AD-A075 501 OHIO STATE UNIV RESEARCH FOUNDATION COLUMBUS F/G 20/4
INVESTIGATION OF THE BOUNDARY LAYER BEHAVIOR ON TURBINE AIRFOIL--ETC(U)
AUG 79 L S HAN, W R COX, A CHAIT F33615-75-C-2052
UNCLASSIFIED OSURF-760256/784174 AFAPL-TR-79-2011 NL

1 OF 3
ADA 075501

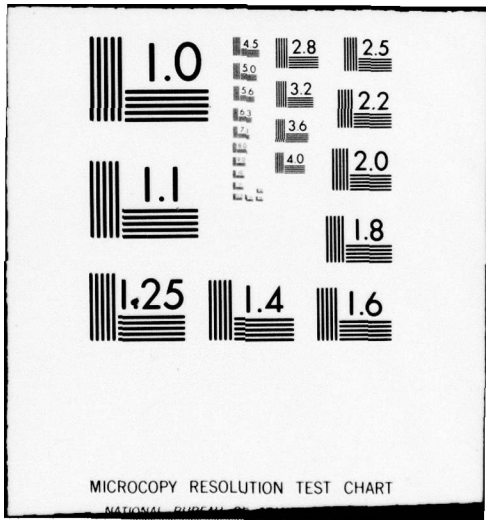
1.0
1.1
1.25
1.4
1.6
1.8
2.0
2.2
2.5
2.8
3.2
3.6
4.0
4.5
5.0
5.6
6.3
7.1
8.0
9.0
MICROCOPY RESOLUTION TEST CHART

AFAPL-TR-79-2011

LEVEL II

AD A075501

INVESTIGATION OF THE BOUNDARY LAYER BEHAVIOR ON TURBINE AIRFOILS

LIT S. HAN
WESLEY R. COX
ARNON CHAIT

THE OHIO STATE UNIVERSITY RESEARCH FOUNDATION
1314 KINNEAR ROAD
COLUMBUS, OHIO 43212

AUGUST 1979

DDC FILE COPY

TECHNICAL REPORT AFAPL-TR-79-2011
Final Report June 1975 – December 1978

Approved for public release; distribution unlimited.

AIR FORCE AERO PROPULSION LABORATORY
AIR FORCE WRIGHT AERONAUTICAL LABORATORIES
AIR FORCE SYSTEMS COMMAND
WRIGHT-PATTERSON AIR FORCE BASE, OHIO 45433

NOTICE

When Government drawings, specifications, or other data are used for any purpose other than in connection with a definitely related Government procurement operation, the United States Government thereby incurs no responsibility nor any obligation whatsoever; and the fact that the government may have formulated, furnished, or in any way supplied the said drawings, specifications, or other data, is not to be regarded by implication or otherwise as in any manner licensing the holder or any other person or corporation, or conveying any rights or permission to manufacture, use, or sell any patented invention that may in any way be related thereto.

This report has been reviewed by the Information Office (OI) and is releasable to the National Technical Information Service (NTIS). At NTIS, it will be available to the general public, including foreign nations.

This technical report has been reviewed and is approved for publication.

KERVYN D. MACH
Project Engineer

JOSEPH C. HURST, Major, USAF
Chief, Components Branch

FOR THE COMMANDER

ERNEST C. SIMPSON
Director, Turbine Engine Division

If your address has changed, if you wish to be removed from our mailing list, or if the addressee is no longer employed by your organization please notify AFAPL/TBC, W-PAFB, OH 45433 to help us maintain a current mailing list.

Copies of this report should not be returned unless return is required by security considerations, contractual obligations, or notice on a specific document.

AIR FORCE/56780/18 September 1979 — 50

(9) Final rept. 16 Jun 75 - 15 Dec 78

UNCLASSIFIED

SECURITY CLASSIFICATION OF THIS PAGE (When Data Entered)

(19) REPORT DOCUMENTATION PAGE

READ INSTRUCTIONS BEFORE COMPLETING FORM

1. REPORT NUMBER (18) AFAPL-TR-79-2011	2. GOVT ACCESSION NO. / 3. RECIPIENT'S CATALOG NUMBER
4. TITLE (and Subtitle) (6) INVESTIGATION OF THE BOUNDARY LAYER BEHAVIOR ON TURBINE AIRFOILS.	5. TYPE OF REPORT & PERIOD COVERED Technical 6/16/75 - 12/15/78
	6. PERFORMING ORG. REPORT NUMBER (14) OSURF-760256/784174
7. AUTHOR(s) (10) Lit S. Han, Wesley R. Cox and Arnon Chait	8. CONTRACT OR GRANT NUMBER(s) (15) F33615-75-C-2052
9. PERFORMING ORGANIZATION NAME AND ADDRESS The Ohio State University Research Foundation 1314 Kinnear Road Columbus, Ohio 43212	10. PROGRAM ELEMENT, PROJECT, TASK AREA & WORK UNIT NUMBERS (16) 3066-06-14 (17) 06
11. CONTROLLING OFFICE NAME AND ADDRESS AFAPL/TBC Wright Patterson AFB OH 45433	12. REPORT DATE (11) August 1979
	13. NUMBER OF PAGES (12) 274
14. MONITORING AGENCY NAME & ADDRESS (if different from Controlling Office)	15. SECURITY CLASS. (of this report) UNCLASSIFIED
	15a. DECLASSIFICATION/DOWNGRADING SCHEDULE

16. DISTRIBUTION STATEMENT (of this Report)

Approved for public release; distribution unlimited.

17. DISTRIBUTION STATEMENT (of the abstract entered in Block 20, if different from Report)

18. SUPPLEMENTARY NOTES

19. KEY WORDS (Continue on reverse side if necessary and identify by block number)

turbine airfoil, turbine cascade, pressure side, Goertler waves. Goertler vortices, traveling waves, surface roughness, Karman vortices, concave side, boundary-layer transition

20. ABSTRACT (Continue on reverse side if necessary and identify by block number)

Smoke flow visualization, hot-wire anemometer, and pressure distribution studies were conducted to determine some of the wake and pressure surface boundary layer transition region characteristics along an enlarged two-dimensional turbine airfoil model in cascade. Smooth surface as well as rough surface airfoils were used in the study, which utilized a continuous, subsonic, specially built wind-tunnel. The flow provided a range of blade chord Reynolds numbers from 7.9E + 5 to 1.5E + 6 at turbulence levels of 0.6 to 0.8%. A pressure surface transition region was found to exist from

DD FORM 1 JAN 73 1473

UNCLASSIFIED

SECURITY CLASSIFICATION OF THIS PAGE (When Data Entered)

267 360

JOB

Block 20 (cont.)

about S/C = 0.43 to the trailing edge for the smooth surface airfoil, and up to S/C = 0.1 for a rough surface airfoil. The transition region for a smooth surface was initiated through the formation of Goertler vortices which were found to break down through the action of traveling Tollmien-Schlichting waves. Other phenomena observed include various trailing edge vortex formations which may be linked to the intermittency of the boundary layer near the trailing edge, and a low frequency traveling wave formed in conjunction with the appearance of traveling waves. An empirical relationship was developed for the traveling wave frequency. Comparison was made with stability theory and empirical methods of predicting transition. Linear stability theory was found to predict the Goertler wavelength, but not that of the traveling waves. For various rough surfaces, transition was initiated both at lower inlet velocities and upper chord locations than was initiated for the smooth surface. A completely turbulent boundary layer was observed at various combinations of flow velocities, chord locations, and roughness sizes.

TABLE OF CONTENTS

TABLE OF CONTENTS (cont'd)

TABLE OF CONTENTS (cont'd)

LIST OF ILLUSTRATIONS

LIST OF ILLUSTRATIONS (cont'd)

LIST OF ILLUSTRATIONS (cont'd)

LIST OF ILLUSTRATIONS (cont'd)

LIST OF ILLUSTRATIONS (cont'd)

LIST OF TABLES

LIST OF TABLES (cont'd)

LIST OF SYMBOLS

Symbol	Definition
Roman	
a	Spacing of vortices in wake vortex street (Fig. D.2)
a_1	Spacing of adjacent vortices in wake vortex street (Fig. D.2)
a_w	Disturbance wave speed (λf)
c	Contraction ratio (upstream area/downstream area)
C	Chord length
c_p	Specific heat at constant pressure of the fluid
d	Diameter
f	Frequency
g_o	Gravitational constant
h	Spacing between rows in wake vortex street (Fig. D.2)
H	Shape factor (δ_1/δ_2)
H	Distance between parallel wind tunnel walls
M	Mach number
M_1	Hot-wire anemometer noise signal
M_2	Signal from hot-wire anemometer at operating temperature (turbulence signal)
M_3	Hot-wire anemometer square wave signal
p	Static pressure
P_o	Stagnation, or total, pressure

Symbol	Definition
q^2	Turbulence intensity $(\overline{u'^2} + \overline{v'^2} + \overline{w'^2})$
R	Blade curvature (negative for convex)
Re	Reynolds number
Re_c	Reynolds number based on chord length $(\frac{\rho UC}{\mu})$
Re_x	Reynolds number based on x-dimension $(\frac{U_\infty x}{\nu})$
$Re_{\Delta x}$	Reynolds number based on change in x-dimension across transition region $(\frac{U_\infty \Delta x}{\nu})$
Re/l	Unit Reynolds number (U_∞/ν)
Re_δ	Reynolds number based on boundary layer thickness $(\frac{U_\infty \delta}{\nu})$
Re_{δ_1}	Reynolds number based on displacement thickness $(\frac{U_\infty \delta_1}{\nu})$
Re_{δ_2}	Reynolds number based on momentum thickness $(\frac{U_\infty \delta_2}{\nu})$
s	Surface distance measured from stagnation point of airfoil
S	Strouhal number (fd/U_∞)
t	Time
Tu	Free-stream turbulence level (u'/U_∞)
u	Velocity component parallel to surface (x-direction)
U	Local free-stream velocity
U_e	Local boundary layer edge velocity
U_{inlet}	Average velocity at test section inlet
U_∞	Free-stream velocity
(u'/U_∞)	Free-stream turbulence level
$\frac{\sqrt{\overline{u'^2}}}{U_\infty}$	Free-stream turbulence level (RMS value)
v	Velocity component normal to surface (y-direction)

Symbol	Definition
w	Velocity component parallel to surface (z-direction)
x	Coordinate parallel to solid surface (normal to axis of curvature for two-dimensional model)
X	Distance between center of circular cylinder (Fig. 3.14) and airfoil stagnation point as measured in free-stream flow direction
y	Coordinate normal to solid surface
Y	Displacement of circular cylinder relative to downstream airfoil stagnation point
z	Coordinate parallel to solid surface, but normal to x-axis
Greek	
α	Wave number ($2\pi/\lambda$)
β	Amplification factor exponent
β	Disturbance frequency
δ	Boundary layer thickness
δ_1	Boundary layer displacement thickness $\left[\int_{y=0}^{\infty} \left(1 - \frac{u}{U_\infty} \right) dy \right]$
δ_2	Boundary layer momentum thickness $\left[\int_{y=0}^{\infty} \frac{u}{U_\infty} \left(1 - \frac{u}{U_\infty} \right) dy \right]$
λ	Wavelength
λ_δ	Pohlhausen parameter based on boundary layer thickness $\left(\frac{\delta^2}{\nu} \frac{dU}{dx} \right)$
λ_{δ_1}	Pohlhausen parameter based on displacement thickness $\left(\frac{\delta_1^2}{\nu} \frac{dU_\infty}{dx} \right)$
λ_{δ_2}	Pohlhausen parameter based on momentum thickness $\left(- \frac{\delta_2^2}{\nu} \frac{dU_\infty}{dx} \right)$
λ_G	Görtler vortex wavelength
λ_{TS}	Tollmien-Schlichting wavelength

Symbol	Definition
μ	Fluid viscosity
ν	Kinematic viscosity of fluid (μ/ρ)
ρ	Fluid density
Subscripts	
cr	Critical, or value at the critical point
e	Edge of boundary layer or wake
G	Denotes characteristics related to Görtler vortices
tr	Value of the parameter at transition
TS	Denotes characteristics related to Tollmien-Schlichting waves
w	Evaluated at the solid surface
∞	Free-stream value
Superscripts	
'	Fluctuation or time varying quantity
—	Mean value or average quantity

SECTION I

INTRODUCTION

Boundary layer flow and upstream wake effects have long been recognized as important to the performance of turbine airfoils. Airfoil boundary layer behavior influences properties such as heat transfer rates, lift and drag coefficients, and even the wake shape and dimensions. Upstream wakes often play a role in determining blade structural stresses by influencing flow-induced vibration and flutter.[1,2] When a principal frequency of the upstream wake (most probably the wake crossing frequency) is close to a blade natural frequency, resonance can be expected to lead to premature fatigue failure of the blade. With the current emphasis on longer operating periods between scheduled maintenance, on increased engine life, and on more efficient performance, consideration of upstream wake effects on the airfoil boundary layer may yield design improvements not previously considered.

Generally, the demand for increased gas turbine efficiency has forced designers to seek methods of using higher inlet gas temperatures. As emphasized by Ludwig,[3] an increase in turbine inlet temperature of 100°F can result in a power increase of 10% combined with a cycle efficiency increase between 1-1/2 and 4-1/2%. Unfortunately, turbine blade temperatures and stresses place severe limitations on the allowable inlet temperature. Gas turbine designers have generally relied upon exotic materials such as cobalt- and nickel-based alloys to permit local blade temperatures as high as 1900°F.[4] However, the ability of such materials to withstand the combination of high stresses and high temperatures found in gas turbines is rapidly being exceeded.

Much research is being directed toward the development of efficient cooling methods. Convection, film, and impingement cooling methods have been shown to be effective and may permit inlet temperatures of at least 2500°F. Transpiration cooling designs which use less cooling fluid and permit higher inlet gas temperatures are currently being studied. Because each of these methods requires the extraction of cooling air from the compressor, the possible increase in efficiency realized by a higher inlet temperature is greatly lessened through the decrease in mass of the working fluid. For this reason, blade cooling systems must be optimized to achieve higher engine efficiencies.

Design of efficient blade cooling systems requires considerable knowledge of boundary layer behavior around the surface of the airfoil.

The surface temperature distribution is directly influenced by local convective heat transfer coefficients which are strongly influenced by boundary layer flow. The importance of boundary layer behavior is readily understood when one considers that the heat transfer coefficient in the laminar boundary layer is as little as one third of the coefficient for turbulent boundary layer flow. Because most turbine airfoil boundary layers are initially laminar and become turbulent somewhere along the surface, the transition region location, extent, and properties also become important. Many designers have assumed that the pressure surface boundary layer becomes turbulent almost immediately after the airfoil stagnation point. However, Cumsty[5] has recently found a transition region extending from 50 to 95% chord along the surface of a two-dimensional turbine airfoil model in a stationary cascade operated at a blade chord Reynolds number of about 2×10^5. In addition, Walker and Markland[6,7] were able to successfully predict suction surface heat transfer, but had little success for cascade pressure surfaces, leading them to conclude that much of the pressure surface boundary layer must be "intermittently turbulent." Brown and Martin[8] also concluded that available prediction techniques failed to describe the boundary layer flow and heat transfer characteristics along the pressure surface of a turbine airfoil, especially for favorable pressure gradients. The former assumption would thus give the maximum cooling that might be needed for the pressure surface, but knowledge of the actual transition region location and extent could permit a reduction in coolant needed for laminar or transitional regions of the boundary layer.

The location of the transition region can be influenced by various factors, many of which are listed below.[9,10]

1) Pressure gradient
2) Free-stream turbulence level
3) Unit Reynolds number
4) Shock wave/boundary layer interaction
5) Mach number
6) Surface roughness
7) Surface curvature
8) Temperature gradients
9) Suction or blowing
10) Passing wakes or unsteady flow
11) Wind tunnel dimensions
12) Surface vibrations
13) Acoustical phenomena

These factors are not linear in their application, and data obtained for individual effects does not necessarily indicate the trends that might be expected when the factors are combined. For instance, surface roughness normally too fine to influence transition region location can suddenly become important and cause early transition if the boundary layer should be greatly thinned by a combination of favorable pressure gradient, convex curvature, and surface cooling, each of which by

itself would normally delay the start of transition.[9] This large number of influencing factors also complicates the comparison of data from different test facilities because each installation has a unique combination of characteristics that may influence boundary layer development.

In order to determine the effects of an upstream wake on boundary layer transition, the characteristics of the wake itself must first be established. As is the case for boundary layer studies, theoretical and experimental wake studies have generally been based on simple geometries such as flat plates or circular cylinders placed at various incidence angles with respect to the flow. Other studies have involved flow past individual airfoils or two-dimensional airfoil cascades. The flow around an actual turbine airfoil is highly three-dimensional and difficult to analyze either theoretically or experimentally. However, some recent studies have been made of the flow behind turbomachinery cascades.[11,12,13,14]

The study of wake effects on a downstream cascade of airfoils has been approached theoretically and experimentally by only a few investigators. Because of the complexity of the flow, theoretical analysis for wake effects on downstream boundary layer development is often heavily simplified and limited in scope. The upstream wakes are often modeled using experimental data from individual airfoils or other surfaces and by assuming that the cascade wake is simply a summation of individual airfoil wakes, a direct violation of continuity. In addition, the close spacing of the cascades in turbomachinery can permit the velocity profiles of the downstream cascade to influence the upstream cascade's wake profile in the subsonic flow.[15] Experimental study of wake effects is, fortunately, less difficult but also yields a less general result. A number of boundary layer studies have included examination of the effects of acoustic or wake phenomena on the transition region, often utilizing circular cylinders for wake production. One such study was made by Kiock[16] who used an oscillating grid of circular cylinders upstream of a turbine airfoil cascade. Through these experiments, considerable upstream wake influence has been shown on the suction surface boundary layer transition region.

The current study has been directed toward experimentally defining pressure surface boundary layer transition region and wake characteristics of an enlarged two-dimensional turbine airfoil cascade. A literature survey has been made to determine the most probable effects of upstream wakes on the transition region. The pressure surface was chosen for study because transition along this surface has been ignored in most turbine airfoil calculations. Also, no significant study has been made of upstream wake effects on the pressure surface boundary layer. The cascade facility constructed for this study was designed to accommodate circular cylinders to create upstream wakes. It is hoped that such a study would be accomplished, since some of the work has already been done during the current research project.

SECTION II

THEORETICAL AND EXPERIMENTAL BACKGROUND

2.1 GENERAL DESCRIPTION OF BOUNDARY LAYER TRANSITION AND STABILITY THEORY

Despite considerable theoretical and experimental efforts during the more than 70 years since Prandtl[17] first described the boundary layer concept in 1904, the mechanism of boundary layer transition is still not fully understood. Experimental efforts have succeeded in finding many characteristics of the transitioning boundary layer, but have failed to show the actual mechanism leading to transition. Likewise, stability theory has done much to show how a laminar boundary layer can become unstable and the trends to be expected under the influence of different effects; but the theory has not yet shown what takes place between the point of neutral stability (critical point) and the onset of transition. Schlichting[18] suggests that more work resembling that of Stuart[19] needs to be attempted using nonlinear stability theory to solve the problem. Kistler,[20] on the other hand, suggests that the Navier-Stokes equations commonly used for stability theory calculations may fail to completely represent physical conditions in the boundary layer, and proposes the use of molecular theory instead. Kistler further states that, in severe velocity gradients, air can act as a non-Newtonian fluid causing many of the usual boundary layer assumptions to become invalid. Whatever the case, complete theoretical representation of the transitioning boundary layer is not currently available although many properties are already known.

When the laminar boundary layer is first developing, all disturbances, regardless of frequency, are damped. After the laminar boundary layer has developed sufficiently, a point of neutral stability is reached. At this point, disturbances of certain critical frequencies are neither damped nor amplified. The Reynolds number at which this condition occurs is called the critical Reynolds number and may be predicted by linear stability theory. Past the point of neutral stability, some disturbances are amplified to form either standing streamwise (Taylor-Görtler) vortices, or traveling spanwise (Tollmien-Schlichting) waves which continue to be amplified. After sufficient amplification, these waves interact with the mean flow causing large nonlinearities. At some point, turbulent spots (first noted by Emmons[21]) separate from the waves and grow in size until they merge to form a completely turbulent boundary layer.

By using kerosene vapor, Brown,[22 23] Knapp,[24] and Knapp and Roache[25] were able to observe boundary layer transition (Tollmien-Schlichting) on an ogive-nosed circular cylinder (Fig. 1). As opposed to some previous thoughts that transition was a relatively continuous process varying only in spatial position, the boundary layer transition was found, through the use of high-speed motion picture photography, to occur as a sequence of events followed by a period of time during which the boundary layer was essentially laminar except beyond the maximum transition region limit where the boundary layer was turbulent at all times. The transition process first consisted of Tollmien-Schlichting waves (in this case, forming rings around the cylinder) which were amplified until three-dimensional deformations occurred to form vortex trusses. These trusses then broke down, accompanied by a tearing off of turbulent spots just prior to the development of fully turbulent boundary layer flow. The turbulent spots tearing away from the vortex trusses bear a resemblance to the growth of turbulent spots described by Emmons,[21] Mitchner,[26] and Schubauer and Klebanoff.[27] In fact, McCormick[28] showed excellent correlation between Emmons'[21] spot theory and the data of Knapp.[24] After this vortex breakdown, the boundary layer transition region became essentially laminar and the whole process started again, although it might be initiated at a slightly different spatial location. This cycle was found to occur at approximately one-fifth the disturbance wave frequency and was felt to relate to the intermittent characteristics of transition observed by other authors (Refs. 21, 29, 30, 31). Brown[22] offered the explanation that a favorable pressure gradient resulting from the development of turbulent flow might be responsible for the observed laminar periods.

The introduction of sound having a frequency about the same as the disturbance wave frequency (about 0.8 to 1.2 times the natural frequency[32]) was found to decrease or eliminate the laminar period, making the process relatively continual, and to fix the initial appearance of the Tollmien-Schlichting waves spatially. Sound of frequency close to the frequency of occurrence of the laminar periods was found to cause the laminar periods to occur more regularly at the acoustic frequency and to become more pronounced. When the boundary layer was subjected to cross flows of sufficient intensity, Brown[32] found spot or transient transition resembling that of Emmons[21] to be very noticeable with very little of the organized motion just described.

Smoke flow visualization experiments by Bergh and Berg[33] along the surface of a symmetrical airfoil also showed traveling waves of an almost constant frequency, amplifying until turbulent patches appeared to tear away from the waves. Neither the intermittent laminar period, if present, nor details of the three-dimensional deformation could have been observed. however, because the camera axis paralleled the blade span and stroboscopic techniques were used, showing only periodic phenomena as discussed by Brown.[22] The use of sound to disturb the boundary layer showed that a small frequency range near the Tollmien-Schlichting wave frequency could amplify the waves slightly and alter

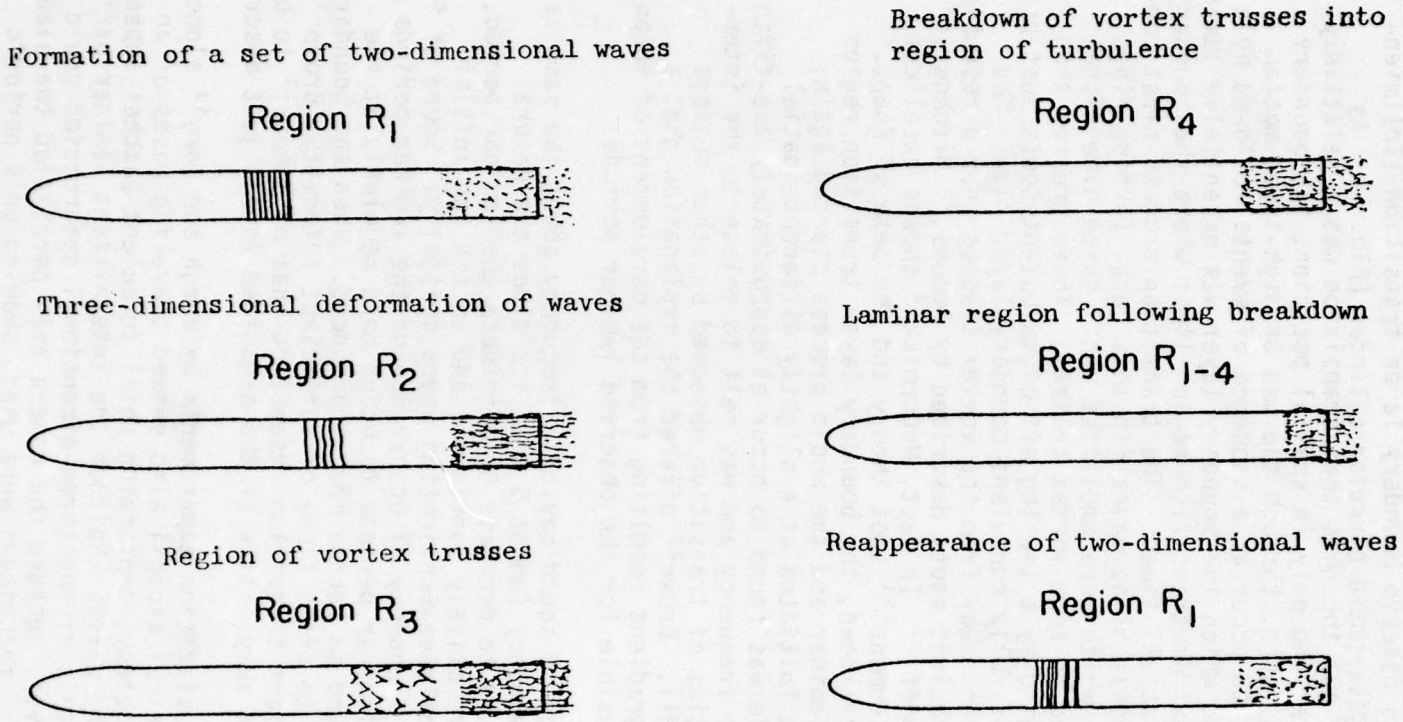

Figure 1. Temporal Development of Boundary Layer Transition

their frequency to conform to the source. Sound at frequencies greatly different from the natural wave frequency again yielded almost negligible effect on the boundary layer development.

Based on the experimental results of Schubauer and Klebanoff,[27] Lin and Benney[34] developed a nonlinear theory which showed the likelihood of streamwise vortices (axes aligned with the flow direction) forming as the Tollmien-Schlichting waves are amplified. This theory was further developed by Nelson and Craik[35] and by Antar and Collins.[36] These vortices were found to be strongest when the streamlines created by the Tollmien-Schlichting waves were convex,[34] possibly explaining the deformation described by Knapp and Roache[24,25] as region R_2 in Fig. 1.

The phenomenon discussed thus far is termed "natural transition" and is the basis for most stability theory analyses. In practice, natural transition can be expected to occur at small disturbance levels (low free-stream turbulence level) on smooth surfaces in the absence of a strong adverse pressure gradient. However, Bennett[37] observed natural transition of the Tollmien-Schlichting type at free-stream turbulence levels (u'/U_∞) as high as 0.42%. In the presence of large free-stream velocity fluctuations or a large adverse pressure gradient, it is often assumed that the mean flow pressure fluctuations cause severe deformations in the velocity profile leading to separation of the laminar boundary layer, and development of a turbulent boundary layer once the flow reattaches to the surface. The form of instability to be expected in any given situation depends on the geometry of the surface and the nature of the surrounding flow. For most cases of low free-stream turbulence level and favorable or mildly adverse pressure gradients, Tollmien-Schlichting instability becomes dominant at low degrees of concavity. In cases of high free-stream turbulence level and severe adverse pressure gradients, laminar separation can be expected to precede boundary layer transition.

In most cases, stability theory is based on the Navier-Stokes equations, the continuity equation, and sometimes the energy equation. The velocity components are comprised of a mean velocity component and a fluctuating component (assumed small). The velocity, written as the sum of these two components, is then substituted into the equations and terms are eliminated through order of magnitude analysis. Physical considerations are used to further eliminate terms and to supply boundary conditions for solution of the equations. Reduction of the equations in this manner generally yields the well-known Orr-Sommerfeld equation.[17] Elimination of viscous terms results in the frictionless stability equation that yields a point of inflection in the velocity profile as the condition for boundary layer instability to occur. Often, a two-dimensional disturbance has been assumed and has been shown by Squire[38] to be the dominant disturbance for two-dimensional incompressible flow. However, Dunn and Lin[39] showed that in compressible flow, the three-dimensional disturbances could, under certain conditions, be more critical than the two-dimensional.

Generally, reduction of the stability equations yields a linear or nearly linear equation that can be solved by numerical analysis. However, transition tends to be a highly nonlinear phenomenon and linear theory cannot be expected to predict what happens beyond the point of neutral stability. Also, stability theory is based on the concept of infinitesimal disturbances and is unable to predict the effect of free-stream turbulence in real situations. For these reasons, some efforts have been directed toward the development of nonlinear theory which, if successful, may help to describe boundary layer development beyond the critical point.[19,40]

2.1.1 Effect of Free-Stream Disturbances

The importance of free-stream disturbances was first discovered when it was found that identical spheres placed in different test facilities at the same Reynolds number gave greatly different values for the drag coefficient. Since that time, the development of instrumentation such as the hot-wire anemometer and frequency analysis equipment has greatly simplified the problems of determining the free-stream turbulence level, its spectrum, and its effect on transition. Free-stream disturbances are often categorized as free-stream turbulence, acoustic phenomena (discrete frequencies), and unsteady flow. In addition, surface vibration may have a similar effect on the transition region. In a gas turbine all of these may have a significant effect on the boundary layer flow.

Generally, the effect of increased free-stream turbulence intensity is to decrease the transition Reynolds number (cause early transition). However, stability theory has shown that the boundary layer is more sensitive to disturbances at certain frequencies than it is to others. Therefore, information about the magnitude of the free-stream turbulence level must be supplemented by knowledge of the frequency spectrum. This was confirmed by the experiments of Spangler and Wells[41,42] who studied flat plate transition in a zero pressure gradient while paying particular attention to the frequency spectrum of the disturbances. By varying the frequency spectrum of the disturbance it was found that the transition Reynolds number varied in much the same way stability theory would predict for the critical Reynolds number. The boundary layer was found to be sensitive to the intensity of disturbances at certain frequencies while it was very much insensitive to others. It was found that, for these sensitive frequencies, the location of transition could be controlled by varying the intensity of the disturbance. Only a slight change in the fundamental disturbance frequency was needed to reduce greatly the sensitivity of the boundary layer. Through careful control of the free-stream turbulence level and spectrum, a flat plate transition Reynolds number of 4.9×10^6 was achieved for free-stream turbulence levels below 0.1%. Similar results were found by Collins and Zelenevitz[43] and Brown and Goddard[44] who found that acoustic phenomena at certain frequencies not only could control the transition region location, but also could cause

reattachment of a separated laminar boundary layer, sometimes leading to "bubble transition."

Heckl and Jackson[45] studied the effects of distributed surface vibration on the boundary layer flow. It was suggested that the wave speed ($a_w = \lambda f$) of the disturbance rather than the disturbance frequency determines the effect on boundary layer transition. The boundary layer was found to be most sensitive to a wave speed such that $a_w = 0.35U_\infty$. This was considered true whether the disturbance was surface vibration or acoustic phenomena. Reshotko,[46] however, suggests using the dimensionless parameter $\beta\nu/U_\infty^2$ where β is a characteristic frequency of the disturbance spectrum. As a result of a 50,000 ft change in altitude (standard atmosphere) this number changes by one order of magnitude. Reshotko thus suggested that the change in this parameter with pressure can also account for the unit Reynolds number effects observed in various test facilities.

Theoretical studies of the interaction between free-stream disturbances and the laminar boundary layer were made by Criminale[47] and by Wazzan, Li, and Taghavi.[48] Wazzan, Li, and Taghavi found that free-stream vorticity could strongly affect the transition Reynolds number, especially when calculations were based on amplification factors such as used by Smith.[49] Criminale[47] developed a theory to estimate the effects of discrete sources of turbulence at specified locations in the free-stream on boundary layer stability. Free-stream pressure fluctuations were felt to be more critical than vorticity. The eigenvalue solutions of linear stability theory based on infinitesimal disturbances were found to become fully valid only when the disturbance was assumed very far from the surface relative to the boundary layer thickness.[47]

Unsteady flow measurements were made by Satyanarayana[50] for the wakes and boundary layers of an isolated symmetric airfoil and a cascade of the same airfoils. The flow was made unsteady by deformation of the tunnel walls as sinusoidal traveling waves. The boundary layer along the isolated airfoil was found to change cyclically from laminar to turbulent and back to laminar along each surface. For the cascade (stagger angle = 45°), however, the boundary layers along the lower surfaces (geometrically corresponding to turbine cascade suction surfaces) of the cascade were fully turbulent while the upper surface boundary layers were found to fluctuate in the same way as the isolated airfoil. Time-mean velocity profiles were also shown to be greatly different from the unsteady wake profiles. Like other complex flow situations, the theory for unsteady flow is difficult and much is left to be accomplished toward full solution of practical cases. Yalamanchili and Erickson[51] have presented a numerical solution technique as well as a review of the limited literature in this field.

2.1.2 Pressure Gradient Effects

Besides the free-stream turbulence level, the effects of imposed pressure gradients upon boundary layer transition cannot be ignored for

airfoil boundary layer calculations. In a favorable pressure gradient, the start of transition is delayed and the length of the transition region is increased. A mild positive pressure gradient produces an inflection point in the velocity profile and, thus, leads to early transition and a shortened transition region. Large adverse (positive) pressure gradients lead to laminar separation with possible reattachment and early transition. Large favorable (negative) pressure gradients can completely stabilize the boundary layer to two-dimensional disturbances and even cause an existing turbulent boundary layer to revert to laminar flow.[52,53] For mild pressure gradients, transition is similar to that observed for zero pressure gradients, although the location may be different.

The effects of pressure gradients have been studied theoretically and experimentally. The pressure gradient is generally nondimensionalized by the Polhausen parameter [$\lambda_\delta = (\delta^2/\nu)\left(\frac{dU_\infty}{dx}\right) = -\left(\frac{\delta^2}{\rho\nu U_\infty}\right)\left(\frac{dp}{dx}\right)$ or $\lambda_{\delta_2} = -\frac{\delta_2^2}{\nu}\frac{dU_\infty}{dx}$]. Tani[54] suggests that the critical Reynolds number based on displacement thickness ($U_\infty\delta_1/\nu$) is roughly proportional to $e^{0.6\lambda\delta}$ for $-3 < \lambda < 3$ based on flat plate studies (for a flat plate in zero pressure gradient $(U_\infty\delta_1/\nu)_{crit} \sim 420$).[17] The beginning of the transition region, however, does not vary quite as rapidly. The transition Reynolds number ($U_\infty\delta_1/\nu$) was found to vary as $e^{0.08\lambda_\delta}$ for the same range.

2.2 PREDICTION OF TOLLMIEN-SCHLICHTING TRANSITION REGION LOCATION

2.2.1 Empirical Equations

As already discussed, linearized stability theory is capable of predicting only the point of neutral stability. As the initial disturbances are amplified, interactions with the free-stream flow create highly nonlinear conditions which make theoretical prediction of transition very difficult. A number of methods for predicting transition region location have been developed, however, generally based on a combination of theory and experimental evidence.

Among the simpler prediction methods available are those involving empirical equations based on experimental data. One such equation, developed by Van Driest and Blumer,[55] is based on the data of Dryden,[56] Schubauer and Skramstad,[55] and Hall and Hislop[57] for flat plate boundary layer transition in a zero pressure gradient. The resulting equation is given as follows:

$$1690/Re_x^{\frac{1}{2}} = 1 + 19.6\, Re_x^{\frac{1}{2}}(u'/U_\infty)^2 \qquad (1)$$

where Re_x is the Reynolds number based on the distance from the leading edge and (u'/U_∞) is the free-stream turbulence level. The form

of the equation is derived from the Taylor[58] assumption that transition in the presence of free-stream pressure disturbances takes place following distortion (and separation) of the laminar boundary layer and that the vorticity Reynolds number $[(y^2/\nu)(du/dy)]_{max}$ is a suitable index for determining when transition has occurred. The number 1690 in the equation represents the vorticity Reynolds number at transition. As a result of the higher transition Reynolds number obtained at low free-stream turbulence levels, Wells[41] rewrote Eq. (1) using slightly different constants:

$$2220/(Re_x)^{\frac{1}{2}} = 1 + 38.2\ (Re_x)^{\frac{1}{2}}(u'/U_\infty)^2 \qquad (2)$$

To consider the effects of pressure gradient, Van Driest and Blumer[55] used the Polhausen fourth-degree velocity profile along with the same assumptions used for Eq. (1) to develop the following equation:

$$9860/Re_\delta = 1 - 0.0485\ \bar{\lambda}_\delta + 3.36\ Re_\delta\ (u'/U_\infty)^2 \qquad (3)$$

where Re_δ is the transition Reynolds number and λ_δ is the Polhausen pressure parameter, both based on boundary layer thickness. Van Driest and Blumer recalculated the equation for the Falkner-Skan velocity profile[59] and found reasonable agreement between the two solutions.

Hall and Gibbings[60] compared a number of boundary layer transition equations and techniques with available experimental data dealing with the effects of free-stream turbulence level and pressure gradients. For turbulence levels greater than 3%, Hall and Gibbings found that Eqs. (1 through 3) did not accurately reflect existing experimental data. Equation (3) was also found inaccurate for favorable pressure gradients such as might be expected along the pressure surface of a turbine airfoil. In addition to examining prediction techniques proposed by others, Hall and Gibbings also developed a prediction method of their own involving the use of empirical equations. By plotting all available experimental data on a semi-logarithmic scale, Hall and Gibbings obtained the following empirical equation for predicting the start of a transition region with a zero pressure gradient:

$$\log_e\,(Re_{\delta_2} - 190) = -103\ (u'/U_\infty) + 6.88 \qquad (4)$$

An equation for the end of the transition region was developed by assuming the turbulent boundary layer started at zero thickness at the start of the transition region and grew according to the one-seventh power law, a method originally suggested by Dhawan and Narasimha.[61] The following equation is the result of such an assumption:

$$Re_{\delta_2 end} = 0.036 \left(Re_{x_{tr}} \right)^{0.8} \quad (5)$$

By assuming that the end of the transition region followed the same asymptotic behavior at high turbulence levels as the start, the following equation was obtained by Hall and Gibbings[60]:

$$\log_e \left(Re_{\delta_2 end} - 320 \right) = - 44.75 \left(u'/U_\infty \right) + 7.70 \quad (6)$$

An interesting result of the curve is that the minimum value for fully turbulent flow is $Re_{\delta_2} = 320$, the same value as was proposed previously by Preston.[62]

In order to consider the effects of pressure gradients on the transition region, two separate techniques were proposed by Hall and Gibbings depending on whether the gradient was positive or negative. For $\lambda_{\delta_2} < 0$, curves of constant Re_{δ_1} were drawn by using Eq. (4) a boundary condition at $\lambda_{\delta_2} = 0$. For $\lambda_{\delta_2} > 0$, the curves were drawn parallel to the Pretsch[63] stability curve, again being fit by Eq. (4) at $\lambda_{\delta_2} = 0$. Because the curves were chosen to fit the data, rather close agreement was found. However, no evidence was provided that the technique would still be successful if the free-stream turbulence level were increased in a nonzero pressure gradient. In fact, Dunham[64] stated that recent work shows the empirical curves based on Eq. (4) give too low a value for $Re_{x_{tr}}$ for $(u'/U_\infty) > 3$. Also, the curve does nothing to further understanding of the mechanism of transition. Nevertheless, it can be useful for estimating the extent of the transition region.

Dunham[64] developed the following equation for calculation of natural transition when the cross-sectional area normal to the flow is varying (as in a turbine blade cascade):

$$Re_{\delta_2} = \left[0.27 + 0.73 \exp \left(-0.8 \, \overline{Tu} \right) \right] \left[550 + 680 \left(1 + \overline{Tu} + 21 \lambda_{\delta_2} \right)^{-1} \right] \quad (7)$$

such that $-21\lambda_{\delta_2} - \overline{Tu} > 0.75$. The equation is based on the work of Batchelor[65] and makes use of a mean value for turbulence level $\left[\overline{Tu} = 1/2(Tu_\infty + Tu) \right]$, where Tu_∞ is the upstream turbulence level (u'/U_∞) and Tu is the turbulence level at the station being considered as given by

$$\frac{Tu}{Tu_\infty} = \sqrt{\frac{1}{2c}\left(1 + \frac{F}{c^3}\right)} \tag{8}$$

where c is the area ratio of the upstream position to the local position (c > 1 indicating a contraction), and F is given by one of the following relations:

$$F = \frac{\tan^{-1}\sqrt{c^{-3} - 1}}{\sqrt{c^{-3} - 1}} \quad \text{, when } c < 1$$

or (9)

$$F = \frac{\log_e\left[c^{1.5}\left(1 + \sqrt{1 - c^{-3}}\right)\right]}{\sqrt{1 - c^{-3}}} \quad \text{, when } c > 1$$

Dunham suggested that transition would never occur for most practical cases if $-21\lambda_{\delta_2} - \overline{Tu}$ were greater than 0.75. Dunham also suggested a technique for predicting transition in an adverse pressure gradient following a laminar separation bubble rather than amplified Tollmien-Schlichting waves. This technique is discussed in Refs. 9 and 64. The criterion for separation was given as the point where $\lambda_{\delta_2} = +0.09$.

2.2.2 Spatial Amplification Factors

In order to permit the estimation of transition region location through the use of stability theory, rather than purely empirical methods, Jaffe, Okamura, and Smith[49] suggested the use of spatial amplification factors as an indicator of transition. As with most other stability theory analyses, the techniques developed by Smith and his coworkers are based on the Orr-Sommerfeld equation. However, unlike much stability theory that assumes temporal growth of the disturbance, spatial growth is assumed. The linear amplification factor presumably represents a ratio between the disturbance amplitude at transition and the amplitude at the critical point. However, as discussed by Stuart,[19] interactions between the growing disturbance and the free-stream, as well as three dimensional deformations of the disturbance wave, limit the growth to much less than represented by the spatial amplification factor calculated at transition.

A justification for using spatial amplification factors was provided by Liepmann[66] who suggested that transition would occur whenever the Reynolds stress reaches the magnitude of the laminar shear stress. As opposed to empirical equations, the use of amplification factors

permits the estimation of transition region location for varying curvature, pressure gradient, and other factors that can be calculated by stability theory without need to obtain considerable experimental data to extend the range. Hall and Gibbings[60] found that the use of spatial amplification factors gives relatively accurate results in favorable pressure gradients, but not in adverse pressure gradients. This, however, would indicate possible use in turbine airfoil boundary layer calculations where favorable pressure gradients are generally encountered along most of the airfoil surface.

As already mentioned, the amplification factor calculations of Smith were based on the Orr-Sommerfeld equation given as follows[18,49]:

$$(U-c)(\phi'' - \alpha^2\phi) - U''\phi = -\frac{i}{\alpha Re_\delta}(\phi'''' - 2\alpha^2\phi'' + \alpha^4\phi) \qquad (10)$$

where the primed quantities represent derivatives with respect to y/δ, α is a complex number of which the imaginary part is the disturbance amplification rate and the real part is the wave number, $U = u/U_\infty$, and c is a complex number where the real part represents the phase speed. A two-dimensional spatial disturbance resembling Tollmien-Schlichting waves was assumed. The calculation is initiated outside the boundary layer and proceeds to the surface using a finite difference approximation. By iteration, a disturbance wavelength is selected such that the amplification factor becomes a maximum at the surface location being considered. When transition is found to occur, the wavelength exhibiting the highest amplification number at that point is assumed to represent the disturbance causing the transition.

By calculation of the amplification factors for a large variety of Tollmien-Schlichting data along flat plates and bodies of revolution, Smith found a range of $e^{6.8}$ to $e^{12.1}$ for the spatial amplification factor. The average was found to be about e^{10}, comparing favorably to values of e^9 previously found by Smith and Gamberoni[67] and e^7 or e^8 by Van Ingen.[68] Because the stability theory on which the Orr-Sommerfeld equation and subsequent amplification factor calculations were based assumes zero free-stream turbulence, the data selected for comparison generally represented low free-stream turbulence levels. It can be expected, however, that an increase in free-stream turbulence would result in a decreased calculated value for the spatial amplification factor at transition. In fact, the previously mentioned Liepmann criteria (Reynolds stress (τ_T) having the same order of magnitude as the laminar shear stress (τ_L) yields transition)[66] tend to confirm this expectation when presented in the following form:

$$[(\tau_T)\,\max/\tau_L] = (1/c_{f1})[Kb\,(u'/U_\infty)^2 a^2(x)]\max \qquad (11)$$

where b = v'/u' (the ratio of y fluctuation velocity component to x

velocity fluctuation component), c_{f1} is the laminar skin friction coefficient, and $K = u'v'/uv$ (the correlation coefficient). Both the free-stream turbulence level (u'/U_∞) and the spatial amplification factor ($a(x)$) can thus be expected, by the Liepmann criteria, to play an important role in determining transition location. Increased free-stream turbulence would require a decrease in amplification factor if a fixed shear stress ratio were assumed to indicate transition.

2.2.3 Turbulence Models

In order to theoretically consider the effects of free-stream turbulence on transition, McDonald and Fish[69] used a turbulence model and finite difference techniques to estimate the transition region location and extent. Turbulence models are widely used for calculating turbulent boundary layers, and a number of models are reviewed in a report by Burggraf.[70] Typically these models fall into three categories; i.e., (1) those which define eddy viscosity by an explicit relationship of local flow properties, (2) those which use an auxiliary differential equation to define the transport of turbulence kinetic energy together with explicit relations for other turbulence properties, and (3) those in which the turbulence properties are defined by a system of differential equations.[70]

McDonald and Fish chose to develop a system of the third type by defining the stagnation temperature $\overline{T}_o$, total apparent stress τ, and total effective heat flux Q in the following manner:

$$\overline{T}_o = \overline{T} + \overline{u}^2/2c_p$$

$$\overline{\tau} = \overline{\mu}\,\partial\overline{u}/\partial y - \overline{\rho}\,\overline{u'v'}$$

and (12)

$$Q = \overline{k}\,\partial\overline{T}/\partial y - \overline{\rho}\,c_p\,\overline{v'T'}$$

A turbulence kinetic energy equation was derived by writing the velocities as sums of mean and fluctuating components and inserting the resulting expressions in place of velocity terms in the Navier-Stokes equations. The i-th equation of motion was then multiplied by the i-th velocity component expression, and the resulting equations were summed. The resulting equation was then reduced by various approximations, yielding the following form:

$$\frac{\partial}{\partial x}\left(\frac{1}{2}\,\bar{\rho}\bar{u}\overline{q^2}\right)+\frac{\partial}{\partial y}\left(\frac{1}{2}\,\bar{\rho}\bar{v}\overline{q^2}\right)=-\,\bar{\rho}\overline{u'v'}\,\frac{\partial\bar{u}}{\partial y}-\frac{\partial}{\partial y}\left(\overline{p'v'}+\frac{1}{2}\,\bar{\rho}\overline{q^2v'}+\frac{1}{2}\,\overline{\rho' q^2 v'}\right)$$

$$-\,\bar{\rho}\varepsilon-\bar{\rho}\left(\overline{u'^2}-\overline{v'^2}\right)\frac{\partial\bar{u}}{\partial x}+\bar{\nu}\,\frac{\partial^2}{\partial y^2}\left(\overline{q^2}/2+\overline{v'^2}\right) \qquad (13)$$

where $\overline{q^2}$ (the turbulence intensity) $= \overline{u'^2} + \overline{v'^2} + \overline{w'^2}$ and ε represents the sum of the turbulent dissipation terms. The resulting equation was then integrated with respect to y, and structural scales a_n and L, together with a mixing length ℓ, were applied where

$$a_1 = \frac{-\overline{u'v'}}{\bar{q}^2} \quad ; \quad a_2 = \frac{\overline{u'^2}}{\bar{q}^2} \quad ; \quad a_3 = \frac{\overline{v'^2}}{\bar{q}^2} \qquad (14)$$

$$L = \frac{\left(-\overline{u'v'}\right)^{3/2}}{\varepsilon} \quad ; \quad \ell = \frac{\left(-\overline{u'v'}\right)^{1/2}}{\partial\bar{u}/\partial y}$$

Through a computer solution of the resulting equations, the start and length of the transition region were predicted. The effects of free-stream turbulence, pressure gradient, surface roughness, and heat transfer can all be handled by the technique. Velocity profiles, skin friction coefficients, and heat transfer were predicted for flat plates as well as for turbine airfoils with a relatively high degree of success.

2.3 STUDIES OF GOERTLER VORTEX FORMATION

Along the pressure surface of a turbine airfoil, the boundary-layer transition region is likely to be characterized by Görtler vortices which undergo deformations to develop into fully turbulent flow. These vortices can best be described as contrarotating vortices having axes parallel to the principal flow direction (see Fig. 2). Görtler vortices are most likely to occur along concave surfaces such that $\delta_2/R > 0.0005$ (where δ_2 is the boundary layer momentum thickness and R is the radius of curvature) before Tollmien-Schlichting waves would be expected to form. In addition, it is also possible for the Görtler instability to occur wherever the streamlines become concave in the direction of flow (such as flow near a stagnation region[17]) or when the forces are analogous to the centrifugal forces acting on the flow along a concave surface (such as ionized flow over a charged plate[71]). As a result, it is conceivable that turbine airfoil pressure surface transition could be initiated by Görtler instability near the stagnation point as well as along the concave region of the airfoil surface.

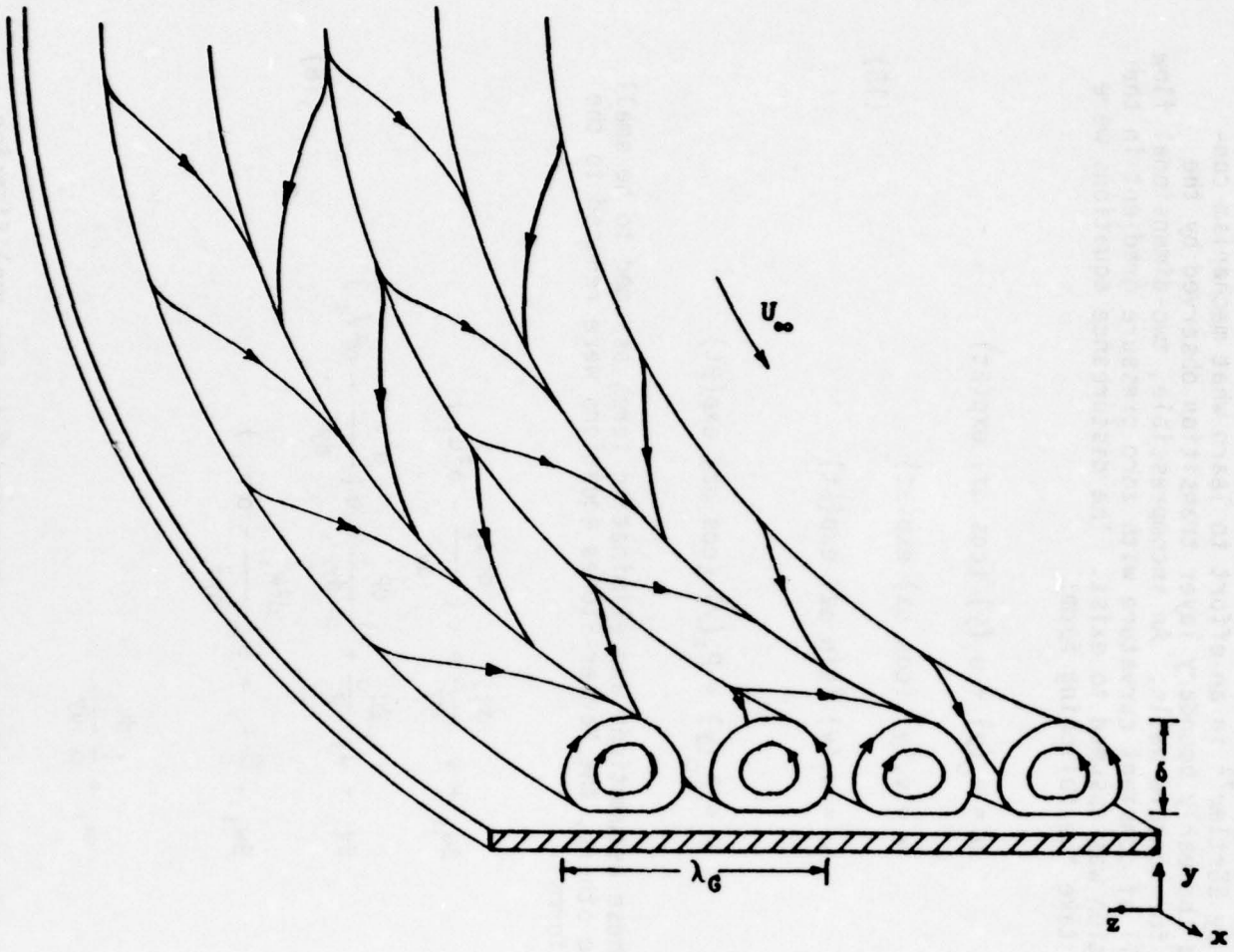

Figure 2. Gortler Vortices in Flow Over Concave Surface

2.3.1 Early Theoretical and Experimental Discoveries

The mathematical concept of contrarotating streamwise vortices leading to boundary layer transition along a concave surface was first postulated by Görtler[72] in an effort to learn what mechanism contributed to the early boundary layer transition observed by the Clausers[73] for concave walls. An incompressible, two-dimensional flow along a wall of constant curvature with zero pressure gradient in the flow direction was assumed to exist. The disturbance equations were assumed to take the following form:

$$\begin{aligned} u &= u_o(y) + u_1(y)\ (\cos \alpha z)\ \exp(\beta t) \\ v &= v_1(y)\ (\cos \alpha z)\ \exp(\beta t) \\ w &= w_1(y)\ (\sin \alpha z)\ \exp(\beta t) \end{aligned} \tag{15}$$

and

$$P = P_o(y) + P_1(y)\ (\cos \alpha z)\ \exp(\beta t)$$

By using these assumptions and eliminating terms assumed to be small relative to others, the Navier-Stokes equations were reduced to the following forms:

$$\begin{aligned} \beta u_1 + v_1 \frac{du_o}{dy} &= \nu \left(\frac{d^2 u_1}{dy^2} - \alpha^2 u_1 \right) \\ \beta v_1 + u_1 \frac{2u_o}{R} + \frac{1}{\rho} \frac{dP_1}{dy} &= \nu \left(\frac{d^2 v_1}{dy^2} - \alpha^2 v_1 \right) \\ \beta w_1 - \frac{\alpha}{\rho} P_1 &= \nu \left(\frac{d^2 w_1}{dy^2} - \alpha^2 w_1 \right) \end{aligned} \tag{16}$$

and

$$w_1 = \frac{1}{\alpha} \frac{dv_1}{dy}$$

where α is the disturbance wave number and β is the amplification factor exponent coefficient. Using the above equations and an assumed Blasius profile, boundary layer flow along a concave surface was found to become unstable much earlier than it would for Tollmien-Schlichting waves previously found for flat plate flow. However, as shown by Hämmerlin,[74] Smith,[75] and Aihara,[40] additional terms such as the mean

velocity component normal to the wall must be retained to gain reliable information about the critical point and other features of the disturbance.

Görtler also recommended the nondimensional parameter $(U_\infty \delta_2/\nu)(\delta_2/R)^{1/2}$, based on momentum thickness, as being significant for determining the transition region location, because its value was relatively constant regardless of assumed velocity profile. As discussed by Aihara,[40] this parameter represents the multiple average of two ratios, the dissipation of kinetic energy to the production of kinetic energy and the dissipation of vorticity energy to the production of vorticity energy. Görtler found a lower limit of 0.58 for instability to occur, and comparison with the Clausers'[73] data gave Görtler parameter values of 8.6 and 10.6 for full transition.

The first real confirmation of the Görtler theory was provided through the experimental studies of Liepmann.[66,76] For mildly convex curvature ($|\delta_2/R| \leq 0.001$) transition was found to occur at about the same Reynolds number as for a flat plate, the Blausius velocity profile was found to be valid, and free-stream turbulence and pressure gradients were found to affect transition in the same manner as for flat plate transition. For concave curvature, however, Liepmann found results greatly different from flat plate behavior, but in agreement with the Görtler theory. The Blasius profile was again found to be reasonably valid for the range of effective radius of curvature studied ($|\delta_2/R| \leq 0.001$). It was also shown that the effect of pressure gradient on transition for concave surfaces is either zero or very small and could probably be ignored for many practical cases. For effective curvatures less than $\delta_2/R = 0.00005$, it was found that the Tollmien-Schlichting instability was the principal cause of transition. For $\delta_2/R > 0.0005$, Görtler instability was found to be the principal cause of transition. For values of δ_2/R between 0.00005 and 0.0005, a continuous change was seen to take place from transition caused by Görtler vortices to transition caused by Tollmien-Schlichting waves. The Görtler parameter was found not to be constant, but to vary with δ_2/R and with the free-stream turbulence level. The Görtler parameter was found to have a value of 9.0 for $R/\delta_2 \approx 4 \times 10^3$ and a free-stream turbulence level of 0.06%, and a value of 7.3 for $R/\delta_2 \approx 10^4$ at the same turbulence level. The value of 9.0 changed to 6.0 for a turbulence level of 0.3%.

2.3.2 Spatial Amplification Factors VS the Gortler Parameter

Because of the simplifications involved in the Görtler analysis, Smith[75] developed a means of solving the equations by approximate methods. One of these involved numerical solution by a digital computer, requiring considerable computer time when Smith made his analysis. The method seems to show promise in predicting actual transition as well as in finding the point of instability. It makes use of spatial amplification factors as already described for Tollmien-Schlichting transition prediction. The coordinate system used by Smith

was based on an x-axis along the surface which was not necessarily of constant curvature. The y-axis was selected to be always normal to the surface with singularities (intersections of surface normals) occurring well outside the boundary layer (assuming a radius of curvature much larger than the boundary layer thickness, a valid assumption for most turbomachine applications). The z-axis paralleled the axis of local curvature. The assumed disturbance was of the following form:

$$\begin{aligned} u(x,y) &= u_o(x,y) + u_1(y) \cos \alpha z \exp(\int \beta(x)dx) \\ v(x,y) &= v_o(x,y) + v_1(y) \cos \alpha z \exp(\int \beta(x)dx) \\ w(x,y) &= \quad 0 \quad + w_1(y) \sin \alpha z \exp(\int \beta(x)dx) \end{aligned} \tag{17}$$

and

$$p(x,y) = p_o(x,y) + p_1(y) \cos \alpha z \exp(\int \beta(x)dx)$$

In contrast with the Görtler analysis, it is to be noted that the variation of radius and pressure gradient has been taken into consideration by allowing both the mean properties and the amplification factor to change as functions of x. Also, the mean velocity in the y-direction is no longer zero but may have a value to allow for suction or blowing. The factors $\partial u_o/\partial x$, $\partial v_o/\partial x$, $\partial k/\partial x$ (where $k = 1/R$), $\partial \beta/\partial x$, and $\partial P_o/\partial x$ were found to be insignificant in comparison with other terms in the equations of motion as were assumed in the Görtler analysis. The equations of motion were then nondimensionalized and several terms were dropped based on order of magnitude assumptions and a study of the range of values the nondimensional parameters could be expected to take in actual flow situations. For $\beta = 0$ (neutral stability), and beyond the boundary layer, the equations reduced to the following pair containing only constant coefficients:

$$\frac{d^2u}{d\eta^2} - (Re_\delta V + K)\frac{du}{d\eta} - \left(A^2 - Re_\delta \frac{dV}{d\eta}\right)u - \left(Re_\delta \frac{dU}{d\eta} - KRe_\delta U\right)v = 0$$

and

$$2KRe_\delta Uu + \frac{1}{A^2}\frac{d^4v}{d\eta^4} - \left(\frac{ReV}{A^2} + \frac{2K}{A^2}\right)\frac{d^3v}{d\eta^3} - \left(\frac{Re_\delta}{A^2}\frac{dV}{d\eta} + 2 - \frac{KRe_\delta V}{A^2}\right)\frac{d^2v}{d\eta^2}$$

$$+ \left[ReV + K\left(\frac{Re_\delta}{A^2}\frac{dV}{d\eta} + 2\right)\right]\frac{dv}{d\eta} + \left(Re_\delta \frac{dV}{d\eta} + A^2\right)v = 0$$

where (18)

$$Re_\delta = \frac{U_o \delta}{\nu} \quad , \quad U = \frac{u_o}{U_o} \quad , \quad V = \frac{v_o}{U_o} \quad , \quad w_o = 0$$

$$u = \frac{u_1}{U_o} \quad , \quad v = \frac{v_1}{U_o}$$

$$A = \alpha\delta \quad , \quad \eta = \frac{y}{\delta}$$

$$K = k\delta = \frac{\delta}{R} \quad , \quad \frac{du}{d\eta} = \frac{\delta}{U_o}\frac{du_1}{dy} \quad , \quad \frac{d^2u}{d\eta^2} = \frac{\delta^2}{U_o}\frac{d^2u_1}{dy^2}$$

By specifying K, six solutions are found for u or v. By numerical integration methods, each solution can be extended to $\eta = 0$, giving the boundary layer shape. Similar equations containing additional terms can be used when β does not equal zero and permit determination of K, B, A, or R by numerical methods outlined by Smith, provided the other three constants are known or assumed.

Smith[75] made a comparison with experimental data to see what improvement might be gained over use of the Görtler analysis. The Görtler parameter for the various experimental data spans values from about 2 to 20, which would lead to large errors in predicting transition. It should be noted, however, that, except for two cases on the Griffith airfoil,[76] the range is from 5 to 10, which would be much more acceptable in the prediction of transition. It should also be noted that the greatest discrepancies occur in the presence of boundary layer suction. The amplification factor, $\int\beta(x)dx$, maintained a relatively constant value which was approximately 10. On this basis, Smith recommended the use of the spatial amplification factor instead of the Görtler parameter for predicting transition. As noted previously, $\exp(\int\beta\, dx)$ represents a ratio between the magnitude of the disturbance at the point of neutral stability and the magnitude at the start of the transition region based on linear theory.

Nothing can be learned from Smith's analysis about the actual magnitude of the vortices at transition, although it is quite likely that transition is more a function of the magnitude of the vortices and their frequency spectrum, than it is of amplification factor alone. It is interesting to note that analysis of Tollmien-Schlichting transition based on spatial amplification factors also yields values around 9 or 10 for $\int\beta(x)dx$.[49,67] A nonlinear analysis by Stuart,[19] however, indicates that amplification of the disturbance is actually much less than indicated by the linear amplification factor because of interactions between the free-stream flow and the transitioning boundary layer.

2.3.3 Other Experimental Studies of Gortler Vortices

Tillman[78] experimented with the growth of a boundary layer impulsively started on the inside of a circular cylinder. Small particles were suspended in water to permit flow visualization. Görtler vortices were observed by using high-speed motion picture photography (up to 4000 frames per second). The first appearance of vortices occurred regularly when the Görtler parameter reached a value of about 6.5. However, transition to fully turbulent flow did not occur until values between 9 and 14 were reached. Initially, the vortices appeared as parallel lines, but meandered as full transition was approached. At the highest velocity studied, the transition greatly resembled that of Tollmien-Schlichting waves leading to Emmons' spots along with the Görtler vortices observed in the other tests.

Tani, et al.[54,79,80] experimentally studied transition on a curved plate in a range of curvatures up to $\delta_1/R = 10^{-3}$. By using vibrating ribbons and rows of wings, studies were made of the transition with and without artificially generated disturbances. The pressure gradient was carefully made zero and the plates had constant curvature, with a constant free-stream velocity. Tani concluded that Görtler vortices are not directly responsible for transition on concave surfaces, but instead cause a spanwise variation of boundary layer thickness which leads to a mechanism similar to that observed on flat plates with pre-existing streamwise vortices or spanwise variation in boundary layer thickness. The use of displacement thickness in the Görtler parameter, however, makes comparison of Tani's results much more dependent on the velocity profile than has been the case in other studies. This would make the data difficult to use directly for situations other than uniformly concave surfaces. However, a Blasius profile is probably again a good assumption, and the data could be converted to read in terms of momentum thickness.

By using a water tunnel with tellurium dye streak markers Wortmann[80] succeeded in visualizing the Görtler vortices along a concave surface and in determining the three-dimensional velocity profile within the vortices. In order to induce vortex formation in the desired region, perturbation wings were used. As a result of these techniques, Wortmann was able to distinguish several stages in the deformation of symmetrical Görtler vortices into fully turbulent flow. Initially, the peaks and valleys were observed to move somewhat in the spanwise direction resulting in oblique interfaces between the vortices as opposed to the original interfaces which were normal to the surface. On one side of these oblique interfaces, the boundary layer velocity profile was found to have two reversals. A reduction in the tunnel velocity or in the intensity of the vortices was found to restore the perpendicular interfaces. By using an additional perturbation airfoil outside the boundary layer above the central vortex, observation of further (third order) deformation of the vortices was made possible. In this case the oblique interfaces were still present, but the

vortices were found to meander along the flow direction much as was seen for the Taylor vortices in Tillman's[78] experiments.

Also using a water tunnel, Bippes and Görtler[82] used hydrogen bubbles to visualize the flow for stereo photography. In order to fix the location of vortex formation, heating coils, aligned with the flow were used to initiate a disturbance of known wavelength (determined by the spacing of the units). The vortices produced in this manner were reproduceable and were sufficiently small for comparison with linear theory in the region of weak amplification. Without the heating coils, the vortices varied in their locations along the surface, attributed by the authors to the random disturbances already present in the flow field. Photogrammetric evaluation of the stereo pairs combined with hot-wire anemometer readings yielded considerable information about the breakdown of the vortices into turbulent flow. Observation of the developing vortices and associated velocity profiles yielded results very much similar to those found previously by Wortmann.[81] As the vortices grew in size, they were seen to deform and a meandering motion similar to that observed by Wortmann[81] and by Tillman[78] was observed. (In a hot-wire anemometer study for air flow over a concave surface, however, McCormack, Welker, and Kelleher[83] observed no meandering motion of the vortices.) After the meandering motion, a corkscrew motion developed as a Tollmien-Schlichting instability appeared to be superimposed on the Görtler instability.[82] Hot-wire studies of the flow indicated no Tollmien-Schlichting instability characteristics prior to visual observation of them. A turbulence level of 30% was indicated within the superimposed region.

Despite the detailed data available for transition along uniformly curved surfaces in a zero pressure gradient, experiments describing accurately the mechanism of transition for the environment of a turbine airfoil appear to be needed. Evidence provided by Dunham and Edwards[61] and by Walker and Markland[6,7] shows an extended region along the pressure surface where the heat transfer characteristics lie in between those of purely laminar and of purely turbulent boundary layer flow. In contrast, the transition region along the suction surface is generally well defined and finite. In addition, theoretical predictions of heat transfer along the pressure surface were greatly in error, while suction surface calculations have proved relatively successful.[6,7,61]

Cumsty[5] utilized surface visualization techniques and hot-wire anemometry to explore the transitioning boundary layer along the pressure surface of a turbine airfoil model at chord Reynolds numbers of 2 to 2.5 x 10^5. Several theoretical prediction methods for transition indicated full transition should occur by approximately 65% of full chord (based on Görtler parameter value and on spatial amplification factors). The experimental results, however, showed full transition to turbulence did not occur until after 95% of full chord despite the fact that it was initiated prior to 50% full chord. The reliance upon talcum powder erosion, china clay, and pitot probe

techniques prevented acquisition of data concerning the time history of the transitioning boundary layer. The methods did satisfactorily indicate Görtler vortex formation and gave a measurement of the wavelength (spacing) which was found to have a minimum value about one-third of the maximum across the airfoil. Hot-wire anemometer studies indicated similarities to Tollmien-Schlichting transition prior to 95% full chord.

2.3.4 Other Theoretical Studies

Despite the extensive experimental data now available for transition along concave surfaces, much of the available data (as well as theory) is limited to the case of constant curvature with zero pressure gradient in the mean flow direction. This presents a problem when applying the data to varying curvature in a favorable pressure gradient such as occurs in the case of a turbine airfoil. In order to help overcome this limitation, Tobak[84] made a theoretical study of the effects of local curvature on Görtler instability. The analysis closely followed that originally made by Görtler, with changes made primarily for a wall curvature varying as a function of x (distance from the leading edge) instead of constant curvature. The Navier-Stokes equations and equation of continuity were reduced by assuming constant free-stream velocity, boundary layer velocity profile a function only of y for the unperturbed flow, and that the curvature $r_o(x)$ extending for a distance 2a between two flat surfaces, has at most a small variation. Results of the study showed that for small values of a_α, only the net turning angle of the concave surface is significant in determining instability. For $a_\alpha > 1$ (where $\alpha = 2\pi/\lambda_G$), and for $a/\delta_2 > 50$, there is little change in the neutral stability curves calculated by Gortler.

Kobayashi[85] theoretically studied the effect of suction or blowing on the Görtler instability. The study was limited to the case of constant wall curvature, with a radius of curvature much greater than the boundary layer momentum thickness, and a uniform free-stream velocity. The suction distribution was chosen as $v_o = - C(\nu U_\infty/x)^{1/2}/2$ along the surface, based on Schlichting.[17] The disturbance velocity distribution was defined in the same manner as Smith.[75] The results tend to show that suction increases the value of the Görtler parameter for neutral stability while blowing has little effect on the neutral stability curve. Although blowing is not predicted to change the value of the Görtler parameter, the transition region location is changed because of the increased boundary layer thickness. This result may prove to be of great importance in the study of turbine blade transition with transpiration or similar cooling methods.

Aihara[40] utilized nonlinear theory to examine the growth of Görtler vortices beyond the point of neutral stability. The neutral stability curve based on his approximations bore strong resemblance to that of Smith.[75] As a result of the analysis, the originally sinusoidal disturbance patterns were shown to distort as neighboring

vortices interfered with additional growth. In addition, the results show possible analytical prediction of the meandering motion experimentally observed by Tillman,[78] Wortmann,[81] and Bippes and Gortler.[82]

2.4 SURFACE ROUGHNESS EFFECTS ON TRANSITION

The influence of surface roughness on boundary layer transition has long been recognized. The general nature of the surface roughness influence is to induce early transition as compared with a smooth surface. The mechanism by which surface roughness can favor early transition can be explained by stability theory, although a fully unique theoretical description of the process is not yet clear.

The practical importance of this problem is well established, and almost any real-life boundary layer problem will include the influence of surface roughness and therefore, qualitative and quantitative models for various types of surface roughness should be established in order to describe its influence on the particular problem. In the case of a turbine airfoil, the highly complex three-dimensional boundary layer on both sides (pressure and suction) of the airfoil could be influenced very significantly by the presence of surface roughness. Roughness could be caused by a manufacturing process, but mainly by a continuous exposure to the extremely hostile environment created by combustion chamber output gases. The temperatures in the first stage of an advanced modern jet engine can reach about 1371°C (2500°F). A combination of extremely high temperatures and continuous impacts by foreign particles could cause deposits to build up, as well as extensive erosion of the blade surface. The irregularity of a surface created by this process resembles the situation of a three-dimensional distributed irregular roughness.

Bammert and Sandstede[138,139] conducted experiments in order to determine the actual efficiency loss from a gas turbine with blades coated with different grades of sandpaper. They found very significant efficiency losses, up to 14% total efficiency loss with 10^{-2} roughness size divided by chord length. General Electric has learned that turbine blades which had been exposed to a service condition at the sea-level for only fifty hours will show higher blade temperatures as compared with new blades. This phenomenon could be caused by a significant change in the boundary layer structure due to changes in the surface roughness of the partially serviced blade. With greater demand for higher overall engine efficiency, these losses cannot be ignored, and a more complete understanding of the roughness influence in the particular conditions of a turbine airfoil needs to be pursued.

A common explanation of the general influence of roughness elements on the laminar boundary layer is that they impose additional disturbances to those already existing in the boundary layer. Such new disturbances could be more critical than the ones already present, and thus could cause earlier transition because lower amplification rates will be needed to reach transition. If existing disturbances are more critical than the ones generated by roughness elements, it can be

expected that the existing disturbances will cause transition. Smith and Clutter[140] studied the problem of the smallest height of roughness capable of affecting boundary layer transition for various two- and three-dimensional elements and concluded that a two-dimensional roughness element is more conducive to boundary layer transition than a three-dimensional roughness element of similar dimensions because the former introduces larger disturbances. However, they also recognized that since the two-dimensional elements produce two-dimensional disturbances which must evolve into three-dimensional vortices before producing a complete transition, the actual location of transition behind the roughness element might be further away for the two-dimensional element as compared with the three-dimensional one.

Klebanoff and Tidstrom[141] conducted an experimental investigation of the effect of two-dimensional roughness of elements on boundary layer transition. Their measurements were geared toward understanding the mechanism by which a roughness element causes transition and they include detailed measurements of the velocity distribution and disturbances of frequency spectra, intensity, growth, and decay. Their findings are perhaps among the most important ones from the many studies done on the subject, and it is felt that much of the previous work, which will be explained later, reflects only indirectly the mechanism by which roughness induces transition. Klebanoff and Tidstrom concluded that the effect of a two-dimensional roughness element on boundary layer transition can be classified as a stability-governed phenomenon. Their point of view on the influence of roughness elements is that it does not necessarily introduce new disturbances, which add to the existing ones, but that in the region immediately behind the element they destabilize the influence of the flow on the existing disturbances, thus hastening the downstream development of the instability. The phenomenon of transition found right behind the element is not inconsistent with the previous explanation since the destabilization process could be rather short, depending primarily on the nature of the velocity profile found behind the element. The type of the inflectional velocity profile is governed by the size and shape of the element, which are known to have direct effects on its influence on transition. An explanation based on the stability-governed phenomenon is also consistent with the known effects of two-dimensional elements at higher Mach numbers. As mentioned before, their study involved extensive, detailed measurements of disturbance frequencies, intensities and growth and decay rates. The amplification (growth) rates in the recovery zone (the zone immediately behind the element) were found to be much greater than in the corresponding region in the smooth plate where the classical Blasius profiles exist. This important finding shows that the authors' opinion concerning the destabilizing influence of the roughness element is a more correct way of understanding the mechanism by which a roughness element causes transition than to say merely that a roughness element adds additional disturbances to the existing ones.

Most studies on the influence of roughness on transition have been concerned with establishing a criterion for transition caused by the roughness element. The most common criterion is the roughness Reynolds number, which is defined as the velocity at the element peak times the element height divided by the kinematic viscosity at the roughness element. The critical Reynolds number, as quoted by many investigators, covers a very very wide range. This kind of data presentation does not help to clarify the issue since a large number of correlation parameters - such as element height divided by boundary layer thickness (either displacement or momentum thickness), the roughness shape, the Reynolds number based on displacement or momentum thickness as well as other parameters - are used in the data presentation. Without minimizing the importance of such factors, they only reflect indirectly the mechanisms by which roughness affects transition, and, as Klebanoff and Tidstrom noted, it has reached the point of diminishing returns as far as an understanding of the basic mechanism is concerned.

Smith and Clutter's[140] results concerning two- and three-dimensional roughness elements show the following critical Reynolds numbers (i.e., the Reynolds number of a critical roughness which caused a 5% decrease in the natural transition Reynolds number):

Roughness	Range of Critical Roughness Reynolds Number
Spanwise wires	60-260
Row of 1/16" dia discs	100-550
¼" wide strip of sandpaper type	178-330

The values for the roughness Reynolds number needed to move transition to the roughness itself are:

Roughness	Average Roughness Reynolds Number
Spanwise wire	300
Row of 1/16" dia discs	600
¼" wide strip of sandpaper type	400

Smith and Clutter[140] also investigated the effect of Mach number on critical roughness, and found that the mechanism at high Mach numbers is not inconsistent with the low-speed mechanism by which roughness causes transition, i.e., critical roughness is that roughness which first induces local distribances such as local separation and vortices. Tani[54] suggested that a value of 826 for the Reynolds number, based on a flat-plate free-stream velocity, cylindrical wire diameter and free-stream

kinematic viscosity, which causes transition to occur by the wire on a flat plate. Tani also agreed with the common opinion concerning three-dimensional elements which states that the affect of three-dimensional elements is more critical in nature than two-dimensional ones. Klebanoff, Schubauer and Tidstrom[142] found an average value of 577 of the roughness Reynolds number for transition induced by single spheres, with velocity at the top of sphere and sphere diameter used in the definition of the roughness Reynolds number. Doenhoff and Horton[143] determined a value of 600 of the roughness Reynolds number, defined as above, to induce transition in a sandpaper-type of distributed roughness with the maximum probable roughness height used to determine the roughness Reynolds number. Braslow[150] used the square root of the roughness Reynolds number for correlation of various experimental results of three-dimensional elements and shows values consistent with those found by Klebanoff, et al.[142] and Schaubauer, Doenhoff and Horton[143] as well as other investigators. The effect of favorable pressure gradient on the critical value of roughness Reynolds number appears to be insignificant.[145,146,147]

SECTION III

TEST FACILITIES AND INSTRUMENTATION

3.1 WIND TUNNEL

A cascade facility used for previous wake effects studies[15] was modified to accept the larger airfoil models and provide two-dimensional flow as free of vibration and turbulence as reasonably possible for the boundary layer studies. Many of the sections described in the previous report were modified or completely redesigned and built new. This includes the screen section and screens, test section, and transition section, as well as much of the supporting structures.

The wind tunnel used was of open circuit design. The entrance of the tunnel was in the same room as the test section while the motor, fan, and 30-in. diameter exhaust duct were located in an adjoining room (Fig. 3). Return flow was provided by open doors and an exhaust fan opening between the two rooms. The design and selection of the ducts, fan and motor in the equipment room are described completely by Diller.[104] Briefly, power for the wind tunnel was provided by a Model X6938 Sirocco fan driven by a General Electric Model TLC24 15-hp D.C. motor. The motor was in turn powered by a motor-generating unit. The speed could be varied from 0 to 650 rpm (15,400 scfm) by a rheostat mounted near the tunnel working section. The fan was placed downstream from the test section to reduce fan noise in the air stream. Air flow between the test section and the fan was controlled by a 24-in. square plywood duct passing through an opening in the wall between the test area and the equipment room. At the fan inlet, a multi-vaned turning section was used along with a sheet metal transition section to adapt the round fan inlet to the square duct. The fan and motor were mounted on concrete bases secured to the floor, while the ducts were supported on stands made of steel channel.

The remaining wind tunnel sections were located within the same room as the test section and are shown in Figs. 4 and 5. Because the turbine airfoil models turn the flow, the flow direction changes within the test section. For this reason, the entrance section axis was placed at an angle of approximately 72.5° with respect to the horizontal while the test section exit axis was approximately horizontal.

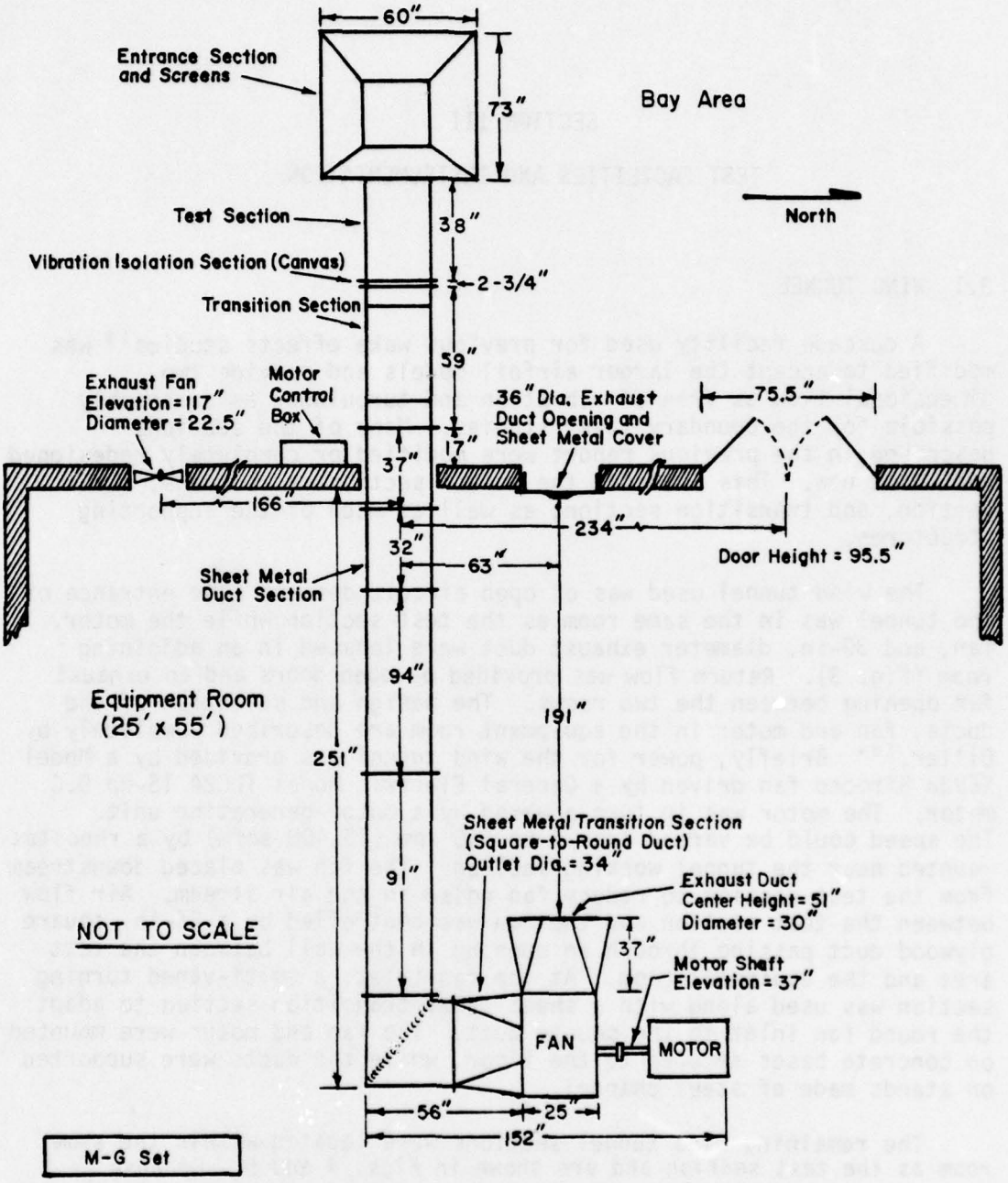

Figure 3. Wind Tunnel Layout (Top View)

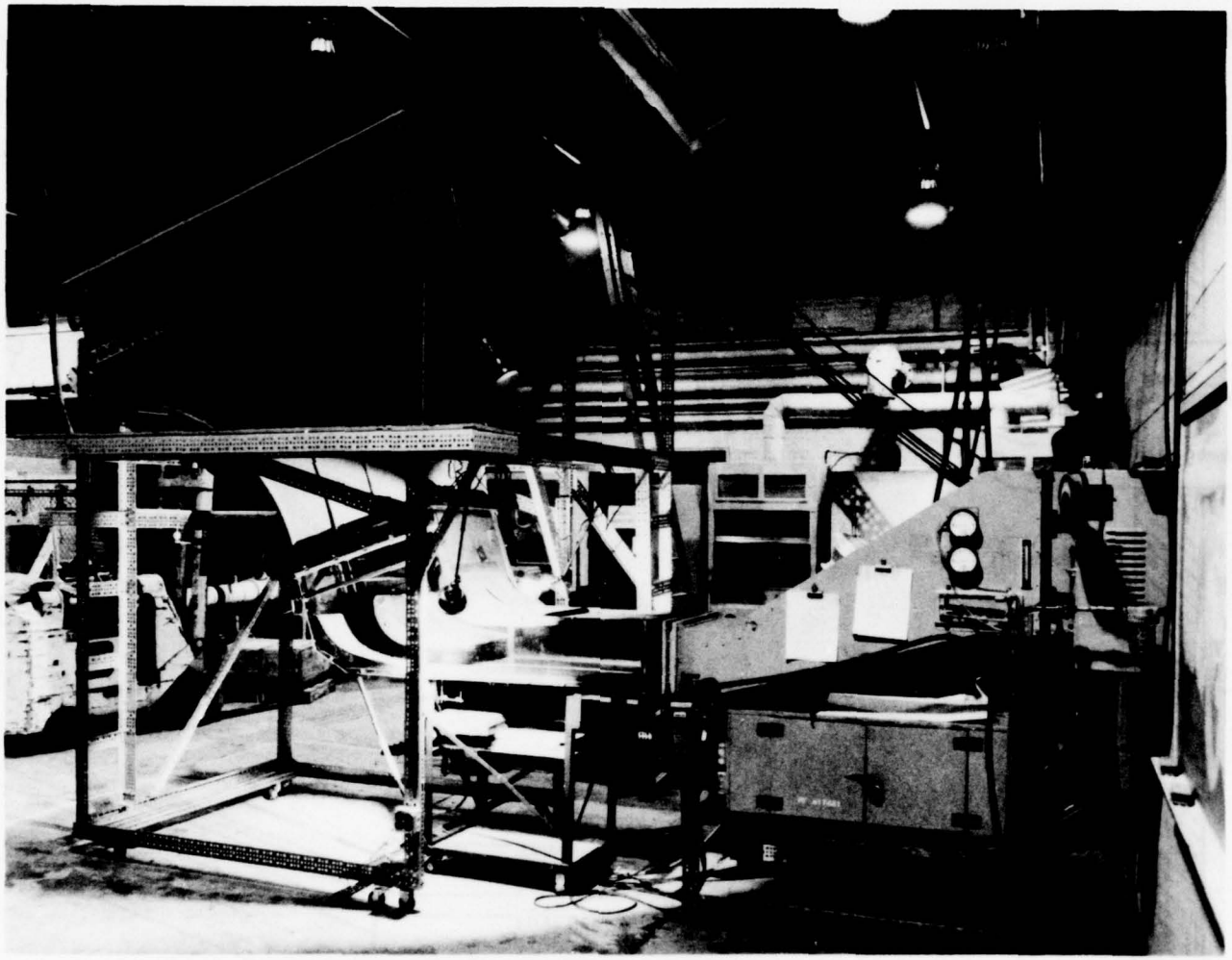

Figure 4 Side View of Wind Tunnel

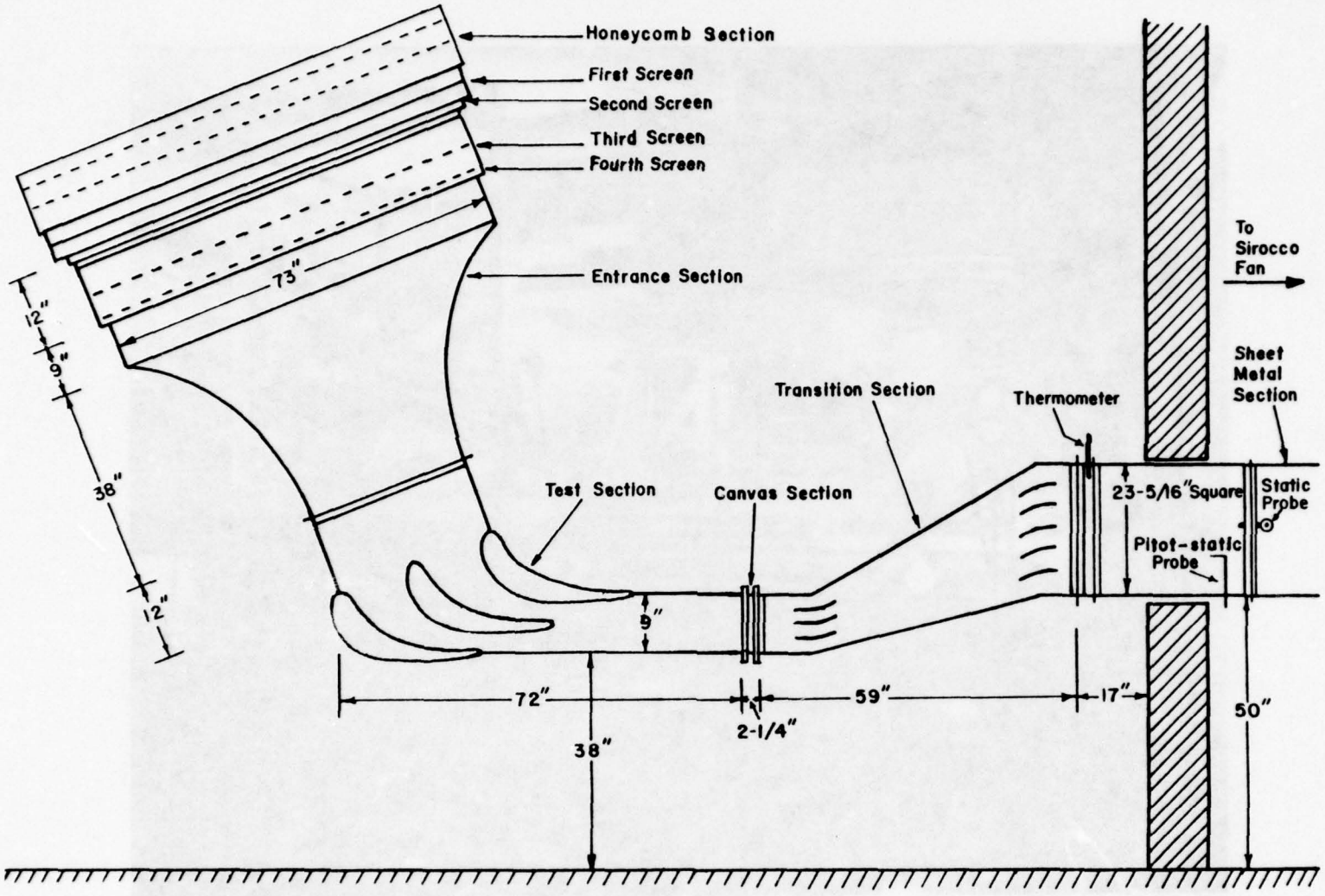

Figure 5. Wind Tunnel Sections and Dimensions

An entrance section and screens were provided for turbulence reduction and to insure flow uniformity. These sections were retained from the previous study and are detailed in Figs. 6 and 7. A screen section (Fig. 6) containing four 60 x 73 in. screens of 24 mesh per inch, 0.0075 in. diameter stainless steel wire cloth was placed at the entrance to the tunnel. These screens were placed so that the downstream screens were approximately 2, 9, and 14 in. from the first screen. A plastic sheet, attached to one end of the screen section, was used to cover the screens between runs so dust would not collect in the test section. A catwalk along all four sides of the supporting structures was used for handling this cover and maintaining the smoke generator and screens.

Following the screens, an entrance section of 20 ga. galvanized sheet metal was used. This section had an elliptical taper from an area of 60 x 73 in. to 24 x 30 in., giving a contraction ratio of 6.08. This ratio yielded a maximum screen Reynolds number, based on wire diameter, of less than 34 for all tunnel operating speeds. As discussed by Dryden and Schubauer,[105] a screen Reynolds number greater than 35 could lead to vortex shedding. The first 9 in. of the entrance section was of constant area to provide a short settling section following the screens. Dimensions of the entrance section are given in Fig. 7.

As can be seen in Fig. 7, the entrance section is formed using a simple elliptical surface, tangent at the exit, but meeting the settling section at an angle. As demonstrated by Morel,[106,107] the optimum profile for such an entrance section would be two curves, tangent at the entrance and exit, and at the match point. For high contraction ratios, irregularities at the low velocity end appear to have little adverse affect on the function of the contraction cone. For small contraction ratios, however, Morel showed that separation at the low velocity end could lead to undesirable flow profiles at the nozzle exit. Because this entrance section had not shown any problems during the previous studies, however, it was retained.

In the previous studies, the pop-riveted seams had been filled with solder, but still contained voids and roughness that could yield undesirable turbulence. For this study, the seams were filled with body epoxy and smoothed to match the adjoining surfaces. Body epoxy was also used to make fillets for the entrance section corners. A flange to mate with the new test section was added and that joint was also smoothed with body epoxy. Unlike the previous studies, the entrance section was coupled directly to the test section. Threaded holes in the entrance section flange accepted bolts inserted through clearance holes in the test section flange.

Preliminary smoke studies made when the other wind tunnel sections were completed showed a need for additional turbulence reduction through the addition of a honeycomb section to the wind tunnel entrance as shown in Fig. 5. The honeycomb (Fig. 8) consisted of

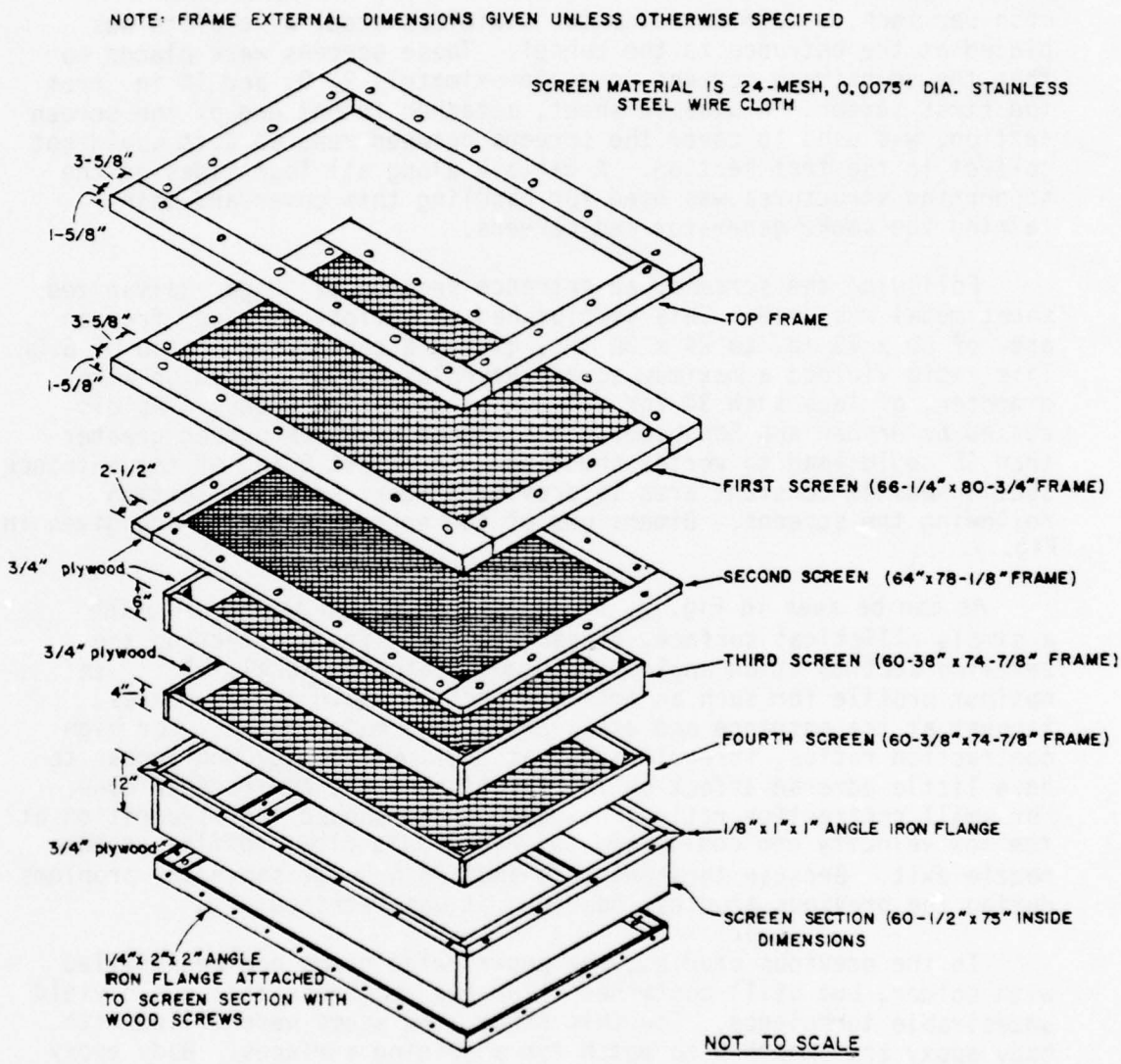

Figure 6. Screen Section and Screens

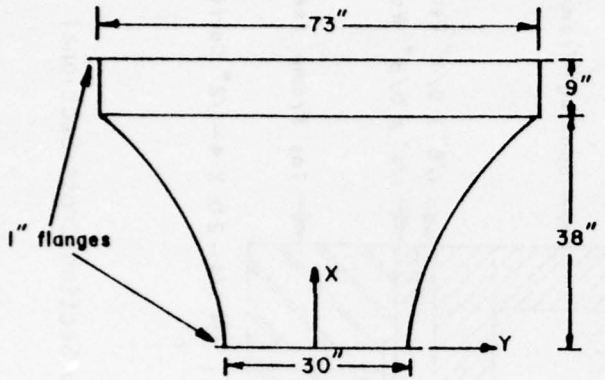

(inches)		
X	Y	Z
0	15	12
3 5/8	15 1/8	12 1/8
7 3/16	15 7/16	12 3/8
10 13/16	16	12 13/16
14 1/2	16 7/8	13 1/2
18 1/4	18	14 3/8
22	19 1/2	15 1/2
25 13/16	21 7/16	16 31/32
30 1/16	24	18 13/16
34 3/4	27 5/8	21 7/16
37 3/16	30 7/16	23 5/16

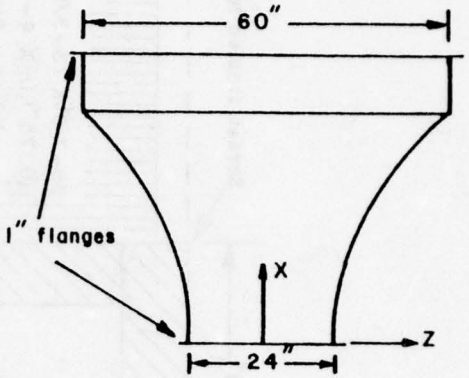

Figure 7. Entrance Section Coordinates

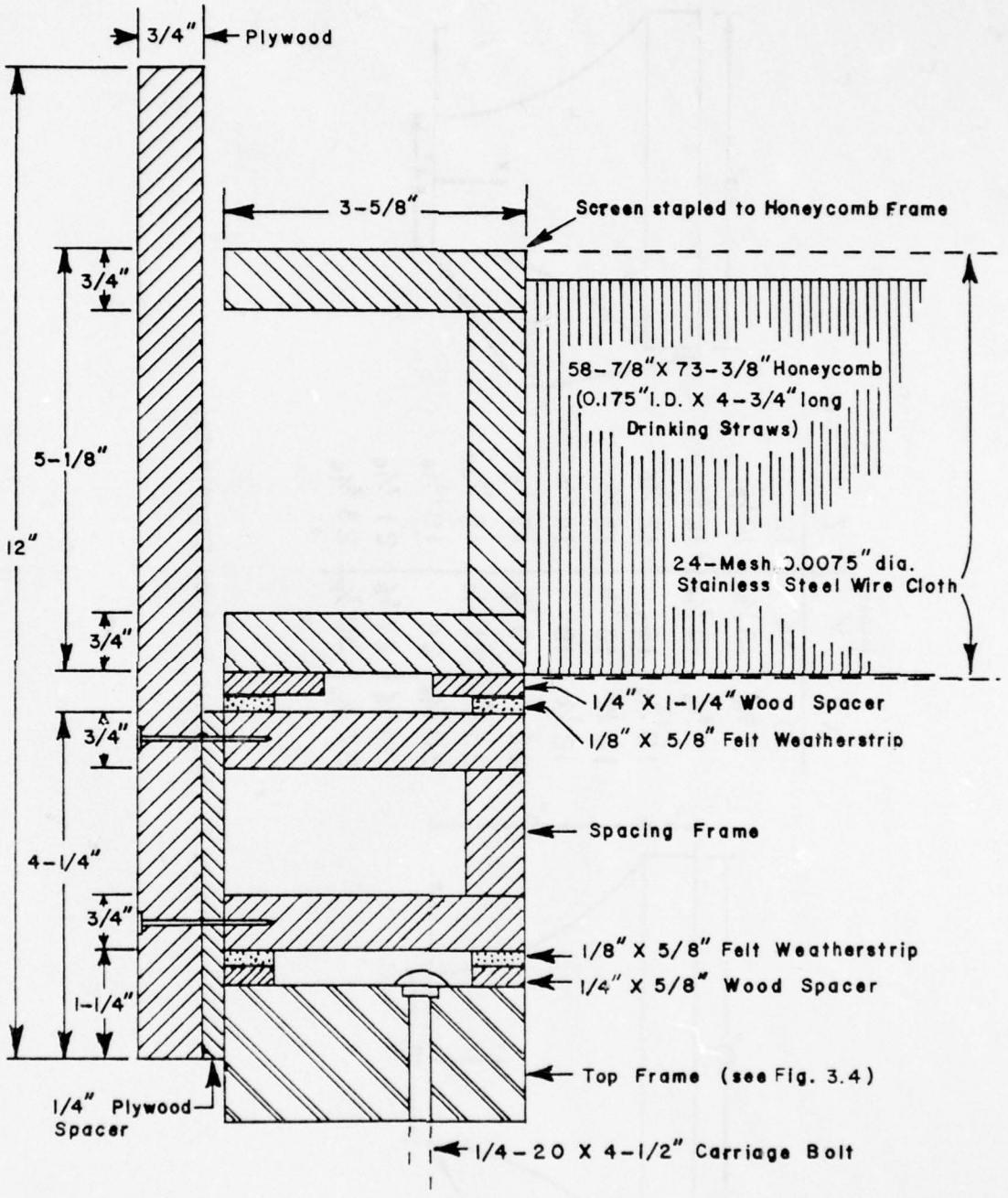

Figure 8. Honeycomb Section Cross-Sectional View

approximately 176,000 milk straws (0.175 in. I.D. x 4-3/4 in. long with 0.007 in. wall thickness) tightly packed into a frame made from 1 in. x 4 in. pine. Screens were stapled to the honeycomb frame before and after the straws, both to hold the straws in place (because of the nearly horizontal placement of the section) and to further reduce the turbulence following the honeycomb. As demonstrated by Loehrke and Nagib,[108] a screen placed at the exit plane of the straws yields optimum performance from the honeycomb section. Loehrke and Nagib also suggested the use of straws having a length-to-diameter ratio of less than 10, but showed significant effects for ratios as large as 45. The straws selected have a ratio of 27. The honeycomb frame slid into place within the honeycomb section, seating on a spacer of felt weatherstrip to seal against leaks around the honeycomb. A spacer frame kept the honeycomb about 5 in. above the first screen section screen. Ths spacing frame seated on the top frame of the screen section (as identified in Figs. 6 and 8).

Initial estimates of flow losses showed that greater losses would occur through the honeycomb section alone than occurred previously in the entire screen section. However, loss calculations for the entire wind tunnel showed that this would result in no more than a 6% reduction in the maximum velocity. Calibration studies made following the installation of the honeycomb showed a change in velocity from 44.8 fps to 42.8 fps for similar fan speeds and atmospheric conditions, a reduction of only 4.5%. At the same time turbulence was reduced from approximately 0.8 to 0.6% and the smoke streams were greatly improved for flow visualization purposes.

The entrance, screen, and honeycomb sections were mounted on a cart made from Interlake 300-12 slotted angle and described in previous reports. For this study, however, the cart was given additional reinforcement and extra castors were added to handle the increased weight of the honeycomb section.

A completely new test section (Fig. 9) was built, eliminating features of the previous test section and having new features required for the boundary layer study. A welded external skeleton of 1/8 x 3/4 x 3/4 in. angle iron was used to support the airfoil models and tunnel wall panels. Unlike the previous test section, where the plywood tunnel wall panels were fastened directly together, this permitted removal of one panel at a time, without destroying the structural integrity of the test section. The provision of spare, interchangeable panels permitted test section modifications to be made with a minimum amount of delay in the testing program. The upper and lower walls of the test section were made of 3/4 in. plywood and were trimmed with a router to the 24-in. width of the section. These were attached to the angle iron frame by wood screws placed through the frame from the outside. The side panels were made from 3/8 in. scratch resistant plexiglass (DuPont Abcite) and 3/4 in. plywood. They were attached to the frame by machine screws placed through clearance holes in the side panels and tapped holes in the frame. Abcite was also used

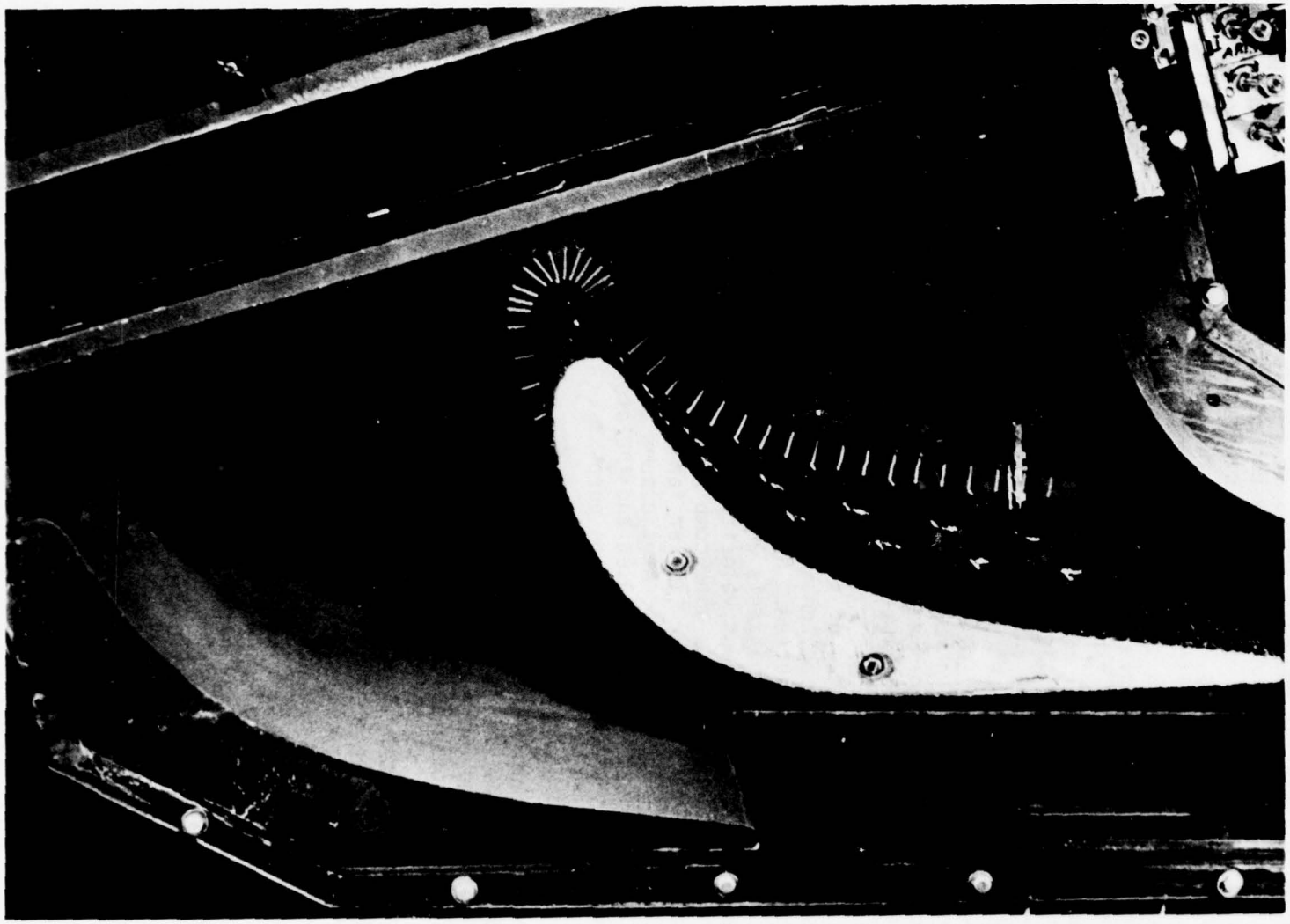

Figure 9 Test Section

to make lighting slits 1-1/2 in. wide in the upper and lower panels of the test section. The outer blades of the cascade served as part of the tunnel wall and were attached directly to the test section frame. The adjoining walls were milled to mate with the blades at the leading and trailing edges. The center blade was supported by bolts through holes in the side panels. Tubing from the instrumented blade extended through a slot in the plywood side panel. A pair of adjustable blade supports was permanently mounted in the floor of the test section. These were used to help support the blade when one of the side panels was removed, but were concealed in the floor when the wind tunnel was in operation. This permitted removal of the side panels for modification or maintenance without need to uncouple any of the tunnel sections. The interior of the test section was sanded smooth and painted flat black to facilitate smoke flow visualization.

Because the ductwork leading to the fan and the test section were of different heights and cross-sectional areas, a transition section was required. Although previous studies[15,109,110] had utilized a similar transition section, redesign was necessary to reduce vibration initiated by flow separation (stall) that had been found to exist at the first bend. With this in mind, the turning angles were decreased by raising the test section until the difference in center height between it and the ductwork was 19 in. The addition of two sets of turning vanes (three vanes in the 9 x 24-in. section, five in the 24-in. square section) helped to further reduce the tendency for separation to occur. The design of these turning vanes was based on data by Stuart, Warner, and Roberts.[111] The vanes were fabricated by rolling all but a 2-in. wide portion of 18 ga. x 10 in. x 25.2 in. galvanized sheet stock to provide a smooth curve yielding the appropriate turning angle. Mounting tabs were cut and bent at the ends making the final span of the vanes 24 in. The 2-in. straight portion of the vanes served as the trailing edge suggested by Stuart, et al., to control the flow. The portion of the transition section between the turning vane cascades acts as a subsonic diffuser for the wind tunnel. The possibility of stall occurring in this diffuser portion was examined using data from Kline[112] and from Kline, Abbott, and Fox[113] using a length-to-minimum-width ratio of 4.7 and diffuser angle of 16.8°. Based on those figures, the diffuser section was predicted to be on the verge of stall, indicating a possible need for splitter vanes. However, experience with the completed section has not shown such a need.

The need for vibration isolation also led to several other changes in the wind tunnel. Wedges were driven between the sides of the duct and the wall at the opening between the two rooms. This was found to effectively isolate vibration transmitted from the fan. Considerable vibration still existed in the equipment room duct walls, but very little was transmitted beyond the sheet metal duct section just inside the wall (Fig. 7). It was felt earlier that some means might have to be found to stiffen the carts supporting the entrance, test, and transition sections, but the wedges and transition section

design changes proved so effective in reducing vibration that only slight additional bracing was applied to the entrance and transition section carts, and no attempt was made to raise the carts onto more solid supports. In addition to the other solutions, a short canvas isolation section was constructed for use in between the test and transition sections. Two frames of 3/4 in. plywood were built with suitable internal dimensions and with tee-nuts spaced to match the holes in the test and transition section flanges. A gap of 3/4 in. was made between the frames and the canvas was stapled to them, providing a slightly elastic wall for the flow channel.

3.2 AIRFOIL CASCADE

For this study, a cascade of three airfoil models was used to simulate the turbine airfoil cascade. The airfoil profile was based on a turbine blade design used by Lander[114] and employed in previous wake studies by Cox and Han.[15] This profile was enlarged to a chord length of 21 in., resulting in the coordinates shown in Fig. 10 and Tables A.1 and A.2 (see Appendix A for Tables A.1 and A.2). The span was 24 in., resulting in an aspect ratio of 1.143. Such extreme enlargement was necessary to achieve the desired Reynolds number at flow velocities suitable for the required visualization techniques and to provide dimensions large enough for detailed boundary layer exploration. Because surface curvature is of considerable importance in any discussion of boundary layer transition on a concave surface, the surface curvature was calculated for both the pressure and suction surfaces and is presented in Fig. 11.

The airfoil models were produced by casting epoxy over a canvas covered wood frame. A pattern (Fig. 12) was made by forming epoxy filler over a core made of hardwood sandwiched between two aluminum end plates which had been machined to the final dimensions of the airfoil profile. The end plates were aligned on a surface plate and the assembly was bolted rigidly together. Epoxy filler was then formed over the wood core to approximately the right shape and then sanded to conform to the end plates. Once this pattern was completed, a fiberglass mold with hardwood moldbox, also shown in Fig. 12, was made.

A total of six airfoils were cast using the completed mold, each having special features needed for the study. Plywood ribs were assembled with pine spars to make frames (Fig. 13) over which heavy canvas was attached. The end ribs of each of these frames had 1/4-20NC tee-nuts installed for locating and holding the core in the mold. On the three airfoils cast for use in the center of the cascade, these tee-nuts were also used for mounting in the test section. Additional threaded fittings were attached to the end frames for attachment of the upper and lower airfoils to the test section frame. Once these airfoil cores were attached to the mold, United States Gypsum type C-301 casting resin was poured into the mold to form the completed airfoil. Voids and other imperfections in the completed airfoil surface were filled with Tuf-Fill and sanded smooth. In this way, each

TEST AIRFOIL
SECTION DATA (in.)

X	Y
0.000	0.000
0.300	-0.180
0.600	-0.222
1.200	0.000
1.800	0.390
3.000	1.140
4.500	1.890
6.000	2.400
7.500	2.640
8.400	2.685
9.000	2.670
10.500	2.550
12.000	2.340
13.500	2.025
15.000	1.650
16.500	1.200
18.000	0.750
19.300	0.355
19.500	0.315
21.000	0.300
19.500	1.200
16.500	2.580
13.500	3.960
10.500	5.220
9.000	5.670
6.900	5.880
4.500	5.550
3.000	4.830
2.250	4.320
1.500	3.690
0.750	2.880
0.000	1.680
-0.220	1.050
-0.240	0.660
-0.165	0.300
-0.027	0.030
0.000	0.000

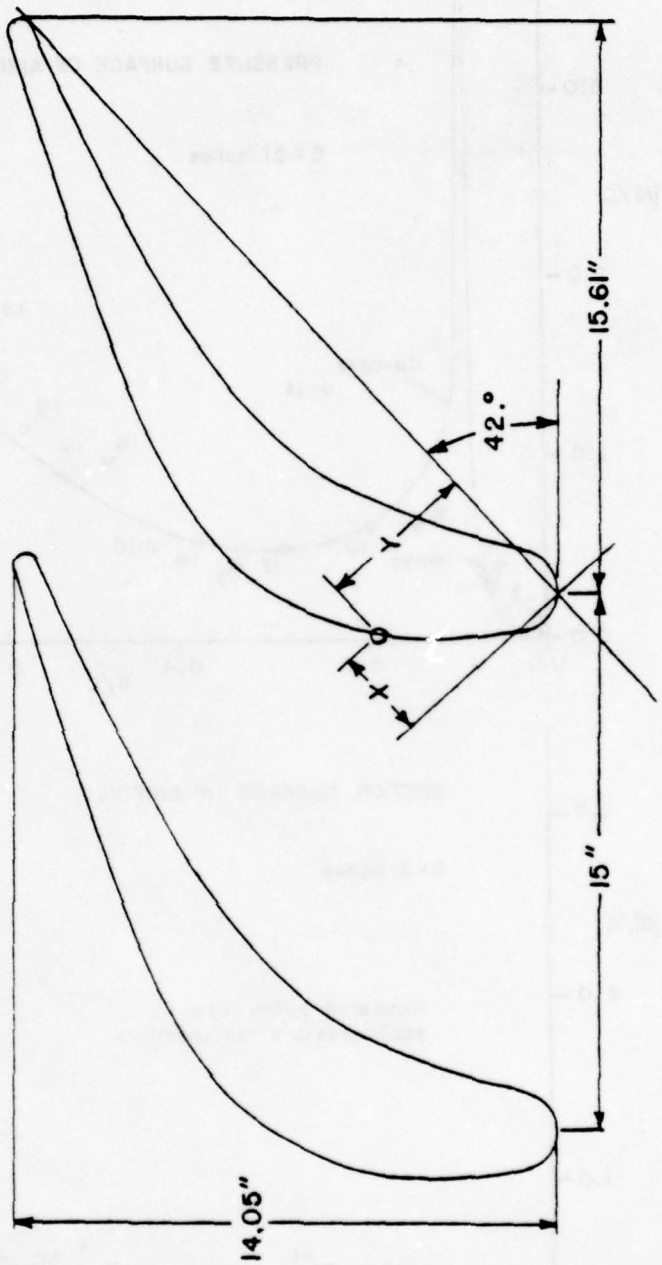

Leading Edge Radius: 0.781 in.
Trailing Edge Radius: 0.355 in.
Span Length: 24 in.

Figure 10. Airfoil Coordinates

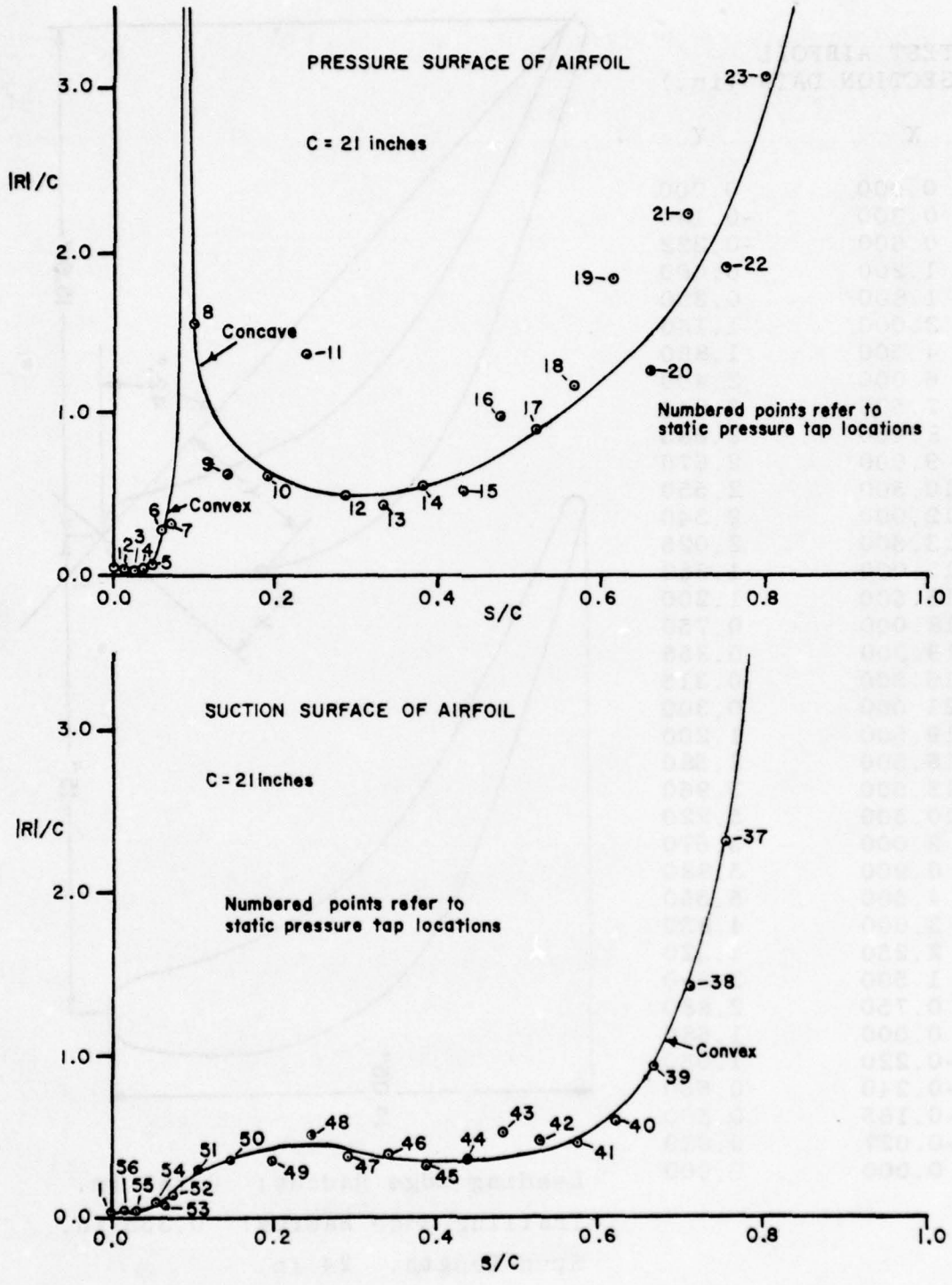

Figure 11. Airfoil Surface Curvature

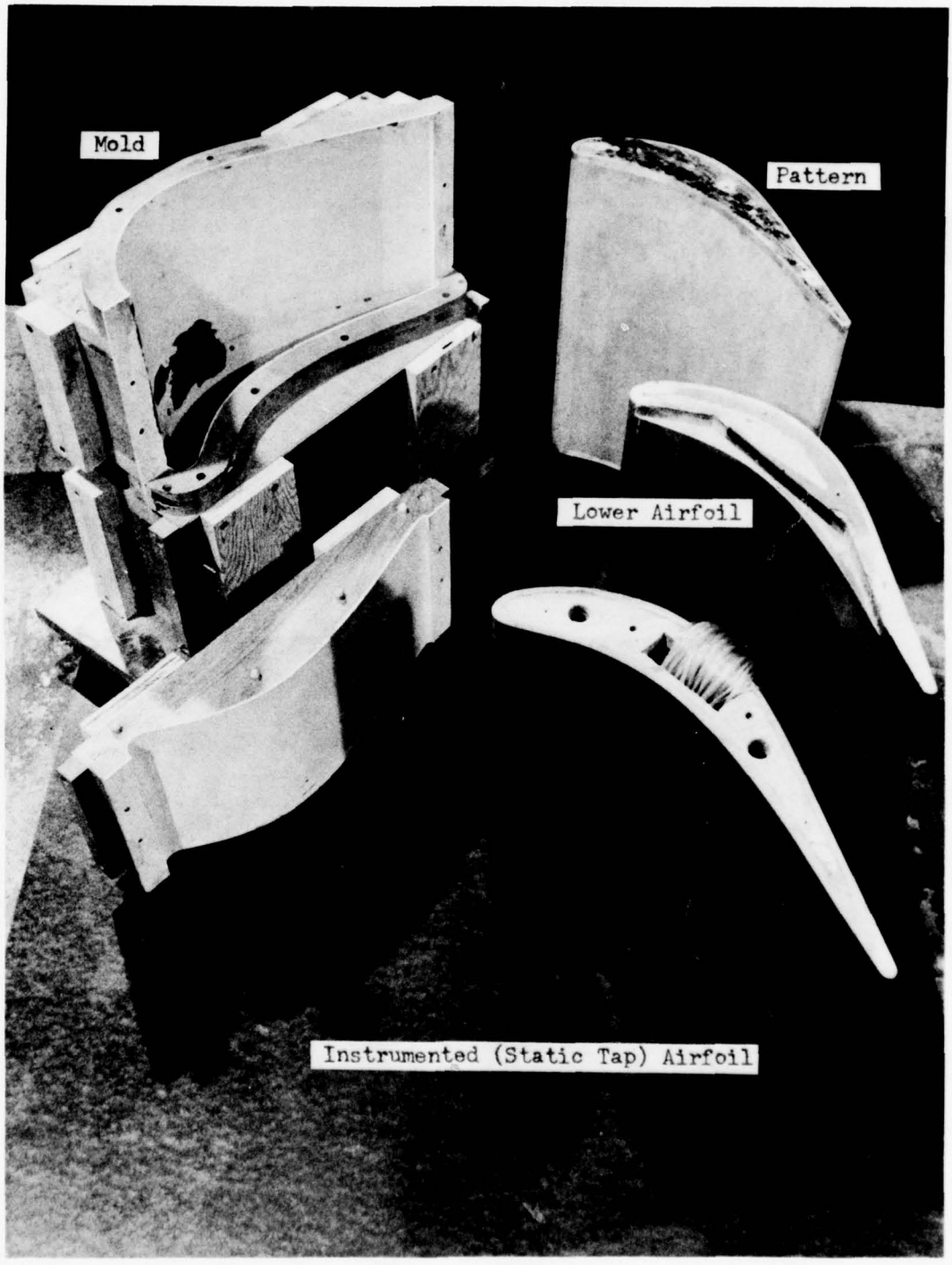

Figure 12 Pattern, Mold, and Airfoil Models

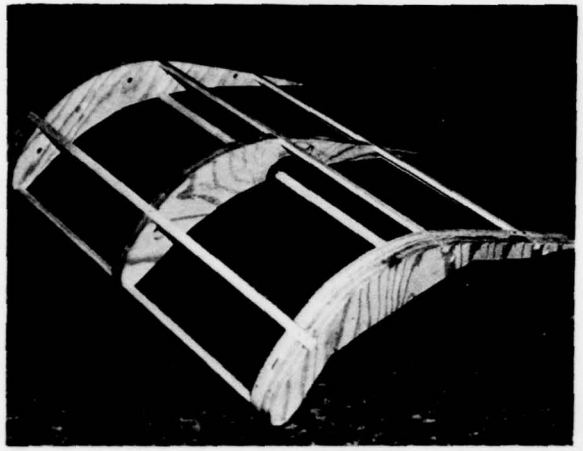

a. Upper airfoil, plane surface

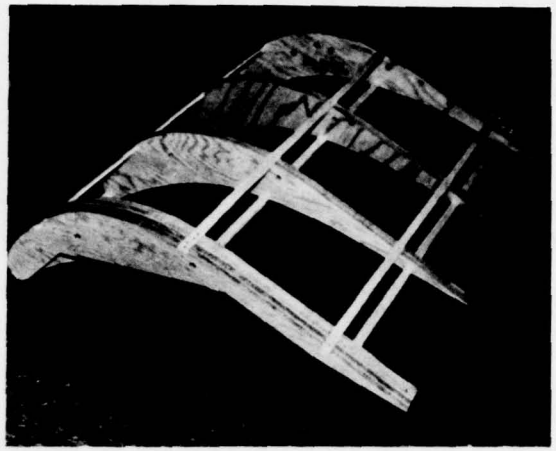

b. Upper airfoil, lighting slit cut in center

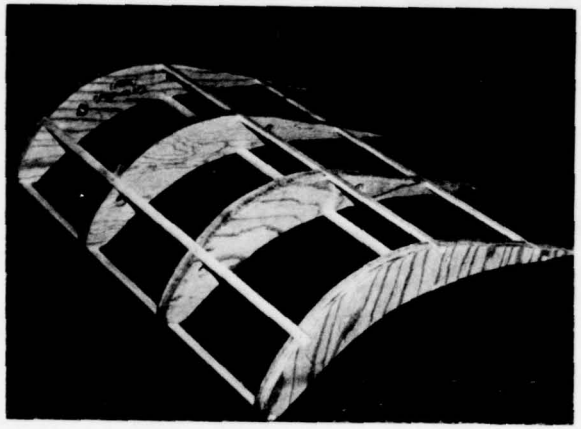

c. Center airfoil

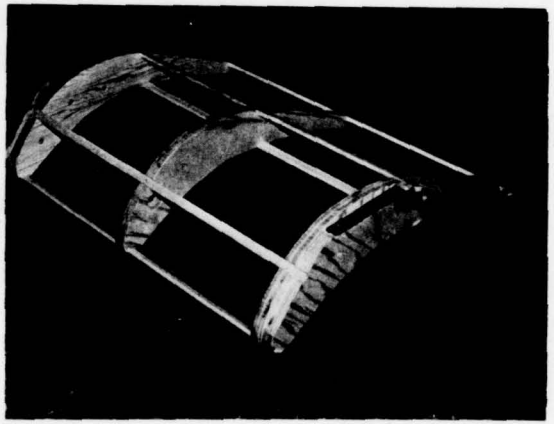

d. Lower airfoil

Figure 13 Airfoil Core Frames

of the airfoil surfaces had the same dimensions despite differences in the features and fittings of each airfoil. Measurement of the surface roughness of the completed airfoils showed an RMS value of about 32 to 64 μin.

As already mentioned, each of the airfoils was slightly different. One of the airfoils (Fig. 13) was fitted for mounting to the lower test section frame. The pressure surface of this airfoil served as part of the cascade as well as part of the lower wall of the test section. Two of the airfoils were fitted for attachment to the upper test section frame, their suction surfaces intended for use as part of the test section wall. The surface of one of these blades was left as cast, but the other airfoil had a 3/8 in. thick window of Abcite (clear, abrasion resistant plexiglass) placed in its center for flow visualization purposes. While the curvature and narrow width of this window (2.0 in.) rendered it unsuitable for most viewing purposes, it was ideal for lighting the pressure surface of the test airfoil. Three airfoils were made for use in the center of the cascade. Two of these airfoils were cast with plain gray surfaces as previously described. One of these, however, was painted with black epoxy paint in the pattern shown in Fig. 14 for flow visualization purposes. Into the surface of the third airfoil, fifty-six 1/32 in. static taps were cast at the midspan locations given in Fig. 15 and Tables A.1 and A.2. Holes were drilled into the mold and 1/32 in. steel wire was inserted into the holes. Tygon tubing (1/16 in. I.D.) was slipped over brass tubing which was in turn slipped over the wire so that the end of the brass tube would be beneath the surface of the airfoil. The airfoil core was made in two sections. The first section was placed in the mold prior to insertion of the wires and tubes. The epoxy was then poured to the height of this core section. The tubes and wires were then inserted and the other core section was added after the Tygon tubing was fished through slots in the core frame. Epoxy was again poured, resulting in an instrumented airfoil with the Tygon tubes extending through one side for attachment to a rotary valve and ultimately to a pressure transducer or inclined manometer. During the casting process, taps 24-27 and 29 became plugged. Taps 25 and 26 were successfully drilled out, but the others remained plugged as shown in Fig. 15. This was not felt to be detrimental to the study, because the pressure gradient is not expected to change rapidly in this region.

Placement of the airfoils within the test section is shown in Fig. 16. In order to simulate the wake from upstream turning vanes or blades, a circular cylinder was placed upstream of the central or test airfoil. The displacement of this circular cylinder relative to the test airfoil stagnation point is labeled as Y and is considered to be positive when the circular cylinder is displaced towards the right in the figure. The turbine airfoil models were mounted so as to have a solidity ratio (C/s) of 1.4 and a cascade stagger angle of 48°.

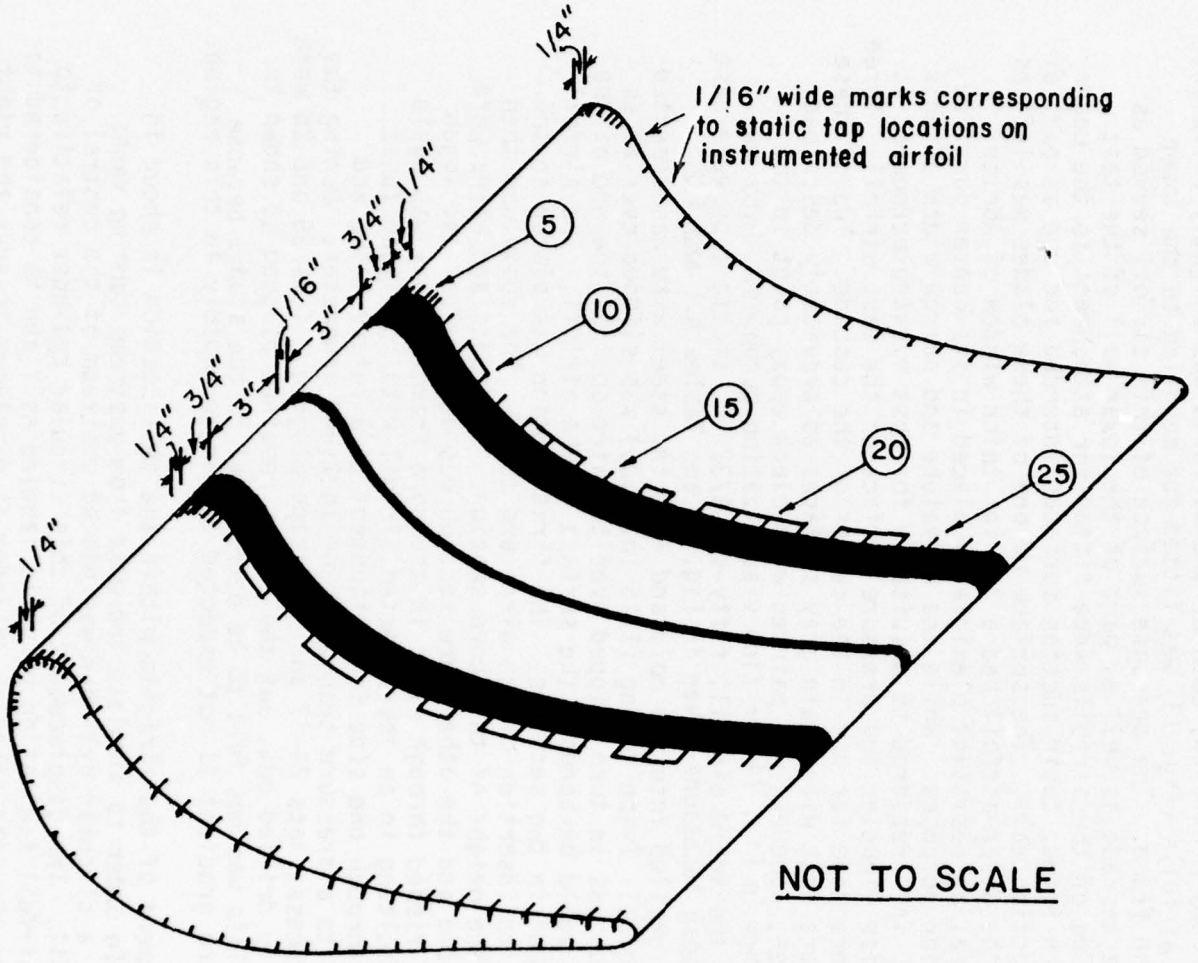

NOTE: All shaded areas and lines represent natural silver-gray color. Remaining regions of airfoil model painted black.

Figure 14. Airfoil Paint Scheme

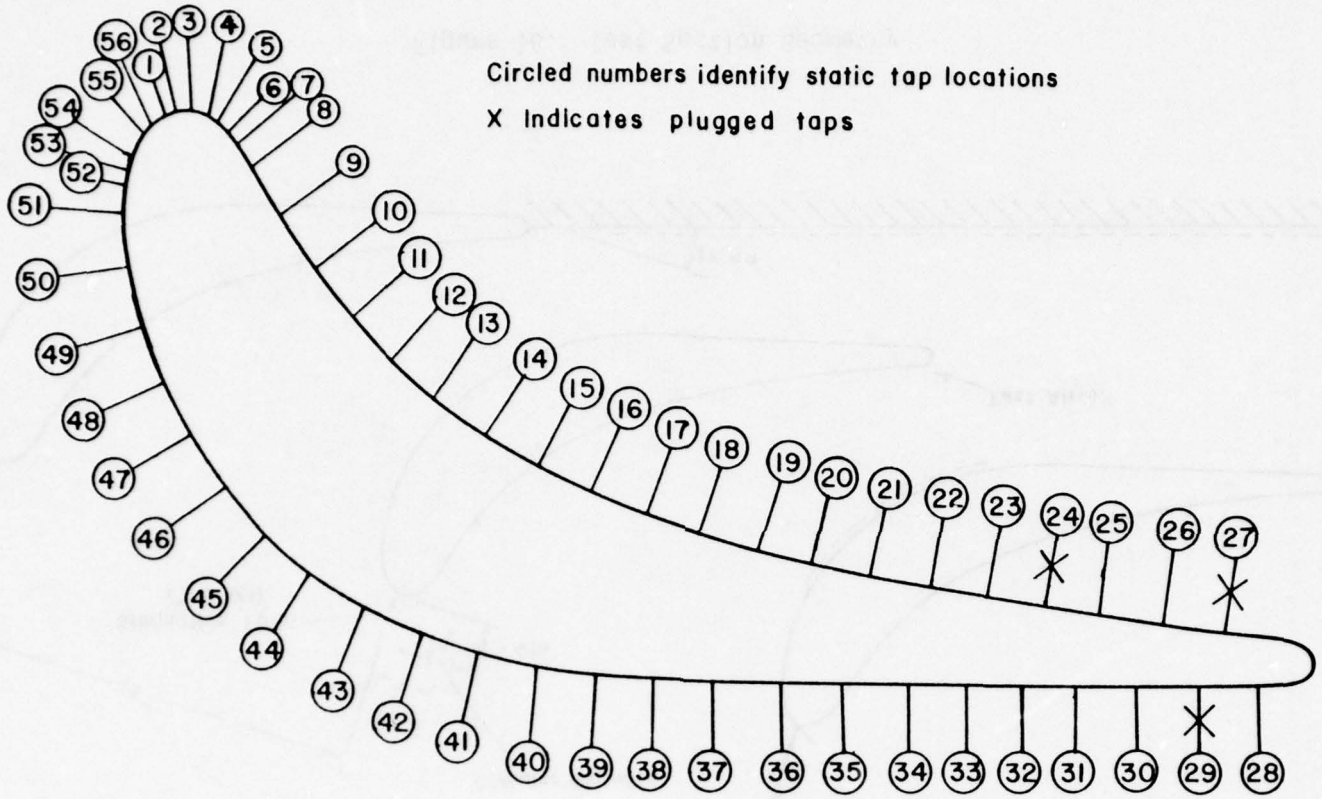

Figure 15. Instrumented Airfoil Static Tap Locations

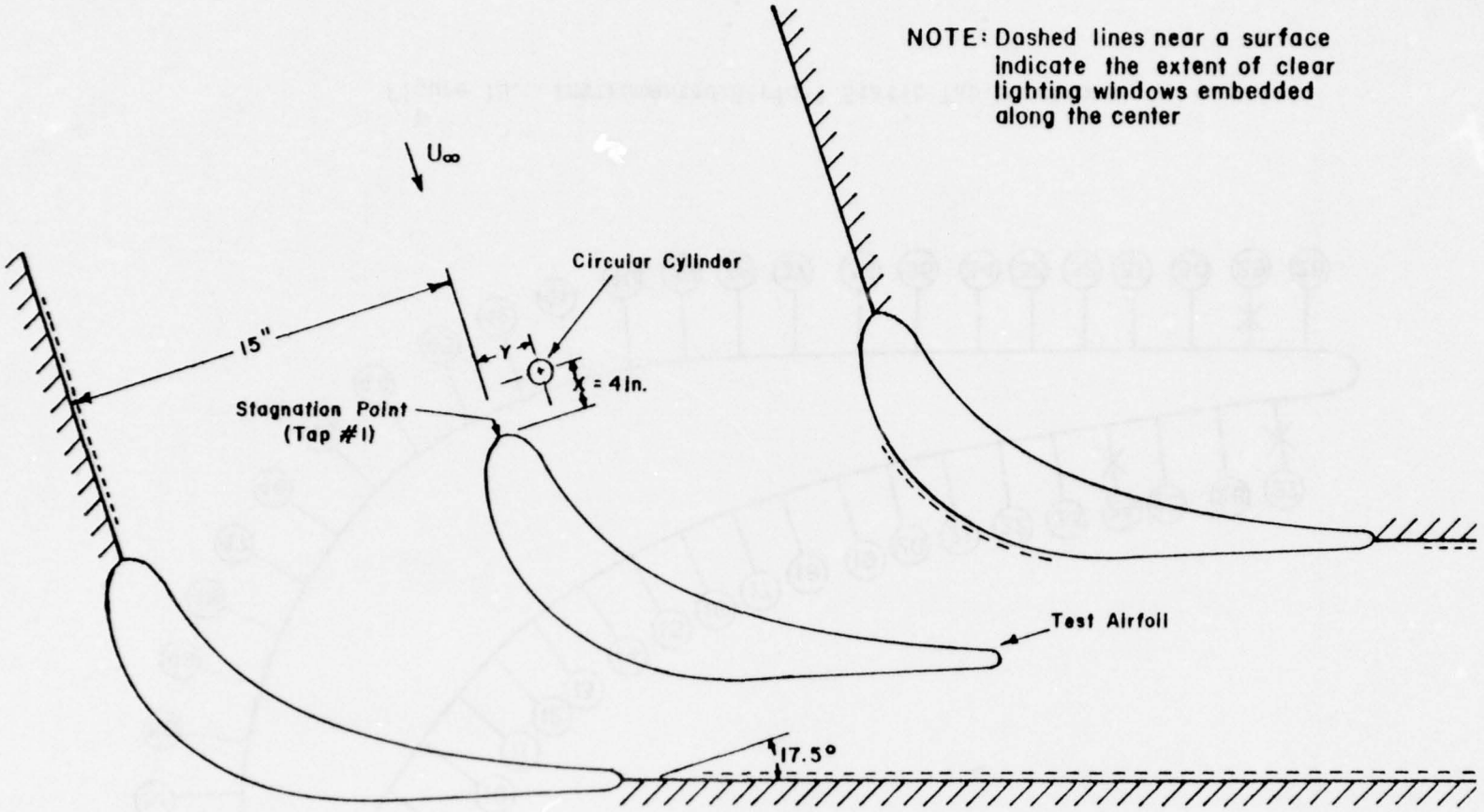

Figure 16. Test Section Geometry

3.3 CIRCULAR CYLINDER TRANSPORT MECHANISM

In order to simplify the task of positioning the upstream circular cylinders, a transport mechanism was designed and installed along the test section side walls (Fig. 17). Basically this transport consists of two screw shafts coupled by a chain drive to transmit equal linear motion to the two rod supports. A continuous mechanical counter permits direct reading of the rod displacement (Y) to the nearest 0.01 in. Through the use of different mounting arrangements, rods of any desired size can be used. The transport mechanism was installed so that the rods move in a line approximately 4 in. from the test airfoil stagnation point and can be moved from one side of the cascade to the other. Moving the cylinders involves only turning a crank and reading the displacement on the counter.

By placing the rod traverse line approximately 4 in. from the airfoil leading edge, several advantages were realized. First, no interference was encountered with the various insertion ports previously drilled in the plywood test section side. Also, one of the instrument ports utilized for wind tunnel calibration was used to study rod wake characteristics by fixing a hot-wire probe in position through the port and moving the rod past it. The 4-in. clearance also proves to be realistic for turbine construction as it would represent only about 0.4 in. for the original turbine airfoil profile.

Although the rod transport was used to move only a single cylinder to a fixed location as described above, the design of the transport offers considerable versatility that could prove valuable in subsequent studies. More than one rod can be installed and moved simultaneously by adding additional rod transport carriages to each screw shaft. A motor could easily be added to the transport. This motor would permit remote control of the mechanism or, if microswitches were installed to limit travel, could provide continuous periodic motion of the rod(s) similar to that used by Kiock[16] for a study of the effects of turbulent wakes on suction surface boundary layer transition.

3.4 HOT-WIRE ANEMOMETERS

For turbulence studies, hot-wire anemometers and associated equipment (Fig. 18) were used. As in previous studies[15,109] a Flow Corporation Model HWB-3 hot-wire anemometer with HWP-B probes was used for the wind tunnel calibration measurements. A TSI Model 1261 probe was obtained for boundary layer measurements and a TSI Model 1050 constant temperature two-channel hot-wire anemometer became available as the study progressed. In addition, a TSI Model 1076 true RMS meter and a Federal Scientific Model UA-500 Ubiquitous Spectrum Analyzer were used to study the turbulence signals.

The hot-wire probes were tipped with Wollaston wire (0.0004 in. diameter platinum core with silver coating) and etched with a stream of 10% nitric acid from a burette. The etching process was accelerated by

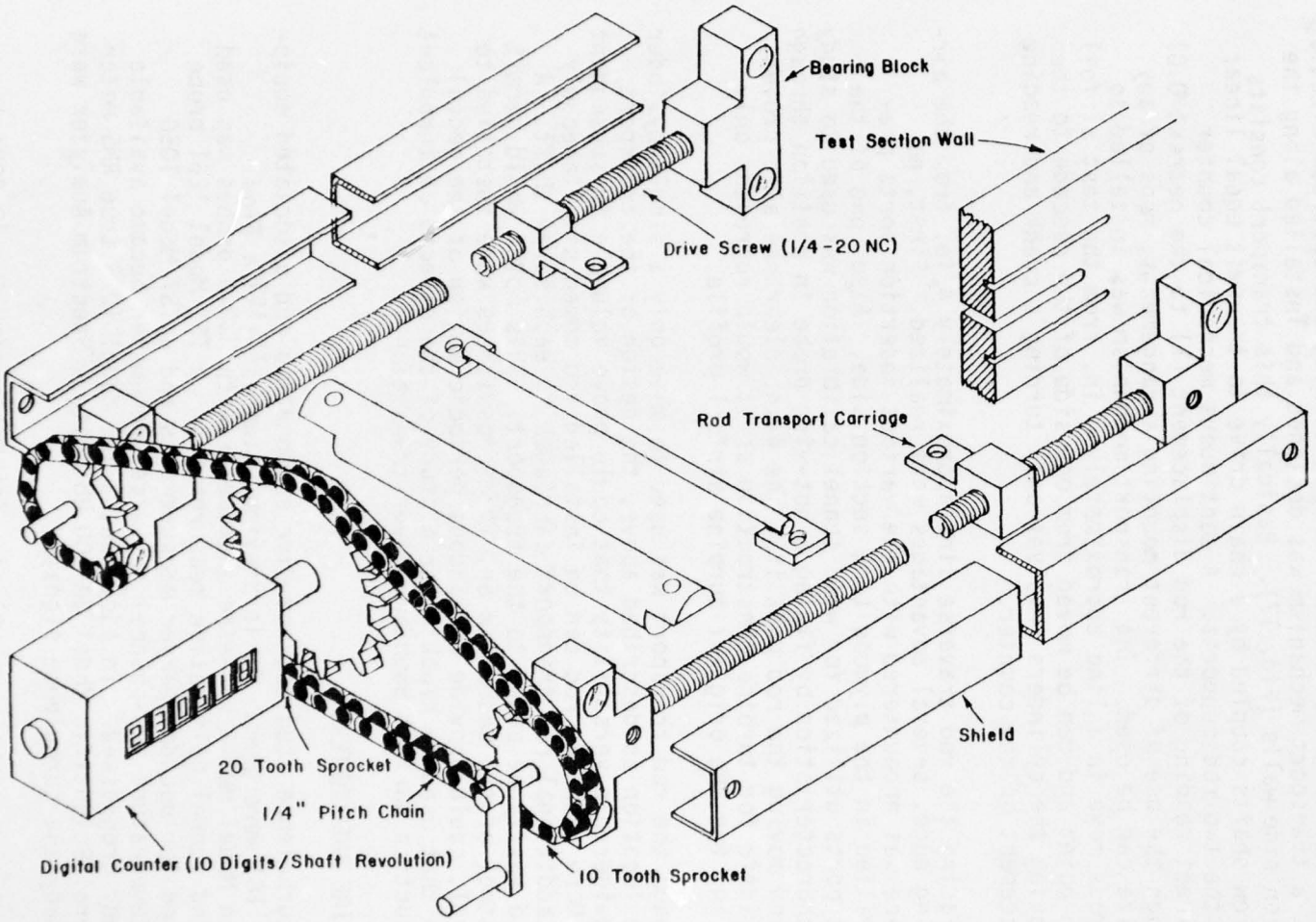

Figure 17. Rod Transport Mechanism

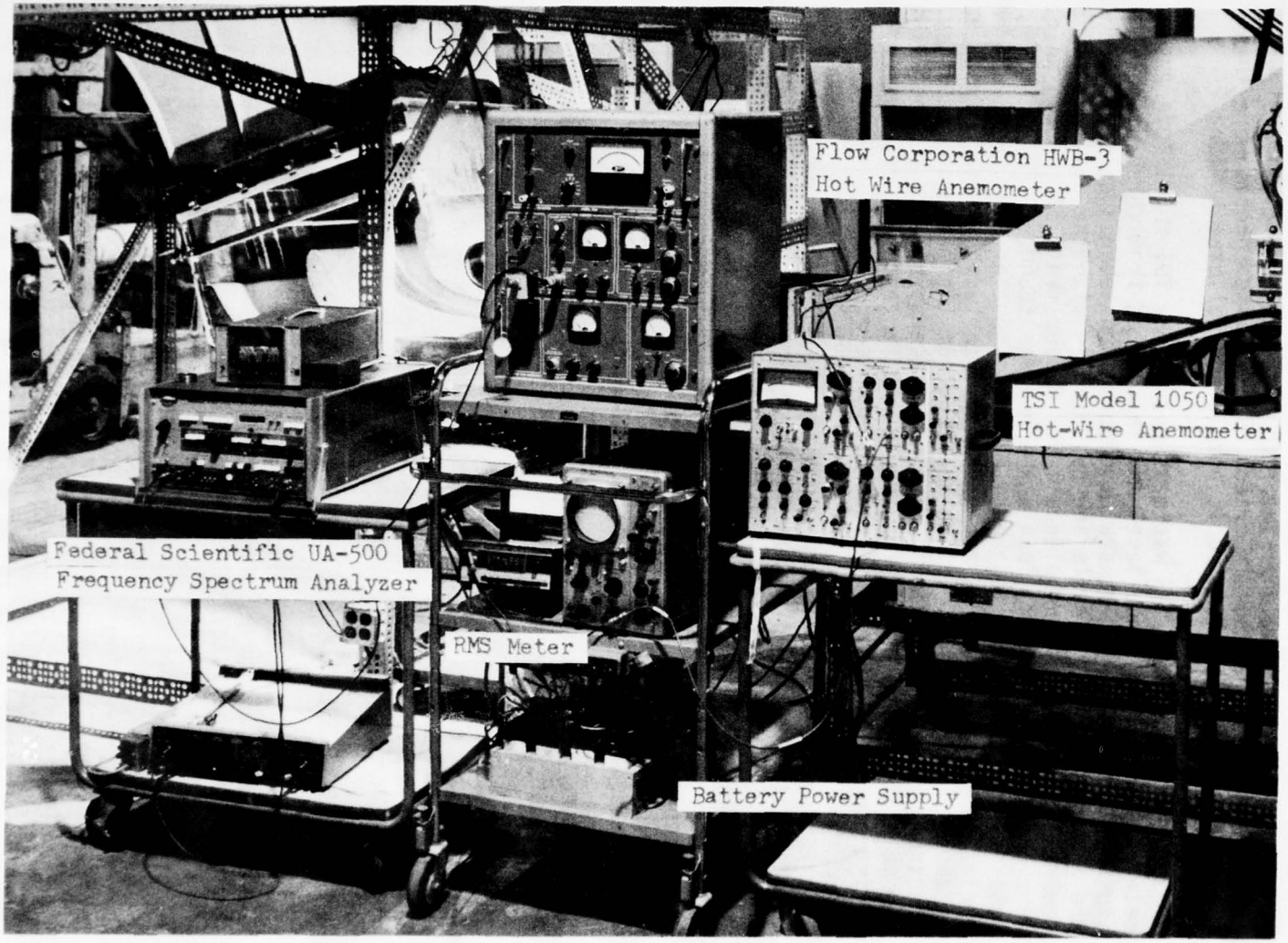

Figure 18 Hot-wire instrumentation

applying a 6V potential to the wire, with a platinum electrode in the acid, as suggested by Bradshaw.[115] A surplus machine slide positioned the wire relative to the acid stream and provided control over the width of the etched region. The etched probes were cleaned first in water, then alcohol, and air dried. The finished probes were then calibrated against an isentropic nozzle and calibration tank.

Output from the HWB-3 was measured by the TSI Model 1076 RMS meter, and the turbulence level was calculated from three signals (noise, turbulence, and square wave) based on techniques described in the Flow Corporation manuals and by Cox.[109] With the availability of the new TSI unit, the turbulence level measurements of the two units were compared and rather close agreement was found. A 20 kHz low-pass filter was applied to the amplifier output of the HWB-3, and the amplifier itself served as a high-pass filter with a cutoff frequency of about 2 Hz, thus restricting the range of the measured frequency spectrum. However, Hopkins[116] showed little turbulence beyond 2 kHz for velocities of 50 to 90 fps in a 2 x 2 ft test section, thus validating the range of output frequencies chosen.

During the course of this study, a TSI Model 1050 two-channel constant temperature hot-wire anemometer was made available. By using a Model 1052 linearizer, the output of this unit is somewhat easier to interpret than the direct output of the HWB-3, from which velocities or turbulence levels must be calculated. In addition, a Model 1057 signal conditioner and Model 1015C correlator were both available for use. The available frequency range of the TSI unit was proved to be up to at least 8 kHz, based on a new technique by Horak and Velkoff.[157]

In order to establish the frequency spectrum of the turbulence level measurements, a Federal Scientific Model UA-500 Ubiquitous Real-Time Spectrum Analyzer was used with either of the hot-wire anemometers. This instrument, when used with an X-Y plotter, plots the spectrum of any of the hot-wire outputs on regular graph paper. However, complete analysis of the signal requires some time because each of the points must be recorded by the observer and punched onto data cards for calculation by the FORTRAN program described in Appendix B.

3.5 PRESSURE SENSITIVE INSTRUMENTATION

Because of the desire to study instantaneous events within the boundary layer and wake, pressure sensitive instrumentation was employed only for obtaining auxiliary data such as the free-stream velocity and airfoil static pressure distribution. Because of the lengths of tubing involved, all of the pressure sensitive instruments used, including the pressure transducer, yielded rather long response times, thus preventing their use for the higher frequencies encountered in the wake and boundary layer.

As in previous studies,[15,109] pressures were measured using a Setra Model 233 pressure transducer (Fig. 19) and Dwyer inclined manometers. Output from the pressure transducer was read from a Dana

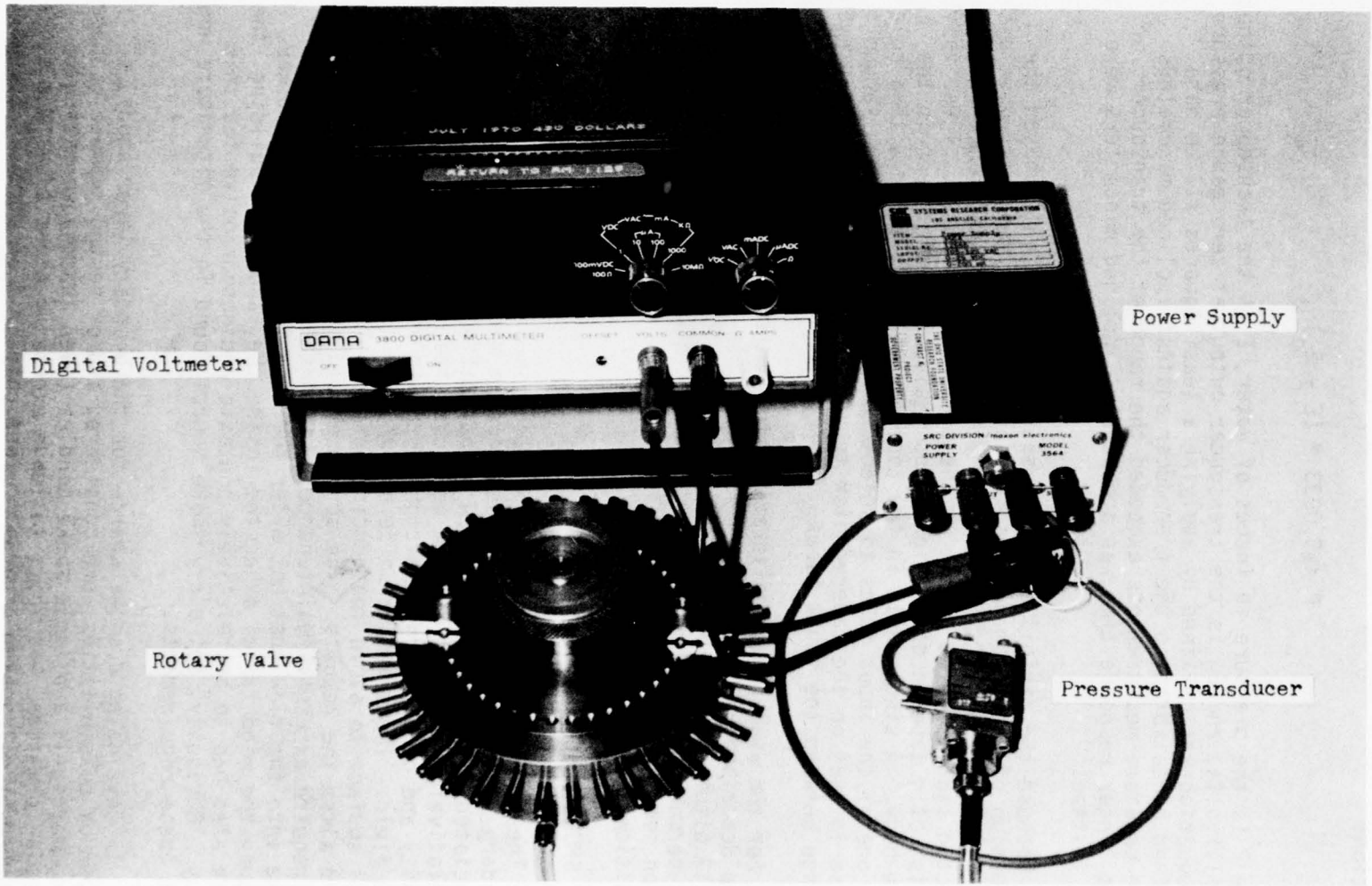

Figure 19 Rotary Valve, Pressure Transducer, and Digital Voltmeter

Model 3800 digital voltmeter and converted to pressure by the following equation:

$$P = 0.0033 * (E - E_o) ,$$

where P is the pressure in inches of water, E is the transducer output in millivolts, and E_o is the transducer output at zero gauge pressure. The equation was obtained by applying a least squares fit to data obtained by calibrating the transducer against inclined manometers. Where pressure measurements exceeded the range of the transducer, or where longer response time was acceptable, inclined manometers were used instead.

Because the airfoil static pressure distribution involved the collection of data from 53 taps, two of the 40-position rotary valves (Fig. 19) described by Cox and Han[15] were used to connect one selected static tap at a time to the pressure transducer. These valves consist of a tapered disk which turns inside a mating taper in the valve body. A single hole in the tapered disk is aligned with a hole from one of the input tubes to select the desired pressure. Vacuum grease is used on the tapered disk to act as a lubricant and to prevent leakage between the input tubes.

For the wind tunnel calibration study, the standard pitot-static probe described by Cox and Han[15] was used. In addition, a Dwyer Model 167-12 pitot-static tube and Model A-302 static pressure probe were semi-permanently mounted in the square duct downstream of the transition section (Fig. 5) to serve as a reference for wind tunnel flow conditions.

3.6 SMOKE GENERATOR

The problems associated with selection of a smoke source for boundary layer flow visualization are much more restrictive than those associated with free-stream flow visualization. The smoke must possess a relatively small but uniform particle size, but must be of sufficient density and contrast to permit photographic and visual studies of the flow field. There must also be minimal buildup of deposits on the model surface to avoid introducing boundary layer disturbances that would alter the results. The source should be convenient to use and not require excessive maintenance or preparation. Introduction of smoke into the flow must not alter the flow in any significant way. Because the wind tunnel exhausted inside the laboratory building, the smoke also had to be relatively nontoxic and noncorrosive for this study. Obviously, not every smoke source found in the literature would meet these requirements.

In developing a smoke source for the boundary layer study, a number of possibilities were considered and/or tested. Smoke produced by commercially available smoke candles (even those advertising no deposit formation) was found to leave excessive deposits as was smoke produced by oil soaked cigars,[117] wood chips,[118] or straw[119] burned in

an oxygen-poor environment, and ammonium chloride.[120] The use of tobacco smoke, dry ice, and wick-type oil or kerosene sources was ruled out because of insufficient density. The use of $TiCl_4$ [121] or $SnCl_4$ [122] was ruled out because of the formation of hydrochloric acid. The use of particles such as balsa dust[123] or PVC[124] particles was considered impractical because of the relatively large particle size and the additional problem of filtering them out of the tunnel exhaust.

As a result, a smoke generator employing kerosene dripped onto a hot surface was developed. The only drawbacks found for this source were the potential explosion hazard of vaporized kerosene (other users of kerosene have indicated no problems) and the somewhat obnoxious fumes associated with long periods of use, limiting the length of time during which the smoke could be used. Since the development of this source, Parker and Brusse[125] have reported the development of a liquid nitrogen/water vapor smoke generator that might have proven even more satisfactory, but this information was obtained too late for use in this study.

The principal design details for the smoke generator are shown in Figs. 20 and 21. As shown in Fig. 20, the evaporation unit consists of a 3/4 in. copper tube flattened over a 1/4 x 3/4 in. bar. Kerosene spray tubes were silver soldered into holes in the flattened tube and to another feed tube connected to the kerosene supply. A Chromalox Model SE2507, 750W strip heater was attached to studs on the underside of the evaporation chamber to provide the necessary heat. By attaching the strip heater in this manner, a replacement heater can be installed rapidly should the need ever occur. Insulation was wrapped around the entire unit to further improve the efficiency. A condensate reservoir or trap, made from standard pipe fittings, was attached to the outlet pipe of the evaporation unit to collect kerosene which might condense during transmission to the smoke probe.

In operation, kerosene was released by a solenoid operated valve and sprayed onto the heated evaporation surface. Shop air was passed through the evaporation chamber, mixing with the evaporated kerosene and carrying it through flexible, insulated tubing to the smoke probe at the wind tunnel entrance. The solenoid controlled valve was open only while a button was depressed at the viewing position near the test section. The smoke color and density determined when additional kerosene must be introduced. A bluish color in the smoke indicated a lack of sufficient kerosene, while a lack of density could be indicative of either too little or too much. If too much kerosene were introduced, a slight delay would occur before the kerosene was heated sufficiently for full operation.

To permit control of the smoke stream position from viewing locations near the test section, the smoke probe was attached to a motorized traverse (Fig. 22). The rail, carriage, and screw shaft for this traverse were obtained as parts for a Genie Model GS-450 garage door opener. A 1/15-hp reversible AC motor was adapted to drive

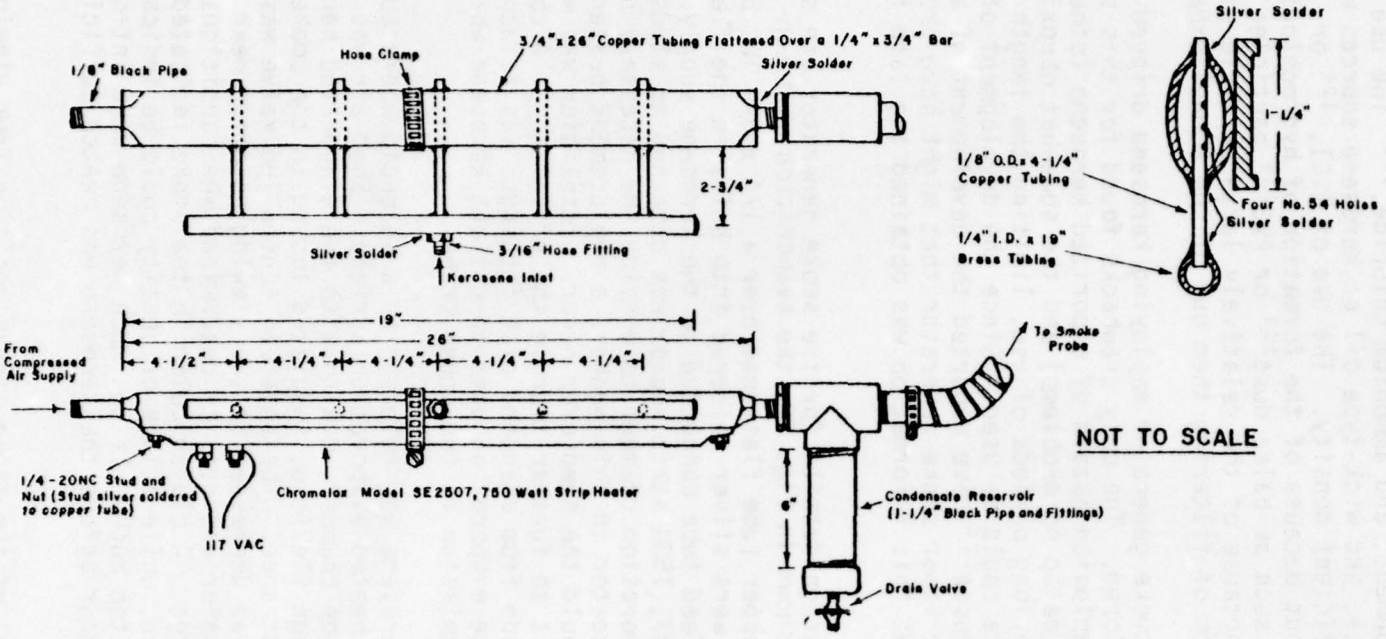

Figure 20. Smoke Generator Evaporation Unit and Condensate Reservoir

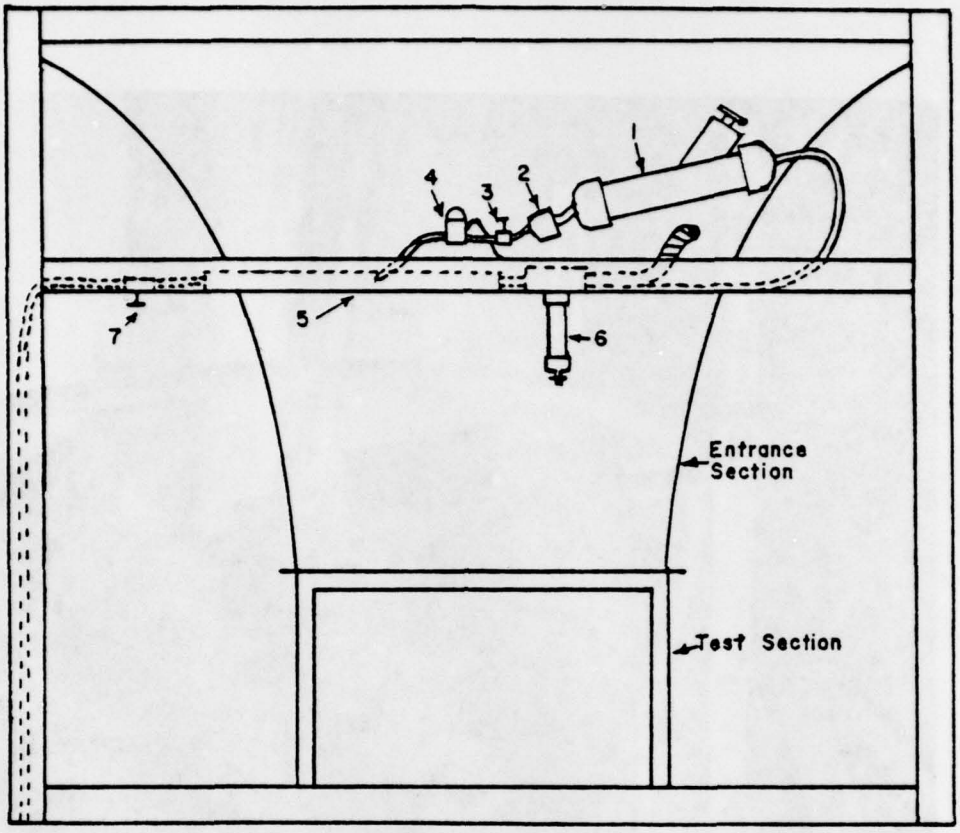

Wind Tunnel Rear View

Not To Scale

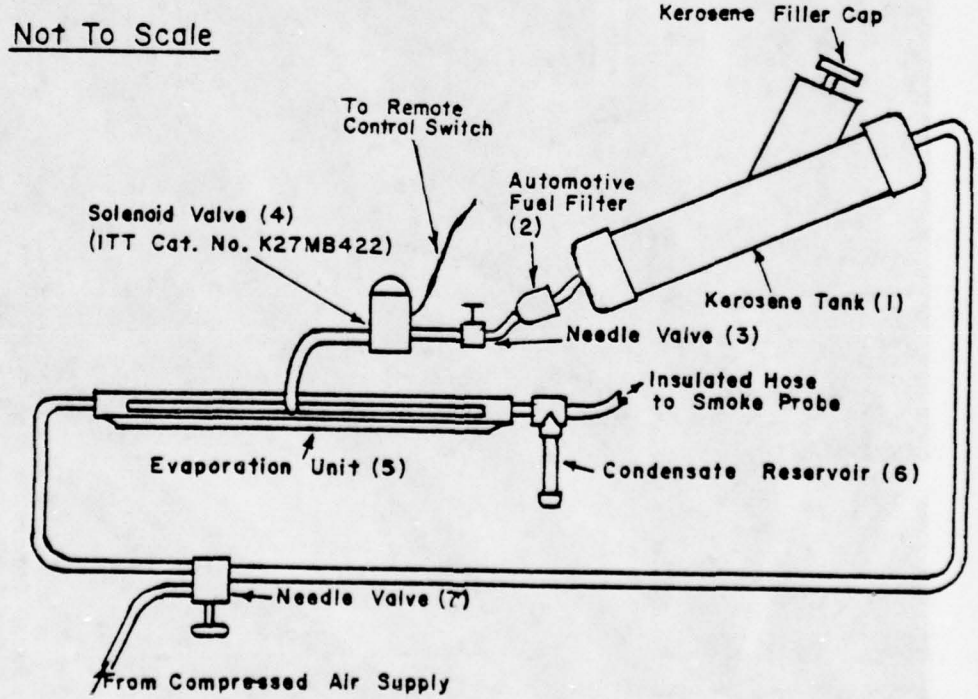

Figure 21. Smoke Generator Location and Schematic

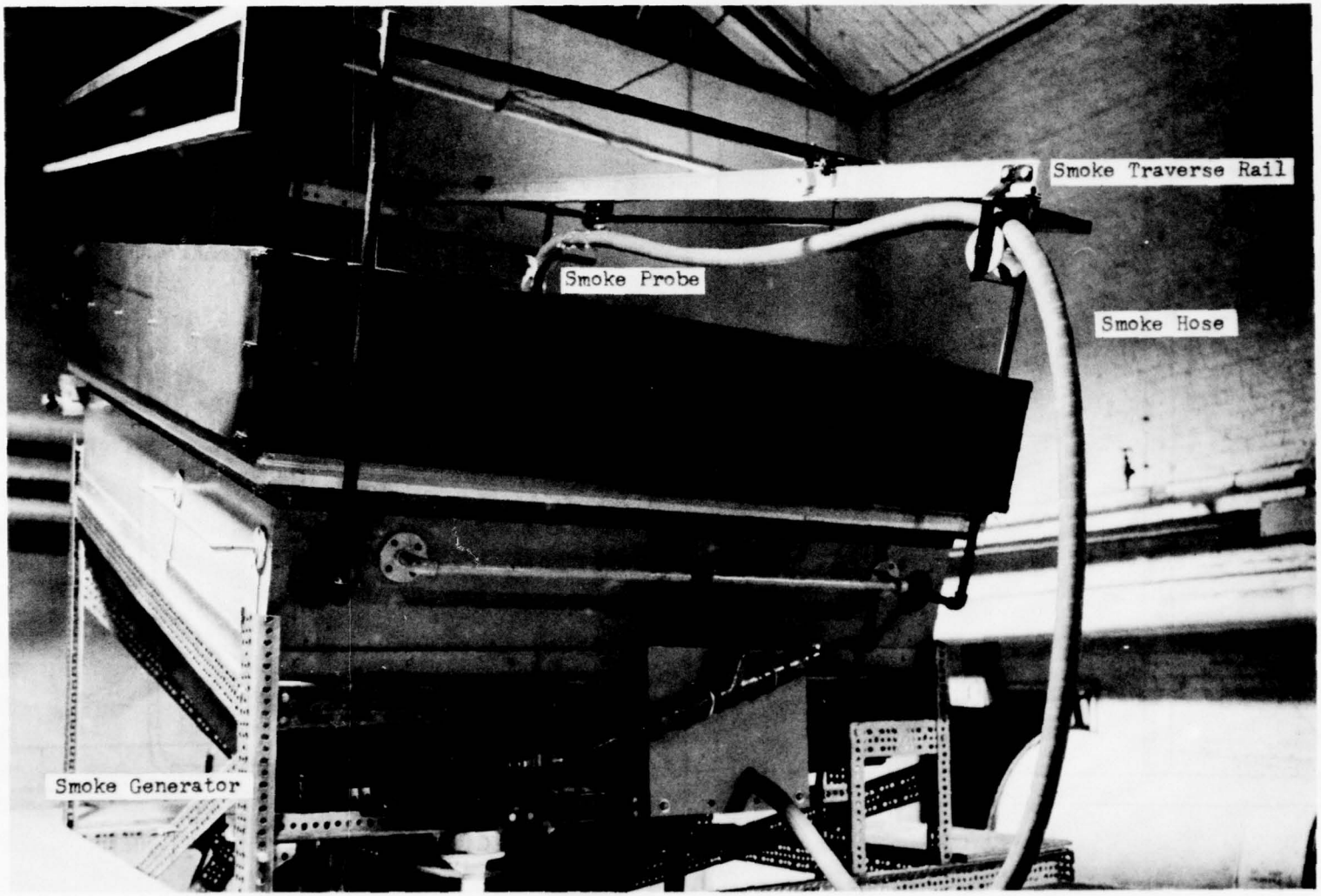

Figure 22 Smoke Traverse, Probe, and Generator

the traverse and could be controlled by a remote switch at the viewing position. By using this traverse, the smoke stream could be conveniently positioned anywhere within a predetermined plane extending between the two outside airfoil surfaces of the cascade. By clamping the traverse rail in a new position on the supporting structure, this plane could be located anywhere between the two wind tunnel side walls.

3.7 PHOTOGRAPHIC AND LIGHTING EQUIPMENT

Because flow visualization was a critical part of the investigation, the choice of phtographic equipment and lighting techniques was considered to be of major importance. The use of still and of motion picture photography required that more than one lighting technique be employed. The lighting conditions in turn placed restrictions on film and equipment selection. Even the test section had to be designed with due consideration for photographic needs.

As in most photography, proper lighting is necessary for good flow visualization results. As shown by experimentation and discussed by other researchers,[33,122] light sources for smoke flow visualization seem to work best when placed at 45 to 90° with respect to the camera axis or when the smoke is backlit. In addition, Brown[126] recommends limiting the light to only the region of interest through the use of slit lighting, thus increasing the contrast between the smoke filament and the black background. He also recommended the use of push processing to increase the contrast of the final negative. The test section was designed with 1-1/2 in. and 2 in. wide slits of 3/8 in. Abcite embedded in the walls along the center line. Also, one of the upper airfoils was provided with a similar lighting slit as discussed in the airfoil models section. These slits were judged to be adequate for most lighting needs, with the use of cardstock to produce narrower slits if necessary. Because the intensity of the illumination was limited by various factors, the room was darkened during photography to eliminate undesirable reflections from the plexiglass surfaces. In order to prevent light from reaching the camera directly from the source, shields of 1/8 in. tempered hardboard, as suggested by Clark,[122] were contoured to fit snugly against the test and entrance sections.

Lighting was provided by floodlamps and/or high-speed flash depending on the desired effects. Hospital bed lamps provided adjustable sockets from above. Five fixed sockets were mounted underneath the test section. Reflector floodlamps were used in these fixtures as needed. A portable fan was used to cool the underside of the test section when the floodlamps were in use. In addition, two General Radio type 1531-A Strobotacs and a Honeywell Strobonar Auto 770 flash unit were used for high-speed still photography. The Strobotacs have a flash duration of 0.8 to 3 μs depending upon the flashing rate. In addition, the Strobotacs can be fired in a single burst or can be set to flash at a rate between 1.8 and 417 Hz. In order to synchronize the flash units with the camera shutter, a 9-ft extension cord and multiple connectors were used to connect the flash units to the camera.

For still photography, a 35mm single-lens reflex camera (Mamiya-Sekor DSX 1000) was generally used. The camera was tripod mounted and a 90 to 250mm f4.5 Macro zoom telephoto lens was used with extension tubes to further reduce the minimum focusing distance. For high-speed motion pictures, a 16mm Fastex Model WF3 was used. This camera permitted 16mm movies to be made with speeds as high as 4000 frames per second. Timing marks on the film permitted accurate timing of events observed in the movies.

High-speed film (Tri-X) was used during most of the study. As recommended by Brown,[126] this film was often push processed (under-exposed, over-developed) with Accufine or other developers to increase contrast and depth-of-field. In addition, the negatives were generally printed on Polycontrast paper with a contrast-4 filter, because of the low contrast within the smoke stream.

3.8 HOT-WIRE TRAVERSE MECHANISM

The introduction of a hot-wire anemometer system to the boundary layer study would have been extremely difficult without the aid of a traverse mechanism which could penetrate the boundary layer without much interference to the flow, while supporting a hot-wire boundary layer probe. Such a mechanism was designed and built, since no commercial unit or sub-assemblies were available. The mechanism consists of a rotating arm around a pivot point near the tunnel wall, a middle arm which can be driven inside and out of the main rotating arm, and a hot-wire probe holder which can be driven relative to the middle arm (Figs. 23-25). The exact location of the pivot point and the general configurations of the mechanism were designed optimally using a computer, so that maximum pressure-side surface distance could be covered while maintaining a minimal interference with the flow field. The design which was finally built can cover the pressure side from tap #6 to tap #24 (Fig. 15). The rotating and the middle arms were constructed from square brass tubing cut and soldered in the appropriate shape. Threaded rods and flexible shaft assemblies control the relative motions of the middle arm and the hot-wire probe holder. Special surface prongs connected to a microswitch provide an exact determination of surface contract, thus allowing an accurate measurement of the hot wire probe distance from the surface. Further insertion of the surface prongs toward the surface helps stabilize the overall structure tip vibrations completely. The complete mechanism now resembles a beam supported at both ends, and not an unstable design of a cantilever beam vibrating at its free end. These vibrations were mentioned in Cumsty's[5] study and caused severe difficulties in judging the true mean position of the probe and in using the wire near the wall. Most of the mechanism structure is covered with a thin brass foil shaped as an airfoil so as to minimize drag and interference with the flow field. The three basic motions the mechanism is capable of achieving (i.e., one rotation and two linear motions) allow the hot-wire

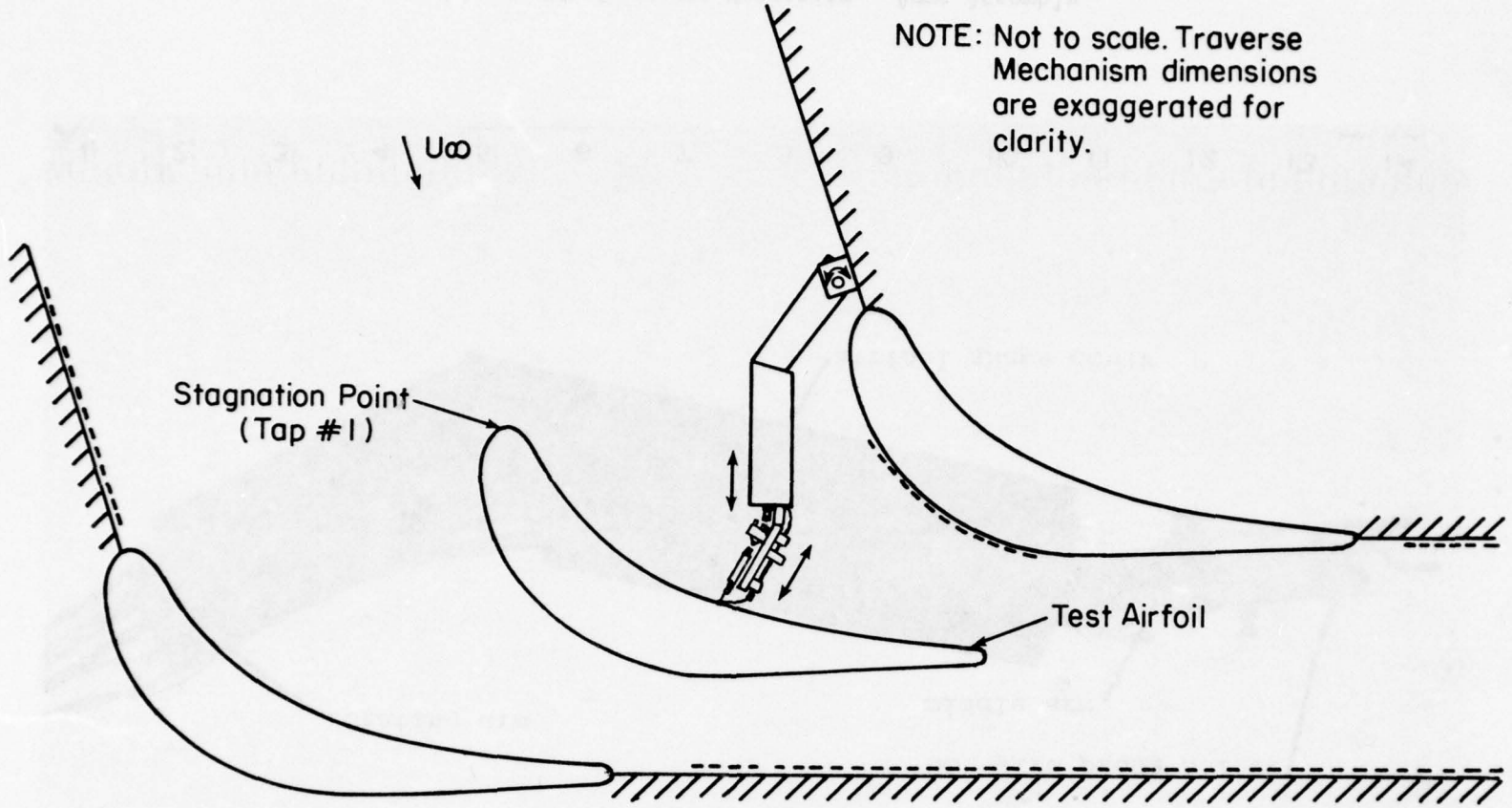

Fig. 23 Traverse Mechanism

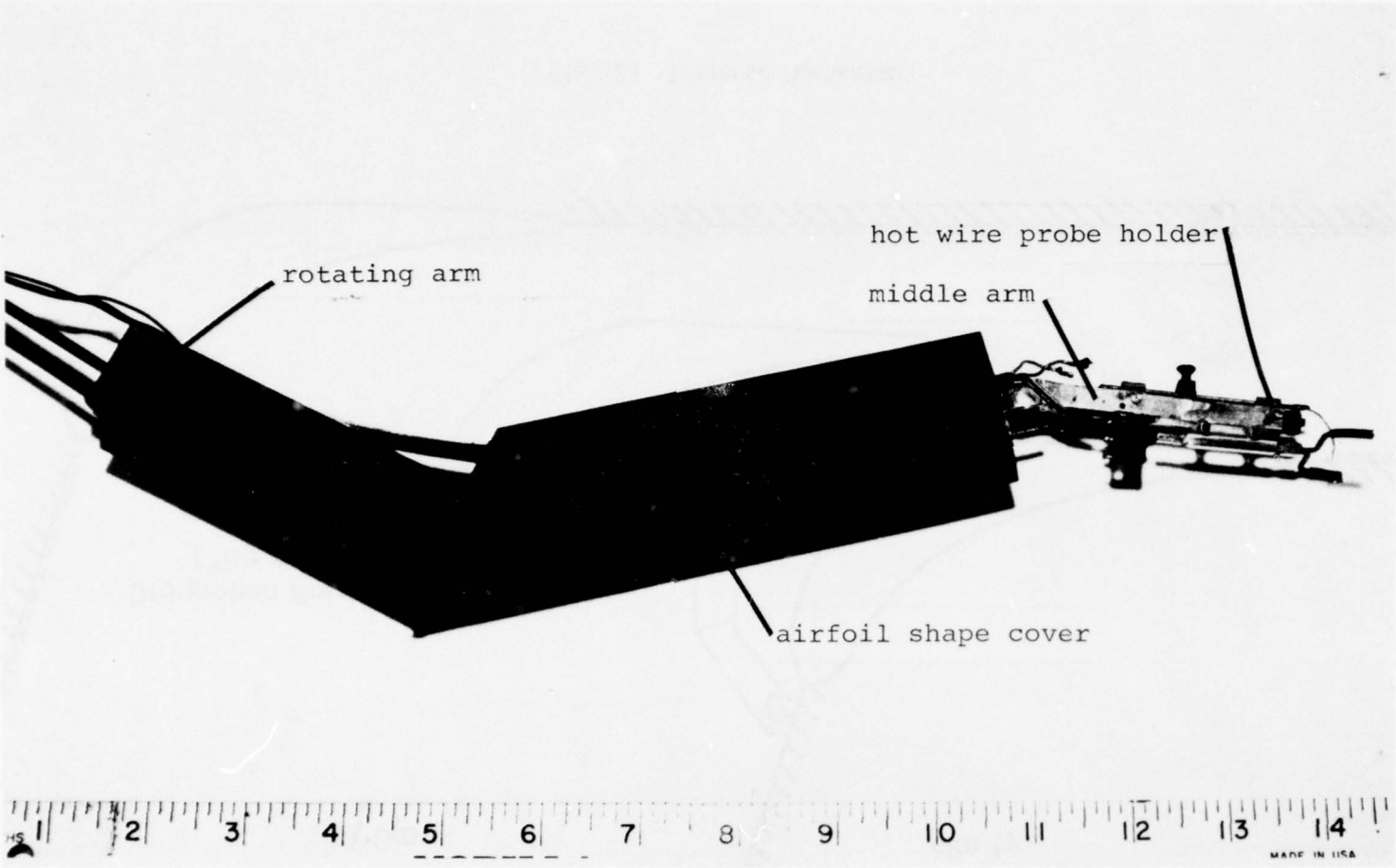

Figure 24 Traverse Mechanism - Arms Assembly

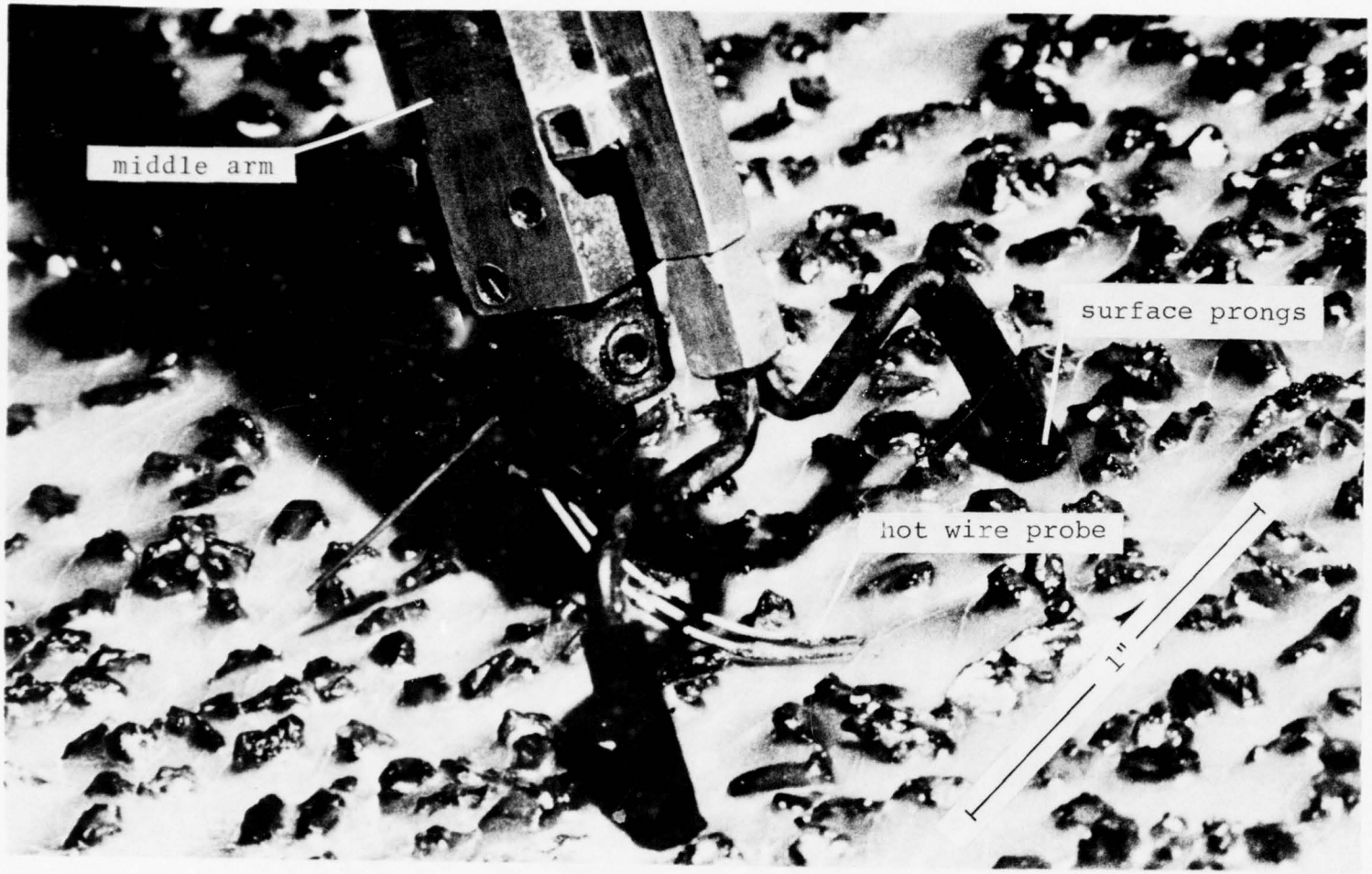

Figure 25 Traverse Mechanism - Hot Wire Probe Close-up View with Rough Surface

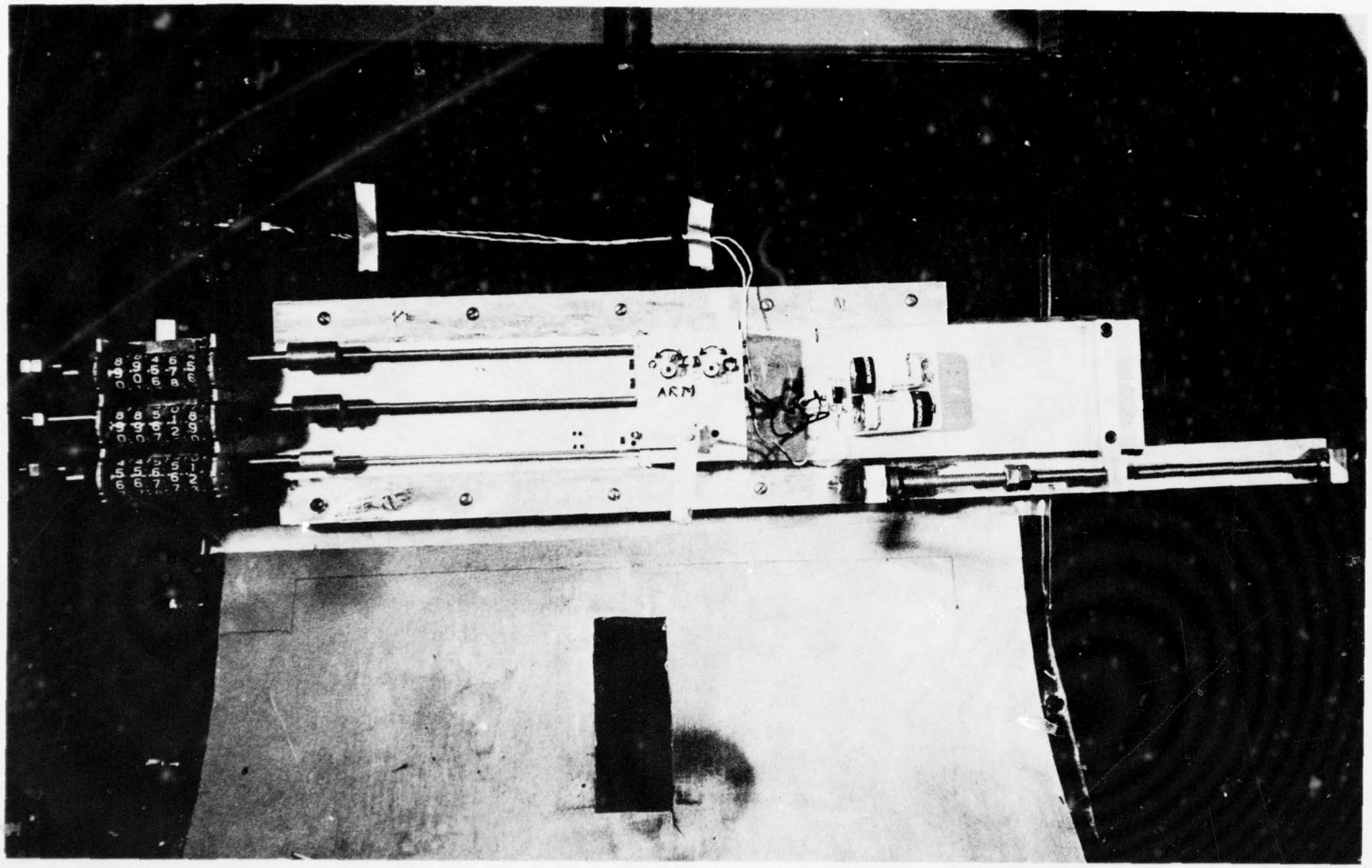

Figure 26 Traverse Mechanism Control Assembly - Side View

probe to reach the desired chord locations. All three motions are controlled through flexible shafts from outside the tunnel (Fig. 26) where the motions are transmitted via worm gear assemblies to mechanical counters, which read the exact probe location within 0.001 inch. An additional motion available is a spanwise motion of the whole mechanism, which allows possible investigation of spanwise vortices present in the tunnel.

Experiments were conducted to determine the frequency spectrum of the wake behind the mechanism. This study was especially important because certain frequencies can affect the boundary layer transition, as shown by several investigators. Brown[32] found that a disturbance frequency ranging from 0.8 to 1.2 times the Tollmien-Schlishting wave frequency will have a considerable effect on transition. Sound frequency close to the approximate laminar periods frequency between the Tollmien-Schlichting waves has been shown to stabilize the occurrence of these periods, while sound of the Tollmien-Schlichting wave may eliminate the laminar period and stabilize the frequency of the Tollmien-Schlichting waves. The frequency spectra found in this study for regions behind the airfoil-shaped part of the mechanism show no predominant frequency, but the square-shaped middle arm produced a Von-Karman vortex street at various velocities as is shown in Table 1. The Strouhal member was found to be equal to 0.3 on the average, based on 0.25" square side dimension of the middle arm, and the free-stream velocity at the arm location. Using Brown's[32] results and the Tollmien-Schlichting wave frequency, the wake of the traverse mechanism was found to have no apparent influence on the boundary layer transition properties, since its frequency was only a small fraction of the frequency of the Tollmien-Schlichting waves. Another important feature of the mechanism is that the vibrations of the overall structure were eliminated almost completely.

3.9 SURFACE ROUGHNESS

A three-dimensional randomly distributed roughness may be the best description of the type of roughness created by erosion or deposits by the high temperature gas from a gas turbine combustion chamber. In order to simulate such roughness in a wind tunnel study, commercially available sand-paper type roughnesses are inexpensive and easy-to-use substitutes. Previous studies on the subject using sand particles were performed by many investigators. Important studies by Bammert and Sandstede[138,139] on actual cascade performance with various roughness sizes show a significant drop in turbine efficiency of up to 14% with roughness size on the order of 10^{-2} chord length. The same studies result in a 6% drop of absolute efficiency for 10^{-3} relative roughness. Three different sand-paper roughness sizes were chosen based on various empirical relationships concerning the probable critical size for transition of three-dimensional sand-type roughness. Such empirical relationships were quoted by Doenhoff and Horton[143], Smith and Clutter[140], Gibbings[148], Loftin[149], Klebanoff, Schubauer and Tidstrom[142], Braslow, Knox and Horton[146], and Guven, Patel and Farell[151,152].

TABLE 1

TRAVERSE MECHANISM WAKE FREQUENCY ANALYSIS

Freestream Velocity (fps)	Frequency Peak (Hz)	Strauhal Number $(f \cdot L)/U_\infty$
23.3	344	0.3076
26.5	372	0.2925
29.8	448	0.3132
35.4	516	0.3037
40.9	560	0.2852
43.7	600	0.2860
46.6	660	0.2951
49.5	720	0.3030
	Average	0.30

In this study commercially available 3M-Resinite floor surfacing papers with grit numbers of 12, 20 and 36 were purchased. Figure 25 shows the relative sizes of these roughness sizes. The 3M-Resinite papers have three-dimensional particles glued on base papers with maximum paper thickness of about 0.05 inch. After several trials, the best results were achieved when the base papers were stripped off, resulting in a very thin layer of paper which was glued to the blade surface with contact cement.

In order to determine the average and maximum roughness heights, several investigators used the grain sizes quoted by the manufacturer. Such a determination could yield great errors because between 20-50% of the particle is lying under a layer of glue, and thus only the exposed particle portion should be used in order to determine the real roughness size affecting the boundary layer, and in developing empirical equations based on roughness height. A Bausch and Lomb 10x narrow-focus microscope was used to measure a statistical sample of each paper in order to determine various properties of t-e particle height distribution. It was found that grit numbers 12, 20 and 36 have an average particle height of 1.168, 0.513 and 0.162 mm., respectively, which correspond to 2.2×10^{-3}, 9.6×10^{-4} and 3.0×10^{-4} roughness height divided by chord length.

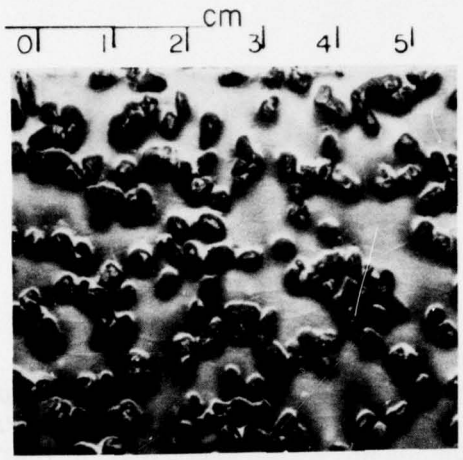

GRIT 12

AVERAGE ROUGHNESS

HEIGHT: 1.168 mm

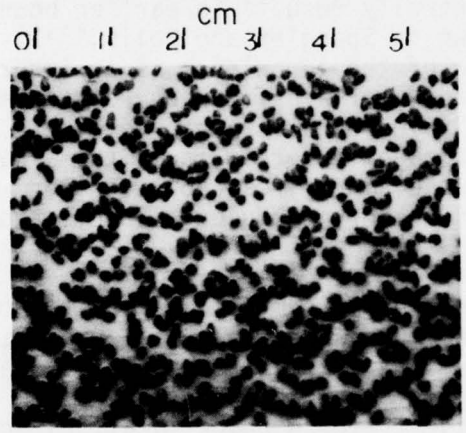

GRIT 20

AVERAGE ROUGHNESS

HEIGHT: 0.513 mm

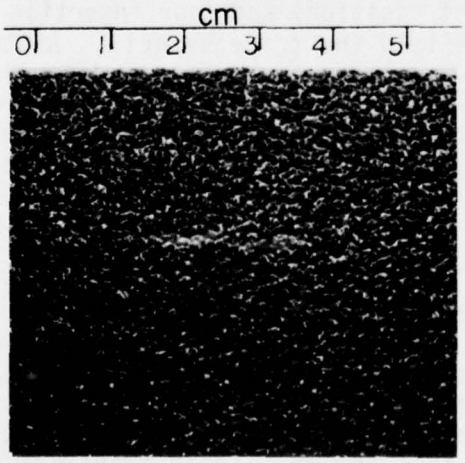

GRIT 36

AVERAGE ROUGHNESS

HEIGHT: 0.162 mm

Figure 27. 3-M Resinite Floor Surfacing Papers

SECTION IV

EXPERIMENTAL RESULTS

4.1 TEST SECTION CALIBRATION STUDY

In order to realistically compare boundary layer transition data from one test facility with data from another, characteristics such as unit Reynolds number, free-stream turbulence level, and the frequency spectrum of the turbulence should be known. For example, an increase in free-stream turbulence level generally results in earlier boundary layer transition. However, as shown by Spangler and Wells,[41,42] knowledge of the frequency spectrum of the turbulence is as important as knowledge of the magnitude, because certain frequency components exhibit more influence on boundary layer behavior than do others. In order to establish the characteristics of the test facility, a calibration study was made upstream of the airfoil cascade to determine the free-stream velocity, unit Reynolds number, turbulence level, and turbulence frequency spectra.

In order to determine the mean free-stream velocity upstream of the cascade, a velocity calibration study was made based on a traverse grid of 16 points, each assumed to be representative of one-sixteenth of the duct area upstream of the airfoil cascade. The locations of the test section instrument ports and the traverse point locations are shown in Fig. 28. Four numbered port positions and four insertion distances (3, 9, 15, and 21 in.) defined the traverse grid. A standard pitot-static probe was used with an inclined manometer to determine the velocities. Complete velocity traverses were made for six different wind tunnel velocities. The lowest average velocity studied completely was 22.21 fps, while the highest was 42.81 fps. A velocity traverse was also made at a fan speed of 650 rpm, the highest practical speed for this installation, yielding a maximum average velocity of 52.9 fps. During examination of the data, it was noted that the velocities obtained for instrument port No. 1 were almost consistently 95% of the average mean velocity, those at port No. 2 were 100%, No. 3 were 98%, and No. 4 were 107%. In contrast, the spanwise variations in velocity (traversed from a single port) were generally less than 1%. Because the velocity measurements were made only 9 in. upstream of the 21 in. chord length airfoil models, it seemed likely that the blades could be influencing the flow profile. For this reason, linear traverses using a smaller (2 in. spacing) grid size were conducted 9 in. from the north wall of the test section. The results of one of these traverses are shown in Fig. 29. The characteristic velocity profiles found just

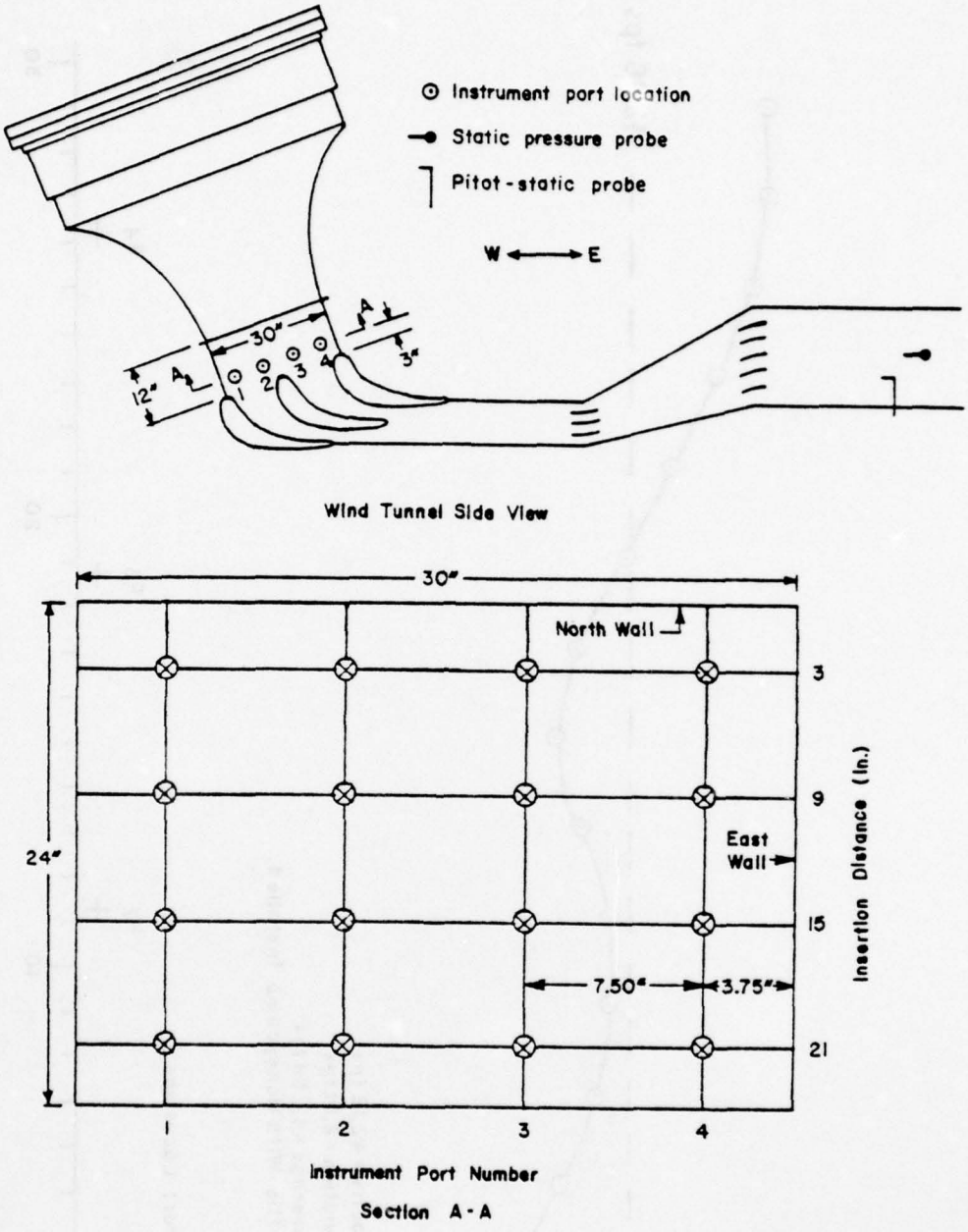

Figure 28. Test Section Calibration Geometry

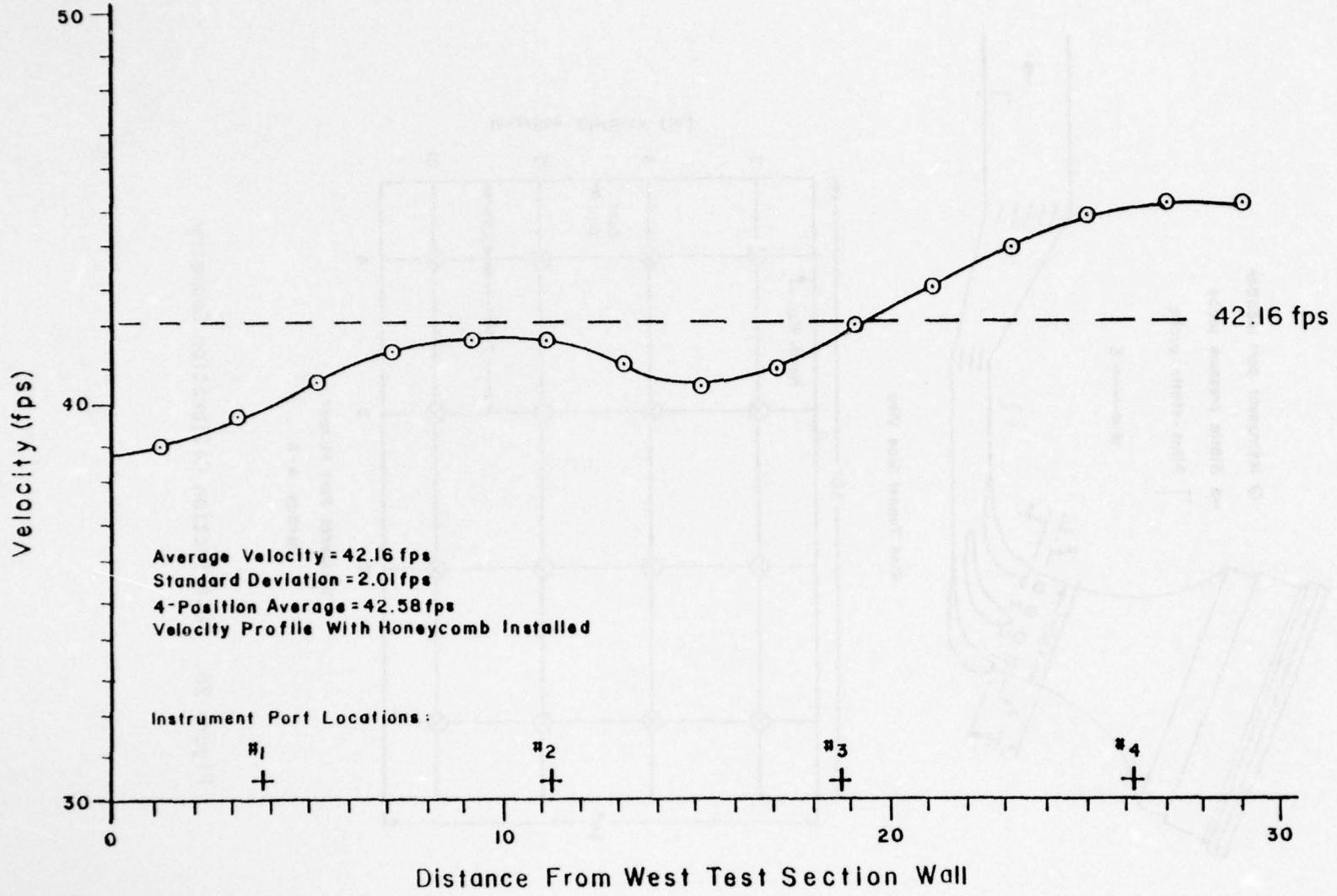

Figure 29. Test Section Velocity Traverse

upstream of turbine airfoil cascade models by Cox and Han[15] are very much evident in the graph. It might be noted that the blade stagnation points are at 0, 15, and 30 in. on the graph, pressure surfaces are to the right, and suction surfaces are to the left. A general slope also seems to be superimposed on the curve, possibly related to the use of only three airfoils in the cascade. Certainly this indicates that the airfoils do not truly represent an infinite cascade. Comparing the results of the linear traverses with those of the corresponding four points of the 16-point velocity traverses yields an error in average velocity of less than 1%. Therefore, the 16-point traverse is felt to adequately represent the average velocity even though the velocity profile is not uniform normal to the airfoil span.

Following completion of the velocity calibration study, a free-stream turbulence level study was conducted with the Flow Corporation HWB-3 hot-wire anemometer and HWP-B probe using the same instrument port positions and 16-point traverse described in Fig. 28 for the velocity study. Because of the time involved in turbulence level measurements, complete data sets were made for only four of the free-stream velocities studied during the velocity calibration. In general, the free-stream turbulence level was relatively uniform, varying from an average of 0.56% to 0.70% depending upon the average mean velocity (Table 2). However, the points 3 in. from the north wall showed a marked increase in turbulence level to values of 1.99% to 2.3%. In order to better define this turbulence increase, several traverses were made at positions No. 1 and No. 4 using a much smaller distance between traverse points than was used for the 16-point grid. Some of the results are shown in Fig. 30. Because the M_1 (noise) and M_3 (square) wave reference) signals would have varied little during the traverse, the M_2 (turbulence) signal was monitored as an indication of the turbulence level while the probe was moved away from the wall. As could be expected, the turbulence level is highest near the wall, but outside of the boundary layer, and starts to decay to the free-stream value with increasing distance from the wall. However, at a distance of about 3 in. from the north wall (the south, plexiglass, wall exhibited no such phenomena) a second turbulence peak was observed regardless of wind tunnel velocity for the range studied. The principal frequencies and magnitude of this peak were a function of velocity, but the peak existed for the entire range. No satisfactory explanation has been found for the turbulence peak, but it was felt unlikely to affect the intended studies, so correction was not attempted.

Table 2 gives a summary of the free-stream inlet velocity and turbulence data obtained during the calibration study. The inlet velocities were measured as just described, but the average outlet velocities were calculated based on the test section contraction ratio (10:3). The unit Reynolds numbers were calculated based on a kinematic viscosity of 1.64×10^{-4} ft^2/s at a temperature of 70°F. The blade chord Reynolds number was based on the outlet unit Reynolds number and a chord length of 1.75 ft. During the calibration study, records were kept of the average atmospheric properties within the lab, representing

TABLE 2

SUMMARY OF TEST SECTION CALIBRATION DATA

Inlet Velocity (fps)	Average Outlet Velocity (fps)	Inlet Unit Reynolds Number (1/ft)	Outlet Unit Reynolds Number (1/ft)	Inlet Turbulence Level (%)	Blade Chord Reynolds Number	Inlet Static Pressure (in. H_2O)
22.21	74.03	1.35×10^5	4.50×10^5	0.690	7.88×10^5	-0.152
29.01	96.70	1.76×10^5	5.88×10^5	0.564	1.03×10^6	-0.280
33.74	112.5	2.05×10^5	6.84×10^5	--	1.20×10^6	-0.356
36.30	121.0	2.21×10^5	7.35×10^5	0.700	1.29×10^6	-0.407
40.45	134.8	2.46×10^5	8.19×10^5	--	1.43×10^6	-0.511
42.81	142.7	2.60×10^5	8.67×10^5	0.641	1.52×10^6	-0.550

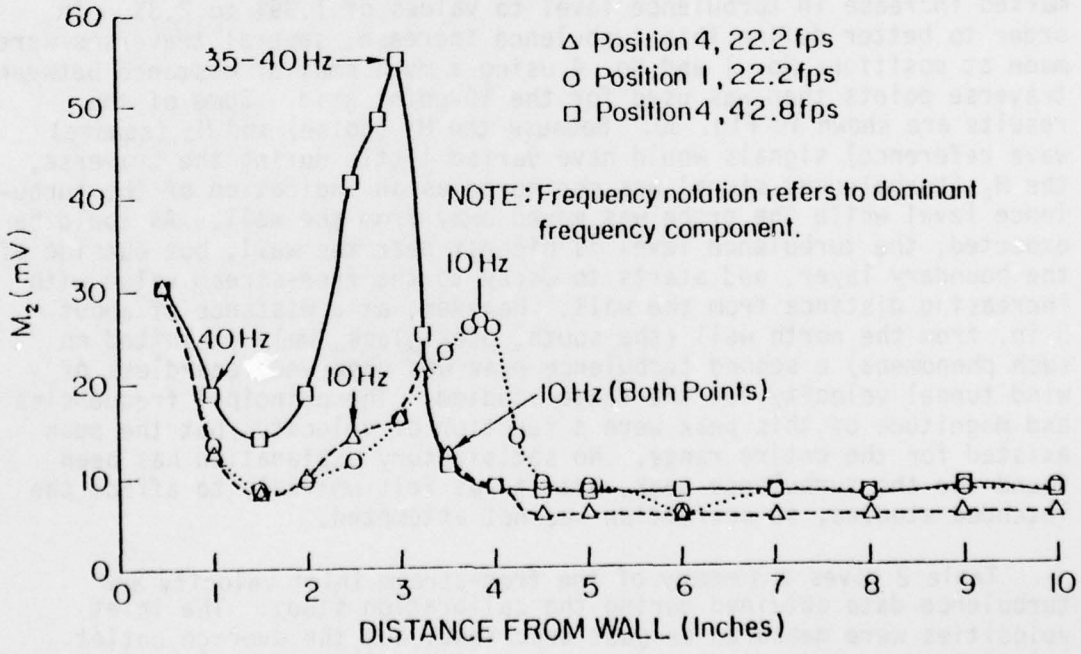

Figure 30. Variation of M_2 with Distance from Test Section North Wall

the average wind tunnel inlet and reference conditions. During April and May (when the studies were conducted), the average dry bulb temperature was found to be 68°F, varying from 66 to 71°F. The atmospheric pressure varied from 29.38 to 29.62 in. Hg with an average value of 29.55. These conditions resulted in an average atmospheric density of 0.074 lbm/ft^3. The average humidity ratio was 0.0080 (55% relative humidity), ranging from 0.0062 (45%) to 0.0094 (62%). Because these data were obtained during months approximating the average annual climatic conditions, the data should represent an overall average for the laboratory conditions encountered during the study.

As a result of the improvements made on the wind tunnel, the maximum free-stream velocity was increased to nearly 80% higher than that of previous studies.[15,109,110] At the same time, free-stream turbulence and wall vibration have been significantly reduced within the test section. The addition of transition section turning vanes has also greatly reduced the surge noted previously in the wind tunnel. Although reduced, some pressure fluctuations were still noted at the higher velocities of the calibration study. Observation of these fluctuations for periods of not less than one minute showed that the fluctuations of dynamic and static pressures measured by instruments mounted downstream of the transition section, and of the dynamic pressure upstream of the airfoils, was on the order of 1% for all velocities, with the highest reported fluctuation from a mean value being 1.7%. While no such data were taken for the previous wind tunnel configuration, this is known to be a significant improvement.

Once the turbulence calibration was completed, the turbulence spectrum was studied at the minimum and maximum velocities. A preliminary study using oscilloscope traces showed a predominate 10 Hz frequency component for a free-stream velocity of 42.8 fps. The full frequency spectrum from about 2 to 20,000 Hz (range restricted by hot-wire anemometer instrumentation including a 20 kHz low-pass filter) was then studied using a Federal Scientific Model UA-500 Ubiquitous Spectrum Analyzer and the Flow Corporation HWB-3 hot-wire anemometer. Because of the time and effort involved in studying the frequency spectra, complete data sets were taken only for free-stream velocities of 22.2 and 42.8 fps, representing the minimum and maximum upstream velocities planned for use during the study. To analyze the graphs obtained from the frequency spectrum analyzer, the data were punched on computer data cards and analyzed using a FORTRAN program (see Appendix B). In preparing these data cards, a uniform frequency interval was considered, but peaks were also included to make certain no important features were omitted. Peaks that occurred in the hot-wire output frequency spectra at 60, 120 Hz, etc., were ignored in analyzing the data as these have been attributed to electrical noise. Some of the results have been plotted in Figs. 31 and 32. By examining graphs for all four of the interior traverse points, it was found that data taken through instrument port No. 3 with an insertion depth of 15 in. most closely represents each of the other points and the average of all four for the velocities considered. For this reason, frequency

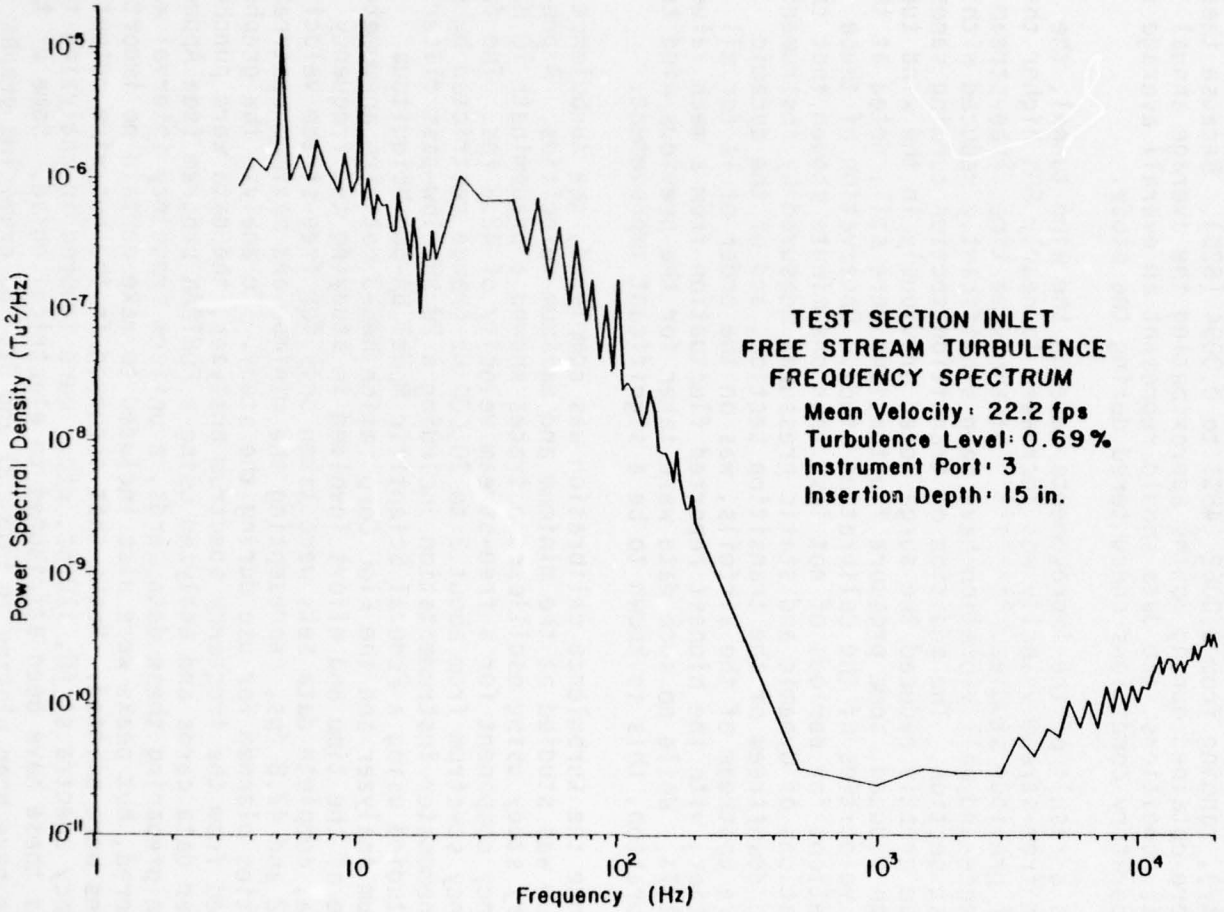

Figure 31. Test Section Inlet Turbulence Frequency Spectrum (U_∞ = 22.2 fps)

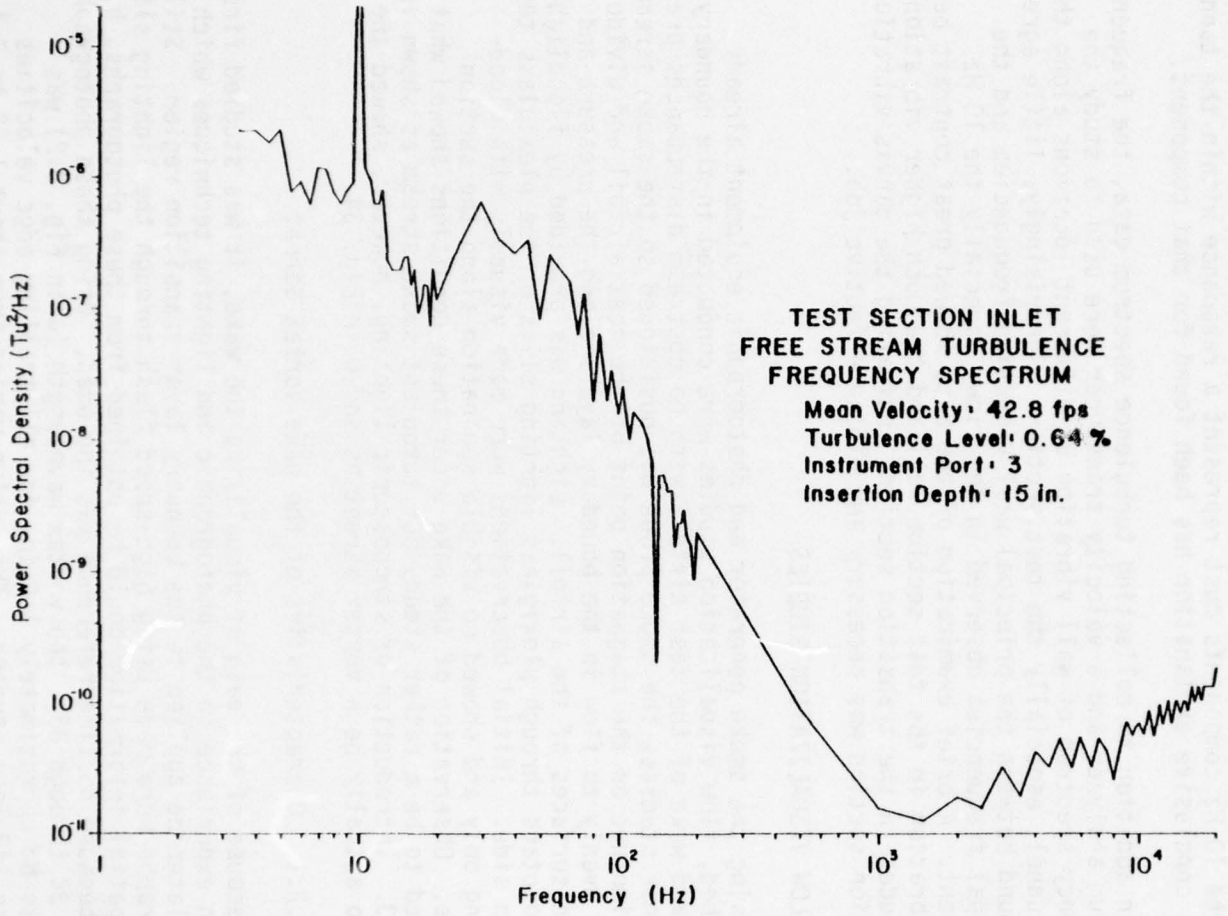

Figure 32. Test Section Inlet Turbulence Frequency Spectrum (U_∞ = 42.8 fps)

spectrum data taken at that position has been assumed representative of all four points.

By plotting Figs. 31 and 32 on logarithmic scales, the complete frequency spectra are shown. As can be seen in those figures, rather dominant frequency components occur at 10 Hz (and at 5 Hz for 22.2 fps). At higher frequencies, the amplitude drops considerably. It is assumed that the 10 Hz components must represent a resonance within the tunnel, but no conclusive explanation has been found for that component.

In addition to collecting turbulence spectrum data, the frequency spectrum analyzer and a velocity transducer were used to study the frequency spectrum of wall vibration at different locations along the wind tunnel, especially the test section. Surprisingly, little agreement was found between the principal wall vibration frequencies and the principal frequencies observed in the flow, especially the 10 Hz component. A brief examination of the data showed great contrast between the vibration in the test section wall and the much higher vibration amplitudes in the transition section, indicating the canvas vibration isolation section was necessary and did an effective job.

4.2 FLOW VISUALIZATION STUDIES

Using the smoke generator and photographic equipment already described, flow visualization studies were conducted in the boundary layer and wake of the test airfoil with no upstream distrubances present. For these studies, the smoke probe was positioned so the smoke stream would impinge on the stagnation point of the test airfoil and divide nearly evenly to flow in the boundary layers along the pressure and suction surfaces of the airfoil. Lighting was provided by floodlights or Strobotacs through plexiglass lighting slits or the plexiglass test section side. Initial observations were made visually with flood-lighting only and showed no visible separation along the suction surface. Observation of the wake under these conditions showed what appeared to be a rather steady but turbulent smoke stream as shown in Fig. 33. Introduction of stroboscopic lighting, however, showed the wake to actually be a vortex street as shown in Fig. 34.

4.2.1. Characteristics of the Wake Vortex Street

Because of the ease of visualizing the wake, it was studied first to gain experience in the photographic and lighting techniques which would later be applied to the boundary layer transition region. Still photographs were made using high-speed flash through the lighting slits. Only spatial information could be obtained from these photographs, however, because no time reference was included. Using these photographs (Figs. 34 through 36), the vortex wavelength (a in Fig. D.2) was found to be approximately 1.9 in. for all trailing edge velocities (74.0 to 143 fps) studied. This value varied from about 1.62 to 2.1 in. for specific vortex pairs, but the average for a given velocity appeared to always be around 1.9. The values for a_1 and h as defined

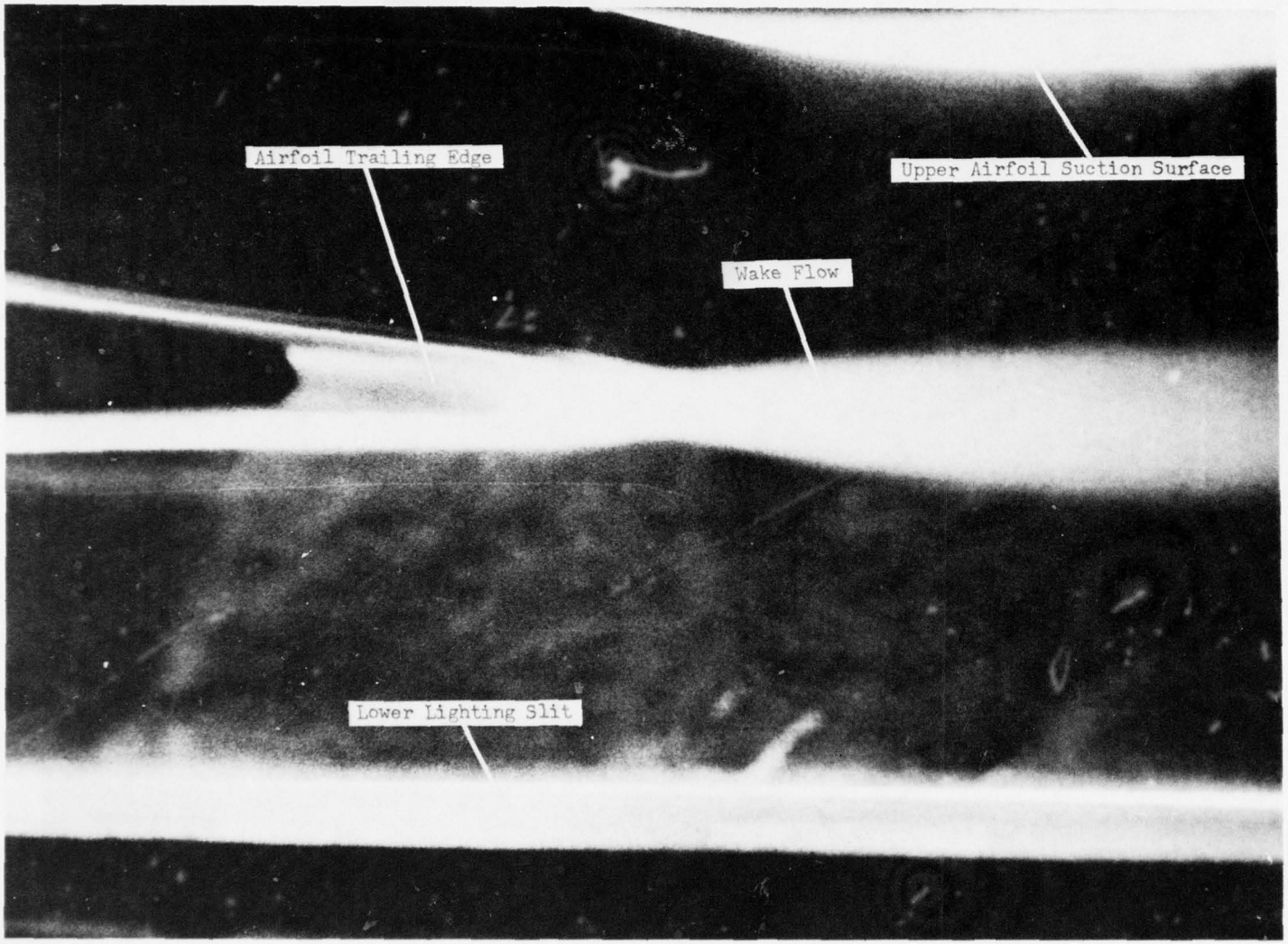

Figure 33 Airfoil Wake Appearance when Lit by Floodlights

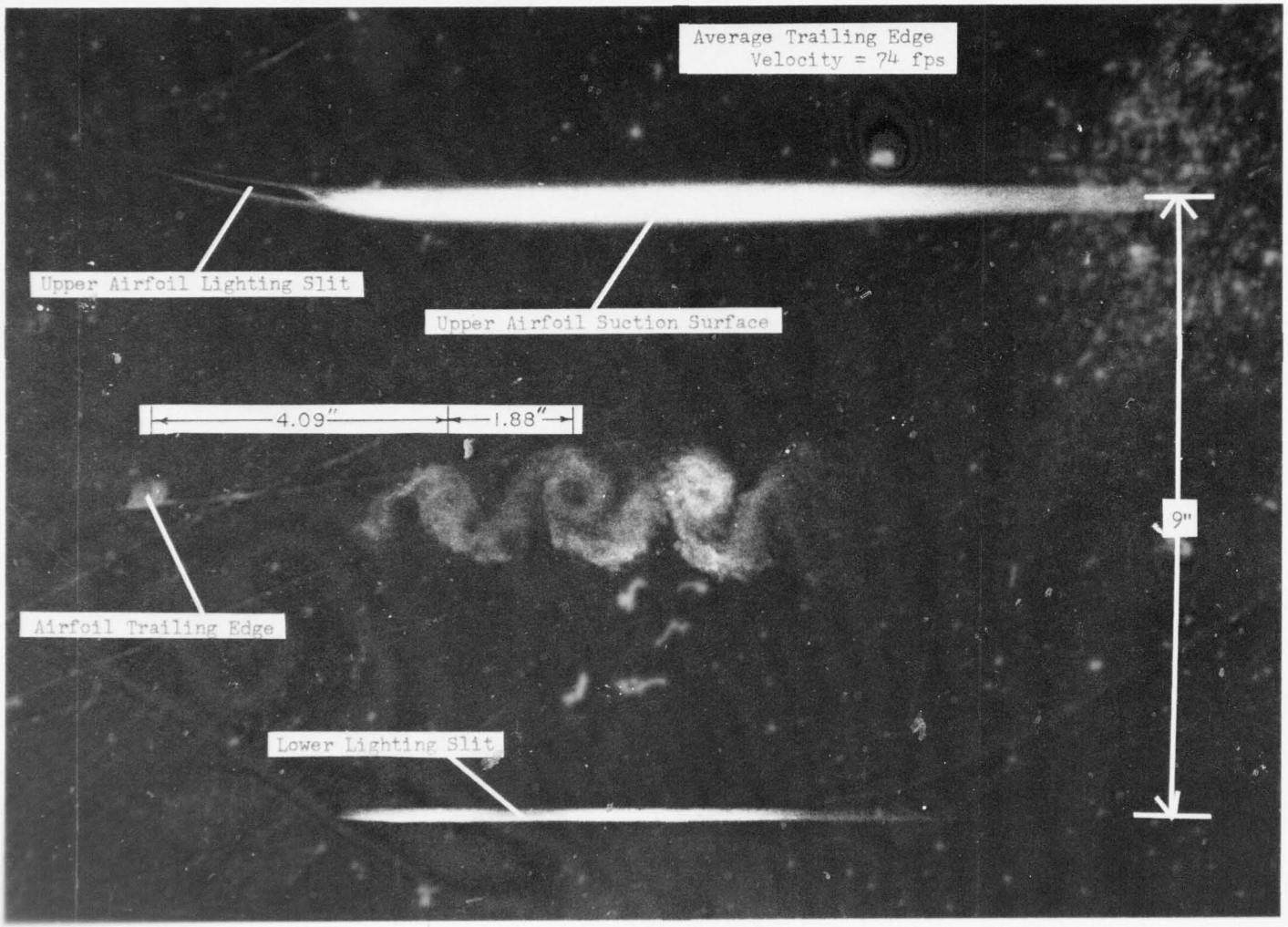

Figure 34 Wake Vortex Street as Seen with High-Speed Flash

AD-A075 501 OHIO STATE UNIV RESEARCH FOUNDATION COLUMBUS F/G 20/4
INVESTIGATION OF THE BOUNDARY LAYER BEHAVIOR ON TURBINE AIRFOIL--ETC(U)
AUG 79 L S HAN, W R COX, A CHAIT F33615-75-C-2052
UNCLASSIFIED OSURF-760256/784174 AFAPL-TR-79-2011 NL

2 OF 3
ADA 075501

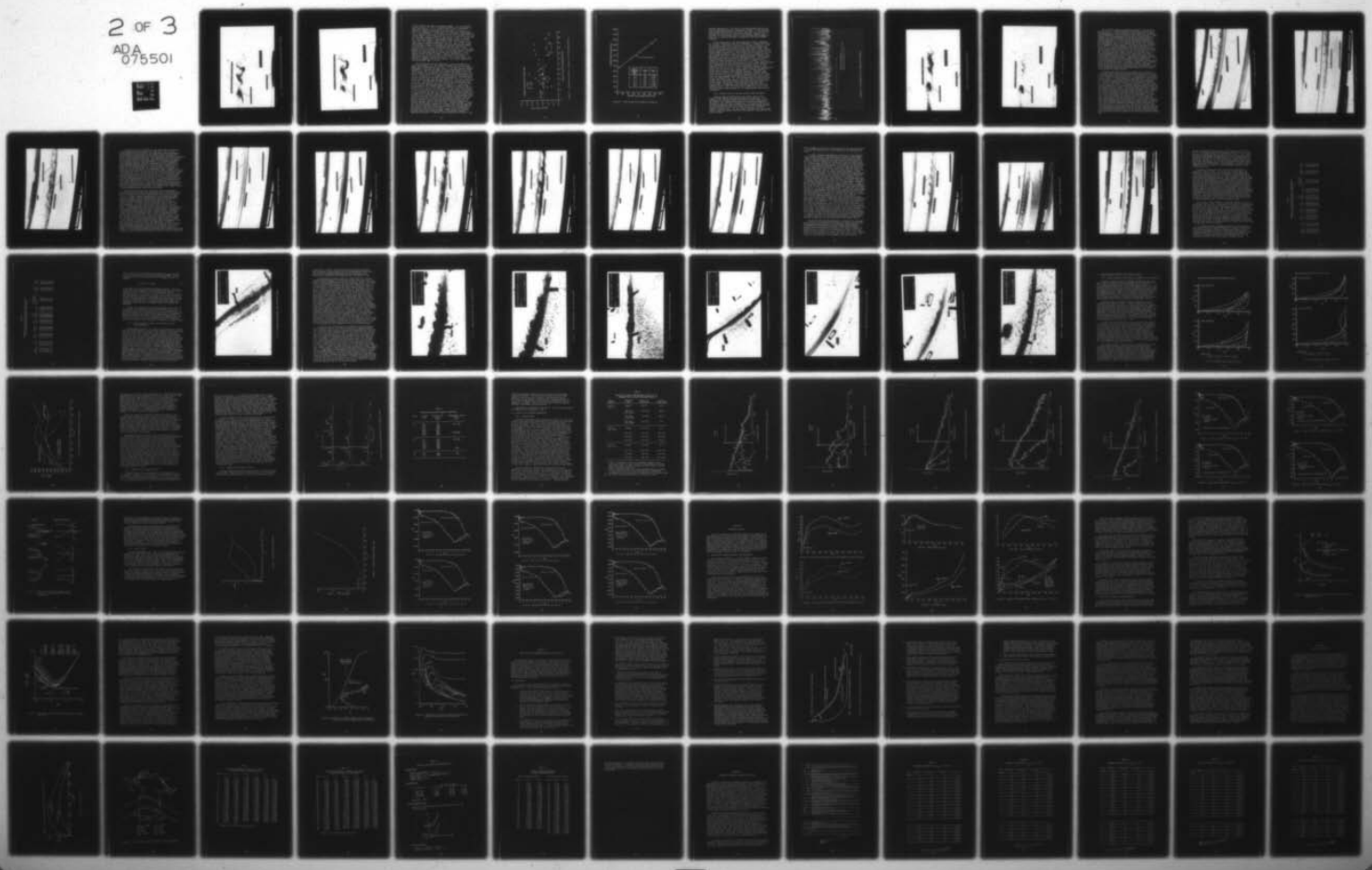

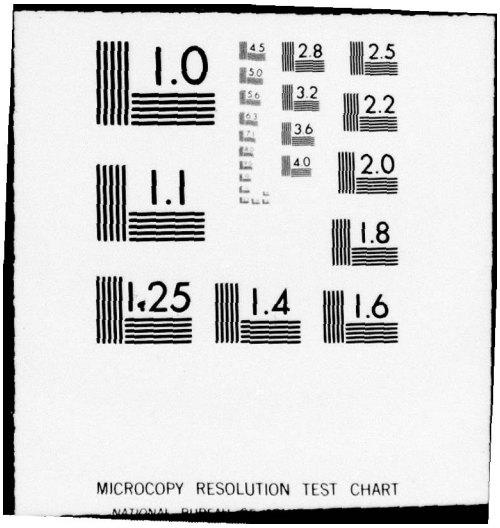
1.0
1.1
1.25
1.4
1.6
1.8
2.0
2.2
2.5
2.8
3.2
3.6
4.0
4.5
5.0
5.6
6.3
MICROCOPY RESOLUTION TEST CHART

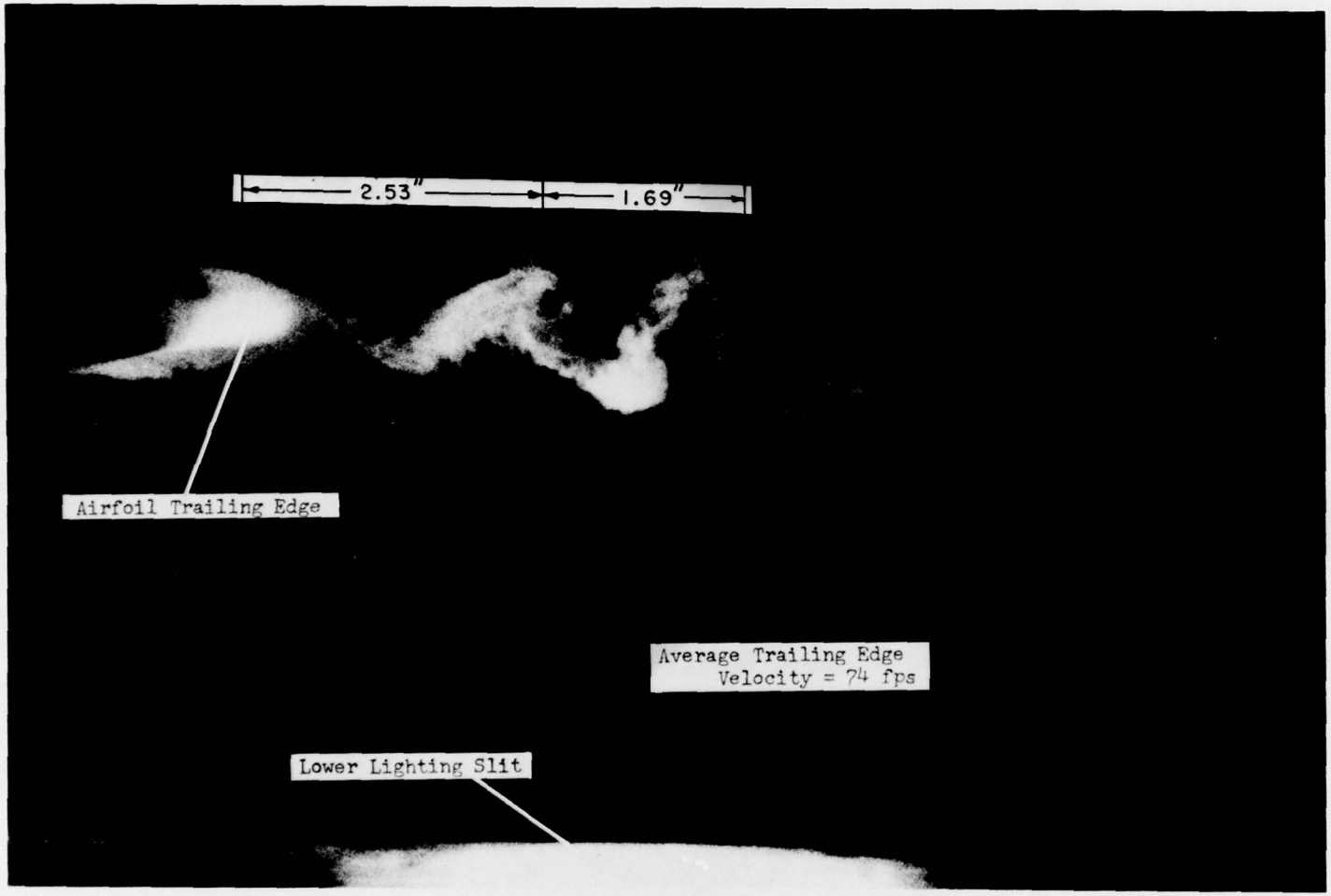

Figure 35 Wake Vortex Street (Average Trailing Edge Velocity = 74 fps)

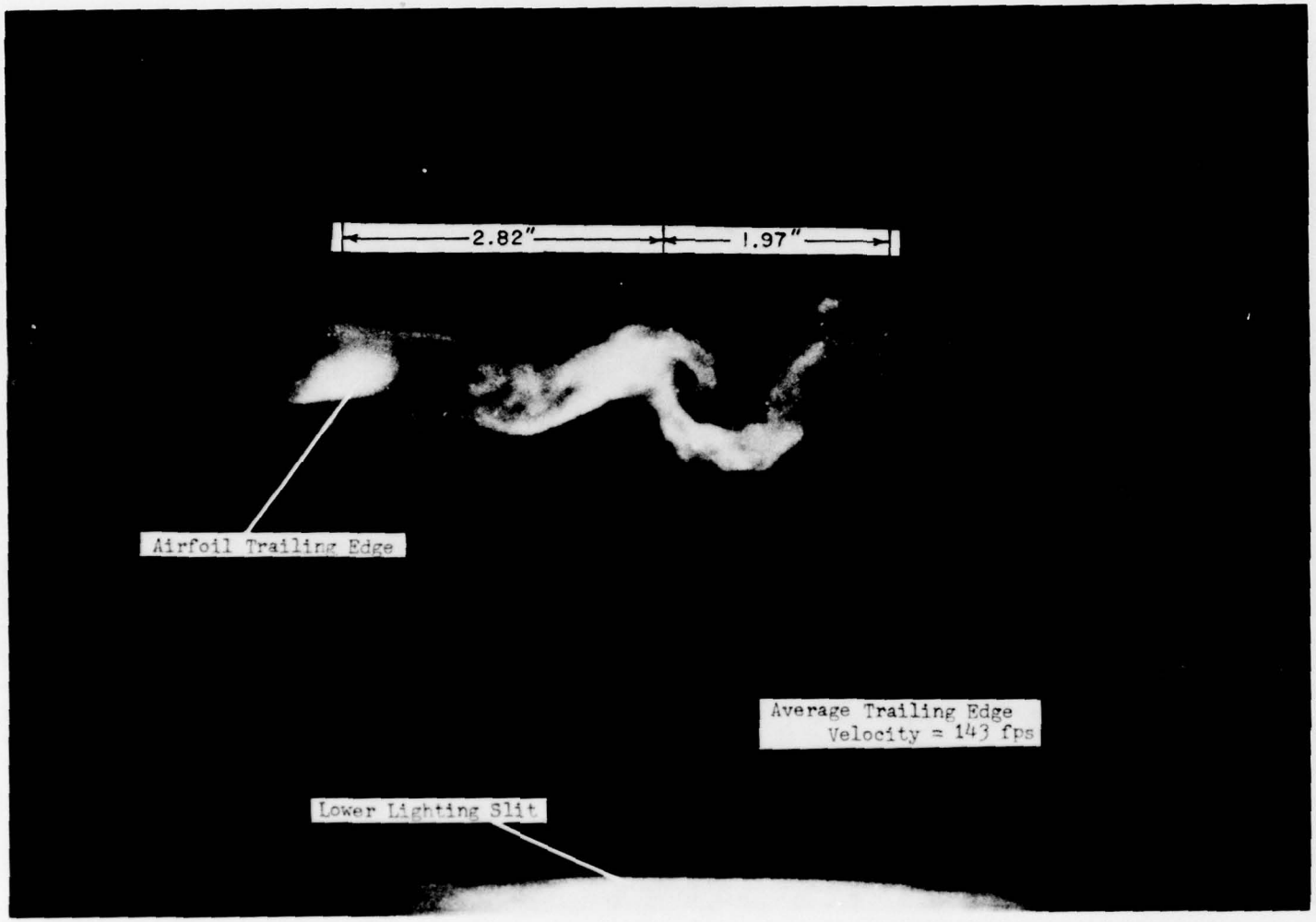

Figure 36 Wake Vortex Street (Average Trailing Edge Velocity = 143 fps)

in Fig. D.2 were not nearly so constant, however. For a true Karman vortex street, $a_1/a = 0.5$. Through examination of a large number of wake vortex photos, a_1/a was found to vary from 0.5 to 0.736. Generally, however, the average value was found to be approximately 0.57. This asymmetry is likely due to the difference in development of the two boundary layers which separate at the trailing edge to form the vortex street. Even the shapes of the vortices in each of the two rows are noticeably different as can be seen clearly in Figs. 34 through 36. From linear theory, a stable Karman vortex street ($a_1/a = 0.5$) occurs only for a spacing ratio (h/a) of 0.281. As discussed in the theory section, however, experimental data has shown various values with observed increases as distance from the trailing edge increases. As can be seen in Fig. 37, considerable variation exists in the spacing ratio as a function of distance from the airfoil trailing edge, especially for the highest velocity. For the lowest velocity (74 fps), however, the data does tend to average near the theoretical value, especially near the trailing edge. Accurate determination of the spacing ratio is difficult, however, especially at the higher velocities, because the smoke diffuses to such an extent that vortex centers are generally not sharply defined. This partly accounts for the large scatter seen in Fig. 37.

The vortices were visually observed at various frequencies by using the Strobotacs, but the highest frequency at which they would appear nearly stationary was only 10 Hz. To further study the temporal development of the trailing edge vortices, high-speed motion pictures (generally at 1000 to 1500 frames per second) were made by using the Fastax camera. By this method, the vortices were found to have a frequency of about 536 to 562 Hz for an average trailing edge velocity of 74 fps. To confirm this, an HWP-B hot-wire probe was inserted through the test section floor and positioned approximately 1.5 in. from the airfoil trailing edge along the wake centerline. The results are shown in Fig. 38. As can be seen from that figure, the frequency data confirms the values obtained from the high-speed movies. Using the data of Fig. 38 and a trailing edge radius of 0.355 in., a value of 0.46 was obtained for the Strouhal number as compared to values of approximately 0.21 for circular cylinders normal to the flow direction and of 0.18 for flat plates at zero incidence. In many studies, the maximum airfoil thickness has been used in determining the Strouhal number, but it appears likely that the local trailing edge radius may better represent the local conditions determining the vortex street characteristics. Support for this may be found in the assumption of Roshko[91] that the point of separation at the trailing edge determines the vortex row spacing (h) which in turn determines the vortex wavelength (a) to maintain maximum stability for the street. Likewise, Gongwer[128] found that the trailing edge thickness for a semicircular trailing edge was the critical length for determining frequency, while leading edge and tip dimensions exhibited little effect. As long as the separation points occur along the trailing edge, changes in the trailing edge thickness should thus produce changes in the shedding frequency. Heskestad and Olberts,[129] however, found considerable variation in the

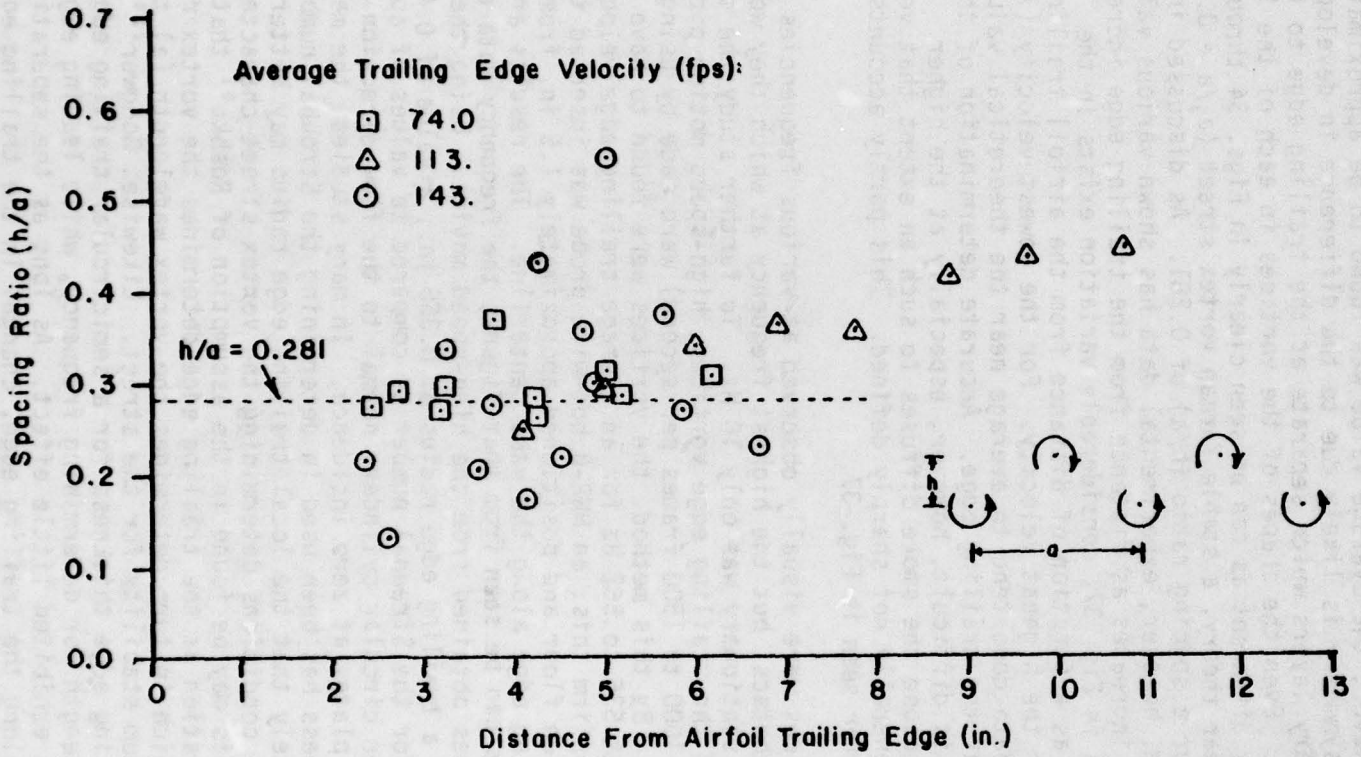

Figure 37. Vortex Spacing Ratio as a Function of Trailing Edge Distance

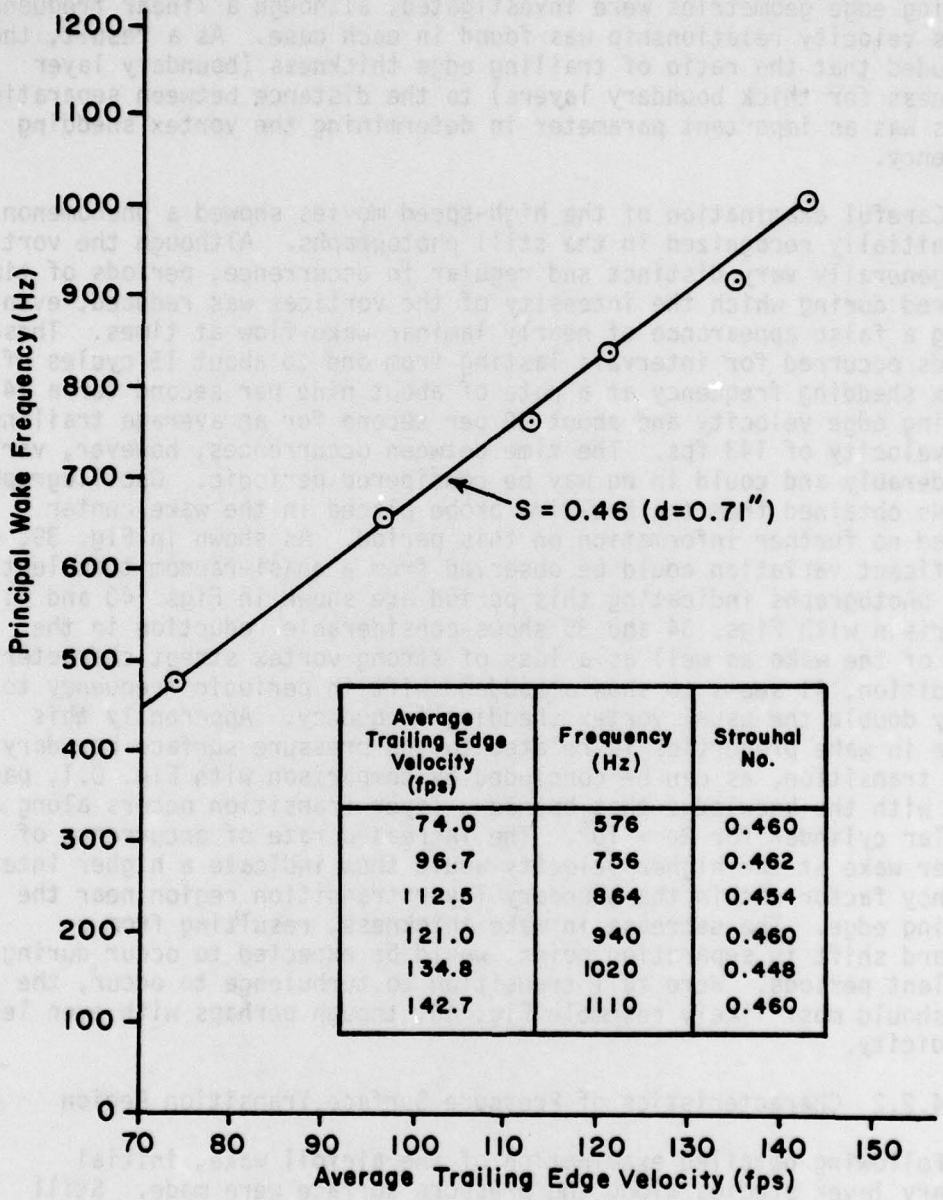

Average Trailing Edge Velocity (fps)	Frequency (Hz)	Strouhal No.
74.0	576	0.460
96.7	756	0.462
112.5	864	0.454
121.0	940	0.460
134.8	1020	0.448
142.7	1110	0.460

Figure 38. Airfoil Wake Vortex Shedding Frequencies

shedding frequencies of a flat plate of uniform thickness when various trailing edge geometries were investigated, although a linear frequency versus velocity relationship was found in each case. As a result, they concluded that the ratio of trailing edge thickness (boundary layer thickness for thick boundary layers) to the distance between separation points was an important parameter in determining the vortex shedding frequency.

Careful examination of the high-speed movies showed a phenomenon not initially recognized in the still photographs. Although the vortices were generally very distinct and regular in occurrence, periods of time occurred during which the intensity of the vortices was reduced, even giving a false appearance of nearly laminar wake flow at times. These periods occurred for intervals lasting from one to about 15 cycles of the vortex shedding frequency at a rate of about nine per second for a 74 fps trailing edge velocity and about 30 per second for an average trailing edge velocity of 143 fps. The time between occurrences, however, varied considerably and could in no way be considered periodic. Oscillograph records obtained from the hot-wire probe placed in the wake center yielded no further information on this period. As shown in Fig. 39, no significant variation could be observed from a quasi-random turbulent signal. Still photographs indicating this period are shown in Figs. 40 and 41. Comparison with Figs. 34 and 35 shows considerable reduction in the width of the wake as well as a loss of strong vortex street characteristics. In addition, 41 seems to show a sudden shift in periodic frequency to nearly double the usual vortex shedding frequency. Apparently this change in wake properties is related to the pressure surface boundary layer transition, as can be concluded by comparison with Fig. D.1, page along with the knowledge that boundary layer transition occurs along a circular cylinder for $Re > 10^5$. The increased rate of occurrence of the thinner wake at the higher velocity would thus indicate a higher intermittency factor within the boundary layer transition region near the trailing edge. The decrease in wake thickness, resulting from a rearward shift in separation point, would be expected to occur during turbulent periods. Were full transition to turbulence to occur, the wake should most likely resemble Fig. 40, though perhaps with even less periodicity.

4.2.2 Characteristics of Pressure Surface Transition Region

Following detailed examination of the airfoil wake, initial boundary layer studies along the pressure surface were made. Still photographs of the smoke streaks were taken at various stations along the surface, with reference being made to the static tap numbering indicated in Figs. 14 and 15, respectively. High speed flash was used for these photographs, with the lights placed to shine through the test section plexiglass side wall at an angle of about 30 to 40° with respect to the lens axis. This was necessary because slit lighting was found to give poor contrast resulting from excessive illumination of the airfoil surface.

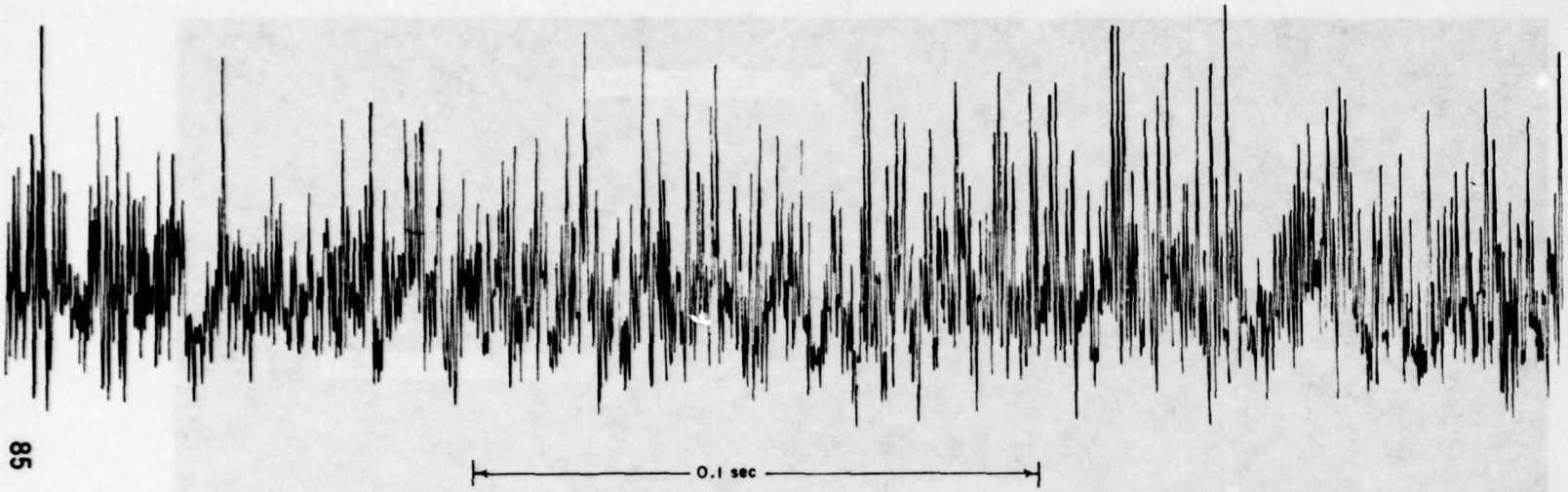

Wake Hot-Wire Anemometer Signal
Probe Located 2" Downstream of Airfoil Trailing Edge
Average Trailing Edge Velocity = 143 fps

Figure 39. Oscillograph Trace of Wake Hot-Wire Signal

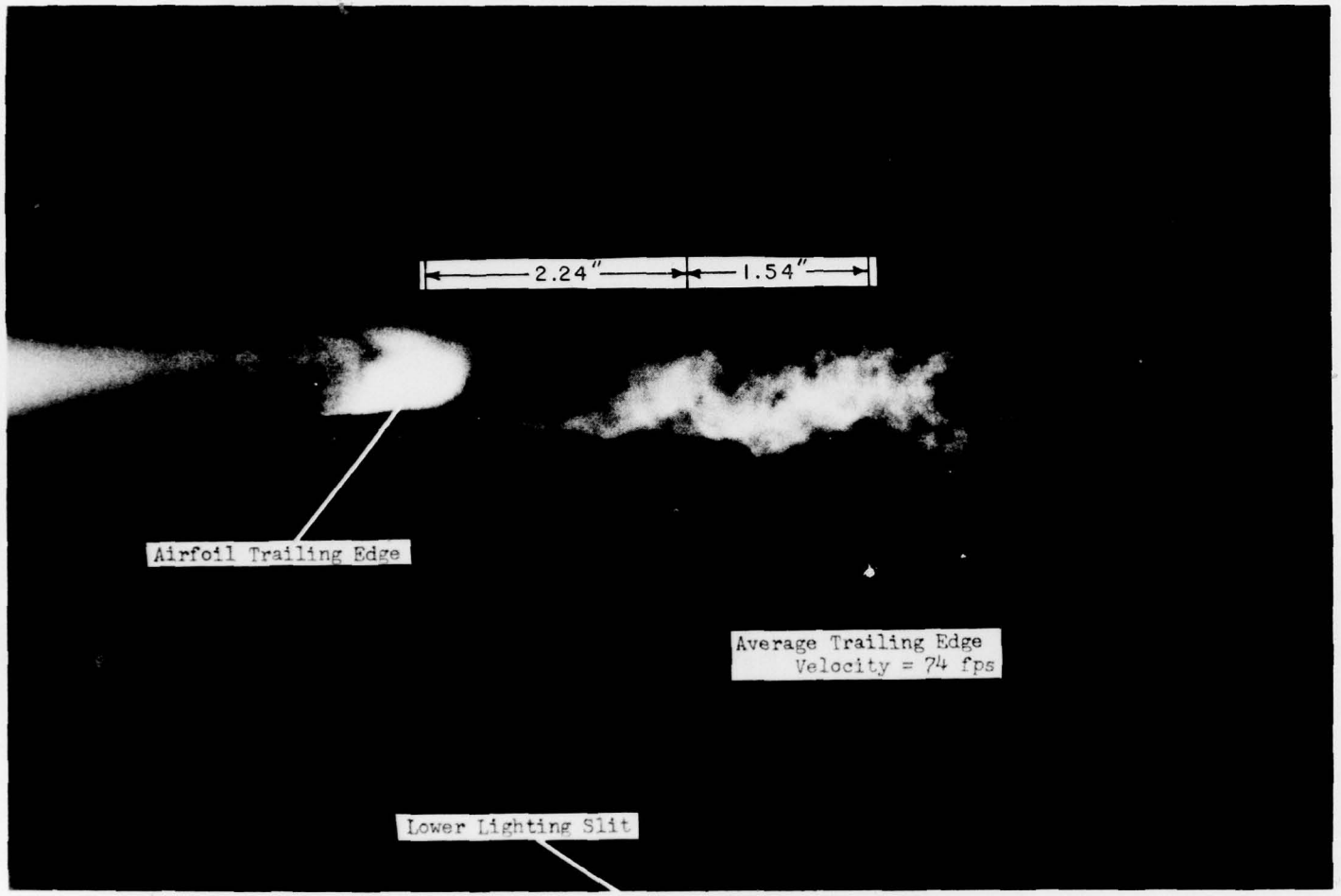

Figure 40 Wake with Reduced Vortex Activity

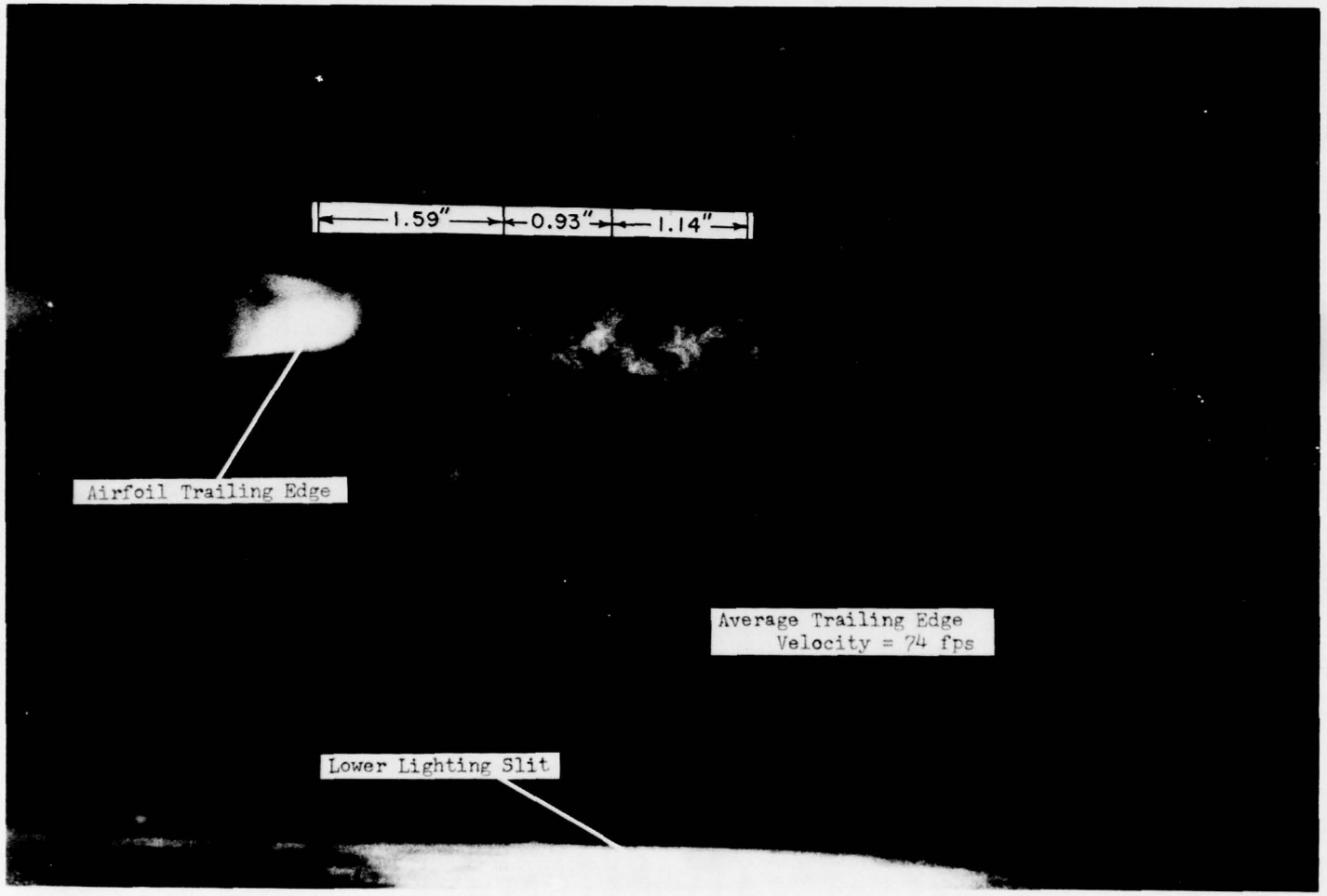

Figure 41 Wake, Showing Frequency Shift

One of the more dramatic photographs obtained in this manner is shown in Fig. 42. In this photograph, the sequence of events during the deformation of a Gortler vortex pair may be observed. As shown through hydrodynamic flow visualization along concave surfaces in other studies,[54,79-82] the deformation of the Gortler vortices appears to resemble amplified Tollmien-Schlichting waves superimposed on the original vortex pair. In fact, some of the regions identified by Knapp and Roache[25] (Fig. 1) for Tollmien-Schlichting transition may be correlated with some of the features shown in Fig. 42. Regions R_1 and R_2 (possible R_2 only, because of the pre-existing Gortler instability) of Fig. 1 would correspond to the initial appearance and growth of the traveling (Tollmien-Schlichting) waves along the vortex pairs as seen in the left side of Fig. 42. In the right of Fig. 42, the traveling waves then proceed to break into turbulent flow. As already mentioned, several other recent studies have also noted Tollmien-Schlichting characteristics following the growth of Gortler vortices along a concave surface. Indeed, Tani[54] suggested that transition along a concave surface resembled Tollmien-Schlichting transition observed for flat plate flow in the presence of pre-existing spanwise velocity variations. In addition, Cumsty,[5] using a hot-wire probe along a turbine airfoil model pressure surface, observed frequency characteristics (high frequency bursts superimposed on slugs of low-speed flow) resembling Tollmien-Schlichting transition downstream of Gortler vortex formation.

Through visual observation of the boundary layer flow with a stroboscopic light source, the developing vortices were found to take on the appearance of an expanding helix. This observation is very much similar to those of Bippes and Gortler[82] for hydrodynamic flow along a concave surface. In a two-dimensional photograph such as Fig. 42, the amplified waves superimposed on the vortices bear some resemblance to the profile reported by Mitchner[26] for the growth of a turbulent spot along a solid surface. In addition, Steurer[130] reported a similar sawtooth appearance as T-S waves deformed three-dimensionally along an ogive-nosed circular cylinder. On the other hand, this may be only the appearance of the helix pattern when shown two-dimensionally. Because of the narrow dimension of the smoke stream impinging on the airfoil, only two or three adjacent Gortler vortices may be observed at one time in any of the smoke flow visualization photographs. As can be seen in Fig. 42, however, even adjacent vortices do not appear to develop and deform at exactly the same rate. In that figure, the upper vortex shows an earlier amplification of the Tollmien-Schlichting waves and a subsequent earlier breakdown to turbulent flow. Likewise, Figs. 43 and 44 show considerable difference in the development of adjacent vortices. In Fig. 43, one of the vortices is nearly turbulent, while the adjacent vortex appears to show only weak amplification of the Tollmien-Schlichting wave. In Fig. 44, one of the vortices has again broken down into nearly turbulent flow while the adjacent vortex shows the district periodic pattern of the amplified Tollmien-Schlichting wave.

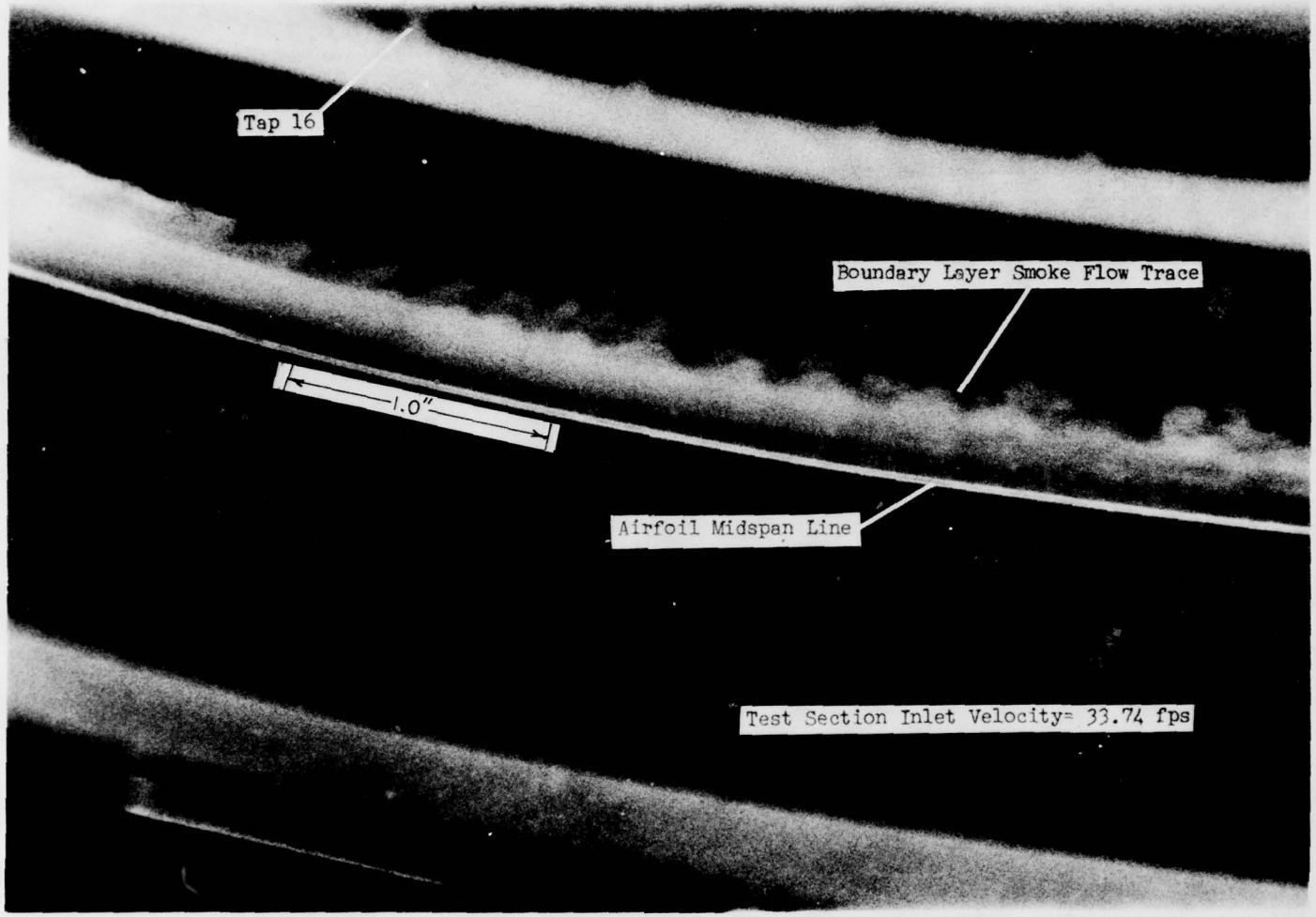

Figure 42 Boundary Layer Transition Region

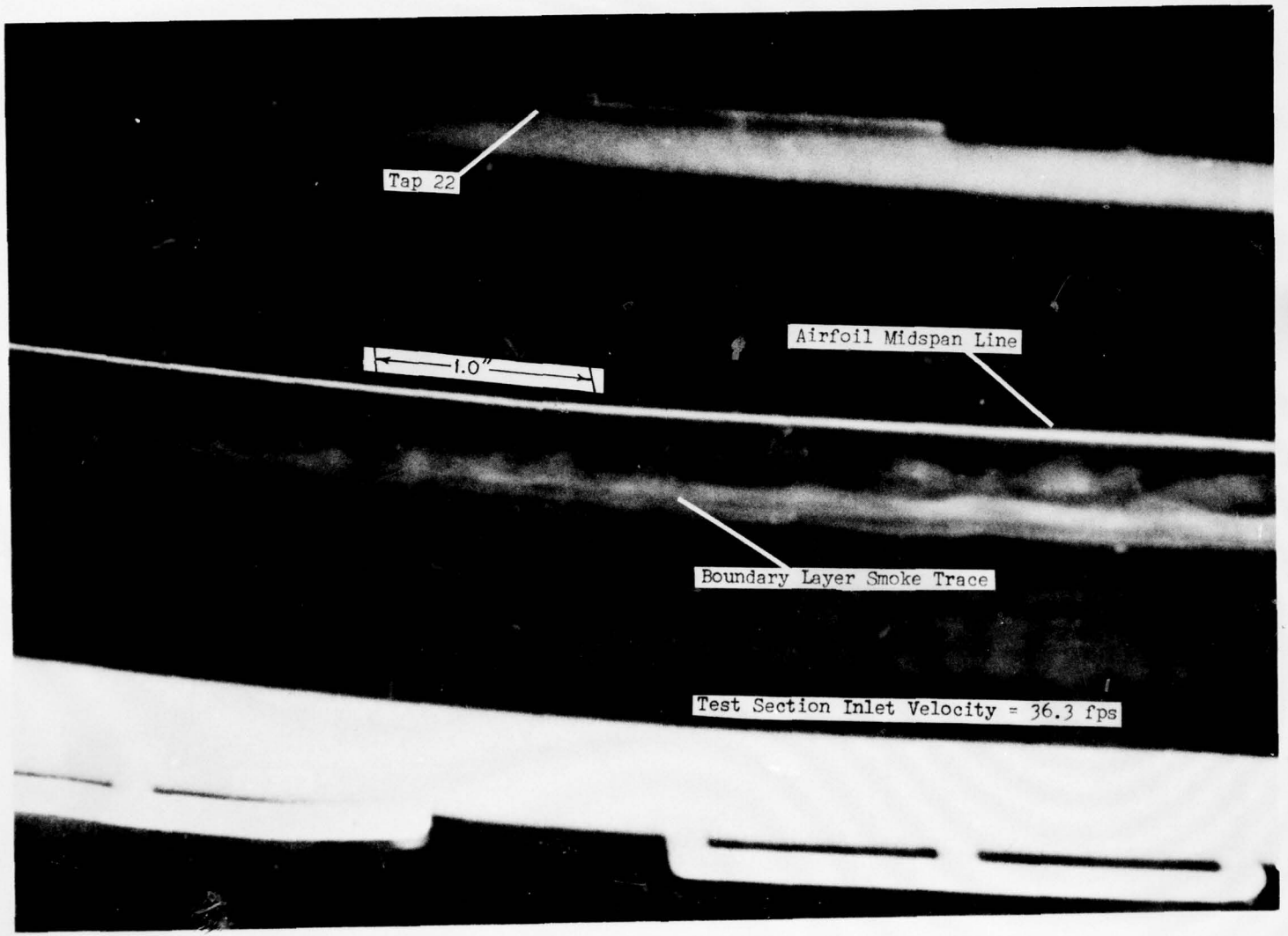

Figure 43 Boundary Layer Transition Region

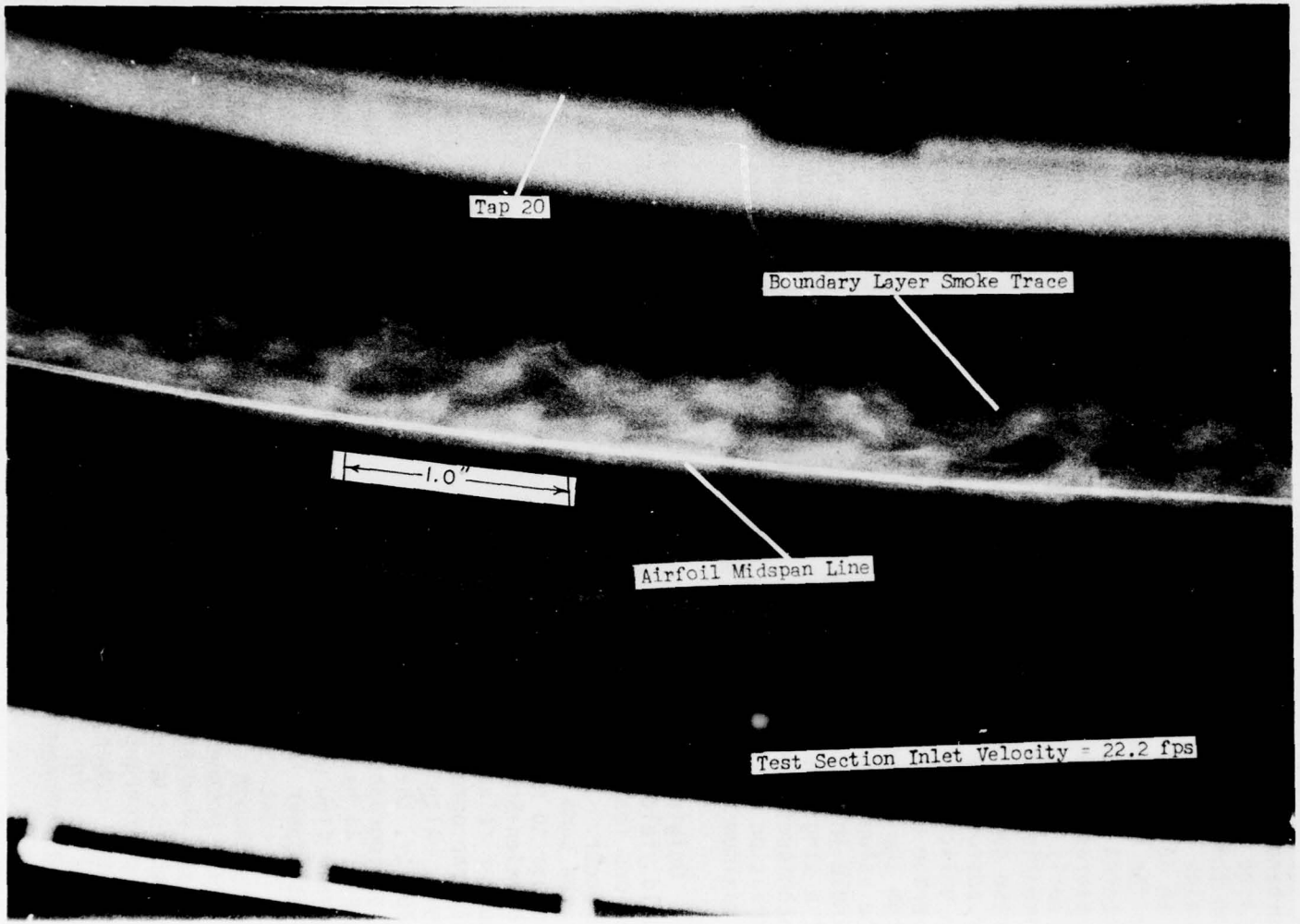

Figure 44 Boundary Layer Transition Region

By measuring the still photographs, some characteristic dimensions of the boundary layer disturbances have been found. When the disturbance growth is roughly equal in two adjacent vortices, measurements may be made in a plane parallel to the airfoil surface using Fig. 14, and the corresponding markings seen in the photographs to establish reference scales in each coordinate direction. One important dimension in dealing with Gortler vortices is the vortex spacing, or wavelength, as measured in the spanwise direction (the wavelength, λ_G, is twice the measured spacing between adjacent vortices). Unfortunately, this dimension is measurable only when two adjacent vortices of similar dimensions show clearly in a given photograph. It is thus possible to obtain this dimension from very few of the many photographs studied. However, from these data it was found that the spacing is relatively constant with a value of approximately 0.3 in. In fact, no distinct trend was seen with changes in velocity, with values lying within 20% of 0.3 in. being found as the average at each of the four inlet velocities studied. Values measured from the photographs ranged from 0.24 to 0.47 in. with more than half of the values lying between 0.27 and 0.33 in. It should be noted that for a single inlet velocity (22.2 fps) the values ranged from 0.25 to 0.47 in. at a single surface position. Using china clay and talcum powder erosion techniques, Cumsty[5] was able to obtain traces showing vortex wavelength variation across the entire blade span of a turbine airfoil model, finding a maximum wavelength about three times the minimum.

Originally it was hoped that a composite of still photographs would yield information about the approximate spatial locations at which various features of the transitioning boundary layer might be expected to occur. Instead, series of photographs (Figs. 44 through 50) taken at the same spatial location showed features ranging from apparently laminar to nearly turbulent flow despite the fact that periodic (Tollmien-Schlichting) waves were observed visually just prior to shutter release. In order to display photographs from a single film, only photographs for a test section inlet velocity of 22.2 fps are shown. Although dimensions and locations may be expected to vary with velocity, the general shape of features in these figures is representative of photographs taken for the full velocity range studied. The details in Fig. 44 have already been discussed. Figures 45 and 46 show nearly laminar flow within the boundary layer. Small Tollmien-Schlichting waves appear in the right of Fig. 45 while no waves are visible in Fig. 46. In contrast, Figs. 47 and 48 show nearly turbulent boundary layer flow although some of the periodicity clearly shown in Figs. 42 and 44 is still present. Even more interesting were several photographs in the same set showing apparently laminar flow downstream of Tollmien-Schlichting waves (in contrast with Fig. 45) as shown in Figs. 49 and 50. These photographs would seem to indicate that transition in this case follows a sequence somewhat resembling that described by Knapp and Roache[24,25] for Tollmien-Schlichting transition, where a group of amplified T-S waves proceeds downstream and eventually breaks up into fully turbulent

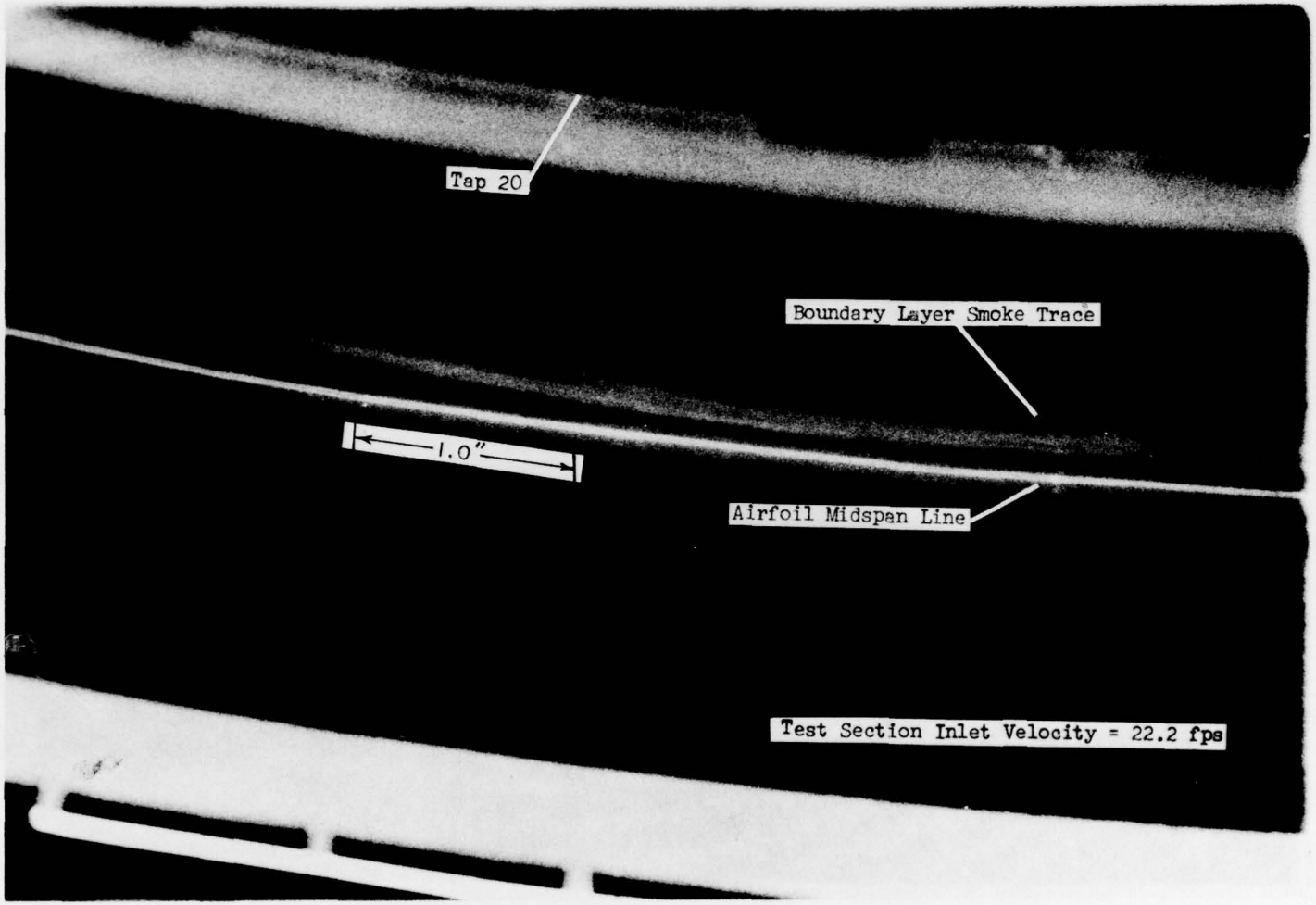

Figure 45 **Boundary Layer Transition Region**

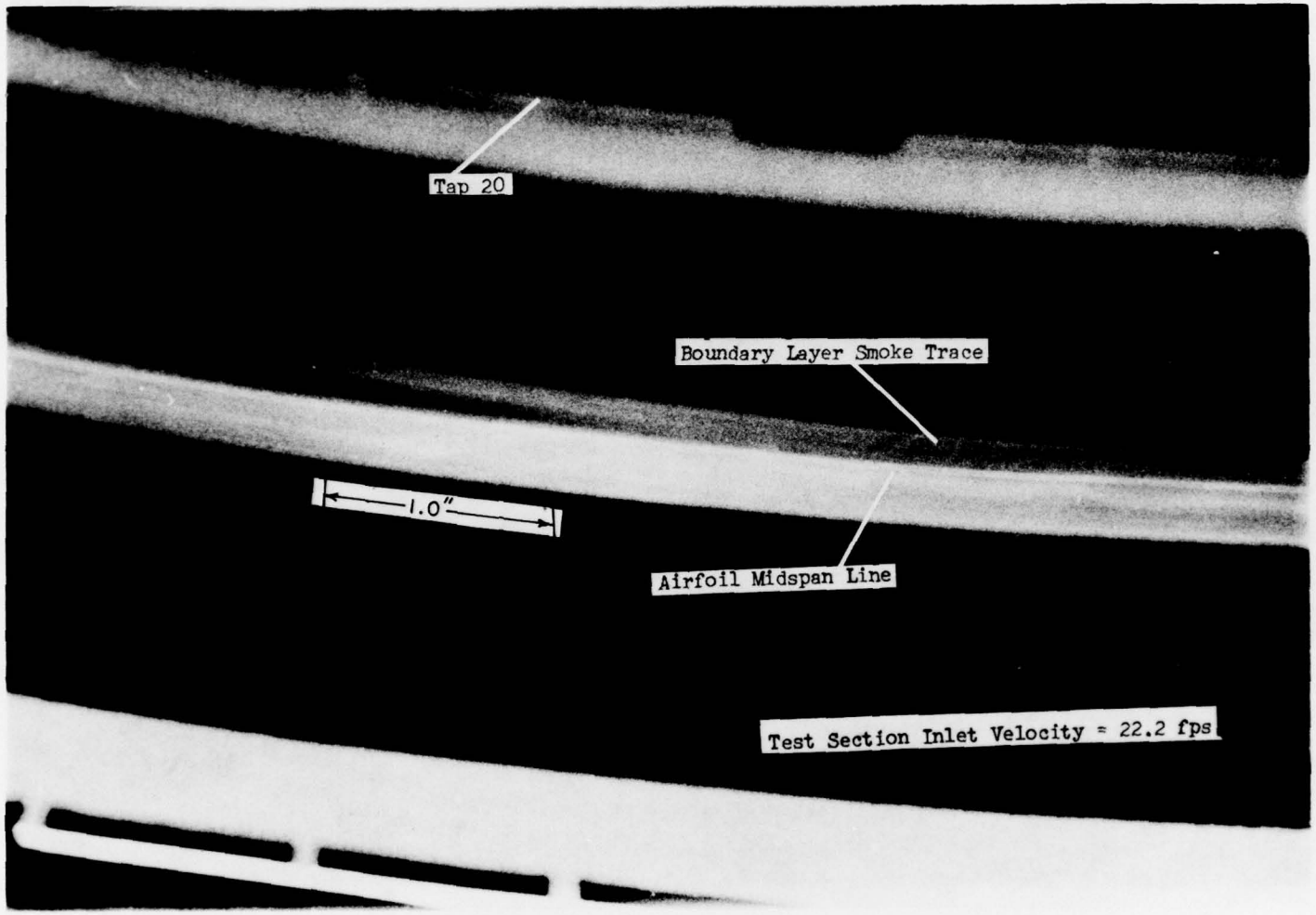

Figure 46 Boundary Layer Transition Region

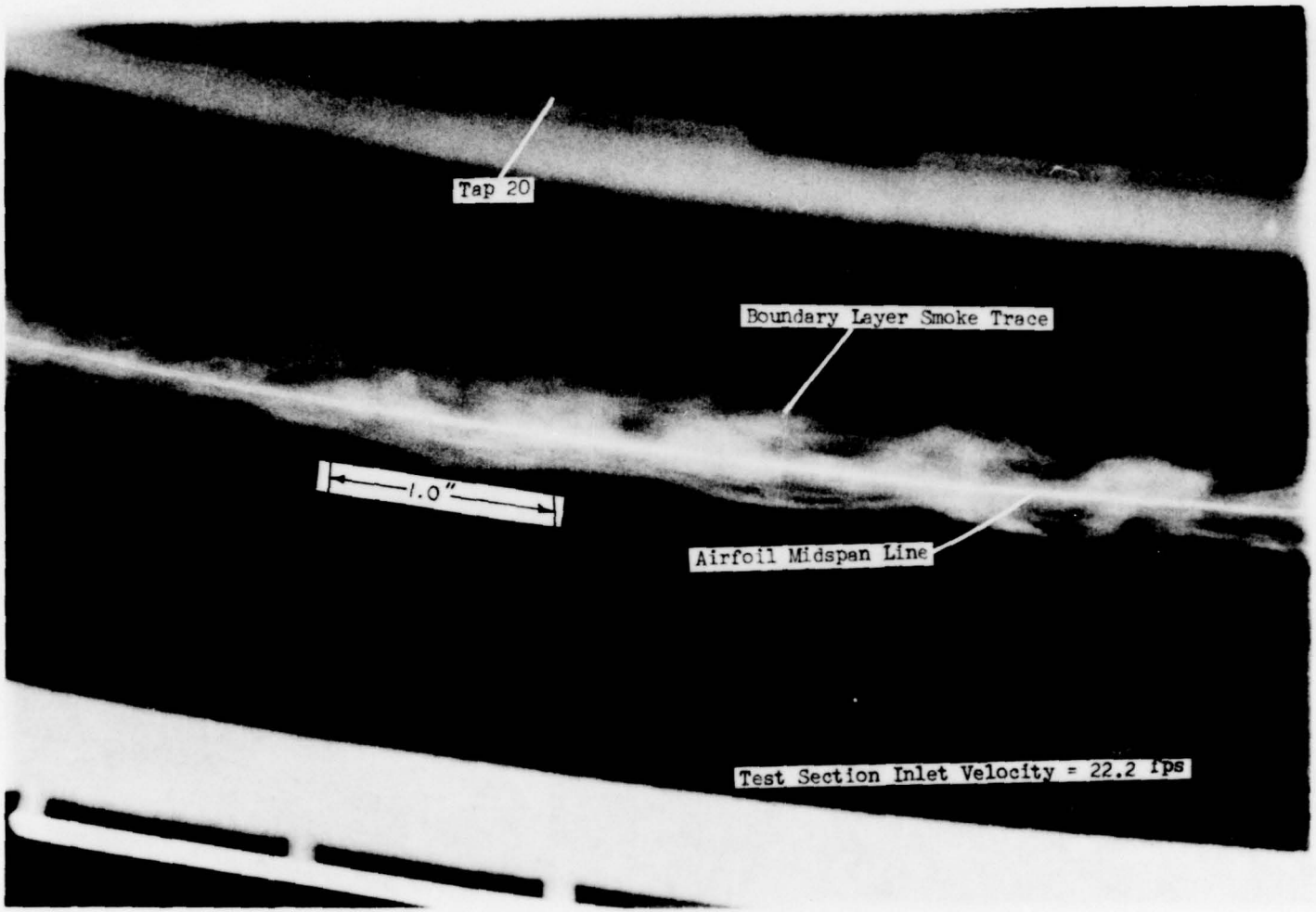

Figure 47 Boundary Layer Transition Region

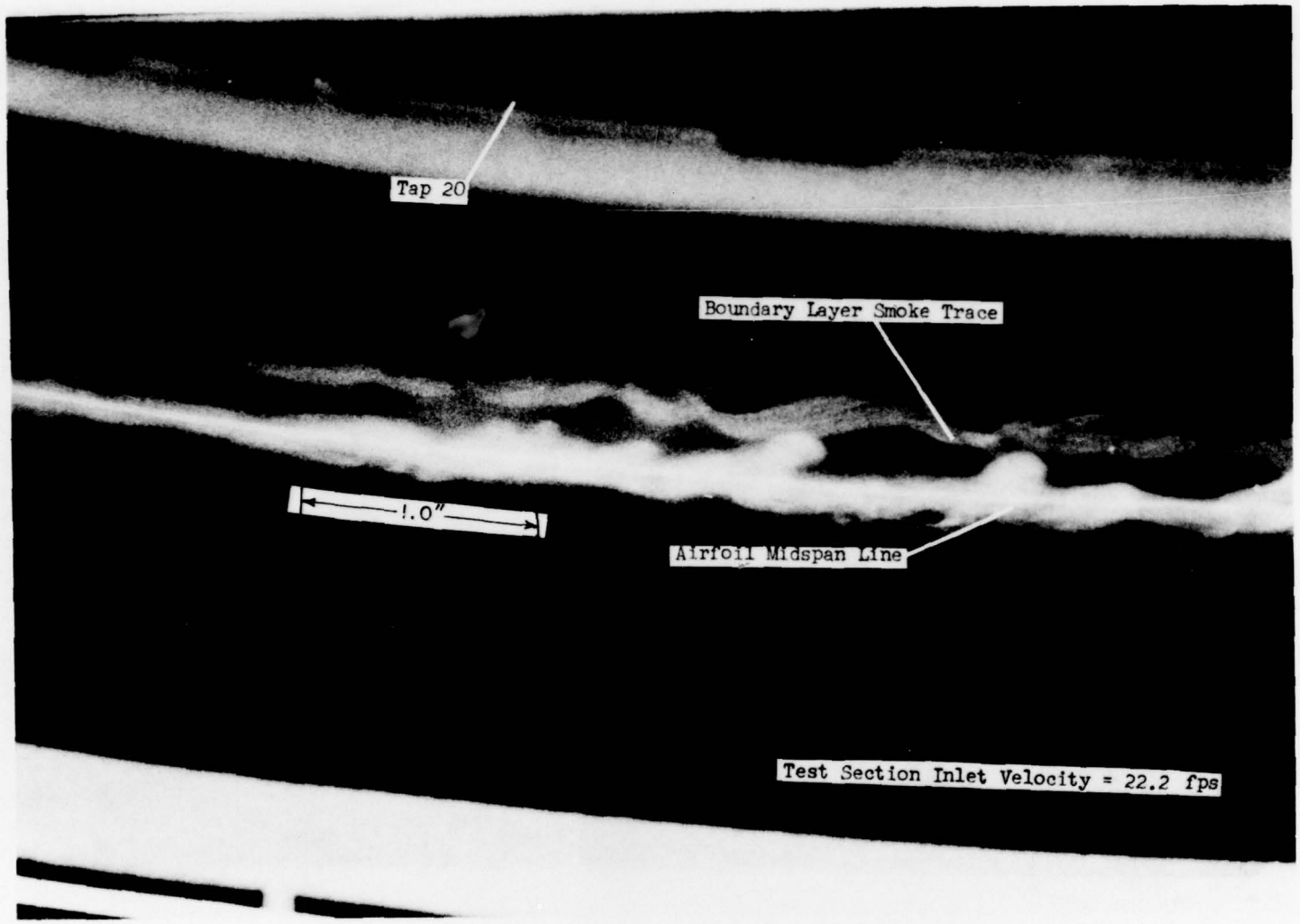

Figure 48 Boundary Layer Transition Region

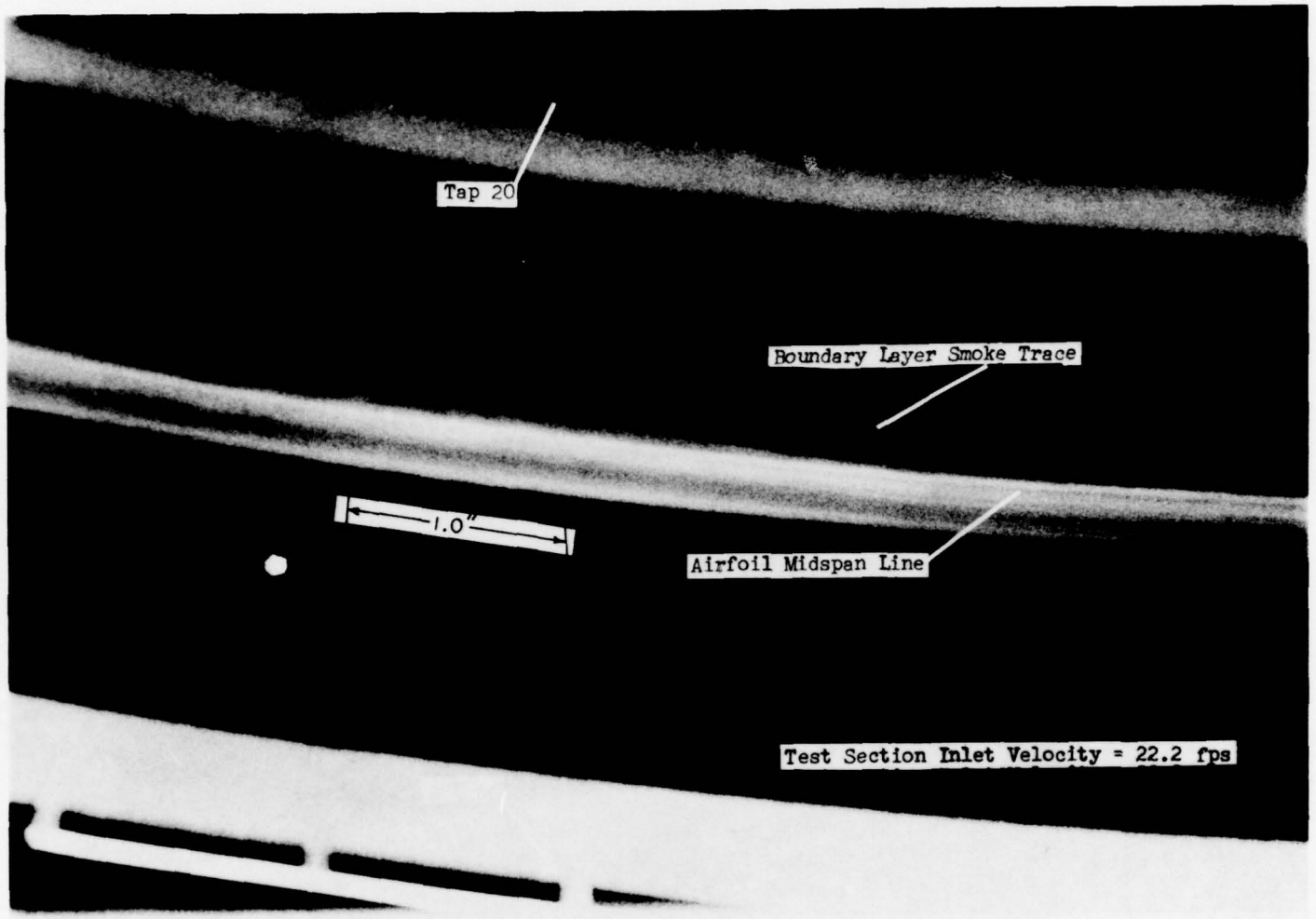

Figure 49 Boundary Layer Transition

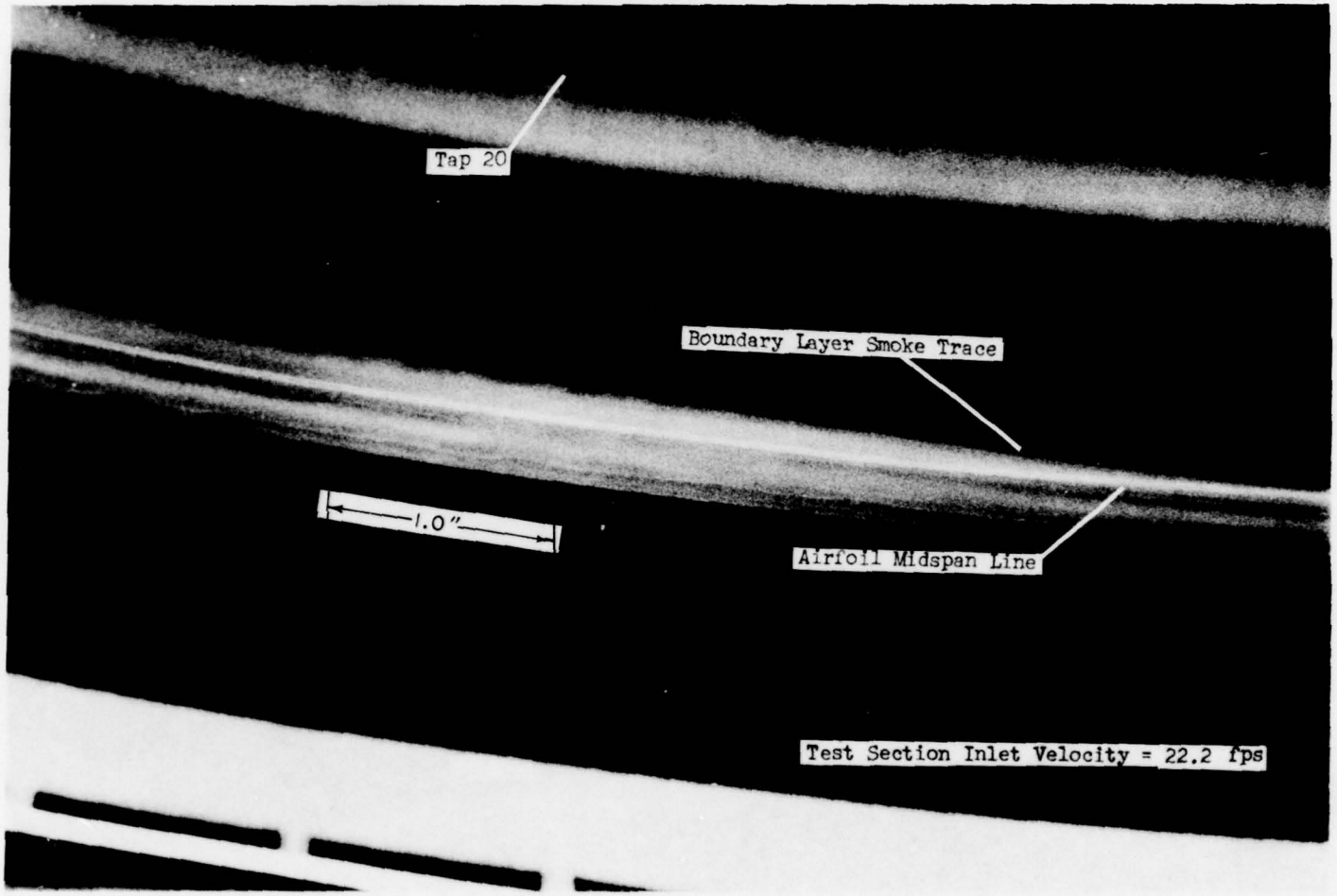

Figure 50 Boundary Layer Transition Region

flow, followed by a period of time during which the transition region is essentially laminar prior to the formation of the next group of waves.

In order to better understand the time history of the boundary layer transition region, high-speed motion pictures (1000 to 4000 frames per second) were taken at various stations along the airfoil surface. These were made only for test section inlet velocities of 22.2 and 42.8 fps. Because of problems with lighting intensity and the higher frequencies present, the films taken at an inlet velocity of 42.8 fps proved to be much harder to analyze and less information has thus been obtained from them. In order to study the films on a frame-by-frame basis (even for the lower inlet velocity studied, the frequencies were too high for regular projection speeds), a hand-operated editor was used. One of the first observations obtained from the films is that groups of Tollmien-Schlichting waves proceed downstream, breaking up into nearly turbulent flow, although a fully turbulent boundary layer was never observed. These groups were found to consist of as few as one or two or as many as fifteen or more waves, in agreement with observations from the still photographs. Between each of these groups was a period of nearly laminar flow. At both of the velocities studied, the earliest appearance of the waves seemed to be at tap 13 (s/C = 0.33) although they occurred more regularly around tap 16 (s/C = 0.47) and further downstream. In addition to the groups of waves, a low frequency variation of the boundary layer smoke stream thickness appeared to take place starting around tap 8 (s/C = 0.10). This variation was in the form of a traveling wave. When the crest of this wave was somewhere between taps 13 (s/C = 0.33) and 17 (s/C = 0.51), the previously mentioned wave (Tollmien-Schlichting) groups were found to form. Rarely were these events out of phase with each other. The frequency of this wave was found to vary considerably for a given inlet velocity. At a test section inlet velocity of 22.2 fps, the frequency was found to vary from about 20 to 54 Hz with most occurrences giving values of 20 to 35 Hz. For an inlet velocity of 42.8 fps, the frequency was much higher, with a value of about 65 Hz being found. As mentioned before, however, difficulties with the higher speed movies prevented comprehensive data from being obtained. The source of these low frequency waves was not found, although there is a possibility that they may somehow be excited by surface pressure variations caused by trailing edge vortex shedding, by free-stream velocity fluctuations, or even by the transition process itself.

The Tollmien-Schlichting wavelengths, as measured in the streamwise direction, were fortunately much easier to obtain than were the Görtler wavelengths because a single photograph could show many occurrences (Fig. 51) with only a single Gortler vortex visible. However, the Tollmien-Schlichting wave is more likely to change its wavelength and/or frequency as it progresses downstream, while the Görtler vortex wavelength may remain relatively fixed. This change is likely to occur, because the Tollmien-Schlichting wave speed ($\lambda_{TS}f$) is likely to be proportional to the boundary layer edge velocity. In

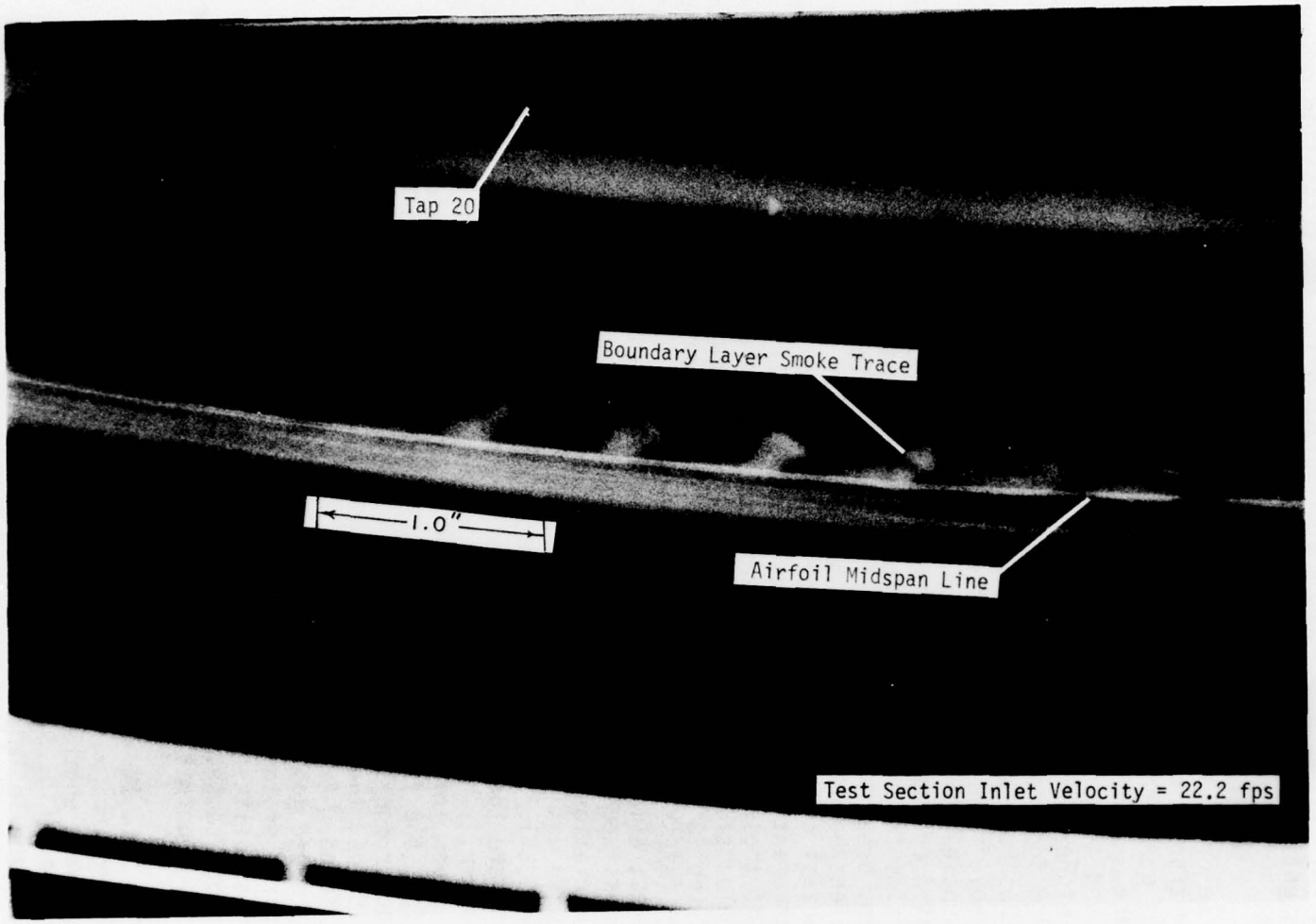

Figure 51 Boundary Layer Transition Region

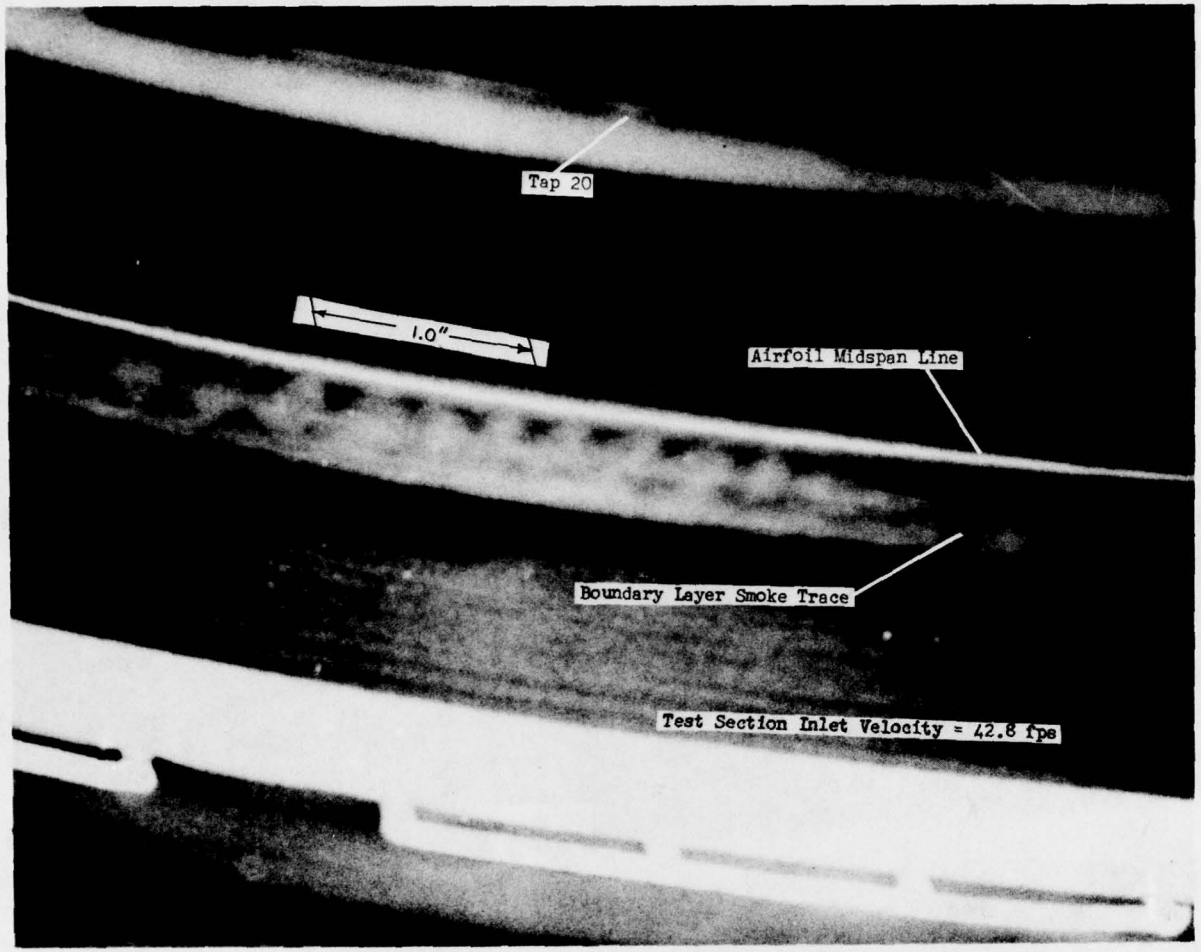

Figure 52 Boundary Layer Transition Region

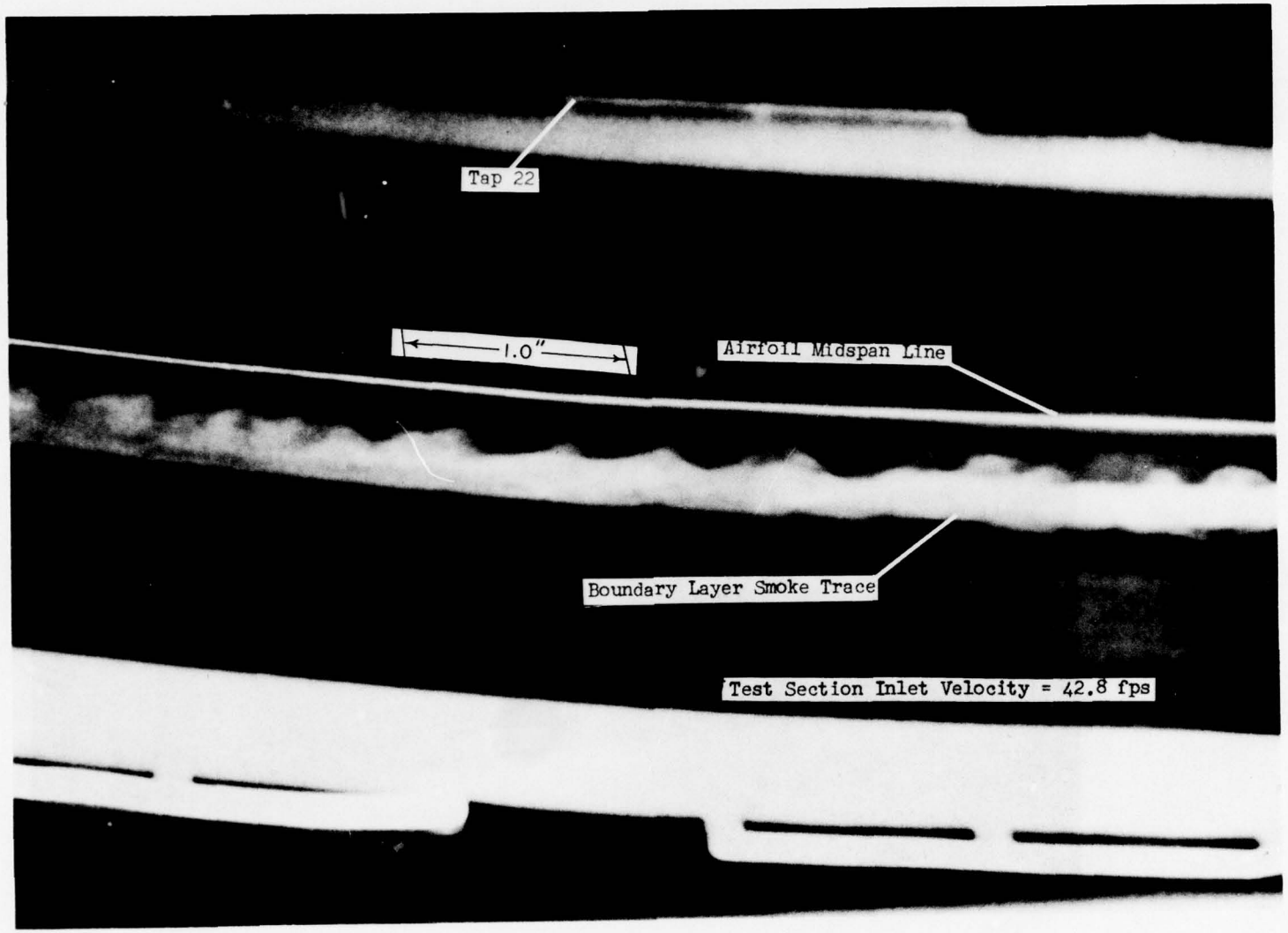

Figure 53 Boundary Layer Transition

addition, frequency shifts may occur, as seen clearly in the left of Fig. 51. By using the static tap reference lines of Fig. 14, a scale may easily be obtained along the center of the airfoil. This is done by drawing lines between corresponding static tap reference marks and noting the intersections along the center line. These intersections represent a spacing of 1 in. over most of the concave surface. Using this scale, the spacing (λ_{TS}) of the Tollmien-Schlichting waves may be obtained by direct measurement of the photographs. As can be seen by comparison of Fig. 52 with Fig. 51 the wavelength decreases as the velocity increases.

A summary of observations made from the still photographs is presented in Tables 3 and 4. As can be seen in those tables, the value of λ_{TS} tends to increase with increasing distance downstream. Also, with the exception of taps 15 through 17, the wavelength tends to decrease with increasing velocity. Taps 15 through 17 may not represent a significant departure from the trends, however, because the data of Table 3 for those locations was obtained from a single photograph which may not have represented accurately the average value. Most of the available data for an inlet velocity of 22.2 fps were found downstream of tap 18. Through analysis of the high-speed motion pictures the wave speed ($\lambda_{TS} f_{TS}$) was found to be nearly equal to or slightly greater than the local boundary layer edge velocity. The wave speed at a given spatial location was found to be relatively constant, especially when compared with the frequency and wavelength data which varied considerably. The wave speed approximately equal to the edge velocity contrasts sharply with a wave speed of 35% of the edge velocity found by Heckl and Jackson[45] as being the most likely to lead to transition initiated by amplification of Tollmien-Schlichting waves.

As a result of these findings, a calculated frequency (U_e/λ_{TS}) is presented in Tables 3 and 4. Because the value given for λ_{TS} represents an average value, the calculated frequency is expected to represent an average value at that position. The frequency data obtained from the motion pictures somewhat comfirm this. For a test section inlet velocity of 22.2 fps, the observed frequencies were found to vary from 563 to 840 Hz with an average value of 657 Hz at tap 19, and from 660 to 1080 Hz with an average value of 931 Hz at tap 22. As already discussed, motion picture data for an inlet velocity of 42.8 fps were rather incomplete, but showed a frequency somewhere around 2000 Hz at tap 22. As can be seen in Figs. 52 and 53, even still photographs of the smoke are much less distinct at the higher velocity, making visualization data that much more difficult to obtain.

In a combined hot-wire anemometer and smoke flow visualization study similar to that of Knapp and Roache,[24,25] Steurer[130] found that, for Tollmien-Schlichting transition along an ogive-nosed circular cylinder, the frequency varied as the 3/2 power of the velocity and as surface distance to the -0.6 power. Using average wavelengths of 0.392 in. at an inlet velocity of 42.8 fps and 0.538 in. at 22 fps (from data in Tables 3 and 4) along with an average value of

TABLE 3

SUMMARY OF TOLLMIEN-SCHLICHTING WAVELENGTH DATA
(TEST SECTION INLET VELOCITY = 22.2 fps)

Tap Interval	U_e (fps)	$\lambda_{TS_{min}}$ (in.)	$\lambda_{TS_{max}}$ (in.)	$\lambda_{TS_{avg}}$ (in.)	$\frac{U_e}{\lambda_{avg}}$ (1/sec)	s (ft)	$\frac{(U_e/\lambda_{avg})}{(U_e^{3/2}/s^{1.3})}$	δ_2 ($\times 10^{-4}$) (ft)	$\frac{\lambda_{avg}}{\delta_2}$
15-16	22.0	0.198	0.264	0.239	1104.6	0.777	7.71	8.99	22.2
16-17	24.6	0.215	0.339	0.256	1153.1	0.858	7.75	9.01	23.7
18-19	30.5	0.404	0.657	0.525	697.14	1.022	4.26	8.82	49.6
19-20	34.3	0.417	0.887	0.628	655.41	1.104	3.71	8.57	61.1
20-21	38.7	0.379	0.848	0.642	723.36	1.187	3.75	8.28	64.6
21-22	43.3	0.309	1.323	0.691	752.0	1.270	3.60	8.07	71.3
22-23	48.9	0.343	1.167	0.717	818.4	1.353	3.54	7.97	75.0
23-24	55.5	--	--	0.609	1093.6	1.437	4.23	8.07	62.9

TABLE 4

SUMMARY OF TOLLMIEN-SCHLICHTING WAVELENGTH DATA
(TEST SECTION INLET VELOCITY = 42.8 fps)

Tap Interval	U_e (fps)	$\lambda_{TS_{min}}$ (in.)	$\lambda_{TS_{max}}$ (in.)	$\lambda_{TS_{avg}}$ (in.)	$\frac{U_e}{\lambda_{avg}}$ (1/sec)	s (ft)	$\frac{(U_e/\lambda_{avg})}{(U_e^{3/2}/s^{1.3})}$	δ_2 ($\times 10^{-4}$) (ft)	$\frac{\lambda_{avg}}{\delta_2}$
15-16	44.24	0.245	0.406	0.319	1164.2	0.777	4.08	6.43	41.0
16-17	49.41	0.282	0.415	0.362	1637.9	0.858	3.87	6.49	46.5
17-18	52.22	0.298	0.585	0.399	1660.8	0.940	3.84	6.42	51.8
18-19	61.99	0.292	0.604	0.383	1942.2	1.022	4.11	6.30	50.7
19-20	69.77	0.310	0.577	0.399	2098.3	1.104	4.10	6.12	54.3
20-21	78.59	0.292	0.666	0.412	2289.0	1.187	4.11	5.92	58.0
21-22	88.22	0.252	0.557	0.434	2439.3	1.270	4.01	5.73	63.1
22-23	99.79	0.305	0.539	0.427	2804.4	1.353	4.16	5.53	64.3

0.46 in. at 36.3 fps, and letting the parameter ($cU_{inlet}/\lambda TS$, where c is an arbitrary constant) represent the average frequency, the frequency was found to vary almost directly with $U_{inlet}^{3/2}$, yielding the relation

$$U_{inlet}/\overline{\lambda}_{TS} = 5\,U_{inlet}^{1.5} \tag{19}$$

in agreement with the relationship presented by Steurer. The calculated local average frequency, however, was found to vary with surface distance to the -1.3 power. This is represented by the term $[(U_e/\lambda_{avg})/(U_e^{1.5}/^{1.3})]$ in Tables 3 and 4. The fact that the values for this term are more consistent at the higher inlet velocity (42.8 fps) is not surprising, because the wavelengths were also found to be more uniform in photographs taken at that velocity, perhaps because of the nearness to full transition. As opposed to use of this term, the wavelength might instead be associated directly with boundary layer dimensions.

In order to investigate the relationship between wavelength (λ_G) and boundary layer momentum thickness, the quantity (λ_{avg}/δ_2) was calculated at each station (Tables 3 and 4). The value used for δ_2 is that calculated for an assumed laminar boundary layer (see Appendix C). Because the boundary layer would likely grow more rapidly within the transition region than for the calculated laminar boundary layer, the variation of λ_{avg}/δ_2 with surface distance may be less if measured velocity profiles were used to determine the momentum thickness integral.

4.2.3. Surface Roughness Effects on the Pressure Surface Transition Region

The techniques involved in the study of the boundary layer development under the influence of various surface roughnesses were essentially similar to those used for the smooth surface studies. High-speed flashes were utilized, aligned at an angle of 30^o to 40^o with respect to the lens axis. This study was somewhat more comples than previous studies, as detailed results produced in the smooth surface studies were more difficult to achieve in the rough surface studies, because of the interfering small turbulent wakes which originated immediately beyond sand particles, starting sometimes close to leading stagnation point. It was almost impossible to recognize whether a turbulent wake behind a certain particle was responsible for a complete breakdown of the laminar boundary layer, or had no influence at all, as it was completely dissipated somewhere downstream of the particle. The high-speed photographs emphasize this special feature of the distributed roughness. Figure 54 shows an upstream view of the boundary layer with grit #12, where many small roughness wakes are originating very close to the surface and are mixing with other wakes, resulting in what can be seen as an overall blur close to the surface. Careful examination of this photograph did reveal important additional information concerning the type of transition

Figure 54 **Rough Surface Boundary Layer Transition Region**

experienced. A group of Tollmien-Schlichting traveling waves were superimposed on a quite unclear, but still recognizable, Gortler wave and can still be observed downstream, forming an expanding helix mentioned in the smooth surface boundary layer development studies.

An interesting fact about Figure 54 is that transition is being propagated and developed by T-S waves and Gortler waves, even after the rather turbulent roughness wakes occurring upstream. Another interesting feature is the chordwise position at which these events take place. The T-S waves were initiated between taps #8 and #9; with smooth surface at the same velocity, the T-S waves were never found upstream of taps #12 or #13. However, a low frequency oscillation in the boundary layer was found to exist around tap #8 of the smooth blade, later resulting in the T-S wave formation downstream. This fact, which was discovered in the smooth surface studies, might help to explain partially the early appearance of the T-S waves. If the roughness wakes were not directly responsible for a complete breakdown in the boundary layer, they might have played an important role by substantially increasing the amplitude of the disturbances as well as by supplying additional high-intensity disturbances of a much broader spectrum than the original disturbances. This feature is unique to a distributed roughness, as a single roughness element will produce only one wake. A wake of sufficiently high intensity, containing frequencies to which the boundary layer is sensitive (critical frequencies), may cause a transition. On the other hand, a single roughness element not producing such disturbances will not influence transition. In contrast, a continuous generation of disturbances over a broad spectrum by the distributed roughness will directly affect the boundary layer development with a sufficient magnitude of critical frequencies. Thus the early formation of the T-S waves could be partially explained by an increase in the magnitude of the disturbances with broader spectra which were generated continuously in the boundary layer by the continuous presence of the roughness particles on the blade surface.

Figs. 54-61 show various stages of the boundary layer development on the pressure side with different grit numbers of roughness, several inlet velocities, and a number of upstream and downstream chord locations. Fig. 55 shows a rather turbulent boundary layer around tap 18 with grit #12 and an inlet velocity of 22.2 fps. At 22.2 fps tap 15 with grit #20 shows also a turbulent boundary layer development (Fig. 56), where the same grit number at a downstream location with a higher inlet velocity (Fig. 57) produces a complete turbulent boundary layer. Fig. 58 shows transitional flow upstream with grit #20 and 29.0 fps inlet velocity. The type of transition is quite unclear in this photograph. Grit #36 produces a laminar boundary layer and tap 12, and the transition process by T-S waves is clearly initiated around tap 15 (see Figs. 59-60). Fig. 61 shows another stage of transition with large nonlinearities in the boundary layer. A large number of photographs were obtained covering most of the available combinations of inlet velocity/grit #/chord location. Higher inlet velocities presented a problem of smoke intensity, but analysis was still possible, although good quality photographs were never obtained. A complete description of the influence of roughness on the boundary layer transition region was not available using only still photographs, and the aid of the hot-wire frequency analysis results were issential in finding the exact type and extent of the transition region.

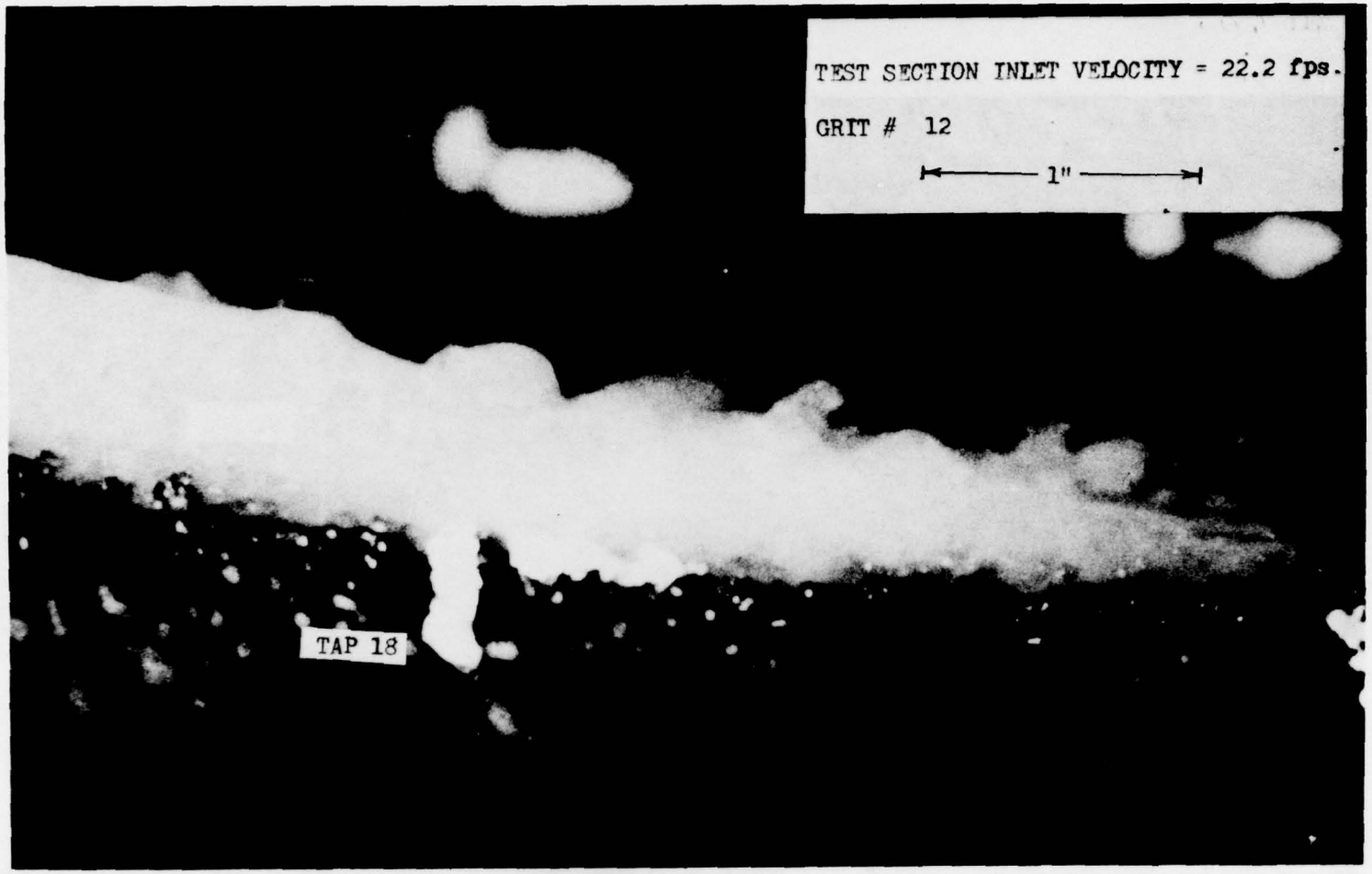

Figure 55 Rough Surface Boundary Layer Transition Region

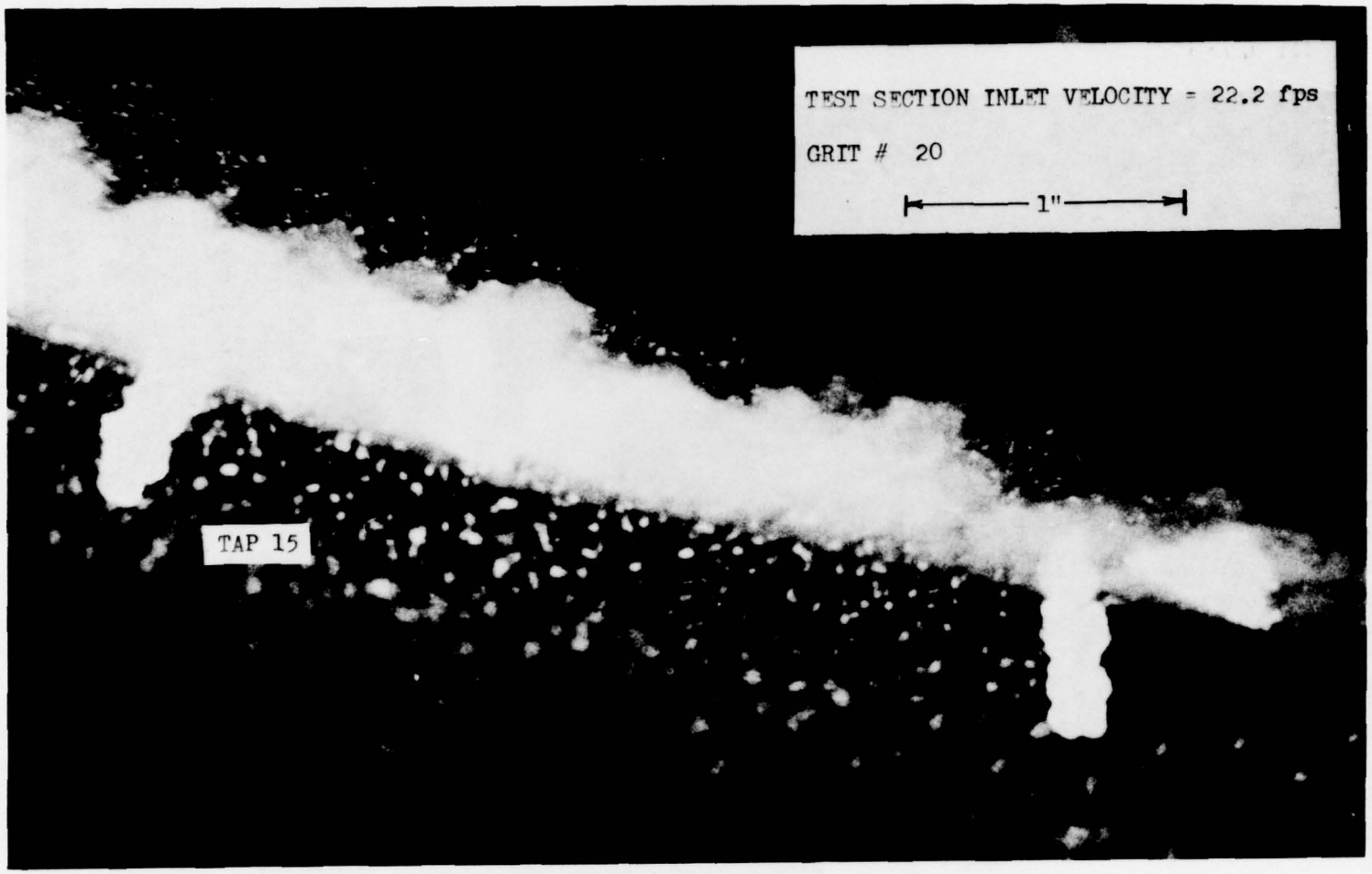

Figure 56 Rough Surface Boundary Layer Transition Region

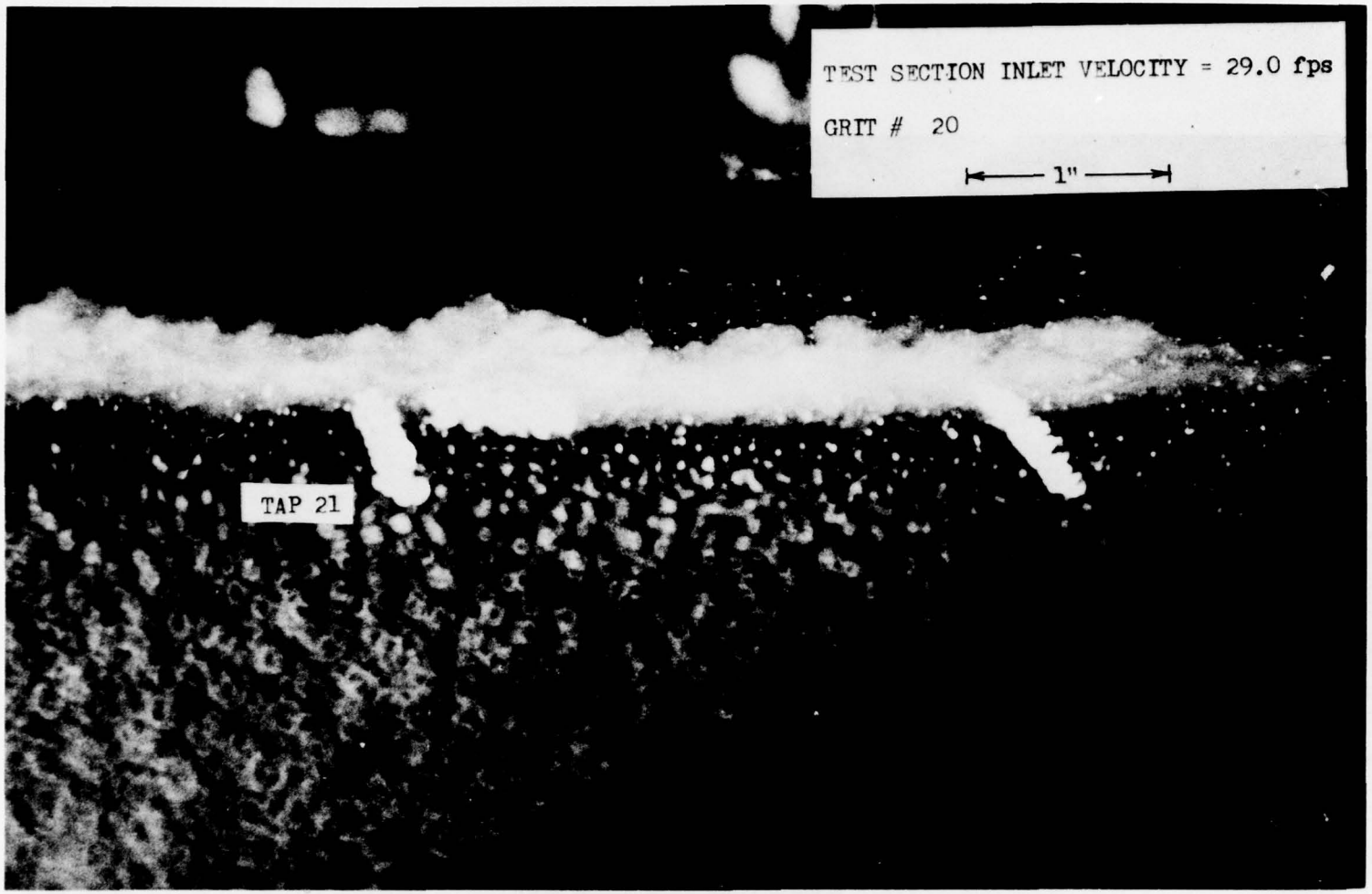

Figure 57 Rough Surface Boundary Layer Transition Region

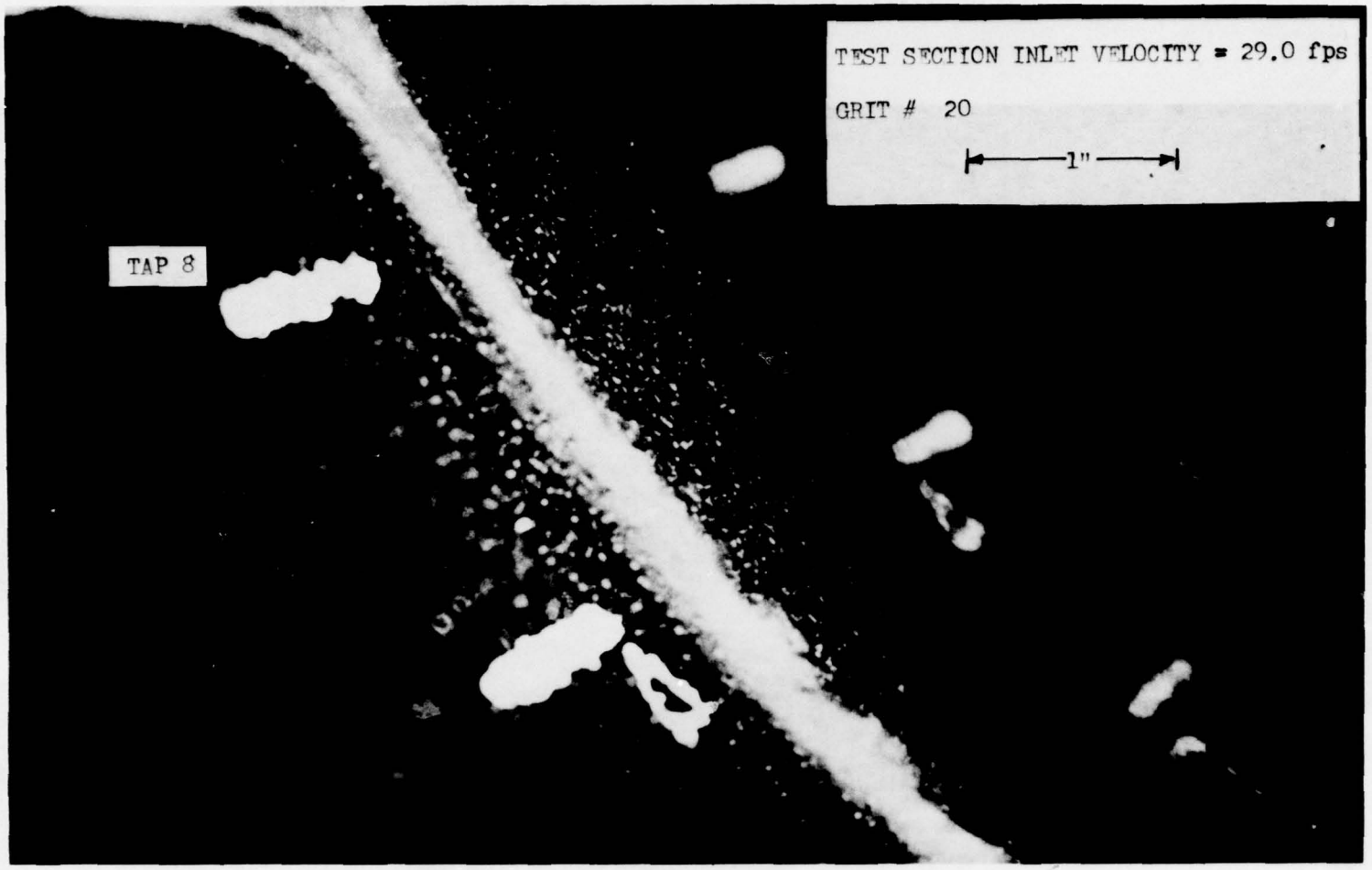

Figure 58 Rough Surface Boundary Layer Transition Region

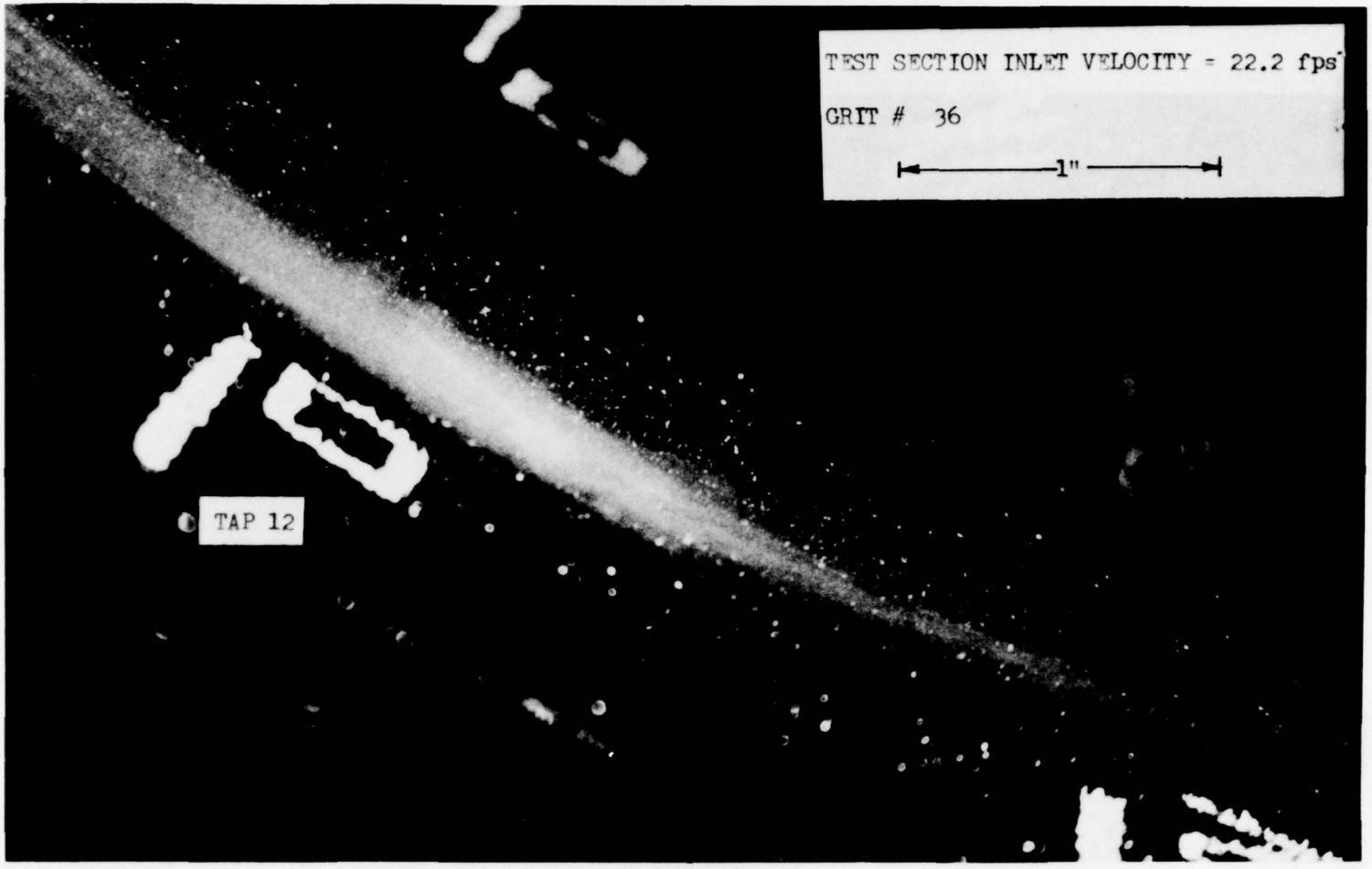

Figure 59 Rough Surface Boundary Layer Transition Region

Figure 60 Rough Surface Boundary Layer Transition Region

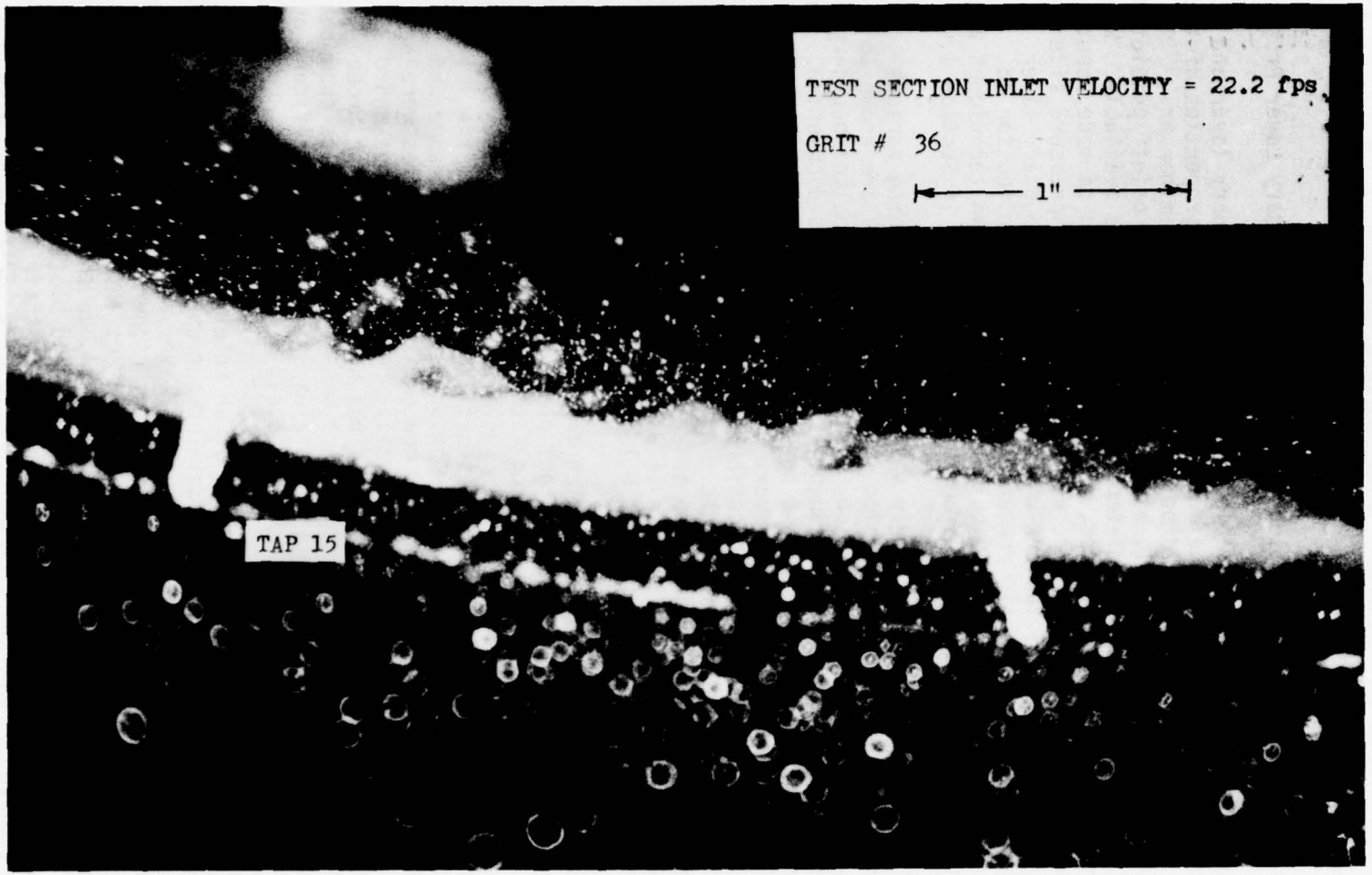

Figure 61 Rough Surface Boundary Layer Transition Region

4.3 PRESSURE SURFACE BOUNDARY LAYER HOT-WIRE STUDIES

4.3.1. Smooth Surface Velocity Profiles and Boundary Layer Properties

In order to use the available techniques for boundary layer and heat-transfer calculations, one must estimate various properties of the flow. Such an estimation could be performed using a laminar or turbulent boundary layer model, with fixed "transition point" predicted by one or more of the many semi-empirical relationships available. When the problem is not very involved, good prediction could be made about the needed parameters. However, as in the case of the pressure side of a turbine blade, several factors which influence the boundary layer development exist, and their presence complicates the situation to such an extent that severe difficulties arise when known techniques are used to predict heat-transfer parameters, as mentioned in Section 1.

A hot-wire study is extremely valuable in determining various properties of the transition region. Velocity profiles are known to be a good indication of transition, as laminar and turbulent boundary layer velocity profiles were throughly investigated and documented. The traverse mechanism was used with a hot-wire, boundary layer probe (TSI model 1261) and a hot-wire (TSI model 1050) constant-temperature anemometer. The probes were precalibrated with a special calibrating tank utilizing an isentropic nozzle. As mentioned in Section 3.8, the traverse mechanism was designed to an accuracy of 0.001 inch. Such an accuracy was not essential because it was proved that the boundary layer thickness is of the order of 0.1 inch.

The wall proximity problem which arises when a hot-wire probe is used very close to a cool wall did not play any role in the analysis of the results. As Wills,[156] Oka and Kostic,[153] Rhen,[154] and Kanevce and Oka[155] show, the problem arises usually much closer to the wall than was used in this study. This is quite fortunate since the calibration needed for the wall correction is rather cumbersome and inaccurate. As an additional safety measure, several studies were conducted on the test blade, and velocity profiles of various chord locations and several speeds were obtained while the hot-wire probe was driven toward the wall until contact was reached. Results show that the wall influence on the velocity profiles starts to be significant only less than 0.005 inch away from the surface.

The velocity profiles (Fig. 62) at an inlet velocity of 22.2 fps resemble a laminar boundary layer development upstream, and the distinct fullness of a turbulent boundary layer as they proceed downstream. However, additional studies at higher inlet velocities of 29.01, 36.3, and 42.8 fps reveal more important information concerning the characteristics of transition which occurs on the pressure-side of a turbine blade. The velocity profiles were plotted at the same inlet velocity and various chord locations, so their development can be investigated as they proceed downstream; Figs. 62-63 show these profiles for 22.2, 29.01, 36.3, and 42.8 fps inlet velocities. The

Note: Several Data Points were Omitted for Clarity.

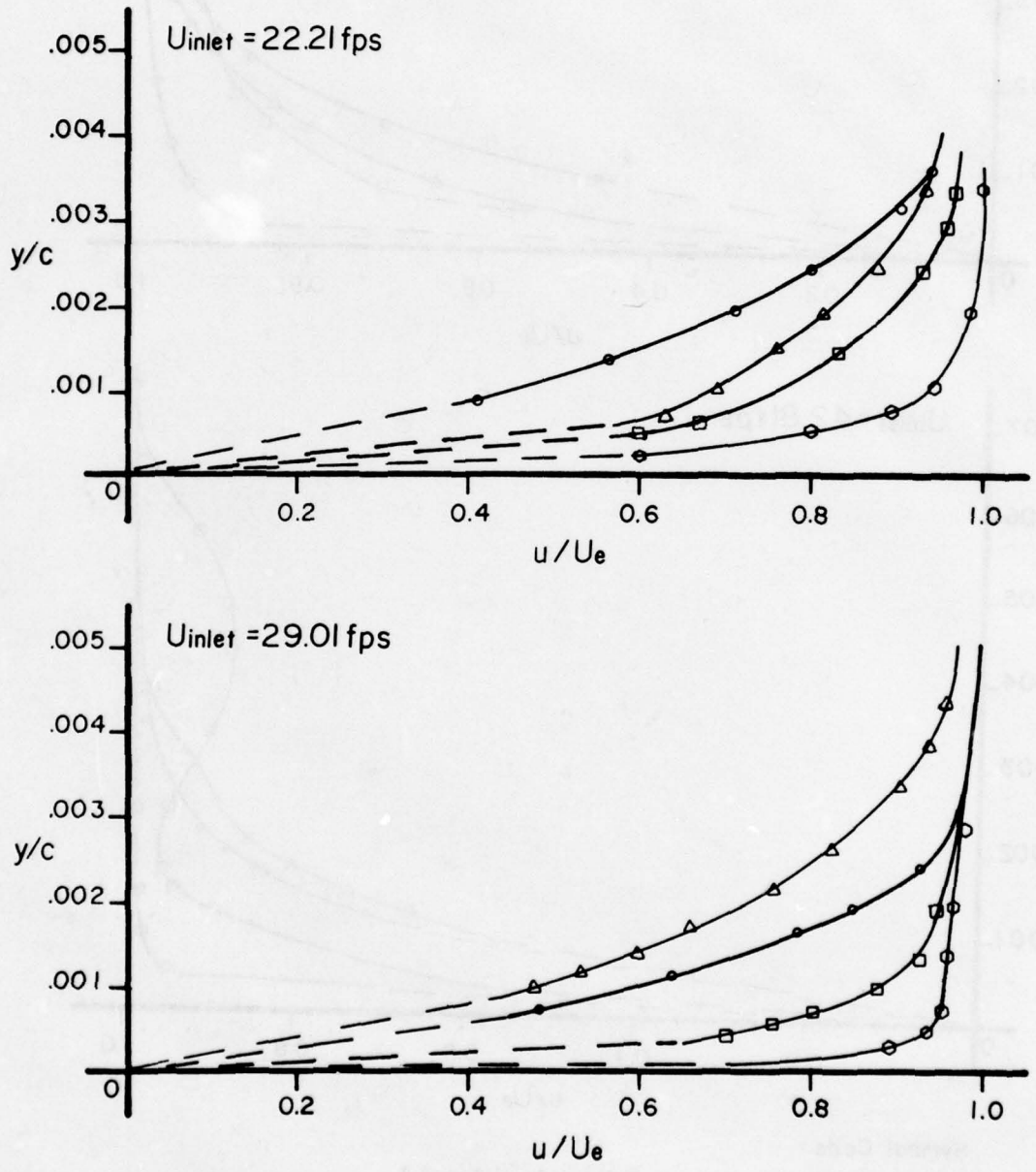

Symbol Code:

○ Tap 9 ; △ Tap 13 ; □ Tap 18 ; ⬡ Tap 24

Fig. 62 Boundary Layer Velocity Profiles

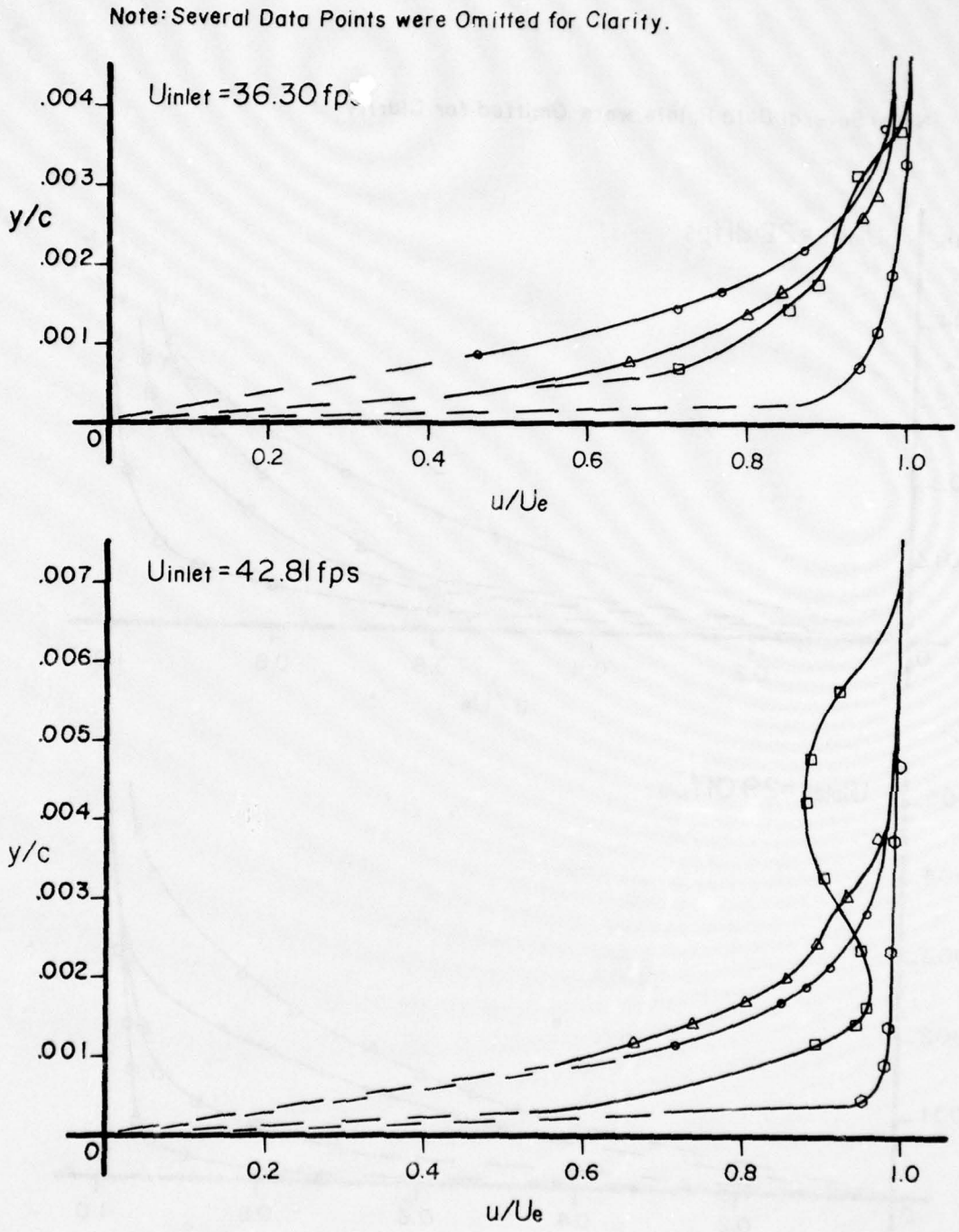

Fig. 63 Boundary Layer Velocity Profiles

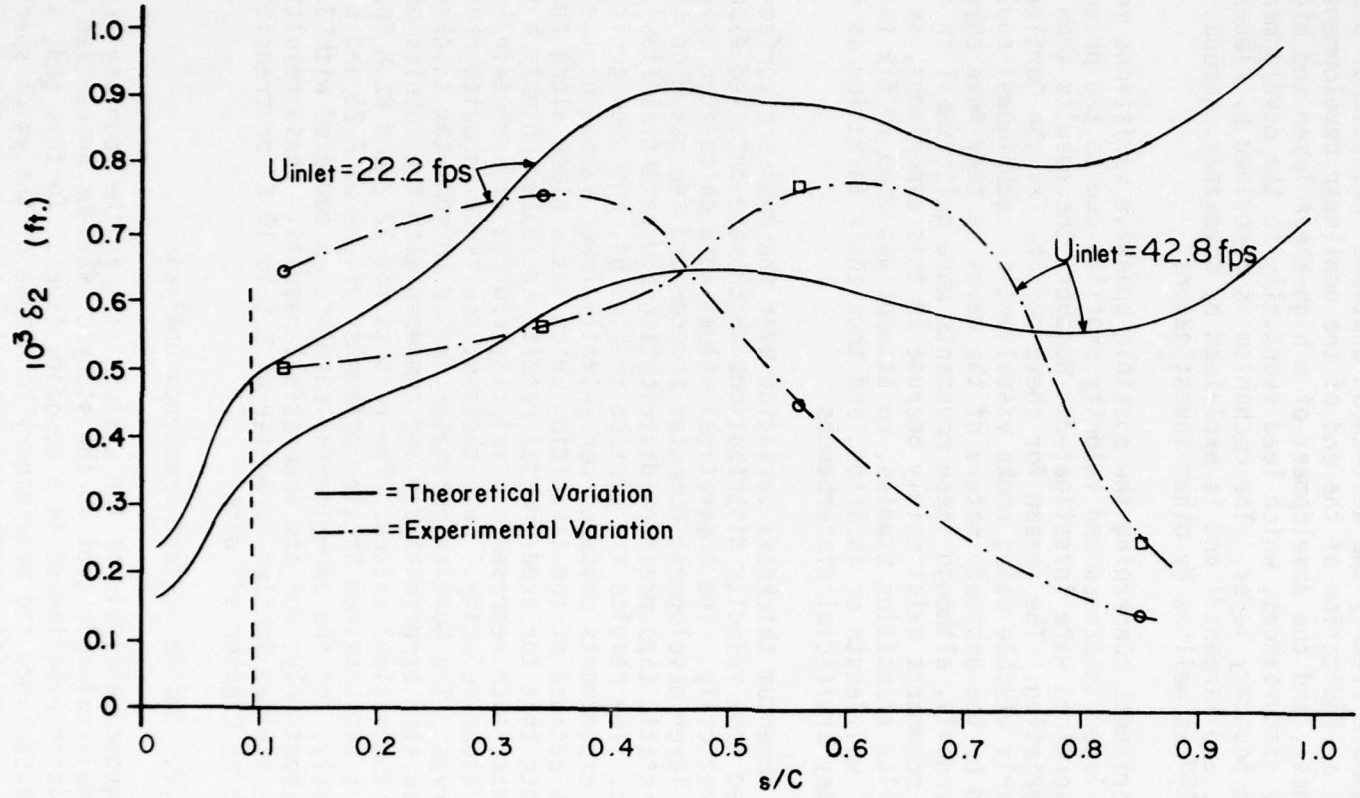

Fig. 64 Boundary Layer Momentum thickness variations

upstream velocity profiles (tap 9) show generally a laminar boundary layer development, but as we go downstream (taps 13, 18), inflectional profiles appear, and further downstream profiles (tap 24) show generally turbulent profiles. The distinct "kinks" in the profiles around mid-chord resemble clearly the well-known unstable inflectional profiles, which are an indication of the end of the nonlinear development of disturbances, and the development of a high-shear layer and high-frequency disturbances, which lead eventually to the development of a turbulent boundary layer. The mechanism is described by Klebanoff, Tidstrom, and Sargent[31] and is explained by Kovasznay, Komoda, and Vasudeva[158] as well as by other investigators.

Experiments concerning the possible spanwise variations in the boundary layer thickness and velocity profiles due to the presence of Gortler vortices were investigated. However, the results show very little variation. The reason for these results (as the Gortler vortices were clearly visible using smoke visualization techniques) could be explained by the unsteady nature of the waves as they move spanwise rather randomly, although these movements were quite small in amplitude. Spanwise movements exist mainly because in this experiment, as compared with similar transition studies, no attempt was made to fix the Gortler vortices' wavelength or location, and thus their formation is entirely free of any artificial disturbances.

The momentum thickness variation over the pressure surface was calculated from velocity distributions which were obtained experimentally and theoretically. The theoretical values were calculated using a boundary layer development computer program and are based on the measured static taps pressure distribution and potential flow calculations. The results are plotted in Fig. 64, and show generally that the experiments produced consistently lower values of the momentum thickness because of the transition which takes place along the pressure side. Note that the experimental results are based on only a few data points; each represents a velocity profile at a certain location and free steam velocity. Nevertheless, the trend is quite obvious in these curves. The Gortler parameter, based on momentum thickness, was then calculated experimentally and compared with the results obtained from the theoretical values. The results for 22.2 and 42.8 fps inlet velocities show maximum Gortler parameter values of 2.25 and 5.35, respectively, for the experimental results, as compared with 3.34 and 4.06, respectively, for the theoretical results. These results are below the minimum Gortler parameter of 8.6 to 10.6 for transition, as indicated by Clauser's[73] data.

4.3.2. Smooth Surface Frequency Analysis

Frequency analysis of the disturbances in the boundary layer is an extremely valuable tool in the study of various properties and types of transition experienced in a boundary layer. To this end, a great deal of experience and preliminary knowledge of the exact spectrum of the free-stream disturbances are essential before any conclusions can be

drawn from the results. It is known that the boundary layer is more sensitive to disturbances of certain frequencies than it is to others; therefore, a complete frequency spectrum survey was performed in the wind tunnel test-section in the calibration stage and was partially repreted again just before any new data in the boundary layer were taken. The extreme care taken in this work was later proven essential when the actual data was analyzed, since several peaks which appeared in the frequency spectrum at various stages were shown to be a direct result of the free-stream disturbances. The output signal from the TSI Model 1050 hot-wire anemometer was fed into a Federal Scientific Model UA-500 Ubiquitous Real-Time Spectrum Analyser with an X-Y plotter, and the spectrum of the signal was then directly plotted on standard graph paper.

The results obtained in this manner were used mainly for two kinds of analyses. The first kind of results obtained were the Tollmien-Schlichting wave frequencies which were compared with the results from the high-speed photography studies. Tollmien-Schlichting wave frequencies were observed as a moving frequency peak among stationary peaks on the frequency spectra. Further examination and comparison of several spectra at the same chord location and various inlet velocities, or at the same inlet velocity and various chord locations, revealed information as to the growth of certain frequencies, This type of study, considered important in obtaining spatial amplification factors for predicting transition[49], was used in this study to ascertain how the frequency spectrum is constituted, an indication of the development of a turbulent boundary layer. A sample of the data (the study involves an analysis of several hundred graphs) is presented in Fig. 65 where results from the same chord location at speeds of about 16 to 29 fps inlet velocities are presented. A shift of the high amplitude region toward higher frequencies with increasing speed is noticeable, as well as the development of stationary peaks inherent in the free-stream disturbances present in the tunnel. The high-speed photographic methods were performed at 22.2 and 42.8 fps inlet velocities. The hot-wire analysis was done at three downstream locations and covered up to seven different inlet velocities between 22.2 and 52.9 fps. Table 5 presents these data and compares the hot-wire with the photographic results. The hot-wire results confirm the photographic results at the low range, and show somewhat lower values for the higher inlet velocity of 42.8 fps, although within an acceptable accuracy. This comparison lends credence to the results through a mutual corroboration by the hot-wire method and the flow visualization study.

4.3.3. Rough Surface Frequency Analysis

The same techniques used for the smooth surface analysis were used in this study. Three chord locations were chosen (i.e., taps #8, #15 and #24) which represent upstream, midchord, and downstream locations.

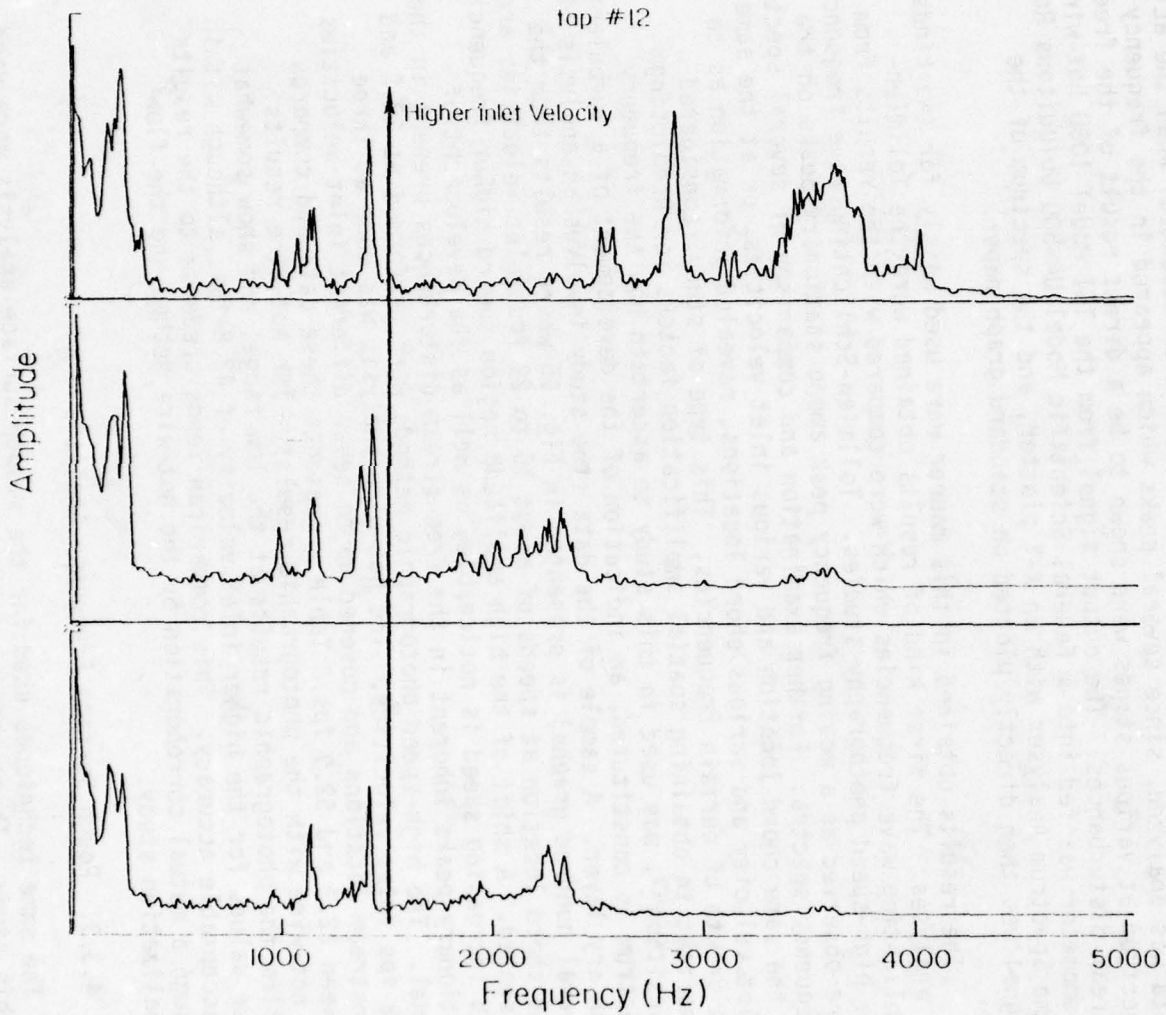

Figure 65 Smooth Surface Boundary Layer Frequency Spectrum

TABLE 5

TOLLMIEN-SCHLICHTING FREQUENCIES COMPARISON

Tap #	U inlet (fps)	Hot-wire freq. results (Hz)	Photographic analysis results (Hz)
22	22.2	750	752- 818
	29	1130	
	33.7	1330	
	36.3	1450	
	40.4	1650	
	42.8	1780	2439-2804
	52.9	2060	
23	22.2	1020	818-1093
	29	1340	
	33.7	1640	
	36.3	1840	
	40.4	2050	
	42.8	2290	2804
24	22.2	1000	1093
	29	1520	

A hot-wire probe was lowered toward the surface, and the frequency spectrum was observed. The same vertical distance from the blade surface was used for each grit number at the same chord station. Generally, the spectrum was very narrow, with low-amplitude peaks up to a certain inlet velocity; it then started to broaden quickly (depending on grit number, inlet velocity and chord location) producing sometimes a completely turbulent spectrum.

Sample data are presented in Figs. 66-70. The conclusions obtained from these data are presented in Table 6.

4.4 AIRFOIL STATIC PRESSURE DISTRIBUTION

4.4.1. Smooth Surface

Using the instrumented airfoil described in section 3.2, the static pressure distributions were determined for test section inlet velocities of 22.2, 29.0, 36.3, and 42.8 fps, with no upstream obstructions (circular cylinders). Only 53 of the 56 static taps were usable, one being plugged on the suction surface and two on the pressure surface as indicated in Fig. 15. In Figs. 71 through 74, data for the plugged tap experimental values has been supplied by a cubic spline fit using adjacent measured data points. In these figures, the experimental data are plotted along with the potential flow calculations performed by Dr. Kervyn Mach of the USAF Aero Propulsion Laboratory based on cascade geometric data as described in Appendix A. As can be seen in the figures, relatively close agreement was obtained, expecially for the pressure surface distribution. The trailing edge distribution, especially for the suction surface, shows a rather large discrepancy. This may be explained easily when one examines the theoretical work of Gostelow.[103] Through potential flow analysis, Gostelow found that a discrepancy in the rear stagnation point location of only 0.001 chord could cause a rather large shift in the trailing edge static pressure distribution. In fact, the static pressure distribution showed significant changes over much (approximately 60 to 90%) of the airfoil surfaces. An exaggerated view of the trailing edge results is shown in Fig. 75. From that figure, it can be seen that the potential flow calculation used for Figs. 71 through 74 seems to be based on a rear stagnation point oriented somewhat toward the suction surface, probably assumed to be at the tangent point of the suction surface and the trailing edge curvature. The experimental data, however, would appear to show a rear stagnation point much closer to the trailing edge center.

One must be careful, however, when interpreting these data, because the pressure taps permitted the measurement only of mean values rather than instantaneous values. The trailing edge vortices shown by visualization and hot-wire techniques occur at much higher frequencies than the response of the static pressure instrumentation. As discussed by Morkovin,[86] these vortices are capable of influencing the instantaneous pressure distribution over much of a circular cylinder surface, and could be expected to do the same for an airfoil. Probably the best

TABLE 6

ANALYSIS OF RESULTS FROM FREQUENCY SPECTRA OF THE BOUNDARY LAYER ON SMOOTH AND ROUGH SURFACES

Chord position	Roughness Size	"Start" of Transition*	"End" of Transition**
Tap #8 S/C = 0.1	Smooth	N.O.***	N.O.
	Grit #12 ($\bar{k}$=1.168mm)	<22.2 fps	29 fps
	Grit #20 ($\bar{k}$=0.513mm)	22.2 fps	>29 fps
	Grit #36 ($\bar{k}$=0.162mm)	36.3 fps	N.O.
Tap #15 S/C = 0.43	Smooth	<22.2 fps	N.O.
	Grit #12	<22.2 fps	22.2 fps
	Grit #20	<22.2 fps	>22.2 fps
	Grit #36	<22.2 fps	29 fps
Tap #24 S/C = 0.85	Smooth	<22.2 fps	N.O.
	Grit #12	<<22.2 fps	<<22.2 fps
	Grit #20	<22.2 fps	<22.2 fps
	Grit #36	<22.2 fps	22.2 fps

* "Start" of transition refers to a noticeable increase in disturbances intensities. Rapid growth of disturbances was recorded beyond that point. However, this does not refer to the "critical point" of the Stability Theory.

** "End" of transition refers to a condition beyond which an increase in inlet velocity did not produce any additional disturbances (frequency-wise), or increase in the intensities of the existing ones.

*** N.O. means "not observed according to the above criteria."

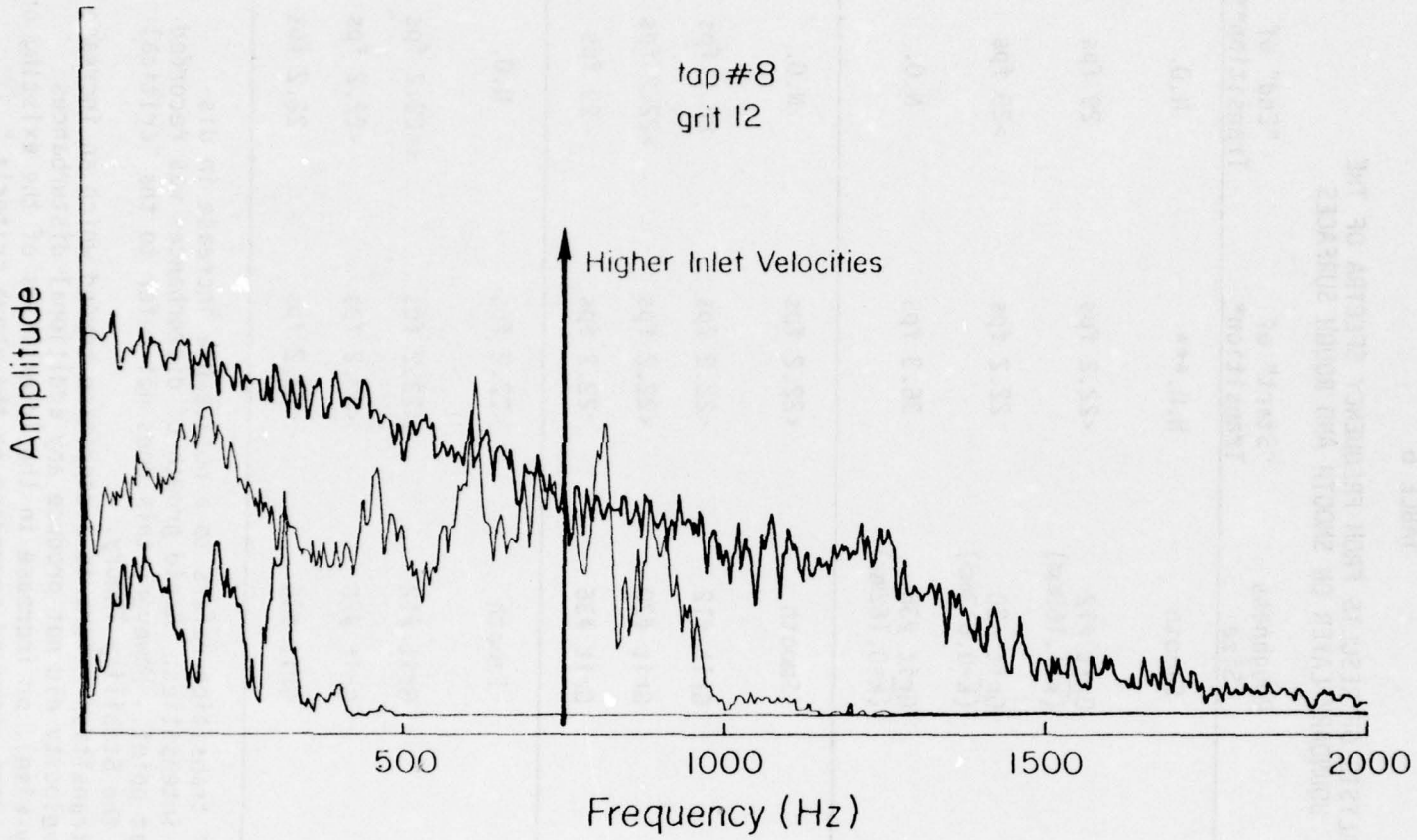

Figure 66. Rough Surface Boundary Layer Frequency Spectrum

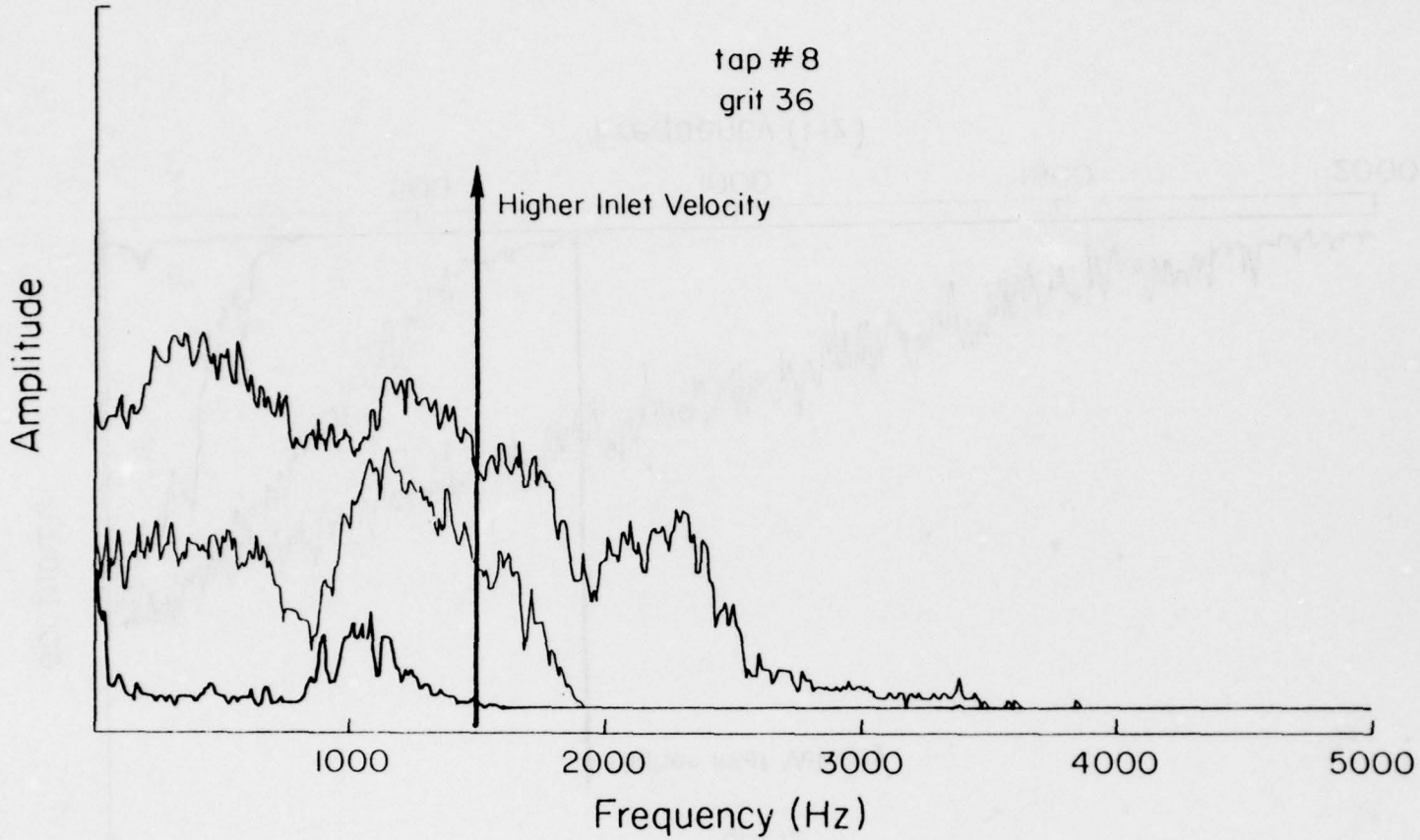

Figure 67. Rough Surface Boundary Layer Frequency Spectrum

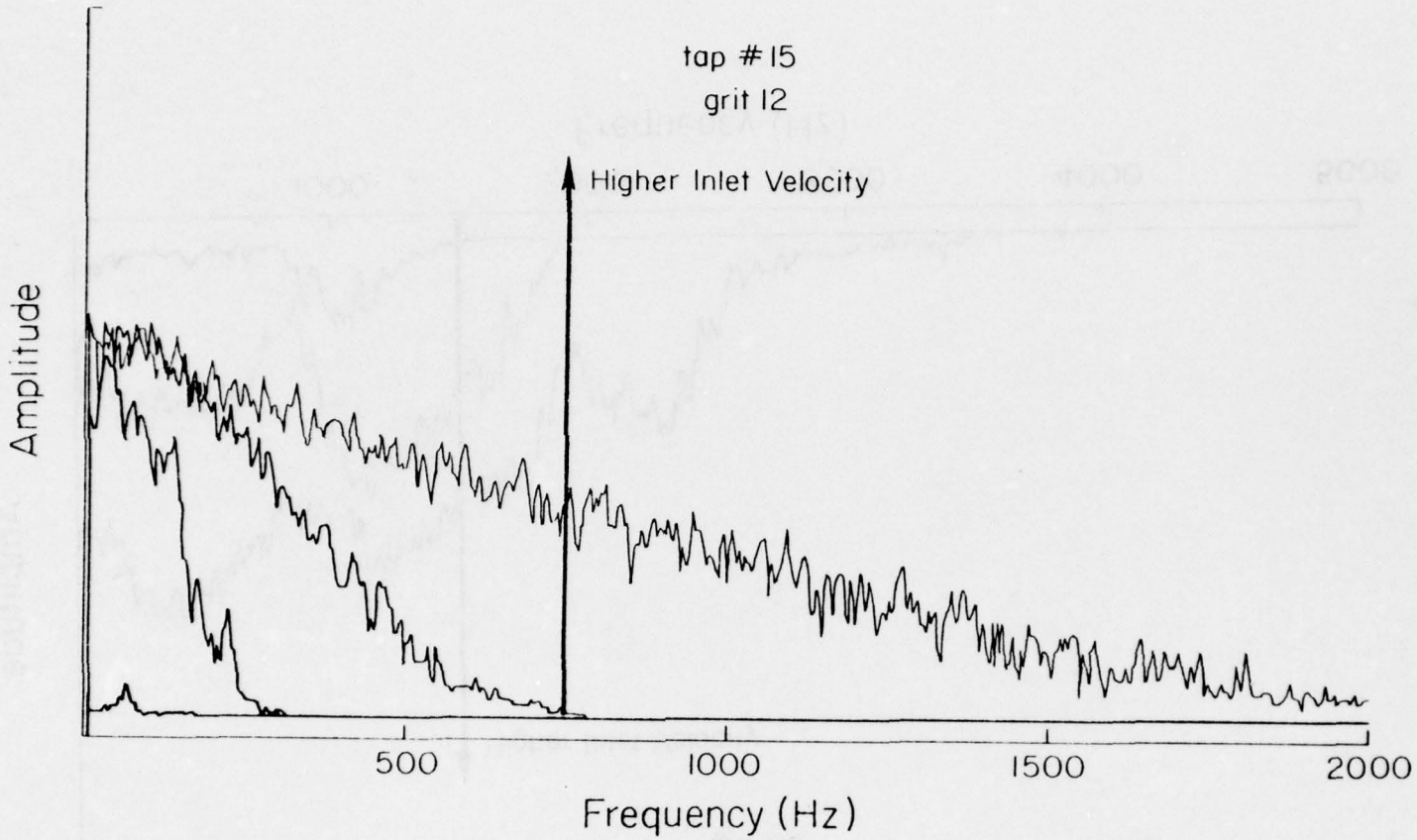

Figure 68. Rough Surface Boundary Layer Frequency Spectrum

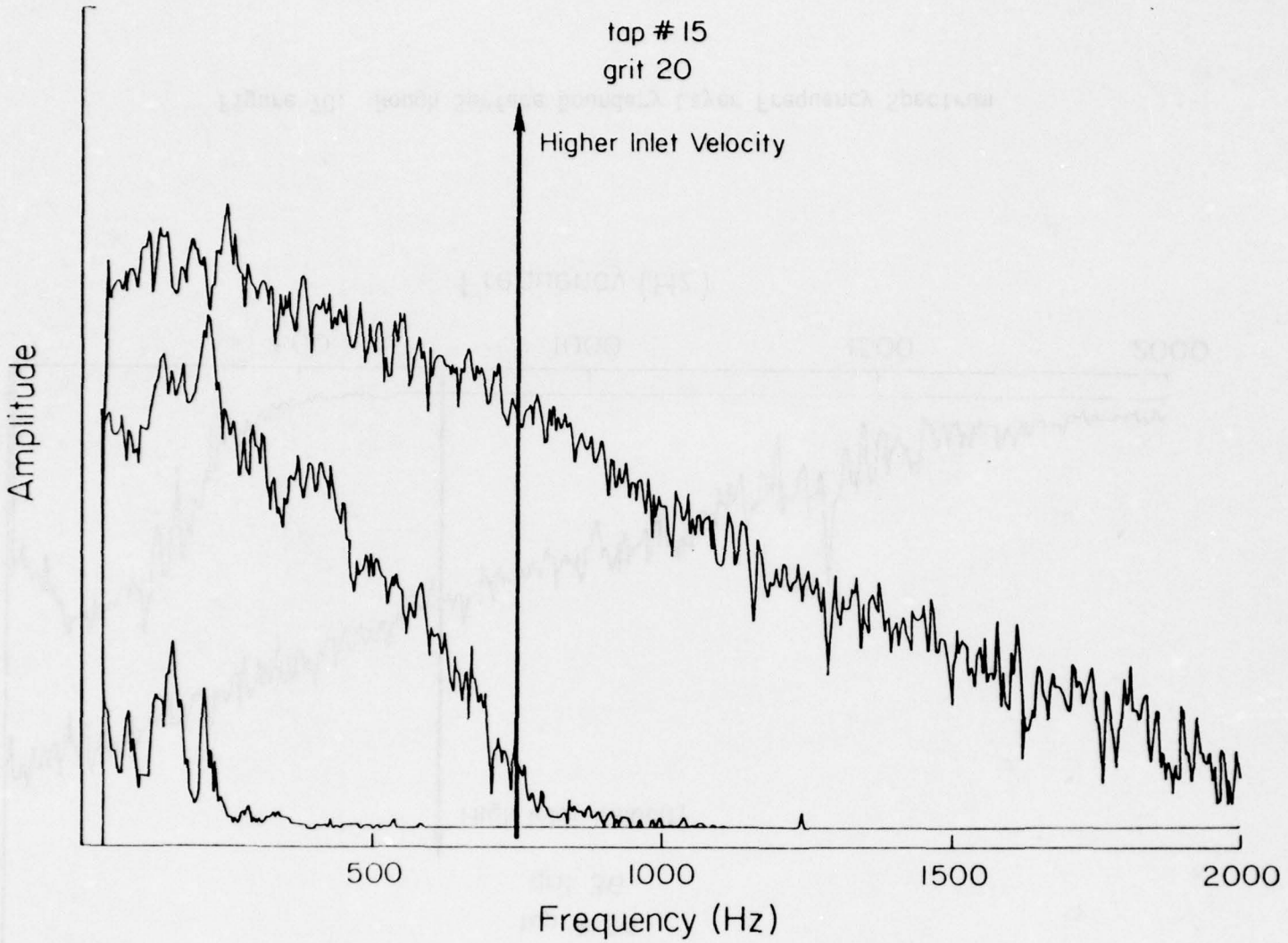

Figure 69. Rough Surface Boundary Layer Frequency Spectrum

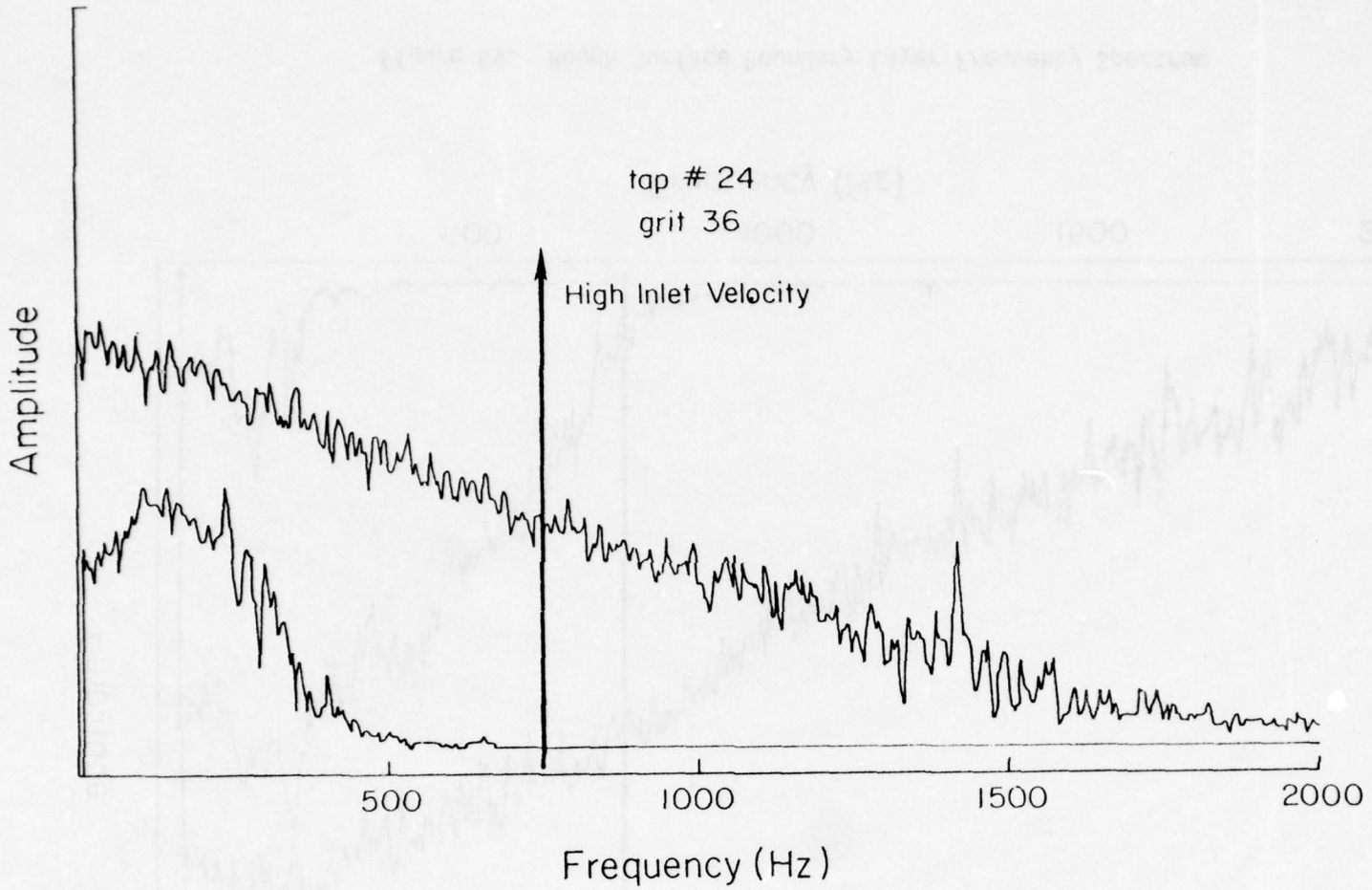

Figure 70. Rough Surface Boundary Layer Frequency Spectrum

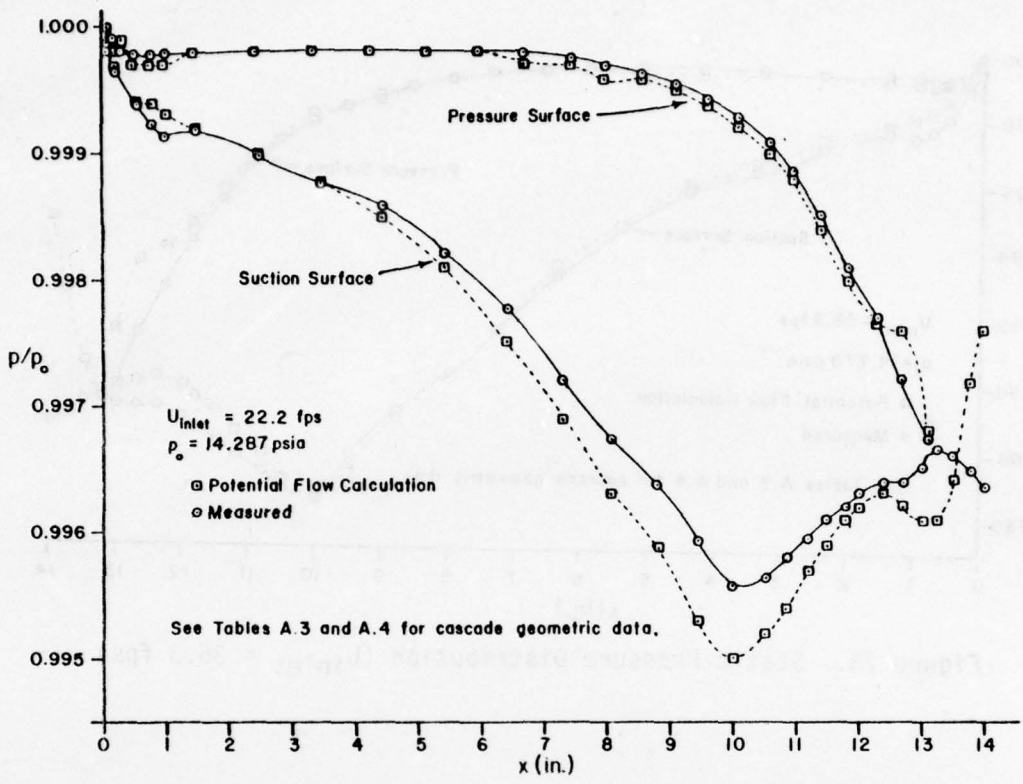

Figure 71. Static Pressure Distribution (U_{inlet} = 22.2 fps)

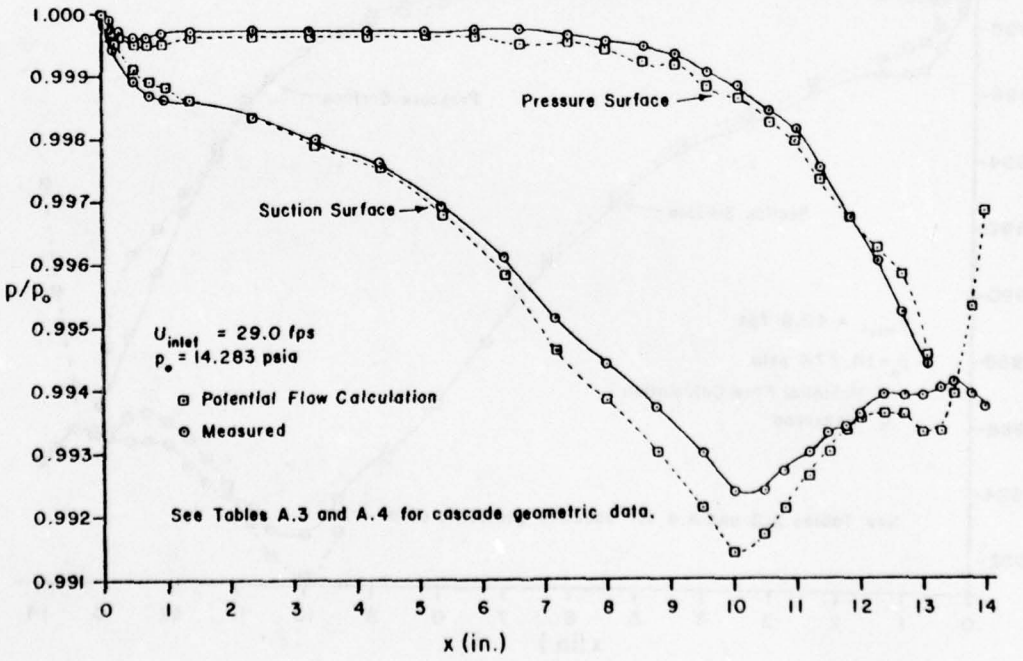

Figure 72. Static Pressure Distribution (U_{inlet} = 29.0 fps)

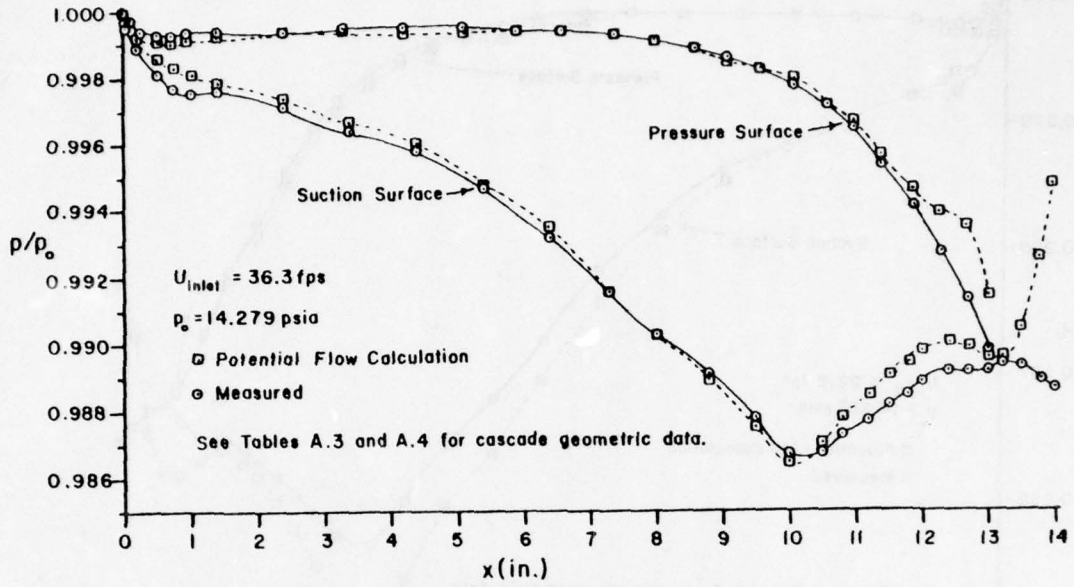

Figure 73. Static Pressure Distribution (U_{inlet} = 36.3 fps)

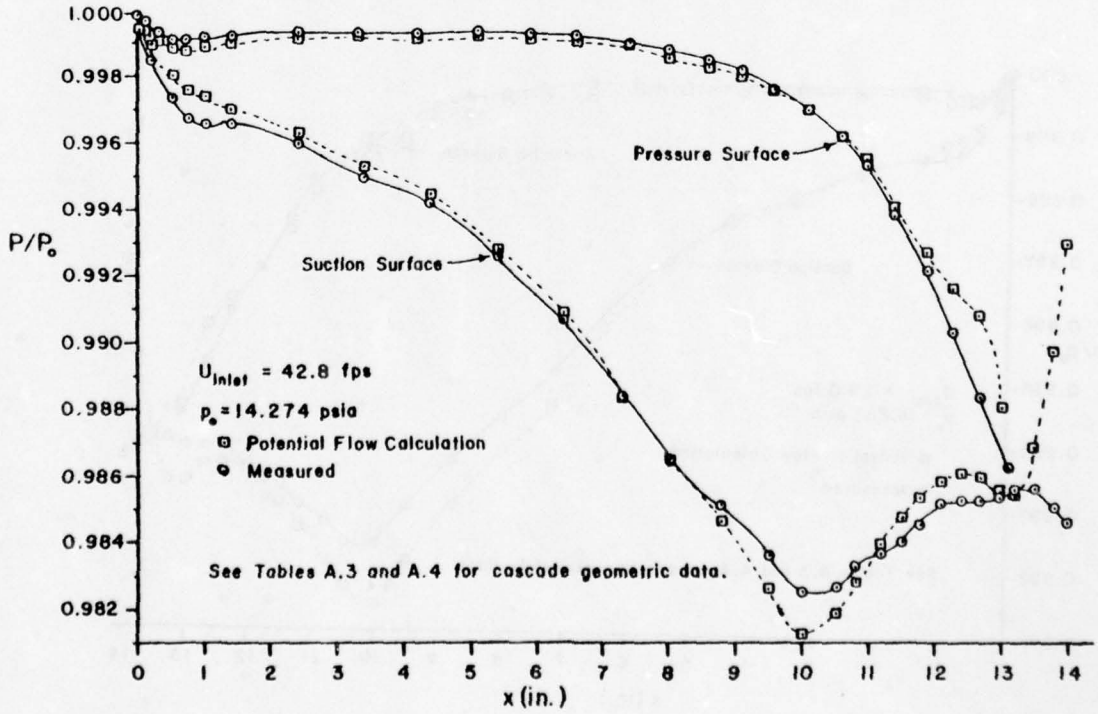

Figure 74. Static Pressure Distribution (U_{inlet} = 42.8 fps)

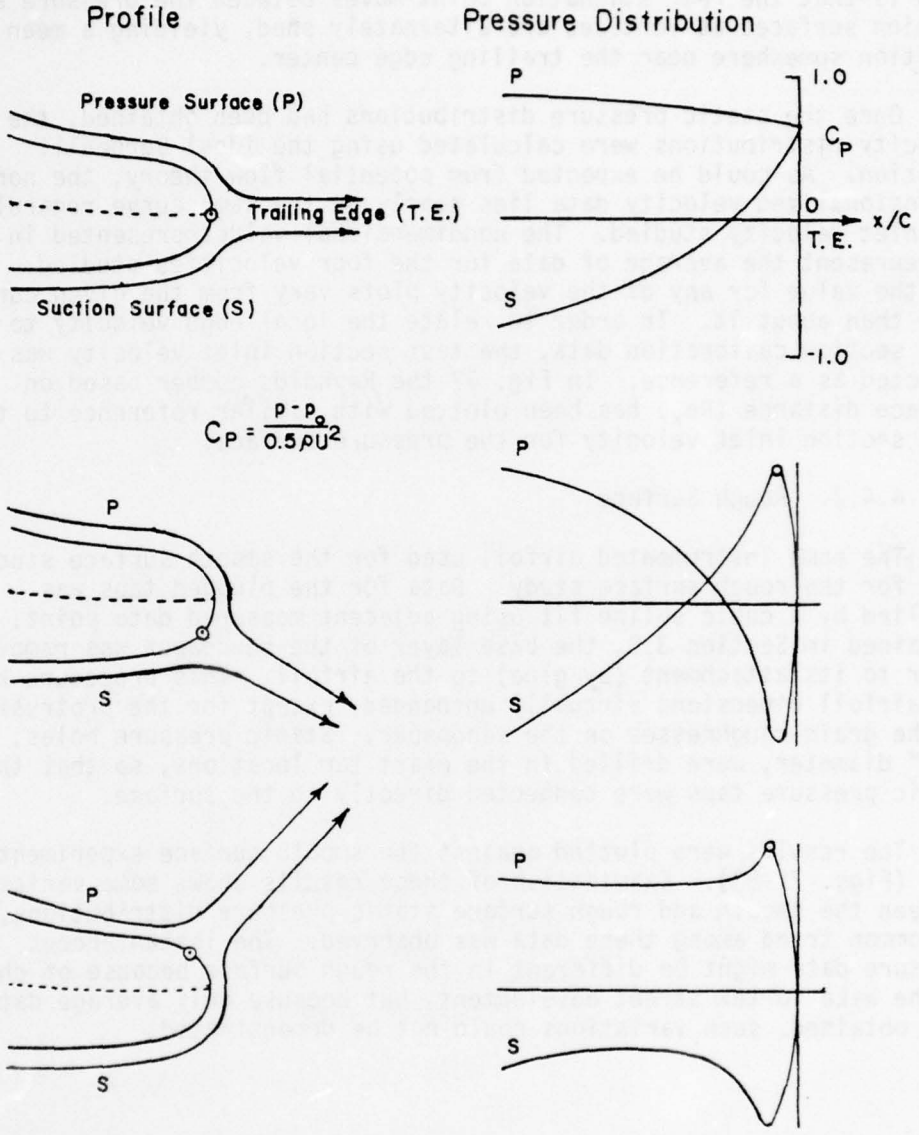

Figure 75. Effect of Assumed Rear Stagnation Point Location on Trailing Edge Static Pressure Distribution

explanation of the experimental curves given in Figs. 71 through 74 then is that the rear stagnation point moves between the pressure and suction surfaces as vortices are alternately shed, yielding a mean position somewhere near the trailing edge center.

Once the static pressure distributions had been obtained, the velocity distributions were calculated using the ideal Bernoulli equation. As could be expected from potential flow theory, the non-dimensionalized velocity data lies nearly on the same curve regardless of inlet velocity studied. The nondimensional values presented in Fig. 76 represent the average of data for the four velocities studied. Rarely did the value for any of the velocity plots vary from the given curve by more than about 1%. In order to relate the local edge velocity to the test section calibration data, the test section inlet velocity was selected as a reference. In Fig. 77 the Reynolds number based on surface distance (Re_x) has been plotted with similar reference to the test section inlet velocity for the pressure surface.

4.4.2. Rough Surface

The same instrumented airfoil used for the smooth surface study was used for the rough surface study. Data for the plugged taps was supplied by a cubic spline fit using adjacent measured data point. As explained in Section 3.9, the base layer of the sandpaper was removed prior to its attachment (by glue) to the airfoil. This procedure kept the airfoil dimensions virtually unchanged, except for the protrusions of the grain-roughnesses on the sandpaper. Static pressure holes, 1/32" diameter, were drilled in the exact tap locations, so that the static pressure taps were connected directly to the surface.

The results were plotted against the smooth surface experimental data (Figs. 78-83). Examination of these results shows some variations between the smooth and rough surface static pressure distributions, but no common trend among these data was observed. The instantaneous pressure data might be different in the rough surface because of changes in the wake vortex street development, but because only average data were obtained, such variations could not be demonstrated.

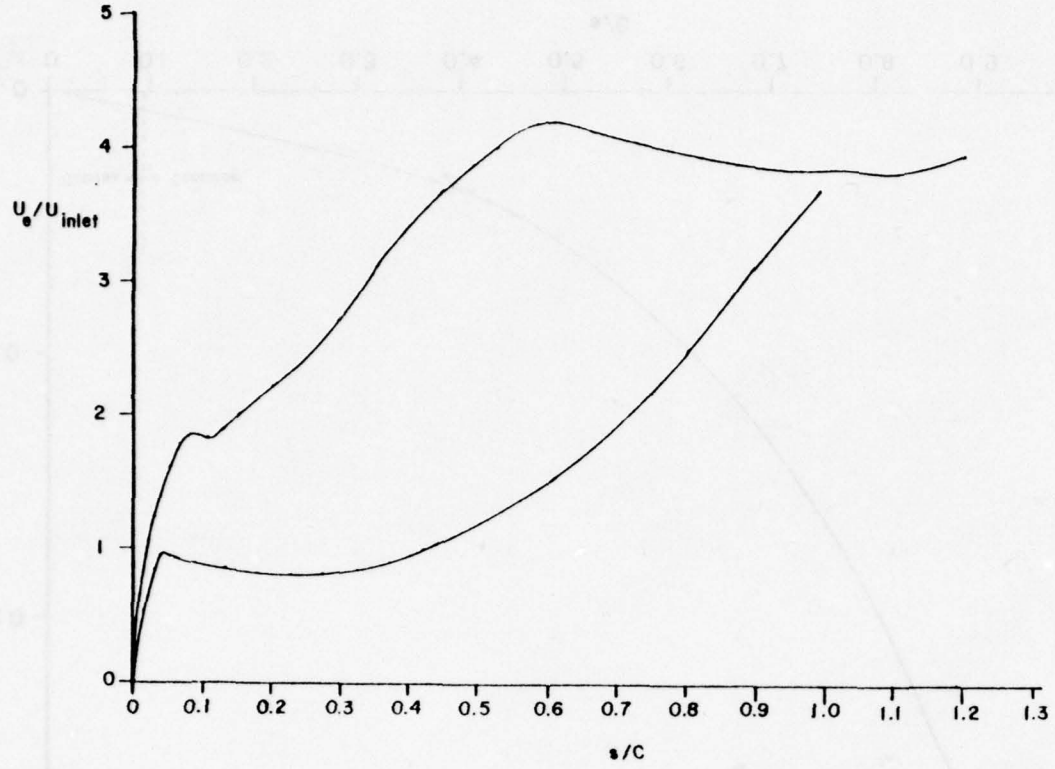

Figure 76. Edge Velocity Distribution

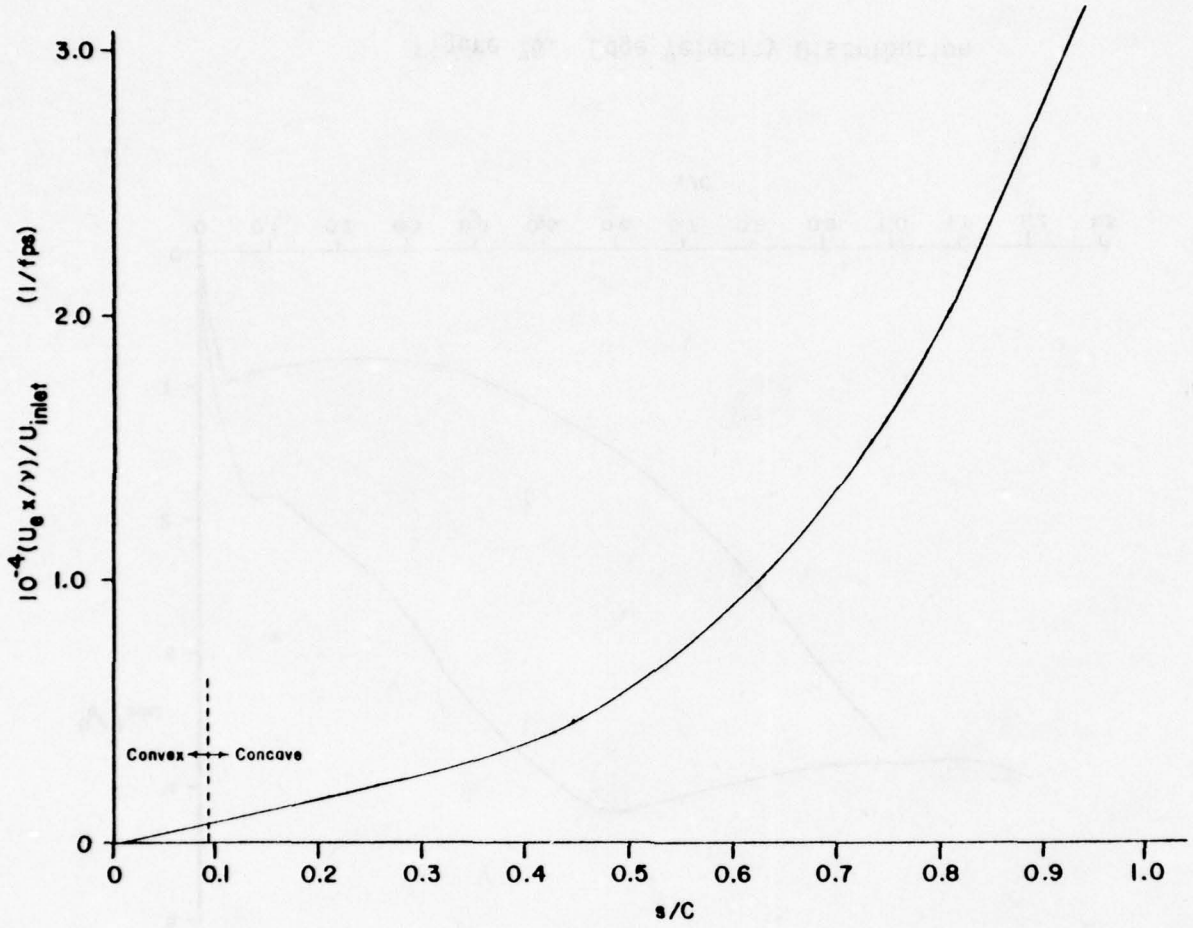

Figure 77. Growth of Reynolds Number (Re_x)

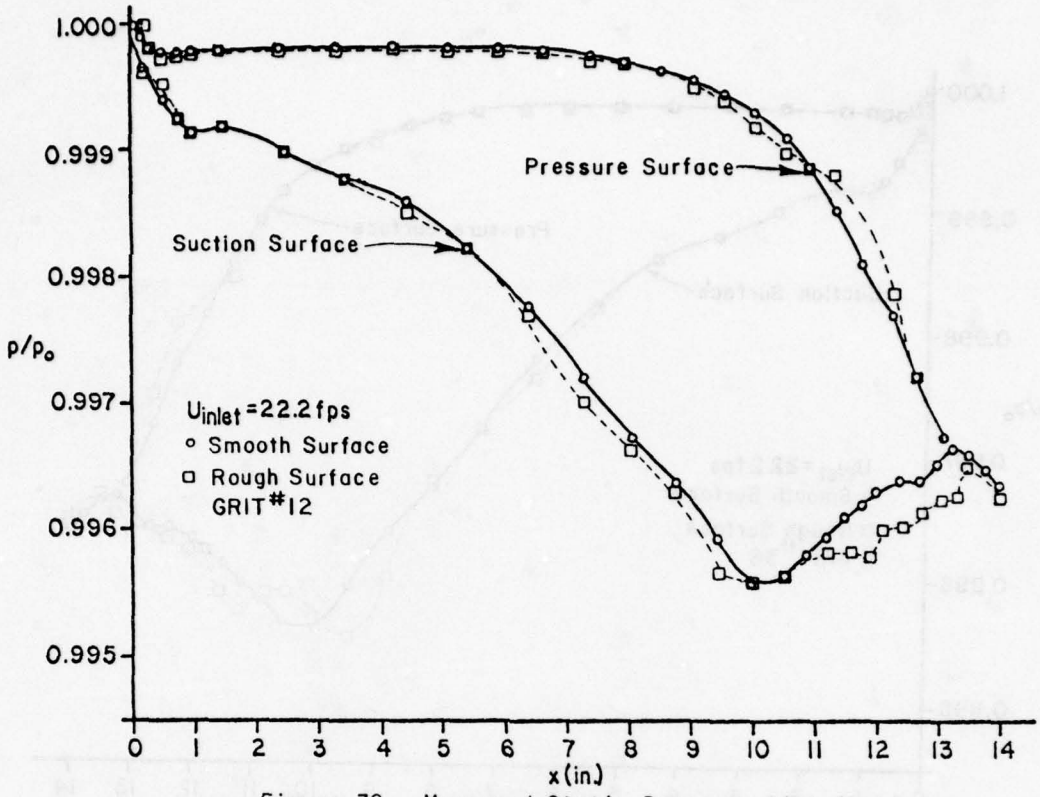

Figure 78. Measured Static Pressure Distribution

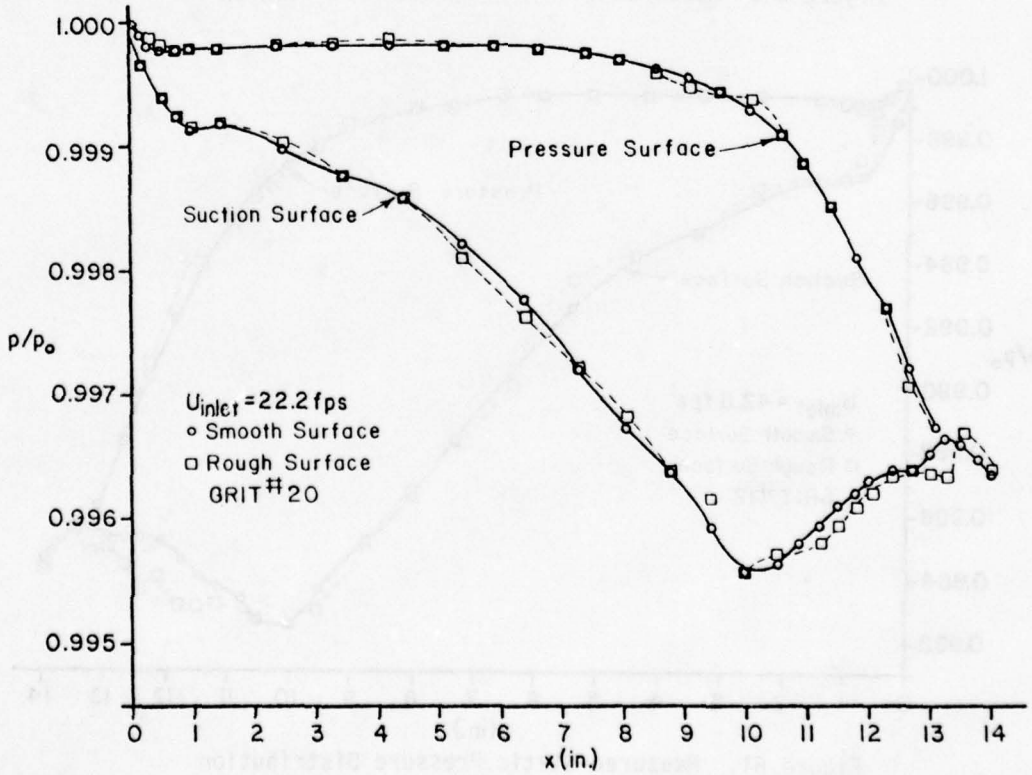

Figure 79. Measured Static Pressure Distribution

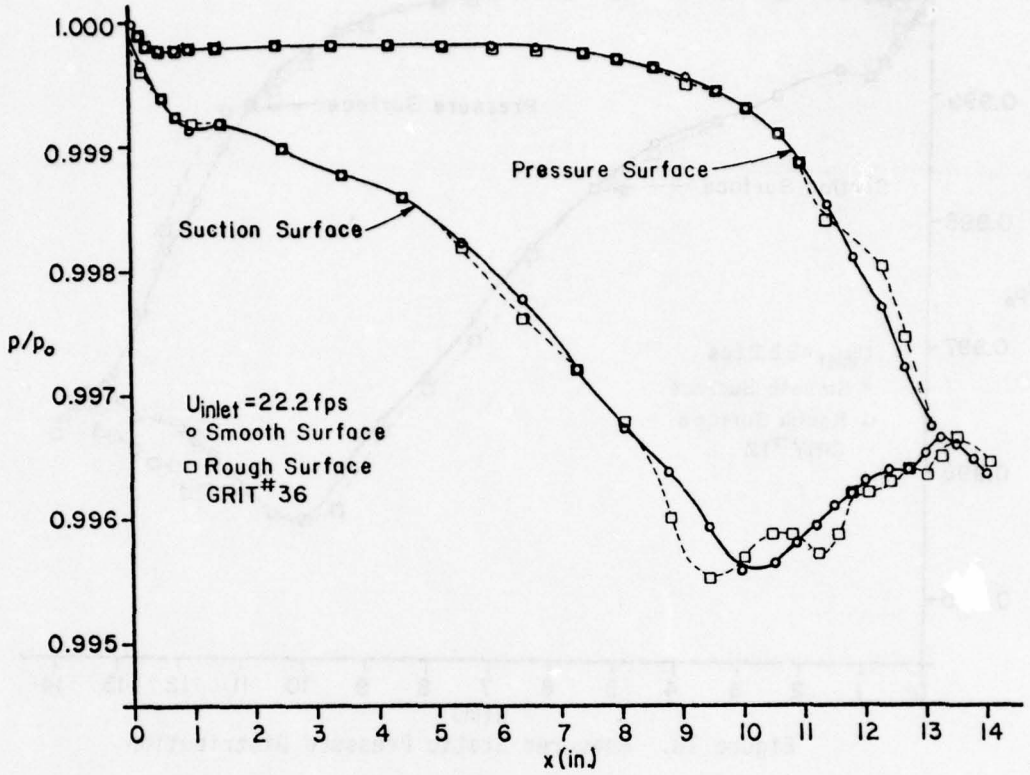

Figure 80. Measured Static Pressure Distribution

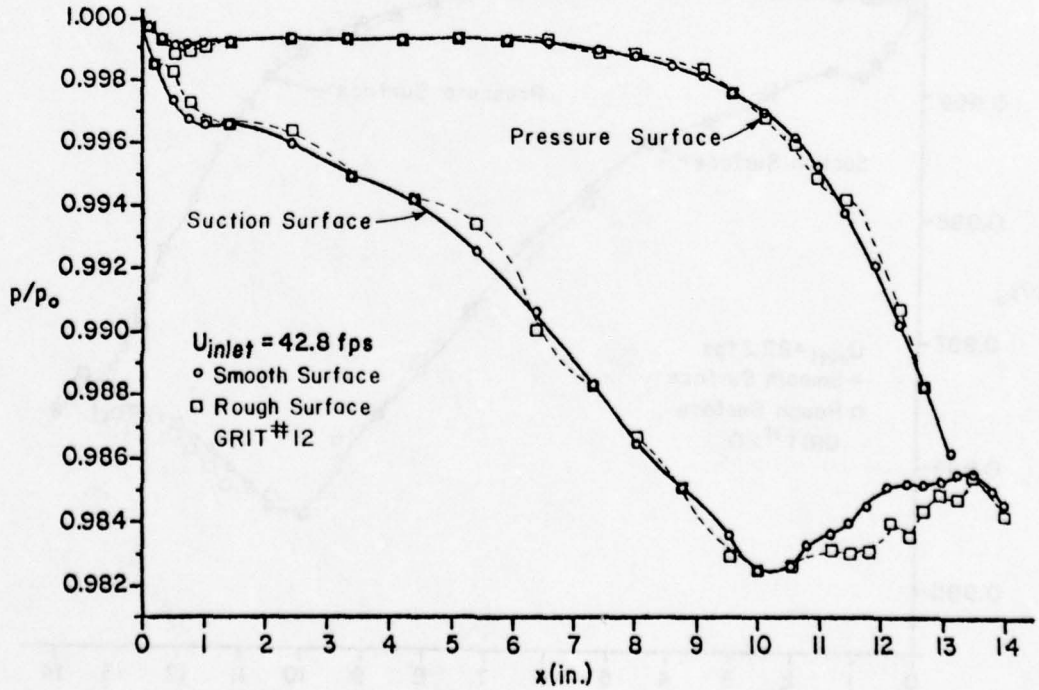

Figure 81. Measured Static Pressure Distribution

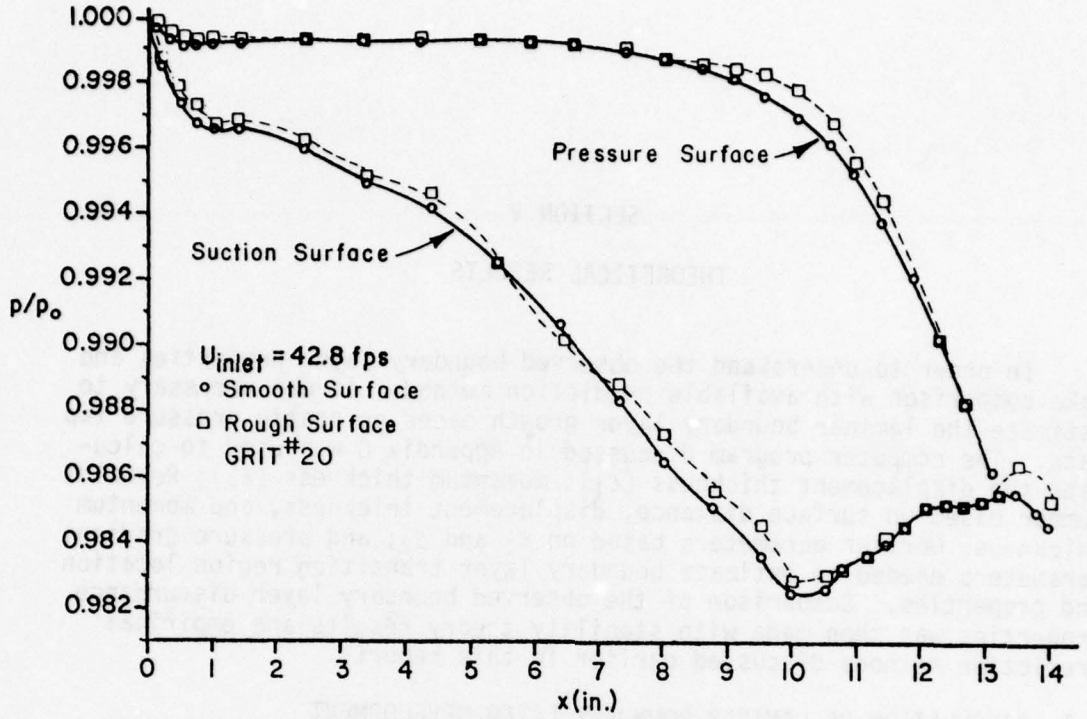

Figure 82. Measured Static Pressure Distribution

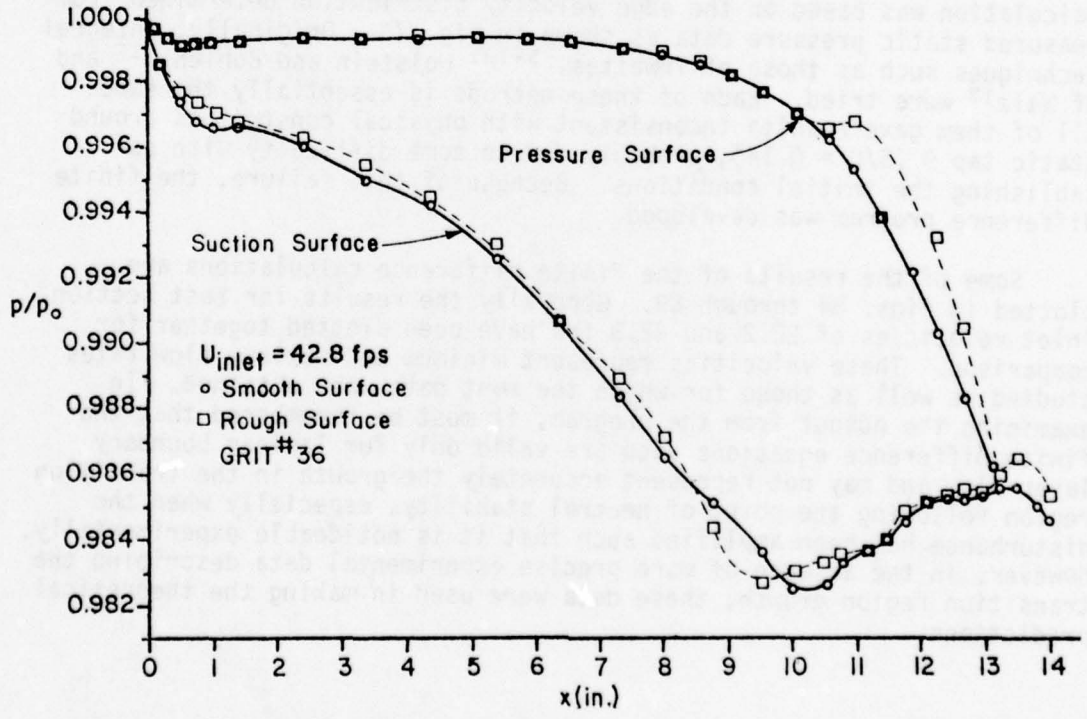

Figure 83. Measured Static Pressure Distribution

SECTION V

THEORETICAL RESULTS

In order to understand the observed boundary layer properties and make comparison with available prediction methods, it was necessary to estimate the laminar boundary layer growth based on static pressure tap data. The computer program discussed in Appendix C was used to calculate the displacement thickness (δ_1); momentum thickness (δ_2); Reynolds number based on surface distance, displacement thickness, and momentum thickness; Gortler parameters based on δ_1 and δ_2; and pressure gradient parameters needed to estimate boundary layer transition region location and properties. Comparison of the observed boundary layer disturbance properties was then made with stability theory results and empirical prediction methods discussed earlier in this report.

5.1 CALCULATION OF LAMINAR BOUNDARY LAYER DEVELOPMENT

As discussed in Appendix C, a finite difference scheme was used to calculate the boundary layer dimensions and velocity profile. This calculation was based on the edge velocity distribution determined from measured static pressure data as shown in Fig. 75. Originally, integral techniques such as those of Thwaites, [5,131] Holstein and Bohlen, [17] and of Walz[17] were tried. Each of these methods is essentially the same. All of them gave results inconsistent with physical constraints around static tap 9 (S/C = 0.14), probably due to some difficulty with establishing the initial conditions. Because of this failure, the finite difference program was developed.

Some of the results of the finite difference calculations are plotted in Figs. 84 through 89. Generally the results for test section inlet velocities of 22.2 and 42.8 fps have been plotted together for comparison. These valocities represent minimum and maximum flow rates studied as well as those for which the most data were obtained. In examining the output from the program, it must be remembered that the finite difference equations used are valid only for laminar boundary layer flow and may not represent accurately the growth in the transition region following the point of neutral stability, especially when the disturbance has been amplified such that it is noticeable experimentally. However, in the absence of more precise experimental data describing the transition region growth, these data were used in making the theoretical predictions.

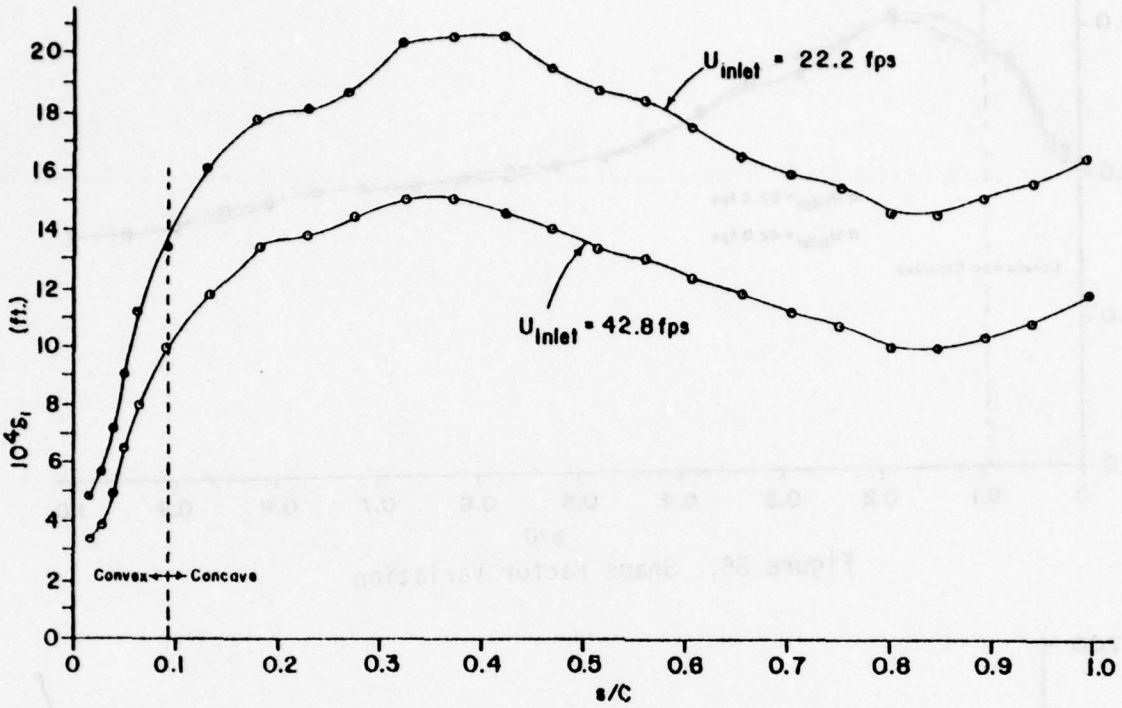

Figure 84. Pressure Surface Boundary Layer Displacement Thickness Variation

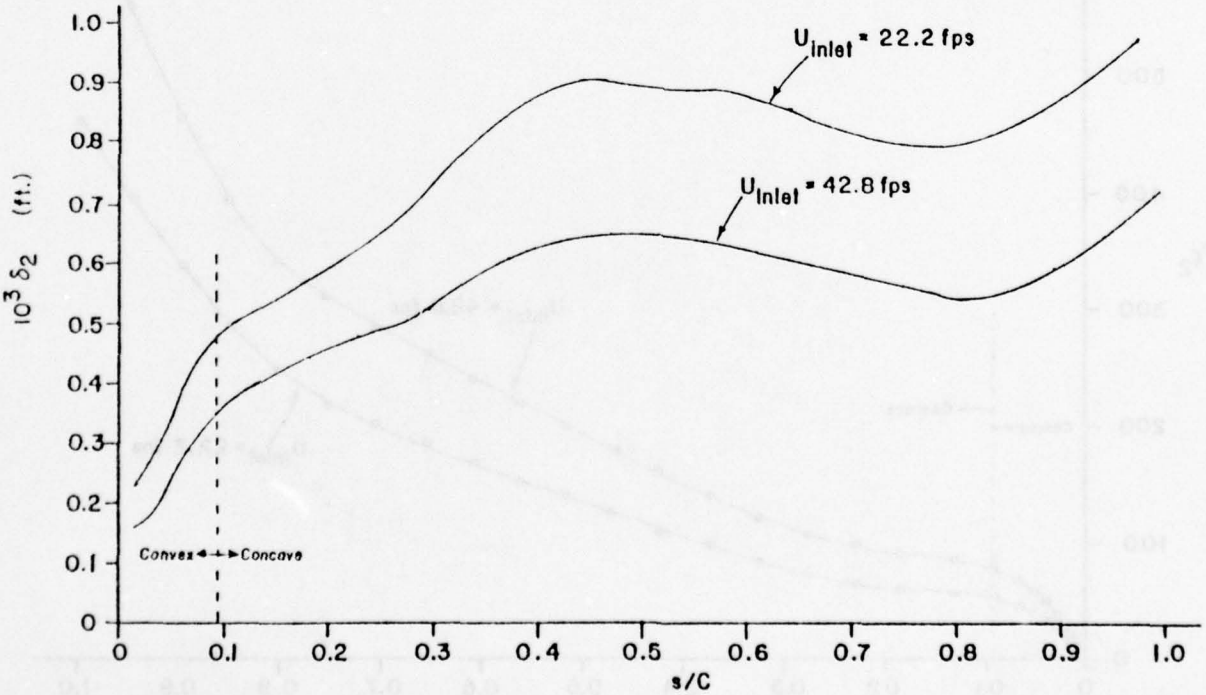

Figure 85. Pressure Surface Boundary Layer Momentum Thickness Variation

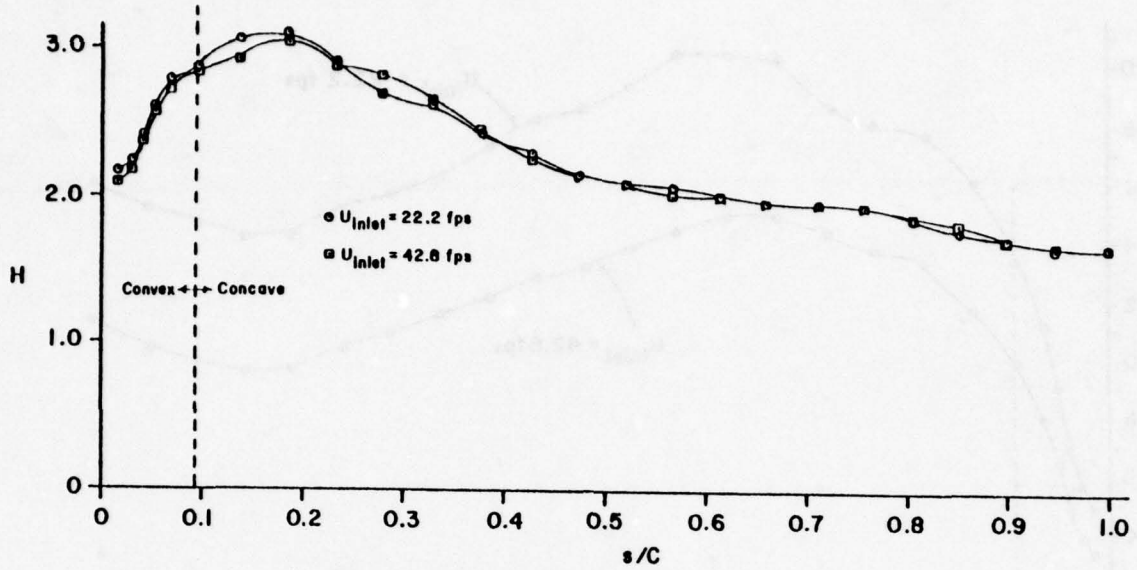

Figure 86. Shape Factor Variation

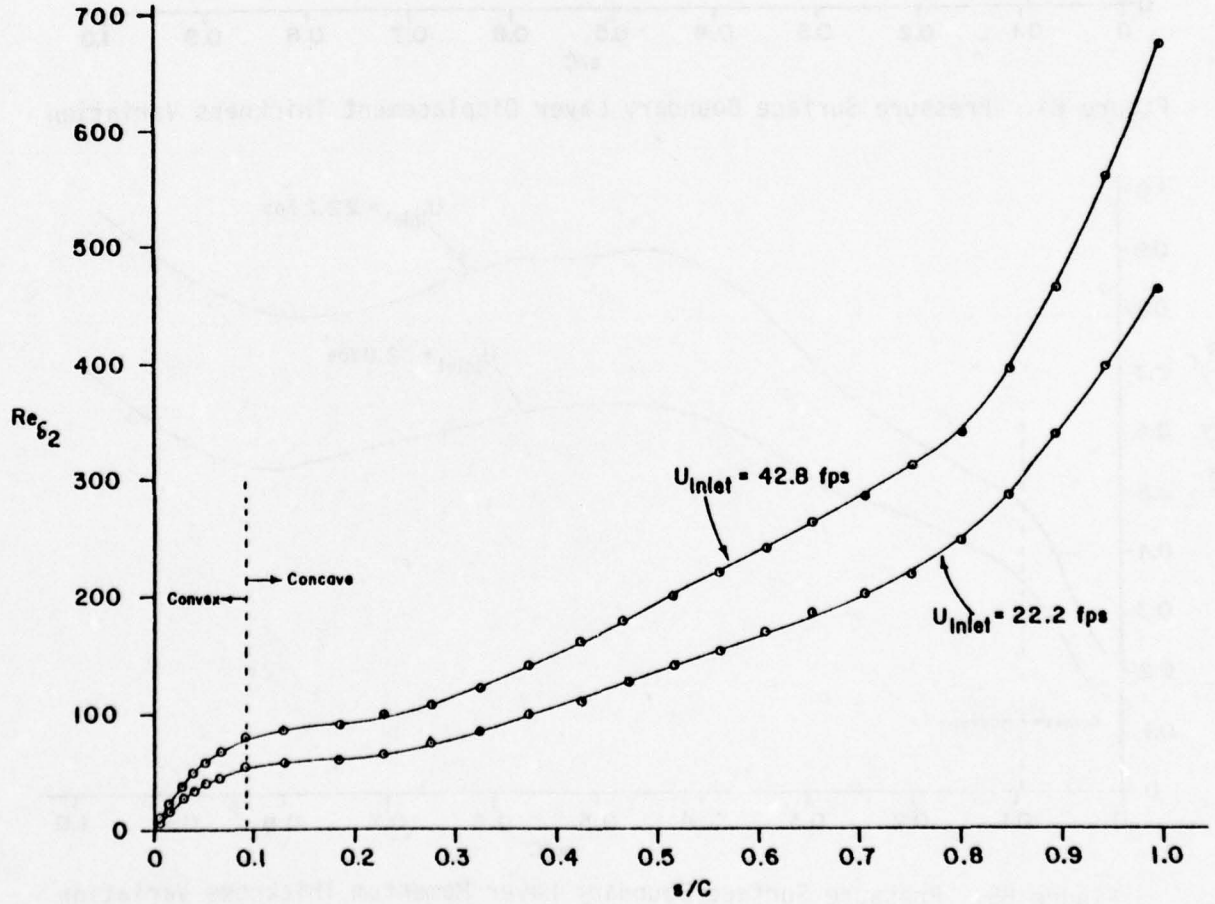

Figure 87. Variation of Re_{δ_2}

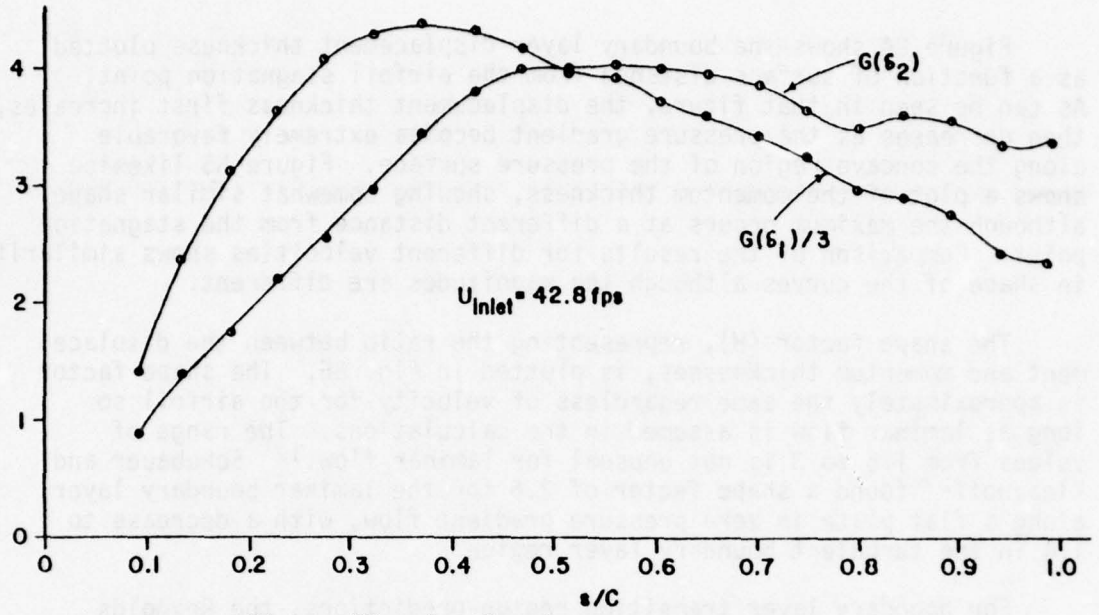

Figure 88. Gortler Parameter Variation

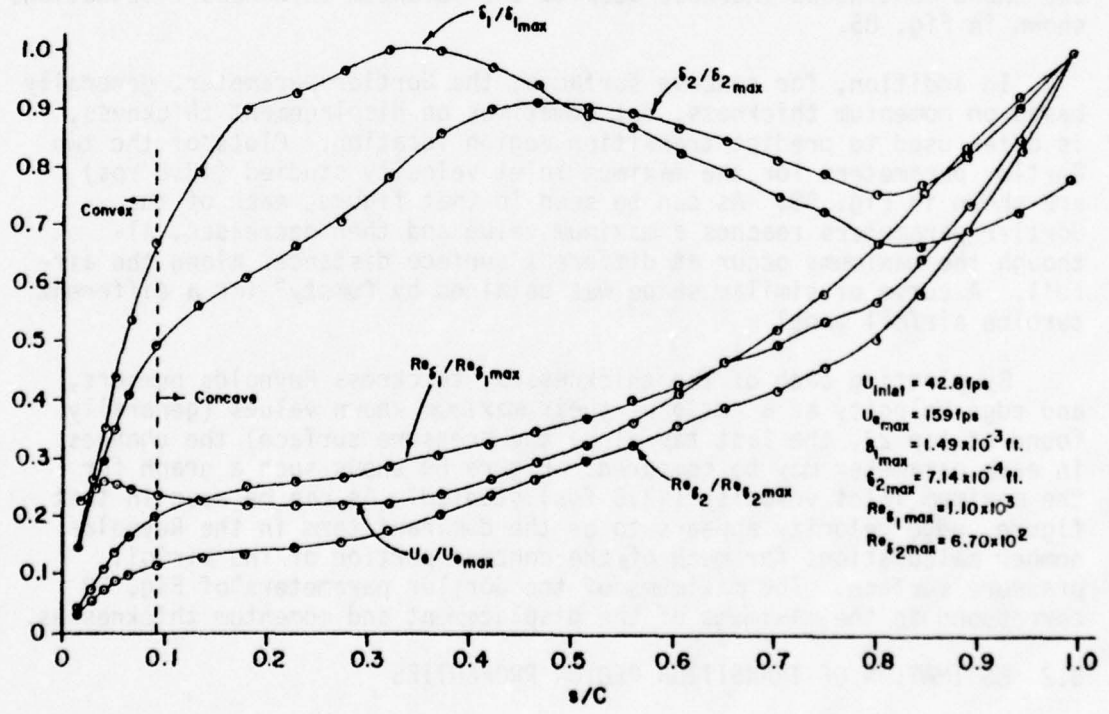

Figure 89. Comparison of Boundary Layer Parameters (U_{inlet} = 42.8 fps)

Figure 84 shows the boundary layer displacement thickness plotted as a function of surface distance from the airfoil stagnation point. As can be seen in that figure, the displacement thickness first increases, then decreases as the pressure gradient becomes extremely favorable along the concave region of the pressure surface. Figure 85 likewise shows a plot of the momentum thickness, showing somewhat similar shape although the maximum occurs at a different distance from the stagnation point. Comparison of the results for different velocities shows similarity in shape of the curves although the magnitudes are different.

The shape factor (H), representing the ratio between the displacement and momentum thicknesses, is plotted in Fig. 86. The shape factor is approximately the same regardless of velocity for the airfoil so long as laminar flow is assumed in the calculations. The range of values from 1.6 to 3 is not unusual for laminar flow.[17] Schubauer and Klebanoff[27] found a shape factor of 2.6 for the laminar boundary layer along a flat plate in zero pressure gradient flow, with a decrease to 1.4 in the turbulent boundary layer region.

For boundary layer transition region predictions, the Reynolds number should be based on the momentum or displacement thickness rather than surface distance, to indicate the magnitude of boundary layer growth. The momentum thickness Reynolds number is plotted in Fig. 87 and shows continuous increase despite the momentum thickness fluctuations shown in Fig. 85.

In addition, for concave surfaces, the Gortler parameter, generally based on momentum thickness, but sometimes on displacement thickness, is often used to predict transition region location. Plots of the two Gortler parameters for the maximum inlet velocity studied (42.8 fps) are shown in Fig. 88. As can be seen in that figure, each of the Gortler parameters reaches a maximum value and then decreases, although the maximums occur at different surface distances along the airfoil. A curve of similar shape was obtained by Cumsty[5] for a different turbine airfoil model.

By plotting each of the thicknesses, thickness Reynolds numbers, and edge velocity as a ratio of their maximum known values (generally found at tap 27, the last tap along the pressure surface) the changes in each parameter may be compared. Figure 89 shows such a graph for the maximum inlet velocity (42.8 fps) studied. As can be seen in that figure, edge velocity appears to be the dominant term in the Reynolds number calculations for much of the concave portion of the airfoil pressure surface. The maximums of the Gortler parameters of Fig. 88 correspond to the maximums of the displacement and momentum thicknesses.

5.2 ESTIMATION OF TRANSITION REGION PROPERTIES

As a result of the laminar flow calculations just discussed, some of the transition region properties, such as location and disturbance wavelengths, can be estimated. This has been done through the use of empirical equations and stability theory calculations of other authors.

For transition along concave surfaces, the Gortler parameter $[(U_\infty \delta_2/\nu)\ \delta_2/R]$ is generally considered an indication of transition. Gortler[72] showed that a value of 0.58 for the Gortler parameter, based on δ_2, is the minimum for neutral stability to occur. Examination of Fig. 88 and the appendix data shows that this value occurs prior to static tap 8 (s/C = 0.10), the first tap in the concave region, for all velocities studied. A value between 6(Tu = 0.3%) and 9(Tu = 0.06%) for $G(\delta_2)$ was found by Liepmann[66,76] to indicate transition. Forest[137] has also reported a previously unpublished value of 4.5 (Tu = 4%). The highest value found along the airfoil in this study was only about 4 at an inlet velocity of 42.8 fps (Tu = 0.64%), and full transition was not observed.

When the Gortler parameter is based on displacement thickness, a value of 38 may be considered an indication of transition in zero pressure gradients as shown in Fig. 90.[54] $G(\delta_1)$ never exceeded 13.2, however, and the maximum values (plotted in Fig. 90) still fall far short of the transition value of 38. The values of $G(\delta_1)$ from this study, however, are based on the calculated growth of a laminar boundary layer. Actual boundary layer growth should be greater beyond the point of neutral stability, thus an experimentally measured displacement thickness might give a somewhat larger value.

At all velocities, the Görtler parameter was found to reach maximum values at about the same surface location [static tap 14 (s/C = 0.38) for $G(\delta_1)$ and tap 18 (s/C = 0.57) for $G(\delta_2)$]. Very little variation of the parameter was found with increasing velocity. The maximum value of $G(\delta_2)$ was found to be 3.35 for a test section inlet velocity of 22.2 fps, while the value was 4.07 for a velocity of 42.8 fps. From the flow visualization studies, the earliest indication of transition occurred prior to tap 13 (s/C = 0.33) with the Tollmien-Schlichting waves occurring soon after. It is likely that the formation of Görtler vortices started soon after tap 8 (s/C = 0.10), the point of neutral stability, and may have been indicated experimentally by the observed low frequency oscillation of the boundary layer which was first observed near that location.

In addition to the Görtler parameter, spatial amplification factors such as those used by Smith[75] could be used to predict transition and the growth of the disturbance from the point of neutral stability. However, time did not permit the calculation of amplification factors for comparison in this study.

An important dimension of Gortler vortices is the wavelength (λ_G). The curves of Fig. 91 are based on the stability theory calculations of Tobak.[84] By knowing the arclength (2a) of constant curvature, a stability curve is found which relates $\alpha\delta_2$ to $G(\delta_2)$, where $\alpha = 2\pi/\lambda_G$. Generally, the vortex wavelength causing instability can be expected to be that which causes the earliest instability. In Fig. 91 this would occur at $G(\delta_2) = 0.58$ and $\alpha\delta_2 = 0.164$, assuming a large plate of constant curvature. For the airfoil pressure surface of this study,

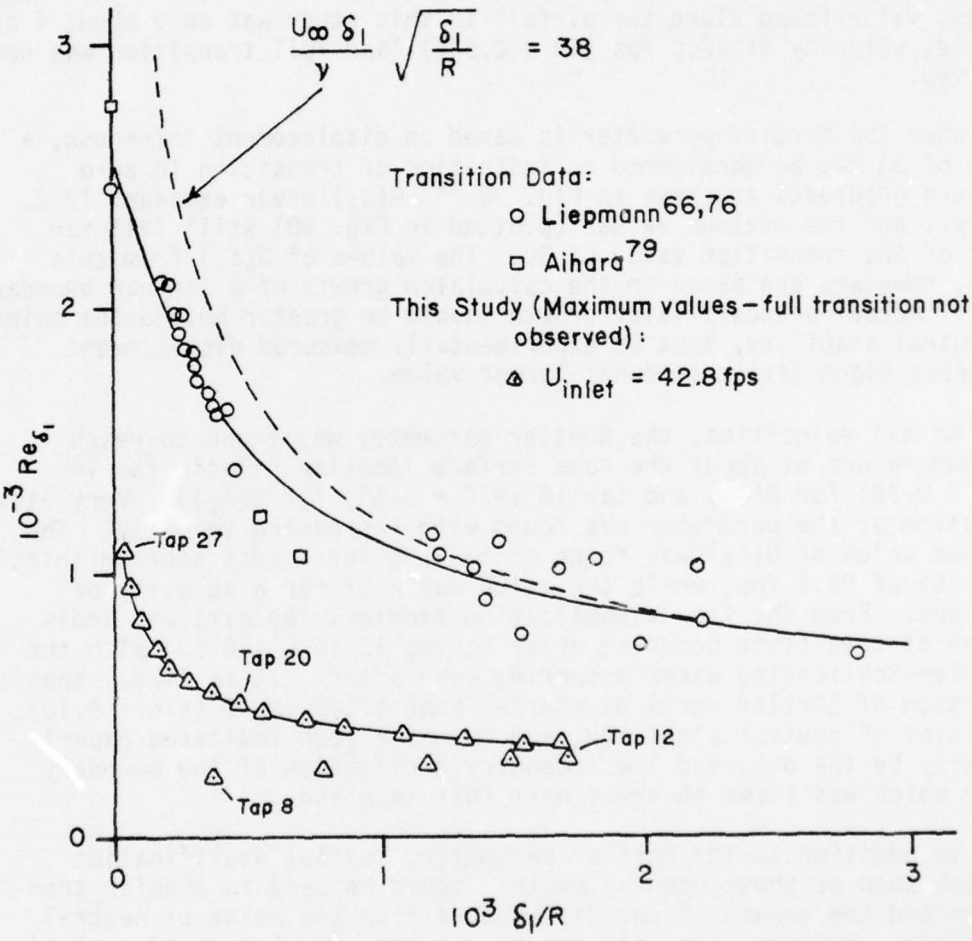

Figure 90. Comparison of $G(\delta_1)$ Values of this Study with Values at Transition from Tani

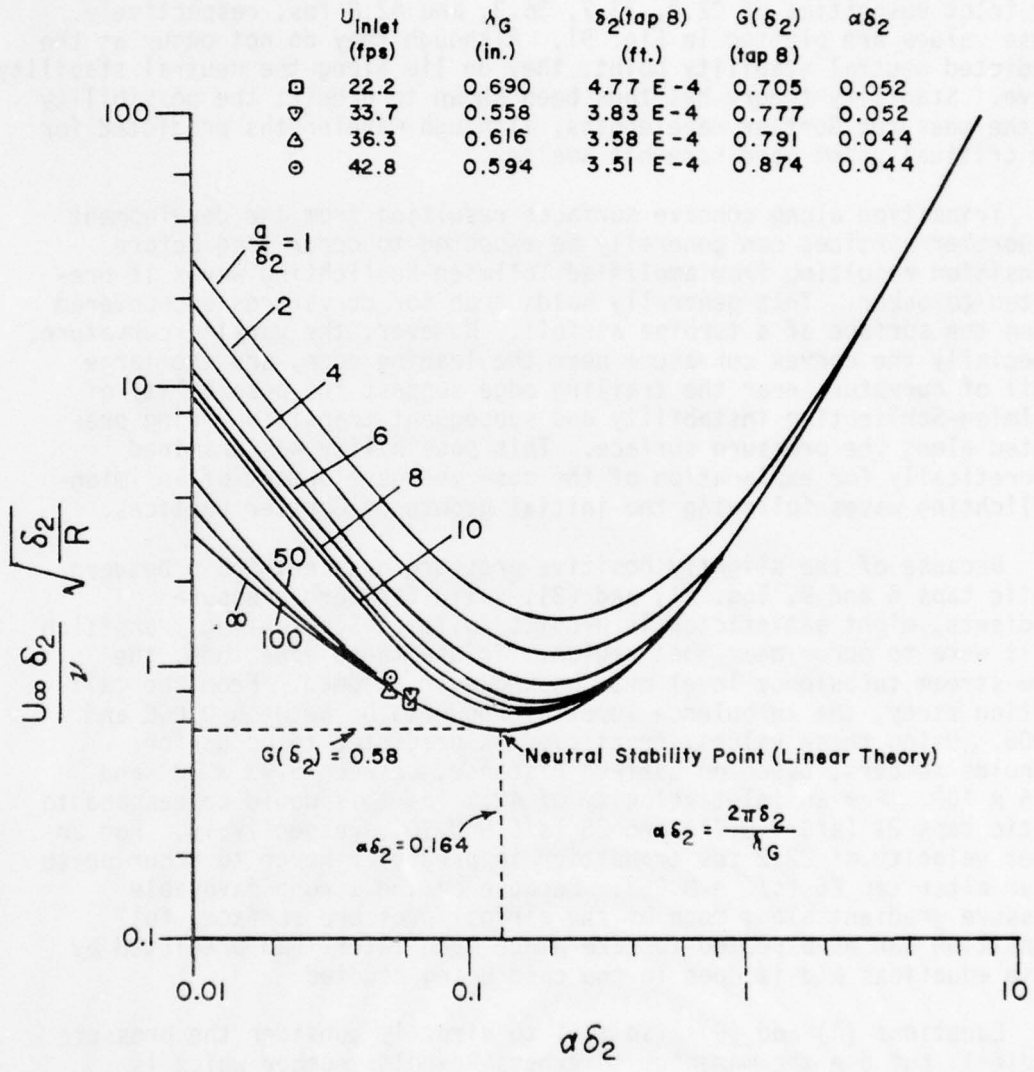

Figure 91. Comparison of Gortler Wavelengths with Stability Theory Due to Tobak

$a/\delta_2 > 50$. The value of λ_G would thus be estimated as 0.22 and 0.16 in. for inlet velocities of 22.2 and 42.8 fps, based on the momentum thickness calculated at tap 8 (s/C = 0.10). The average values of λ_G obtained from the flow visualization studies were 0.69, 0.56, 0.63, and 0.59 in. for inlet velocities of 22.2, 33.7, 36.3, and 42.8 fps, respectively. These values are plotted in Fig. 91. Although they do not occur at the predicted neutral stability point, they do lie along the neutral stability curve. Stability theory has thus been shown to predict the possibility of the measured Gortler wavelengths, although wavelengths predicted for the critical point were somewhat smaller.

Transition along concave surfaces resulting from the development of Gortler vortices can generally be expected to occur long before transition resulting from amplified Tollmien-Schlichting waves is predicted to occur. This generally holds true for curvatures encountered along the surface of a turbine airfoil. However, the varying curvature, especially the convex curvature near the leading edge, and the large radii of curvature near the trailing edge suggest the possibility of Tollmien-Schlichting instability and subsequent transition being predicted along the pressure surface. This possibility was examined theoretically for explanation of the observed development of Tollmien-Schlichting waves following the initial growth of Gortler vortices.

Because of the slightly positive pressure gradient found between static taps 5 and 9, Eqs. (1) and (2), valid for zero pressure gradients, might satisfactorily predict Tollmien-Schlichting transition if it were to occur near that region. To use these equations, the free-stream turbulence level must be known or assumed. From the calibration study, the turbulence level is known to be between 0.006 and 0.008. Using these values, transition is predicted to occur for Reynolds numbers, based on surface distance, between 5.93×10^5 and 1.16×10^6. For an inlet velocity of 42.8 fps this would correspond to static taps 21 (s/C = 0.71) and 25 (s/C = 0.90), respectively. For an inlet velocity of 22.2 fps transition is predicted never to occur or to occur after tap 26 (s/C = 0.95). Because of the strong favorable pressure gradient along much of the airfoil pressure surface, full transition can be expected to take place much later than predicted by these equations and it does in the case being studied.

Equations (4) and (6) also fail to directly consider the pressure gradient, but use the momentum thickness Reynolds number which is influenced by pressure gradients. These equations offer the additional advantage of predicting the beginning and end of the Tollmien-Schlichting transition region. Using these equations, transition was predicted never to start for an inlet velocity of 22.2 fps. For an inlet velocity of 42.8 fps, the transition region was predicted to start after tap 26 (s/C = 0.95), but never to reach full transition. Using a turbulence level of 0.008, Re_{δ_2} was found to equal 616 for the beginning of the transition region and to equal 1863 for the end, greatly in excess of the values obtained from the laminar flow calculations for the region ($0.43<s/C<0.57$) within which traveling waves

were first observed at all inlet velocities of this study. Therefore, in the presence of the Gortler vortices, the Tollmien-Schlicting waves occur even much earlier than predicted by Eq. (4). In order to directly consider the pressure gradient effects, an equation such as Eq. (3) can also be used, but this equation yields even higher values for the transition Reynolds numbers in this instance than do Eqs. (4) and (6).

The earlier transition due to the presence of Gortler vortices is not surprising, because it was this early transition along concave surfaces that led to their initial discovery. However, determination of the critical Reynolds number (shown in Fig. 92) also fails to predict the occurrence of Tollmien-Schlichting waves where observed. In that figure the data for an inlet velocity of 42.8 fps is plotted against a stability curve obtained by schlichting.[17] The pressure gradient parameter $[\lambda_\delta = (\delta^2/\upsilon)dU_e/dx]$ was estimated by assuming a Blasius profile and converting the values of DEL2U from the laminar boundary program listed in Appendix C. As can be seen in Fig. 92, the data come closest to neutral stability around tap 7 or 8, the same region where the Gortler vortices reach neutral stability. Although this could help to explain the occurrence of Tollmien-Schlichting waves in the current study, similar explanation does not exist for similar characteristics described in Refs. 5, 54, and 79 through 82.

In order to see what estimates might be obtained for the Tollmien-Schlichting wavelengths (λ_{TS}) from linear theory, reference was made to Fig. 93. In that figure, the data obtained at an inlet velocity of 42.8 fps at various stations along the airfoil have been plotted with stability curves from Ref. 17. The data points lie within the predicted unstable regions for adverse rather than the favorable pressure gradients found along most of the pressure surface. To a large extent, this is because of the smaller Reynolds numbers at which the traveling waves were found in this study. However, the wavelengths observed for taps 15 and 16 are larger than would be predicted for zero or negative pressure gradients, even for much larger Reynolds numbers. With the varying pressure gradients and early occurrence of traveling waves found in this study, Fig. 93 would thus seem to offer little assistance in predicting the Tollmien-Schlichting wavelengths associated with deformation of Gortler vortices.

It would appear that little information about the Tollmien-Schlichting wavelengths or location can be obtained from the linear stability theory. As would be expected, transition, even instability, is predicted to occur long after Tollmien-Schlichting waves are actually initiated through deformation of the Gortler vortices. This suggests that nonlinear theory such as that of Aihara[40] must be developed further before theoretical prediction of the observed features of transition following deformation of the Gortler vortices may be possible. In contrast, the linear theory does appear to predict adequately the point of neutral stability and the possible wavelengths associated with the Gortler vortices.

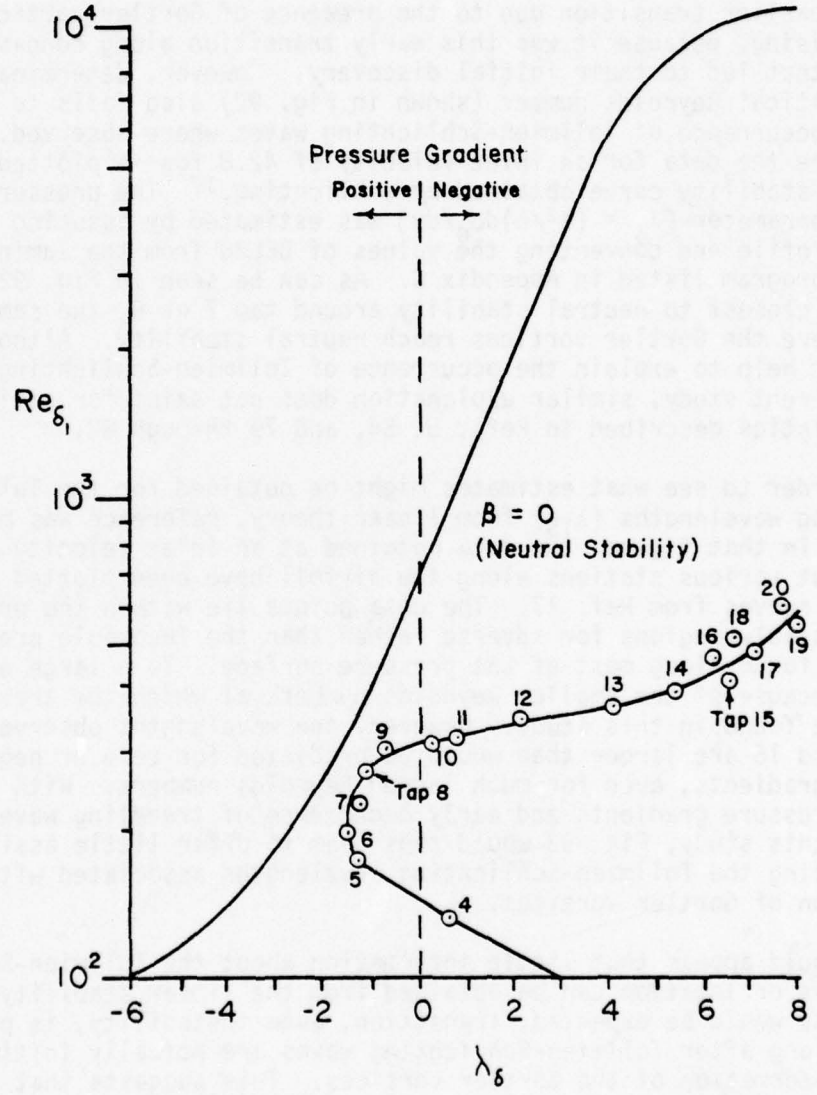

Figure 92. Comparison of Laminar Boundary Layer Calculations with Critical Reynolds Number Curve of Schlichting

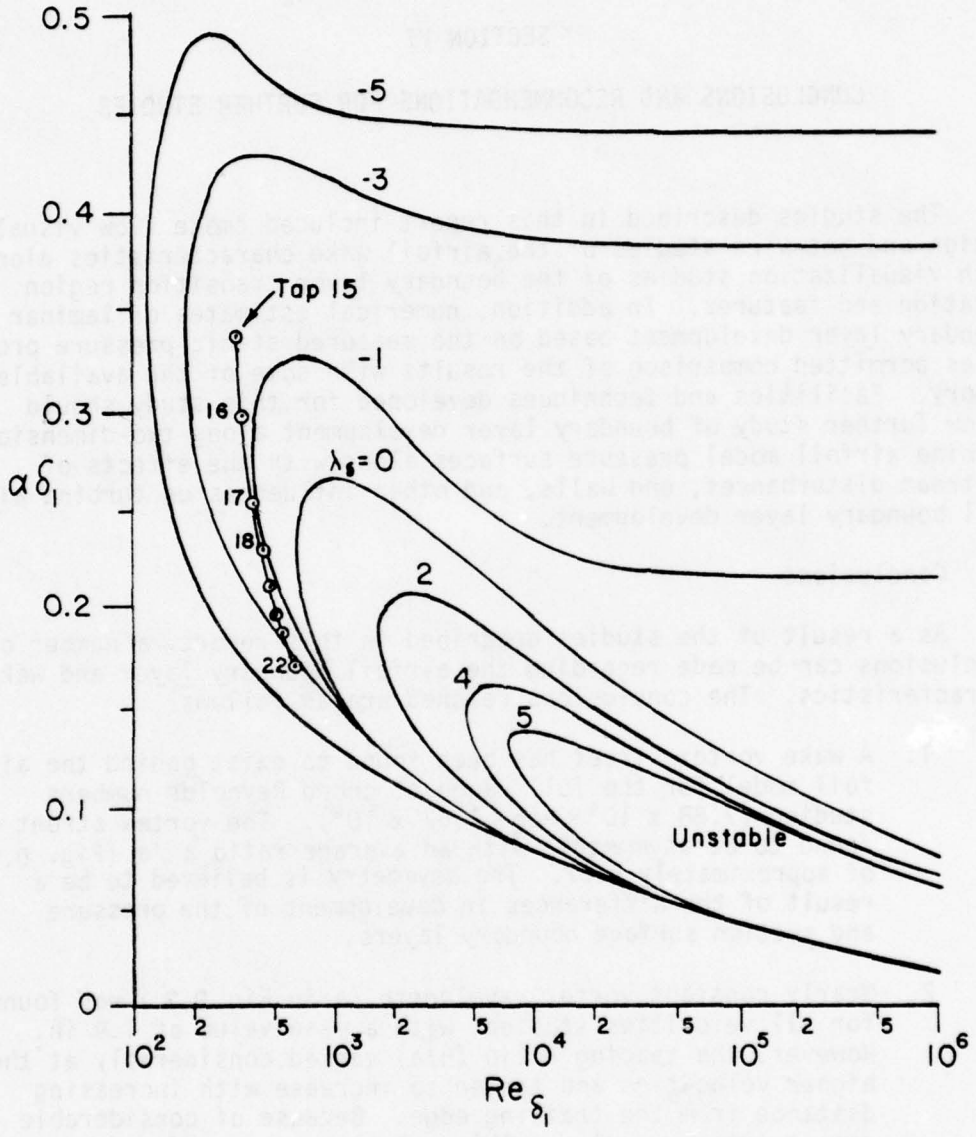

Figure 93. Comparison of Tollmien-Schlichting Wave Data with Neutral Stability Curves of Schlichting

SECTION VI

CONCLUSIONS AND RECOMMENDATIONS FOR FURTHER STUDIES

The studies described in this report included smoke flow visualization and hot-wire studies of the airfoil wake characteristics along with visualization studies of the boundary layer transition region location and features. In addition, numerical estimates of laminar boundary layer development based on the measured static pressure profiles permitted comparison of the results with some of the available theory. Facilities and techniques developed for this study should allow further study of boundary layer development along two-dimensional turbine airfoil model pressure surfaces along with the effects of upstream disturbances, end walls, and other influences on turbine airfoil boundary layer development.

6.1 Conclusions

As a result of the studies described in this report, a number of conclusions can be made regarding the airfoil boundary layer and wake characteristics. The conclusions reached are as follows:

1. A wake vortex street has been found to exist behind the airfoil model for the full range of chord Reynolds numbers studied ($7.88 \times 10^5 < Re_C < 1.52 \times 10^6$). The vortex street was found to be asymmetric with an average ratio a_1/a (Fig. D.2) of approximately 0.57. The asymmetry is believed to be a result of the differences in development of the pressure and suction surface boundary layers.

2. Nearly constant vortex wavelength (a in Fig. D.2) was found for all velocities studied, with a mean value of 1.9 in. However, the spacing ratio (h/a) varied considerably at the higher velocities and tended to increase with increasing distance from the trailing edge. Because of considerable data scatter, no discernible relationship was found between the spacing ratio and distance behind the airfoil trailing edge.

3. In agreement with Ref. 128, the airfoil trailing edge radius appears to be a significant parameter in determining the vortex shedding frequency from turbine airfoils having a semicircular trailing edge. The Strouhal number based on the trailing edge diameter was found to be 0.46.

4. Considerable variation of the wake thickness was found to occur, especially at a blade chord Reynolds number of 1.5×10^6. At times, vortex shedding appears to cease, yielding a turbulent wake of much less thickness. Although the occurrence of these changes is by no means periodic, the turbulent wake was found to appear approximately nine times per second with an inlet velocity of 22.2 fps and about thirty times per second with an inlet velocity of 42.8 fps. This appears to be directly related to full boundary layer transition to turbulence and may serve as an indication of when turbulent boundary layer development actually takes place on the pressure surface. This result may prove very valuable for cascade or rotor testing where wake measurements are often easier to obtain than are boundary layer measurements.

5. The observed vortex street properties of the airfoil wake are sufficiently similar to those of a circular cylinder to permit substitution of circular cylinders for upstream airfoils in wake effects studies.

6. Transition along the pressure surface of the model is initiated by the formation of Görtler vortices having a point of neutral stability prior to $s/C = 0.10$, based on Görtler criteria such that $G(\delta_2) > 0.58$, for all test section inlet velocities studied.

7. In agreement with the results of Refs. 5, 54, and 79 through 82, the Görtler vortices were found to deform through the action of what appear to be superimposed traveling, or Tollmien-Schlichting, waves. These waves follow a sequence of events very much similar to those described in Refs. 22 through 25 for Tollmien-Schlichting transition along an ogive-nosed circular cylinder. The Tollmien-Schlichting waves observed in this study were found to occur in groups ranging from one to fifteen waves, grow, and then break into a turbulent boundary layer, followed by a period when the entire transition region appeared to go essentially laminar.

8. Adjacent Görtler vortices were found to deform, through the action of traveling waves, at slightly different surface distances.

9. The first regular occurrence of the Tollmien-Schlichting waves occurred for $0.43 < s/C < 0.57$ for the velocities studied. Nowhere along the airfoil pressure surface was a turbulent boundary layer found to exist at all times.

10. A low frequency traveling wave variation of the boundary layer thickness was found to precede the Tollmien-Schlichting wave development. When the thickness reached a maximum between $s/C = 0.43$ and 0.57, a group of Tollmien-Schlichting

waves was found to form. A diagram of this observation is shown in Fig. 94. The frequency of this wave was found to vary from 20 to 54 Hz with most values between 20 and 35 Hz at a test section inlet velocity of 22.2 fps ($Re_c = 7.88 \times 10^5$). For a test section inlet velocity of 42.8 fps ($Re_c = 1.52 \times 10^6$), the value was found to increase, possibly to as much as 65 Hz. These values accompany Tollmien-Schlichting wave frequencies on the order of 600 and 2000 Hz at the respective velocities.

11. Stability theory was shown to give relatively good agreement with the measured Görtler vortex wavelength (λ_G). The wavelength did not agree with the usual prediction for the critical point, however. Stability theory was not shown to predict the observed Tollmien-Schlichting wavelengths (λ_{TS}), however.

12. The wave speed ($\lambda_{TS}f$) of the Tollmien-Schlichting waves was found to be roughly equal to or slightly greater than the local edge velocity (U_e). This is in contrast to the results of Heckl and Jackson[45] which would indicate a disturbance wave speed approximately 35% of the edge velocity.

13. The local Tollmien-Schlichting wave frequency was found proportional to $U_e^{1.5}/\delta^{1.3}$.

14. Tollmien-Schlichting transition, even instability, is not generally predicted to occur along the airfoil pressure surface for the conditions studied. However, a slight positive pressure gradient between s/C = 0.05 and 0.14 results in a possible point of neutral stability at nearly the same location as neutral stability for the Görtler instability. However, this does not explain the observations of Tollmien-Schlichting waves following Görtler vortices found in Refs. 54 and 79 through 82 for flow along concave surfaces of constant curvature in zero pressure gradients.

15. Upstream boundary layer velocity profiles show generally a laminar boundary layer development, but as they proceed downstream inflexional profiles start to appear around mid-chord which indicate the end of the nonlinear development of disturbances, and the development of a high shear-layer and high-frequency disturbances, which lead eventually to the development of a turbulent boundary layer. Downstream profiles resemble turbulent profiles, but one should be careful not to conclude directly that a completely turbulent boundary layer exists downstream, and should consult with the visual and hot-wire frequency data which indicate an "intermittently turbulent" boundary layer development.

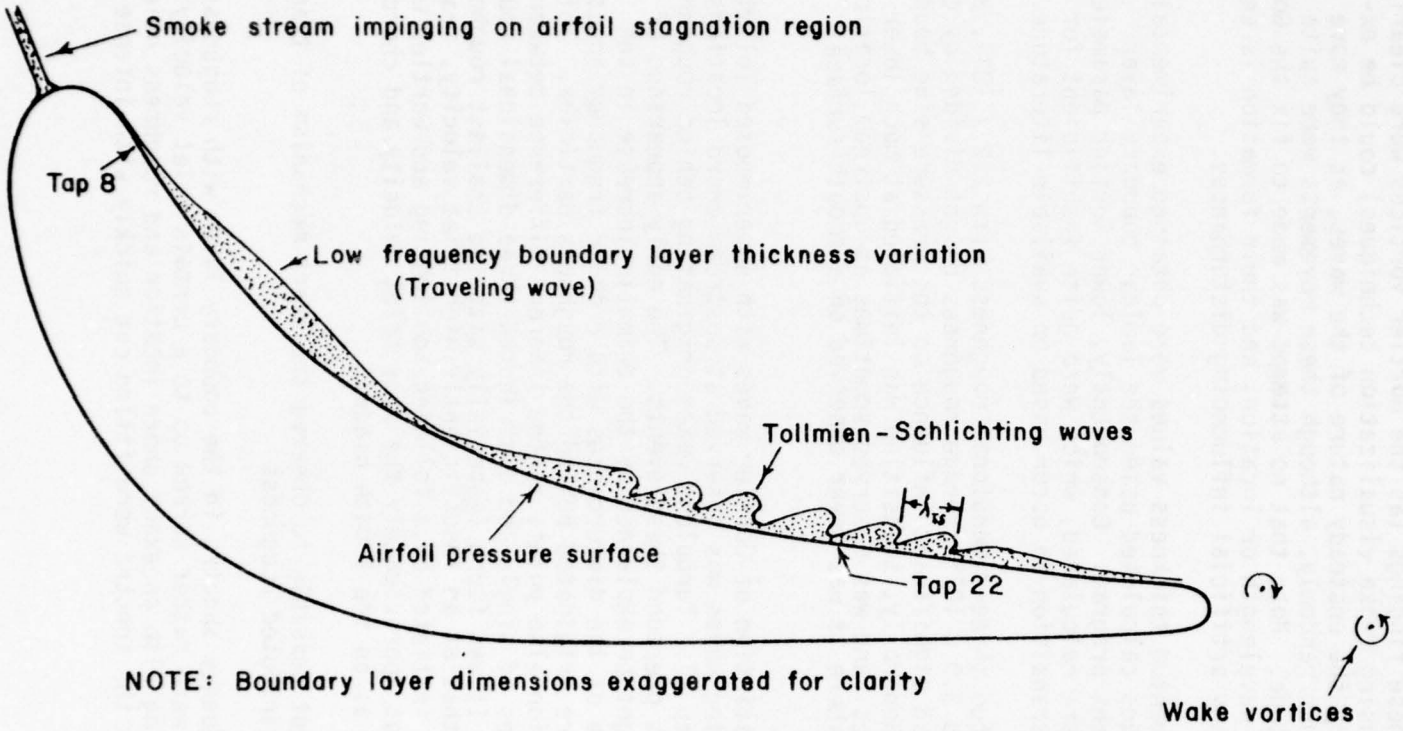

Figure 94. Diagram of Observed Boundary Layer Transition Region Features

16. Few spanwise velocity variations were found on the pressure side. These findings (as the Gortler vortices were clearly visible using smoke visualization techniques) could be explained by the unsteady nature of the waves, as they move spanwise rather randomly, although these movements were quite small in amplitude. Note that no attempt was made to fix the Gortler vortices wavelength or location, and their formation is entirely free of any artificial influencing disturbances.

17. Lower momentum thickness values were obtained experimentally than values calculated using the laminar boundary layer development program. Consequently, lower Gortler parameter values were calculated, which were quite insufficient for full Gortler transition to occur based on available literature.

18. Distributed three-dimensional roughness with 2.2×10^{-3}, 9.6×10^{-4}, and 3.0×10^{-4} average roughness height divided by chord length had significant influence on the pressure side boundary layer. Generally, transition was initiated at much lower inlet velocities, and was observed sometimes at upstream locations (tap 8) where it was never observed on a smooth surface.

19. Early initiation of Gortler waves with superimposed Tollmien-Schlichting waves was observed at upstream chord locations (up to tap 8). Turbulent wakes originating behind roughness particles preceded these events. The early appearance of these waves might be explained by the dramatic increase in the amplitude of the disturbances with broader frequency spectrum, which were originated behind the roughness particles. This observation also points to the inherent difference between the influences of single and distributed three-dimensional roughnesses. It was found (especially with the smallest roughness height) that at an insufficiently high inlet velocity, transition was initiated by a Tollmien-Schlichting and Gortler wave system, at approximately the same inlet velocity and chord location as on the smooth blade.

20. It was not possible to observe the exact mechanism of transition with distributed roughness.

21. The frequency spectra in the boundary layer with roughness present were rather narrow up to a certain inlet velocity (depending also on exact chord location and roughness height), and then the spectra were filled out quickly with intense

higher frequency disturbances. This is in contrast with the smooth surface transition spectra, which were full with distinct "spikes," and gradually got filled in with higher frequencies as complete transition was approached. The Tollmien-Schlicting waves which were observed upstream in some of the roughness studies were quite hard to locate on the frequency spectra because of the large number of intense disturbances present.

22. Small variations without any clear trend were observed between the smooth and rough surfaces static pressure distributions.

6.2 Recommendations for Further Studies

As a result of the observations obtained during the current study a number of ideas for future studies come to mind. The ability to visualize basic transition region features suggests that many influences on the pressure surface transition region could be studied with some detail. In addition, some further study of the wake region may be justified as a result of the vortex street observations.

The relationship between the observed low frequency boundary layer thickness variation and the groups of high frequency Tollmien-Schlichting waves also needs to be studied. In addition, the source of this low frequency variation needs to be identified to see whether it may be related to trailing edge conditions, stagnation region flow, some fundamental part of the natural transition process, or even to other channel flow dynamics of the tunnel. Study should also be made to determine whether a variation of this sort was also responsible for the groups of Tollmien-Schlichting waves observed in Refs. 24 and 25 for transition initiated by amplification of Tollmien-Schlichting waves rather than Görtler vortices.

The similarities between transition initiated by Görtler vortices and by Tollmien-Schlichting waves within the nonlinear region prior to full turbulence suggest that comparative study be made to see if some fundamental features might be found for both types of natural transition. The Lin-Benney[34] region of Tollmien-Schlichting transition is characterized by the deformation of the traveling waves through the formation of streamwise vortices. (Note that these vortices tend to form when the wave streamlines are convex. Could this be related in some way to the initiation of high-frequency Tollmien-Schlichting waves to deform the Görtler vortices when the boundary layer thickness variation was also convex?) Similarly, for Görtler transition along a concave surface, the streamwise vortices are deformed through the formation of traveling waves resembling Tollmien-Schlichting waves. At the same time as experimental studies of this nature are pursued, further development of nonlinear theory might also help to explain the observed similarities and differences.

Turbine airfoil pressure surface boundary layer transition has generally been ignored by designers as being insignificant. However, several recent turbine blade studies (Refs. 8, 132, and 134) have indicated either an inability to predict heat transfer rates accurately, confused transition region measurements, or an extensive transition region along the pressure surface. As a result, the low velocity two-dimensional cascades utilized in this study and by Cumsty[5] give some insight to other turbine airfoil experimental results. This should justify continued efforts to study the observed boundary layer transition region features to give improved turbine blade flow predictions as well as increased fundamental knowledge of the processes of boundary layer transition.

In order to describe more fully the mechanism of transition and relate it to events observed during this study and others, detailed study is needed to determine the instantaneous physical parameters associated with the observed sequence of events. Such parameters would include the instantaneous static pressure, detailed description of the velocity flow field as a function of time, and other parameters that might help show what forces the events to take place. Very likely such a study would involve the use of a combination of experimental techniques such as hot-wire anemometry, laser-Doppler anemometry, flow visualization using smoke or neutrally buoyant bubbles, surface-mounted pressure transducers, and other techniques that can yield instantaneous rather than average values for a number of points in the boundary layer. A data acquisition system would do much to facilitate the collection of such data.

The results of this study may show that while it is true that the boundary layer on the pressure-side of a turbine blade may be transitional, and thus the heat transfer rates will be different from laminar or turbulent calculations, it may be the case that the actual heat transfer rates after only a short period of time in service will resemble the rates obtained by turbulent calculations. This idea is further supported if one realizes that such relative roughness sizes used in this study are quite representative (if not underestimated) of the real surface roughness sizes of a turbine airfoil in service. Another interpretation of these results may point to a probable deficiency in ground testing of jet-engines. Jet-engine operating at high altitudes may not experience such intensive erosion as a jet-engine operating in ground conditions.

During the last several months of the project new sophisticated electronic equipment was purchased, and became available in the Department of Mechanical Engineering. A dual-channel Fast Fourier Transform Analyser with excellent automatic correlation capabilities is now available. This instrument can directly interact with the existing TSI dual-channel hot-wire anemometer. The FFT analyser can also interact with the new Department's Digital PDP 11/60 (which has A/D conversion capabilities), and

the large amount of data can be handled and processed virtually instantaneously and printed or plotted with great ease. With the aid of such a system, many previously unanswered questions may be investigated. Possible correlation between a complete turbulent boundary layer and the intermittent turbulent wake might be observed, which may prove very valuable for cascade or rotor testing as explained in Section 6.1 A study of the correlation between the low frequency waves observed in the boundary layer and the appearance of the T-S waves might help in gaining better understanding of transition in general.

In order to explore the mechanism by which single or distributed three-dimensional roughness causes transition, experimental work such as the study by Klebanoff et al[141] is needed. Rather interesting phenomena observed in this study (such as the early appearance of T-S and Gortler wave systems on rough surface) could be explained in such a study.

In addition, many other boundary layer studies of considerable importance to turbine airfoil design could be attempted with only minor modifications to the existing facilities. The effects of the various boundary regions on the heat transfer rate may be studied by embedding small heating units in the airfoil surface and raising slightly the temperature of the airfoil surface or, to represent more closely the cooling of a turbine airfoil, by embedding refrigerating coils in the airfoil surface and measuring the resulting heat transfer rate. Hub or turbine wall effects and accompanying secondary flow could be simulated by installing a plate normal to the airfoil surface in the center of the test section.

One more problem encountered with the current study is that the Reynolds numbers are too low to produce full transition along the airfoil pressure surface. If studies of the complete transition region are to be made, higher velocities may be needed to encourage full transition. The magnitude of this higher velocity is uncertain, because the theoretical study indicates only a slight change in the Görtler parameter even when the flow velocity is doubled. However, the transition region was seen to break into nearly turbulent flow rather often, and the wake indicated frequent transition to turbulent boundary layer flow at the highest inlet velocity used in the current study. To increase the velocities in the existing facilities, a fan and motor of greater capacity would be needed. In addition, modifications might be required to prevent stall in the transition section and to improve the screen and entrance sections even more than was done for this study.

The wake vortex street found behind the airfoil also suggests some additional study. Parmakian and Jacobson[136] showed that a rather small change in trailing edge thickness can result in significant reduction of turbine vibration for hydrodynamic flow. A study of the effects of different trailing edge dimensions or geometries on the wake vortex street dimensions and frequencies might thus prove valuable.

APPENDIX A

CASCADE GEOMETRIC DATA

Figures A.1 and A.2 and Tables A.1 through A.4 present the airfoil and cascade geometric data used for all calculations made after the airfoil models were cast. These values may differ slightly from the data presented in Fig. 10, because the coordinates for that figure were developed by enlarging the Lander[114] coordinate data for a chord length of 21 in. The data of Fig. 10 were then used as a reference for producing the pattern from which the mold was made. However, much of the pattern had to be worked by hand, so the completed instrument airfoil was measured by using a mill table to obtain the results presented in this appendix.

Figure A.1 shows the profile of the test airfoil, along with the coordinate system used in Tables A.1 and A.2. Tables A.1 and A.2 present the coordinates for all the static tap locations shown in Fig. 15, and calculated distance(s) from tap 1, and the surface curvature (R) as calculated from the coordinates of that tap and the adjacent taps on either side. Both the surface distance and the curvature have also been nondimensionalized with respect to a chord length of 21 in. The curvature data are the same as presented in Fig. 11, and fluctuate somewhat, because a small error in the coordinates for a single tap location will give a much larger error for the curvature calculation which is based on fitting a circle through each set of three coordinate pairs.

In order to obtain calculated potential flow data for comparison with the experimental results, the geometric information presented in Fig. A.2 and Tables A.3 and A.4 was sent to the project sponsors at the USAF Aero Propulsion Laboratory. Tables A.3 and A.4 give the revised coordinate system used (axis aligned with flow direction) along with some of the airfoil and flow data submitted for the calculation. In preparing these data, it was found that, through an undetected previous error, the flow was not aligned to impinge directly on tap 1 which had been assumed to be the stagnation point. Instead, the flow impinged at an angle with tap 1 of about 7^0 toward the pressure surface. All of the data in Tables A.3 and A.4 and Fig. A.2 have been changed to reflect this fact. Figure A.2 describes some of the geometric parameters specifically required for the potential flow calculations. In that figure, $\Delta\beta_1$ and $\Delta\beta_2$ represent the angles formed by tangents to the leading and trailing edge curvature circles at the points where the airfoil surface is tangent to them. The trailing edge radius was chosen to match the coordinates of Tables A.3 and A.4 when plotted,

NOTE: Airfoil model outline drawn to one-third full scale

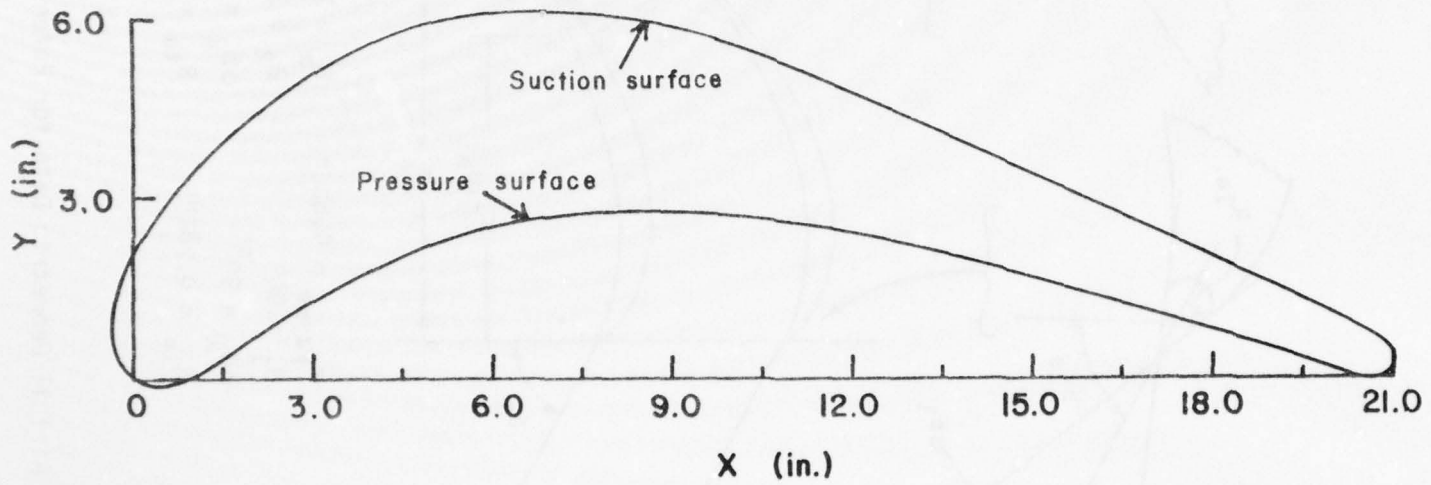

Figure A.1 Test Blade Profile

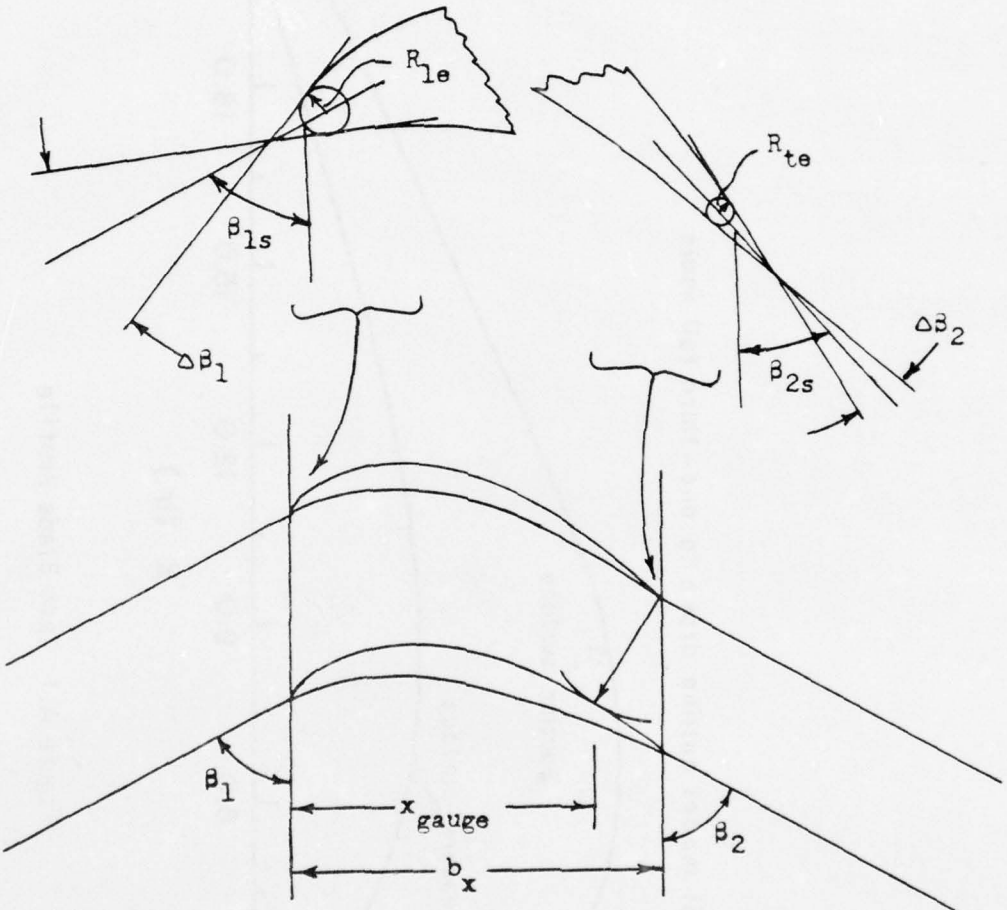

$x_{gauge} = 9.625"$ $\quad b_x = 14.183"$

$\beta_1 = 90^\circ$ $\quad \beta_2 = 17.5^\circ$

$\Delta\beta_1 = 90^\circ$ $\quad \Delta\beta_2 = 8.1^\circ$

$R_{le} = 0.781"$ $\quad R_{te} = 0.398"$

Figure A.2 Airfoil Geometric Data for Potential Flow Calculations

TABLE A.1

STATIC TAP COORDINATES, CURVATURE, AND SURFACE DISTANCE FOR AIRFOIL PRESSURE SURFACE

Tap No.	X(in.)	Y(in.)	R*(in.)	R/C*	s(in.)	s/C
1	0.0	0.0	-0.968	-0.0461	0.0	0.0
2	0.160	-0.135	-0.674	-0.0321	0.236	0.0113
3	0.415	-0.226	-0.767	-0.0365	0.487	0.0232
4	0.661	-0.227	-0.796	-0.0379	0.744	0.0354
5	0.909	-0.146	-1.471	-0.0701	0.997	0.0475
6	1.121	-0.034	-5.856	-0.2788	1.246	0.0593
7	1.342	0.095	-6.458	-0.3075	1.555	0.0740
8	1.746	0.363	32.977	1.5703	2.112	0.1006
9	2.595	0.899	10.950	0.5214	2.979	0.1419
10	3.461	1.342	12.307	0.5860	3.969	0.1890
11	4.394	1.728	29.065	1.3841	4.969	0.2366
12	5.336	2.080	10.592	0.5044	5.970	0.2843
13	6.248	2.336	9.003	0.4287	6.962	0.3315
14	7.272	2.489	11.265	0.5364	7.975	0.3798
15	8.339	2.555	10.425	0.4964	8.990	0.4281
16	9.259	2.524	20.826	0.9917	9.966	0.4746
17	10.249	2.445	18.982	0.9039	10.939	0.5209
18	11.223	2.316	25.006	1.1908	11.929	0.5681
19	12.211	2.145	38.660	1.8410	12.917	0.6151
20	13.154	1.957	25.755	1.2264	13.902	0.6620
21	14.143	1.720	47.287	2.2518	14.897	0.7094
22	15.093	1.471	40.822	1.9439	15.895	0.7569
23	16.064	1.191	65.374	3.1130	16.900	0.8048
24	17.037	0.894	78.452	3.7358	17.914	0.8531
25	18.009	0.611	120.582	5.7420	18.918	0.9009
26	18.942	0.331	53.624	2.5535	19.905	0.9479
27	19.891	0.065				

*Negative sign indicates convex curvature.

TABLE A.2

STATIC TAP COORDINATES, CURVATURE, AND SURFACE DISTANCE FOR AIRFOIL SUCTION SURFACE

Tap No.	X(in.)	Y(in.)	R*(in.)	R/C*	s(in.)	s/C
1	0.0	0.0	-0.968	-0.0461	0.0	0.0
56	-0.149	0.204	-0.955	-0.0455	0.243	0.0116
55	-0.240	0.443	-1.110	-0.0529	0.548	0.0261
54	-0.260	0.892	-1.885	-0.0897	0.910	0.0434
53	-0.216	1.179	-1.690	-0.0805	1.226	0.0584
52	-0.146	1.400	-2.658	-0.1266	1.541	0.0734
51	0.070	1.853	-6.150	-0.2929	2.104	0.1002
50	0.616	2.708	-7.436	-0.3541	2.985	0.1422
49	1.258	3.465	-6.997	-0.3332	3.988	0.1899
48	2.013	4.133	-10.459	-0.4981	4.993	0.2378
47	2.830	4.726	-7.766	-0.3698	6.007	0.2860
46	3.730	5.214	-7.714	-0.3673	7.024	0.3345
45	4.672	5.574	-6.237	-0.2970	8.028	0.3823
44	5.624	5.773	-7.625	-0.3631	9.037	0.4303
43	6.699	5.850	-10.325	-0.4917	10.075	0.4798
42	7.722	5.819	-9.694	-0.4616	11.101	0.5286
41	8.690	5.689	-9.756	-0.4646	12.104	0.5764
40	9.694	5.447	-12.136	-0.5779	13.103	0.6240
39	10.601	5.148	-19.831	-0.9443	14.095	0.6712
38	11.557	4.779	-29.932	-1.4254	15.093	0.7187
37	12.465	4.393	-48.741	-2.3210	16.085	0.7659
36	13.347	3.997	-103.652	-4.9358	17.065	0.8126
35	14.257	3.578	-11.044	-0.5259	18.056	0.8598
34	15.192	3.246	-10.274	-0.4893	19.042	0.9068
33	16.059	2.842	-11.258	-0.5361	20.005	0.9526
32	16.948	2.516	-6.458	-0.3075	20.987	0.9994
31	17.887	1.993	-12.812	-0.6101	22.001	1.0476
30	18.755	1.596	-1343.291	-63.9662	22.997	1.0951
29	19.665	1.179	-956.845	-45.5641	23.987	1.1423
28	20.579	0.759				

*Negative sign indicates convex curvature.

TABLE A.3

POTENTIAL FLOW CALCULATION GEOMETRIC DATA

Cascade Data:

Airfoil Chord Length: 21 in.
Airfoil Spacing: 15 in. (Solidity Ratio: 1.4)
Airfoil Span: 24 in. (Aspect Ratio: 1.143)
Stagger Angle: 50°
Angle of Attack: 50°

Upstream Data:

Inlet Velocity (U)	Inlet Static Pressure (In. H_2O gauge)	(In. Hg abs.)	(PSI abs.)
22.21 fps	-0.152	29.158	14.287
29.01 fps	-0.280	29.149	14.283
36.30 fps	-0.407	29.140	14.279
42.81 fps	-0.550	29.130	14.274

Temperature: 80°F

Airfoil Geometric Data:

See Table A.4 for measured airfoil coordinates given in the following system:

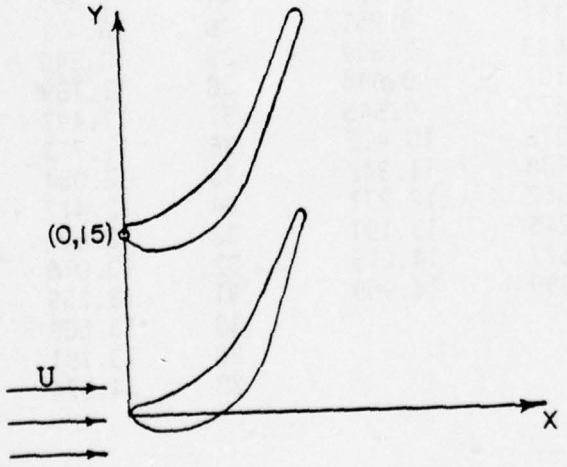

Trailing Edge Data:

Radius of Curvature: 0.398 in.
Center of Curvature: (13.785, 15.547)

TABLE A.4

AIRFOIL SURFACE COORDINATES
(REVISED COORDINATE SYSTEM)

Airfoil Pressure Surface			Airfoil Suction Surface		
Tap No.	XP(in.)	YP(in.)	Tap No.	XP(in.)	YP(in.)
1	0.0	0.0	1	0.0	0.0
2	0.003	0.209	56	0.056	-0.246
3	0.102	0.461	55	0.177	-0.472
4	0.262	0.648	54	0.503	-0.781
5	0.486	0.782	53	0.748	-0.937
6	0.710	0.868	52	0.961	-1.029
7	0.952	0.950	51	1.444	-1.163
8	1.419	1.080	50	2.448	-1.312
9	2.381	1.369	49	3.440	-1.324
10	3.283	1.732	48	4.440	-1.192
11	4.187	2.183	47	5.423	-0.965
12	5.071	2.663	46	6.382	-0.606
13	5.886	3.210	45	7.272	-0.131
14	6.649	3.855	44	8.047	0.457
15	7.399	4.617	43	8.810	1.218
16	7.979	5.332	42	9.458	2.010
17	8.569	6.131	41	9.995	2.826
18	9.111	6.951	40	10.471	3.743
19	9.630	7.809	39	10.840	4.623
20	10.107	8.644	38	11.189	5.587
21	10.577	9.545	37	11.493	6.525
22	11.012	10.426	36	11.773	7.451
23	11.438	11.342	35	12.054	8.413
24	11.852	12.271	34	12.417	9.336
25	12.276	13.191	33	12.681	10.255
26	12.677	14.079	32	13.018	11.140
27	13.099	14.969	31	13.239	12.192
			30	13.509	13.108
			29	13.791	14.068
			28	14.074	15.033

although measurements on the airfoil show the actual local curvature to be closer to 0.355 in. In addition, several of the coordinate points in Tables A.3 and A.4 did not match the surrounding curvature and had to be altered slightly by the sponsors to give a smooth curve for the calculations.

APPENDIX B

PROGRAM FOR FREQUENCY SPECTRUM CALCULATION

In order to determine the frequency spectrum of turbulence level data obtained with the Flow Corporation HWB-3 hot-wire anemometer, the FORTRAN program of this appendix was developed. The output of the HWB-3 hot-wire anemometer consists of three signals, M_1, M_2, and M_3. M_1 represents the noise signal of the equipment and is produced with a very small current (< 3 mA) applied to the wire, thus keeping the wire at nearly the ambient temperature. The second signal, M_2, is taken with the wire at operating temperature, but with constant current, and represents the turbulence signal created by the velocity fluctuations. The third signal, M_3, is produced by the addition of a square wave signal to the M_2 output and serves as a reference signal for the turbulence calculations. As might be expected, the square wave spectrum showed a series of spikes representing the components of a Fourier series. The noise signal included large frequency components at 60 Hz and at multiples such as 120 and 240 Hz. Likewise, the M_2 signal included these same large components, but they were generally cancelled or were ignored during the spectrum calculations.

The procedure used to calculate the turbulence level from the signal spectra is based on the procedure used to calculate the turbulence level as described by Cox.[109] The output of the frequency spectrum analyzer is given in dB versus Hz. The amplitudes are read from data cards and are then converted to their voltage equivalents for the M_1 and M_2 signals, given in the program as SM1 and SM2. A frequency component of the noise signal (SM1) is then squared and subtracted from the corresponding squared frequency component of the turbulence signal (SM2). This quantity is then divided by the square of the RMS value of the square wave signal (VM3) minus the square of the turbulence signal (VM2). The resulting quantity multiplied by a factor, representing the hot-wire calibration curve and the operating conditions which is also squared, gives a component (STU) of the power spectral density curve shown in Figs. 31 and 32 respectively.

The computer output shown in Tables B.1 through B.6 give complete turbulence spectrum data for test section inlet velocities of 22.21 and 42.81 fps. Generally, uniform frequency intervals are considered, but the interval has been varied slightly to allow for peaks in the

```
      $JOB
C1    HOT-WIRE DATA FREQUENCY SPECTRUM ANALYSIS PROGRAM FOR USE WITH
C1A         FEDERAL SCIENTIFIC MODEL UA-500 UBIQUITOUS SPECTRUM ANALYZER
C1B         AND FLOW CORPORATION MODEL HWB-3 HOT-WIRE ANEMOMETER
 1          DIMENSION FREQ(500),VM1DB(500),VM2DB(500),SM1(500),SM2(500),STU(5
     *00)
 2          REAL IZERO,IREF
 3          INTEGER PCNTID,DATE
 4          READ(5,153)NN
 5      153 FORMAT(I5)
 6          DO 150 L=1,NN
 7     1000 READ(5,1)OBSERV,PCNTID,AIRPRS,TATM,TFLOW,DATE,CALCON,BNREF,IREF,RR
     *,A,CMPFRQ,SQWFRQ,RI,RI4,VM1,VM2,VM3,GAIN1,GAIN
     *2,FLSCL1,FLSCL2,BETA,FLSCL3,FLSCL4,CORRCT
 8        1 FORMAT(A4,1X,I5,F5.2,2F5.1,I6,F5.3,F4.0,F7.2,F5.0,F4.1,F4.0,2F6.3,
     *12(F5.2,2F2.1,3F5.2/8F5.3)
C          BNREF = REFERENCE BRIDGE NULL (NO FLOW,WIRE CAPPED)
C          IREF = REFERENCE WIRE CURRENT (NO FLOW,WIRE CAPPED)
C          RR = RESISTANCE RATIO SETTING
C          A = SQUARE WAVE AMPLITUDE SETTING
C          CMPFRQ = AMPLIFIER COMPENSATION FREQUENCY
C          SQWFRQ = SQUARE WAVE FREQUENCY
C          RI = WIRE CURRENT AT OPERATING POINT
C          RI4 = 4*RI (READ DIRECTLY FROM HWB-3 POTENTIOMETER)
C          VM1 = RMS VOLTAGE WITH WIRE COLD (NOISE SIGNAL)
C          VM2 = RMS VOLTAGE WITH WIRE HOT (TURBULENCE SIGNAL)
C          VM3 = RMS VOLTAGE WITH WIRE HOT AND SQUARE WAVE ON (REFERENCE SIGNAL)
C2         GAIN1 = GAIN SETTING (DB) OF REAL TIME FREQUENCY SPECTRUM ANALYZER FOR
C2A             VM1 SPECTRUM
C3         GAIN2 = GAIN SETTING (DB) OF REAL TIME FREQUENCY SPECTRUM ANALYZER FOR
C3A             VM2 SPECTRUM
C4         FLSCL1 = FULL SCALE SETTING (VOLTS) OF REAL TIME FREQUENCY SPECTRUM
C4A             ANALYZER FOR VM1 SPECTRUM
C5         FLSCL2 = FULL SCALE SETTING (VOLTS) OF REAL TIME FREQUENCY SPECTRUM
C5A             ANALYZER FOR VM2 SPECTRUM
 9          IF(EOF(5))1500,1001
1001        READ(5,2)(FREQ(I),VM1DB(I),VM2DB(I),I=1,N)
10        2 FORMAT(3F10.2)
C          FREQ = THE FREQUENCY CORRESPONDING TO THE AMPLITUDE COMPONENTS
C          VM1DB = THE FREQUENCY COMPONENT OF VM1 EXPRESSED IN DECIBELS
C          VM2DB = THE FREQUENCY COMPONENT OF VM1 EXPRESSED IN DECIBELS
11          IZERO=(IREF*(BNREF/RN))**.5
C          IZERO = CORRECTED REFERENCE WIRE CURRENT
12          SMALLI=2.5/(1.+RN*(1.+4.*RR)/1600.)*A
C          SMALLI = HOT WIRE SQUARE WAVE CURRENT (AMPS TO PEAK)
13          F=10.**SMALLI/RI4/(1.-(IZERO**4./RI4)**2)
C          F = CALCULATIONS ON UPPER HALF OF DATA SHEET (FROM FLOW CORPORATION
C          HWB-3 MANUAL & COX THESIS)
14          G=(VM2**2-VM1**2)/(VM3**2-VM2**2)
C          G = CALCULATIONS ON LOWER HALF OF DATA SHEET (FROM FLOW CORPORATION
C          HWB-3 MANUAL & COX THESIS)
15          TU=F*SQRT(G)
C          TU = TURBULENCE INTENSITY
16          FLSCL5=.79*(FLSCL3*1000.)**2/BETA
17          FLSCL6=.79*(FLSCL4*1000.)**2/BETA
18          DO 501 I=1,N
19          SM1(I)=FLSCL5*10.**((VM1DB(I)-GAIN1+CORRCT)/20.*2.)
20          SM2(I)=FLSCL6*10.**((VM2DB(I)-GAIN2+CORRCT)/20.*2.)
21          GS=(SM2(I)-SM1(I))/(VM3**2-VM2**2)
22          STU(I)=GS*F**2
C          STU=TURBULENCE INTENSITY PER HERTZ. UNITS: (TU**2/HZ.)

23        501 CONTINUE
24          WRITE(6,991)PCNTID
25        991 FORMAT('1',23X,'TEST POINT- ',I5///)
26          WRITE(6,992)
27        992 FORMAT(4X,'NO.',7X,'FREQUENCY',7X,'COLD POSITION',7X,'HOT POSITION'
     *,10X,'STU'/18X,'HZ',14X,'DB/HZ',15X,'DB/HZ',14X,'1/HZ'/)
28          WRITE(6,993)(TU,(FREQ(I),VM1DB(I),VM2DB(I),STU(I),I=1,N)
29        993 FORMAT(2X,F3.2//(16,F8.1,13X,F4.1,16X,F4.1,9X,E12.3/))
30        150 CONTINUE
31       7734 STOP
32            END

      $ENTRY
```

TABLE B-1

FREQUENCY SPECTRUM DATA (U_{inlet} = 22.2 fps)

YU	FREQUENCY HZ	COLD POSITION DB/HZ	HOT POSITION DB/HZ	STD 1/HZ
0.008221				
	3.5	-47.	-38.	0.851E-06
	4.0	-47.	-36.	0.142E-05
	4.5	-48.	-37.	0.113E-05
	5.0	-47.	-35.	0.132E-05
	5.2	-48.	-27.	0.122E-04
	5.5	-52.	-38.	0.935E-06
	6.0	-53.	-36.	0.151E-05
	6.5	-52.	-38.	0.935E-06
	7.0	-57.	-35.	0.193E-05
	7.5	-56.	-37.	0.121E-05
	8.0	-53.	-38.	0.943E-06
	8.5	-59.	-39.	0.755E-06
	9.0	-57.	-36.	0.153E-05
	9.5	-60.	-39.	0.757E-06
	10.0	-56.	-38.	0.956E-06
	10.4	-57.	-26.	0.154E-04
	10.5	-59.	-40.	0.606E-06
	11.0	-52.	-38.	0.967E-06
	11.5	-60.	-41.	0.482E-06
	12.0	-54.	-39.	0.749E-06
	12.5	-60.	-40.	0.608E-06
	13.0	-60.	-40.	0.609E-06
	13.5	-60.	-42.	0.381E-06
	14.0	-60.	-42.	0.381E-06
	14.5	-59.	-39.	0.765E-06
	15.0	-60.	-41.	0.482E-06
	15.5	-61.	-42.	0.383E-06
	16.0	-61.	-44.	0.240E-06
	16.5	-60.	-41.	0.482E-06
	17.0	-61.	-43.	0.303E-06
	17.5	-60.	-48.	0.412E-07
	18.0	-61.	-43.	0.303E-06
	18.5	-61.	-44.	0.240E-06
	19.0	-61.	-44.	0.240E-06
	19.5	-60.	-42.	0.381E-06
	20.0	-60.	-44.	0.238E-06

TABLE B-2

FREQUENCY SPECTRUM DATA (U_{inlet} = 22.2 fps)

YU	FREQUENCY HZ	CALC POSITION DB/HZ	MOT POSITION DB/HZ	ST 1/HZ
0.098221				
	25.0	-59.	-26.	0.104E-05
	30.0	-58.	-29.	0.653E-06
	35.0	-59.	-28.	0.653E-06
	40.0	-59.	-29.	0.653E-06
	45.0	-59.	-32.	0.262E-06
	50.0	-59.	-28.	0.653E-06
	55.0	-60.	-34.	0.165E-06
	60.0	-32.	-29.	0.397E-06
	65.0	-60.	-36.	0.104E-06
	70.0	-59.	-31.	0.330E-06
	75.0	-59.	-37.	0.824E-07
	80.0	-61.	-34.	0.165E-06
	85.0	-60.	-40.	0.412E-07
	90.0	-60.	-36.	0.130E-06
	95.0	-60.	-41.	0.325E-07
	100.0	-60.	-34.	0.165E-06
	105.0	-60.	-43.	0.204E-07
	110.0	-62.	-42.	0.258E-07
	115.0	-60.	-43.	0.204E-07
	120.0	-30.	-30.	0.402E-00
	125.0	-60.	-45.	0.127E-07
	130.0	-61.	-44.	0.162E-07
	135.0	-60.	-45.	0.127E-07
	140.0	-61.	-44.	0.162E-07
	145.0	-63.	-47.	0.809E-08
	150.0	-61.	-47.	0.794E-08
	155.0	-60.	-47.	0.799E-08
	160.0	-62.	-48.	0.633E-08
	165.0	-60.	-49.	0.482E-08
	170.0	-61.	-47.	0.794E-08
	175.0	-60.	-49.	0.482E-08
	180.0	-50.	-50.	0.000E-00
	185.0	-60.	-51.	0.289E-08
	190.0	-62.	-51.	0.304E-08
	195.0	-60.	-50.	0.374E-08
	200.0	-62.	-52.	0.230E-08

TABLE B-3

FREQUENCY SPECTRUM DATA (U_{inlet} = 22.2 fps)

YU	FREQUENCY HZ	CCLD POSITION DB/HZ	HOT POSITION DB/HZ	STD 1/HZ
0.0C8221				
	500.C	-61.	-5C.	0.325E-10
	1000.C	-59.	-51.	0.241E-10
	1500.C	-60.	-5C.	0.325E-10
	2000.C	-57.	-5C.	0.239E-10
	2500.C	-57.	-50.	0.289E-10
	3000.C	-58.	-5C.	0.314E-10
	3500.C	-60.	-48.	0.536E-10
	4000.C	-58.	-49.	0.397E-10
	4500.C	-60.	-47.	0.634E-10
	5000.C	-59.	-48.	0.527E-10
	5500.C	-60.	-45.	0.111E-09
	6000.C	-60.	-47.	0.634E-10
	6500.C	-60.	-45.	0.111E-09
	7000.C	-61.	-47.	0.834E-10
	7500.C	-6C.	-44.	0.140E-09
	8000.C	-61.	-46.	0.879E-10
	8500.C	-60.	-44.	0.140E-09
	9000.C	-60.	-46.	0.879E-10
	9500.C	-61.	-44.	0.140E-09
	10000.C	-60.	-45.	0.111E-09
	10500.C	-61.	-44.	0.141E-09
	11000.C	-58.	-44.	0.138E-09
	11500.C	-62.	-43.	0.179E-09
	12000.C	-47.	-41.	0.215E-09
	12500.C	-62.	-43.	0.179E-09
	13000.C	-60.	-42.	0.224E-09
	13500.C	-62.	-42.	0.225E-09
	14000.C	-64.	-43.	0.179E-09
	14500.C	-61.	-42.	0.225E-09
	15000.C	-61.	-43.	0.177E-09
	15500.C	-58.	-42.	0.222E-09
	16000.C	-59.	-42.	0.223E-09
	16500.C	-60.	-41.	0.283E-09
	17000.C	-62.	-42.	0.224E-09
	17500.C	-60.	-41.	0.283E-09
	18000.C	-61.	-41.	0.224E-09
	18500.C	-59.	-4C.	0.356E-09
	19000.C	-61.	-41.	0.283E-09
	19500.C	-59.	-40.	0.356E-09
	20000.C	-60.	-41.	0.283E-09

TABLE B-4

FREQUENCY SPECTRUM DATA (U_{inlet} = 42.8 fps)

TU	FREQUENCY HZ	COLD POSITION DB/HZ	HOT POSITION DB/HZ	STU 1/HZ
0.006481				
	3.5	-53.	-31.	0.243E-05
	4.0	-55.	-31.	0.243E-05
	4.5	-59.	-32.	0.194E-05
	5.0	-53.	-31.	0.243E-05
	5.5	-53.	-36.	0.757E-06
	6.0	-59.	-35.	0.969E-06
	6.5	-57.	-37.	0.608E-06
	7.0	-59.	-34.	0.122E-05
	7.5	-60.	-34.	0.122E-05
	8.0	-59.	-36.	0.769E-06
	8.5	-59.	-37.	0.610E-06
	9.0	-59.	-36.	0.769E-06
	9.5	-60.	-35.	0.970E-06
	10.1	-52.	-15.	0.373E-04
	10.5	-60.	-34.	0.122E-05
	11.0	-60.	-35.	0.970E-06
	11.5	-61.	-37.	0.611E-06
	12.0	-53.	-37.	0.563E-06
	12.5	-61.	-36.	0.770E-06
	13.0	-61.	-41.	0.242E-06
	13.5	-61.	-42.	0.192E-06
	14.0	-61.	-42.	0.192E-06
	14.5	-60.	-42.	0.191E-06
	15.0	-61.	-41.	0.242E-06
	15.5	-61.	-41.	0.242E-06
	16.0	-61.	-43.	0.152E-06
	16.5	-61.	-42.	0.192E-06
	17.0	-61.	-45.	0.948E-07
	17.5	-61.	-44.	0.120E-06
	18.0	-61.	-43.	0.152E-06
	18.5	-61.	-43.	0.152E-06
	19.0	-61.	-46.	0.748E-07
	19.5	-61.	-42.	0.192E-06
	20.0	-61.	-44.	0.122E-06

TABLE B-5

FREQUENCY SPECTRUM DATA (U_{inlet} = 42.8 fps)

YU	FREQUENCY HZ	CCLD POSITION DB/HZ	FLT POSITION DB/HZ	SYS L/HZ
0.026481				
	25.0	-55.	-28.	0.329E-06
	30.0	-55.	-25.	0.658E-06
	35.0	-58.	-28.	0.330E-06
	40.0	-56.	-29.	0.262E-06
	45.0	-55.	-28.	0.329E-06
	50.0	-59.	-34.	0.824E-07
	55.0	-55.	-29.	0.261E-06
	60.0	-29.	-29.	0.102E-02
	65.0	-55.	-31.	0.165E-06
	70.0	-58.	-35.	0.655E-07
	75.0	-59.	-32.	0.131E-06
	80.0	-58.	-40.	0.205E-07
	85.0	-59.	-35.	0.650E-07
	90.0	-60.	-40.	0.329E-07
	95.0	-60.	-38.	0.329E-07
	100.0	-60.	-41.	0.163E-07
	105.0	-60.	-39.	0.260E-07
	110.0	-60.	-43.	0.102E-07
	115.0	-60.	-41.	0.163E-07
	120.0	-30.	-30.	0.200E-02
	125.0	-60.	-42.	0.129E-07
	130.0	-61.	-43.	0.103E-07
	135.0	-60.	-45.	0.638E-08
	140.0	-60.	-57.	0.207E-09
	145.0	-60.	-46.	0.502E-08
	150.0	-60.	-46.	0.502E-08
	155.0	-60.	-47.	0.395E-08
	160.0	-59.	-47.	0.389E-08
	165.0	-60.	-51.	0.145E-08
	170.0	-60.	-49.	0.241E-08
	175.0	-60.	-49.	0.241E-08
	180.0	-46.	-44.	0.305E-08
	185.0	-60.	-50.	0.187E-08
	190.0	-60.	-51.	0.145E-08
	195.0	-60.	-53.	0.835E-09
	200.0	-60.	-50.	0.197E-08

AD-A075 501 OHIO STATE UNIV RESEARCH FOUNDATION COLUMBUS F/G 20/4
INVESTIGATION OF THE BOUNDARY LAYER BEHAVIOR ON TURBINE AIRFOIL--ETC(U)
AUG 79 L S HAN, W R COX, A CHAIT F33615-75-C-2052
UNCLASSIFIED OSURF-760256/784174 AFAPL-TR-79-2011 NL

3 OF 3
ADA 075501

END
DATE FILMED
12-79
DDC

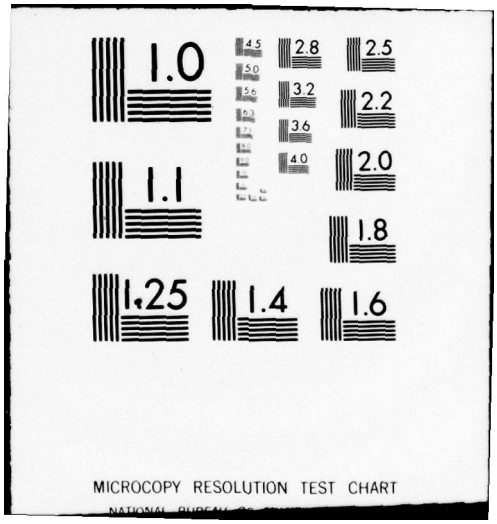
1.0
1.1
1.25
1.4
1.6
1.8
2.0
2.2
2.5
2.8
3.2
3.6
4.0
4.5
5.0
5.6
6.3
MICROCOPY RESOLUTION TEST CHART

TABLE B-6

FREQUENCY SPECTRUM DATA (U_{inlet} = 42.8 fps)

YU	FREQUENCY HZ	COLD POSITION DB/HZ	HOT POSITION DB/HZ	STO 1/HZ
0.0C6481				
	500.C	-60.	-43.	0.888E-10
	1000.0	-53.	-50.	0.153E-10
	1500.C	-60.	-51.	0.126E-10
	2000.C	-57.	-49.	0.192E-10
	2500.C	-60.	-50.	0.163E-10
	3000.C	-58.	-47.	0.332E-10
	3500.C	-60.	-49.	0.210E-10
	4000.C	-58.	-46.	0.425E-10
	4500.C	-60.	-47.	0.343E-10
	5000.C	-60.	-45.	0.554E-10
	5500.C	-60.	-47.	0.343E-10
	6000.C	-59.	-45.	0.549E-10
	6500.C	-61.	-47.	0.346E-10
	7000.C	-58.	-45.	0.543E-10
	7500.C	-61.	-46.	0.440E-10
	8000.C	-60.	-44.	0.256E-10
	8500.C	-62.	-46.	0.443E-10
	9000.C	-60.	-44.	0.702E-10
	9500.C	-62.	-45.	0.560E-10
	10000.C	-57.	-44.	0.634E-10
	10500.C	-63.	-45.	0.563E-10
	11000.C	-60.	-43.	0.888E-10
	11500.C	-64.	-45.	0.565E-10
	12000.C	-60.	-41.	0.992E-10
	12500.C	-64.	-44.	0.713E-10
	13000.C	-60.	-42.	0.1125-09
	13500.C	-64.	-44.	0.713E-10
	14000.C	-61.	-42.	0.1135-09
	14500.C	-64.	-43.	0.899E-10
	15000.C	-60.	-42.	0.1125-09
	15500.C	-60.	-43.	0.888E-10
	16000.C	-57.	-41.	0.1405-09
	16500.C	-62.	-42.	0.113E-09
	17000.C	-60.	-41.	0.1425-09
	17500.C	-62.	-42.	0.113E-09
	18000.C	-60.	-41.	0.1425-09
	18500.C	-61.	-41.	0.1425-09
	19000.C	-60.	-41.	0.1425-09
	19500.C	-61.	-41.	0.1425-09
	20000.C	-59.	-40.	0.1795-09

M_1 ("Cold Position") and M_2 ("Hot Position") data. The data are given in the raw form (dB/Hz) and in the calculated power spectral density (STU) form. It is this final column which was plotted in Figs. 31 and 32.

APPENDIX C

CALCULATION OF THE LAMINAR BOUNDARY LAYER PROFILES ON A TURBINE AIRFOIL MODEL

In order to estimate transition region location, it is first necessary to calculate the development of the laminar boundary layer. As a result of the failure of certain integral techniques (the Karman-Pohlhausen approximation and the Walz integral equations described in Ref. 17 and the Thwaites method described in Ref. 5) to yield realistic values for this study, the finite difference program described in this appendix was developed with the assistance of Professor Han of the OSU Mechanical Engineering Department. Using measured or calculated (potential flow) static pressure data for the airfoil, the program computes the boundary layer profiles and parameters required by the transition prediction techniques discussed elsewhere in this report.

The edge velocity (u_e) profile is found by applying the idealized Bernoulli equation to the static pressure distribution measured with the instrumented airfoil, thus fixing boundary conditions at some distance from the wall. As an alternative, the velocity distribution from a potential flow calculation may be used. Figure C.1 shows a velocity distribution for the airfoil pressure surface used in this study, where u_e is the velocity outside the boundary layer and x is the surface distance measured from the airfoil stagnation point. These velocities are calculated by the subroutine UFREE which also interpolates (cubic spline curve fit) to five velocities at 15 equally spaced points between each pair of static taps.

Because the boundary layer thickness is initially zero at the stagnation point (x = 0), the Hiemenz similarity transformation (Schlichting,[17] pages 87 through 91) for stagnation region flow was utilized to initiate the calculations. The stagnation region ($x = 0$ to $x = x_{st}$) is defined from Fig. C.1 by determining the location (x_{st}) where the edge velocity (u_{st}) is 5% of the maximum edge velocity calculated for the airfoil. The edge velocity in this region is then approximated by the following relation defined in Fig. C.2:

$$u_e = \beta x \ . \qquad \text{C-1}$$

Using the notation given by Schlichting,[17] one has

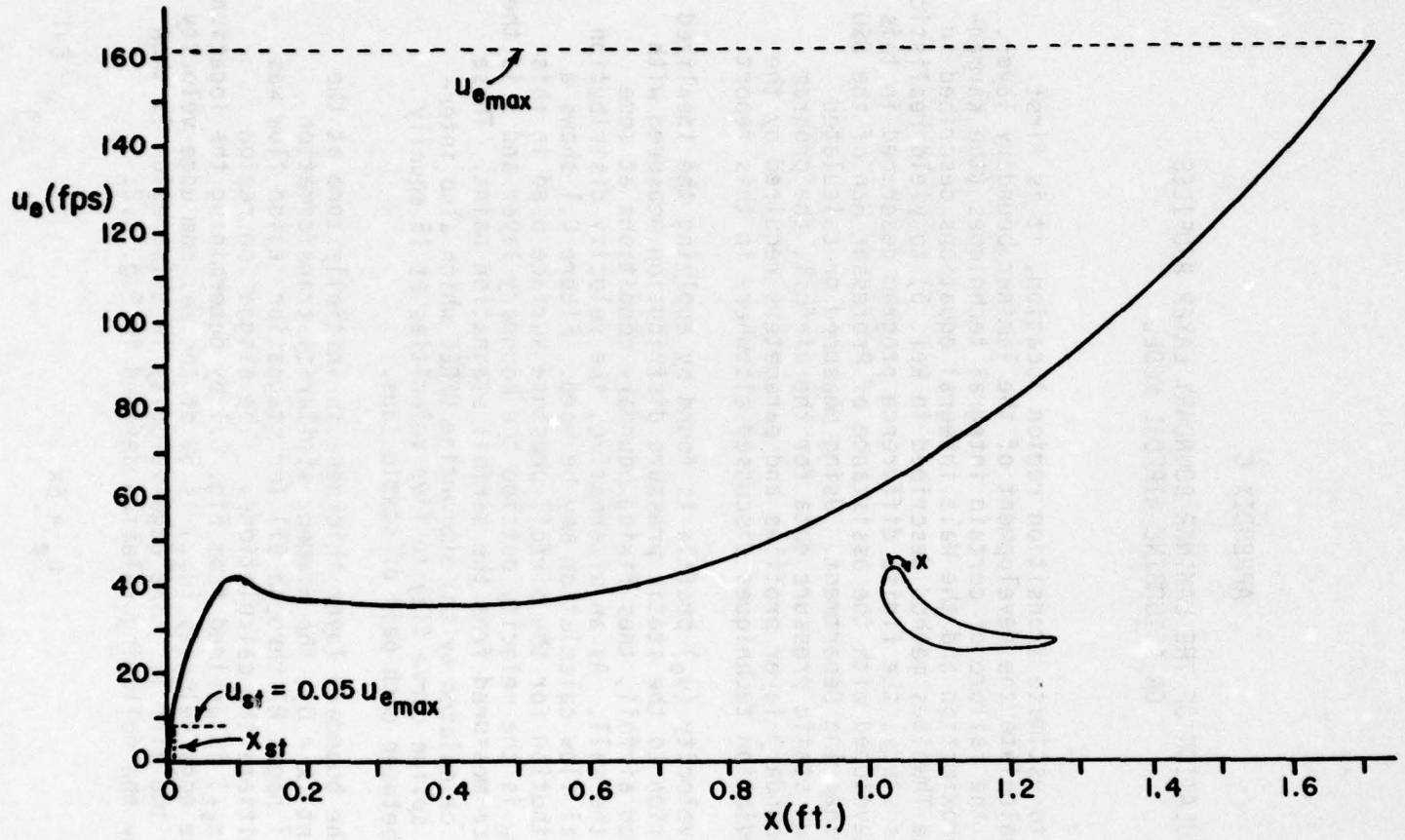

Figure C.1 Edge Velocity Distribution (Pressure Surface)

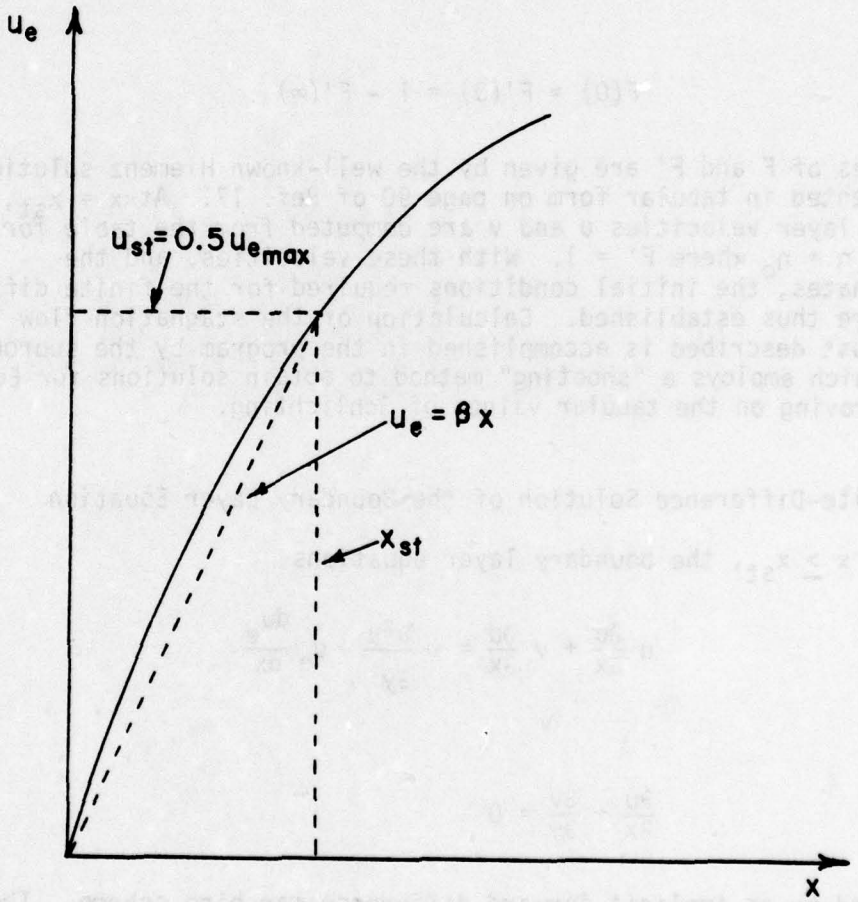

Figure C.2 Stagnation Region Nomenclature

$$u = \beta x F'(\eta) \ ,$$

$$v = - \sqrt{\beta\nu}\, F(\eta) \ , \qquad \text{C-2}$$

and

$$\eta = y\sqrt{\beta/\nu} \ ,$$

where the function F is governed by

$$F'^2 - FF'' = 1 + F''' \qquad \text{C-3}$$

and

$$F(0) = F'(0) = 1 - F'(\infty) \ .$$

The values of F and F' are given by the well-known Hiemenz solution and are presented in tabular form on page 90 of Ref. 17. At $x = x_{st}$, the boundary layer velocities u and v are computed from the table for $\eta = 0$ to $\eta = \eta_o$ where $F' = 1$. With these velocities, and the y-coordinates, the initial conditions required for the finite difference method are thus established. Calculation of the stagnation flow in the manner just described is accomplished in the program by the subroutine START, which employs a "shooting" method to obtain solutions for Eq. C-3, thus improving on the tabular values of Schlichting.

C.1 Finite-Difference Solution of the Boundary Layer Equation

For $x \geq x_{st}$, the boundary layer equations

$$u \frac{\partial u}{\partial x} + v \frac{\partial u}{\partial x} = \nu \frac{\partial^2 u}{\partial y^2} + u_e \frac{du_e}{dx} \qquad \text{C-4}$$

and

$$\frac{\partial u}{\partial x} + \frac{\partial v}{\partial y} = 0$$

are solved by an implicit forward difference marching scheme. The normal derivatives, $\partial u/\partial y$ and $\partial^2 u/\partial y^2$, are computed by central difference formulae. At a given station, x(j), the velocities u and v in the boundary layer are assumed known. A forward finite difference scheme is then used to calculate the velocities u and v at a new station x(j+1). Using this finite difference approach and the notation of Fig. C.3, the terms of Eq. C-4 are expressed as follows:

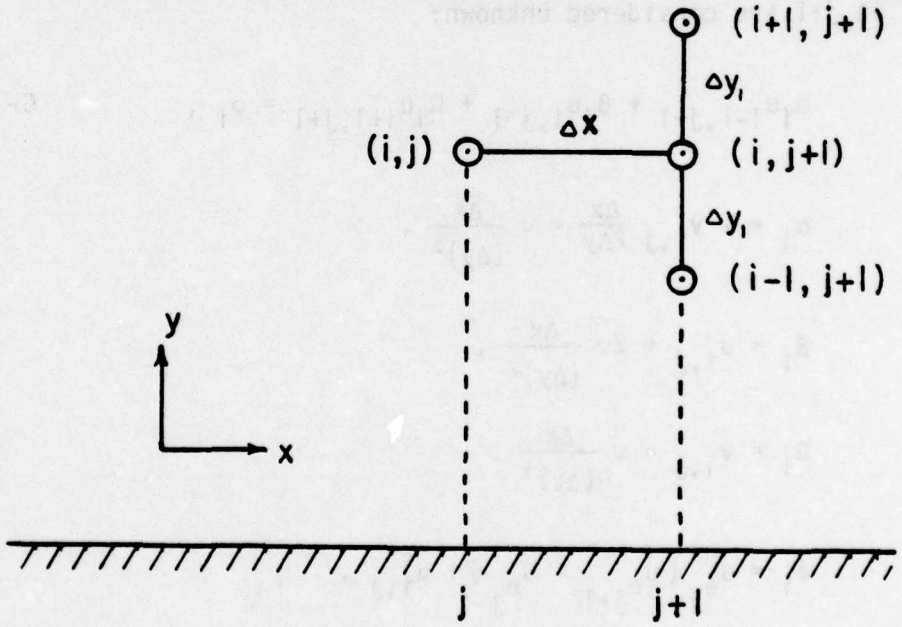

Figure C.3 Forward Marching Finite Difference Grid Nomenclature

$$u \frac{\partial u}{\partial x} = u_{i,j} (u_{i,j+1} - u_{i,j}) / \Delta x$$

$$v \frac{\partial u}{\partial y} = v_{i,j} (u_{i+1,j+1} - u_{i-1,j+1}) / 2\Delta y_1$$

$$\nu \frac{\partial^2 u}{\partial y^2} = \nu (u_{i+1,j+1} - 2u_{i,j+1} + u_{i-1,j+1}) / (\Delta y_1)^2 \qquad \text{C-5}$$

$$u_e \frac{du_e}{dx} = u_{e_j} (u_{e_{j+1}} - u_{e_j}) / \Delta x$$

By replacing terms of Eq. C-4 with the above expressions, and rearranging slightly, the following equation results, where the velocities at j+1 are considered unknown:

$$\alpha_i u_{i-1,j+1} + \beta_i u_{i,j+1} + \Omega_i u_{i+1,j+1} = \phi_i \ , \qquad \text{C-6}$$

where

$$\alpha_i = - v_{i,j} \frac{\Delta x}{2\Delta y} - \nu \frac{\Delta x}{(\Delta y)^2} \ ,$$

$$\beta_i = u_{i,j} + 2\nu \frac{\Delta x}{(\Delta y)^2} \ ,$$

$$\Omega_i = v_{i,j} - \nu \frac{\Delta x}{(\Delta y)^2} \ ,$$

and

$$\phi_i = u_{e_j} (u_{e_{j+1}} - u_{e_j}) + u_{i,j}^2 \ ,$$

and where i = 2, 3, ..., k; such that k denotes the edge of the boundary layer. For i = k, the equation reduces to the following ($u_{k+1,j+1} = u_{e_{j+1}}$):

$$
\begin{aligned}
\beta_2 u_2 + \Omega_2 u_3 &= \phi_2 \\
\alpha_3 u_2 + \beta_3 u_3 + \Omega_3 u_4 &= \phi_3 \\
\alpha_4 u_3 + \beta_4 u_4 + \Omega_4 u_5 &= \phi_4 \\
&\ddots \\
\alpha_k u_{k-1} + \beta_k u_k &= \phi_k \ ,
\end{aligned}
\qquad \text{C-7}
$$

where u_2, u_3 denote $u_{2,j+1}$, $u_{3,j+1}$, etc. Through Gaussian elimination, proceeding from the bottom of the coefficient matrix, the velocities $u_{i,j+1}$ are determined. In order to determine $v_{i,j+1}$, the continuity equation was also written in finite difference form by writing the terms as follows:

$$
\frac{\partial u}{\partial x} = \frac{u_{i,j+1} - u_{i,j}}{2\Delta x} + \frac{u_{i-1,j+1} - u_{i-1,j}}{2\Delta x}
\qquad \text{C-8}
$$

and

$$
\frac{\partial v}{\partial y} = \frac{v_{i,j+1} - v_{i-1,j+1}}{\Delta y} \ ,
$$

thus utilizing the average value for $\partial u/\partial x$ over the grid interval for the $\partial v/\partial y$ term. Substituting these finite difference terms into the continuity equation and rearranging results in the following form:

$$
v_{i,j+1} = v_{i-1,j+1} - \frac{\Delta y}{2\Delta x}\left(u_{i,j+1} - u_{i,j} + u_{i-1,j+1} - u_{i-1,j} \right) , \qquad \text{C-9}
$$

which is solved by applying the boundary condition that $v_{1,j+1} = 0$. The solution then gives values for all $v_{i,j+1}$.

C.2 Use of Variable Spacings

In order to obtain better accuracy with the forward difference solution, the grid size near the wall was made finer than the grid at some distance from the wall. At the initial point, $x = x_{st}$, the boundary layer is represented by a grid of 300 divisions. Nearest the wall, a region of 50 intervals dy_1 is selected such that $dy_2 = 2dy_1$. A third region of 50 steps is selected such that $dy_3 = 2dy_2$. The remaining 150 steps are selected to have a spacing such that $dy_4 = 2dy_3$.

An additional 300 steps having the same spacing as the fourth region constitutes the free-stream portion of the grid which is assumed to have constant velocity at x_{st}.

As the calculation proceeds along the surface, the boundary layer velocity profile grows into the free-stream region of the finite difference grid. As this growth occurs, the value of k is increased from an initial value of 300. In order to control the change in k value, the value of $u_{k,j+1}$ is tested and, if found equal to or less than 0.995 u_{e_j}, a new grid point is added to k from the 300 allotted for the free stream. When the boundary layer has grown such that all the allocated grid points (in this program, 601) have been used, the grid spacings dy_1, dy_2, dy_3, and dy_4 are doubled, again reducing the number of grid points in the boundary layer to 301. The user of the program must then examine the output to confirm that no sudden changes in the calculated values occur when the grid size is increased, by comparing values on both sides of the change.

Because of the variation of grid spacings with increasing y, junctions exist within the grid where the y spacings are unequal as shown in Fig. C.4. In order to derive more accurate finite difference solutions of the differential equations at the junctions, the velocities at these three points are fit by a second-order polynomial as follows:

$$u_1 = u_{i-1,j+1} ,$$

$$u_2 = u_{i,j+1} ,$$

$$u_3 = u_{i+1,j+1} , \qquad \text{C-10}$$

and

$$R = \frac{dy_2}{dy_1} ,$$

where the notation is given in Fig. C.4.

Assume

$$u = ay^2 + by + c ,$$

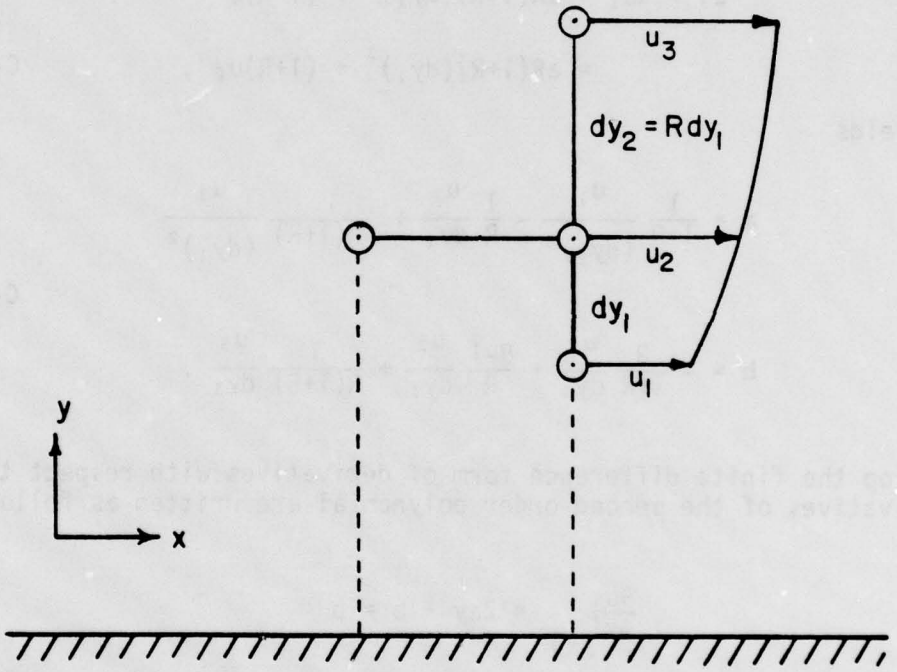

Figure C.4 Grid Junction Nomenclature

then

$$u_1 = a(dy_1)^2 - b\,dy_1 + c\ ,$$

$$u_2 = c\ ,$$

and

$$u_3 = aR^2(dy_1)^2 + bR\,dy_1 + c\ . \qquad \text{C-11}$$

Solving the above simultaneous equations:

$$u_3 + Ru_1 = aR(1+R)(dy_1)^2 + (1+R)c$$

$$= aR(1+R)(dy_1)^2 + (1+R)u_2\ , \qquad \text{C-12}$$

which yields

$$a = \frac{1}{1+R}\frac{u_1}{(dy_1)^2} - \frac{1}{R}\frac{u_2}{dy_1} + \frac{1}{R(1+R)}\frac{u_3}{(dy_1)^2}$$

and

$$b = -\frac{R}{1+R}\frac{u_1}{dy_1} + \frac{R-1}{R}\frac{u_2}{dy_1} + \frac{1}{R(1+R)}\frac{u_3}{dy_1}\ . \qquad \text{C-13}$$

To develop the finite difference form of derivatives with respect to y, the derivatives of the second-order polynomial are written as follows:

$$\left.\frac{\partial u}{\partial y}\right)_{y=0} = 2ay + b = b$$

and

$$\frac{\partial^2 u}{\partial y^2} = 2a\ . \qquad \text{C-14}$$

Using the finite difference derivative terms for the x-direction as given in Eq. C-5, along with the above y derivative terms, the new coefficients for Eq. C-6 may be written as follows:

$$\alpha_i = -\frac{cR}{1+R} v_{i,j} - \frac{2\ cc}{1+R} \nu \ ,$$

$$\beta_i = u_{i-1,j} + \frac{(R-1)c}{R} v_{i,j} + \frac{2\nu}{R} cc \ ,$$

$$\Omega_i = \frac{c}{R(1+R)} v_{i,j} - \frac{2\nu}{R(1+R)} cc \ , \qquad \text{C-15}$$

and

$$\phi_i = u^2_{i-1,j} + u_{e_j} (u_{e_{j+1}} - u_{e_j}) \ ,$$

where

$$c = \Delta x/dy_1$$

and

$$cc = \Delta x/(dy_1)^2 \ .$$

(For other junctions, dy_1 is replaced with dy_m and $R = dy_{m+1}/dy_m$.) Other than the above coefficient modifications, the calculations at the grid junctions are performed in the same manner as for other grid points.

C.3 General Description of the Computer Program

The FORTRAN program presented on the following pages was prepared utilizing the finite difference equations just described and consists of the main program with four subroutines: START, MARCH, PROPY, and UFREE. The main program in this case is arranged to provide boundary layer data for flat plate or circular cylinder flow as well as the two-dimensional airfoil model. The type of flow to be studied is governed by the integer variable L which equals one for flat plate, two for normal circular cylinder, and three for two-dimensional airfoil model flow. By running the program for the flat plate and circular cylinder cases, which have well-known solutions, it was possible to check the program for possible errors.

Calculations are initiated by calling the subroutine START. This subroutine sets the number of intervals in each grid region of the finite difference program and establishes the free-stream velocity field for flat plate or circular cylinder flow. For two-dimensional airfoil models, subroutine UFREE is called. This subroutine reads data cards containing dimensional data for the airfoil along with experimental static pressure data. UFREE then uses the idealized Bernoulli equation to calculate the free-stream velocity distribution and then uses a cubic spline curve fitting routine to interpolate 15 additional data points between each static tap. Interpolations are also used to reconstruct data for the three plugged taps along the perimeter of the

airfoil. Control then returns to START. Subroutine START then uses a shooting method to calculate the Hiemenz solution at x_{st} as described previously and initializes the boundary layer velocity grid.

Subroutine PROPY is then called to calculate the momentum and displacement thickness integrals by means of Simpson's 1/3 rule applied to three grid points at a time. The main program then computes all the desired boundary layer parameters (such as Reynolds number) based on the current (j) data and the information obtained for that station is then printed.

Subroutine MARCH is then called and the calculation then proceeds to the next x station using the forward finite difference scheme already described. Control is then returned to the main program which again calls PROPY, and this loop continues until the calculations have proceeded along the entire surface or until the output is terminated because of an error such as a negative displacement thickness.

```
FORTRAN IV G1  RELEASE 2.0              MAIN              DATE = 77346        10/37/55              PAGE 0001

0001                  COMMON    REX(401),CAPK(401),RE1(401),RE2(401),DE1(401),DE2(401),
                     *F2D(401),F2(401)
0002                  COMMON D1(401),D(401),DUDX(401),DUDX2(401),VAU,CUR(30)
0003                  COMMON AL(601),BET(601),GME(601),FEE(601),UC(601),UM(601),VO(601),
                     *VN(601),YP(601)
0004                  DIMENSION UUE(601)
0005                  DIMENSION DEL1(30),DEL2(30),XYAP(30),UINF(30),REYX(30),REYD1(30),
                     1REYD2(30),GD1(30),GD2(30),D1OR(30),D2OR(30),POHD2(30)
0006                  REAL HFAC(30)
0007                  NNNN=0
0008            1111  L=2
0009                  L=3
0010                  L=1
                C***  L=1,2,3 FOR FP,CYL,AND 2D STG FLW
0011                  LA=3
0012                  LB=3
0013                  VISC=.00015
0014                  VNU=VISC
                C****  THIS VALUE OF VISC WILL BE OVERRIDEN BY SUEPRG UFREE FOR L=3** 2-D STG FL
0015                  DO 4567 L=LA,LB
0016                  IMIN=100
0017                  CALL STAK1(L,DY1,DY2,DY3,DY4,N12,N23,N34,MED,NMAX,IST,ITP,BETA,VIS
                     *C,XMAX,XSTRT,UST)
0018                  VNU=VISC
0019                  IA=IST
0020                  IB=ITP
0021                  NMT=2
0022                  NINT=4
0023                  NINT=12
0024                  NINT=40
0025                  XO=XSTRT
0026                  UFO=UST
0027                  JRND=-120
0028                  K=1
0029                  KP=1
0030                  ITAP=2
0031                  NPR=1
0032                  WRITE(6,741) L
0033            741   FORMAT(1H1//
                     *      5X,'L',I2,5X,'(L=1,2,3,FOR FL PL,CYL,2D STG FLOW)'//
                     *8X,'X-FT',6X,'DPLT-IKFT',3X,'MMT-IKFT',5X,'DEL2U',7X,'DZL2U',9X,
                     *'UFREE',6X,'DUDXT',6X,'DUDYN',8X,'K',5X,'MEC'//
                     *5X,'NOTE**  X=DIST FRM STG PT,** DPLT=DISPLACEMENT THK(FT),** MMT=
                     *MOMENTUM THK(FT)'/13X,'DEL2U=DISPL**2*DUDX/VISC(NON DIM),** DZL2U=
                     *M4)**2*DUDX/VISC(NON DIM),** UFREE=FREE ST VEL(FPS),**'/
                     *13X,'DUDXT=VEL GRD ALONG X(FT/S/FT),** DUDYN=NORMAL VEL GRDT(FT/S/
                     *FT)***,K=KO IF INTGTN STEPS'//)
0034                  DO 555 I=IA,IB
0035                  NINT=I+NINT/2
0036                  UFO=U(I)
0037                  XO=D(I)
0038                  CALL PROPY(DY1,DY2,DY3,DY4,N12,N23,N34,MED      ,SZ,SO, UFO)
0039                  IF(I-3) 1551,655,655
0040            655   CONTINUE
0041            1551  IF(SO) 15,15,1551
0042              15  DO 1665 KI=1,MED
0043            1665  UUE(KI)=UC(KI)/UFO
0044                  WRITE(6,7665)(KI,UUE(KI),UO(KI),UP(KI),KI=1,MED,2)
```

```
                7665 FORMAT(110,3E15.6)
                     WRITE(6,7115)
                7115 FORMAT(10(5X,'PRG STOPPED, DISPLMNT THK IS NEG'/))
                     CALL EXIT
                1551 CONTINUE
                     DU=U(I+1)-U(I)
                     DXTCT=D(I+1)-D(I)
                     DXSTP=DXTCT/NINT
                     DUDY=(4.*UC(2)-UO(3))/2./DY1
                     DUDXT=DUDX(I)
                     DEL2U=SO**2*DUDXT/VISC
                     DZL2U=SZ**2*DUDXT/VISC
                     IF(L-3) 17,711,17
                 711 NET=I-1
                     ITAP=1+NET/15
                     MEXX=I-1-15*(ITAP-1)
                     IF(MEXX) 17,799,17
                 799 CONTINUE
                     WRITE(6,9151 ITAP
                  17 CONTINUE
                     DEL(I)=SO
                     DF2(I)=SZ
                     REX(I)=U(I)*D(I)/VISC
                     IF(U(I)) 761,761,767
                 767 CAPK(I)=VISC*DUDX(I)/U(I)**2
                     GO TO 762
                 761 CAPK(I)=99999999.
                 762 CONTINUE
                     F2U(I)=DEL2U
                     F2Z(I)=DZL2U
                     RE1(I)=DEL(I)*U(I)/VISC
                     RE2(I)=DF2(I)*U(I)/VISC
                1915 FORMAT(12X,
                    *'(REX=',E12.4,')',(VISC*DUDX/U*U=',E12.4,'),(D1*U/VISC=',
                    *E12.4,'),(D2*U/VISC=',E12.4,')')
                     WRITE(6,44) XO,SO,SZ,DEL2U,DZL2U,UFC,DUDXT,DUDY,NINT,MED,I
                     WRITE(6,1915) REX(I),CAPK(I),RE1(I),RE2(I)
                 915 FORMAT(//5X,20('*'),3X,'NEXT LINE FOR TAP NO=',I5)
                     KP=KP+1
                     IF(KP-22) 514,5155,5155
                5155 WRITE(6,7411)
                     KP=1
                 514 CONTINUE
                     IF(L-3)1700,1701,1701
                1701 IF(MEXX) 1700,1702,1700
                1702 DEL1(ITAP)=DEL(I)
                     DEL2(ITAP)=DF2(I)
                     XTAP(ITAP)=XO
                     UINF(ITAP)=UFO
                     REYX(ITAP)=REX(I)
                     REYD1(ITAP)=RE1(I)
                     REYD2(ITAP)=RE2(I)
                     HEAD(ITAP)=DEL(I)/DF2(I)
                     IMAX=ITAP
                     IF(ITAP-8)1704,1703,1703
                1703 D1OR(ITAP)=DEL(I)/CUR(ITAP)
                     D2OR(ITAP)=DF2(I)/CUR(ITAP)
                     GDL(ITAP)=RE1(I)*SQRT(D1OR(ITAP))
```

```
0101                GD2(ITAP)=KE2(I)*SQRT(D20R(ITAP))
0102             1704 PUHC2(ITAP)=DZL2U
0103                IF(ITAP-MIN)1705,1700,1700
0104             1705 MIN=ITAP
0105             1700 CONTINUE
0106                IF(L-2) 11,14,11
0107               14 ANG=XC*180./3.1416
0108                WRITE(6,133) ANG
0109              133 FORMAT(5X,'ANG(DEG)=',E15.4)
0110               44 FORMAT(4X,8E12.4,3I7)
0111               11 CONTINUE
0112                   IF(L-1) 51,51,88
0113               51 FX=(SD*DUDY/UFO)/(.332*1.728)
0114                WRITE(6,456) FX
0115              456 FORMAT(' ******   FX=1?', E15.4/)
0116               88 CONTINUE
0117                DO 333 NST=1,NINT
0118                UFN=UFC+(CL/NINT)
0119                JRND=JRND+1
0120                CALL MARCH(DY1,DY2,DY3,DY4,N12,N23,N34,MED,L,DXSTP,JRND,UFO,UFN)
0121                IF(L-3)  111,336,336
0122              336 DO 1234 J=1,PMAX
0123                IF(UN(J)-UFN) 1234,1234,2345
0124             2345 UN(J)=UFN
0125             1234 CONTINUE
0126              111 CONTINUE
0127                IF(JRND) 31,31,39
0128               39 JRND=-120
0129               31 CONTINUE
0130                RATIO=UN(MED-5)/UFN
0131                IF(RATIO-.998) 7,7,77
0132                7 MED=MED+1
0133               77 CONTINUE
0134                IF(MED-599) 76,76,1776
0135             1776 KM=0
0136                DO 2776 M=151,601,3
0137                KM=KM+1
0138                YS(150+KM)=YO(M)
0139                UO(150+KM)=UO(M)
0140                VO(150+KM)=VO(M)
0141                UN(150+KM)=UN(M)
0142             2776 VN(150+KM)=VN(M)
0143                DY4=DY4*3.
0144                MED=301
0145                DO 3421 M=301,601
0146                UN(M)=UFN
0147                UO(M)=UFC
0148             3421 VN(M)=VN(M-1)-(DY4/DXSTP)*(UFN-UFO)
0149               76 CONTINUE
0150                DO 4455 M=1,601
0151                UC(M)=UN(M)
0152             4455 VO(M)=VN(M)
0153                XO=XO+DXSTP
0154                UFO=UFN
0155              333 CONTINUE
0156                K=K+1
0157              555 CONTINUE
0158                CALL  PLTG(IST,IIP,0)
```

```
0159                    DO 1713 NPRINT=1,3
0160                    IF(L-3) 1713,1714,1714
0161              1714  WRITE(6,1720)
0162                    IF(IMNI.GE.8) GO TO 1711
0163                    DO 1710 J=IMIN,7
0164              1710  WRITE(6,1721) J,CUR(J),XTAP(J),DEL1(J),DEL2(J),POHD2(J),UINF(J),
                       1REYX(J),FFAC(J)
0165              1711  CONTINUE
0166                    IF(IMAX.LT.8) GO TO 1713
0167                    DO 1712 J=8,IMAX
0168              1712  WRITE(6,1721) J,CUR(J),XTAP(J),DEL1(J),DEL2(J),POHD2(J),UINF(J),
                       1REYX(J),FFAC(J)
0169              1720  FORMAT('1'///5X,'N',8X,'K',7X,'S',7X,'DEL1',6X,'DEL2',6X,'DZL2U',
                       16X,'UINF',6X,'REYX',7X,'H'/12X,'(FT)',4X,'(FT)',6X,'(FT)',6X,'(FT
                       1)',7X,'(FPS)'//)
0170              1721  FORMAT(' ',2X,I3,4X,F7.3,F8.3,2X,1P3E10.2,0PF9.3,1X,1PE10.2,0PF8.3
                       1)
0171              1814  WRITE(6,1820)
0172                    IF(IMIN.GE.8) GO TO 1811
0173                    DO 1810 J=IMIN,7
0174              1810  WRITE(6,1821) J,REYD1(J),REYD2(J)
0175              1811  CONTINUE
0176                    IF(IMAX.LT.8) GO TO 1713
0177                    DO 1812 J=8,IMAX
0178              1812  WRITE(6,1821) J,REYD1(J),REYD2(J),DLOR(J),GD1(J),D2OR(J),GD2(J)
0179              1713  CONTINUE
0180              1820  FORMAT('1'///5X,'N',8X,'REYD1',5X,'REYD2',5X,'DEL1/R',4X,'G(DE1)',
                       14X,'DEL2/R',4X,'G(DE2)'//)
0181              1821  FORMAT(' ',2X,I3,4X,1P3E10.2,0PF10.3,1X,1PE10.2,0PF9.3)
0182                    ANNA=ANNA+1
0183                    IF(ANNA.EQ.3) GO TO 4567
0184                    GO TO 1111
0185              4567  CONTINUE
0186                    CALL EXIT
0187                    END
```

```
0001                  SUBROUTINE START(L,DY1,DY2,DY3,DY4,N12,N23,N34,MED,NMAX,IST,ITP,BE
                     *TA,VISC ,XMAX,XSTRT,USI)
0002                  COMMON   RFX(401),CAPK(401),RE1(401),RE2(401),DE1(401),DE2(401),
                     *F2D(401),F27(401)
0003                  COMMON D(401),U(401),DUDX(401),DUDX2(401),VFU,CUR(30)
0004                  COMMON AL(601),BET(601),OME(601),FFF(601),UC(601),UN(601),VO(601),
                     *VN(601),VR(601)
0005                  N12=51
0006                  N23=101
0007                  N34=151
0008                  MED=301
0009                  NMAX=601
0010                  GO TO (21,22,23),L
0011               23 CALL UFREE
0012                  VISC=VNU
0013                  XMAX=D(399)
0014                  UMAX=U(399)
0015                  ITP=399
0016                  GO TO 2233
0017               22 UINF=100.
0018                  XMAX=3.1416
0019                  ITP=201
0020                  UMAX=100.
0021                  DO 122 I=1,ITP
0022                  D(I)=XMAX*FLOAT(I-1)/(ITP-1)
0023              122 U(I)=100.*SIN(D(I))
0024             2233 CONTINUE
0025                  DO 3322 I=1,ITP
0026                  IF(U(I)-.05*UMAX) 491,499,499
0027              499 USI=U(I)
0028                  IST=I
0029                  XSI=D(I)
0030                  BETA=USI/XST
0031                  GO TO 4949
0032              491 CONTINUE
0033             3322 CONTINUE
0034             4949 XSTRT=XSI
0035                  DO 17 I=1,601
0036               17 BET(I)=1.
0037                  MAX=0
0038                  MIN=0
0039                  F2MAX=1.4
0040                  F2MIN=1.2
                 C**** SOLVE 2-D STAGIN EQ
0041                1 F2AV=.5*(F2MAX+F2MIN)
0042                  ER=(F2MAX-F2MIN)/F2AV
0043                3 AL(1)=0.
0044                  BET(1)=0.
0045                  OME(1)=F2AV
0046                  DX=.05
0047                  DO 4 I=2,601
0048                  MFX=I
0049                  F3=BET(I-1)**2-AL(I-1)*OME(I-1)-1.
0050                  F4=BET(I-1)*OME(I-1)-AL(I-1)*F3
0051                  AL(I)=AL(I-1)+DX*(BET(I-1)+DX*(OME(I-1)/2.+DX*(F3/6.+DX*F4/24.)))
0052                  BET(I)=BET(I-1)+DX*(OME(I-1)+DX*(F3/2.+DX*F4/6.))
0053                  OME(I)=OME(I-1)+DX*(F3+DX*F4/2.)
0054                  IF(BET(I)-1.) 5,55,55
```

```
0055                5 IF(CME(I)) 44,44,4
0056                4 CONTINUE
0057                  I=600
0058                  WRITE(6,199) AL(I),BET(I),OME(I),F2MAX,F2AV,F2MIN
0059              199 FORMAT(5X,'OUTPUT FROM START, FORMAT 199--PRGM IN TROUBLE',
                     *6E15.5,5X,'AL,BET,OME,F2MAX,F2AV,F2MIN'/)
0060                  RETURN
0061               55 IF(ER-.0001) 999,999,255
0062              255 MAX=1
0063                  F2MAX=F2AV
0064                  IF(MIN) 551,551,1
0065              551 F2MIN=F2MIN/1.1
0066                  GO TO 1
0067               44 IF(ER-.0001) 88,88,355
0068               88 F2AV=F2MAX
0069                  GO TO 3
0070              355 MIN=1
0071                  F2MIN=F2AV
0072                  IF(MAX) 661,661,1
0073              661 F2MAX=F2MAX*1.1
0074                  GO TO 1
0075              999 WRITE(6,1881) F2MIN,F2AV,F2MAX,MEX
0076                  WRITE(6,1991) (K,AL(K),BET(K),OME(K),K=1,MEX)
0077             1991 FORMAT(2(I6,3E12.4))
0078             1881 FORMAT(5X,'OUTPUT FROM 2-D STG-EQ-OK'/10X,'F2MIN,F2AV,F2MAX,MEX',
                     *3E15.6,I10//2(4X,'I',1X,5X,'F',6X,4X,'FP',6X,3X,'FPP',6X)/)
0079                  MA=MEX-1
0080                  DO 2991 I=MA,NMAX
0081                  BET(I)=1.
0082             2991 AL(I)=AL(MA)+DX *(I-MA)
0083                  DO 3991  I=1,NMAX
0084             3991 OME(I)= DX*(I-1)*SQRT(VISC/BETA)
                 C**** OME(I)=YABS IN FEET
0085                  DO 5951 I=1,NMAX
0086                  IF(BET(I)-.995) 5991,5999,5999
0087             5999 MEX=I
0088                  GO TO 7991
0089             5951 CONTINUE
0090             7991 CONTINUE
0091                  YMED=CME(MEX)
0092               12 CONTINUE
0093                  DO 91 I=1,N12
0094               91 YB(I)=YMED*FLOAT(I-1)/1550.
0095                  K=N12+1
0096                  DO 92 I=K,N23
0097               92 YB(I)=YMED*FLOAT(2*(I-N12)+N12-1)/1550.
0098                  K=N23+1
0099                  DO 93 I=K,N34
0100               93 YB(I)=YMED*FLOAT(4*(I-N23)+2*N23-N12-1)/1550.
0101                  K=N34+1
0102                  DO 94 I=K,NMAX
0103               94 YB(I)=YMED*FLOAT(8*(I-N34)+4*N34-2*N23-N12-1)/1550.
0104                  DY1=YMED/1550.
0105                  DY2=2.*DY1
0106                  DY3=2.*DY2
0107                  DY4=2.*DY3
0108                  IF(L-1) 61,61,69
0109               69 YB(1)=0.
```

```
0110                    DO 165 N=2,300
0111                    YFIX=YB(N)
0112                    MIXX=MEX+1
0113                    DO 699 I=2,MIXX
0114                    PR=(YFIX-OME(I))*(YFIX-OME(I-1))
0115                    IF(PR) 1699,1695,699
0116                1695 RATIO=(YFIX-OME(I-1))/(OME(I)-OME(I-1))
0117                    UO(N)=UST*(BET(I-1)+RATIO*(BET(I)-BET(I-1)))
0118                    VO(N)=-SQRT(VISC*BETA)*(AL(I-1)+RATIO*(AL(I)-AL(I-1)))
0119                    GO TO 169
0120                 699 CONTINUE
0121                 165 CONTINUE
0122                    UO(1)=0.
0123                    VO(1)=0.
0124                    DV=ABS(VO(300)-VO(299))
0125                    DO 799 I=300,NMAX
0126                    UO(I)=UST
0127                 799 VO(I)=VO(300)-DV*(I-300)
0128                    WRITE(6,1799) XST,UST,BETA,VISC
0129                1799 FORMAT(1H1,5X,'STARTING VELOCITIES AT (FT) XST=',E15.5/33X,'UST=',
                       *E15.5/32X,'BETA=',E15.5/32X,'VISC=',E15.5//2(3X,'I',2X,5X,'U',9X,5
                       *X,'V',9X,5X,'Y',9X)/20X,'UNITS=FEET,SEC'/)
0130                    WRITE(6,1599)   (I,UO(I),VO(I),YB(I),I=1,301)
0131                1599 FORMAT(  2(I6,3E15.5))
0132                    WRITE(6,1229)
0133                1229 FORMAT(50(' *')/)
0134                    WRITE(6,1599)   (I,UO(I),VO(I),YB(I),I=301,NMAX,4)
0135                    RETURN
0136                  21 IST=1
0137                    ITP=201
0138                    DO 921 I=IST,ITP
0139                    U(I)=10.
0140                 921 O(I)=20.*FLOAT(I-IST)/(ITP-IST)
0141                    UST=U(IST)
0142                    UO(1)=0.
0143                    DO 1921 I=2,601
0144                    UO(I)=10.
0145                1921 VO(I)=0.
0146                    VO(1)=0.
0147                    YMED=.2
0148                    YMED=.05
0149                    XSTRT=0.
0150                    GO TO 12
0151                  61 RETURN
0152                    END
```

```
FORTRAN IV G1  RELEASE 2.0              MARCH              DATE = 77346        10/37/55                PAGE 0001

0001                    SUBROUTINE MARCH(DY1,DY2,DY3,DY4,N12,N23,N34,MFD,L,DX,JRN,UFO,UFN)
0002                    COMMON    REX(401),CAPK(401),RE1(401),RE2(401),DE1(401),DE2(401),
                       *F2D(401),F22(401)
0003                    COMMON D(401),U(401),DUDX(401),DUDX2(401),VAU,CUR(30)
0004                    COMMON AL(601),BET(601),CME(601),FEE(601),UC(601),UM(601),VO(601),
                       *VN(601),YB(601)
0005                    VISC=VNU
0006                    MSTOP=MFD+1
0007                    MEXT=MFD+2
0008                    C=DX/DY1
0009                    CC=C/DY1
0010                    AL(2)=-VO(2)*C*.5-VISC*CC
0011                    BET(2)=UO(2)+2.*VISC*CC
0012                    CME(2)=VO(2)*C*.5-VISC*CC
0013                    FEE(2)=UFN*UFO+(UC(2)**2-UFO**2)
0014                    MSTOP=MFD+1
0015                    DO 199 I=2,MSTOP
0016                    IF(I-N12) 4,5,6
0017                  4 DY=DY1
0018                    C=DX/DY1
0019                    CC=C/DY1
0020                 54 AL(I)=-VO(I)*C*.5-VISC*CC
0021                    BET(I)=UO(I)+2.*VISC*CC
0022                    CME(I)=VO(I)*C*.5-VISC*CC
0023                    FEE(I)=UFN*UFO+(UO(I)-UFO)*(UO(I)+UFO)
0024                    GO TO 199
0025                  5 DY=DY1
0026                    R=DY2/DY1
0027                    C=DX/DY
0028                    CC=DX/DY**2
0029                 55 AL(I)=-VO(I)*C*R/(1.+R)-2.*VISC*CC/(1.+R)
0030                    BET(I)=UO(I)+C*VO(I)*(R-1.)/R+2.*VISC*CC/R
0031                    CME(I)=VO(I)*C/P/(1.+R)-2.*VISC*CC/R/(1.+R)
0032                    FEE(I)=UFN*UFO+(UO(I)-UFO)*(UO(I)+UFO)
0033                    GO TO 199
0034                  6 IF(I-N23) 14,15,16
0035                 14 DY=DY2
0036                    C=DX/DY
0037                    CC=C/DY
0038                    GO TO 54
0039                 15 DY=DY2
0040                    R=DY3/DY2
0041                    C=DX/DY
0042                    CC=C/DY
0043                    GO TO 55
0044                 16 IF(I-N34) 24,25,26
0045                 24 DY=DY3
0046                    C=DX/DY
0047                    CC=C/DY
0048                    GO TO 54
0049                 25 DY=DY3
0050                    R=DY4/DY3
0051                    C=DX/DY
0052                    CC=C/DY
0053                    GO TO 55
0054                 26 DY=DY4
0055                    C=DX/DY
0056                    CC=C/DY
```

```
0057                    GO TO 94
0058                159 CONTINUE
0059                    FEE(MSTOP)=FEE(MSTOP)-OME(MSTOP)*UFN
0060                    DO 1299 I=2,MSTOP
0061                    AL(I)=AL(I)/BET(I)
0062                    OME(I)=OME(I)/BET(I)
0063                    FEE(I)=FEE(I)/BET(I)
0064                    BET(I)=1.
0065                1299 CONTINUE
0066                    MSHORT=MSTOP-1
0067                    DO 299 I=2,MSHORT
0068                    J=MSHORT+2-I
0069                    BET(J)=BET(J)-AL(J+1)*OME(J)/BET(J+1)
0070                 299 FEE(J)=FEE(J)-FEE(J+1)*OME(J)/BET(J+1)
0071                    UN(1)=0.
0072                    DO 3299 I=2,MSTOP
0073                3299 UN(I)=(FEE(I)-AL(I)*UN(I-1))/BET(I)
0074                    DO 4299 I=MSTOP,NMAX
0075                4299 UN(I)=UFN
0076                    VN(NOW=0.
0077                    VN(1)=VBLOW
0078                    DO 499 I=2,NMAX
0079                    IF(I-N12) 54,54,854
0080                  54 DY=DY1
0081                     GO TO 954
0082                 854 IF(I-N23)  254,254,754
0083                 254 DY=DY2
0084                     GO TO 954
0085                 754 IF(I-N34)  354,354,654
0086                 354 DY=DY3
0087                     GO TO 954
0088                 654 DY=DY4
0089                 954 VN(I)=VN(I-1)-(DY/DX )*(UN(I)-UO(I)+UN(I-1)-UO(I-1))*.5
0090                 499 CONTINUE
0091                   3 CONTINUE
0092                  34 CONTINUE
0093                     RETURN
0094                     END
```

```
FORTRAN IV G1  RELEASE 2.0            PROPY          DATE = 77346      10/37/55          PAGE 0001

0001                  SUBROUTINE PROPY(DY1,DY2,DY3,DY4,M12,M23,M34,MED,SZ,SD,UFO)
0002                  COMMON   REX(401),CAPK(401),RF1(401),RE2(401),DE1(401),DE2(401),
                     *F2D(401),F2Z(401)
0003                  COMMON D(401),U(401),DUDX(401),DUDX2(401),VNU,CUR(30)
0004                  COMMON AL(601),BET(601),OME(601),FEE(601),UC(601),UN(601),VO(601),
                     *VN(601),YB(601)
0005                  SD=C.
0006                  SZ=0.
0007                  DO 999 IR=1,4
0008                  GO TO (1,2,3,4),IR
0009                1 IST=1
0010                  IEND=49
0011                  DY=DY1
0012                  GO TO 5
0013                2 IST=51
0014                  IEND=99
0015                  DY=DY2
0016                  GO TO 5
0017                3 DY=DY3
0018                  IST=101
0019.                 IEND=149
0020                  GO TO 5
0021                4 DY=DY4
0022                  IST=151
0023                  IEND=MED-2
0024                5 FD1=1.-UO(IST)/UFO
0025                  FZ1=FD1*(UC(IST)/UFO)
0026                  DO 555 I=IST,IEND,2
0027                  FD2=1.-UO(I+1)/UFO
0028                  FZ2=FD2*(UC(I+1)/UFO)
0029                  FD3=1.-UO(I+2)/UFO
0030                   FZ3=FD3*(UO(I+2)/UFO)
0031                  SD=SD+(FD1+4.*FD2+FD3)*(DY/3.)
0032                  SZ=SZ+(FZ1+4.*FZ2+FZ3)*(DY/3.)
0033                  FD1=FD3
0034                  FZ1=FZ3
0035              555 CONTINUE
0036              999 CONTINUE
0037                  RETURN
0038                  END
```

```
FORTRAN IV G1  RELEASE 2.0            PLTG              DATE = 77346        10/37/55        PAGE 0001

0001                  SUBROUTINE PLTG(IST,ITP,NPLOT)
0002                  COMMON   REX(401),CAPK(401),RE1(401),RE2(401),DE1(401),DE2(401),
                     *F2D(401),F2Z(401)
0003                  COMMON D(401),U(401),DUDX(401),DUDX2(401),VAV,CUR(30)
0004                  COMMON AL(601),BET(601),OME(601),FEE(601),UC(601),UN(601),VO(601),
                     *VH(601),YB(601)
0005                  RETURN
0006                  END
```

```
FORTRAN IV G1  RELEASE 2.0              UFREE              DATE = 77346          10/37/55          PAGE 0001

0001                    SUBROUTINE UFREE
0002                    COMMON    RE2(401),CAPK(401),RE1(401),RE2(401),DE1(401),DE2(401),
                       *F2D(401),F22(401)
0003                    COMMON D(401),U(401),DUDX(401),DUDX2(401),VNU,CUR(30)
0004                    COMMON AL(601),BET(601),OME(601),FEE(601),UC(601),UN(601),VO(601),
                       *VN(601),VR(60
0005                    DIMENSION PP(60),PTAPI(60)
0006                    DIMENSION PTAP(60),PTAPN(60),TRNOUT(60),VT(60),STOT(30)
0007                    COMPLEX*16 OBSER,DATE
0008                    REAL DF(27)/27*1./
0009                    REAL YI(27)
0010                    REAL C1(26,3)
0011                    REAL WK(156)
0012                    REAL*8 BLAPOS
0013                119 READ(5,1) MFAM,BLAPOS,OBSER,DATE,ATPRES,TRANZE,PSTAG,V,FLWTMP
                      C,PSTAT
0014                  1 FORMAT(I5,A5,4A5 ,F5.2,F5.1,F5.2,F5.2,F5.1,F5.2)
0015                    READ(5,2) (TRNOUT(I),I=1,56)
0016                  2 FORMAT(10F8.1)
0017                    READ(5,109) (STOT(I),I=1,27)
0018                109 FORMAT(8F10.3)
0019                    READ(5,1091) (CUR(I),I=1,27)
                C
                C  CONVERT TRANSDUCER OUTPUT INTO INCHES OF H20 AND INTERPOLATES A
                C  VALUE FOR THE PLUGGED TAPS
0020                    A=.0033
0021                    B=-A*TRANZE
0022                    DO 3 I=1,56
0023                    IF(I.EQ.24) GO TO 105
0024                    IF(I.EQ.27) GO TO 106
0025                    IF(I.EQ.29) GO TO 107
0026                108 PTAP(I)=A*TRNOUT(I)+B
0027                    GO TO 3
0028                105 TRNOUT(I)=(TRNOUT(25)+TRNOUT(23))/2.
0029                    GO TO 108
0030                106 TRNOUT(I)=TRNOUT(26)+(TRNOUT(26)-TRNOUT(25))
0031                    GO TO 108
0032                107 TRNOUT(I)=(TRNOUT(28)+TRNOUT(30))/2.
0033                    GO TO 108
0034                  3 CONTINUE
                C
                C  CALCULATES DENSITY OF AIR
0035                    T=FLWTMP+460.
0036                    P=(ATPRES/2.036)*144.
0037                    RG=53.34
0038                    RHO=P/(RG*T)
                C
                C  CALCULATES VELOCITY AT EACH TAP USING BERNOULLI
0039                    DO 103 I=1,56
0040                    IF(PTAP(I).GE.0.) GO TO 100
0041                    W=ABS((PSTAG-PTAP(I))*5.204*2*32.17)/RHO)
0042                    GO TO 35
0043                100 W=0.
0044                 35 VT(I)=SQRT(W)
                C
0045                    VISC=.0427*(FLWTMP-50.)*.000064
0046                    VISC  =VISC/(RHO*3600)
0047                103 CONTINUE
```

```
0048                    D(1)=0.
0049                    NI=2
0050                    DO 761 I=2,27
0051                    J=I-1
0052                    VINC=(STOT(I)-STOT(J))/15.
0053                    NF=NI+14
0054                    DO 762 K=NI,NF
0055                    L=K-1
0056                    D(K)=D(L)+VINC
0057                762 CONTINUE
0058                    NI=NI+15
0059                761 CONTINUE
0060                    DO 737 I=392,400
0061                    J=I-1
0062                    D(I)=D(J)+.075
0063                737 CONTINUE
0064                    VT(1)=0.0
0065                    M1=400
0066                    SM=.02
0067                    IC=26
0068                    NDIM=27
0069                    CALL DCSSCU(STOT,VT,DF,NDIM,SM,Y1,C1,IC,WK,IER1)
0070                    CALL DCSFVU(STOT,VT,NDIM,C1,IC,D,0,M1,IER2)
0071                    CALL DCSEVU(STOT,VT,NDIM,C1,IC,D,DUDX,M1,DUDX2,M1,IER3)
0072                    DO 773 I=1,400
0073                    DUDX(I)=DUDX(I)*12.
0074                    DUDX2(I)=DUDX2(I)*144.
0075                     D(I)=D(I)/12.
0076                773 CONTINUE
0077                    VSV=VISC
0078                    DUDX(1)=DUDX(2)
0079                    DUDX2(1)=DUDX2(2)
0080                    WRITE(6,1773)
0081             1773 FORMAT(1H1//20(5X,'DATA PROCESSED BY SUBPRG UFREE, SEE NEXT PAGE'/
                    *),1H1//
                    *2(5X,'I',4X,'D-FT FR STG PT',4X,'U(FPS)',6X,'DUDX(1/S)',6X)/)
0082                    WRITE(6,1883)(I,D(I),U(I),DUDX(I),I=1,399)
0083             1883 FORMAT(I2,I10,3E15.5)
0084                    WRITE(6,2273)
0085             2273 FORMAT(/3(5X,'END OF UFREE OUTPUT.*********',/),1H1)
0086                    RETURN
0087                    END
```

I	D-FT FR STG PT	U(F/S)	DUDX(1/S)	I	D-FT FR STG PT	U(F/S)	DUDX(1/S)
1	0.C	0.0	0.53505E+03	2	C.42222E-03	0.22595E+00	0.53505E+03
3	0.84444E-03	0.45178E+00	0.53464E+03	4	C.12667E-02	0.67738E+00	0.53397E+03
5	0.16889E-02	0.90265E+00	0.53303E+03	6	C.21111E-02	0.11275E+01	0.53182E+03
7	0.25333E-02	0.13517E+01	0.53034E+03	8	C.29556E-02	0.15753E+01	0.52859E+03
9	0.33778E-02	0.17980E+01	0.52657E+03	10	C.38000E-02	0.20199E+01	0.52429E+03
11	0.42222E-02	0.22407E+01	0.52173E+03	12	C.46444E-02	0.24604E+01	0.51891E+03
13	0.50667E-02	0.26789E+01	0.51582E+03	14	C.54889E-02	0.28960E+01	0.51246E+03
15	0.59111E-02	0.31116E+01	0.50883E+03	16	C.63333E-02	0.33256E+01	0.50493E+03
17	0.77278E-C2	0.42100E+01	0.49181E+C3	18	C.91222E-02	0.48869E+01	0.47909E+03
19	0.10517E-01	0.55463E+01	0.46678E+03	20	C.11911E-01	0.61889E+01	0.45488E+03
21	0.13306E-C1	0.68151E+01	0.44338E+03	22	C.14700E-01	0.74256E+01	0.43228E+03
23	0.16094E-01	0.80209E+01	0.42160E+03	24	C.17489E-01	0.86016E+01	0.41131E+03
25	0.18883E-C1	0.91682E+01	0.40143E+03	26	C.20278E-01	0.97213E+01	0.39196E+03
27	0.21672E-C1	0.10261E+02	0.38289E+03	28	C.23067E-01	0.10789E+02	0.37423E+03
29	0.24461E-01	0.11305E+02	0.36597E+03	30	C.25855E-01	0.11810E+02	0.35812E+03
31	0.27250E-C1	0.12304E+02	0.35067E+03	32	C.28678E-01	0.12672E+02	0.34300E+03
33	0.30105E-C1	0.13156E+02	0.33483E+03	34	C.31533E-01	0.13628E+02	0.32616E+03
35	0.32961E-01	0.14087E+02	0.31699E+03	36	C.34389E-01	0.14533E+02	0.30731E+03
37	0.35817E-01	0.14964E+02	0.29714E+03	38	C.37244E-01	0.15381E+02	0.28646E+03
39	0.38672E-01	0.15782E+02	0.27528E+03	40	C.40100E-01	0.16167E+02	0.26360E+03
41	0.41528E-01	0.16535E+02	0.25141E+03	42	C.42955E-01	0.16885E+02	0.23873E+03
43	0.44383E-C1	0.17216E+02	0.22554E+03	44	C.45811E-01	0.17528E+02	0.21185E+03
45	0.47239E-01	0.17821E+02	0.19766E+03	46	C.48667E-01	0.18093E+02	0.18297E+03
47	0.50072E-01	0.18399E+02	0.16857E+03	48	C.51478E-01	0.18626E+02	0.15478E+03
49	0.52883E-01	0.18834E+02	0.14160E+03	50	C.54289E-01	0.19025E+02	0.12904E+03
51	0.55694E-01	0.19197E+02	0.11709E+03	52	C.57100E-01	0.19354E+02	0.10575E+03
53	0.58505E-C1	0.19495E+02	0.95022E+02	54	C.59911E-01	0.19621E+02	0.84910E+02
55	0.61317E-01	0.19734E+02	0.75410E+02	56	C.62722E-01	0.19834E+02	0.66524E+02
57	0.64128E-C1	0.19921E+02	0.58251E+02	58	C.65533E-01	0.19998E+02	0.50590E+02
59	0.66939E-C1	0.20064E+02	0.43543E+C2	60	C.68344E-01	0.20120E+02	0.37109E+02
61	0.69750E-C1	0.20168E+02	0.31287E+02	62	C.71133E-01	0.20164E+02	0.25979E+02
63	0.72517E-01	0.20157E+02	0.20910E+02	64	C.73900E-01	0.20222E+02	0.16081E+02
65	0.75283E-C1	0.20241E+02	0.11490E+02	66	C.76666E-01	0.20254E+02	0.71394E+01
67	0.78050E-C1	0.20261E+02	0.30276E+01	68	C.79433E-01	0.20263E+02	-0.84502E+00
69	0.80817E-C1	0.20259E+02	-0.44784E+01	70	C.82200E-01	0.20250E+02	-0.78725E+01
71	0.83583E-C1	0.20237E+02	-0.11027E+02	72	C.84966E-01	0.20220E+02	-0.13943E+02
73	0.86350E-C1	0.20199E+02	-0.16619E+02	74	C.87733E-01	0.20174E+02	-0.19057E+02
75	0.89116E-C1	C.20146E+02	-0.21255E+C2	76	C.90500E-01	0.20115E+02	-0.23213E+02
77	0.92216E-01	C.20083E+02	-0.25350E+02	78	C.93933E-01	0.20038E+02	-0.27198E+02
79	0.95649E-C1	C.19990E+02	-0.28756E+02	80	C.97366E-01	0.19939E+02	-0.30225E+02
81	0.99083E-01	0.15887E+02	-0.31034E+02	82	C.10080E+00	0.19833E+02	-0.31693E+02
83	0.10252E+C0	0.19778E+02	-0.32093E+02	84	C.10423E+00	0.19723E+02	-0.32203E+02
85	0.10595E+00	0.19668E+02	-0.32023E+02	86	C.10767E+00	0.19613E+02	-0.31554E+02
87	0.10938E+00	0.19560E+02	-0.30796E+02	88	C.11110E+00	0.19508E+02	-0.29747E+02
89	0.11282E+C0	0.19458E+02	-0.28409E+02	90	C.11453E+00	0.19410E+02	-0.27682E+02
91	0.11625E+CC	0.19368E+02	-0.24864E+02	92	C.11934E+00	0.19288E+02	-0.21304E+02
93	0.12244E+C0	0.19228E+02	-0.18055E+02	94	C.12553E+00	0.19176E+02	-0.15119E+02
95	0.12863E+00	0.19134E+02	-0.12495E+02	96	C.13172E+00	0.19099E+02	-0.10184E+02
97	0.13482E+00	0.19076E+02	-0.81853E+01	98	C.13791E+00	0.19048E+02	-0.64993E+01
99	0.14100E+C0	0.19030E+02	-0.51258E+01	100	C.14410E+00	0.19016E+02	-0.40648E+01
101	0.14719E+C0	C.19004E+02	-0.33163E+01	102	C.15029E+00	0.18995E+02	-0.28804E+01
103	0.15338E+00	0.18986E+02	-0.27571E+01	104	C.15648E+00	0.18978E+02	-0.29463E+01
105	0.15957E+00	0.18968E+02	-0.34480E+01	106	C.16267E+00	0.18956E+02	-0.42622E+01
107	0.16748E+0C	0.18942E+02	-0.57150E+C1	108	C.17230E+00	0.18911E+02	-0.70513E+01
109	0.17712E+C0	0.18874E+02	-0.82712E+01	110	C.18193E+00	0.18831E+02	-0.93747E+01
111	0.18675E+00	0.18784E+02	-0.10362E+02	112	C.19157E+00	0.18732E+02	-0.11232E+02
113	0.19638E+C0	0.18672E+02	-0.11987E+02	114	C.20120E+00	0.18616E+02	-0.12624E+02
115	0.20601E+C0	0.18554E+02	-0.13146E+02	116	C.21083E+00	0.18490E+02	-0.13551E+02
117	0.21565E+C0	0.18424E+02	-0.13840E+C2	118	C.22046E+00	0.18357E+02	-0.14012E+02

121	0.23491E+00	0.18154E+02	-0.13830E+02	122	C.24041E+00	0.18077E+02	-0.13541E+02
123	0.24591E+00	C.18003E+02	-0.13213E+02	124	C.25141E+00	0.17932E+02	-0.12846E+02
125	0.25691E+00	0.17862E+02	-0.12438E+02	126	C.26241E+00	0.17795E+02	-0.11991E+02
127	0.26791E+00	0.17730E+02	-0.11504E+02	128	C.27341E+00	0.17668E+02	-0.10978E+02
129	0.27891E+00	0.17609E+02	-0.10412E+02	130	C.28441E+00	0.17554E+02	-0.98362E+01
131	0.28991E+00	0.17502E+02	-0.91609E+01	132	C.29541E+00	0.17453E+02	-0.84759E+01
133	0.30091E+00	0.17408E+02	-0.77512E+01	134	C.30641E+00	0.17368E+02	-0.69869E+01
135	0.31191E+00	0.17332E+02	-0.61830E+01	136	C.31741E+00	0.17300E+02	-0.53393E+01
137	0.32297E+00	0.17273E+02	-0.44833E+01	138	C.32853E+00	0.17250E+02	-0.36592E+01
139	0.33408E+00	0.17232E+02	-0.28673E+01	140	C.33964E+00	0.17218E+02	-0.21074E+01
141	0.34519E+00	0.17209E+02	-0.13797E+01	142	C.35075E+00	0.17203E+02	-0.68399E+00
143	0.35630E+00	0.17201E+02	-0.20406E-01	144	C.36186E+00	0.17203E+02	0.61108E+00
145	0.36741E+00	0.17208E+02	0.12105E+01	146	C.37297E+00	0.17216E+02	0.17778E+01
147	0.37853E+00	0.17227E+02	0.23130E+01	148	C.38408E+00	0.17242E+02	0.28161E+01
149	0.38964E+00	0.17259E+02	0.32871E+01	150	C.39519E+00	0.17278E+02	0.37260E+01
151	0.40075E+00	0.17300E+02	0.41329E+01	152	C.40631E+00	0.17324E+02	0.44987E+01
153	0.41187E+00	0.17350E+02	0.48137E+01	154	C.41743E+00	0.17378E+02	0.50781E+01
155	0.42299E+00	0.17406E+02	0.52917E+01	156	C.42855E+00	0.17436E+02	0.54546E+01
157	0.43411E+00	0.17467E+02	0.55668E+01	158	C.43968E+00	0.17498E+02	0.56282E+01
159	0.44524E+00	0.17529E+02	0.56389E+01	160	C.45080E+00	0.17561E+02	0.55988E+01
161	0.45636E+00	0.17592E+02	0.55081E+01	162	C.46192E+00	0.17622E+02	0.53666E+01
163	0.46748E+00	0.17651E+02	0.51743E+01	164	C.47304E+00	0.17679E+02	0.49314E+01
165	0.47860E+00	0.17706E+02	0.46377E+01	166	C.48416E+00	0.17731E+02	0.42932E+01
167	0.48968E+00	0.17754E+02	0.39742E+01	168	C.49519E+00	0.17775E+02	0.37498E+01
169	0.50070E+00	0.17795E+02	0.36203E+01	170	C.50621E+00	0.17815E+02	0.35854E+01
171	0.51172E+00	0.17835E+02	0.36454E+01	172	C.51723E+00	0.17856E+02	0.38002E+01
173	0.52274E+00	0.17877E+02	0.40497E+01	174	C.52825E+00	0.17900E+02	0.43940E+01
175	0.53376E+00	0.17926E+02	0.48331E+01	176	C.53927E+00	0.17954E+02	0.53669E+01
177	0.54479E+00	0.17985E+02	0.59956E+01	178	C.55030E+00	0.18020E+02	0.67190E+01
179	0.55581E+00	0.18059E+02	0.75371E+01	180	C.56132E+00	0.18103E+02	0.84501E+01
181	0.56683E+00	0.18153E+02	0.94578E+01	182	C.57246E+00	0.18208E+02	0.10492E+02
183	0.57809E+00	0.18270E+02	0.11440E+02	184	C.58371E+00	0.18337E+02	0.12302E+02
185	0.58934E+00	0.18408E+02	0.13077E+02	186	C.59497E+00	0.18484E+02	0.13766E+02
187	0.60060E+00	0.18563E+02	0.14368E+02	188	C.60622E+00	0.18645E+02	0.14884E+02
189	0.61185E+00	0.18730E+02	0.15313E+02	190	C.61748E+00	0.18818E+02	0.15656E+02
191	0.62311E+00	0.18906E+02	0.15913E+02	192	C.62873E+00	0.18996E+02	0.16083E+02
193	0.63436E+00	0.19087E+02	0.16167E+02	194	C.63999E+00	0.19178E+02	0.16164E+02
195	0.64562E+00	0.19269E+02	0.16075E+02	196	C.65125E+00	0.19359E+02	0.15900E+02
197	0.65688E+00	0.19449E+02	0.15727E+02	198	C.66252E+00	0.19537E+02	0.15648E+02
199	0.66816E+00	0.19626E+02	0.15663E+02	200	C.67380E+00	0.19714E+02	0.15771E+02
201	0.67944E+00	0.19804E+02	0.15973E+02	202	C.68508E+00	0.19894E+02	0.16268E+02
203	0.69072E+00	0.19987E+02	0.16657E+02	204	C.69636E+00	0.20082E+02	0.17139E+02
205	0.70200E+00	0.20181E+02	0.17715E+02	206	C.70763E+00	0.20282E+02	0.18384E+02
207	0.71327E+00	0.20388E+02	0.19147E+02	208	C.71891E+00	0.20499E+02	0.20003E+02
209	0.72455E+00	0.20614E+02	0.20953E+02	210	C.73019E+00	0.20735E+02	0.21997E+02
211	0.73583E+00	0.20862E+02	0.23134E+02	212	C.74125E+00	0.20990E+02	0.24243E+02
213	0.74667E+00	0.21124E+02	0.25292E+02	214	C.75209E+00	0.21264E+02	0.26283E+02
215	0.75752E+00	0.21409E+02	0.27214E+02	216	C.76294E+00	0.21559E+02	0.28087E+02
217	0.76836E+00	0.21714E+02	0.28900E+02	218	C.77378E+00	0.21873E+02	0.29654E+02
219	0.77921E+00	0.22035E+02	0.30349E+02	220	C.78463E+00	0.22202E+02	0.30985E+02
221	0.79005E+00	0.22371E+02	0.31562E+02	222	C.79547E+00	0.22544E+02	0.32080E+02
223	0.80089E+00	0.22719E+02	0.32538E+02	224	C.80632E+00	0.22896E+02	0.32938E+02
225	0.81174E+00	0.23076E+02	0.33278E+02	226	C.81716E+00	0.23257E+02	0.33559E+02
227	0.82257E+00	0.23440E+02	0.33791E+02	228	C.82797E+00	0.23623E+02	0.33985E+02
229	0.83338E+00	0.23807E+02	0.34141E+02	230	C.83878E+00	0.23992E+02	0.34259E+02
231	0.84419E+00	0.24177E+02	0.34339E+02	232	C.84959E+00	0.24363E+02	0.34381E+02
233	0.85500E+00	0.24549E+02	0.34385E+02	234	C.86041E+00	0.24735E+02	0.34352E+02
235	0.86581E+00	0.24920E+02	0.34280E+02	236	C.87122E+00	0.25105E+02	0.34170E+02
237	0.87662E+00	0.25290E+02	0.34022E+02	238	C.88203E+00	0.25473E+02	0.33837E+02
239	0.88743E+00	0.25655E+02	0.33613E+02	240	C.89284E+00	0.25836E+02	0.33351E+02
241	0.89824E+00	0.26016E+02	0.33052E+02	242	C.90374E+00	0.26197E+02	0.32765E+02
243	0.90924E+00	0.26377E+02	0.32552E+02	244	C.91474E+00	0.26555E+02	0.32415E+02
245	0.92024E+00	0.26733E+02	0.32351E+02	246	C.92574E+00	0.26911E+02	0.32362E+02
247	0.93124E+00	0.27089E+02	0.32448E+02	248	C.93674E+00	0.27268E+02	0.32608E+02
249	0.94224E+00	0.27448E+02	0.32843E+02	250	C.94774E+00	0.27630E+02	0.33152E+02
251	0.95324E+00	0.27813E+02	0.33536E+02	252	C.95874E+00	0.27999E+02	0.33995E+02
253	0.96424E+00	0.28187E+02	0.34528E+02	254	C.96974E+00	0.28379E+02	0.35135E+02
255	[illegible]	[illegible]	[illegible]	256	[illegible]	[illegible]	0.36574E+02

257	0.98623E+00	0.28675E+02	0.37360E+02	258	C.99172E+00	0.29182E+02	0.38135E+02
259	0.99721E+00	0.29394E+02	0.38899E+02	260	C.10027E+01	0.29609E+02	0.39651E+02
261	0.10082E+01	0.29829E+02	0.40392E+02	262	C.10137E+01	0.30053E+02	0.41122E+02
263	0.10192E+01	0.30281E+02	0.41840E+02	264	C.10247E+01	0.30512E+02	0.42546E+02
265	0.10301E+01	0.30744E+02	0.43242E+02	266	C.10356E+01	0.30987E+02	0.43925E+02
267	0.10411E+01	0.31236E+02	0.44598E+02	268	C.10466E+01	0.31476E+02	0.45259E+02
269	0.10521E+01	0.31727E+02	0.45908E+02	270	C.10576E+01	0.31980E+02	0.46546E+02
271	0.10631E+01	0.32238E+02	0.47173E+02	272	C.10685E+01	0.32497E+02	0.47780E+02
273	0.10740E+01	0.32761E+02	0.48363E+02	274	C.10795E+01	0.33027E+02	0.48922E+02
275	0.10850E+01	0.33296E+02	0.49457E+02	276	C.10904E+01	0.33568E+02	0.49968E+02
277	0.10959E+01	0.33843E+02	0.50456E+02	278	C.11014E+01	0.34120E+02	0.50919E+02
279	0.11069E+01	0.34400E+02	0.51358E+02	280	C.11123E+01	0.34682E+02	0.51773E+02
281	0.11178E+01	0.34967E+02	0.52164E+02	282	C.11233E+01	0.35253E+02	0.52531E+02
283	0.11287E+01	0.35541E+02	0.52874E+02	284	C.11342E+01	0.35832E+02	0.53193E+02
285	0.11397E+01	0.36124E+02	0.53488E+02	286	C.11452E+01	0.36417E+02	0.53758E+02
287	0.11506E+01	0.36715E+02	0.53999E+02	288	C.11562E+01	0.37014E+02	0.54199E+02
289	0.11617E+01	0.37314E+02	0.54357E+02	290	C.11673E+01	0.37615E+02	0.54474E+02
291	0.11728E+01	0.37916E+02	0.54549E+02	292	C.11783E+01	0.38218E+02	0.54583E+02
293	0.11839E+01	0.38519E+02	0.54576E+02	294	C.11894E+01	0.38821E+02	0.54527E+02
295	0.11949E+01	0.39122E+02	0.54437E+02	296	C.12004E+01	0.39423E+02	0.54305E+02
297	0.12060E+01	0.39723E+02	0.54132E+02	298	C.12115E+01	0.40021E+02	0.53918E+02
299	0.12170E+01	0.40319E+02	0.53662E+02	300	C.12225E+01	0.40614E+02	0.53365E+02
301	0.12281E+01	0.40908E+02	0.53027E+02	302	C.12336E+01	0.41202E+02	0.52751E+02
303	0.12392E+01	0.41494E+02	0.52644E+02	304	C.12447E+01	0.41786E+02	0.52707E+02
305	0.12503E+01	0.42079E+02	0.52939E+02	306	C.12558E+01	0.42373E+02	0.53340E+02
307	0.12613E+01	0.42671E+02	0.53911E+02	308	C.12669E+01	0.42972E+02	0.54651E+02
309	0.12724E+01	0.43277E+02	0.55560E+02	310	C.12780E+01	0.43588E+02	0.56638E+02
311	0.12835E+01	0.43905E+02	0.57886E+02	312	C.12891E+01	0.44230E+02	0.59303E+02
313	0.12946E+01	0.44563E+02	0.60889E+02	314	C.13002E+01	0.44906E+02	0.62644E+02
315	0.13057E+01	0.45258E+02	0.64569E+02	316	C.13112E+01	0.45622E+02	0.66663E+02
317	0.13168E+01	0.45995E+02	0.68782E+02	318	C.13224E+01	0.46389E+02	0.70751E+02
319	0.13280E+01	0.46789E+02	0.72569E+02	320	C.13336E+01	0.47199E+02	0.74237E+02
321	0.13392E+01	0.47610E+02	0.75755E+02	322	C.13447E+01	0.48044E+02	0.77112E+02
323	0.13503E+01	0.48478E+02	0.78338E+02	324	C.13559E+01	0.48919E+02	0.79404E+02
325	0.13615E+01	0.49364E+02	0.80320E+02	326	C.13671E+01	0.49815E+02	0.81086E+02
327	0.13727E+01	0.50269E+02	0.81701E+02	328	C.13782E+01	0.50727E+02	0.82166E+02
329	0.13838E+01	0.51186E+02	0.82480E+02	330	C.13894E+01	0.51647E+02	0.82844E+02
331	0.13950E+01	0.52109E+02	0.82658E+02	332	C.14006E+01	0.52575E+02	0.82563E+02
333	0.14062E+01	0.53040E+02	0.82402E+02	334	C.14119E+01	0.53503E+02	0.82176E+02
335	0.14175E+01	0.53965E+02	0.81884E+02	336	C.14231E+01	0.54426E+02	0.81526E+02
337	0.14288E+01	0.54884E+02	0.81103E+02	338	C.14344E+01	0.55339E+02	0.80614E+02
339	0.14400E+01	0.55792E+02	0.80059E+02	340	C.14457E+01	0.56241E+02	0.79438E+02
341	0.14513E+01	0.56687E+02	0.78752E+02	342	C.14569E+01	0.57128E+02	0.78001E+02
343	0.14626E+01	0.57565E+02	0.77183E+02	344	C.14682E+01	0.57998E+02	0.76300E+02
345	0.14738E+01	0.58425E+02	0.75351E+02	346	C.14795E+01	0.58846E+02	0.74317E+02
347	0.14851E+01	0.59258E+02	0.73374E+02	348	C.14906E+01	0.59665E+02	0.72563E+02
349	0.14962E+01	0.60068E+02	0.71903E+02	350	C.15018E+01	0.60468E+02	0.71394E+02
351	0.15074E+01	0.60865E+02	0.71036E+02	352	C.15129E+01	0.61260E+02	0.70829E+02
353	0.15185E+01	0.61655E+02	0.70773E+02	354	C.15241E+01	0.62050E+02	0.70869E+02
355	0.15297E+01	0.62446E+02	0.71115E+02	356	C.15352E+01	0.62843E+02	0.71513E+02
357	0.15408E+01	0.63244E+02	0.72061E+02	358	C.15464E+01	0.63648E+02	0.72761E+02
359	0.15520E+01	0.64056E+02	0.73612E+02	360	C.15576E+01	0.64469E+02	0.74614E+02
361	0.15631E+01	0.64888E+02	0.75767E+02	362	C.15686E+01	0.65306E+02	0.76868E+02
363	0.15741E+01	0.65730E+02	0.77831E+02	364	C.15796E+01	0.66159E+02	0.78596E+02
365	0.15851E+01	0.66592E+02	0.79183E+02	366	C.15905E+01	0.67027E+02	0.79593E+02
367	0.15960E+01	0.67464E+02	0.79924E+02	368	C.16015E+01	0.67902E+02	0.79870E+02
369	0.16070E+01	0.68340E+02	0.79754E+02	370	C.16125E+01	0.68776E+02	0.79451E+02
371	0.16180E+01	0.69211E+02	0.78971E+02	372	C.16234E+01	0.69642E+02	0.78313E+02
373	0.16289E+01	0.70069E+02	0.77478E+02	374	C.16344E+01	0.70491E+02	0.76464E+02
375	0.16399E+01	0.70907E+02	0.75272E+02	376	C.16454E+01	0.71316E+02	0.73902E+02
377	0.16513E+01	0.71753E+02	0.72368E+02	378	C.16573E+01	0.72140E+02	0.70938E+02
379	0.16633E+01	0.72599E+02	0.69615E+02	380	C.16692E+01	0.73011E+02	0.68398E+02
381	0.16752E+01	0.73415E+02	0.67286E+02	382	C.16811E+01	0.73813E+02	0.66280E+02
383	0.16871E+01	0.74205E+02	0.65380E+02	384	C.16931E+01	0.74593E+02	0.64585E+02
385	0.16990E+01	0.74976E+02	0.63897E+02	386	C.17050E+01	0.75355E+02	0.63314E+02
387	0.17109E+01	0.75731E+02	0.62837E+02	388	C.17169E+01	0.76104E+02	0.62466E+02
389	0.17229E+01	0.76476E+02	0.62201E+02	390	C.17288E+01	0.76846E+02	0.62042E+02
391	0.17348E+01	0.77215E+02	0.61988E+02	392	C.17410E+01	0.77603E+02	0.62045E+02
393	0.17473E+01	0.77991E+02	0.62219E+02	394	C.17535E+01	0.78381E+02	0.62509E+02
395	0.17598E+01	0.78773E+02	0.62915E+02	396	C.17660E+01	0.79168E+02	0.63430E+02
397	0.17723E+01	0.79566E+02	0.64077E+02	398	C.17785E+01	0.79969E+02	0.64832E+02
399	0.17848E+01	0.80377E+02	0.65704E+02				

END OF UFREE OUTPUT.**********
END OF UFREE OUTPUT.**********
END OF UFREE OUTPUT.**********

OUTPUT FROM 2-D SIG-FG-OK
F2MIN,F2AV,F2MAX,MEX 0.123272E+01 0.123277E+01 0.123282E+01 75

I	F	FP	FPP	I	F	FP	FPP
1	0.0	0.0	0.1233E+01	2	0.1520E-02	0.6039E-01	0.1183E+01
3	0.5997E-02	0.1183E+00	0.1133E+01	4	0.1331E-01	0.1737E+00	0.1083E+01
5	0.2333E-01	0.2266E+00	0.1035E+01	6	0.3593E-01	0.2772E+00	0.9862E+00
7	0.5100E-01	0.3251E+00	0.9387E+00	8	0.6842E-01	0.3710E+00	0.8920E+00
9	0.8807E-01	0.4145E+00	0.8463E+00	10	0.1098E+00	0.4557E+00	0.8017E+00
11	0.1336E+00	0.4947E+00	0.7583E+00	12	0.1593E+00	0.5315E+00	0.7161E+00
13	0.1867E+00	0.5663E+00	0.6751E+00	14	0.2159E+00	0.5991E+00	0.6355E+00
15	0.2466E+00	0.6299E+00	0.5973E+00	16	0.2788E+00	0.6588E+00	0.5605E+00
17	0.3124E+00	0.6860E+00	0.5251E+00	18	0.3474E+00	0.7114E+00	0.4911E+00
19	0.3836E+00	0.7351E+00	0.4586E+00	20	0.4209E+00	0.7572E+00	0.4276E+00
21	0.4592E+00	0.7779E+00	0.3980E+00	22	0.4586E+00	0.7971E+00	0.3698E+00
23	0.5389E+00	0.8149E+00	0.3431E+00	24	0.5801E+00	0.8314E+00	0.3177E+00
25	0.6221E+00	0.8467E+00	0.2937E+00	26	0.6647E+00	0.8608E+00	0.2711E+00
27	0.7081E+00	0.8738E+00	0.2498E+00	28	0.7521E+00	0.8858E+00	0.2298E+00
29	0.7967E+00	0.8968E+00	0.2111E+00	30	0.8418E+00	0.9069E+00	0.1934E+00
31	0.8873E+00	0.9162E+00	0.1770E+00	32	0.9334E+00	0.9246E+00	0.1616E+00
33	0.9798E+00	0.9323E+00	0.1474E+00	34	0.1027E+01	0.9394E+00	0.1341E+00
35	0.1074E+01	0.9458E+00	0.1218E+00	36	0.1121E+01	0.9516E+00	0.1105E+00
37	0.1169E+01	0.9568E+00	0.1000E+00	38	0.1217E+01	0.9616E+00	0.9035E-01
39	0.1265E+01	0.9659E+00	0.8148E-01	40	0.1313E+01	0.9697E+00	0.7334E-01
41	0.1362E+01	0.9732E+00	0.6599E-01	42	0.1411E+01	0.9763E+00	0.5908E-01
43	0.1460E+01	0.9791E+00	0.5288E-01	44	0.1509E+01	0.9816E+00	0.4724E-01
45	0.1558E+01	0.9839E+00	0.4212E-01	46	0.1607E+01	0.9859E+00	0.3748E-01
47	0.1656E+01	0.9876E+00	0.3329E-01	48	0.1706E+01	0.9892E+00	0.2951E-01
49	0.1755E+01	0.9906E+00	0.2611E-01	50	0.1805E+01	0.9918E+00	0.2305E-01
51	0.1854E+01	0.9929E+00	0.2032E-01	52	0.1904E+01	0.9939E+00	0.1787E-01
53	0.1954E+01	0.9947E+00	0.1569E-01	54	0.2004E+01	0.9954E+00	0.1375E-01
55	0.2053E+01	0.9961E+00	0.1202E-01	56	0.2103E+01	0.9966E+00	0.1049E-01
57	0.2153E+01	0.9971E+00	0.9141E-02	58	0.2203E+01	0.9975E+00	0.7949E-02
59	0.2253E+01	0.9979E+00	0.6900E-02	60	0.2303E+01	0.9982E+00	0.5979E-02
61	0.2353E+01	0.9985E+00	0.5172E-02	62	0.2403E+01	0.9988E+00	0.4466E-02
63	0.2452E+01	0.9990E+00	0.3851E-02	64	0.2502E+01	0.9991E+00	0.3315E-02
65	0.2552E+01	0.9993E+00	0.2850E-02	66	0.2602E+01	0.9994E+00	0.2447E-02
67	0.2652E+01	0.9995E+00	0.2099E-02	68	0.2702E+01	0.9996E+00	0.1799E-02
69	0.2752E+01	0.9997E+00	0.1541E-02	70	0.2802E+01	0.9998E+00	0.1320E-02
71	0.2852E+01	0.9999E+00	0.1130E-02	72	0.2902E+01	0.9999E+00	0.9686E-03
73	0.2952E+01	0.1000E+01	0.8309E-03	74	0.3002E+01	0.1000E+01	0.7139E-03
75	0.3052E+01	0.1000E+01	0.6148E-03				

STARTING VELOCITIES AT (FT) XST= 0.77278E-02
UST= 0.42100E+01
BETA= 0.54479E+03
VISC= 0.16770E-03

UNITS=FEET,SEC/

I	U	V	Y	I	U	V	Y
1	0.0	0.0	0.0	2	0.86932E-02	-0.15711E-04	0.94858E-06
3	0.17386E-01	-0.31422E-04	0.18972E-05	4	0.26080E-01	-0.47134E-04	0.28457E-05
5	0.34773E-01	-0.62845E-04	0.37943E-05	6	0.43466E-01	-0.78556E-04	0.47429E-05
7	0.52159E-01	-0.94267E-04	0.56915E-05	8	0.60852E-01	-0.10998E-03	0.66400E-05
9	0.69546E-01	-0.12569E-03	0.75886E-05	10	0.78239E-01	-0.14140E-03	0.85372E-05
11	0.86932E-01	-0.15711E-03	0.94858E-05	12	0.95625E-01	-0.17282E-03	0.10434E-04
13	0.10432E+00	-0.18853E-03	0.11383E-04	14	0.11301E+00	-0.20425E-03	0.12331E-04
15	0.12170E+00	-0.21996E-03	0.13280E-04	16	0.13040E+00	-0.23567E-03	0.14229E-04
17	0.13909E+00	-0.25138E-03	0.15177E-04	18	0.14778E+00	-0.26709E-03	0.16126E-04
19	0.15648E+00	-0.28280E-03	0.17074E-04	20	0.16517E+00	-0.29851E-03	0.18023E-04
21	0.17386E+00	-0.31422E-03	0.18972E-04	22	0.18256E+00	-0.32994E-03	0.19920E-04
23	0.19125E+00	-0.34565E-03	0.20869E-04	24	0.19994E+00	-0.36136E-03	0.21817E-04
25	0.20864E+00	-0.37707E-03	0.22766E-04	26	0.21733E+00	-0.39278E-03	0.23714E-04
27	0.22602E+00	-0.40849E-03	0.24663E-04	28	0.23472E+00	-0.42420E-03	0.25612E-04
29	0.24341E+00	-0.43991E-03	0.26560E-04	30	0.25210E+00	-0.45563E-03	0.27509E-04
31	0.26052E+00	-0.49440E-03	0.28457E-04	32	0.26886E+00	-0.54068E-03	0.29406E-04
33	0.27719E+00	-0.58695E-03	0.30354E-04	34	0.28553E+00	-0.63322E-03	0.31303E-04
35	0.29386E+00	-0.67949E-03	0.32252E-04	36	0.30219E+00	-0.72577E-03	0.33200E-04
37	0.31053E+00	-0.77204E-03	0.34149E-04	38	0.31886E+00	-0.81831E-03	0.35097E-04
39	0.32720E+00	-0.86459E-03	0.36046E-04	40	0.33553E+00	-0.91086E-03	0.36994E-04
41	0.34386E+00	-0.95713E-03	0.37943E-04	42	0.35220E+00	-0.10034E-02	0.38892E-04
43	0.36053E+00	-0.10497E-02	0.39840E-04	44	0.36886E+00	-0.10960E-02	0.40789E-04
45	0.37720E+00	-0.11422E-02	0.41737E-04	46	0.38553E+00	-0.11885E-02	0.42686E-04
47	0.39387E+00	-0.12348E-02	0.43634E-04	48	0.40220E+00	-0.12810E-02	0.44583E-04
49	0.41053E+00	-0.13273E-02	0.45532E-04	50	0.41887E+00	-0.13736E-02	0.46480E-04
51	0.42720E+00	-0.14199E-02	0.47429E-04	52	0.43387E+00	-0.15124E-02	0.49326E-04
53	0.44054E+00	-0.16050E-02	0.51223E-04	54	0.47720E+00	-0.16975E-02	0.53120E-04
55	0.49387E+00	-0.17900E-02	0.55017E-04	56	0.51000E+00	-0.19268E-02	0.56915E-04
57	0.52595E+00	-0.20779E-02	0.58812E-04	58	0.54191E+00	-0.22290E-02	0.60709E-04
59	0.55782E+00	-0.23801E-02	0.62606E-04	60	0.57381E+00	-0.25312E-02	0.64503E-04
61	0.58977E+00	-0.26823E-02	0.66400E-04	62	0.60572E+00	-0.28334E-02	0.68297E-04
63	0.62167E+00	-0.29844E-02	0.70195E-04	64	0.63762E+00	-0.31355E-02	0.72092E-04
65	0.65358E+00	-0.32866E-02	0.73989E-04	66	0.66953E+00	-0.34377E-02	0.75886E-04
67	0.68548E+00	-0.35888E-02	0.77783E-04	68	0.70144E+00	-0.37399E-02	0.79680E-04
69	0.71739E+00	-0.38910E-02	0.81578E-04	70	0.73325E+00	-0.40495E-02	0.83475E-04
71	0.74849E+00	-0.42566E-02	0.85372E-04	72	0.76374E+00	-0.44637E-02	0.87269E-04
73	0.77899E+00	-0.46708E-02	0.89166E-04	74	0.79423E+00	-0.48779E-02	0.91063E-04
75	0.80947E+00	-0.50850E-02	0.92960E-04	76	0.82471E+00	-0.52921E-02	0.94858E-04
77	0.83996E+00	-0.54991E-02	0.96755E-04	78	0.85520E+00	-0.57062E-02	0.98652E-04
79	0.87045E+00	-0.59133E-02	0.10055E-03	80	0.88569E+00	-0.61204E-02	0.10245E-03
81	0.90053E+00	-0.63275E-02	0.10434E-03	82	0.91618E+00	-0.65346E-02	0.10624E-03
83	0.93142E+00	-0.67417E-02	0.10814E-03	84	0.94667E+00	-0.69488E-02	0.11003E-03
85	0.96156E+00	-0.71831E-02	0.11193E-03	86	0.97610E+00	-0.74437E-02	0.11383E-03
87	0.99064E+00	-0.77042E-02	0.11573E-03	88	0.10052E+01	-0.79648E-02	0.11762E-03
89	0.10157E+01	-0.82254E-02	0.11952E-03	90	0.10343E+01	-0.84859E-02	0.12142E-03
91	0.10488E+01	-0.87464E-02	0.12331E-03	92	0.10634E+01	-0.90070E-02	0.12521E-03
93	0.10779E+01	-0.92675E-02	0.12711E-03	94	0.10925E+01	-0.95281E-02	0.12901E-03
95	0.11070E+01	-0.97886E-02	0.13090E-03	96	0.11215E+01	-0.10049E-01	0.13280E-03
97	0.11361E+01	-0.10310E-01	0.13470E-03	98	0.11506E+01	-0.10570E-01	0.13659E-03
99	0.11652E+01	-0.10831E-01	0.13849E-03	100	0.11791E+01	-0.11137E-01	0.14039E-03
101	0.11930E+01	-0.11443E-01	0.14229E-03	102	0.12207E+01	-0.12071E-01	0.14608E-03
103	0.12484E+01	-0.12694E-01	0.14988E-03	104	0.12761E+01	-0.13317E-01	0.15367E-03
105	0.13038E+01	-0.13940E-01	0.15746E-03	106	0.13315E+01	-0.14563E-01	0.16126E-03
107	0.13592E+01	-0.15186E-01	0.16505E-03	108	0.13861E+01	-0.15871E-01	0.16885E-03
109	0.14124E+01	-0.16591E-01	0.17264E-03	110	0.14388E+01	-0.17311E-01	0.17644E-03
111	0.14651E+01	-0.18031E-01	0.18023E-03	112	0.14915E+01	-0.18751E-01	0.18402E-03
113	0.15178E+01	-0.19471E-01	0.18782E-03	114	0.15442E+01	-0.20191E-01	0.19161E-03

115	0.15701E+01	-0.20941E-01	0.19541E-03	116	0.15951E+01	-0.21753E-01	0.19920E-03
117	0.16201E+01	-0.22565E-01	0.20300E-03	118	0.16451E+01	-0.23378E-01	0.20679E-03
119	0.16702E+01	-0.24190E-01	0.21058E-03	120	0.16952E+01	-0.25002E-01	0.21438E-03
121	0.17202E+01	-0.25814E-01	0.21817E-03	122	0.17452E+01	-0.26627E-01	0.22197E-03
123	0.17689E+01	-0.27527E-01	0.22576E-03	124	0.17927E+01	-0.28427E-01	0.22956E-03
125	0.18164E+01	-0.29327E-01	0.23335E-03	126	0.18401E+01	-0.30226E-01	0.23714E-03
127	0.18638E+01	-0.31126E-01	0.24094E-03	128	0.18876E+01	-0.32026E-01	0.24473E-03
129	0.19113E+01	-0.32926E-01	0.24853E-03	130	0.19341E+01	-0.33883E-01	0.25232E-03
131	0.19566E+01	-0.34866E-01	0.25612E-03	132	0.19790E+01	-0.35849E-01	0.25991E-03
133	0.20015E+01	-0.36831E-01	0.26370E-03	134	0.20239E+01	-0.37814E-01	0.26750E-03
135	0.20464E+01	-0.38796E-01	0.27129E-03	136	0.20688E+01	-0.39779E-01	0.27509E-03
137	0.20908E+01	-0.40792E-01	0.27888E-03	138	0.21120E+01	-0.41853E-01	0.28268E-03
139	0.21333E+01	-0.42914E-01	0.28647E-03	140	0.21545E+01	-0.43975E-01	0.29026E-03
141	0.21757E+01	-0.45036E-01	0.29406E-03	142	0.21969E+01	-0.46097E-01	0.29785E-03
143	0.22181E+01	-0.47158E-01	0.30165E-03	144	0.22393E+01	-0.48225E-01	0.30544E-03
145	0.22593E+01	-0.49236E-01	0.30924E-03	146	0.22793E+01	-0.50495E-01	0.31303E-03
147	0.22993E+01	-0.51630E-01	0.31682E-03	148	0.23194E+01	-0.52765E-01	0.32062E-03
149	0.23394E+01	-0.53900E-01	0.32441E-03	150	0.23594E+01	-0.55035E-01	0.32821E-03
151	0.23794E+01	-0.56170E-01	0.33200E-03	152	0.24174E+01	-0.58563E-01	0.33959E-03
153	0.24552E+01	-0.60573E-01	0.34718E-03	154	0.24929E+01	-0.63382E-01	0.35477E-03
155	0.25301E+01	-0.65822E-01	0.36236E-03	156	0.25656E+01	-0.68363E-01	0.36994E-03
157	0.26011E+01	-0.70904E-01	0.37753E-03	158	0.26366E+01	-0.73445E-01	0.38512E-03
159	0.26720E+01	-0.76056E-01	0.39271E-03	160	0.27042E+01	-0.78721E-01	0.40030E-03
161	0.27375E+01	-0.81385E-01	0.40789E-03	162	0.27708E+01	-0.84050E-01	0.41548E-03
163	0.28022E+01	-0.86820E-01	0.42306E-03	164	0.28335E+01	-0.89601E-01	0.43065E-03
165	0.28647E+01	-0.92381E-01	0.43824E-03	166	0.28955E+01	-0.95190E-01	0.44583E-03
167	0.29247E+01	-0.98079E-01	0.45342E-03	168	0.29540E+01	-0.10097E+00	0.46101E-03
169	0.29832E+01	-0.10386E+00	0.46860E-03	170	0.30113E+01	-0.10681E+00	0.47619E-03
171	0.30386E+01	-0.10980E+00	0.48377E-03	172	0.30660E+01	-0.11279E+00	0.49136E-03
173	0.30933E+01	-0.11578E+00	0.49895E-03	174	0.31189E+01	-0.11886E+00	0.50654E-03
175	0.31444E+01	-0.12194E+00	0.51413E-03	176	0.31699E+01	-0.12503E+00	0.52172E-03
177	0.31949E+01	-0.12814E+00	0.52931E-03	178	0.32187E+01	-0.13131E+00	0.53689E-03
179	0.32424E+01	-0.13449E+00	0.54448E-03	180	0.32662E+01	-0.13766E+00	0.55207E-03
181	0.32889E+01	-0.14089E+00	0.55966E-03	182	0.33110E+01	-0.14414E+00	0.56725E-03
183	0.33331E+01	-0.14740E+00	0.57484E-03	184	0.33552E+01	-0.15066E+00	0.58243E-03
185	0.33758E+01	-0.15399E+00	0.59001E-03	186	0.33963E+01	-0.15732E+00	0.59760E-03
187	0.34168E+01	-0.16065E+00	0.60519E-03	188	0.34368E+01	-0.16401E+00	0.61278E-03
189	0.34558E+01	-0.16741E+00	0.62037E-03	190	0.34748E+01	-0.17081E+00	0.62796E-03
191	0.34939E+01	-0.17422E+00	0.63555E-03	192	0.35119E+01	-0.17767E+00	0.64313E-03
193	0.35295E+01	-0.18113E+00	0.65072E-03	194	0.35471E+01	-0.18460E+00	0.65831E-03
195	0.35647E+01	-0.18807E+00	0.66590E-03	196	0.35810E+01	-0.19160E+00	0.67349E-03
197	0.35972E+01	-0.19513E+00	0.68108E-03	198	0.36135E+01	-0.19866E+00	0.68867E-03
199	0.36293E+01	-0.20221E+00	0.69625E-03	200	0.36443E+01	-0.20580E+00	0.70384E-03
201	0.36593E+01	-0.20938E+00	0.71143E-03	202	0.36743E+01	-0.21297E+00	0.71902E-03
203	0.36884E+01	-0.21659E+00	0.72661E-03	204	0.37022E+01	-0.22023E+00	0.73420E-03
205	0.37160E+01	-0.22381E+00	0.74179E-03	206	0.37298E+01	-0.22751E+00	0.74937E-03
207	0.37424E+01	-0.23119E+00	0.75696E-03	208	0.37551E+01	-0.23488E+00	0.76455E-03
209	0.37678E+01	-0.23856E+00	0.77214E-03	210	0.37801E+01	-0.24227E+00	0.77973E-03
211	0.37917E+01	-0.24599E+00	0.78732E-03	212	0.38034E+01	-0.24972E+00	0.79491E-03
213	0.38150E+01	-0.25345E+00	0.80250E-03	214	0.38259E+01	-0.25721E+00	0.81008E-03
215	0.38366E+01	-0.26098E+00	0.81767E-03	216	0.38472E+01	-0.26475E+00	0.82526E-03
217	0.38578E+01	-0.26852E+00	0.83285E-03	218	0.38676E+01	-0.27232E+00	0.84044E-03
219	0.38773E+01	-0.27613E+00	0.84803E-03	220	0.38871E+01	-0.27994E+00	0.85562E-03
221	0.38964E+01	-0.28375E+00	0.86320E-03	222	0.39053E+01	-0.28759E+00	0.87079E-03
223	0.39142E+01	-0.29143E+00	0.87838E-03	224	0.39231E+01	-0.29527E+00	0.88597E-03
225	0.39314E+01	-0.29913E+00	0.89356E-03	226	0.39395E+01	-0.30300E+00	0.90115E-03
227	0.39476E+01	-0.30687E+00	0.90874E-03	228	0.39556E+01	-0.31074E+00	0.91632E-03
229	0.39630E+01	-0.31464E+00	0.92391E-03	230	0.39703E+01	-0.31854E+00	0.93150E-03
231	0.39777E+01	-0.32243E+00	0.93909E-03	232	0.39848E+01	-0.32634E+00	0.94668E-03
233	0.39914E+01	-0.33027E+00	0.95427E-03	234	0.39981E+01	-0.33419E+00	0.96186E-03
235	0.40048E+01	-0.33811E+00	0.96944E-03	236	0.40110E+01	-0.34205E+00	0.97703E-03
237	0.40170E+01	-0.34599E+00	0.98462E-03	238	0.40231E+01	-0.34994E+00	0.99221E-03
239	0.40291E+01	-0.35389E+00	0.99980E-03	240	0.40345E+01	-0.35785E+00	0.10074E-02
241	0.40400E+01	-0.36182E+00	0.10150E-02	242	0.40455E+01	-0.36578E+00	0.10226E-02
243	0.40507E+01	-0.36976E+00	0.10302E-02	244	0.40557E+01	-0.37374E+00	0.10377E-02
245	0.40606E+01	-0.37773E+00	0.10453E-02	246	0.40655E+01	-0.38171E+00	0.10529E-02
247	0.40701E+01	-0.38571E+00	0.10605E-02	248	0.40745E+01	-0.38971E+00	0.10681E-02
249	0.40790E+01	-0.39371E+00	0.10757E-02	250	0.40831E+01	-0.39771E+00	0.10833E-02

251	0.40874E+01	-0.40173E+00	0.10909E-02	252	0.40914E+01	-0.40575E+00	0.10985E-02
253	0.40954E+01	-0.40977E+00	0.11062E-02	254	0.40992E+01	-0.41379E+00	0.11136E-02
255	0.41028E+01	-0.41782E+00	0.11212E-02	256	0.41064E+01	-0.42185E+00	0.11288E-02
257	0.41100E+01	-0.42588E+00	0.11364E-02	258	0.41132E+01	-0.42992E+00	0.11440E-02
259	0.41164E+01	-0.43396E+00	0.11516E-02	260	0.41197E+01	-0.43801E+00	0.11592E-02
261	0.41228E+01	-0.44205E+00	0.11667E-02	262	0.41257E+01	-0.44610E+00	0.11743E-02
263	0.41286E+01	-0.45016E+00	0.11819E-02	264	0.41314E+01	-0.45421E+00	0.11895E-02
265	0.41342E+01	-0.45827E+00	0.11971E-02	266	0.41367E+01	-0.46233E+00	0.12047E-02
267	0.41393E+01	-0.46646E+00	0.12123E-02	268	0.41419E+01	-0.47046E+00	0.12199E-02
269	0.41442E+01	-0.47454E+00	0.12275E-02	270	0.41465E+01	-0.47860E+00	0.12350E-02
271	0.41488E+01	-0.48267E+00	0.12426E-02	272	0.41510E+01	-0.48675E+00	0.12502E-02
273	0.41530E+01	-0.49083E+00	0.12578E-02	274	0.41551E+01	-0.49490E+00	0.12654E-02
275	0.41571E+01	-0.49898E+00	0.12730E-02	276	0.41590E+01	-0.50307E+00	0.12806E-02
277	0.41608E+01	-0.50715E+00	0.12882E-02	278	0.41626E+01	-0.51124E+00	0.12958E-02
279	0.41644E+01	-0.51533E+00	0.13033E-02	280	0.41660E+01	-0.51942E+00	0.13109E-02
281	0.41676E+01	-0.52351E+00	0.13185E-02	282	0.41692E+01	-0.52760E+00	0.13261E-02
283	0.41708E+01	-0.53170E+00	0.13337E-02	284	0.41722E+01	-0.53580E+00	0.13413E-02
285	0.41736E+01	-0.53989E+00	0.13489E-02	286	0.41750E+01	-0.54399E+00	0.13565E-02
287	0.41763E+01	-0.54809E+00	0.13641E-02	288	0.41776E+01	-0.55219E+00	0.13716E-02
289	0.41788E+01	-0.55630E+00	0.13792E-02	290	0.41801E+01	-0.56040E+00	0.13868E-02
291	0.41812E+01	-0.56451E+00	0.13944E-02	292	0.41823E+01	-0.56861E+00	0.14020E-02
293	0.41834E+01	-0.57272E+00	0.14096E-02	294	0.41844E+01	-0.57683E+00	0.14172E-02
295	0.41854E+01	-0.58094E+00	0.14248E-02	296	0.41863E+01	-0.58505E+00	0.14323E-02
297	0.41873E+01	-0.58916E+00	0.14399E-02	298	0.41882E+01	-0.59327E+00	0.14475E-02
299	0.41890E+01	-0.59739E+00	0.14551E-02	300	0.42100E+01	-0.60150E+00	0.14627E-02
301	0.42100E+01	-0.60561E+00	0.14703E-02				

301	0.42100E+01	-0.60561E+00	0.14703E-02	305	0.42100E+01	-0.62207E+00	0.15006E-02
309	0.42100E+01	-0.63852E+00	0.15310E-02	313	0.42100E+01	-0.65498E+00	0.15614E-02
317	0.42100E+01	-0.67143E+00	0.15917E-02	321	0.42100E+01	-0.68789E+00	0.16221E-02
325	0.42100E+01	-0.70434E+00	0.16524E-02	329	0.42100E+01	-0.72080E+00	0.16828E-02
333	0.42100E+01	-0.73725E+00	0.17131E-02	337	0.42100E+01	-0.75371E+00	0.17435E-02
341	0.42100E+01	-0.77016E+00	0.17738E-02	345	0.42100E+01	-0.78662E+00	0.18042E-02
349	0.42100E+01	-0.80307E+00	0.18345E-02	353	0.42100E+01	-0.81953E+00	0.18649E-02
357	0.42100E+01	-0.83598E+00	0.18953E-02	361	0.42100E+01	-0.85244E+00	0.19256E-02
365	0.42100E+01	-0.86889E+00	0.19560E-02	369	0.42100E+01	-0.88535E+00	0.19863E-02
373	0.42100E+01	-0.90180E+00	0.20167E-02	377	0.42100E+01	-0.91826E+00	0.20470E-02
381	0.42100E+01	-0.93471E+00	0.20774E-02	385	0.42100E+01	-0.95117E+00	0.21077E-02
389	0.42100E+01	-0.96762E+00	0.21381E-02	393	0.42100E+01	-0.98408E+00	0.21684E-02
397	0.42100E+01	-0.10005E+01	0.21988E-02	401	0.42100E+01	-0.10170E+01	0.22292E-02
405	0.42100E+01	-0.10334E+01	0.22595E-02	409	0.42100E+01	-0.10499E+01	0.22899E-02
413	0.42100E+01	-0.10664E+01	0.23202E-02	417	0.42100E+01	-0.10828E+01	0.23506E-02
421	0.42100E+01	-0.10993E+01	0.23809E-02	425	0.42100E+01	-0.11157E+01	0.24113E-02
429	0.42100E+01	-0.11322E+01	0.24416E-02	433	0.42100E+01	-0.11486E+01	0.24720E-02
437	0.42100E+01	-0.11651E+01	0.25023E-02	441	0.42100E+01	-0.11815E+01	0.25327E-02
445	0.42100E+01	-0.11980E+01	0.25631E-02	449	0.42100E+01	-0.12144E+01	0.25934E-02
453	0.42100E+01	-0.12309E+01	0.26238E-02	457	0.42100E+01	-0.12474E+01	0.26541E-02
461	0.42100E+01	-0.12638E+01	0.26845E-02	465	0.42100E+01	-0.12803E+01	0.27148E-02
469	0.42100E+01	-0.12967E+01	0.27452E-02	473	0.42100E+01	-0.13132E+01	0.27755E-02
477	0.42100E+01	-0.13296E+01	0.28059E-02	481	0.42100E+01	-0.13461E+01	0.28362E-02
485	0.42100E+01	-0.13625E+01	0.28666E-02	489	0.42100E+01	-0.13790E+01	0.28970E-02
493	0.42100E+01	-0.13954E+01	0.29273E-02	497	0.42100E+01	-0.14119E+01	0.29577E-02
501	0.42100E+01	-0.14284E+01	0.29880E-02	505	0.42100E+01	-0.14448E+01	0.30184E-02
509	0.42100E+01	-0.14613E+01	0.30487E-02	513	0.42100E+01	-0.14777E+01	0.30791E-02
517	0.42100E+01	-0.14942E+01	0.31094E-02	521	0.42100E+01	-0.15106E+01	0.31398E-02
525	0.42100E+01	-0.15271E+01	0.31701E-02	529	0.42100E+01	-0.15435E+01	0.32005E-02
533	0.42100E+01	-0.15600E+01	0.32309E-02	537	0.42100E+01	-0.15765E+01	0.32612E-02
541	0.42100E+01	-0.15929E+01	0.32916E-02	545	0.42100E+01	-0.16094E+01	0.33219E-02
549	0.42100E+01	-0.16258E+01	0.33523E-02	553	0.42100E+01	-0.16423E+01	0.33826E-02
557	0.42100E+01	-0.16587E+01	0.34130E-02	561	0.42100E+01	-0.16752E+01	0.34433E-02
565	0.42100E+01	-0.16916E+01	0.34737E-02	569	0.42100E+01	-0.17081E+01	0.35040E-02
573	0.42100E+01	-0.17245E+01	0.35344E-02	577	0.42100E+01	-0.17410E+01	0.35647E-02
581	0.42100E+01	-0.17575E+01	0.35951E-02	585	0.42100E+01	-0.17739E+01	0.36255E-02
589	0.42100E+01	-0.17904E+01	0.36558E-02	593	0.42100E+01	-0.18068E+01	0.36862E-02
597	0.42100E+01	-0.18234E+01	0.37165E-02	601	0.42100E+01	-0.18397E+01	0.37469E-02

L 3 (L=1,2,3,FOR FL PL,CYL,2L STG FLOW)

X-FT	DPLT-THFT	MMT-THFT	DFL2U	DZL2U	UFREE	DUDXT	DUDYW	K	MFD	
NOTE** X=DIST FRM STG PT,** DPLT=DISPLACEMENT THK(FT),** MMT=MOMENTUM THK(FT) DFL2U=DISPL**2*DUDX/VISC(NON DIM),** DZL2U=MMT**2*DUDX/VISC(NON DIM),** UFREE=FREE ST VEL(FPS),** DUDXT=VEL GRD ALONG X(FT/S/FT),** DUDYW=NORMAL VEL GRDT(FT/S/FT)***,K=NO IF INTGTN STEPS										
0.1720E-02	0.3587E-03	0.1613E-03	0.3773E+00	0.7634E-01	0.4210E+01	0.4918E+03	0.9164E+04	21	301	17
(REX= 0.1940E+03),(VISC*DUDX/U*U= 0.4653E-02),(D1*U/VISC= 0.9005E+01),(D2*U/VISC= 0.4050E+01)										
0.9122E-02	0.3905E-04	0.1760E-03	0.4366E+00	0.8847E-01	0.4887E+01	0.4791E+03	0.1005E+05	11	317	18
(REX= 0.2658E+03),(VISC*DUDX/U*U= 0.3364E-02),(D1*U/VISC= 0.1139E+02),(D2*U/VISC= 0.5128E+01)										
0.1052E-01	0.4121E-03	0.1973E-03	0.4726E+00	0.9759E-01	0.5546E+01	0.4668E+03	0.1104E+05	6	328	19
(REX= 0.3478E+03),(VISC*DUDX/U*U= 0.2545E-02),(D1*U/VISC= 0.1363E+02),(D2*U/VISC= 0.6193E+01)										
0.1191E-01	0.4264E-03	0.1950E-03	0.4932E+00	0.1031E+00	0.6189E+01	0.4549E+03	0.1206E+05	4	334	20
(REX= 0.4396E+03),(VISC*DUDX/U*U= 0.1992E-02),(D1*U/VISC= 0.1574E+02),(D2*U/VISC= 0.7197E+01)										
0.1331E-01	0.4375E-03	0.2067E-03	0.5060E+00	0.1065E+00	0.6815E+01	0.4434E+03	0.1302E+05	3	338	21
(REX= 0.5407E+03),(VISC*DUDX/U*U= 0.1601E-02),(D1*U/VISC= 0.1778E+02),(D2*U/VISC= 0.8156E+01)										
0.1470E-01	0.4463E-03	0.2051E-03	0.5135E+00	0.1085E+00	0.7426E+01	0.4323E+03	0.1395E+05	2	341	22
(REX= 0.6509E+03),(VISC*DUDX/U*U= 0.1315E-02),(D1*U/VISC= 0.1976E+02),(D2*U/VISC= 0.9083E+01)										
0.1609E-01	0.4544E-03	0.2089E-03	0.5191E+00	0.1097E+00	0.8021E+01	0.4216E+03	0.1480E+05	2	343	23
(REX= 0.7658E+03),(VISC*DUDX/U*U= 0.1099E-02),(D1*U/VISC= 0.2173E+02),(D2*U/VISC= 0.9990E+01)										
0.1749E-01	0.4611E-03	0.2120E-03	0.5213E+00	0.1103E+00	0.8602E+01	0.4113E+03	0.1568E+05	2	345	24
(REX= 0.8970E+03),(VISC*DUDX/U*U= 0.9323E-03),(D1*U/VISC= 0.2365E+02),(D2*U/VISC= 0.1088E+02)										
0.1888E-01	0.4668E-03	0.2148E-03	0.5215E+00	0.1104E+00	0.9168E+01	0.4014E+03	0.1652E+05	2	347	25
(REX= 0.1032E+04),(VISC*DUDX/U*U= 0.8009E-03),(D1*U/VISC= 0.2552E+02),(D2*U/VISC= 0.1174E+02)										
0.2028E-01	0.4721E-03	0.2172E-03	0.5209E+00	0.1103E+00	0.9721E+01	0.3920E+03	0.1733E+05	2	349	26
(REX= 0.1175E+04),(VISC*DUDX/U*U= 0.6956E-03),(D1*U/VISC= 0.2737E+02),(D2*U/VISC= 0.1259E+02)										
0.2161E-01	0.4771E-03	0.2195E-03	0.5196E+00	0.1100E+00	0.1026E+02	0.3829E+03	0.1810E+05	2	351	27
(REX= 0.1326E+04),(VISC*DUDX/U*U= 0.6098E-03),(D1*U/VISC= 0.2919E+02),(D2*U/VISC= 0.1343E+02)										
0.2307E-01	0.4817E-03	0.2216E-03	0.5178E+00	0.1096E+00	0.1079E+02	0.3742E+03	0.1884E+05	2	353	28
(REX= 0.1484E+04),(VISC*DUDX/U*U= 0.5391E-03),(D1*U/VISC= 0.3099E+02),(D2*U/VISC= 0.1426E+02)										
0.2446E-01	0.4862E-03	0.2236E-03	0.5159E+00	0.1091E+00	0.1131E+02	0.3660E+03	0.1955E+05	2	355	29
(REX= 0.1649E+04),(VISC*DUDX/U*U= 0.4802E-03),(D1*U/VISC= 0.3278E+02),(D2*U/VISC= 0.1508E+02)										
0.2586E-01	0.4906E-03	0.2255E-03	0.5139E+00	0.1086E+00	0.1181E+02	0.3581E+03	0.2022E+05	2	357	30
(REX= 0.1821E+04),(VISC*DUDX/U*U= 0.4306E-03),(D1*U/VISC= 0.3455E+02),(D2*U/VISC= 0.1588E+02)										
********** NEXT LINE FOR TAP PG= 3										
0.2725E-01	0.4947E-03	0.2274E-03	0.5118E+00	0.1081E+00	0.1230E+02	0.3507E+03	0.2087E+05	2	359	31
(REX= 0.1999E+04),(VISC*DUDX/U*U= 0.3884E-03),(D1*U/VISC= 0.3630E+02),(D2*U/VISC= 0.1668E+02)										
0.2864E-01	0.5078E-03	0.2330E-03	0.5275E+00	0.1082E+00	0.1267E+02	0.3430E+03	0.1997E+05	2	361	32
(REX= 0.2167E+04),(VISC*DUDX/U*U= 0.3582E-03),(D1*U/VISC= 0.3837E+02),(D2*U/VISC= 0.1738E+02)										
0.3011E-01	0.5088E-03	0.2324E-03	0.5169E+00	0.1078E+00	0.1316E+02	0.3348E+03	0.2163E+05	2	363	33
(REX= 0.2362E+04),(VISC*DUDX/U*U= 0.3244E-03),(D1*U/VISC= 0.3991E+02),(D2*U/VISC= 0.1823E+02)										
0.3153E-01	0.5108E-03	0.2336E-03	0.5074E+00	0.1061E+00	0.1363E+02	0.3262E+03	0.2232E+05	2	365	34
(REX= 0.2562E+04),(VISC*DUDX/U*U= 0.2945E-03),(D1*U/VISC= 0.4151E+02),(D2*U/VISC= 0.1898E+02)										
0.3296E-01	0.5141E-03	0.2352E-03	0.4997E+00	0.1046E+00	0.1409E+02	0.3170E+03	0.2291E+05	2	367	35
(REX= 0.2769E+04),(VISC*DUDX/U*U= 0.2679E-03),(D1*U/VISC= 0.4319E+02),(D2*U/VISC= 0.1976E+02)										
0.3439E-01	0.5175E-03	0.2368E-03	0.4914E+00	0.1028E+00	0.1453E+02	0.3073E+03	0.2341E+05	2	369	36
(REX= 0.2980E+04),(VISC*DUDX/U*U= 0.2440E-03),(D1*U/VISC= 0.4488E+02),(D2*U/VISC= 0.2052E+02)										
0.3582E-01	0.5213E-03	0.2388E-03	0.4815E+00	0.1004E+00	0.1496E+02	0.2971E+03	0.2382E+05	2	371	37
(REX= 0.3196E+04),(VISC*DUDX/U*U= 0.2225E-03),(D1*U/VISC= 0.4652E+02),(D2*U/VISC= 0.2124E+02)										

L 3 (L=1,2,3,FOR FL PL,CYL,2D STG FLOW)

X-FT	DPLT-THFT	MMT-THFT	DEL2U	DZL2U	UFREE	DUDXT	DUDYW	K	MED	
NOTE** X=DIST FRM STG PT,** DPLT=DISPLACEMENT THK(FT),** MMT=MOMENTUM THK(FT) DEL2U=DISPL**2*DUDX/VISC(NON DIM),** DZL2U=MMT**2*DUDX/VISC(NON DIM),** UFREE=FREE ST VEL(FPS),** DUDXT=VEL GRD ALONG X(FT/SFT),** DUDYW=NORMAL VEL GRDT(FT/SFT)***,K=NO IF INTGTN STEPS										
0.3724E-01	0.5257E-03	0.2398E-03	0.4721E+00	0.9818E-01	0.1538E+02	0.2865E+03	0.2421E+05	2	373	38
(REX= 0.3416E+04),(VISC*DUDX/U*U= 0.2031E-03),(D1*U/VISC= 0.4822E+02),(D2*U/VISC= 0.2199E+02)										
0.3867E-01	0.5305E-03	0.2415E-03	0.4620E+00	0.9575E-01	0.1578E+02	0.2753E+03	0.2450E+05	2	375	39
(REX= 0.3639E+04),(VISC*DUDX/U*U= 0.1853E-03),(D1*U/VISC= 0.4992E+02),(D2*U/VISC= 0.2273E+02)										
0.4010E-01	0.5350E-03	0.2430E-03	0.4499E+00	0.9280E-01	0.1617E+02	0.2636E+03	0.2472E+05	2	377	40
(REX= 0.3866E+04),(VISC*DUDX/U*U= 0.1691E-03),(D1*U/VISC= 0.5158E+02),(D2*U/VISC= 0.2342E+02)										
0.4153E-01	0.5405E-03	0.2449E-03	0.4380E+00	0.8993E-01	0.1653E+02	0.2514E+03	0.2490E+05	2	379	41
(REX= 0.4054E+04),(VISC*DUDX/U*U= 0.1542E-03),(D1*U/VISC= 0.5329E+02),(D2*U/VISC= 0.2415E+02)										
0.4296E-01	0.5463E-03	0.2469E-03	0.4249E+00	0.8680E-01	0.1688E+02	0.2387E+03	0.2499E+05	2	381	42
(REX= 0.4325E+04),(VISC*DUDX/U*U= 0.1404E-03),(D1*U/VISC= 0.5501E+02),(D2*U/VISC= 0.2486E+02)										
0.4438E-01	0.5520E-03	0.2487E-03	0.4098E+00	0.8317E-01	0.1722E+02	0.2255E+03	0.2501E+05	2	383	43
(REX= 0.4556E+04),(VISC*DUDX/U*U= 0.1276E-03),(D1*U/VISC= 0.5667E+02),(D2*U/VISC= 0.2553E+02)										
0.4581E-01	0.5587E-03	0.2505E-03	0.3943E+00	0.7952E-01	0.1753E+02	0.2119E+03	0.2498E+05	2	385	44
(REX= 0.4788E+04),(VISC*DUDX/U*U= 0.1156E-03),(D1*U/VISC= 0.5839E+02),(D2*U/VISC= 0.2622E+02)										
0.4724E-01	0.5658E-03	0.2532E-03	0.3773E+00	0.7555E-01	0.1782E+02	0.1977E+03	0.2486E+05	2	387	45
(REX= 0.5020E+04),(VISC*DUDX/U*U= 0.1044E-03),(D1*U/VISC= 0.6012E+02),(D2*U/VISC= 0.2690E+02)										
********** NEXT LINE FOR TAP NO= 4										
0.4867E-01	0.5728E-03	0.2552E-03	0.3580E+00	0.7107E-01	0.1809E+02	0.1830E+03	0.2465E+05	2	389	46
(REX= 0.5250E+04),(VISC*DUDX/U*U= 0.9374E-04),(D1*U/VISC= 0.6180E+02),(D2*U/VISC= 0.2754E+02)										
0.5007E-01	0.5768E-03	0.2577E-03	0.3344E+00	0.6674E-01	0.1840E+02	0.1686E+03	0.2534E+05	2	391	47
(REX= 0.5493E+04),(VISC*DUDX/U*U= 0.8351E-04),(D1*U/VISC= 0.6328E+02),(D2*U/VISC= 0.2827E+02)										
0.5148E-01	0.5863E-03	0.2598E-03	0.3172E+00	0.6229E-01	0.1863E+02	0.1548E+03	0.2433E+05	2	393	48
(REX= 0.5717E+04),(VISC*DUDX/U*U= 0.7482E-04),(D1*U/VISC= 0.6511E+02),(D2*U/VISC= 0.2885E+02)										
0.5288E-01	0.5955E-03	0.2623E-03	0.2994E+00	0.5811E-01	0.1883E+02	0.1416E+03	0.2388E+05	2	395	49
(REX= 0.5939E+04),(VISC*DUDX/U*U= 0.6694E-04),(D1*U/VISC= 0.6688E+02),(D2*U/VISC= 0.2946E+02)										
0.5429E-01	0.6050E-03	0.2656E-03	0.2816E+00	0.5405E-01	0.1902E+02	0.1290E+03	0.2345E+05	2	397	50
(REX= 0.6159E+04),(VISC*DUDX/U*U= 0.5979E-04),(D1*U/VISC= 0.6863E+02),(D2*U/VISC= 0.3007E+02)										
0.5569E-01	0.6147E-03	0.2678E-03	0.2638E+00	0.5009E-01	0.1920E+02	0.1171E+03	0.2300E+05	2	399	51
(REX= 0.6375E+04),(VISC*DUDX/U*U= 0.5328E-04),(D1*U/VISC= 0.7036E+02),(D2*U/VISC= 0.3066E+02)										
0.5710E-01	0.6246E-03	0.2707E-03	0.2460E+00	0.4621E-01	0.1935E+02	0.1057E+03	0.2254E+05	2	401	52
(REX= 0.6590E+04),(VISC*DUDX/U*U= 0.4735E-04),(D1*U/VISC= 0.7208E+02),(D2*U/VISC= 0.3124E+02)										
0.5851E-01	0.6346E-03	0.2737E-03	0.2283E+00	0.4244E-01	0.1949E+02	0.9502E+02	0.2207E+05	2	403	53
(REX= 0.6801E+04),(VISC*DUDX/U*U= 0.4193E-04),(D1*U/VISC= 0.7379E+02),(D2*U/VISC= 0.3181E+02)										
0.5991E-01	0.6452E-03	0.2767E-03	0.2108E+00	0.3876E-01	0.1962E+02	0.8491E+02	0.2159E+05	2	405	54
(REX= 0.7010E+04),(VISC*DUDX/U*U= 0.3699E-04),(D1*U/VISC= 0.7549E+02),(D2*U/VISC= 0.3237E+02)										
0.6132E-01	0.6556E-03	0.2797E-03	0.1934E+00	0.3519E-01	0.1973E+02	0.7541E+02	0.2109E+05	2	407	55
(REX= 0.7215E+04),(VISC*DUDX/U*U= 0.3247E-04),(D1*U/VISC= 0.7718E+02),(D2*U/VISC= 0.3292E+02)										
0.6272E-01	0.6667E-03	0.2828E-03	0.1763E+00	0.3173E-01	0.1983E+02	0.6652E+02	0.2060E+05	2	409	56
(REX= 0.7418E+04),(VISC*DUDX/U*U= 0.2836E-04),(D1*U/VISC= 0.7884E+02),(D2*U/VISC= 0.3345E+02)										
0.6413E-01	0.6777E-03	0.2860E-03	0.1595E+00	0.2840E-01	0.1992E+02	0.5825E+02	0.2009E+05	2	411	57
(REX= 0.7618E+04),(VISC*DUDX/U*U= 0.2462E-04),(D1*U/VISC= 0.8050E+02),(D2*U/VISC= 0.3397E+02)										
0.6555E-01	0.6888E-03	0.2891E-03	0.1431E+00	0.2521E-01	0.2000E+02	0.5059E+02	0.1962E+05	2	413	58
(REX= 0.7814E+04),(VISC*DUDX/U*U= 0.2122E-04),(D1*U/VISC= 0.8214E+02),(D2*U/VISC= 0.3447E+02)										

L 3 (L=1,2,3,FOR FL PL,CYL,2D STG FLOW)

X-FT	DPLT-THFT	MMT-THFT	DEL2U	DZL2U	UFREE	DUDXT	DUDYW	K	MED	
NOTE** X=DIST FRM STG PT,** DPLT=DISPLACEMENT THK(FT),** MMT=MOMENTUM THK(FT) DEL2U=DISPL**2*DUDX/VISC(NON DIM),** DZL2U=MMT**2*DUDX/VISC(NON DIM),** UFREE=FREE ST VEL(FPS),** DUDXT=VEL GRD ALONG X(FT/S/FT),** DUDYW=NORMAL VEL GRD(FT/S/FT)***,K=NO IF INTGTN STEPS										
0.6694E-01	0.7002E-03	0.2923E-03	0.1273E+00	0.2218E-01	0.2006E+02	0.4354E+02	0.1913E+05	2	415	59
(REX= 0.8008E+04),(VISC*DUDX/U*U= 0.1814E-04),(D1*U/VISC= 0.8376E+02),(D2*U/VISC= 0.3497E+02)										
0.6834E-01	0.7116E-03	0.2955E-03	0.1120E+00	0.1932E-01	0.2012E+02	0.3711E+02	0.1864E+05	2	417	60
(REX= 0.8200E+04),(VISC*DUDX/U*U= 0.1537E-04),(D1*U/VISC= 0.8537E+02),(D2*U/VISC= 0.3545E+02)										
********** NEXT LINE FOR TAP NO= 5										
0.6975E-01	0.7232E-03	0.2987E-03	0.9758E-01	0.1665E-01	0.2017E+02	0.3129E+02	0.1815E+05	2	419	61
(REX= 0.8388E+04),(VISC*DUDX/U*U= 0.1290E-04),(D1*U/VISC= 0.8697E+02),(D2*U/VISC= 0.3592E+02)										
0.7113E-01	0.7392E-03	0.3015E-03	0.8464E-01	0.1408E-01	0.2016E+02	0.2598E+02	0.1679E+05	2	421	62
(REX= 0.8553E+04),(VISC*DUDX/U*U= 0.1072E-04),(D1*U/VISC= 0.8888E+02),(D2*U/VISC= 0.3625E+02)										
0.7252E-01	0.7502E-03	0.3055E-03	0.7018E-01	0.1163E-01	0.2020E+02	0.2091E+02	0.1695E+05	2	423	63
(REX= 0.8733E+04),(VISC*DUDX/U*U= 0.8597E-05),(D1*U/VISC= 0.9035E+02),(D2*U/VISC= 0.3679E+02)										
0.7390E-01	0.7614E-03	0.3096E-03	0.5566E-01	0.9156E-02	0.2022E+02	0.1608E+02	0.1659E+05	2	425	64
(REX= 0.8911E+04),(VISC*DUDX/U*U= 0.6595E-05),(D1*U/VISC= 0.9187E+02),(D2*U/VISC= 0.3726E+02)										
0.7528E-01	0.7736E-03	0.3125E-03	0.4102E-01	0.6690E-02	0.2024E+02	0.1149E+02	0.1617E+05	2	427	65
(REX= 0.9086E+04),(VISC*DUDX/U*U= 0.4703E-05),(D1*U/VISC= 0.9339E+02),(D2*U/VISC= 0.3771E+02)										
0.7667E-01	0.7858E-03	0.3159E-03	0.2629E-01	0.4248E-02	0.2025E+02	0.7139E+01	0.1576E+05	2	429	66
(REX= 0.9259E+04),(VISC*DUDX/U*U= 0.2919E-05),(D1*U/VISC= 0.9490E+02),(D2*U/VISC= 0.3815E+02)										
0.7805E-01	0.7980E-03	0.3192E-03	0.1150E-01	0.1840E-02	0.2026E+02	0.3028E+01	0.1534E+05	2	431	67
(REX= 0.9430E+04),(VISC*DUDX/U*U= 0.1237E-05),(D1*U/VISC= 0.9641E+02),(D2*U/VISC= 0.3857E+02)										
0.7943E-01	0.8103E-03	0.3226E-03	-0.3308E-02	-0.5244E-03	0.2026E+02	-0.8450E+00	0.1493E+05	2	433	68
(REX= 0.9597E+04),(VISC*DUDX/U*U= -0.3452E-06),(D1*U/VISC= 0.9790E+02),(D2*U/VISC= 0.3898E+02)										
0.8082E-01	0.8227E-03	0.3259E-03	-0.1807E-01	-0.2837E-02	0.2026E+02	-0.4478E+01	0.1451E+05	2	435	69
(REX= 0.9763E+04),(VISC*DUDX/U*U= -0.1830E-05),(D1*U/VISC= 0.9938E+02),(D2*U/VISC= 0.3937E+02)										
0.8220E-01	0.8352E-03	0.3292E-03	-0.3275E-01	-0.5089E-02	0.2025E+02	-0.7873E+01	0.1412E+05	2	437	70
(REX= 0.9926E+04),(VISC*DUDX/U*U= -0.3220E-05),(D1*U/VISC= 0.1009E+03),(D2*U/VISC= 0.3976E+02)										
0.8358E-01	0.8478E-03	0.3325E-03	-0.4727E-01	-0.7271E-02	0.2024E+02	-0.1103E+02	0.1372E+05	2	439	71
(REX= 0.1009E+05),(VISC*DUDX/U*U= -0.4516E-05),(D1*U/VISC= 0.1023E+03),(D2*U/VISC= 0.4013E+02)										
0.8497E-01	0.8605E-03	0.3358E-03	-0.6157E-01	-0.9376E-02	0.2022E+02	-0.1394E+02	0.1333E+05	2	441	72
(REX= 0.1024E+05),(VISC*DUDX/U*U= -0.5719E-05),(D1*U/VISC= 0.1038E+03),(D2*U/VISC= 0.4049E+02)										
0.8635E-01	0.8733E-03	0.3391E-03	-0.7558E-01	-0.1139E-01	0.2020E+02	-0.1662E+02	0.1295E+05	2	443	73
(REX= 0.1040E+05),(VISC*DUDX/U*U= -0.6831E-05),(D1*U/VISC= 0.1052E+03),(D2*U/VISC= 0.4084E+02)										
0.8773E-01	0.8862E-03	0.3423E-03	-0.8923E-01	-0.1332E-01	0.2017E+02	-0.1906E+02	0.1258E+05	2	445	74
(REX= 0.1055E+05),(VISC*DUDX/U*U= -0.7852E-05),(D1*U/VISC= 0.1066E+03),(D2*U/VISC= 0.4118E+02)										
0.8912E-01	0.8991E-03	0.3455E-03	-0.1024E+00	-0.1513E-01	0.2015E+02	-0.2125E+02	0.1222E+05	2	447	75
(REX= 0.1071E+05),(VISC*DUDX/U*U= -0.8782E-05),(D1*U/VISC= 0.1080E+03),(D2*U/VISC= 0.4151E+02)										
********** NEXT LINE FOR TAP NO= 6										
0.9050E-01	0.9120E-03	0.3487E-03	-0.1151E+00	-0.1684E-01	0.2012E+02	-0.2321E+02	0.1187E+05	2	449	76
(REX= 0.1086E+05),(VISC*DUDX/U*U= -0.9621E-05),(D1*U/VISC= 0.1094E+03),(D2*U/VISC= 0.4183E+02)										
0.9222E-01	0.9255E-03	0.3525E-03	-0.1295E+00	-0.1879E-01	0.2008E+02	-0.2535E+02	0.1172E+05	2	451	77
(REX= 0.1104E+05),(VISC*DUDX/U*U= -0.1054E-04),(D1*U/VISC= 0.1108E+03),(D2*U/VISC= 0.4222E+02)										
0.9393E-01	0.9405E-03	0.3558E-03	-0.1435E+00	-0.2053E-01	0.2004E+02	-0.2720E+02	0.1121E+05	2	453	78
(REX= 0.1122E+05),(VISC*DUDX/U*U= -0.1136E-04),(D1*U/VISC= 0.1124E+03),(D2*U/VISC= 0.4251E+02)										
0.9565E-01	0.9555E-03	0.3592E-03	-0.1565E+00	-0.2212E-01	0.1999E+02	-0.2876E+02	0.1084E+05	2	455	79
(REX= 0.1140E+05),(VISC*DUDX/U*U= -0.1207E-04),(D1*U/VISC= 0.1139E+03),(D2*U/VISC= 0.4281E+02)										

L 3 (L=1,2,3,FOR FL PL,CYL,2D STG FLOW)

X-FT	DPLT-THFT	MMT-THFT	DEL2U	DZL2U	UFREE	DUDXT	DUDYW	K	MED	
NOTE** X=DIST FRM STG PT,** DPLT=DISPLACEMENT THK(FT),** MMT=MOMENTUM THK(FT) DEL2U=DISPL**2*DUDX/VISC(NON DIM),** DZL2U=MMT**2*DUDX/VISC(NON DIM),** UFREE=FREE ST VEL(FPS),** DUDXT=VEL GRD ALONG X(FT/S/FT),** DUDYW=NORMAL VEL GRDT(FT/S/FT)***,K=NO IF INTGTN STEPS										
0.9737E-01	0.9702E-03	0.3626E-03	-0.1686E+00	-0.2353E-01	0.1594E+02	-0.3002E+02	0.1049E+05	2	457	80
(REX= 0.1158E+05),(VISC*DUDX/U*U= -0.1266E-04),(D1*U/VISC= 0.1154E+03),(D2*U/VISC= 0.4311E+02)										
0.9908E-01	0.9851E-03	0.3659E-03	-0.1794E+00	-0.2475E-01	0.1589E+02	-0.3100E+02	0.1016E+05	2	459	81
(REX= 0.1175E+05),(VISC*DUDX/U*U= -0.1315E-04),(D1*U/VISC= 0.1168E+03),(D2*U/VISC= 0.4339E+02)										
0.1008E+00	0.9998E-03	0.3693E-03	-0.1889E+00	-0.2577E-01	0.1583E+02	-0.3169E+02	0.9851E+04	2	461	82
(REX= 0.1192E+05),(VISC*DUDX/U*U= -0.1351E-04),(D1*U/VISC= 0.1182E+03),(D2*U/VISC= 0.4367E+02)										
0.1025E+00	0.1014E-02	0.3727E-03	-0.1969E+00	-0.2658E-01	0.1578E+02	-0.3209E+02	0.9566E+04	2	463	83
(REX= 0.1209E+05),(VISC*DUDX/U*U= -0.1376E-04),(D1*U/VISC= 0.1196E+03),(D2*U/VISC= 0.4395E+02)										
0.1042E+00	0.1029E-02	0.3761E-03	-0.2032E+00	-0.2716E-01	0.1572E+02	-0.3220E+02	0.9305E+04	2	465	84
(REX= 0.1226E+05),(VISC*DUDX/U*U= -0.1388E-04),(D1*U/VISC= 0.1210E+03),(D2*U/VISC= 0.4423E+02)										
0.1059E+00	0.1043E-02	0.3794E-03	-0.2076E+00	-0.2749E-01	0.1567E+02	-0.3202E+02	0.9066E+04	2	467	85
(REX= 0.1243E+05),(VISC*DUDX/U*U= -0.1388E-04),(D1*U/VISC= 0.1223E+03),(D2*U/VISC= 0.4450E+02)										
0.1077E+00	0.1057E-02	0.3828E-03	-0.2101E+00	-0.2758E-01	0.1561E+02	-0.3155E+02	0.8851E+04	2	469	86
(REX= 0.1259E+05),(VISC*DUDX/U*U= -0.1376E-04),(D1*U/VISC= 0.1236E+03),(D2*U/VISC= 0.4477E+02)										
0.1094E+00	0.1070E-02	0.3862E-03	-0.2103E+00	-0.2739E-01	0.1556E+02	-0.3080E+02	0.8660E+04	2	471	87
(REX= 0.1276E+05),(VISC*DUDX/U*U= -0.1350E-04),(D1*U/VISC= 0.1248E+03),(D2*U/VISC= 0.4505E+02)										
0.1111E+00	0.1083E-02	0.3897E-03	-0.2081E+00	-0.2693E-01	0.1551E+02	-0.2975E+02	0.8497E+04	2	473	88
(REX= 0.1292E+05),(VISC*DUDX/U*U= -0.1311E-04),(D1*U/VISC= 0.1260E+03),(D2*U/VISC= 0.4533E+02)										
0.1128E+00	0.1096E-02	0.3931E-03	-0.2035E+00	-0.2618E-01	0.1546E+02	-0.2841E+02	0.8358E+04	2	475	89
(REX= 0.1309E+05),(VISC*DUDX/U*U= -0.1258E-04),(D1*U/VISC= 0.1272E+03),(D2*U/VISC= 0.4561E+02)										
0.1145E+00	0.1108E-02	0.3966E-03	-0.1961E+00	-0.2512E-01	0.1541E+02	-0.2678E+02	0.8246E+04	2	477	90
(REX= 0.1326E+05),(VISC*DUDX/U*U= -0.1192E-04),(D1*U/VISC= 0.1283E+03),(D2*U/VISC= 0.4590E+02)										
********** NEXT LINE FOR IAP NO= 7										
0.1162E+00	0.1120E-02	0.4001E-03	-0.1859E+00	-0.2374E-01	0.1537E+02	-0.2486E+02	0.8163E+04	2	479	91
(REX= 0.1342E+05),(VISC*DUDX/U*U= -0.1112E-04),(D1*U/VISC= 0.1293E+03),(D2*U/VISC= 0.4621E+02)										
0.1193E+00	0.1143E-02	0.4068E-03	-0.1660E+00	-0.2102E-01	0.1529E+02	-0.2130E+02	0.7889E+04	2	481	92
(REX= 0.1373E+05),(VISC*DUDX/U*U= -0.9603E-05),(D1*U/VISC= 0.1315E+03),(D2*U/VISC= 0.4679E+02)										
0.1224E+00	0.1163E-02	0.4138E-03	-0.1457E+00	-0.1844E-01	0.1523E+02	-0.1805E+02	0.7873E+04	2	483	93
(REX= 0.1404E+05),(VISC*DUDX/U*U= -0.8190E-05),(D1*U/VISC= 0.1334E+03),(D2*U/VISC= 0.4744E+02)										
0.1255E+00	0.1182E-02	0.4204E-03	-0.1259E+00	-0.1593E-01	0.1518E+02	-0.1512E+02	0.7830E+04	2	485	94
(REX= 0.1435E+05),(VISC*DUDX/U*U= -0.6895E-05),(D1*U/VISC= 0.1351E+03),(D2*U/VISC= 0.4807E+02)										
0.1286E+00	0.1199E-02	0.4267E-03	-0.1071E+00	-0.1357E-01	0.1513E+02	-0.1250E+02	0.7804E+04	2	487	95
(REX= 0.1468E+05),(VISC*DUDX/U*U= -0.5724E-05),(D1*U/VISC= 0.1368E+03),(D2*U/VISC= 0.4868E+02)										
0.1317E+00	0.1215E-02	0.4327E-03	-0.8962E-01	-0.1137E-01	0.1510E+02	-0.1018E+02	0.7786E+04	2	489	96
(REX= 0.1500E+05),(VISC*DUDX/U*U= -0.4682E-05),(D1*U/VISC= 0.1383E+03),(D2*U/VISC= 0.4928E+02)										
0.1348E+00	0.1230E-02	0.4384E-03	-0.7380E-01	-0.9381E-02	0.1507E+02	-0.8185E+01	0.7776E+04	2	491	97
(REX= 0.1533E+05),(VISC*DUDX/U*U= -0.3774E-05),(D1*U/VISC= 0.1398E+03),(D2*U/VISC= 0.4985E+02)										
0.1379E+00	0.1244E-02	0.4438E-03	-0.5994E-01	-0.7634E-02	0.1505E+02	-0.6499E+01	0.7765E+04	2	493	98
(REX= 0.1566E+05),(VISC*DUDX/U*U= -0.3004E-05),(D1*U/VISC= 0.1413E+03),(D2*U/VISC= 0.5041E+02)										
0.1410E+00	0.1257E-02	0.4488E-03	-0.4828E-01	-0.6160E-02	0.1503E+02	-0.5126E+01	0.7752E+04	2	495	99
(REX= 0.1600E+05),(VISC*DUDX/U*U= -0.2374E-05),(D1*U/VISC= 0.1426E+03),(D2*U/VISC= 0.5094E+02)										
0.1441E+00	0.1269E-02	0.4538E-03	-0.3906E-01	-0.4991E-02	0.1502E+02	-0.4065E+01	0.7732E+04	2	497	100
(REX= 0.1634E+05),(VISC*DUDX/U*U= -0.1885E-05),(D1*U/VISC= 0.1439E+03),(D2*U/VISC= 0.5145E+02)										

L 3 (L=1,2,3,FOR FL PL,CYL,2D STG FLOW)

X-FT	DPLT-THFT	MMT-THFT	DEL2D	DZL2D	UFREE	DUDXT	DUDYW	K	MED	
NOTE** X=DIST FRM STG PT,** DPLT=DISPLACEMENT THK(FT),** MMT=MOMENTUM THK(FT) DEL2D=DISPL**2*DUDX/VISC(NON DIM),** DZL2D=MMT**2*DUDX/VISC(NON DIM),** UFREE=FREE ST VEL(FPS),** DUDXT=VEL GRD ALONG X(FT/S/FT),** DUDYW=NORMAL VEL GRDT(FT/S/FT)***,K=NO IF INTGTN STEPS										
0.1472E+00	0.1282E-02	0.4583E-03	-0.3248E-01	-0.4154E-02	0.1900E+02	-0.3316E+01	0.7704E+04	2	499	101
(REX=	0.1668E+05),(VISC*DUDX/U*U=	-0.1540E-05),(D1*U/VISC=	0.1452E+03),(D2*U/VISC=	0.5194E+02)						
0.1504E+00	0.1293E-02	0.4626E-03	-0.2873E-01	-0.3676E-02	0.1899E+02	-0.2880E+01	0.7665E+04	2	501	102
(REX=	0.1702E+05),(VISC*DUDX/U*U=	-0.1339E-05),(D1*U/VISC=	0.1465E+03),(D2*U/VISC=	0.5240E+02)						
0.1534E+00	0.1305E-02	0.4667E-03	-0.2799E-01	-0.3581E-02	0.1899E+02	-0.2757E+01	0.7612E+04	2	503	103
(REX=	0.1736E+05),(VISC*DUDX/U*U=	-0.1283E-05),(D1*U/VISC=	0.1477E+03),(D2*U/VISC=	0.5284E+02)						
0.1565E+00	0.1316E-02	0.4705E-03	-0.3045E-01	-0.3889E-02	0.1898E+02	-0.2946E+01	0.7543E+04	2	505	104
(REX=	0.1771E+05),(VISC*DUDX/U*U=	-0.1372E-05),(D1*U/VISC=	0.1490E+03),(D2*U/VISC=	0.5324E+02)						
0.1596E+00	0.1328E-02	0.4741E-03	-0.3627E-01	-0.4621E-02	0.1897E+02	-0.3448E+01	0.7456E+04	2	507	105
(REX=	0.1805E+05),(VISC*DUDX/U*U=	-0.1607E-05),(D1*U/VISC=	0.1502E+03),(D2*U/VISC=	0.5362E+02)						
********** NEXT LINE FOR TAP NO= 8										
0.1627E+00	0.1340E-02	0.4774E-03	-0.4564E-01	-0.5794E-02	0.1896E+02	-0.4262E+01	0.7349E+04	2	509	106
(REX=	0.1839E+05),(VISC*DUDX/U*U=	-0.1989E-05),(D1*U/VISC=	0.1515E+03),(D2*U/VISC=	0.5397E+02)						
0.1675E+00	0.1356E-02	0.4825E-03	-0.6270E-01	-0.7933E-02	0.1894E+02	-0.5715E+01	0.7282E+04	2	511	107
(REX=	0.1892E+05),(VISC*DUDX/U*U=	-0.2671E-05),(D1*U/VISC=	0.1532E+03),(D2*U/VISC=	0.5450E+02)						
0.1723E+00	0.1376E-02	0.4862E-03	-0.7959E-01	-0.9940E-02	0.1891E+02	-0.7051E+01	0.6993E+04	2	513	108
(REX=	0.1943E+05),(VISC*DUDX/U*U=	-0.3307E-05),(D1*U/VISC=	0.1551E+03),(D2*U/VISC=	0.5483E+02)						
0.1771E+00	0.1394E-02	0.4856E-03	-0.9586E-01	-0.1182E-01	0.1887E+02	-0.8271E+01	0.6774E+04	2	515	109
(REX=	0.1993E+05),(VISC*DUDX/U*U=	-0.3894E-05),(D1*U/VISC=	0.1569E+03),(D2*U/VISC=	0.5510E+02)						
0.1819E+00	0.1414E-02	0.4930E-03	-0.1117E+00	-0.1350E-01	0.1883E+02	-0.9375E+01	0.6549E+04	2	517	110
(REX=	0.2043E+05),(VISC*DUDX/U*U=	-0.4433E-05),(D1*U/VISC=	0.1587E+03),(D2*U/VISC=	0.5536E+02)						
0.1867E+00	0.1433E-02	0.4962E-03	-0.1269E+00	-0.1521E-01	0.1878E+02	-0.1036E+02	0.6329E+04	2	519	111
(REX=	0.2092E+05),(VISC*DUDX/U*U=	-0.4925E-05),(D1*U/VISC=	0.1605E+03),(D2*U/VISC=	0.5557E+02)						
0.1916E+00	0.1452E-02	0.4990E-03	-0.1411E+00	-0.1668E-01	0.1873E+02	-0.1123E+02	0.6124E+04	2	521	112
(REX=	0.2140E+05),(VISC*DUDX/U*U=	-0.5369E-05),(D1*U/VISC=	0.1621E+03),(D2*U/VISC=	0.5574E+02)						
0.1964E+00	0.1471E-02	0.5020E-03	-0.1547E+00	-0.1801E-01	0.1868E+02	-0.1199E+02	0.5918E+04	2	523	113
(REX=	0.2187E+05),(VISC*DUDX/U*U=	-0.5763E-05),(D1*U/VISC=	0.1638E+03),(D2*U/VISC=	0.5591E+02)						
0.2012E+00	0.1491E-02	0.5048E-03	-0.1672E+00	-0.1918E-01	0.1862E+02	-0.1262E+02	0.5721E+04	2	525	114
(REX=	0.2233E+05),(VISC*DUDX/U*U=	-0.6109E-05),(D1*U/VISC=	0.1655E+03),(D2*U/VISC=	0.5604E+02)						
0.2060E+00	0.1509E-02	0.5074E-03	-0.1784E+00	-0.2018E-01	0.1855E+02	-0.1315E+02	0.5542E+04	2	527	115
(REX=	0.2279E+05),(VISC*DUDX/U*U=	-0.6404E-05),(D1*U/VISC=	0.1669E+03),(D2*U/VISC=	0.5614E+02)						
0.2108E+00	0.1528E-02	0.5101E-03	-0.1895E+00	-0.2102E-01	0.1849E+02	-0.1355E+02	0.5364E+04	2	529	116
(REX=	0.2324E+05),(VISC*DUDX/U*U=	-0.6647E-05),(D1*U/VISC=	0.1684E+03),(D2*U/VISC=	0.5624E+02)						
0.2156E+00	0.1546E-02	0.5128E-03	-0.1973E+00	-0.2170E-01	0.1842E+02	-0.1384E+02	0.5200E+04	2	531	117
(REX=	0.2369E+05),(VISC*DUDX/U*U=	-0.6818E-05),(D1*U/VISC=	0.1699E+03),(D2*U/VISC=	0.5633E+02)						
0.2205E+00	0.1563E-02	0.5153E-03	-0.2042E+00	-0.2218E-01	0.1836E+02	-0.1401E+02	0.5058E+04	2	533	118
(REX=	0.2413E+05),(VISC*DUDX/U*U=	-0.6973E-05),(D1*U/VISC=	0.1711E+03),(D2*U/VISC=	0.5640E+02)						
0.2253E+00	0.1581E-02	0.5179E-03	-0.2096E+00	-0.2250E-01	0.1829E+02	-0.1407E+02	0.4918E+04	2	535	119
(REX=	0.2457E+05),(VISC*DUDX/U*U=	-0.7053E-05),(D1*U/VISC=	0.1724E+03),(D2*U/VISC=	0.5648E+02)						
0.2301E+00	0.1598E-02	0.5206E-03	-0.2133E+00	-0.2263E-01	0.1822E+02	-0.1401E+02	0.4793E+04	2	537	120
(REX=	0.2500E+05),(VISC*DUDX/U*U=	-0.7075E-05),(D1*U/VISC=	0.1736E+03),(D2*U/VISC=	0.5656E+02)						
********** NEXT LINE FOR TAP NO= 9										
0.2349E+00	0.1613E-02	0.5231E-03	-0.2147E+00	-0.2257E-01	0.1815E+02	-0.1383E+02	0.4692E+04	2	539	121
(REX=	0.2543E+05),(VISC*DUDX/U*U=	-0.7037E-05),(D1*U/VISC=	0.1747E+03),(D2*U/VISC=	0.5663E+02)						

L 3 (L=1,2,3,FOR FL PL,CYL,2D STG FLOW)

X-FT	DPLT-THFT	MMT-THFT	DEL2U	DZL2U	UFREE	DUDXT	DUDYW	K	MED	
NOTE** X=DIST FRM STG PT,** DPLT=DISPLACEMENT THK(FT),** MMT=MOMENTUM THK(FT) DEL2U=DISPL**2*DUDX/VISC(NON DIM),** DZL2U=MMT**2*(DUDX/VISC(NON DIM),** UFREE=FREE ST VEL(FPS),** DUDXT=VEL GRD ALONG X(FT/SEC/FT),** DUDYW=NORMAL VEL GRD(FT/SEC/FT)***,K=NO IF INTGTN STEPS										
0.2464E+00	0.1631E-02	0.5258E-03	-0.2148E+00	-0.2232E-01	0.1809E+02	-0.1354E+02	0.4558E+04	2	541	122
(REX= 0.2591E+05),(VISC*DUDX/U*U= -0.6950E-05),(D1*U/VISC= 0.1758E+03),(D2*U/VISC= 0.5667E+02)										
0.2459E+00	0.1647E-02	0.5288E-03	-0.2136E+00	-0.2204E-01	0.1800E+02	-0.1321E+02	0.4491E+04	2	543	123
(REX= 0.2640E+05),(VISC*DUDX/U*U= -0.6837E-05),(D1*U/VISC= 0.1768E+03),(D2*U/VISC= 0.5677E+02)										
0.2514E+00	0.1661E-02	0.5318E-03	-0.2114E+00	-0.2166E-01	0.1793E+02	-0.1285E+02	0.4418E+04	2	545	124
(REX= 0.2688E+05),(VISC*DUDX/U*U= -0.6700E-05),(D1*U/VISC= 0.1777E+03),(D2*U/VISC= 0.5686E+02)										
0.2569E+00	0.1676E-02	0.5347E-03	-0.2082E+00	-0.2121E-01	0.1786E+02	-0.1244E+02	0.4355E+04	2	547	125
(REX= 0.2736E+05),(VISC*DUDX/U*U= -0.6538E-05),(D1*U/VISC= 0.1785E+03),(D2*U/VISC= 0.5696E+02)										
0.2624E+00	0.1689E-02	0.5377E-03	-0.2046E+00	-0.2067E-01	0.1779E+02	-0.1199E+02	0.4303E+04	2	549	126
(REX= 0.2784E+05),(VISC*DUDX/U*U= -0.6351E-05),(D1*U/VISC= 0.1792E+03),(D2*U/VISC= 0.5706E+02)										
0.2679E+00	0.1701E-02	0.5407E-03	-0.1986E+00	-0.2006E-01	0.1773E+02	-0.1150E+02	0.4260E+04	2	551	127
(REX= 0.2832E+05),(VISC*DUDX/U*U= -0.6137E-05),(D1*U/VISC= 0.1799E+03),(D2*U/VISC= 0.5717E+02)										
0.2734E+00	0.1713E-02	0.5438E-03	-0.1921E+00	-0.1936E-01	0.1767E+02	-0.1098E+02	0.4228E+04	2	553	128
(REX= 0.2881E+05),(VISC*DUDX/U*U= -0.5898E-05),(D1*U/VISC= 0.1805E+03),(D2*U/VISC= 0.5729E+02)										
0.2789E+00	0.1724E-02	0.5468E-03	-0.1845E+00	-0.1857E-01	0.1761E+02	-0.1041E+02	0.4205E+04	2	555	129
(REX= 0.2929E+05),(VISC*DUDX/U*U= -0.5631E-05),(D1*U/VISC= 0.1810E+03),(D2*U/VISC= 0.5742E+02)										
0.2844E+00	0.1734E-02	0.5500E-03	-0.1758E+00	-0.1769E-01	0.1755E+02	-0.9806E+01	0.4191E+04	2	557	130
(REX= 0.2977E+05),(VISC*DUDX/U*U= -0.5337E-05),(D1*U/VISC= 0.1815E+03),(D2*U/VISC= 0.5757E+02)										
0.2899E+00	0.1743E-02	0.5531E-03	-0.1659E+00	-0.1671E-01	0.1750E+02	-0.9161E+01	0.4186E+04	2	559	131
(REX= 0.3026E+05),(VISC*DUDX/U*U= -0.5016E-05),(D1*U/VISC= 0.1819E+03),(D2*U/VISC= 0.5773E+02)										
0.2954E+00	0.1751E-02	0.5564E-03	-0.1550E+00	-0.1565E-01	0.1745E+02	-0.8476E+01	0.4191E+04	2	561	132
(REX= 0.3074E+05),(VISC*DUDX/U*U= -0.4666E-05),(D1*U/VISC= 0.1823E+03),(D2*U/VISC= 0.5790E+02)										
0.3009E+00	0.1759E-02	0.5597E-03	-0.1430E+00	-0.1448E-01	0.1741E+02	-0.7751E+01	0.4205E+04	2	563	133
(REX= 0.3124E+05),(VISC*DUDX/U*U= -0.4289E-05),(D1*U/VISC= 0.1826E+03),(D2*U/VISC= 0.5810E+02)										
0.3064E+00	0.1765E-02	0.5630E-03	-0.1298E+00	-0.1321E-01	0.1737E+02	-0.6987E+01	0.4227E+04	2	565	134
(REX= 0.3173E+05),(VISC*DUDX/U*U= -0.3884E-05),(D1*U/VISC= 0.1828E+03),(D2*U/VISC= 0.5831E+02)										
0.3119E+00	0.1771E-02	0.5664E-03	-0.1157E+00	-0.1183E-01	0.1733E+02	-0.6183E+01	0.4258E+04	2	567	135
(REX= 0.3224E+05),(VISC*DUDX/U*U= -0.3452E-05),(D1*U/VISC= 0.1830E+03),(D2*U/VISC= 0.5854E+02)										
********** NEXT LINE FOR TAP NO= 10										
0.3174E+00	0.1776E-02	0.5699E-03	-0.1004E+00	-0.1034E-01	0.1730E+02	-0.5339E+01	0.4297E+04	2	569	136
(REX= 0.3276E+05),(VISC*DUDX/U*U= -0.2992E-05),(D1*U/VISC= 0.1832E+03),(D2*U/VISC= 0.5879E+02)										
0.3230E+00	0.1781E-02	0.5735E-03	-0.8484E-01	-0.8793E-02	0.1727E+02	-0.4483E+01	0.4338E+04	2	571	137
(REX= 0.3326E+05),(VISC*DUDX/U*U= -0.2520E-05),(D1*U/VISC= 0.1835E+03),(D2*U/VISC= 0.5907E+02)										
0.3285E+00	0.1786E-02	0.5771E-03	-0.6960E-01	-0.7268E-02	0.1725E+02	-0.3659E+01	0.4384E+04	2	573	138
(REX= 0.3379E+05),(VISC*DUDX/U*U= -0.2062E-05),(D1*U/VISC= 0.1837E+03),(D2*U/VISC= 0.5936E+02)										
0.3341E+00	0.1790E-02	0.5807E-03	-0.5478E-01	-0.5766E-02	0.1723E+02	-0.2867E+01	0.4434E+04	2	575	139
(REX= 0.3433E+05),(VISC*DUDX/U*U= -0.1619E-05),(D1*U/VISC= 0.1839E+03),(D2*U/VISC= 0.5967E+02)										
0.3396E+00	0.1793E-02	0.5843E-03	-0.4041E-01	-0.4290E-02	0.1722E+02	-0.2107E+01	0.4487E+04	2	577	140
(REX= 0.3487E+05),(VISC*DUDX/U*U= -0.1192E-05),(D1*U/VISC= 0.1841E+03),(D2*U/VISC= 0.5999E+02)										
0.3452E+00	0.1796E-02	0.5878E-03	-0.2653E-01	-0.2842E-02	0.1721E+02	-0.1380E+01	0.4543E+04	2	579	141
(REX= 0.3542E+05),(VISC*DUDX/U*U= -0.7813E-06),(D1*U/VISC= 0.1843E+03),(D2*U/VISC= 0.6031E+02)										
0.3507E+00	0.1798E-02	0.5912E-03	-0.1319E-01	-0.1425E-02	0.1720E+02	-0.6840E+00	0.4599E+04	2	581	142
(REX= 0.3598E+05),(VISC*DUDX/U*U= -0.3876E-06),(D1*U/VISC= 0.1844E+03),(D2*U/VISC= 0.6064E+02)										

L 3 (L=1,2,3,FOR FL PL,CYL,2E STG FLOW)

X-FT	DPLT-THKFT	MMT-THKFT	DEL2U	DZL2U	UFREE	DUDXT	DUDYW	K	MED	
NOTE** X=DIST FRM STG PT,** DPLT=DISPLACEMENT THK(FT),** MMT=MOMENTUM THK(FT) DEL2U=DISPL**2*DUDX/VISC(NON DIM),** DZL2U=MMT**2*DUDX/VISC(NON DIM),** UFREE=FREE ST VEL(FPS),** DUDXT=VEL GRD ALONG X(FT/S/FT),** DUDYW=NORMAL VEL GRDT(FT/S/FT)***,K=NO IF INTGTN STEPS										
0.3564E+00	0.1800E-02	0.5946E-03	-0.3942E-03	-0.4301E-04	0.1720E+02	-0.2041E-01	0.4656E+04	2	583	143
(REX= 0.3654E+05),(VISC*DUDX/U*U= -0.1157E-07),(D1*U/VISC= 0.1846E+03),(D2*U/VISC= 0.6098E+02)										
0.3619E+00	0.1802E-02	0.5979E-03	0.1183E-01	0.1302E-02	0.1720E+02	0.6111E+00	0.4715E+04	2	585	144
(REX= 0.3712E+05),(VISC*DUDX/U*U= 0.3463E-06),(D1*U/VISC= 0.1848E+03),(D2*U/VISC= 0.6133E+02)										
0.3674E+00	0.1803E-02	0.6011E-03	0.2346E-01	0.2608E-02	0.1721E+02	0.1210E+01	0.4772E+04	2	587	145
(REX= 0.3770E+05),(VISC*DUDX/U*U= 0.6856E-06),(D1*U/VISC= 0.1850E+03),(D2*U/VISC= 0.6169E+02)										
0.3730E+00	0.1804E-02	0.6042E-03	0.3450E-01	0.3870E-02	0.1722E+02	0.1778E+01	0.4829E+04	2	589	146
(REX= 0.3829E+05),(VISC*DUDX/U*U= 0.1006E-05),(D1*U/VISC= 0.1852E+03),(D2*U/VISC= 0.6203E+02)										
0.3785E+00	0.1805E-02	0.6073E-03	0.4492E-01	0.5087E-02	0.1723E+02	0.2313E+01	0.4887E+04	2	591	147
(REX= 0.3888E+05),(VISC*DUDX/U*U= 0.1307E-05),(D1*U/VISC= 0.1854E+03),(D2*U/VISC= 0.6239E+02)										
0.3841E+00	0.1806E-02	0.6104E-03	0.5474E-01	0.6255E-02	0.1724E+02	0.2816E+01	0.4943E+04	2	593	148
(REX= 0.3949E+05),(VISC*DUDX/U*U= 0.1589E-05),(D1*U/VISC= 0.1856E+03),(D2*U/VISC= 0.6275E+02)										
0.3896E+00	0.1806E-02	0.6133E-03	0.6395E-01	0.7372E-02	0.1726E+02	0.3287E+01	0.4998E+04	2	595	149
(REX= 0.4010E+05),(VISC*DUDX/U*U= 0.1851E-05),(D1*U/VISC= 0.1859E+03),(D2*U/VISC= 0.6311E+02)										
0.3952E+00	0.1807E-02	0.6162E-03	0.7254E-01	0.8435E-02	0.1728E+02	0.3726E+01	0.5052E+04	2	597	150
(REX= 0.4072E+05),(VISC*DUDX/U*U= 0.2093E-05),(D1*U/VISC= 0.1862E+03),(D2*U/VISC= 0.6348E+02)										
********** NEXT LINE FOR TAP NO= 11										
0.4007E+00	0.1807E-02	0.6190E-03	0.8051E-01	0.9442E-02	0.1730E+02	0.4133E+01	0.5104E+04	2	599	151
(REX= 0.4136E+05),(VISC*DUDX/U*U= 0.2316E-05),(D1*U/VISC= 0.1865E+03),(D2*U/VISC= 0.6385E+02)										
0.4063E+00	0.1808E-02	0.6226E-03	0.8773E-01	0.1040E-01	0.1732E+02	0.4499E+01	0.5159E+04	2	302	152
(REX= 0.4197E+05),(VISC*DUDX/U*U= 0.2514E-05),(D1*U/VISC= 0.1868E+03),(D2*U/VISC= 0.6432E+02)										
0.4119E+00	0.1810E-02	0.6273E-03	0.9407E-01	0.1129E-01	0.1735E+02	0.4814E+01	0.5214E+04	2	304	153
(REX= 0.4261E+05),(VISC*DUDX/U*U= 0.2682E-05),(D1*U/VISC= 0.1873E+03),(D2*U/VISC= 0.6490E+02)										
0.4174E+00	0.1813E-02	0.6321E-03	0.9951E-01	0.1210E-01	0.1738E+02	0.5078E+01	0.5264E+04	2	306	154
(REX= 0.4325E+05),(VISC*DUDX/U*U= 0.2820E-05),(D1*U/VISC= 0.1878E+03),(D2*U/VISC= 0.6550E+02)										
0.4230E+00	0.1816E-02	0.6371E-03	0.1041E+00	0.1281E-01	0.1741E+02	0.5292E+01	0.5310E+04	2	308	155
(REX= 0.4390E+05),(VISC*DUDX/U*U= 0.2929E-05),(D1*U/VISC= 0.1885E+03),(D2*U/VISC= 0.6613E+02)										
0.4286E+00	0.1820E-02	0.6422E-03	0.1077E+00	0.1341E-01	0.1744E+02	0.5455E+01	0.5350E+04	2	310	156
(REX= 0.4456E+05),(VISC*DUDX/U*U= 0.3009E-05),(D1*U/VISC= 0.1892E+03),(D2*U/VISC= 0.6677E+02)										
0.4341E+00	0.1824E-02	0.6474E-03	0.1105E+00	0.1391E-01	0.1747E+02	0.5567E+01	0.5385E+04	2	312	157
(REX= 0.4521E+05),(VISC*DUDX/U*U= 0.3060E-05),(D1*U/VISC= 0.1900E+03),(D2*U/VISC= 0.6742E+02)										
0.4397E+00	0.1829E-02	0.6525E-03	0.1123E+00	0.1429E-01	0.1750E+02	0.5628E+01	0.5414E+04	2	314	158
(REX= 0.4588E+05),(VISC*DUDX/U*U= 0.3083E-05),(D1*U/VISC= 0.1909E+03),(D2*U/VISC= 0.6808E+02)										
0.4452E+00	0.1835E-02	0.6577E-03	0.1132E+00	0.1454E-01	0.1753E+02	0.5639E+01	0.5437E+04	2	316	159
(REX= 0.4654E+05),(VISC*DUDX/U*U= 0.3078E-05),(D1*U/VISC= 0.1918E+03),(D2*U/VISC= 0.6875E+02)										
0.4508E+00	0.1841E-02	0.6629E-03	0.1132E+00	0.1467E-01	0.1756E+02	0.5590E+01	0.5455E+04	2	318	160
(REX= 0.4720E+05),(VISC*DUDX/U*U= 0.3045E-05),(D1*U/VISC= 0.1928E+03),(D2*U/VISC= 0.6941E+02)										
0.4564E+00	0.1848E-02	0.6680E-03	0.1122E+00	0.1466E-01	0.1759E+02	0.5508E+01	0.5465E+04	2	320	161
(REX= 0.4787E+05),(VISC*DUDX/U*U= 0.2985E-05),(D1*U/VISC= 0.1939E+03),(D2*U/VISC= 0.7007E+02)										
0.4619E+00	0.1856E-02	0.6732E-03	0.1102E+00	0.1450E-01	0.1762E+02	0.5367E+01	0.5469E+04	2	322	162
(REX= 0.4854E+05),(VISC*DUDX/U*U= 0.2898E-05),(D1*U/VISC= 0.1950E+03),(D2*U/VISC= 0.7073E+02)										
0.4675E+00	0.1864E-02	0.6783E-03	0.1072E+00	0.1419E-01	0.1765E+02	0.5174E+01	0.5466E+04	2	324	163
(REX= 0.4920E+05),(VISC*DUDX/U*U= 0.2785E-05),(D1*U/VISC= 0.1961E+03),(D2*U/VISC= 0.7139E+02)										

L 3 (L=1,2,3,FOR FL PL,CYL,2D STG FLOW)

X-FT	DPLT-TKFT	MMT-TKFT	DEL2U	DZL2U	UFREE	DUDXT	DUDYW	K	MFD	
NOTE** X=DIST FRM STG PT,** DPLT=DISPLACEMENT THK(FT),** MMT=MOMENTUM THK(FT) DEL2U=DISPL**2*DUDX/VISC(NON DIM),** DZL2U=MMT**2*DUDX/VISC(NON DIM),** UFREE=FREE ST VEL(FPS),** DUDXT=VEL GRD ALONG X(FT/S/FT),** DUDYW=NORMAL VEL GRDT(FT/S/FT)***,K=NO IF INTGTN STEPS										
0.4730E+00	0.1872E-02	0.6833E-03	0.1031E+00	0.1373E-01	0.1768E+02	0.4931E+01	0.5456E+04	2	326	164
(REX= 0.4987E+05),(VISC*DUDX/U*U= 0.2646E-05),(D1*U/VISC= 0.1974E+03),(D2*U/VISC= 0.7204E+02)										
0.4786E+00	0.1882E-02	0.6884E-03	0.9791E-01	0.1310E-01	0.1771E+02	0.4638E+01	0.5438E+04	2	328	165
(REX= 0.5053E+05),(VISC*DUDX/U*U= 0.2481E-05),(D1*U/VISC= 0.1987E+03),(D2*U/VISC= 0.7268E+02)										
********** NEXT LINE FOR TAP NO= 12										
0.4842E+00	0.1892E-02	0.6934E-03	0.9160E-01	0.1231E-01	0.1773E+02	0.4293E+01	0.5414E+04	2	330	166
(REX= 0.5119E+05),(VISC*DUDX/U*U= 0.2290E-05),(D1*U/VISC= 0.2000E+03),(D2*U/VISC= 0.7331E+02)										
0.4857E+00	0.1902E-02	0.6984E-03	0.8572E-01	0.1156E-01	0.1775E+02	0.3974E+01	0.5394E+04	2	332	167
(REX= 0.5184E+05),(VISC*DUDX/U*U= 0.2114E-05),(D1*U/VISC= 0.2013E+03),(D2*U/VISC= 0.7393E+02)										
0.4952E+00	0.1913E-02	0.7034E-03	0.8181E-01	0.1106E-01	0.1778E+02	0.3750E+01	0.5361E+04	2	334	168
(REX= 0.5249E+05),(VISC*DUDX/U*U= 0.1990E-05),(D1*U/VISC= 0.2027E+03),(D2*U/VISC= 0.7455E+02)										
0.5007E+00	0.1924E-02	0.7084E-03	0.7991E-01	0.1083E-01	0.1780E+02	0.3620E+01	0.5333E+04	2	336	169
(REX= 0.5313E+05),(VISC*DUDX/U*U= 0.1917E-05),(D1*U/VISC= 0.2042E+03),(D2*U/VISC= 0.7517E+02)										
0.5062E+00	0.1935E-02	0.7135E-03	0.8007E-01	0.1089E-01	0.1782E+02	0.3585E+01	0.5310E+04	2	338	170
(REX= 0.5377E+05),(VISC*DUDX/U*U= 0.1895E-05),(D1*U/VISC= 0.2056E+03),(D2*U/VISC= 0.7580E+02)										
0.5117E+00	0.1946E-02	0.7188E-03	0.8235E-01	0.1123E-01	0.1784E+02	0.3645E+01	0.5293E+04	2	340	171
(REX= 0.5442E+05),(VISC*DUDX/U*U= 0.1922E-05),(D1*U/VISC= 0.2070E+03),(D2*U/VISC= 0.7644E+02)										
0.5172E+00	0.1957E-02	0.7241E-03	0.8683E-01	0.1188E-01	0.1786E+02	0.3800E+01	0.5284E+04	2	342	172
(REX= 0.5507E+05),(VISC*DUDX/U*U= 0.1999E-05),(D1*U/VISC= 0.2084E+03),(D2*U/VISC= 0.7709E+02)										
0.5227E+00	0.1968E-02	0.7295E-03	0.9355E-01	0.1285E-01	0.1788E+02	0.4050E+01	0.5282E+04	2	344	173
(REX= 0.5572E+05),(VISC*DUDX/U*U= 0.2125E-05),(D1*U/VISC= 0.2098E+03),(D2*U/VISC= 0.7777E+02)										
0.5283E+00	0.1979E-02	0.7350E-03	0.1026E+00	0.1416E-01	0.1790E+02	0.4394E+01	0.5290E+04	2	346	174
(REX= 0.5638E+05),(VISC*DUDX/U*U= 0.2300E-05),(D1*U/VISC= 0.2112E+03),(D2*U/VISC= 0.7846E+02)										
0.5338E+00	0.1988E-02	0.7407E-03	0.1139E+00	0.1581E-01	0.1793E+02	0.4833E+01	0.5308E+04	2	348	175
(REX= 0.5705E+05),(VISC*DUDX/U*U= 0.2522E-05),(D1*U/VISC= 0.2125E+03),(D2*U/VISC= 0.7917E+02)										
0.5393E+00	0.1998E-02	0.7464E-03	0.1277E+00	0.1783E-01	0.1795E+02	0.5367E+01	0.5337E+04	2	350	176
(REX= 0.5773E+05),(VISC*DUDX/U*U= 0.2792E-05),(D1*U/VISC= 0.2138E+03),(D2*U/VISC= 0.7990E+02)										
0.5448E+00	0.2006E-02	0.7521E-03	0.1439E+00	0.2022E-01	0.1799E+02	0.5996E+01	0.5377E+04	2	352	177
(REX= 0.5842E+05),(VISC*DUDX/U*U= 0.3108E-05),(D1*U/VISC= 0.2151E+03),(D2*U/VISC= 0.8066E+02)										
0.5503E+00	0.2014E-02	0.7580E-03	0.1624E+00	0.2302E-01	0.1802E+02	0.6719E+01	0.5429E+04	2	354	178
(REX= 0.5913E+05),(VISC*DUDX/U*U= 0.3470E-05),(D1*U/VISC= 0.2164E+03),(D2*U/VISC= 0.8145E+02)										
0.5558E+00	0.2020E-02	0.7639E-03	0.1834E+00	0.2622E-01	0.1806E+02	0.7537E+01	0.5494E+04	2	356	179
(REX= 0.5985E+05),(VISC*DUDX/U*U= 0.3876E-05),(D1*U/VISC= 0.2175E+03),(D2*U/VISC= 0.8226E+02)										
0.5613E+00	0.2026E-02	0.7698E-03	0.2068E+00	0.2986E-01	0.1810E+02	0.8450E+01	0.5571E+04	2	358	180
(REX= 0.6059E+05),(VISC*DUDX/U*U= 0.4324E-05),(D1*U/VISC= 0.2187E+03),(D2*U/VISC= 0.8310E+02)										
********** NEXT LINE FOR TAP NO= 13										
0.5668E+00	0.2030E-02	0.7757E-03	0.2325E+00	0.3394E-01	0.1815E+02	0.9458E+01	0.5663E+04	2	360	181
(REX= 0.6135E+05),(VISC*DUDX/U*U= 0.4813E-05),(D1*U/VISC= 0.2198E+03),(D2*U/VISC= 0.8397E+02)										
0.5725E+00	0.2034E-02	0.7819E-03	0.2588E+00	0.3825E-01	0.1821E+02	0.1049E+02	0.5794E+04	2	362	182
(REX= 0.6215E+05),(VISC*DUDX/U*U= 0.5307E-05),(D1*U/VISC= 0.2208E+03),(D2*U/VISC= 0.8489E+02)										
0.5781E+00	0.2036E-02	0.7879E-03	0.2828E+00	0.4234E-01	0.1827E+02	0.1144E+02	0.5909E+04	2	364	183
(REX= 0.6298E+05),(VISC*DUDX/U*U= 0.5748E-05),(D1*U/VISC= 0.2218E+03),(D2*U/VISC= 0.8583E+02)										
0.5837E+00	0.2038E-02	0.7936E-03	0.3046E+00	0.4620E-01	0.1834E+02	0.1230E+02	0.6026E+04	2	366	184
(REX= 0.6382E+05),(VISC*DUDX/U*U= 0.6136E-05),(D1*U/VISC= 0.2228E+03),(D2*U/VISC= 0.8678E+02)										

L 3 (L=1,2,3,FOR FL PL,CYL,2D STG FLOW)

X-FT	DPLT-THKFT	MMT-THKFT	DEL2U	DZL2U	UFREE	DUDXT	DUDYW	K	NED	
NOTE** X=DIST FRM SIG PT,** DPLT=DISPLACEMENT THK(FT),** MMT=MOMENTUM THK(FT) DEL2U=DISPL**2*DUDX/VISC(NON DIM),** DZL2U=MMT**2*DUDX/VISC(NON DIM),** UFREE=FREE ST VEL(FPS),** DUDXT=VEL GRD ALONG X(FT/S/FT),** DUDYW=NORMAL VEL GRDT(FT/S/FT)***,K=NO IF INTGTN STEPS										
0.5893E+00	0.2039E-02	0.7992E-03	0.3242E+00	0.4980E-01	0.1641E+02	0.1308E+02	0.6137E+04	2	368	185
(REX= 0.6469E+05),(VISC*DUDX/U*U= 0.6472E-05),(D1*U/VISC= 0.2238E+03),(D2*U/VISC= 0.8772E+02)										
0.5950E+00	0.2040E-02	0.8045E-03	0.3415E+00	0.5313E-01	0.1648E+02	0.1377E+02	0.6248E+04	2	370	186
(REX= 0.6558E+05),(VISC*DUDX/U*U= 0.6757E-05),(D1*U/VISC= 0.2248E+03),(D2*U/VISC= 0.8867E+02)										
0.6006E+00	0.2040E-02	0.8096E-03	0.3565E+00	0.5616E-01	0.1656E+02	0.1437E+02	0.6358E+04	2	372	187
(REX= 0.6648E+05),(VISC*DUDX/U*U= 0.6993E-05),(D1*U/VISC= 0.2258E+03),(D2*U/VISC= 0.8962E+02)										
0.6062E+00	0.2040E-02	0.8145E-03	0.3694E+00	0.5888E-01	0.1665E+02	0.1488E+02	0.6460E+04	2	374	188
(REX= 0.6740E+05),(VISC*DUDX/U*U= 0.7180E-05),(D1*U/VISC= 0.2268E+03),(D2*U/VISC= 0.9055E+02)										
0.6119E+00	0.2040E-02	0.8191E-03	0.3801E+00	0.6127E-01	0.1673E+02	0.1531E+02	0.6558E+04	2	376	189
(REX= 0.6834E+05),(VISC*DUDX/U*U= 0.7320E-05),(D1*U/VISC= 0.2279E+03),(D2*U/VISC= 0.9148E+02)										
0.6175E+00	0.2040E-02	0.8235E-03	0.3886E+00	0.6331E-01	0.1682E+02	0.1566E+02	0.6652E+04	2	378	190
(REX= 0.6929E+05),(VISC*DUDX/U*U= 0.7415E-05),(D1*U/VISC= 0.2289E+03),(D2*U/VISC= 0.9241E+02)										
0.6231E+00	0.2040E-02	0.8277E-03	0.3950E+00	0.6501E-01	0.1691E+02	0.1591E+02	0.6737E+04	2	380	191
(REX= 0.7025E+05),(VISC*DUDX/U*U= 0.7466E-05),(D1*U/VISC= 0.2300E+03),(D2*U/VISC= 0.9332E+02)										
0.6287E+00	0.2041E-02	0.8317E-03	0.3993E+00	0.6634E-01	0.1900E+02	0.1608E+02	0.6816E+04	2	382	192
(REX= 0.7122E+05),(VISC*DUDX/U*U= 0.7474E-05),(D1*U/VISC= 0.2311E+03),(D2*U/VISC= 0.9421E+02)										
0.6344E+00	0.2041E-02	0.8356E-03	0.4017E+00	0.6736E-01	0.1509E+02	0.1617E+02	0.6888E+04	2	384	193
(REX= 0.7220E+05),(VISC*DUDX/U*U= 0.7442E-05),(D1*U/VISC= 0.2323E+03),(D2*U/VISC= 0.9510E+02)										
0.6400E+00	0.2042E-02	0.8392E-03	0.4020E+00	0.6788E-01	0.1518E+02	0.1616E+02	0.6948E+04	2	386	194
(REX= 0.7319E+05),(VISC*DUDX/U*U= 0.7370E-05),(D1*U/VISC= 0.2335E+03),(D2*U/VISC= 0.9597E+02)										
0.6456E+00	0.2043E-02	0.8427E-03	0.4003E+00	0.6808E-01	0.1527E+02	0.1608E+02	0.7002E+04	2	388	195
(REX= 0.7418E+05),(VISC*DUDX/U*U= 0.7261E-05),(D1*U/VISC= 0.2348E+03),(D2*U/VISC= 0.9683E+02)										
********** NEXT LINE FOR TAP NO= 14										
0.6512E+00	0.2045E-02	0.8461E-03	0.3966E+00	0.6788E-01	0.1536E+02	0.1590E+02	0.7049E+04	2	390	196
(REX= 0.7518E+05),(VISC*DUDX/U*U= 0.7115E-05),(D1*U/VISC= 0.2361E+03),(D2*U/VISC= 0.9767E+02)										
0.6569E+00	0.2047E-02	0.8494E-03	0.3931E+00	0.6766E-01	0.1545E+02	0.1573E+02	0.7097E+04	2	392	197
(REX= 0.7618E+05),(VISC*DUDX/U*U= 0.6973E-05),(D1*U/VISC= 0.2374E+03),(D2*U/VISC= 0.9851E+02)										
0.6625E+00	0.2050E-02	0.8526E-03	0.3921E+00	0.6783E-01	0.1554E+02	0.1565E+02	0.7127E+04	2	394	198
(REX= 0.7718E+05),(VISC*DUDX/U*U= 0.6875E-05),(D1*U/VISC= 0.2388E+03),(D2*U/VISC= 0.9932E+02)										
0.6682E+00	0.2053E-02	0.8558E-03	0.3935E+00	0.6840E-01	0.1563E+02	0.1566E+02	0.7164E+04	2	396	199
(REX= 0.7819E+05),(VISC*DUDX/U*U= 0.6820E-05),(D1*U/VISC= 0.2402E+03),(D2*U/VISC= 0.1001E+03)										
0.6738E+00	0.2055E-02	0.8585E-03	0.3972E+00	0.6938E-01	0.1571E+02	0.1577E+02	0.7207E+04	2	398	200
(REX= 0.7921E+05),(VISC*DUDX/U*U= 0.6805E-05),(D1*U/VISC= 0.2416E+03),(D2*U/VISC= 0.1010E+03)										
0.6794E+00	0.2058E-02	0.8621E-03	0.4033E+00	0.7079E-01	0.1980E+02	0.1597E+02	0.7256E+04	2	400	201
(REX= 0.8023E+05),(VISC*DUDX/U*U= 0.6830E-05),(D1*U/VISC= 0.2430E+03),(D2*U/VISC= 0.1019E+03)										
0.6851E+00	0.2060E-02	0.8653E-03	0.4116E+00	0.7263E-01	0.1589E+02	0.1627E+02	0.7314E+04	2	402	202
(REX= 0.8127E+05),(VISC*DUDX/U*U= 0.6893E-05),(D1*U/VISC= 0.2444E+03),(D2*U/VISC= 0.1026E+03)										
0.6907E+00	0.2062E-02	0.8685E-03	0.4222E+00	0.7491E-01	0.1599E+02	0.1666E+02	0.7380E+04	2	404	203
(REX= 0.8232E+05),(VISC*DUDX/U*U= 0.6993E-05),(D1*U/VISC= 0.2457E+03),(D2*U/VISC= 0.1035E+03)										
0.6964E+00	0.2063E-02	0.8716E-03	0.4350E+00	0.7765E-01	0.2008E+02	0.1714E+02	0.7456E+04	2	406	204
(REX= 0.8339E+05),(VISC*DUDX/U*U= 0.7127E-05),(D1*U/VISC= 0.2471E+03),(D2*U/VISC= 0.1044E+03)										
0.7020E+00	0.2064E-02	0.8748E-03	0.4500E+00	0.8083E-01	0.2018E+02	0.1771E+02	0.7543E+04	2	408	205
(REX= 0.8447E+05),(VISC*DUDX/U*U= 0.7295E-05),(D1*U/VISC= 0.2484E+03),(D2*U/VISC= 0.1053E+03)										

L 3 (I=1,2,3,FOR FL PL,CYL,2D STG FLOW)

X-FT	DPLT-THFT	MMT-THFT	DFL2U	DZL2U	UFREE	DUDXT	DUDYW	K	MED	
NOTE** X=DIST FRM SIG PT,** DPLT=DISPLACEMENT THK(FT),** MMT=MOMENTUM THK(FT)										
DFL2U=DISPL**2*DUDX/VISC(NON DIM),** DZL2U=MMT**2*DUDX/VISC(NON DIM),** UFREE=FREE ST VEL(FPS),**										
DUDXT=VEL GRD ALONG X(FT/S/FT),** DUDYW=NORMAL VEL GRDT(FT/S/FT)***,K=NO IF INTGTN STEPS										
0.7076E+00	0.2064E-02	0.8779E-03	0.4670E+00	0.8449E-01	0.2028E+02	0.1838E+02	0.7643E+04	2	410	206
(REX= 0.8558E+05),(VISC*DUDX/U*U= 0.7495E-05),(D1*U/VISC= 0.2496E+03),(D2*U/VISC= 0.1062E+03)										
0.7133E+00	0.2063E-02	0.8805E-03	0.4861E+00	0.8860E-01	0.2039E+02	0.1915E+02	0.7753E+04	2	412	207
(REX= 0.8671E+05),(VISC*DUDX/U*U= 0.7725E-05),(D1*U/VISC= 0.2509E+03),(D2*U/VISC= 0.1071E+03)										
0.7189E+00	0.2062E-02	0.8839E-03	0.5072E+00	0.9319E-01	0.2050E+02	0.2000E+02	0.7879E+04	2	414	208
(REX= 0.8787E+05),(VISC*DUDX/U*U= 0.7984E-05),(D1*U/VISC= 0.2520E+03),(D2*U/VISC= 0.1080E+03)										
0.7246E+00	0.2060E-02	0.8868E-03	0.5301E+00	0.9825E-01	0.2061E+02	0.2095E+02	0.8016E+04	2	416	209
(REX= 0.8906E+05),(VISC*DUDX/U*U= 0.8269E-05),(D1*U/VISC= 0.2532E+03),(D2*U/VISC= 0.1090E+03)										
0.7302E+00	0.2057E-02	0.8896E-03	0.5547E+00	0.1038E+00	0.2074E+02	0.2200E+02	0.8170E+04	2	418	210
(REX= 0.9028E+05),(VISC*DUDX/U*U= 0.8580E-05),(D1*U/VISC= 0.2543E+03),(D2*U/VISC= 0.1100E+03)										
********** NEXT LINE FOR IAP NO= 15										
0.7358E+00	0.2052E-02	0.8922E-03	0.5810E+00	0.1098E+00	0.2086E+02	0.2313E+02	0.8338E+04	2	420	211
(REX= 0.9154E+05),(VISC*DUDX/U*U= 0.8914E-05),(D1*U/VISC= 0.2553E+03),(D2*U/VISC= 0.1110E+03)										
0.7413E+00	0.2048E-02	0.8944E-03	0.6063E+00	0.1156E+00	0.2099E+02	0.2424E+02	0.8450E+04	2	422	212
(REX= 0.9270E+05),(VISC*DUDX/U*U= 0.9228E-05),(D1*U/VISC= 0.2563E+03),(D2*U/VISC= 0.1119E+03)										
0.7467E+00	0.2042E-02	0.8966E-03	0.6291E+00	0.1212E+00	0.2112E+02	0.2529E+02	0.8631E+04	2	424	213
(REX= 0.9405E+05),(VISC*DUDX/U*U= 0.9505E-05),(D1*U/VISC= 0.2573E+03),(D2*U/VISC= 0.1129E+03)										
0.7521E+00	0.2036E-02	0.8986E-03	0.6498E+00	0.1266E+00	0.2126E+02	0.2628E+02	0.8812E+04	2	426	214
(REX= 0.9536E+05),(VISC*DUDX/U*U= 0.9748E-05),(D1*U/VISC= 0.2582E+03),(D2*U/VISC= 0.1139E+03)										
0.7575E+00	0.2030E-02	0.9004E-03	0.6684E+00	0.1315E+00	0.2141E+02	0.2721E+02	0.9002E+04	2	428	215
(REX= 0.9671E+05),(VISC*DUDX/U*U= 0.9957E-05),(D1*U/VISC= 0.2591E+03),(D2*U/VISC= 0.1149E+03)										
0.7629E+00	0.2022E-02	0.9019E-03	0.6850E+00	0.1362E+00	0.2156E+02	0.2809E+02	0.9190E+04	2	430	216
(REX= 0.9808E+05),(VISC*DUDX/U*U= 0.1013E-04),(D1*U/VISC= 0.2600E+03),(D2*U/VISC= 0.1159E+03)										
0.7684E+00	0.2015E-02	0.9031E-03	0.6997E+00	0.1406E+00	0.2171E+02	0.2890E+02	0.9374E+04	2	432	217
(REX= 0.9948E+05),(VISC*DUDX/U*U= 0.1028E-04),(D1*U/VISC= 0.2609E+03),(D2*U/VISC= 0.1169E+03)										
0.7738E+00	0.2007E-02	0.9042E-03	0.7125E+00	0.1446E+00	0.2187E+02	0.2965E+02	0.9566E+04	2	434	218
(REX= 0.1009E+06),(VISC*DUDX/U*U= 0.1040E-04),(D1*U/VISC= 0.2618E+03),(D2*U/VISC= 0.1179E+03)										
0.7792E+00	0.2000E-02	0.9050E-03	0.7236E+00	0.1482E+00	0.2204E+02	0.3035E+02	0.9753E+04	2	436	219
(REX= 0.1024E+06),(VISC*DUDX/U*U= 0.1048E-04),(D1*U/VISC= 0.2627E+03),(D2*U/VISC= 0.1189E+03)										
0.7846E+00	0.1992E-02	0.9056E-03	0.7329E+00	0.1515E+00	0.2220E+02	0.3099E+02	0.9934E+04	2	438	220
(REX= 0.1039E+06),(VISC*DUDX/U*U= 0.1054E-04),(D1*U/VISC= 0.2637E+03),(D2*U/VISC= 0.1199E+03)										
0.7901E+00	0.1984E-02	0.9060E-03	0.7427E+00	0.1545E+00	0.2237E+02	0.3156E+02	0.1012E+05	2	440	221
(REX= 0.1054E+06),(VISC*DUDX/U*U= 0.1058E-04),(D1*U/VISC= 0.2646E+03),(D2*U/VISC= 0.1209E+03)										
0.7955E+00	0.1976E-02	0.9062E-03	0.7469E+00	0.1571E+00	0.2254E+02	0.3208E+02	0.1030E+05	2	442	222
(REX= 0.1069E+06),(VISC*DUDX/U*U= 0.1059E-04),(D1*U/VISC= 0.2656E+03),(D2*U/VISC= 0.1218E+03)										
0.8009E+00	0.1968E-02	0.9063E-03	0.7516E+00	0.1594E+00	0.2272E+02	0.3254E+02	0.1047E+05	2	444	223
(REX= 0.1085E+06),(VISC*DUDX/U*U= 0.1057E-04),(D1*U/VISC= 0.2666E+03),(D2*U/VISC= 0.1228E+03)										
0.8063E+00	0.1961E-02	0.9062E-03	0.7549E+00	0.1613E+00	0.2290E+02	0.3294E+02	0.1065E+05	2	446	224
(REX= 0.1101E+06),(VISC*DUDX/U*U= 0.1054E-04),(D1*U/VISC= 0.2677E+03),(D2*U/VISC= 0.1237E+03)										
0.8117E+00	0.1953E-02	0.9060E-03	0.7569E+00	0.1629E+00	0.2308E+02	0.3328E+02	0.1082E+05	2	448	225
(REX= 0.1117E+06),(VISC*DUDX/U*U= 0.1048E-04),(D1*U/VISC= 0.2687E+03),(D2*U/VISC= 0.1247E+03)										
********** NEXT LINE FOR IAP NO= 16										
0.8172E+00	0.1946E-02	0.9057E-03	0.7577E+00	0.1641E+00	0.2326E+02	0.3356E+02	0.1098E+05	2	450	226
(REX= 0.1133E+06),(VISC*DUDX/U*U= 0.1040E-04),(D1*U/VISC= 0.2698E+03),(D2*U/VISC= 0.1256E+03)										

L 3 (L=1,2,3,FOR FL PL,CYL,2D STG FLOW)

X-FT	DPLT-THFT	MMT-THFT	DEL2U	DZL2U	UFREE	DUDXT	DUDYW	K	MED	
NOTE** X=DIST FRM STG PT,** DPLT=DISPLACEMENT THK(FT),** MMT=MOMENTUM THK(FT) DEL2U=DISPL**2*DUDX/VISC(NON DIM),** DZL2U=MMT**2*DUDX/VISC(NON DIM),** UFREE=FREE ST VEL(FPS),** DUDXT=VEL GRD ALONG X(FT/S/FT),** DUDYW=NORMAL VEL GRDT(FT/S/FT)***,K=NO IF INTGTN STEPS										
0.8226E+00	0.1939E-02	0.9052E-03	0.7573E+00	0.1651E+00	0.2344E+02	0.3379E+02	0.1115E+05	2	452	227
(REX= 0.1150E+06),(VISC*DUDX/U*U= 0.1031E-04),(D1*U/VISC= 0.2710E+03),(D2*U/VISC= 0.1265E+03)										
0.8280E+00	0.1932E-02	0.9046E-03	0.7563E+00	0.1658E+00	0.2362E+02	0.3399E+02	0.1131E+05	2	454	228
(REX= 0.1166E+06),(VISC*DUDX/U*U= 0.1021E-04),(D1*U/VISC= 0.2721E+03),(D2*U/VISC= 0.1274E+03)										
0.8334E+00	0.1925E-02	0.9040E-03	0.7546E+00	0.1664E+00	0.2381E+02	0.3414E+02	0.1146E+05	2	456	229
(REX= 0.1183E+06),(VISC*DUDX/U*U= 0.1010E-04),(D1*U/VISC= 0.2733E+03),(D2*U/VISC= 0.1283E+03)										
0.8388E+00	0.1919E-02	0.9033E-03	0.7522E+00	0.1667E+00	0.2399E+02	0.3426E+02	0.1160E+05	2	458	230
(REX= 0.1200E+06),(VISC*DUDX/U*U= 0.9981E-05),(D1*U/VISC= 0.2745E+03),(D2*U/VISC= 0.1292E+03)										
0.8442E+00	0.1913E-02	0.9025E-03	0.7493E+00	0.1668E+00	0.2418E+02	0.3434E+02	0.1174E+05	2	460	231
(REX= 0.1217E+06),(VISC*DUDX/U*U= 0.9852E-05),(D1*U/VISC= 0.2758E+03),(D2*U/VISC= 0.1301E+03)										
0.8496E+00	0.1907E-02	0.9018E-03	0.7458E+00	0.1667E+00	0.2436E+02	0.3438E+02	0.1188E+05	2	462	232
(REX= 0.1234E+06),(VISC*DUDX/U*U= 0.9714E-05),(D1*U/VISC= 0.2771E+03),(D2*U/VISC= 0.1310E+03)										
0.8550E+00	0.1902E-02	0.9010E-03	0.7416E+00	0.1664E+00	0.2455E+02	0.3439E+02	0.1201E+05	2	464	233
(REX= 0.1252E+06),(VISC*DUDX/U*U= 0.9569E-05),(D1*U/VISC= 0.2784E+03),(D2*U/VISC= 0.1319E+03)										
0.8604E+00	0.1897E-02	0.9002E-03	0.7370E+00	0.1660E+00	0.2473E+02	0.3435E+02	0.1214E+05	2	466	234
(REX= 0.1269E+06),(VISC*DUDX/U*U= 0.9416E-05),(D1*U/VISC= 0.2798E+03),(D2*U/VISC= 0.1328E+03)										
0.8658E+00	0.1892E-02	0.8994E-03	0.7318E+00	0.1653E+00	0.2492E+02	0.3428E+02	0.1226E+05	2	468	235
(REX= 0.1287E+06),(VISC*DUDX/U*U= 0.9257E-05),(D1*U/VISC= 0.2812E+03),(D2*U/VISC= 0.1336E+03)										
0.8712E+00	0.1888E-02	0.8986E-03	0.7261E+00	0.1645E+00	0.2511E+02	0.3417E+02	0.1237E+05	2	470	236
(REX= 0.1304E+06),(VISC*DUDX/U*U= 0.9092E-05),(D1*U/VISC= 0.2826E+03),(D2*U/VISC= 0.1345E+03)										
0.8766E+00	0.1884E-02	0.8978E-03	0.7198E+00	0.1635E+00	0.2529E+02	0.3402E+02	0.1248E+05	2	472	237
(REX= 0.1322E+06),(VISC*DUDX/U*U= 0.8921E-05),(D1*U/VISC= 0.2841E+03),(D2*U/VISC= 0.1354E+03)										
0.8820E+00	0.1880E-02	0.8971E-03	0.7131E+00	0.1624E+00	0.2547E+02	0.3384E+02	0.1259E+05	2	474	238
(REX= 0.1340E+06),(VISC*DUDX/U*U= 0.8745E-05),(D1*U/VISC= 0.2856E+03),(D2*U/VISC= 0.1363E+03)										
0.8874E+00	0.1877E-02	0.8964E-03	0.7059E+00	0.1611E+00	0.2566E+02	0.3361E+02	0.1268E+05	2	476	239
(REX= 0.1358E+06),(VISC*DUDX/U*U= 0.8564E-05),(D1*U/VISC= 0.2871E+03),(D2*U/VISC= 0.1371E+03)										
0.8928E+00	0.1874E-02	0.8957E-03	0.6982E+00	0.1595E+00	0.2584E+02	0.3335E+02	0.1278E+05	2	478	240
(REX= 0.1375E+06),(VISC*DUDX/U*U= 0.8379E-05),(D1*U/VISC= 0.2887E+03),(D2*U/VISC= 0.1380E+03)										
********** NEXT LINE FOR IAP NO= 17										
0.8982E+00	0.1871E-02	0.8950E-03	0.6900E+00	0.1579E+00	0.2602E+02	0.3305E+02	0.1286E+05	2	480	241
(REX= 0.1393E+06),(VISC*DUDX/U*U= 0.8190E-05),(D1*U/VISC= 0.2903E+03),(D2*U/VISC= 0.1389E+03)										
0.9037E+00	0.1869E-02	0.8945E-03	0.6824E+00	0.1563E+00	0.2620E+02	0.3276E+02	0.1292E+05	2	482	242
(REX= 0.1412E+06),(VISC*DUDX/U*U= 0.8007E-05),(D1*U/VISC= 0.2919E+03),(D2*U/VISC= 0.1397E+03)										
0.9092E+00	0.1867E-02	0.8940E-03	0.6766E+00	0.1551E+00	0.2638E+02	0.3255E+02	0.1300E+05	2	484	243
(REX= 0.1430E+06),(VISC*DUDX/U*U= 0.7847E-05),(D1*U/VISC= 0.2937E+03),(D2*U/VISC= 0.1406E+03)										
0.9147E+00	0.1865E-02	0.8936E-03	0.6726E+00	0.1543E+00	0.2656E+02	0.3241E+02	0.1308E+05	2	486	244
(REX= 0.1448E+06),(VISC*DUDX/U*U= 0.7709E-05),(D1*U/VISC= 0.2954E+03),(D2*U/VISC= 0.1415E+03)										
0.9202E+00	0.1864E-02	0.8933E-03	0.6701E+00	0.1539E+00	0.2673E+02	0.3235E+02	0.1316E+05	2	488	245
(REX= 0.1467E+06),(VISC*DUDX/U*U= 0.7592E-05),(D1*U/VISC= 0.2971E+03),(D2*U/VISC= 0.1424E+03)										
0.9257E+00	0.1862E-02	0.8930E-03	0.6693E+00	0.1539E+00	0.2691E+02	0.3236E+02	0.1325E+05	2	490	246
(REX= 0.1486E+06),(VISC*DUDX/U*U= 0.7494E-05),(D1*U/VISC= 0.2988E+03),(D2*U/VISC= 0.1433E+03)										
0.9312E+00	0.1861E-02	0.8927E-03	0.6700E+00	0.1542E+00	0.2709E+02	0.3245E+02	0.1335E+05	2	492	247
(REX= 0.1504E+06),(VISC*DUDX/U*U= 0.7415E-05),(D1*U/VISC= 0.3006E+03),(D2*U/VISC= 0.1442E+03)										

L 3 (I=1,2,3,FOR FL PL,CYL,2D SIG FLOW)

X-FT	DPLT-TKFT	MMT-TKFT	DFL2U	DZL2U	UFREE	DUDXT	DUDYW	K	MED	
NOTE** X=DIST FRM STG PT,** DPLT=DISPLACEMENT THK(FT),** MMT=MOMENTUM THK(FT) DFL2U=DISPL**2*DUDX/VISC(NON DIM),** DZL2U=MMT**2*DUDX/VISC(NON DIM),** UFREE=FREE ST VEL(FPS),** DUDXT=VEL GRD ALONG X(FT/S/FT),** DUDYW=NORMAL VEL GRD(FT/S/FT)***,K=NO IF INTGTN STEPS										
0.9367E+00	0.1859E-02	0.8925E-03	0.6721E+00	0.1549E+00	0.2727E+02	0.3261E+02	0.1345E+05	2	494	248
(REX=	0.1523E+06),(VISC*DUDX/U*U=	0.7355E-05),(D1*U/VISC=	0.3023E+03),(D2*U/VISC=	0.1451E+03)						
0.9422E+00	0.1858E-02	0.8923E-03	0.6757E+00	0.1559E+00	0.2745E+02	0.3284E+02	0.1356E+05	2	496	249
(REX=	0.1542E+06),(VISC*DUDX/U*U=	0.7311E-05),(D1*U/VISC=	0.3040E+03),(D2*U/VISC=	0.1460E+03)						
0.9477E+00	0.1856E-02	0.8921E-03	0.6827E+00	0.1573E+00	0.2763E+02	0.3315E+02	0.1368E+05	2	498	250
(REX=	0.1561E+06),(VISC*DUDX/U*U=	0.7283E-05),(D1*U/VISC=	0.3057E+03),(D2*U/VISC=	0.1470E+03)						
0.9532E+00	0.1854E-02	0.8919E-03	0.6871E+00	0.1591E+00	0.2781E+02	0.3354E+02	0.1381E+05	2	500	251
(REX=	0.1581E+06),(VISC*DUDX/U*U=	0.7271E-05),(D1*U/VISC=	0.3074E+03),(D2*U/VISC=	0.1479E+03)						
0.9587E+00	0.1851E-02	0.8917E-03	0.6947E+00	0.1612E+00	0.2800E+02	0.3399E+02	0.1396E+05	2	502	252
(REX=	0.1601E+06),(VISC*DUDX/U*U=	0.7272E-05),(D1*U/VISC=	0.3091E+03),(D2*U/VISC=	0.1489E+03)						
0.9642E+00	0.1849E-02	0.8915E-03	0.7036E+00	0.1636E+00	0.2819E+02	0.3453E+02	0.1411E+05	2	504	253
(REX=	0.1621E+06),(VISC*DUDX/U*U=	0.7288E-05),(D1*U/VISC=	0.3107E+03),(D2*U/VISC=	0.1498E+03)						
0.9697E+00	0.1846E-02	0.8912E-03	0.7137E+00	0.1664E+00	0.2838E+02	0.3514E+02	0.1427E+05	2	506	254
(REX=	0.1641E+06),(VISC*DUDX/U*U=	0.7317E-05),(D1*U/VISC=	0.3123E+03),(D2*U/VISC=	0.1508E+03)						
0.9752E+00	0.1842E-02	0.8909E-03	0.7249E+00	0.1695E+00	0.2857E+02	0.3582E+02	0.1445E+05	2	508	255
(REX=	0.1662E+06),(VISC*DUDX/U*U=	0.7357E-05),(D1*U/VISC=	0.3139E+03),(D2*U/VISC=	0.1518E+03)						
********** NEXT LINE FOR TAP NO= 18										
0.9807E+00	0.1839E-02	0.8906E-03	0.7372E+00	0.1730E+00	0.2877E+02	0.3657E+02	0.1464E+05	2	510	256
(REX=	0.1683E+06),(VISC*DUDX/U*U=	0.7409E-05),(D1*U/VISC=	0.3154E+03),(D2*U/VISC=	0.1528E+03)						
0.9862E+00	0.1835E-02	0.8901E-03	0.7498E+00	0.1765E+00	0.2898E+02	0.3736E+02	0.1485E+05	2	512	257
(REX=	0.1704E+06),(VISC*DUDX/U*U=	0.7463E-05),(D1*U/VISC=	0.3170E+03),(D2*U/VISC=	0.1538E+03)						
0.9917E+00	0.1830E-02	0.8856E-03	0.7616E+00	0.1800E+00	0.2918E+02	0.3814E+02	0.1506E+05	2	514	258
(REX=	0.1726E+06),(VISC*DUDX/U*U=	0.7510E-05),(D1*U/VISC=	0.3185E+03),(D2*U/VISC=	0.1548E+03)						
0.9972E+00	0.1825E-02	0.8890E-03	0.7728E+00	0.1833E+00	0.2939E+02	0.3890E+02	0.1528E+05	2	516	259
(REX=	0.1748E+06),(VISC*DUDX/U*U=	0.7550E-05),(D1*U/VISC=	0.3199E+03),(D2*U/VISC=	0.1558E+03)						
0.1003E+01	0.1820E-02	0.8882E-03	0.7832E+00	0.1865E+00	0.2961E+02	0.3965E+02	0.1551E+05	2	518	260
(REX=	0.1770E+06),(VISC*DUDX/U*U=	0.7585E-05),(D1*U/VISC=	0.3213E+03),(D2*U/VISC=	0.1568E+03)						
0.1008E+01	0.1815E-02	0.8873E-03	0.7931E+00	0.1896E+00	0.2983E+02	0.4039E+02	0.1574E+05	2	520	261
(REX=	0.1793E+06),(VISC*DUDX/U*U=	0.7613E-05),(D1*U/VISC=	0.3228E+03),(D2*U/VISC=	0.1578E+03)						
0.1014E+01	0.1809E-02	0.8863E-03	0.8024E+00	0.1926E+00	0.3005E+02	0.4112E+02	0.1597E+05	2	522	262
(REX=	0.1817E+06),(VISC*DUDX/U*U=	0.7636E-05),(D1*U/VISC=	0.3242E+03),(D2*U/VISC=	0.1588E+03)						
0.1019E+01	0.1803E-02	0.8852E-03	0.8111E+00	0.1955E+00	0.3028E+02	0.4184E+02	0.1621E+05	2	524	263
(REX=	0.1840E+06),(VISC*DUDX/U*U=	0.7653E-05),(D1*U/VISC=	0.3256E+03),(D2*U/VISC=	0.1598E+03)						
0.1025E+01	0.1797E-02	0.8840E-03	0.8192E+00	0.1983E+00	0.3051E+02	0.4255E+02	0.1645E+05	2	526	264
(REX=	0.1864E+06),(VISC*DUDX/U*U=	0.7664E-05),(D1*U/VISC=	0.3269E+03),(D2*U/VISC=	0.1609E+03)						
0.1030E+01	0.1791E-02	0.8827E-03	0.8269E+00	0.2009E+00	0.3075E+02	0.4324E+02	0.1671E+05	2	528	265
(REX=	0.1889E+06),(VISC*DUDX/U*U=	0.7671E-05),(D1*U/VISC=	0.3283E+03),(D2*U/VISC=	0.1618E+03)						
0.1036E+01	0.1784E-02	0.8814E-03	0.8340E+00	0.2035E+00	0.3099E+02	0.4393E+02	0.1695E+05	2	530	266
(REX=	0.1914E+06),(VISC*DUDX/U*U=	0.7672E-05),(D1*U/VISC=	0.3297E+03),(D2*U/VISC=	0.1629E+03)						
0.1041E+01	0.1778E-02	0.8799E-03	0.8407E+00	0.2059E+00	0.3123E+02	0.4460E+02	0.1721E+05	2	532	267
(REX=	0.1939E+06),(VISC*DUDX/U*U=	0.7669E-05),(D1*U/VISC=	0.3311E+03),(D2*U/VISC=	0.1639E+03)						
0.1047E+01	0.1771E-02	0.8784E-03	0.8468E+00	0.2082E+00	0.3148E+02	0.4526E+02	0.1747E+05	2	534	268
(REX=	0.1964E+06),(VISC*DUDX/U*U=	0.7661E-05),(D1*U/VISC=	0.3325E+03),(D2*U/VISC=	0.1649E+03)						

L 3 (L=1,2,3,FOR FI PL,CYL,2D STG FLOW)

X-FT	DPLT-TRFT	MMT-TRFT	DEL2U	DZL2U	UFREE	DUDXT	DUDYW	K	MED	
NOTE** X=DIST FRM STG PT,** DPLT=DISPLACEMENT THK(FT),** MMT=MOMENTUM THK(FT)										
DEL2U=DISPL**2*DUDX/VISC(NON DIM),** DZL2U=MMT**2*DUDX/VISC(NON DIM),** UFREE=FREE ST VEL(FPS),**										
DUDXT=VEL GRD ALONG X(FT/S/FT),** DUDYW=NORMAL VEL GRDT(FT/S/FT)***,K=NO IF INTGTN STEPS										
0.1052E+01	0.1765E-02	0.8768E-03	0.8526E+00	0.2104E+00	0.3173E+02	0.4591E+02	0.1773E+05	2	536	269
(REX= 0.1990E+06),(VISC*DUDX/U*U= 0.7849E-05),(D1*U/VISC= 0.3339E+03),(D2*U/VISC= 0.1659E+03)										
0.1058E+01	0.1758E-02	0.8751E-03	0.8579E+00	0.2125E+00	0.3198E+02	0.4655E+02	0.1799E+05	2	538	270
(REX= 0.2017E+06),(VISC*DUDX/U*U= 0.7632E-05),(D1*U/VISC= 0.3353E+03),(D2*U/VISC= 0.1669E+03)										
********** NEXT LINE FOR TAP NO= 19										
0.1063E+01	0.1751E-02	0.8734E-03	0.8627E+00	0.2146E+00	0.3224E+02	0.4717E+02	0.1827E+05	2	540	271
(REX= 0.2044E+06),(VISC*DUDX/U*U= 0.7612E-05),(D1*U/VISC= 0.3367E+03),(D2*U/VISC= 0.1679E+03)										
0.1069E+01	0.1745E-02	0.8715E-03	0.8671E+00	0.2164E+00	0.3250E+02	0.4778E+02	0.1851E+05	2	542	272
(REX= 0.2071E+06),(VISC*DUDX/U*U= 0.7587E-05),(D1*U/VISC= 0.3381E+03),(D2*U/VISC= 0.1689E+03)										
0.1074E+01	0.1738E-02	0.8657E-03	0.8709E+00	0.2181E+00	0.3276E+02	0.4836E+02	0.1878E+05	2	544	273
(REX= 0.2098E+06),(VISC*DUDX/U*U= 0.7557E-05),(D1*U/VISC= 0.3395E+03),(D2*U/VISC= 0.1699E+03)										
0.1079E+01	0.1731E-02	0.8677E-03	0.8741E+00	0.2197E+00	0.3303E+02	0.4892E+02	0.1905E+05	2	546	274
(REX= 0.2126E+06),(VISC*DUDX/U*U= 0.7522E-05),(D1*U/VISC= 0.3409E+03),(D2*U/VISC= 0.1709E+03)										
0.1085E+01	0.1724E-02	0.8658E-03	0.8767E+00	0.2212E+00	0.3330E+02	0.4946E+02	0.1932E+05	2	548	275
(REX= 0.2154E+06),(VISC*DUDX/U*U= 0.7482E-05),(D1*U/VISC= 0.3423E+03),(D2*U/VISC= 0.1719E+03)										
0.1090E+01	0.1717E-02	0.8638E-03	0.8789E+00	0.2223E+00	0.3357E+02	0.4997E+02	0.1960E+05	2	550	276
(REX= 0.2183E+06),(VISC*DUDX/U*U= 0.7437E-05),(D1*U/VISC= 0.3438E+03),(D2*U/VISC= 0.1729E+03)										
0.1096E+01	0.1711E-02	0.8617E-03	0.8806E+00	0.2234E+00	0.3384E+02	0.5046E+02	0.1987E+05	2	552	277
(REX= 0.2212E+06),(VISC*DUDX/U*U= 0.7388E-05),(D1*U/VISC= 0.3452E+03),(D2*U/VISC= 0.1739E+03)										
0.1101E+01	0.1704E-02	0.8596E-03	0.8817E+00	0.2244E+00	0.3412E+02	0.5092E+02	0.2014E+05	2	554	278
(REX= 0.2241E+06),(VISC*DUDX/U*U= 0.7335E-05),(D1*U/VISC= 0.3467E+03),(D2*U/VISC= 0.1749E+03)										
0.1107E+01	0.1698E-02	0.8575E-03	0.8825E+00	0.2252E+00	0.3440E+02	0.5136E+02	0.2041E+05	2	556	279
(REX= 0.2270E+06),(VISC*DUDX/U*U= 0.7278E-05),(D1*U/VISC= 0.3482E+03),(D2*U/VISC= 0.1759E+03)										
0.1112E+01	0.1691E-02	0.8554E-03	0.8828E+00	0.2259E+00	0.3468E+02	0.5177E+02	0.2069E+05	2	558	280
(REX= 0.2300E+06),(VISC*DUDX/U*U= 0.7218E-05),(D1*U/VISC= 0.3497E+03),(D2*U/VISC= 0.1769E+03)										
0.1118E+01	0.1685E-02	0.8532E-03	0.8827E+00	0.2264E+00	0.3497E+02	0.5216E+02	0.2096E+05	2	560	281
(REX= 0.2331E+06),(VISC*DUDX/U*U= 0.7155E-05),(D1*U/VISC= 0.3512E+03),(D2*U/VISC= 0.1779E+03)										
0.1123E+01	0.1678E-02	0.8510E-03	0.8823E+00	0.2269E+00	0.3525E+02	0.5253E+02	0.2123E+05	2	562	282
(REX= 0.2361E+06),(VISC*DUDX/U*U= 0.7089E-05),(D1*U/VISC= 0.3528E+03),(D2*U/VISC= 0.1789E+03)										
0.1129E+01	0.1672E-02	0.8489E-03	0.8815E+00	0.2272E+00	0.3554E+02	0.5287E+02	0.2150E+05	2	564	283
(REX= 0.2392E+06),(VISC*DUDX/U*U= 0.7020E-05),(D1*U/VISC= 0.3544E+03),(D2*U/VISC= 0.1799E+03)										
0.1134E+01	0.1666E-02	0.8467E-03	0.8803E+00	0.2274E+00	0.3583E+02	0.5319E+02	0.2177E+05	2	566	284
(REX= 0.2423E+06),(VISC*DUDX/U*U= 0.6948E-05),(D1*U/VISC= 0.3559E+03),(D2*U/VISC= 0.1809E+03)										
0.1140E+01	0.1660E-02	0.8445E-03	0.8788E+00	0.2275E+00	0.3612E+02	0.5349E+02	0.2204E+05	2	568	285
(REX= 0.2455E+06),(VISC*DUDX/U*U= 0.6874E-05),(D1*U/VISC= 0.3576E+03),(D2*U/VISC= 0.1819E+03)										
********** NEXT LINE FOR TAP NO= 20										
0.1145E+01	0.1654E-02	0.8423E-03	0.8771E+00	0.2274E+00	0.3642E+02	0.5376E+02	0.2230E+05	2	570	286
(REX= 0.2487E+06),(VISC*DUDX/U*U= 0.6798E-05),(D1*U/VISC= 0.3592E+03),(D2*U/VISC= 0.1829E+03)										
0.1151E+01	0.1648E-02	0.8402E-03	0.8749E+00	0.2273E+00	0.3671E+02	0.5400E+02	0.2260E+05	2	572	287
(REX= 0.2519E+06),(VISC*DUDX/U*U= 0.6718E-05),(D1*U/VISC= 0.3609E+03),(D2*U/VISC= 0.1839E+03)										
0.1156E+01	0.1643E-02	0.8381E-03	0.8722E+00	0.2271E+00	0.3701E+02	0.5420E+02	0.2286E+05	2	574	288
(REX= 0.2552E+06),(VISC*DUDX/U*U= 0.6634E-05),(D1*U/VISC= 0.3626E+03),(D2*U/VISC= 0.1850E+03)										
0.1162E+01	0.1637E-02	0.8360E-03	0.8690E+00	0.2265E+00	0.3731E+02	0.5436E+02	0.2312E+05	2	576	289
(REX= 0.2585E+06),(VISC*DUDX/U*U= 0.6547E-05),(D1*U/VISC= 0.3643E+03),(D2*U/VISC= 0.1860E+03)										

L 3 (L=1,2,3,FOR FL PL,CYL,2D STG FLOW)

X-FT	DPLT-THFT	MMT-THFT	DEL2U	DZL2U	UFREE	DUDXT	DUDYW	K	MED	
NOTE** X=DIST FRM STG PT,** DPLT=DISPLACEMENT THK(FT),** MMT=MOMENTUM THK(FT) DEL2U=DISPL**2*DUDX/VISC(NON DIM),** DZL2U=MMT**2*DUDX/VISC(NON DIM),** UFREE=FREE ST VEL(FPS),** DUDXT=VEL GRD ALONG X(FT/S/FT),** DUDYW=NORMAL VEL GRDT(FT/S/FT)***,K=NO IF INTGTN STEPS										
0.1284E+01	0.1559E-02	0.8006E-03	0.8390E+00	0.2212E+00	0.4291E+02	0.5789E+02	0.2820E+05	2	321	311
(REX= 0.3360E+06),(VISC*DUDX/U*U= 0.5036E-05),(D1*U/VISC= 0.4082E+03),(D2*U/VISC= 0.2096E+03)										
0.1289E+01	0.1556E-02	0.8001E-03	0.8558E+00	0.2264E+00	0.4423E+02	0.5930E+02	0.2860E+05	2	323	312
(REX= 0.3460E+06),(VISC*DUDX/U*U= 0.5084E-05),(D1*U/VISC= 0.4103E+03),(D2*U/VISC= 0.2110E+03)										
0.1295E+01	0.1552E-02	0.7997E-03	0.8745E+00	0.2322E+00	0.4456E+02	0.6089E+02	0.2904E+05	2	325	313
(REX= 0.3440E+06),(VISC*DUDX/U*U= 0.5142E-05),(D1*U/VISC= 0.4124E+03),(D2*U/VISC= 0.2125E+03)										
0.1300E+01	0.1548E-02	0.7993E-03	0.8950E+00	0.2387E+00	0.4491E+02	0.6264E+02	0.2951E+05	2	327	314
(REX= 0.3481E+06),(VISC*DUDX/U*U= 0.5210E-05),(D1*U/VISC= 0.4145E+03),(D2*U/VISC= 0.2140E+03)										
0.1306E+01	0.1543E-02	0.7990E-03	0.9172E+00	0.2458E+00	0.4526E+02	0.6457E+02	0.3002E+05	2	329	315
(REX= 0.3524E+06),(VISC*DUDX/U*U= 0.5287E-05),(D1*U/VISC= 0.4165E+03),(D2*U/VISC= 0.2156E+03)										
********** NEXT LINE FOR TAP NO= 22										
0.1311E+01	0.1539E-02	0.7987E-03	0.9411E+00	0.2536E+00	0.4562E+02	0.6666E+02	0.3057E+05	2	331	316
(REX= 0.3567E+06),(VISC*DUDX/U*U= 0.5371E-05),(D1*U/VISC= 0.4186E+03),(D2*U/VISC= 0.2173E+03)										
0.1317E+01	0.1534E-02	0.7983E-03	0.9645E+00	0.2614E+00	0.4600E+02	0.6878E+02	0.3116E+05	2	333	317
(REX= 0.3612E+06),(VISC*DUDX/U*U= 0.5452E-05),(D1*U/VISC= 0.4206E+03),(D2*U/VISC= 0.2190E+03)										
0.1322E+01	0.1528E-02	0.7979E-03	0.9849E+00	0.2686E+00	0.4639E+02	0.7075E+02	0.3178E+05	2	335	318
(REX= 0.3658E+06),(VISC*DUDX/U*U= 0.5514E-05),(D1*U/VISC= 0.4226E+03),(D2*U/VISC= 0.2207E+03)										
0.1328E+01	0.1522E-02	0.7975E-03	0.1003E+01	0.2752E+00	0.4679E+02	0.7257E+02	0.3241E+05	2	337	319
(REX= 0.3705E+06),(VISC*DUDX/U*U= 0.5559E-05),(D1*U/VISC= 0.4247E+03),(D2*U/VISC= 0.2225E+03)										
0.1334E+01	0.1516E-02	0.7971E-03	0.1018E+01	0.2813E+00	0.4720E+02	0.7424E+02	0.3304E+05	2	339	320
(REX= 0.3753E+06),(VISC*DUDX/U*U= 0.5589E-05),(D1*U/VISC= 0.4268E+03),(D2*U/VISC= 0.2243E+03)										
0.1339E+01	0.1511E-02	0.7967E-03	0.1031E+01	0.2867E+00	0.4762E+02	0.7575E+02	0.3367E+05	2	341	321
(REX= 0.3802E+06),(VISC*DUDX/U*U= 0.5603E-05),(D1*U/VISC= 0.4289E+03),(D2*U/VISC= 0.2262E+03)										
0.1345E+01	0.1505E-02	0.7963E-03	0.1041E+01	0.2916E+00	0.4804E+02	0.7712E+02	0.3430E+05	2	343	322
(REX= 0.3852E+06),(VISC*DUDX/U*U= 0.5603E-05),(D1*U/VISC= 0.4311E+03),(D2*U/VISC= 0.2281E+03)										
0.1350E+01	0.1499E-02	0.7960E-03	0.1050E+01	0.2955E+00	0.4848E+02	0.7834E+02	0.3492E+05	2	345	323
(REX= 0.3903E+06),(VISC*DUDX/U*U= 0.5590E-05),(D1*U/VISC= 0.4333E+03),(D2*U/VISC= 0.2301E+03)										
0.1356E+01	0.1494E-02	0.7956E-03	0.1056E+01	0.2997E+00	0.4892E+02	0.7940E+02	0.3554E+05	2	347	324
(REX= 0.3955E+06),(VISC*DUDX/U*U= 0.5565E-05),(D1*U/VISC= 0.4357E+03),(D2*U/VISC= 0.2321E+03)										
0.1361E+01	0.1488E-02	0.7953E-03	0.1061E+01	0.3030E+00	0.4936E+02	0.8032E+02	0.3614E+05	2	349	325
(REX= 0.4008E+06),(VISC*DUDX/U*U= 0.5528E-05),(D1*U/VISC= 0.4381E+03),(D2*U/VISC= 0.2341E+03)										
0.1367E+01	0.1483E-02	0.7951E-03	0.1064E+01	0.3057E+00	0.4982E+02	0.8109E+02	0.3672E+05	2	351	326
(REX= 0.4061E+06),(VISC*DUDX/U*U= 0.5480E-05),(D1*U/VISC= 0.4406E+03),(D2*U/VISC= 0.2362E+03)										
0.1373E+01	0.1478E-02	0.7950E-03	0.1065E+01	0.3079E+00	0.5027E+02	0.8170E+02	0.3729E+05	2	353	327
(REX= 0.4115E+06),(VISC*DUDX/U*U= 0.5422E-05),(D1*U/VISC= 0.4432E+03),(D2*U/VISC= 0.2383E+03)										
0.1378E+01	0.1474E-02	0.7949E-03	0.1065E+01	0.3096E+00	0.5073E+02	0.8211E+02	0.3786E+05	2	355	328
(REX= 0.4169E+06),(VISC*DUDX/U*U= 0.5355E-05),(D1*U/VISC= 0.4459E+03),(D2*U/VISC= 0.2404E+03)										
0.1384E+01	0.1470E-02	0.7950E-03	0.1063E+01	0.3108E+00	0.5119E+02	0.8248E+02	0.3839E+05	2	357	329
(REX= 0.4224E+06),(VISC*DUDX/U*U= 0.5279E-05),(D1*U/VISC= 0.4487E+03),(D2*U/VISC= 0.2426E+03)										
0.1389E+01	0.1466E-02	0.7952E-03	0.1060E+01	0.3116E+00	0.5165E+02	0.8264E+02	0.3891E+05	2	359	330
(REX= 0.4279E+06),(VISC*DUDX/U*U= 0.5196E-05),(D1*U/VISC= 0.4516E+03),(D2*U/VISC= 0.2449E+03)										
********** NEXT LINE FOR TAP NO= 23										
0.1395E+01	0.1463E-02	0.7955E-03	0.1055E+01	0.3119E+00	0.5211E+02	0.8266E+02	0.3940E+05	2	361	331
(REX= 0.4334E+06),(VISC*DUDX/U*U= 0.5105E-05),(D1*U/VISC= 0.4546E+03),(D2*U/VISC= 0.2472E+03)										

L 3 (L=1,2,3,FOR FL PL,CYL,2L STG FLOW)

X-FT	DPLT-TKFT	MMT-TKFT	DEL2U	DZL2U	UFREE	DUDXT	DUDYW	K	MED	
NOTE** X=DIST FRM STG PT,** DPLT=DISPLACEMENT THK(FT),** MMT=MOMENTUM THK(FT) DEL2U=DISPL**2*DUDX/VISC(NON DIM),** DZL2U=MMT**2*DUDX/VISC(NON DIM),** UFREE=FREE ST VEL(FPS),** DUDXT=VEL GRD ALONG X(FT/S/FT),** DUDYW=NORMAL VEL GRDT(FT/S/FT)**,K=NO IF INTGTN STEPS										
0.1401E+01	0.1460E-02	0.7960E-03	0.1049E+01	0.3115E+00	0.5258E+02	0.8256E+02	0.4017E+05	2	363	332
(REX=	0.4391E+06),(VISC*DUDX/U*U=	0.5009E-05),(D1*U/VISC=	0.4577E+03),(D2*U/VISC=	0.2495E+03)						
0.1406E+01	0.1457E-02	0.7966E-03	0.1043E+01	0.3118E+00	0.5304E+02	0.8240E+02	0.4057E+05	2	365	333
(REX=	0.4448E+06),(VISC*DUDX/U*U=	0.4912E-05),(D1*U/VISC=	0.4609E+03),(D2*U/VISC=	0.2519E+03)						
0.1412E+01	0.1455E-02	0.7973E-03	0.1037E+01	0.3115E+00	0.5350E+02	0.8218E+02	0.4111E+05	2	367	334
(REX=	0.4504E+06),(VISC*DUDX/U*U=	0.4814E-05),(D1*U/VISC=	0.4642E+03),(D2*U/VISC=	0.2544E+03)						
0.1418E+01	0.1453E-02	0.7982E-03	0.1031E+01	0.3111E+00	0.5397E+02	0.8188E+02	0.4155E+05	2	369	335
(REX=	0.4561E+06),(VISC*DUDX/U*U=	0.4715E-05),(D1*U/VISC=	0.4677E+03),(D2*U/VISC=	0.2569E+03)						
0.1423E+01	0.1452E-02	0.7992E-03	0.1025E+01	0.3105E+00	0.5443E+02	0.8153E+02	0.4188E+05	2	371	336
(REX=	0.4619E+06),(VISC*DUDX/U*U=	0.4616E-05),(D1*U/VISC=	0.4712E+03),(D2*U/VISC=	0.2594E+03)						
0.1429E+01	0.1451E-02	0.8003E-03	0.1018E+01	0.3098E+00	0.5488E+02	0.8110E+02	0.4235E+05	2	373	337
(REX=	0.4676E+06),(VISC*DUDX/U*U=	0.4515E-05),(D1*U/VISC=	0.4749E+03),(D2*U/VISC=	0.2619E+03)						
0.1434E+01	0.1450E-02	0.8016E-03	0.1011E+01	0.3089E+00	0.5534E+02	0.8061E+02	0.4272E+05	2	375	338
(REX=	0.4733E+06),(VISC*DUDX/U*U=	0.4415E-05),(D1*U/VISC=	0.4786E+03),(D2*U/VISC=	0.2645E+03)						
0.1440E+01	0.1450E-02	0.8031E-03	0.1004E+01	0.3079E+00	0.5579E+02	0.8006E+02	0.4298E+05	2	377	339
(REX=	0.4791E+06),(VISC*DUDX/U*U=	0.4313E-05),(D1*U/VISC=	0.4825E+03),(D2*U/VISC=	0.2672E+03)						
0.1446E+01	0.1450E-02	0.8047E-03	0.9966E+00	0.3067E+00	0.5624E+02	0.7944E+02	0.4340E+05	2	379	340
(REX=	0.4848E+06),(VISC*DUDX/U*U=	0.4212E-05),(D1*U/VISC=	0.4864E+03),(D2*U/VISC=	0.2699E+03)						
0.1451E+01	0.1451E-02	0.8065E-03	0.9888E+00	0.3054E+00	0.5669E+02	0.7875E+02	0.4371E+05	2	381	341
(REX=	0.4906E+06),(VISC*DUDX/U*U=	0.4110E-05),(D1*U/VISC=	0.4905E+03),(D2*U/VISC=	0.2726E+03)						
0.1457E+01	0.1452E-02	0.8084E-03	0.9807E+00	0.3041E+00	0.5713E+02	0.7800E+02	0.4392E+05	2	383	342
(REX=	0.4963E+06),(VISC*DUDX/U*U=	0.4008E-05),(D1*U/VISC=	0.4946E+03),(D2*U/VISC=	0.2754E+03)						
0.1463E+01	0.1453E-02	0.8106E-03	0.9722E+00	0.3024E+00	0.5757E+02	0.7718E+02	0.4427E+05	2	385	343
(REX=	0.5020E+06),(VISC*DUDX/U*U=	0.3906E-05),(D1*U/VISC=	0.4989E+03),(D2*U/VISC=	0.2782E+03)						
0.1468E+01	0.1455E-02	0.8129E-03	0.9634E+00	0.3006E+00	0.5800E+02	0.7630E+02	0.4452E+05	2	387	344
(REX=	0.5078E+06),(VISC*DUDX/U*U=	0.3804E-05),(D1*U/VISC=	0.5032E+03),(D2*U/VISC=	0.2811E+03)						
0.1474E+01	0.1457E-02	0.8153E-03	0.9542E+00	0.2987E+00	0.5842E+02	0.7535E+02	0.4466E+05	2	389	345
(REX=	0.5135E+06),(VISC*DUDX/U*U=	0.3702E-05),(D1*U/VISC=	0.5077E+03),(D2*U/VISC=	0.2840E+03)						
********** NEXT LINE FOR TAP NO= 24										
0.1479E+01	0.1460E-02	0.8179E-03	0.9446E+00	0.2966E+00	0.5885E+02	0.7434E+02	0.4494E+05	2	391	346
(REX=	0.5191E+06),(VISC*DUDX/U*U=	0.3600E-05),(D1*U/VISC=	0.5122E+03),(D2*U/VISC=	0.2870E+03)						
0.1485E+01	0.1463E-02	0.8207E-03	0.9364E+00	0.2947E+00	0.5926E+02	0.7337E+02	0.4486E+05	2	393	347
(REX=	0.5247E+06),(VISC*DUDX/U*U=	0.3504E-05),(D1*U/VISC=	0.5169E+03),(D2*U/VISC=	0.2900E+03)						
0.1491E+01	0.1466E-02	0.8236E-03	0.9303E+00	0.2935E+00	0.5967E+02	0.7256E+02	0.4500E+05	2	395	348
(REX=	0.5303E+06),(VISC*DUDX/U*U=	0.3418E-05),(D1*U/VISC=	0.5217E+03),(D2*U/VISC=	0.2930E+03)						
0.1496E+01	0.1470E-02	0.8268E-03	0.9263E+00	0.2931E+00	0.6007E+02	0.7190E+02	0.4516E+05	2	397	349
(REX=	0.5359E+06),(VISC*DUDX/U*U=	0.3342E-05),(D1*U/VISC=	0.5265E+03),(D2*U/VISC=	0.2961E+03)						
0.1502E+01	0.1474E-02	0.8301E-03	0.9244E+00	0.2933E+00	0.6047E+02	0.7139E+02	0.4534E+05	2	399	350
(REX=	0.5415E+06),(VISC*DUDX/U*U=	0.3275E-05),(D1*U/VISC=	0.5313E+03),(D2*U/VISC=	0.2993E+03)						
0.1507E+01	0.1477E-02	0.8335E-03	0.9245E+00	0.2943E+00	0.6086E+02	0.7104E+02	0.4553E+05	2	401	351
(REX=	0.5471E+06),(VISC*DUDX/U*U=	0.3216E-05),(D1*U/VISC=	0.5362E+03),(D2*U/VISC=	0.3025E+03)						
0.1513E+01	0.1481E-02	0.8370E-03	0.9267E+00	0.2959E+00	0.6126E+02	0.7083E+02	0.4575E+05	2	403	352
(REX=	0.5527E+06),(VISC*DUDX/U*U=	0.3165E-05),(D1*U/VISC=	0.5411E+03),(D2*U/VISC=	0.3057E+03)						

L 3 (L=1,2,3,FOR FL PL,CYL,2D STG FLOW)

X-FT	DPLT-THKFT	MMT-THKFT	DEL2U	DZL2U	UFREE	DUDXT	DUDYW	K	MED	
NOTE** X=DIST FRM STG PT,** DPLT=DISPLACEMENT THK(FT),** MMT=MOMENTUM THK(FT)										
DEL2U=DISPL**2*DUDX/VISC(NON DIM),** DZL2U=MMT**2*DUDX/VISC(NON DIM),** UFREE=FREE ST VEL(FPS),**										
DUDXT=VEL GRD ALONG X(FT/S/FT),** DUDYW=NORMAL VEL GRDT(FT/S/FT)***,K=NO IF INTGTN STEPS										
0.1519E+01	0.1485E-02	0.8406E-03	0.9310E+00	0.2982E+00	0.6166E+02	0.7077E+02	0.4598E+05	2	405	353
(REX= 0.5583E+06),(VISC*DUDX/U*U= 0.3122E-05),(D1*U/VISC= 0.5460E+03),(D2*U/VISC= 0.3090E+03)										
0.1524E+01	0.1489E-02	0.8443E-03	0.9372E+00	0.3012E+00	0.6205E+02	0.7087E+02	0.4624E+05	2	407	354
(REX= 0.5639E+06),(VISC*DUDX/U*U= 0.3087E-05),(D1*U/VISC= 0.5510E+03),(D2*U/VISC= 0.3124E+03)										
0.1530E+01	0.1493E-02	0.8480E-03	0.9434E+00	0.3049E+00	0.6245E+02	0.7112E+02	0.4652E+05	2	409	355
(REX= 0.5696E+06),(VISC*DUDX/U*U= 0.3058E-05),(D1*U/VISC= 0.5560E+03),(D2*U/VISC= 0.3158E+03)										
0.1535E+01	0.1497E-02	0.8518E-03	0.9555E+00	0.3094E+00	0.6284E+02	0.7151E+02	0.4683E+05	2	411	356
(REX= 0.5753E+06),(VISC*DUDX/U*U= 0.3037E-05),(D1*U/VISC= 0.5609E+03),(D2*U/VISC= 0.3192E+03)										
0.1541E+01	0.1501E-02	0.8556E-03	0.9676E+00	0.3146E+00	0.6324E+02	0.7206E+02	0.4717E+05	2	413	357
(REX= 0.5811E+06),(VISC*DUDX/U*U= 0.3021E-05),(D1*U/VISC= 0.5659E+03),(D2*U/VISC= 0.3227E+03)										
0.1546E+01	0.1504E-02	0.8594E-03	0.9817E+00	0.3205E+00	0.6365E+02	0.7276E+02	0.4754E+05	2	415	358
(REX= 0.5869E+06),(VISC*DUDX/U*U= 0.3012E-05),(D1*U/VISC= 0.5709E+03),(D2*U/VISC= 0.3262E+03)										
0.1552E+01	0.1508E-02	0.8632E-03	0.9977E+00	0.3271E+00	0.6406E+02	0.7361E+02	0.4794E+05	2	417	359
(REX= 0.5928E+06),(VISC*DUDX/U*U= 0.3009E-05),(D1*U/VISC= 0.5758E+03),(D2*U/VISC= 0.3297E+03)										
0.1558E+01	0.1511E-02	0.8671E-03	0.1016E+01	0.3345E+00	0.6447E+02	0.7461E+02	0.4838E+05	2	419	360
(REX= 0.5988E+06),(VISC*DUDX/U*U= 0.3011E-05),(D1*U/VISC= 0.5808E+03),(D2*U/VISC= 0.3333E+03)										
********** NEXT LINE FOR IAP NO= 25										
0.1563E+01	0.1514E-02	0.8709E-03	0.1035E+01	0.3426E+00	0.6489E+02	0.7577E+02	0.4886E+05	2	421	361
(REX= 0.6048E+06),(VISC*DUDX/U*U= 0.3018E-05),(D1*U/VISC= 0.5857E+03),(D2*U/VISC= 0.3369E+03)										
0.1569E+01	0.1517E-02	0.8747E-03	0.1055E+01	0.3508E+00	0.6531E+02	0.7689E+02	0.4934E+05	2	423	362
(REX= 0.6108E+06),(VISC*DUDX/U*U= 0.3023E-05),(D1*U/VISC= 0.5906E+03),(D2*U/VISC= 0.3406E+03)										
0.1574E+01	0.1519E-02	0.8785E-03	0.1071E+01	0.3582E+00	0.6573E+02	0.7783E+02	0.4986E+05	2	425	363
(REX= 0.6169E+06),(VISC*DUDX/U*U= 0.3021E-05),(D1*U/VISC= 0.5955E+03),(D2*U/VISC= 0.3443E+03)										
0.1580E+01	0.1522E-02	0.8823E-03	0.1086E+01	0.3648E+00	0.6616E+02	0.7860E+02	0.5038E+05	2	427	364
(REX= 0.6231E+06),(VISC*DUDX/U*U= 0.3011E-05),(D1*U/VISC= 0.6004E+03),(D2*U/VISC= 0.3480E+03)										
0.1585E+01	0.1525E-02	0.8860E-03	0.1097E+01	0.3706E+00	0.6659E+02	0.7918E+02	0.5088E+05	2	429	365
(REX= 0.6294E+06),(VISC*DUDX/U*U= 0.2995E-05),(D1*U/VISC= 0.6054E+03),(D2*U/VISC= 0.3518E+03)										
0.1591E+01	0.1527E-02	0.8897E-03	0.1107E+01	0.3757E+00	0.6703E+02	0.7959E+02	0.5135E+05	2	431	366
(REX= 0.6357E+06),(VISC*DUDX/U*U= 0.2971E-05),(D1*U/VISC= 0.6103E+03),(D2*U/VISC= 0.3556E+03)										
0.1596E+01	0.1530E-02	0.8934E-03	0.1114E+01	0.3799E+00	0.6746E+02	0.7982E+02	0.5182E+05	2	433	367
(REX= 0.6420E+06),(VISC*DUDX/U*U= 0.2941E-05),(D1*U/VISC= 0.6153E+03),(D2*U/VISC= 0.3594E+03)										
0.1602E+01	0.1532E-02	0.8971E-03	0.1118E+01	0.3833E+00	0.6790E+02	0.7988E+02	0.5226E+05	2	435	368
(REX= 0.6484E+06),(VISC*DUDX/U*U= 0.2905E-05),(D1*U/VISC= 0.6204E+03),(D2*U/VISC= 0.3632E+03)										
0.1607E+01	0.1535E-02	0.9008E-03	0.1121E+01	0.3859E+00	0.6834E+02	0.7975E+02	0.5267E+05	2	437	369
(REX= 0.6549E+06),(VISC*DUDX/U*U= 0.2864E-05),(D1*U/VISC= 0.6256E+03),(D2*U/VISC= 0.3671E+03)										
0.1612E+01	0.1538E-02	0.9046E-03	0.1121E+01	0.3877E+00	0.6878E+02	0.7945E+02	0.5302E+05	2	439	370
(REX= 0.6613E+06),(VISC*DUDX/U*U= 0.2817E-05),(D1*U/VISC= 0.6308E+03),(D2*U/VISC= 0.3710E+03)										
0.1618E+01	0.1541E-02	0.9084E-03	0.1119E+01	0.3886E+00	0.6921E+02	0.7897E+02	0.5340E+05	2	441	371
(REX= 0.6677E+06),(VISC*DUDX/U*U= 0.2765E-05),(D1*U/VISC= 0.6361E+03),(D2*U/VISC= 0.3749E+03)										
0.1623E+01	0.1545E-02	0.9123E-03	0.1114E+01	0.3887E+00	0.6964E+02	0.7831E+02	0.5371E+05	2	443	372
(REX= 0.6742E+06),(VISC*DUDX/U*U= 0.2708E-05),(D1*U/VISC= 0.6415E+03),(D2*U/VISC= 0.3789E+03)										
0.1629E+01	0.1548E-02	0.9163E-03	0.1106E+01	0.3879E+00	0.7007E+02	0.7748E+02	0.5398E+05	2	445	373
(REX= 0.6806E+06),(VISC*DUDX/U*U= 0.2646E-05),(D1*U/VISC= 0.6470E+03),(D2*U/VISC= 0.3828E+03)										

L 3 (I=1,2,3,FOR FL PL,CYL,2D STG FLOW)

X-FT	DPLT-THFT	MMT-THFT	DEL2U	DZL2U	UFREE	DUDXT	DUDYW	K	MED	
NOTE** X=DIST FRM STG PT,** DPLT=DISPLACEMENT THK(FT),** MMT=MOMENTUM THK(FT)										
DEL2U=DISPL**2*DUDX/VISC(NON DIM),** DZL2U=MMT**2*DUDX/VISC(NON DIM),** UFREE=FREE ST VEL(FPS),**										
DUDXT=VEL GRD ALONG X(FT/S/FT),** DUDYW=NORMAL VEL GRDT(FT/S/FT)***,K=NO IF INTGTN STEPS										
0.1634E+01	0.1562E-02	0.9603E-03	0.1099E+01	0.3862E+00	0.7049E+02	0.7646E+02	0.5421E+05	2	447	374
(REX= 0.6870E+06),(VISC*DUDX/U*U= 0.2581E-05),(D1*U/VISC= 0.6526E+03),(D2*U/VISC= 0.3868E+03)										
0.1640E+01	0.1557E-02	0.9245E-03	0.1088E+01	0.3836E+00	0.7091E+02	0.7527E+02	0.5439E+05	2	449	375
(REX= 0.6934E+06),(VISC*DUDX/U*U= 0.2511E-05),(D1*U/VISC= 0.6583E+03),(D2*U/VISC= 0.3909E+03)										
********** NEXT LINE FOR TAP NO= 26										
0.1645E+01	0.1562E-02	0.9288E-03	0.1075E+01	0.3802E+00	0.7132E+02	0.7390E+02	0.5454E+05	2	451	376
(REX= 0.6957E+06),(VISC*DUDX/U*U= 0.2437E-05),(D1*U/VISC= 0.6641E+03),(D2*U/VISC= 0.3950E+03)										
0.1651E+01	0.1566E-02	0.9328E-03	0.1058E+01	0.3755E+00	0.7175E+02	0.7237E+02	0.5484E+05	2	453	377
(REX= 0.7065E+06),(VISC*DUDX/U*U= 0.2357E-05),(D1*U/VISC= 0.6700E+03),(D2*U/VISC= 0.3991E+03)										
0.1657E+01	0.1571E-02	0.9370E-03	0.1044E+01	0.3714E+00	0.7218E+02	0.7094E+02	0.5500E+05	2	455	378
(REX= 0.7133E+06),(VISC*DUDX/U*U= 0.2283E-05),(D1*U/VISC= 0.6761E+03),(D2*U/VISC= 0.4033E+03)										
0.1663E+01	0.1576E-02	0.9412E-03	0.1031E+01	0.3678E+00	0.7260E+02	0.6962E+02	0.5501E+05	2	457	379
(REX= 0.7200E+06),(VISC*DUDX/U*U= 0.2215E-05),(D1*U/VISC= 0.6824E+03),(D2*U/VISC= 0.4075E+03)										
0.1669E+01	0.1582E-02	0.9457E-03	0.1021E+01	0.3647E+00	0.7301E+02	0.6840E+02	0.5508E+05	2	459	380
(REX= 0.7267E+06),(VISC*DUDX/U*U= 0.2152E-05),(D1*U/VISC= 0.6887E+03),(D2*U/VISC= 0.4117E+03)										
0.1675E+01	0.1588E-02	0.9503E-03	0.1011E+01	0.3623E+00	0.7341E+02	0.6729E+02	0.5519E+05	2	461	381
(REX= 0.7333E+06),(VISC*DUDX/U*U= 0.2094E-05),(D1*U/VISC= 0.6951E+03),(D2*U/VISC= 0.4160E+03)										
0.1681E+01	0.1594E-02	0.9550E-03	0.1004E+01	0.3604E+00	0.7381E+02	0.6628E+02	0.5518E+05	2	463	382
(REX= 0.7399E+06),(VISC*DUDX/U*U= 0.2040E-05),(D1*U/VISC= 0.7015E+03),(D2*U/VISC= 0.4203E+03)										
0.1687E+01	0.1600E-02	0.9598E-03	0.9983E+00	0.3592E+00	0.7421E+02	0.6538E+02	0.5522E+05	2	465	383
(REX= 0.7465E+06),(VISC*DUDX/U*U= 0.1991E-05),(D1*U/VISC= 0.7081E+03),(D2*U/VISC= 0.4247E+03)										
0.1693E+01	0.1607E-02	0.9648E-03	0.9942E+00	0.3585E+00	0.7459E+02	0.6459E+02	0.5534E+05	2	467	384
(REX= 0.7531E+06),(VISC*DUDX/U*U= 0.1947E-05),(D1*U/VISC= 0.7146E+03),(D2*U/VISC= 0.4291E+03)										
0.1699E+01	0.1613E-02	0.9698E-03	0.9917E+00	0.3584E+00	0.7498E+02	0.6390E+02	0.5536E+05	2	469	385
(REX= 0.7596E+06),(VISC*DUDX/U*U= 0.1906E-05),(D1*U/VISC= 0.7213E+03),(D2*U/VISC= 0.4336E+03)										
0.1705E+01	0.1620E-02	0.9750E-03	0.9909E+00	0.3589E+00	0.7535E+02	0.6331E+02	0.5541E+05	2	471	386
(REX= 0.7661E+06),(VISC*DUDX/U*U= 0.1870E-05),(D1*U/VISC= 0.7279E+03),(D2*U/VISC= 0.4381E+03)										
0.1711E+01	0.1627E-02	0.9802E-03	0.9916E+00	0.3600E+00	0.7573E+02	0.6284E+02	0.5556E+05	2	473	387
(REX= 0.7726E+06),(VISC*DUDX/U*U= 0.1837E-05),(D1*U/VISC= 0.7346E+03),(D2*U/VISC= 0.4426E+03)										
0.1717E+01	0.1634E-02	0.9855E-03	0.9940E+00	0.3617E+00	0.7610E+02	0.6247E+02	0.5562E+05	2	475	388
(REX= 0.7791E+06),(VISC*DUDX/U*U= 0.1809E-05),(D1*U/VISC= 0.7413E+03),(D2*U/VISC= 0.4472E+03)										
0.1723E+01	0.1640E-02	0.9908E-03	0.9981E+00	0.3641E+00	0.7648E+02	0.6220E+02	0.5572E+05	2	477	389
(REX= 0.7857E+06),(VISC*DUDX/U*U= 0.1784E-05),(D1*U/VISC= 0.7481E+03),(D2*U/VISC= 0.4518E+03)										
0.1729E+01	0.1647E-02	0.9962E-03	0.1004E+01	0.3671E+00	0.7685E+02	0.6204E+02	0.5592E+05	2	479	390
(REX= 0.7922E+06),(VISC*DUDX/U*U= 0.1762E-05),(D1*U/VISC= 0.7548E+03),(D2*U/VISC= 0.4565E+03)										
********** NEXT LINE FOR TAP NO= 27										
0.1735E+01	0.1654E-02	0.1002E-02	0.1011E+01	0.3708E+00	0.7722E+02	0.6199E+02	0.5601E+05	2	481	391
(REX= 0.7987E+06),(VISC*DUDX/U*U= 0.1744E-05),(D1*U/VISC= 0.7615E+03),(D2*U/VISC= 0.4612E+03)										
0.1741E+01	0.1660E-02	0.1007E-02	0.1020E+01	0.3749E+00	0.7760E+02	0.6205E+02	0.5616E+05	2	483	392
(REX= 0.8056E+06),(VISC*DUDX/U*U= 0.1728E-05),(D1*U/VISC= 0.7683E+03),(D2*U/VISC= 0.4658E+03)										
0.1747E+01	0.1667E-02	0.1012E-02	0.1031E+01	0.3799E+00	0.7799E+02	0.6222E+02	0.5642E+05	2	485	393
(REX= 0.8126E+06),(VISC*DUDX/U*U= 0.1715E-05),(D1*U/VISC= 0.7751E+03),(D2*U/VISC= 0.4706E+03)										
0.1754E+01	0.1673E-02	0.1017E-02	0.1043E+01	0.3856E+00	0.7838E+02	0.6251E+02	0.5661E+05	2	487	394
(REX= 0.8196E+06),(VISC*DUDX/U*U= 0.1706E-05),(D1*U/VISC= 0.7819E+03),(D2*U/VISC= 0.4754E+03)										

L 3 (L=1,2,3,FOR FL PL,CYL,2D STG FLOW)

X-FT	DPLT-THFT	MMT-THFT	DEL2U	DZL2U	UFREE	DUDXT	DUDYW	K	MED	
NOTE** X=DIST FRM STG PT,** DPLT=DISPLACEMENT THK(FT),** MMT=MOMENTUM THK(FT) DEL2U=DISPL**2*DUDX/VISC(NON DIM),** DZL2U=MMT**2*DUDX/VISC(NON DIM),** UFREE=FREE ST VEL(FPS),** DUDXT=VEL GRD ALONG X(FT/S/FT),** DUDYW=NORMAL VEL GRDT(FT/S/FT)***,K=NO IF INTGTN STEPS										
0.1760E+01	0.1679E-02	0.1022E-02	0.1058E+01	0.3920E+00	0.7877E+02	0.6292E+02	0.5686E+05	2	489	395
(REX= 0.8266E+06),(VISC*DUDX/U*U= 0.1700E-05),(D1*U/VISC= 0.7887E+03),(D2*U/VISC= 0.4801E+03)										
0.1766E+01	0.1685E-02	0.1027E-02	0.1074E+01	0.3993E+00	0.7917E+02	0.6344E+02	0.5723E+05	2	491	396
(REX= 0.8337E+06),(VISC*DUDX/U*U= 0.1697E-05),(D1*U/VISC= 0.7954E+03),(D2*U/VISC= 0.4850E+03)										
0.1772E+01	0.1691E-02	0.1032E-02	0.1092E+01	0.4073E+00	0.7957E+02	0.6408E+02	0.5752E+05	2	493	397
(REX= 0.8408E+06),(VISC*DUDX/U*U= 0.1697E-05),(D1*U/VISC= 0.8022E+03),(D2*U/VISC= 0.4899E+03)										
0.1779E+01	0.1686E-02	0.1038E-02	0.1112E+01	0.4161E+00	0.7997E+02	0.6483E+02	0.5785E+05	2	495	398
(REX= 0.8481E+06),(VISC*DUDX/U*U= 0.1700E-05),(D1*U/VISC= 0.8089E+03),(D2*U/VISC= 0.4947E+03)										
0.1785E+01	0.1701E-02	0.1043E-02	0.1134E+01	0.4255E+00	0.8038E+02	0.6570E+02	0.5833E+05	2	497	399
(REX= 0.8554E+06),(VISC*DUDX/U*U= 0.1706E-05),(D1*U/VISC= 0.8155E+03),(D2*U/VISC= 0.4997E+03)										

TABLE C-1

SUMMARY OF LAMINAR BOUNDARY LAYER CALCULATIONS (U_{inlet} = 22.2 fps)

N	$\bar{u}$ (FPS)	$\bar{v}$ (FPS)	UU11 (FPS)	UU22 (FPS)	DUDZU	VINF (FPS)	REYX	H	RLYD1	RLYD2	DELT/M	GIEF11	DELZ/M	GIDEZ1
3	-0.970	0.927	2.95E-05	2.27E-02	1.09E-01	12.304	2.99E+03	2.378	1.63E+01	1.47E+01				
4	-0.705	0.254	1.73E-02	9.54E-02	1.21E-02	16.003	4.29E+03	2.522	8.42E+01	5.23E+01				
5	-0.123	0.070	7.23E-04	2.99E-04	1.66E-02	20.168	5.39E+03	2.421	1.09E+02	4.18E+01				
6	-0.490	0.090	5.12E-04	3.49E-04	1.68E-02	20.115	1.07E+04	2.615	1.29E+02	4.42E+01				
7	-0.215	0.115	1.14E-03	4.60E-02	2.14E-05	12.405	5.42E+03	2.737	1.94E+02	2.52E+01	2.47E-03	2.215	1.71E-02	2.705
8	-0.600	0.115	1.36E-03	2.97E-02	6.24E-05	12.456	1.42E+04	2.807	1.94E+02	2.52E+01	1.07E-03	5.685	3.43E-02	7.055
9	1.523	0.225	1.61E-03	5.23E-04	2.76E-02	14.154	2.54E+04	3.044	1.83E+02	5.86E+01	1.54E-03	7.185	4.93E-04	1.102
10	1.154	0.317	1.78E-03	5.70E-04	1.03E-02	17.300	3.27E+04	3.117	1.86E+02	6.39E+01	1.91E-03	8.154	6.55E-04	1.634
11	0.949	0.401	1.88E-03	6.45E-02	7.33E-05	17.330	4.13E+04	3.220	1.90E+02	7.23E+01	2.24E-03	9.231	8.08E-04	2.084
12	0.858	0.484	1.96E-03	6.53E-04	7.23E-02	17.331	5.12E+04	3.258	2.29E+02	8.40E+01	2.23E-03	10.418	8.68E-04	2.094
13	0.893	0.567	2.03E-03	7.76E-04	3.39E-02	18.153	6.14E+04	2.617	2.36E+02	9.77E+01	2.09E-03	10.786	8.63E-04	2.078
14	0.980	0.651	2.05E-03	8.46E-04	6.79E-02	19.159	7.52E+04	2.417	2.55E+02	1.11E+02	1.83E-03	10.929	7.97E-04	3.135
15	1.149	0.715	2.05E-03	8.82E-02	1.12E-01	20.594	8.13E+04	2.308	2.70E+02	1.40E+02	1.50E-03	10.300	6.90E-04	3.295
16	1.393	0.811	2.05E-03	9.06E-04	1.62E-01	21.949	1.13E+05	2.114	3.00E+02	1.19E+02	1.17E-03	8.628	5.62E-02	4.291
17	1.593	0.898	1.81E-03	8.95E-04	1.58E-01	26.016	1.39E+05	2.030	3.15E+02	1.53E+02	9.93E-04	9.931	4.80E-04	3.166
18	1.855	0.981	1.84E-03	8.98E-04	1.73E-01	28.773	1.68E+05	2.065	3.32E+02	1.68E+02	7.82E-04	9.413	3.90E-04	3.315
19	2.229	1.054	1.78E-03	8.73E-02	5.15E-01	32.278	2.05E+05	2.092	3.27E+02	1.83E+02	6.26E-04	8.706	3.12E-04	3.264
20	2.643	1.115	1.75E-03	8.52E-04	2.37E-01	36.547	2.49E+05	2.022	3.87E+02	2.06E+02	4.66E-02	8.456	3.42E-02	3.178
21	3.195	1.228	1.59E-03	9.15E-04	2.10E-01	40.908	3.00E+05	1.953	4.12E+02	2.17E+02	3.83E-04	8.166	1.98E-04	3.054
22	4.043	1.311	1.54E-03	1.09E-04	2.54E-01	45.622	3.51E+05	1.927	4.55E+02	2.43E+02	2.55E-04	7.679	1.55E-04	3.078
23	5.168	1.398	1.46E-03	1.22E-02	3.14E-01	52.109	4.33E+05	1.832	5.44E+02	2.92E+02	2.22E-04	7.554	1.25E-04	3.295
24	6.554	1.478	1.42E-03	1.16E-02	2.63E-01	58.842	5.16E+05	1.788	6.49E+02	3.47E+02	1.67E-02	7.139	8.67E-05	3.119
25	10.049	1.543	1.51E-03	9.71E-04	3.43E-01	64.888	6.05E+05	1.738	6.66E+02	3.55E+02	8.68E-05	6.185	5.16E-05	2.833
26	18.000	1.645	1.56E-03	9.29E-04	3.80E-01	71.316	7.00E+05	1.681	7.21E+02	4.61E+02	5.91E-05	5.853	3.58E-05	2.758
27	28.000	1.735	1.65E-03	1.00E-03	3.71E-01	77.215	7.99E+05	1.651						

TABLE C-2

SUMMARY OF LAMINAR BOUNDARY LAYER CALCULATIONS (U_{inlet} = 29.0 fps)

N														
2	0.010	0.024	2.47E-03	1.23E-03	1.58E-01	13.570	1.49E+04	2.111	3.45E+01	1.63E+01				
3	0.068	0.056	2.48E-03	1.30E-03	1.58E-01	23.567	1.72E+04	2.214	9.78E+01	4.11E+01				
5	0.123	0.070	6.27E-04	2.83E-04	1.81E-02	26.318	1.09E+04	2.379	1.25E+02	4.80E+01				
6	0.490	0.090	8.13E-04	3.11E-04	2.67E-02	26.035	1.43E+04	2.413	1.32E+02	5.46E+01				
8	0.735	0.110	1.92E-03	2.43E-03	2.31E-02	52.977	1.71E+02	5.741	1.70E+02	9.22E+01	1.35E-03	2.725	1.91E-02	9.825
8	0.800	0.163	1.24E-03	5.49E-04	2.91E-03	54.214	5.34E+04	5.117	1.15E+03	1.15E+03	1.01E-03	8.669	1.40E-02	1.911
9	1.523	0.235	1.53E-03	5.18E-04	2.68E-02	53.265	6.25E+04	2.056	2.30E+03	1.31E+03	1.45E-03	8.893	4.98E-04	1.721
10	1.155	0.317	1.32E-03	5.35E-04	1.17E-02	52.603	4.25E+04	2.487	2.43E+02	8.24E+01	1.95E-03	0.727	6.60E-04	2.111
11	0.328	0.201	4.85E-03	6.47E-03	4.08E-03	56.209	2.23E+05	2.329	2.23E+03	8.97E+01	4.20E-03	1.852	1.81E-03	2.306
12	0.428	0.481	4.80E-03	6.60E-03	5.66E-03	52.833	2.70E+04	2.807	2.63E+03	9.80E+01	2.20E-03	2.265	4.05E-02	2.784
13	0.893	0.567	1.56E-03	7.21E-04	3.34E-02	22.916	3.71E+04	2.721	2.78E+02	1.15E+02	1.95E-03	2.249	8.06E-04	3.761
14	0.940	0.651	1.51E-03	7.90E-04	8.12E-02	24.531	9.47E+04	2.417	2.96E+02	1.31E+02	1.68E-03	2.129	7.40E-04	3.555
15	1.121	0.719	1.09E-03	6.49E-04	1.68E-01	28.695	1.10E+05	2.767	3.11E+02	1.37E+02	1.35E-03	2.303	6.35E-04	3.773
16	1.111	0.810	1.05E-03	8.34E-04	1.83E-01	29.826	1.44E+05	2.166	3.34E+02	1.61E+02	1.02E-03	10.48	6.15E-04	4.068
17	1.593	0.848	1.69E-03	8.21E-04	1.69E-01	31.419	1.78E+05	2.057	3.62E+02	1.79E+02	8.88E-04	10.78	4.39E-04	3.744
18	1.855	0.981	1.45E-03	8.14E-04	2.06E-01	31.072	2.16E+05	2.023	3.85E+02	1.97E+02	6.89E-04	10.104	3.52E-04	3.694
19	2.220	1.062	1.25E-03	7.92E-04	2.21E-01	32.050	2.60E+05	1.957	4.15E+02	2.11E+02	5.69E-04	9.811	2.89E-04	3.644
20	2.643	1.155	1.48E-03	9.85E-04	2.46E-01	29.335	3.21E+05	1.934	4.24E+02	2.15E+02	4.58E-04	4.911	6.47E-02	3.533
21	3.165	1.278	1.40E-03	1.33E-04	2.35E-01	53.609	3.90E+05	1.908	4.81E+02	2.53E+02	3.36E-04	8.829	1.77E-04	3.358
22	4.043	1.311	1.32E-03	1.14E-04	2.53E-01	54.756	4.45E+05	1.905	5.10E+02	2.74E+02	2.46E-04	8.005	1.32E-04	3.166
23	5.128	1.293	1.26E-03	6.17E-05	2.29E-01	69.951	5.63E+05	1.863	5.65E+02	3.04E+02	1.80E-04	7.150	9.95E-05	3.156
24	6.358	1.278	1.25E-03	6.77E-04	2.60E-01	77.275	6.98E+05	1.818	6.49E+02	3.68E+02	1.27E-04	7.322	9.93E-05	3.132
25	10.049	1.362	1.28E-03	7.27E-04	3.17E-01	85.510	1.03E+06	1.761	7.50E+02	4.44E+02	1.47E-05	6.479	4.63E-05	2.953
26	18.000	1.645	1.34E-03	7.91E-04	3.68E-01	94.030	1.13E+06	1.681	8.81E+02	5.38E+02	5.21E-05	6.364	3.19E-05	3.038
27	28.000	1.935	1.40E-03	8.92E-04	3.88E-01	101.842	1.05E+06	1.637						

TABLE C-3

SUMMARY OF LAMINAR BOUNDARY LAYER CALCULATIONS (U_{inlet} = 36.3 fps)

N	X (FT)	Y (FT)	DEL1 (FT)	DEL2 (FT)	DEL2U	U1NE (FPS)	REYX	H	REYD1	REYD2	DEL1/X	G(DEL1)	DEL2/X	G(DEL2)
1	-0.969	0.021	2.39E-02	1.74E-02	1.19E-01	21.504	2.51E+03	2.178	4.73E+01	2.17E+01				
2	-0.105	0.049	4.23E-04	2.40E-04	7.75E-02	32.252	2.31E+03	2.220	8.08E+01	3.64E+01				
3	-0.123	0.070	5.44E-04	2.23E-04	7.11E-03	36.396	1.49E+04	2.437	1.16E+02	4.19E+01				
4	-0.490	0.090	6.95E-04	2.62E-04	8.94E-02	35.731	1.89E+04	2.658	1.45E+02	5.46E+01				
5	-0.133	0.110	8.50E-04	3.01E-04	1.05E-02	35.620	2.27E+04	2.832	1.71E+02	6.25E+01				
6	-0.122	0.129	1.00E-03	3.58E-04	1.24E-02	35.521	2.71E+04	2.804	2.03E+02	7.00E+01	1.21E-04	1.915	1.20E-04	0.171
7	2.800	0.143	1.05E-03	3.58E-04	1.24E-02	35.521	2.71E+04	2.904	2.28E+02	7.51E+01	1.49E-04	6.457	2.63E-04	1.513
8	1.523	0.235	1.22E-03	4.00E-04	1.59E-02	32.123	4.41E+04	3.043	2.41E+02	7.82E+01	1.16E-03	8.190	3.15E-04	1.512
9	1.152	0.317	1.33E-03	4.33E-04	8.72E-03	30.913	5.73E+04	3.083	2.46E+02	8.45E+01	1.44E-03	9.355	4.95E-04	1.886
10	1.155	0.401	1.36E-03	4.68E-04	9.05E-03	30.213	7.42E+04	2.915	2.66E+02	9.68E+01	1.69E-03	15.940	6.15E-04	2.406
11	0.943	0.424	2.49E-03	5.20E-04	2.08E-02	32.603	8.68E+04	2.749	2.92E+02	1.11E+02	1.74E-03	12.175	6.61E-04	2.850
12	0.858	0.464	2.56E-03	5.91E-04	2.54E-02	32.124	1.06E+05	2.633	3.15E+02	1.28E+02	1.63E-03	12.700	6.62E-04	3.275
13	0.893	0.567	1.60E-03	6.49E-04	6.68E-02	33.146	1.28E+05	2.460	3.35E+02	1.47E+02	1.39E-03	12.476	6.11E-04	3.625
14	0.980	0.651	1.56E-03	6.85E-04	1.20E-01	36.176	1.52E+05	2.278	3.55E+02	1.65E+02	1.13E-03	11.965	5.26E-04	3.786
15	1.120	0.736	1.49E-03	6.91E-04	1.59E-01	40.402	1.79E+05	2.153	3.82E+02	1.83E+02	9.00E-04	11.466	4.30E-04	3.781
16	1.313	0.817	1.43E-03	6.85E-04	1.55E-01	45.663	2.40E+05	2.094	4.13E+02	2.01E+02	7.54E-04	11.349	3.67E-04	3.852
17	1.593	0.898	1.40E-03	6.81E-04	1.94E-01	50.580	2.90E+05	2.055	4.39E+02	2.21E+02	5.85E-04	10.618	2.94E-04	3.784
18	1.955	0.981	1.31E-03	6.57E-04	2.09E-01	57.366	3.36E+05	1.992	4.74E+02	2.40E+02	4.79E-04	10.312	2.43E-04	3.741
19	2.240	1.063	1.27E-03	6.41E-04	2.25E-01	64.150	4.39E+05	1.974	5.06E+02	2.61E+02	3.75E-04	9.796	1.93E-04	3.611
20	2.843	1.145	1.19E-03	6.14E-04	2.16E-01	72.630	5.21E+05	1.943	5.51E+02	2.85E+02	2.89E-04	9.377	1.50E-04	3.493
21	3.185	1.228	1.17E-03	6.04E-04	2.41E-01	80.695	6.18E+05	1.931	5.98E+02	3.25E+02	2.17E-04	8.809	1.18E-04	3.525
22	4.043	1.311	1.11E-03	6.05E-04	3.16E-01	92.904	7.40E+05	1.836	6.72E+02	3.71E+02	1.69E-04	8.726	9.57E-05	3.965
23	5.128	1.395	1.03E-03	5.79E-04	3.07E-01	104.290	8.31E+05	1.782	7.69E+02	4.43E+02	1.14E-04	8.193	6.55E-05	3.583
24	6.338	1.479	1.04E-03	5.98E-04	3.38E-01	115.273	1.05E+06	1.736	8.74E+02	5.19E+02	6.58E-05	7.093	3.91E-05	3.248
25	10.049	1.563	1.14E-03	7.04E-04	3.67E-01	126.388	1.21E+06	1.693	1.00E+03	6.07E+02	4.49E-05	6.726	2.72E-05	3.162
26	18.000	1.695	1.30E-03	7.60E-04	3.65E-01	136.609	1.38E+06	1.654						
27	28.300	1.735	1.26E-03											

TABLE C-4

SUMMARY OF LAMINAR BOUNDARY LAYER CALCULATIONS (U_{inlet} = 42.8 fps)

N														
1	-0.070	0.527	1.781E-02	1.574E-03	1.423E-01	24.999	1.716E+03	2.129	4.481E+01	3.147E+01				
4	-0.105	0.049	1.481E-02	1.76E-02	1.23E-01	41.693	1.01E+05	2.212	8.291E+02	5.63E+01				
5	-0.123	0.030	5.03E-04	2.08E-04	9.66E-03	41.409	1.70E+04	2.416	1.56E+02	5.92E+01				
6	-0.496	0.040	6.52E-04	2.49E-04	4.53E-03	40.644	2.17E+04	2.642	1.86E+02	6.77E+01				
7	-1.115	0.118	8.02E-04	2.92E-04	2.20E-02	39.276	2.60E+04	2.746	2.22E+02	7.91E+01				
8	-2.000	0.119	8.06E-02	3.51E-02	1.77E-01	37.518	6.82E+04	5.448	5.56E+02	1.98E+02	1.57E-04	4.201	1.42E-06	0.844
9	1.523	0.235	1.18E-03	4.60E-04	1.65E-02	36.484	2.06E+04	2.951	2.70E+02	9.00E+01	1.17E-03	9.395	3.78E-04	1.756
10	1.155	0.317	1.54E-03	4.36E-04	1.13E-02	34.995	2.56E+04	3.063	2.95E+02	9.82E+01	1.46E-03	10.877	5.03E-04	2.202
11	0.845	0.382	1.85E-03	4.39E-04	7.98E-03	33.977	2.97E+04	3.201	3.22E+02	1.03E+02	1.69E-03	12.241	6.07E-04	2.574
12	0.588	0.432	2.09E-03	4.43E-04	5.70E-03	33.212	3.01E+04	3.454	3.12E+02	1.13E+02	1.67E-03	12.913	6.22E-04	2.674
13	0.393	0.547	1.59E-03	5.59E-04	1.28E-02	36.065	1.21E+05	5.662	1.37E+02	1.37E+02	1.52E-03	13.127	6.26E-04	3.466
14	0.980	0.671	1.59E-03	6.11E-04	7.78E-02	38.315	1.41E+05	5.429	1.59E+02	1.59E+02	1.10E-03	12.548	5.94E-04	3.814
15	1.610	0.719	1.72E-03	6.31E-04	1.64E-01	21.918	1.62E+05	5.659	1.83E+02	1.74E+02	1.46E-03	12.432	5.92E-04	3.944
16	1.511	0.719	1.60E-03	6.32E-04	1.64E-01	42.561	2.75E+05	5.134	2.11E+02	1.40E+02	1.47E-03	11.844	5.95E-04	4.035
17	1.593	0.838	1.33E-03	6.55E-04	1.73E-01	52.258	2.77E+05	5.067	4.45E+02	2.19E+02	6.99E-04	11.775	3.46E-04	4.016
18	1.855	0.981	1.30E-03	6.39E-04	1.98E-01	58.183	3.37E+05	5.031	4.76E+02	2.41E+02	5.97E-04	11.128	2.77E-04	4.007
19	2.229	1.145	1.28E-03	6.21E-04	4.43E-01	62.720	4.48E+05	5.219	2.14E+03	2.42E+03	1.27E-03	10.520	2.91E-03	3.976
20	2.624	1.248	1.12E-03	6.14E-04	2.31E-01	81.752	4.98E+05	5.864	5.45E+02	2.86E+02	1.91E-04	8.248	1.82E-04	3.853
21	3.185	1.220	5.80E-04	2.74E-04	2.74E-01	83.410	4.05E+05	5.926	5.95E+02	3.10E+02	2.68E-04	9.134	1.40E-04	3.644
22	4.043	1.311	5.68E-03	5.65E-04	5.56E-01	93.005	1.20E+05	5.918	6.32E+02	3.40E+02	1.54E-04	8.041	1.06E-04	3.496
23	5.168	1.354	4.99E-03	2.41E-03	3.01E-01	106.570	1.11E+05	6.029	1.10E+03	3.23E+02	1.54E-03	8.765	9.53E-03	3.605
24	6.548	1.426	4.92E-04	2.31E-04	2.01E-01	120.758	1.06E+06	6.807	6.18E+02	2.27E+02	8.01E-05	8.112	5.91E-05	3.582
25	10.049	1.543	1.06E-03	5.94E-04	3.30E-01	133.448	1.23E+06	7.753	9.40E+02	5.60E+02	4.03E-05	7.208	3.59E-05	3.352
26	15.000	1.645	1.08E-03	6.46E-04	3.79E-01	146.852	1.43E+06	7.680	1.10E+03	6.70E+02	4.17E-04	7.088	2.55E-05	3.384
27	20.000	1.735	1.12E-03	7.15E-04	3.88E-01	159.132	1.63E+06	7.637						

APPENDIX D

WAKES AND WAKE EFFECTS ON TRANSITION

Wakes occur as a direct result of boundary layer development. When the boundary layer flows along each surface join at the trailing edge of an object, the wake profile results. Consequently, anything affecting the boundary layer along either surface will also likely influence the wake characteristics. The wake from one object may in turn influence the boundary layer development along another surface downstream. In a turbine, where one blade row closely follows another, this can cause considerable difficulty in predicting the flow field and heat transfer properties around each airfoil. Because of a minimum velocity at the trailing edge, the wake velocity profile is characterized by an inflection point that yields instabilities in the wake except for very low velocity flows. Generally the resulting wake is characterized by spanwise contrarotating vortices (Karman vortex street), or by turbulent flow. Because of the importance of the wake in determining drag and vibrational forces for aircraft and structures, considerable experimental and theoretical information is available for various geometries. The brief treatment given here should only be considered representative of material available in the open literature.

D.1 Characteristics of Circular Cylinder Wakes

Because of the simple geometry, a large percentage of wake studies have involved the use of circular cylinders placed normal to the flow. For incompressible flows, the wake characteristics are determined principally by the Reynolds number based on free-stream velocity and cylinder diameter. For compressible flows ($M > 0.3$), the Mach number must also be considered.[17]

Figure D.1 shows circular cylinder wake characteristics for various Reynolds number ranges. This figure is based on a presentation by Morkovin[86] in which the results from numerous experimental studies were reviewed to determine wake properties at low free-stream turbulence levels. For extremely low Reynolds numbers ($Re < 1$) the wake flow is essentially laminar and may be calculated by the approximations of Lamb[87] based on similar calculations made by Stokes[17] for the case of creeping flow about a sphere. At such a low Reynolds number (practically unobtainable for gaseous flows) the flow may be considered highly viscous, making it possible to ignore inertial terms in the equations of motion. At slightly higher Reynolds numbers ($3\text{-}5 < Re < 30\text{-}40$) the wake flow is still essentially laminar, but twin vortices have formed behind the cylinder. With artificial excitation of the flow field, however, the wake becomes unstable in this range. At large Reynolds numbers ($10^5 < Re < 3.5 \times 10^6$) the wake (Fig. D.1f) is formed through the development of a laminar separation bubble with transition to turbulence following reattachment, with subsequent

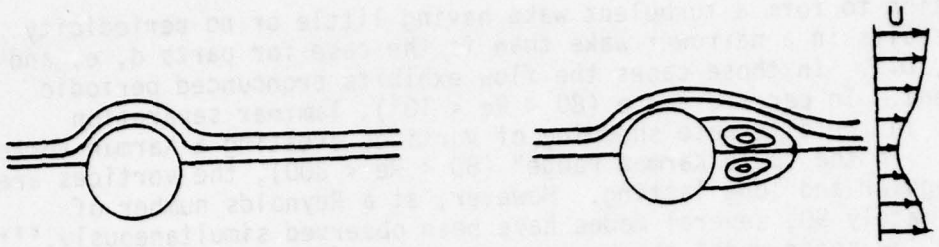

(a.) Very Low Re
(Re<1)

(b.) Twin Vortex Stage
(3-5 < Re < 30-40)

(c.) Incipient Karman Range
(30-40 < Re < 80-90)

(d.) Pure Karman Range
(80-90 < Re < 150-300)

(e.) Subcritical
(150-300 < Re < 1-1.3x10^6)

(f.) Critical and Post-Critical
(1-1.3x10^5 < Re < 3.5x10^6)

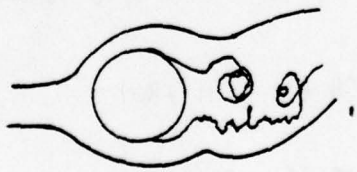

(g.) Transcritical
(3.5x10^6 < Re < ?)

Figure D.1 Circular Cylinder Wake Characteristics for Various Ranges of Reynolds Number

separation to form a turbulent wake having little or no periodicity. This results in a narrower wake than is the case for parts d, e, and g of Fig. D.1. In those cases the flow exhibits pronounced periodic phenomena. In parts d and e ($80 < Re < 10^5$), laminar separation results in the alternate shedding of vortices creating a Karman vortex street. In the "pure Karman range" ($80 < Re < 300$), the vortices are very regular and long lasting. However, at a Reynolds number of approximately 90, several modes have been observed simultaneously.[88,89] In the "low speed mode" the vortex street is highly regular as already described for this region. During the "high speed mode," however, the vortices become highly irregular and unstable. Gastor,[90] however, found no such phenomena and suggested that perhaps some irregularity in the flow created the observed features. In the "subcritical" range ($300 < Re < 10^5$), the vortex street decays much more rapidly than for the "pure Karman range." At very high Reynolds numbers ($Re > 3.5 \times 10^6$), transition to turbulence occurs on the front face of the cylinder resulting in turbulent spearation to form the wake, but again yielding dominant periodicity.

The trailing edge vortices pictured in Figs. D.1d and D.1e, commonly known as a Karman vortex street, have been shown to be present in the wakes of many two-dimensional flow models. The importance of these vortices to structural or mechanical designs has been shown in numerous cases, probably the most dramatic and best known of these being the Tacoma Narrows bridge failure in 1940. For steady flow conditions, these vortices are shed at an approximately regular frequency determined by the cylinder Reynolds number and a second dimensionless parameter known as the Strouhal number ($S = fd/U_\infty$). As an alternative, Roshko[91] suggested the use of another dimensionless parameter (fd^2/ν) rather than the Strouhal number. At relatively low Reynolds numbers, the Strouhal number is a function of the Reynolds number, but becomes relatively constant for high Reynolds numbers ($Re > 300$).

Functional relationships between Re and S have been given by several authors based on available experimental data. Two such formulae reviewed by Goldstein[92] based on work by Tyler and by Rayleigh are as follows:

$$S = 0.198\ (1 - 19.7/Re) \qquad \text{D-1}$$

and

$$S = 0.195\ (1 - 20.1/Re)\ . \qquad \text{D-2}$$

Roshko[91] gave two equations, one for the rising portion of the curve and one for where the curve is relatively flat at higher Reynolds numbers as follows:

$$S = 0.212\ (1 - 21.2/Re) \quad (Re < 150) \qquad \text{D-3}$$

and

$$S = 0.212\ (1 - 12.7/Re) \quad (Re > 300)\ . \qquad D\text{-}4$$

Maximum values of the Strouhal number at large Reynolds numbers have been reported from about 0.18 to 0.48 (Refs. 91 through 92), but generally range from about 0.19 to 0.21 as reflected by the coefficients for Eqs. D-1 through D-4. Similar determinations have also been made for other geometries using a Strouhal number based on maximum thickness rather than cylinder diameter. Strouhal numbers of 0.148 to 0.18 have been reported for flat plates at zero incidence and 0.15 to 0.21 for certain airfoils.[92] Brown and Goddard[44] studied a number of geometries and found Strouhal numbers ranging from 0.08 to 0.22.

Although most theoretical work is based on assumed two-dimensional vortices, most vortices encountered experimentally are three-dimensional even for two-dimensional flow around a two-dimensional model.[94] In fact, most vortices are shed obliquely from circular cylinders.[89,94] However, vibration of the cylinder at approximately the shedding frequency can cause vortices to be shed parallel to the cylinder axis.[89]

The dimensions of the vortex street have also been the subject of much study. Von Karman studied the spacing theoretically and found that the spacing ratio h/a (Fig. D.2) must be equal to 0.281 for a stable vortex street to exist.[17,92] Domm,[95] however, showed that this is true only for the linear theory and that no spacing is entirely stable when second order terms are considered. Much experimental data show higher values of h/a with an observed increase as the flow proceeds downstream. Reported experimental values for h/a range from 0.2 to 0.5,[44,96] but generally are above 0.3 for flow uninfluenced by tunnel wall spacing or sound. Brown and Goddard[44] showed that the spacing ratio could be effectively controlled from 0.246 to 0.5 through the use of sound. Hooker[97] suggested that the apparent center of rotation, as generally determined from still photographs, is displaced outward relative to the true vortex center, because of the translatory motion of the wake, resulting in the greater spacing ratios observed experimentally. Although some experimental data has been corrected for this error,[89] all data given in this report follow the more common trend of recording measurements directly as observed from visualization photographs.

The effects of wind tunnel walls on the circular cylinder wake have also been studied. Okamoto and Takeuchi[96] found that increasing the ratio d/H where d is the cylinder diameter and H is the spacing between test section side walls parallel to the cylinder axis, caused decreases in the ratios a/d, h/d, and h/a. At the same time the velocity of the vortex street and the intensity of the vortices was found to increase. The width of the wake and the boundary layer thickness were both found to decrease with increasing d/H. Probably as a result of the boundary layer thickness change, the separation point moved rearward on the cylinder. The vortex shedding frequency,

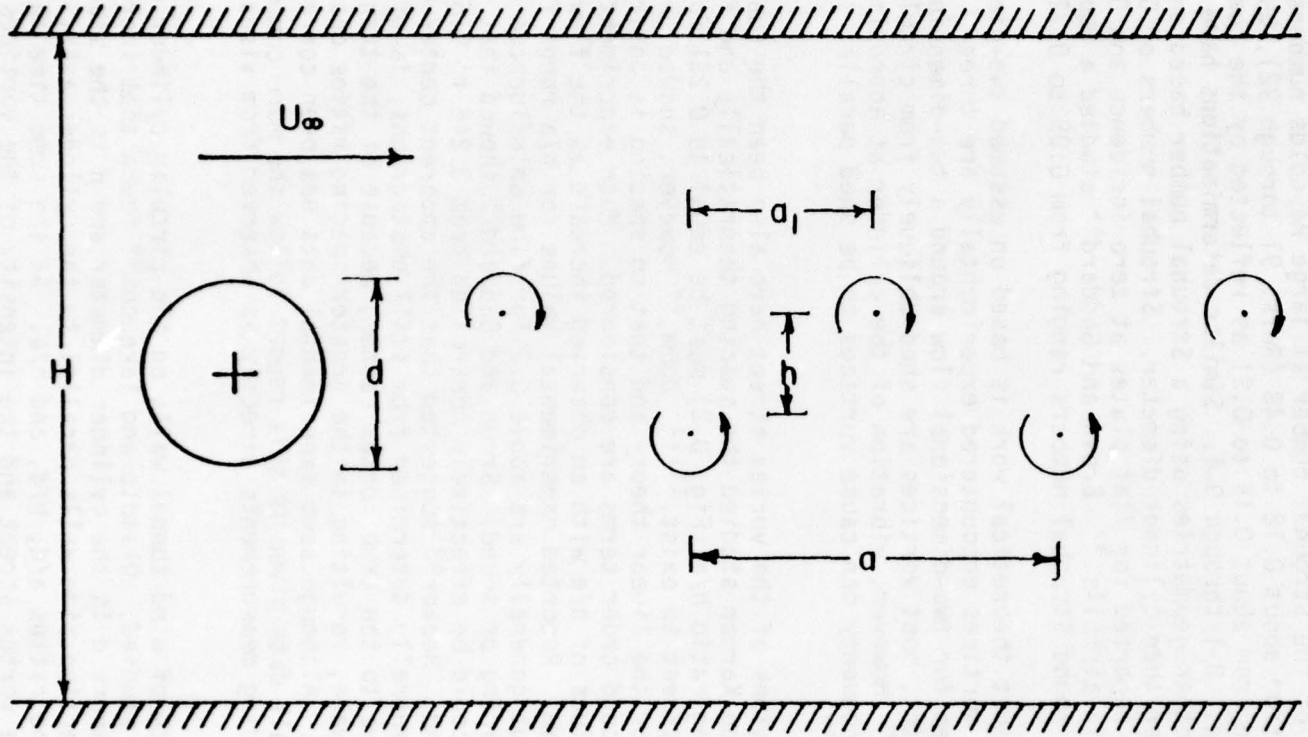

Figure D.2 Nomenclature for Karman Vortex Street Spacing Ratio and Tunnel Wall Effects

however, was found to be independent of d/H and a Strouhal number of 0.191 was reported for Re = 3.22×10^4. Okamoto and Takeuchi suggested that the effect of wind tunnel side walls could be ignored for $d/H < 0.04$, based on their results. Goldstein[92] reported similar results by Thom indicating a change in the minimum Reynolds number from 30 for d/H = 0.025 to 62 for d/H = 0.1 for change from the "twin vortex stage" to the "incipient Karman range."

D.2 Previous Airfoil and Cascade Wake Studies

The importance of wakes to airfoil and cascade studies should not be underestimated in any situation. Not only does the wake have a strong influence on drag, but the lift coefficient and general flow field can be influenced by wake location and characteristics as well. For many years the principal wake data available to designers was that of Silverstein, Katzoff, and Bullivant[98] based on the wake of a single airfoil at subsonic velocities. This data consisted of relatively complete velocity maps as well as empirical equations for much of the trailing edge flow. However. the results do not adequately represent cascade or three-dimensional turbine airfoil trailing edge flow.

More recently, experimental studies have been made of turbine or compressor stage wake flow. For instance, Evans[11] used an X-probe hot-wire anemometer and hybrid computer to explore the velocity and turbulence profiles downstream of a moving compressor stage at midspan. Periodic turbulence was found to be of the same order of magnitude as general free-stream turbulence when the compressor was operated near the design point, but free-stream turbulence was found to be the most significant quantity when the compressor was operated near stall. It was also determined that the power spectral density of the periodic turbulence did not change greatly with changes in axial velocity, while the free-stream turbulence varied in magnitude with increasing flow velocity. The fact that periodic turbulence from passing wakes was of similar magnitude to the background turbulence is very significant to the study of wake effects on turbine blade design. Blade vibration and flutter are more affected by frequencies near the blade natural frequency than by the overall magnitude of the turbulence.

Raj and Lakshminaryana[12] obtained three-dimensional velocity, turbulence and Reynolds stress profiles at various locations behind a turbomachine rotor. Turbulence and wake velocity defects were found to decay at a much faster rate in turbomachines than for flow past cascades or isolated airfoils, probably due to the increased mixing resulting from the three-dimensional flow. It was also found that the wake turbulence and mean velocity defect contributed almost equally to the total unsteadiness in the following blade row. Whitfield, Kelly, and Barry[13] used a rotating single-wire hot-wire anemometer probe to map the flow field behind a turbine rotor and plotted the resulting data as contour maps and vector surfaces. A study by Kerrebrock and Mikolajczak[14] showed considerable blade-to-blade variation in the wake

stagnation temperature profiles behind a compressor rotor, probably a result of minor surface variations affecting individual airfoil boundary layer development.

The complexity of the flow field in a turbine makes direct theoretical estimation of the effect of one stage upon the flow in a successive stage difficult, leading to the common assumption of two-dimensional flow past two-dimensional cascades. Likewise, most wake effects experimental studies have involved two-dimensional cascades, and even the use of circular cylinders or symmetrical airfoils to produce the interfering wake. Dean[99] has shown through theoretical analysis that if work is obtained from a fluid through the use of pressure forces the flow must be unsteady. Therefore, even if the actual wake profiles were to be ignored, unsteady terms must still be retained in the equations of continuity, motion, and energy when applied to turbomachinery.

Kemp and Sears[100] studied wake effects on cascade forces by modeling the upstream cascade wake profiles as a summation of the individual wake profiles previously studied by Silverstein.[98] This approach, however, violates the continuity equation because the velocity defect in the individual airfoil wake does not significantly change the edge velocity while the cascade edge velocities must increase to compensate for the wake velocity defect. Fleeter[101] improved on the model of Kemp and Sears, utilizing cascade flow considerations to calculate the fluctuating forces on the downstream cascade. The importance of using cascade flow theory and considering compressibility effects, even for low velocity subsonic flow, was shown. Hanson[102] also improved upon the model by assuming a rotor instead of a cascade. Both Fleeter and Hanson showed significant periodic pressure fluctuations for the downstream cascade. Both of these studies were based on potential flow theory and did nothing to describe unsteady boundary layer development resulting from the upstream wake passing. In fact, no theoretical study has apparently been made to predict the resulting unsteady boundary layer. Based on the pressure fluctuations calculated by theoretical studies similar to those of Fleeter and of Hanson such a study may be possible although it would likely be very complicated and involve extensive numerical analysis.

In addition to ignoring boundary layer development, studies such as those of Hanson and of Fleeter treat the upstream wake simply as fully turbulent flow surrounded by nonturbulent flow combined with the wake velocity profile. Accurate modeling of the wake is difficult (even for individual turbine airfoils), however, because vortex streets occur downstream of many turbine blades, especially those with large thickness or trailing edge wedge angle. According to Gostelow,[103] the rate of mixing of vorticity and the application of stability criterion represent unresolved problems necessary for the definition of vortex street flow. Gostelow has reviewed several methods currently available for solution of the problem, however. In addition, Gostelow has shown

that inaccurate definition of the rear stagnation point (whether through use of a "Kutta-Joukowsky" condition or by assuming its location at the point of tangency of the airfoil surface to the trailing edge curve) could result in noticeable error in the potential flow calculation over much of the airfoil or cascade surfaces.

Experimental study of wake effects is, fortunately, somewhat less difficult but yields a less general result. A number of boundary layer studies have included examination of the effects of acoustic or wake phenomena on the transition region. For instance, Brown[22] studied the effects of the wake from a circular cylinder placed normal to the flow on boundary layer transition along an ogive-nosed circular cylinder parallel to the flow. The effects of turbomachine or cascade wakes on downstream cascade performance have also been studied by several investigators. Kobayashi, Tanaka, and Maruta,[2] using instrumented flexible stator blades, studied the effects of moving rotor wakes on cascade flutter. The wake profiles were not measured, but variation of the clearance between adjacent cascades showed that the greatest influence occurred for clearances less than 0.5 chord length while almost no effect was found for clearances greater than 1.5 chord lengths. Cox and Han[15] studied the effects of wakes from a stationary cascade of symmetrical airfoils on the surface pressure distribution and on the wakes of a downstream cascade of turbine airfoil models. The greatest changes were observed along the suction (convex) surfaces of the airfoils and when the wakes impinged near the stagnation points of the downstream airfoils. Probably one of the more advanced two-dimensional studies of wake effects recently attempted was that of Kiock.[16] In that study an oscillating grid of circular cylinders was used to produce the high turbulence levels usually associated with turbomachinery. The highly turbulent wakes were found to have a major effect on boundary layer development along the suction side of the airfoil. At low turbulence levels transition along this surface was preceded by a laminar separation bubble. As the magnitude of turbulence increased, the bubble shortened until it disappeared. Further increases in free-stream turbulence level caused the transition region to shift further upstream.

D.3 Experimental Results with Cylinder Wakes

In anticipation for future experiments, where the effects of an upstream circular cylinder wake on the boundary layer could be studied, the vortex shedding frequencies of the circular cylinders placed upstream of the test cascade were studied. The cylinders were positioned at Y = 7.5 in. (Fig. 16). A Flow Corporation HWP-B hot-wire probe and HWB-3 hot-wire anemometer were used to determine the principal wake frequency components for the circular cylinders as shown in Table D.1. The circular cylinders were made of steel drill rod and mounted on the transport mechanism described in Section 3.3. The hot-wire probe was inserted into the tunnel through the instrumentation port in the wind tunnel east wall (Fig. 28), and adjusted so that the element was about 1 in. from the cylinder trailing edge along the wake centerline. The Federal Scientific Model UA-500 frequency spectrum analyzer was used to determine the principal frequency components within the wake.

TABLE D.1

VORTEX SHEDDING CHARACTERISTICS OF CIRCULAR CYLINDERS

Inlet Velocity (fps)	Rod Diameter (in.)	Principal Wake Frequency (Hz)	S $\left(\frac{fd}{U_\infty}\right)$	Re $\left(\frac{U_\infty d}{\nu}\right)$
22.21	3/32	582.0	0.205	1.05×10^3
22.21	1/8	437.0	0.205	1.41×10^3
22.21	3/16	287.0	0.202	2.11×10^3
22.21	1/4	217.0	0.204	2.81×10^3
22.21	3/8	132.0	0.186	4.22×10^3
22.21	1/2	102.4	0.192	5.63×10^3
22.21	3/4	64.4	0.181	8.44×10^3
29.01	3/32	790.0	0.213	1.38×10^3
29.01	1/8	582.0	0.209	1.83×10^3
29.01	3/16	385.0	0.208	2.75×10^3
29.01	1/4	288.0	0.207	3.67×10^3
29.01	3/8	180.4	0.195	5.50×10^3
29.01	1/2	135.2	0.194	7.33×10^3
29.01	3/4	86.0	0.185	1.10×10^4
36.30	3/32	984.0	0.213	1.73×10^3
36.30	1/8	730.0	0.211	2.30×10^3
36.30	3/16	479.0	0.208	3.45×10^3
36.30	1/4	355.0	0.205	4.60×10^3
36.30	3/8	226.0	0.196	6.91×10^3
36.30	1/2	174.0	0.201	9.21×10^3
36.30	3/4	109.6	0.190	1.38×10^4
42.81	3/32	1148.0	0.210	2.03×10^3
42.81	1/8	866.0	0.211	2.71×10^3
42.81	3/16	562.0	0.205	4.06×10^3
42.81	1/4	415.0	0.202	5.42×10^3
42.81	3/8	263.0	0.192	8.13×10^3
42.81	1/2	206.0	0.200	1.08×10^4
42.81	3/4	130.0	0.190	1.63×10^4

TABLE D.2

SUMMARY OF AVERAGE STROUHAL NUMBERS

Rod Diameter (in.)	Strouhal Number (average)	Reynolds Number (minimum)	Reynolds Number (maximum)
3/32	0.210	1.05×10^3	2.03×10^3
1/8	0.209	1.41×10^3	2.71×10^3
3/16	0.206	2.11×10^3	4.06×10^3
1/4	0.205	2.81×10^3	5.42×10^3
3/8	0.192	4.22×10^3	8.13×10^3
1/2	0.197	5.63×10^3	1.08×10^4
3/4	0.187	8.44×10^3	1.63×10^4

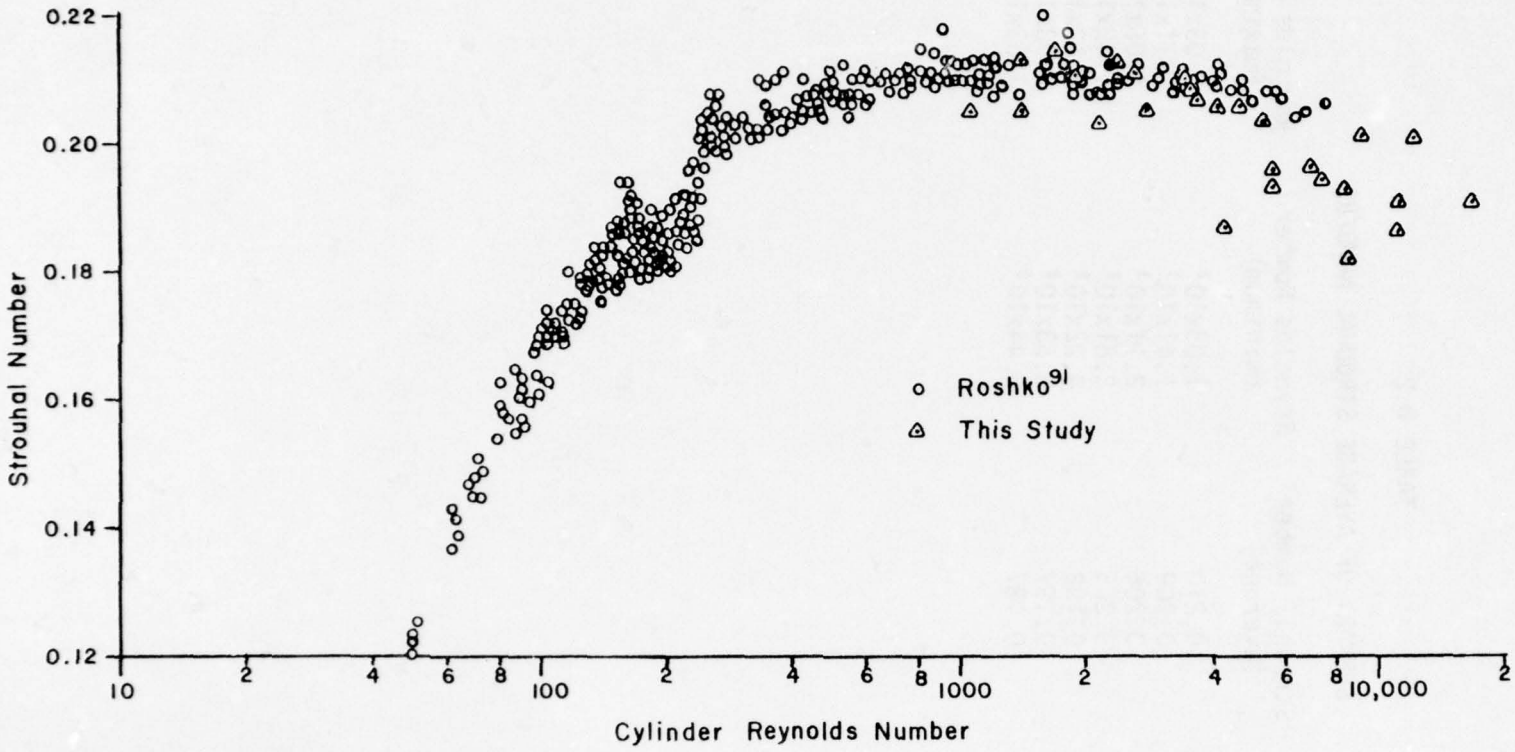

Figure D.3 Comparison of Circular Cylinder Strouhal Numbers with Data from Roshko

The results of the frequency study are given in Tables D.1 and D.2 The Reynolds number range encountered is equivalent to the situation described for Fig. D.1e, where vortex streets exist at frequencies governed by the Strouhal number, but decay much more rapidly than they would for lower Reynolds numbers. The Strouhal numbers encountered are consistent with results of other studies. For some reason, the Strouhal number tends to decrease with an increase in cylinder size, contrary to most other experimental studies and Eqs. D.1 through D.4. The reason for this decrease is not clear. However, experimental data points given by Roshko[91] (Fig. D.3) can be interpreted as showing a slight decrease in Strouhal number ($10^3 < Re < 10^4$) with increasing Reynolds number, although the decrease is less than given in Table D.2, and most authors interpret the value as constant in this region. The possibility of tunnel wall effects was also considered, but Okamoto and Takeuchi[96] showed little change in Strouhal number with changes in d/H and suggested that tunnel wall effects could be ignored for $d/H < 0.04$. In the cases represented by Tables D.1 and D.2, tunnel wall effects could thus be ignored for cylinders less than 1.2 in. in diameter which includes all cylinders studied.

As a result of the initial boundary layer studies and the data of Table 4.2, Table 4.3 and Tables D.1 and D.2, it is possible to make some guesses as to which cylinders should have the greatest effect on the coundary layer transition region. Brown,[32] for instance, has found that a disturbance frequency ranging from 0.8 to 1.2 times the Tollmien-Schlichting wave frequency will have considerable effect on the transition region location and properties. In addition, sound having a frequency close close to the approximate frequency of occurrence of the laminar periods between Tollmien-Schlichting wave groups has been shown to stabilize the occurrence of those periods, while sound of the Tollmien-Schlichting wave frequency may eliminate the laminar periods and stabilize the frequency of the Tollmien-Schlichting waves. The lowest measured Tollmien-Schlichting wave frequency at a test section inlet velocity of 22.2 fps was about 563 Hz. On the basis of Brown's results, only the 3/32 in. and possibly the 1/8 in. cylinders would be expected to affect the transition region location. The laminar periods occurred at a frequency of about 20 to 50 Hz at the same inlet velocity and would likely be stabilized only by cylinders larger than the 3/4 in. cylinder tested. At an inlet velocity of 42.8 fps, only the 3/32 in. cylinder would be expected to influence the Tollmien-Schlichting waves and a cylinder of approximately 1-1/2 in. would probably be necessary to influence the occurrence of the laminar periods.

In order to see the effect of the cylinders on boundary layer smoke flow visualization, a brief study was attempted. Figure D.4 shows the magnitude of the trailing edge vortices developing behind the 1/2 in. diameter cylinder when the cylinder is aligned so the wake impinges on the airfoil stagnation point. As can be seen along the airfoil surface in Fig. D.4, the smoke becomes rather diffuse, making clear boundary layer visualization difficult at best. Test photographs of the airfoil boundary layer with the cylinder in this position yielded little useful information. For this reason, smoke visualization may only be possible when the cylinder is offset with respect to the stagnation point, as was done in the experiments by Brown.[32]

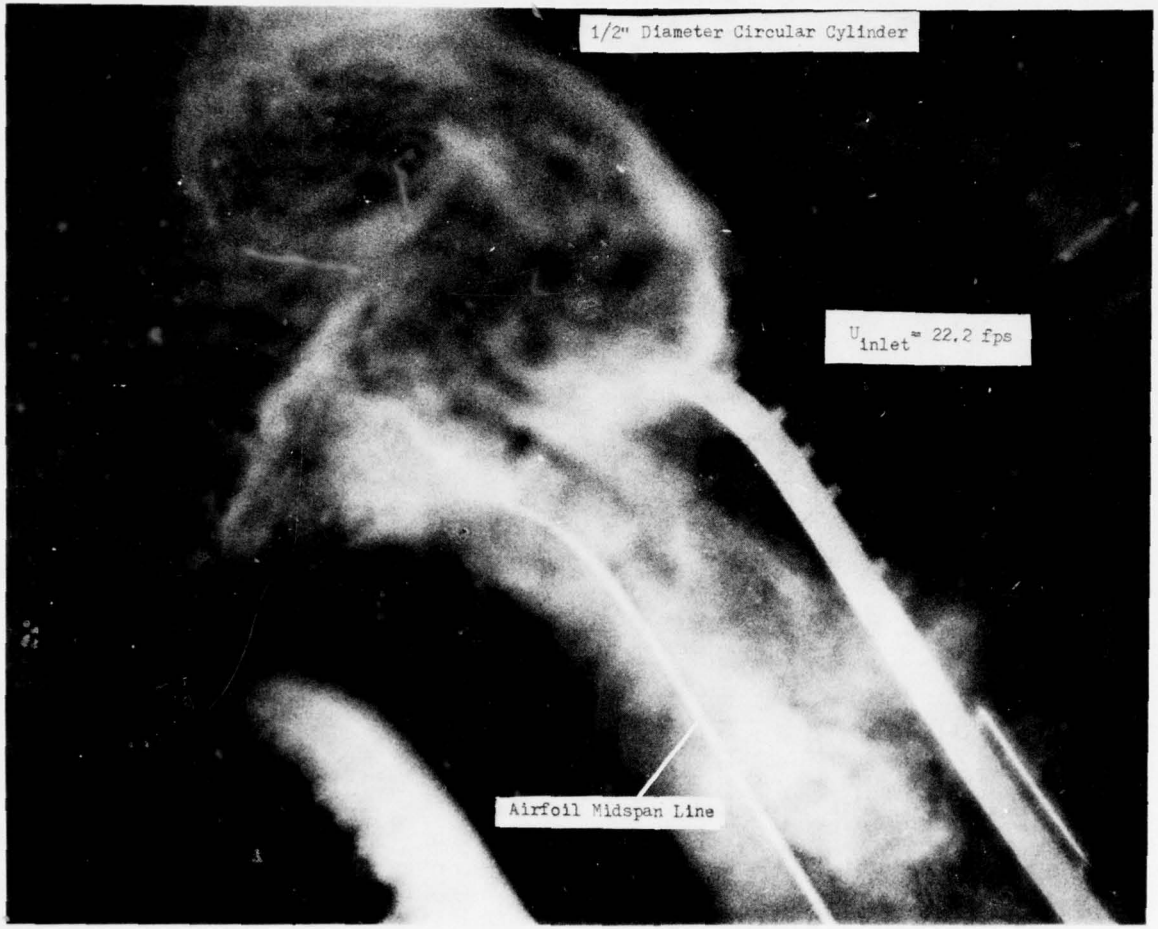

Figure 4.D Smoke in Wake of Upstream Circular Cylinder

REFERENCES

1. Adams, H. T., Elements of Internal Combustion Turbine Theory, Cambridge University Press (1949).

2. Kobayashi, H., H. Tanaka, and H. Maruta, "Effect of Interference Between Moving Blade Rows on Cascade Flutter," Bulletin of the JSME, 18: 116 (February, 1975), 149-150.

3. Ludwig, G. A., "General Electric Gas Turbine Design Philosophy," General Electric Company, GER-2483B (1973).

4. Sawyer, John W., Sawyer's Gas Turbine Engineering Handbook, Gas Turbine Publications, Inc., Stanford, Connecticut, 2nd Ed., Vols. I, II, & III (1972).

5. Cumsty, Richard, "Boundary Layer Development on Turbine Blades in the Presence of Görtler Vorticity," Gas Turbine Laboratory, Cambridge University, Cambridge, England.

6. Walker, L. A., and E. Markland, "Heat Transfer to Turbine Blading in the Presence of Secondary Flow," Int. J. Heat Mass Transfer, 8 (1965), 729-748.

7. Walker, L. A., and E. Markland, "Calculation of Heat Transfer to Turbine Blading in the Presence of Secondary Flow," Int. J. Heat Mass Transfer, 10 (1967), 499-518.

8. Brown, A., and B. W. Martin, "A Review of the Bases of Predicting Heat Transfer to Gas Turbine Rotor Blades," ASME Conference Paper No. 74-GT-27 (1974).

9. Cox, W. R., and L. S. Han, "Gas Turbine Transpiration Cooling Research, Part III: Prediction of Transition Region Location and Extent for the Effects of Surface Curvature, Free-Stream Turbulence, Pressure Gradients, Wall Temperature, and Unit Reynolds Number," U. S. Air Force Aero Propulsion Laboratory, Technical Report AFAPL-TR-76-2, Part III (September 1975).

10. Seyb, N. J., "The Role of Boundary Layers in Axial Flow Turbomachines and the Prediction of Their Effects," AGARDograph No. 164 (1972), 241-260.

11. Evans, R. L., "Turbulence and Unsteadiness Measurements Downstream of a Moving Blade Row," ASME Conference Paper No. 74-GT-73 (1974).

12. Raj, R., and B. Lakshminarayana, "Three-Dimensional Characteristics of Turbulent Wakes Behind Rotors of Axial Flow Turbomachinery," ASME Conference Paper No. 75-GT-1 (1975).

13. Whitfield, C. E., J. C. Kelly, and B. Barry, "A Three-Dimensional Analysis of Rotor Wakes," Aeronautical Quarterly, 23 (1972), 285-300.

14. Kerrebrock, J. L., and A. A. Mikolajczak, "Intra-Stator Transport of Rotor Wakes and Its Effect on Compressor Performance," Journal of Engineering for Power, Trans. ASME, 92 (1970), 359-368.

15. Cox, W. R., and L. S. Han, "Gas Turbine Transpiration Cooling Research, Part I: An Experimental Study of Turbine Airfoil Wakes as Influenced by Upstream Nozzle Vanes," U. S. Air Force Aero Propulsion Laboratory, Technical Report AFAPL-TR-76-2, Part I (November, 1975).

16. Kiock, R., "Influence of the Degree of Turbulence on the Aerodynamic Coefficients of Cascades," AGARDograph No. 164 (1972), 73-88.

17. Schlichting, H., Boundary Layer Theory, McGraw-Hill Book Company, 6th Ed. (1968).

18. Schlichting, H., "A Background of the Problems of Boundary Layer Research," AGARD Report 253 (April, 1960).

19. Stuart, J. T., "On the Nonlinear Mechanics of Hydrodynamic Stability," J. Fluid Mech., 4 pt 1 (1958), 1-21.

20. Kistler, E. L., "Boundary Layer Transition: A Review of Theory, Experiment and Related Phenomena," NASA CR-128540 (February, 1971).

21. Emmons, H. W., "The Laminar Turbulent Transition in a Boundary Layer -- Part I," J. Aeron. Sci., 18: 7 (1951), 490-498.

22. Brown, F. N. M., "Boundary Layer Transition," Naval Ordnance Report 17702 (May, 1963).

23. Brown, F. N. M., "Some Characteristics of the Periodic Vortical Elements Within the Transitioning Boundary Layer," Bureau of Naval Weapons Report (1960).

24. Knapp, C. F., "Analysis of Natural Boundary-Layer Transition," AIAA Student Journal, 4: 4 (1966), 147-152.

25. Knapp, C. F., and P. J. Roache, "Combined Visual and Hot-Wire Anemometer Investigation of Boundary-Layer Transition," AIAA Journal, 6: 1 (1968), 29-36.

26. Mitchner, M., "Propagation of Turbulence from an Instantaneous Point Disturbance," J. Aeron. Sci., 21 (1954), 350-351.

27. Schubauer, G. B., and P. S. Klebanoff, "Contributions to the Mechanics of Boundary Layer Transition," NACA TR 1289 (1956), also NACA TN 3489 (1955).

28. McCormick, M. E., "An Analysis of the Formation of Turbulent Patches in the Transition Boundary Layer," General Dynamics Corporation Electric Boat Division, Groton, Connecticut (April, 1967).

29. Schubauer, G. B., and H. K. Skramstad, "Laminar-Boundary-Layer Oscillations and Transition on a Flat Plate," NACA TR 909 (1948).

30. Hama, F. R., "Boundary Layer Transition Induced by a Vibrating Ribbon on a Flat Plate," Proceedings of the 1960 Heat Transfer and Fluid Mechanics Institute, Stanford University Press, California (1960), 92-105.

31. Klebanoff, P. S., K. D. Tidstrom, and L. M. Sargent, "The Three-Dimensional Nature of Boundary Layer Instability," J. Fluid Mech., 12 pt 1 (1962), 1-34.

32. Brown, F. N. M., "The Organized Boundary Layer," 6th Midwestern Conference on Fluid Mechanics, University of Texas (1959), 331-349.

33. Bergh, H., and B. Berg, "On the Visualization of Laminar Boundary Layer Oscillations and the Transition to Turbulent Flow," ZAMP, 9b: 7, 97-104.

34. Benney, D. J., and C. C. Lin, "On the Secondary Motion Induced by Oscillations in a Shear Flow," Physics of Fluids, 3: 4 (1960), 656-657.

35. Nelson, G., and A. D. D. Craik, "Growth of Streamwise Vorticity in Unstable Boundary Layers," Physics of Fluids, 20: 4 (1977), 698-700.

36. Antar, B. N., and F. G. Collins, "Numerical Calculation of Finite Amplitude Effects in Unstable Laminar Boundary Layers," Physics of Fluids, 18: 3 (1975), 289-297.

37. Bennett, H. W., "An Experimental Study of Boundary Layer Transition," Office of Naval Research, Contract Nonr-673(00) (September, 1953), Kimberly-Clark Corporation.

38. Squire, H. B., "On the Stability of Three-Dimensional Distribution of Viscous Fluid Between Parallel Walls," Proc. Roy. Soc. London, A142 (1933), 621-628.

39. Dunn, D. W., and C. C. Lin, "On the Stability of the Laminar Boundary Layer in a Compressible Fluid," J. Aeron. Sci., 22: 7 (1955), 455-477.

40. Aihara, Y., "Nonlinear Analysis of Görtler Vortices," Physics of Fluids, 19: 11 (1976), 1655-1660.

41. Wells, C. S., "Effects of Free-Stream Turbulence on Boundary Layer Transition," AIAA Journal, 5: 1 (1967), 172-174.

42. Spangler, J. G., and C. S. Wells, "Effects of Free-Stream Disturbances on Boundary Layer Transition," AIAA Journal, 6: 3 (1968), 543-545.

43. Collins, F. G., and J. Zelenevitz, "Influence of Sound Upon Separated Flow Over Wings," AIAA Journal, 13: 3 (1975), 408-410.

44. Brown, F. N. M., and V. P. Goddard, "The Effect of Sound on the Separated Laminar Boundary Layer," U. of Notre Dame Dept. of Aeronautical Engineering, NSF G 11712 (June, 1963).

45. Heckl, M. A., and F. J. Jackson, "Interaction of a Distributed Surface Vibration with an Adjacent Steady Fluid Flow," David Taylor Model Basin, Contract NONR 394400 (September, 1965).

46. Reshotko, E., "Stability Theory as a Guide to the Evaluation of Transition Data," SAMSO Boundary Layer Transition Study Group Meeting (August, 1967), 13-i - 13-22.

47. Criminale, W. O., Jr., "Interaction of the Laminar Boundary Layer with Free-Stream Turbulence," Phys. of Fluids Supplement (1967), S101-S107.

48. Wazzan, A. R., H. Taghavi, and Y. Y. Li, "Effect of Free-Stream Vorticity on Spatial Stability of Incompressible Boundary Layers with Nonparallel Effects," Phys. of Fluids, 19: 3 (1976), 362-365.

49. Jaffe, N. A., T. T. Okamura, and A. M. O. Smith, "The Determination of Spatial Amplification Factors and Their Application to Predicting Transition," AIAA Journal, 8: 2 (1970), 301-308.

50. Satyanarayana, B., "Unsteady Wake Measurements of Airfoils and Cascades," AIAA Journal, 15: 5 (1977), 613-618.

51. Yalamanchili, R. V. S., and A. J. Erickson, "Unsteady Turbulent Boundary Layers with Arbitrary Pressure Gradients," ASME Conference Paper No. 74-WA/HT-34 (1974).

52. Patel, V. C., and M. R. Head, "Reversion of Turbulent to Laminar Flow," J. Fluid Mech., 34 pt 2 (1968), 371-392.

53. Bradshaw, P., "A Note on Reverse Transition," J. Fluid Mech., 35 pt 2 (1969), 387-390.

54. Tani, I., "Boundary Layer Transition," Annual Review of Fluid Mechanics, 1 (1969), 169-196.

55. Van Driest, E. R., and C. B. Blumer, "Boundary Layer Transition: Free-Stream Turbulence and Pressure Gradient Effects," AIAA Journal, 1: 6 (1963), 1303-1306.

56. Dryden, H. L., "Airflow in the Boundary Layer Near a Plate," NACA TR 562 (1936).

57. Hall, A. A., and G. S. Hislop, "Experiments on the Transition of the Laminar Boundary Layer on a Flat Plate," ARC R&M 1843 (1938).

58. Taylor, G. I., "Statistical Theory of Turbulence. V. Effect of Turbulence on Boundary Layer, Theoretical Discussion of Relationship Between Scale of Turbulence and Critical Resistance of Spheres," Proc. Roy. Soc. London, A156 (1936), 307-317.

59. Falkner, B. M., and S. W. Skan, "Some Approximate Solutions of the Boundary Layer Equations," ARC R&M 1314 (1929).

60. Hall, D. J., and J. C. Gibbings, "Influence of Stream Turbulence and Pressure Gradient Upon Boundary Layer Transition," J. Mech. Eng. Sci., 14: 2 (1972), 134-146.

61. Dhawan, S., and R. Narasimha, "Some Properties of Boundary Layer Flow During the Transition from Laminar to Turbulent Motion," J. Fluid Mech., 3 (1958), 418-436.

62. Preston, J. H., "The Minimum Reynolds Number for a Turbulent Boundary Layer and the Selection of a Transition Device," J. Fluid Mech., 3 pt 4 (1958), 373-384.

63. Pretsch, J., "Die Stabilitat einer Ebenen Laminarstromang bei, Druckgefalle und Druckansteig," Jb. d. dt. Laftfahrtfarschung, 1 (1941), 58.

64. Dunham, J., "Predictions of Boundary Layer Transition on Turbomachinery Blades," AGARDograph No. 164 (1972), 55-71.

65. Batchelor, G. K., The Theory of Homogeneous Turbulence, Cambridge University Press (1953).

66. Liepmann, H. W., "Investigation of Boundary Layer Transition on Concave Walls," NACA Wartime Report W-87 (ARC No. 4J28), (February, 1945).

67. Smith, A. M. O., and N. Gamberoni, "Transition, Pressure Gradient and Stability Theory," Douglas Aircraft Co., Report No. ES 26388 (August, 1956).

68. Van Ingen, J. L., "A Suggested Semi-Empirical Method for the Calculation of the Boundary Layer Transition Region," Report Nos. V.T.H. 71, V.T.H. 74 (in English), Delft, Holland (1956).

69. McDonald, H., and P. W. Fish, "Practical Calculations of Transitional Boundary Layers," Intern. J. Heat Mass Transfer, 16 (1973), 1729-1744, also AGARDograph No. 164 (1972), 29-54.

70. Burggraf, O. R., "Comparative Study of Turbulence Models for Boundary Layers and Wakes," USAF Aerospace Research Laboratories Report ARL TR 74-0031 (1974).

71. Chuang, T., and H. Velkoff, "Analytical Studies of the Effects of Ionization on Fluid Flows," The Ohio State University Research Foundation, Technical Report No. 6 (June, 1967).

72. Görtler, H., "On the Three-Dimensional Instability of Laminar Boundary Layers on Concave Walls," NACA TM 1375 (1954), (Translation of: "über eine dreidimensionale Instabilitat laminarer Greneschichten an konkaven Wänden," Ges. D. Wiss. Gottingen, Nachr. a. d. Math., Bd. 2, Nr. 1, 1940).

73. Clauser, M., and F. Clauser, "The Effect of Curvature on the Transition from Laminar to Turbulent Boundary Layer," NACA TN 613 (1937).

74. Hammerlin, G., "Über das Eigenwertproblem der dreidimensionalen Instabilität laminarer Grenzschichten an konkaven Wander." Diss. Freiburg (1954), J. Rat. Mech. Anal., 4, 279-321, see also: ZAMM, 35 (1955), 366-367.

75. Smith, A. M. O., "On the Growth of Taylor-Görtler Vortices Along Highly Concave Walls," Quart. Appl. Math., 13 (1955), 233-262.

76. Liepmann, H. W., "Investigations on Laminar Boundary-Layer Stability and Transition on Curved Boundaries," NACA Wartime Report W-107 (ACR No. 3H30), (August, 1943).

77. Richards, E. J., W. S. Walker, and J. R. Greening, "Tests of a Griffith Aerofoil in the 13 ft. x 9 ft. Wind Tunnel," ARC R&M 2148 (March, 1944).

78. Tillman, W., "Development of Turbulence During the Build-Up of a Boundary Layer at a Concave Wall," Phys. Fluids Supplement (1967), s108 - s111.

79. Tani, I., and Y. Aihara, "Görtler Vortices and Boundary-Layer Transition," ZAMP (Zeitschrift für Angewandte Mathematik und Physik), 22 (1971), 130-143.

80. Tani, I., and H. Komoda, "Boundary-Layer Transition in the Presence of Streamwise Vortices," J. Aeros. Sci., 29 (1962), 440-444.

81. Wortmann, F. X., "Visualization of Transition," J. Fluid Mech., 38 pt 3 (1969), 473-480.

82. Bippes, H., and H. Görtler, "Dreidimensionale Störungen in der Grenzschicht an einer konkaven Wand," Acta Mechanica, 14 (1972), 251-267.

83. McCormack, P. D., H. Welker, and M. Kelleher, "Taylor-Görtler Vortices and Their Effect on Heat Transfer," Journal of Heat Transfer, ASME, 92: 1 (1970), 101-112.

84. Tobak, M., "On Local Görtler Instability," ZAMP (Zeitschrift für Angewandte Mathematik und Physik), 22 (1971), 130-143.

85. Kobayashi, R., "Taylor-Görtler Instability of a Boundary Layer with Suction or Blowing," AIAA Journal, 12: 3 (1974), 394-395.

86. Morkovin, M. V., "Flow Around Circular Cylinder--A Kaleidoscope of Challenging Fluid Phenomena," Symposium on Fully Separated Flows, ASME, New York (1964), 102-118.

87. Lamb, J., Hydrodynamics, 6th Ed., Dover Publications, Inc., New York (1945).

88. Tritton, D. J., "A Note on Vortex Streets Behind Circular Cylinders at Low Reynolds Numbers," J. Fluid Mech., 45 pt 1 (1971), 203-208.

89. Wille, R., "On Unsteady Flows and Transient Motions," Progress in Aeronautical Sciences, Vol. 7, edited by D. Küchemann, Pergamon Press (1966).

90. Gastor, M., "Vortex Shedding from Circular Cylinders at Low Reynolds Numbers," J. Fluid Mech., 46 pt 4 (1971), 749-756.

91. Roshko, A., "On the Development of Turbulent Wakes from Vortex Streets," NACA TR 1191 (1954), also see NACA TN 3169 (1954).

92. Goldstein, S., Modern Developments in Fluid Dynamics, Vol. II, Dover Publications (1965), (Reprint of 1938 publication).

93. Bearman, P. W., "On Vortex Shedding from a Circular Cylinder in the Critical Reynolds Number Regime," J. Fluid Mech., 37 pt 3 (1969), 577-585.

94. Mair, W. A., and D. J. Maull, "Bluff Bodies and Vortex Shedding--A Report on Euromech 17," J. Fluid Mech., 45 pt 2 (1971), 209-224.

95. Domm, U., "The Stability of Vortex Streets with Consideration of the Spread of Vorticity of the Individual Vortices," J. Aeron. Sci., 22: 11 (November, 1955), 750-754.

96. Okamoto, T., and M. Takeuchi, "Effect of Side Walls of Wind-Tunnel on Flow Around Two-Dimensional Circular Cylinder and Its Wake," Bulletin of the JSME, 18: 123 (1975), 1011-1017.

97. Hooker, S. G., "On the Action of Viscosity in Increasing the Spacing Ratio of Vortex Streets," Proc. Roy. Soc. London, A154 (1936).

98. Silverstein, A., S. Katzoff, and W. K. Bullivant, "Downwash and Wake Behind Plain and Flapped Airfoils," NACA TR 651 (1939).

99. Dean, R. C., Jr., "On the Necessity of Unsteady Flow in Fluid Machines," Journal of Basic Engineering, Trans. ASME (March, 1959), 24-28.

100. Kemp, N. H., and W. R. Sears, "The Unsteady Forces Due to Viscous Wakes in Turbomachines," J. Aeron. Sci., (July, 1965), 478-483.

101. Fleeter, S., "Fluctuating Forces Appropriate for the Calculation of Discrete Frequency Noise Generation in Subsonic Turbomachines," J. Acoustical Society of America, 55: 1 (1974), 98-101.

102. Hanson, D. B., "Spectrum of Rotor Noise Caused by Inlet Buide Vane Wakes," J. Acoustical Society of America, 55: 6 (1974), 1247-1251.

103. Gostelow, J. P., "Trailing Edge Flows Over Turbomachine Blades and the Kutta-Joukowsky Condition," ASME Conference Paper No. 75-GT-94 (1975).

104. Diller, K. R., "Design and Calibration of a Low-Speed Wind Tunnel," M. Sc. Thesis, The Ohio State University (1966).

105. Dryden, H. L., and G. B. Schubauer, "The Use of Damping Screens for the Reduction of Wind Tunnel Turbulence," J. Aeron. Sci., 14 (1947), 221-228.

106. Morel, T., "Comprehensive Design of Axisymmetric Wind Tunnel Contractions," ASME Conference Paper No. 75-FE-17 (1975).

107. Morel, T., "Design of Two-Dimensional Wind Tunnel Contractions," Journal of Fluids Engineering, 99: 2 (1977), 371-378, also ASME Conference Paper No. 76-WA/FE-4 (1976).

108. Loehrke, R. I., and H. M. Nagib, "Control of Free-Stream Turbulence by Means of Honeycombs: A Balance Between Suppression and Generation," ASME Conference Paper No. 76-FE-2 (1975).

109. Cox, W. R., "An Experimental Study of Turbine Blade Wake Effects," M. Sc. Thesis, The Ohio State University (1973).

110. Cole, R. J., "An Experimental Study of the Wake Characteristics of a Turbine Blade Cascade," M. Sc. Thesis, The Ohio State University (1974).

111. Stuart, M. C., C. F. Warner, and W. C. Roberts, "Effect of Vanes in Reducing Loss in Elbows in 7-inch Square Ventilating Duct," ASHVE Transactions, 48 (1942), 409-424.

112. Kline, S. J., "On the Nature of Stall," Journal of Basic Engineering, ASME Transactions Series D, 81: 3 (1959), 305-320.

113. Kline, S. J., D. E. Abbott, and R. W. Fox, "Optimum Design of Straight-Walled Diffusers," Journal of Basic Engineering, ASME Transactions Series D, 81: 3 (1959), 321-331.

114. Lander, R. D., "Evaluation of the Effect of Free-Stream Turbulence on the Heat Transfer to Turbine Airfoils," United Aircraft Corp., P & W, Tech. Report AFAPL-TR-69-70, U. S. Air Force (1969).

115. Bradshaw, P., An Introduction to Turbulence and Its Measurement, Pergamon Press (1971).

116. Hopkins, J. P., "An Investigation of Wind Tunnel Turbulence," M. Sc. Thesis, University of Notre Dame (1962).

117. Hansen, A. G., H. Z. Herzig, and G. R. Costello, "A Visualization Study of Secondary Flows in Cascades," NACA TR 1163 (1954), also NACA TN 2947 (1953).

118. Yu, J. P., E. M. Sparrow, and E. R. G. Eckert, "A Smoke Generator for Use in Fluid Flow Visualization," Int. J. Heat Mass Transfer, 15: 3 (1972), 557-558.

119. Brown, F. N. M., "An American Method of Photographing Flow Patterns," Aircraft Engineering, 24: 280 (1952), 164-169.

120. Bryant, L. W., and D. H. Williams, "Discontinuous Flow Around the Edge of a Bluff Obstacle," ARC R&M 962 (1925).

121. Shapiro, A. H., Shape and Flow: The Fluid Dynamics of Drag, Doubleday & Company, Inc. (1961), 122-128 & 151-153.

122. Clark, K. W., "Methods of Visualizing Air Flow with Observations on Several Aerofoils in the Wind Tunnel," ARC R&M 1552 (1933).

123. Taylor, M. K., "A Balsa-Dust Technique for Airflow Visualization and its Application to Flow Through Model Helicopter Rotors in Static Thrust," NACA TN 2220 (1950).

124. Daugherty, J. W., "Study of the Electrostatic Field and Charge Distribution in a Vortex Seeded with Dust," Ph.D. Dissertation, The Ohio State University (1972).

125. Parker, A. G., and J. C. Brusse, "New Smoke Generator for Flow Visualization in Low Speed Wind Tunnels," J. Aircraft, 13: 1 (January, 1976), 57-58.

126. Brown, F. N. M., "A Photographic Technique for the Mensuration and Evaluation of Aerodynamic Patterns," Photographic Engineering, 4: 3, 146-156.

127. Kreith, F., Principles of Heat Transfer, 2nd Ed., International Textbook Company (1965).

128. Gongwer, C. A., "A Study of Vanes Singing in Water," Journal of Applied Mechanics, 19: 4 (1952), 432-438.

129. Heskestad, G., and D. R. Olberts, "Influence of Trailing-Edge Geometry on Hydraulic-Turbine-Blade Vibration Resulting from Vortex Excitation," ASME Conference Paper No. 59-Hyd-7 (1959).

130. Steurer, J. W., "The Instability of the Laminar Boundary Layer and the Mechanisms of Transition on an Ogive Nose Cylinder," M. Sc. Thesis, University of Notre Dame (1960).

131. Thwaites, B. J., "The Approximate Calculation of the Laminar Boundary Layer," Aeronautical Quarterly, I (1949), 245-280.

132. Turner, A. B., "Local Heat Transfer Measurements on a Gas Turbine Blade," J. Mech. Eng. Sci., 13: 1 (1971), 1-12.

133. Andrews, S. J., and N. W. Schofield, "An Experimental Investigation of a Thick-Aerofoil Nozzle Cascade," ARC R&M 2883 (1950).

134. Colladay, R. S., and L. M. Russell, "Flow Visualization of Discrete Hole Film Cooling for Gas Turbine Applications," ASME Conference Paper 75WA/HT-12 (July, 1975).

135. Hale, R. W., P. Tan, R. C. Stowell, and D. E. Ordway, "Development of an Integrated System for Flow Visualization in Air Using Neutrally-Buoyant Bubbles," Sage Action, Inc., Ithaca, New York, SAI-RR7107 (1971).

136. Parmakian, J., and R. S. Jacobson, "Measurement of Hydraulic-Turbine Vibration," Transactions of the ASME, 74: 5 (1952), 733-741.

137. Forest, A. E., "Engineering Predictions of Transitional Boundary Layers," AGARD Report CP-224 (1977), 22-1 - 22-19.

138. Bammert, K., and H. Sandstede, "Measurements Concerning the Influence of Surface Roughness and Profile Changes on the Performance of Gas Turbines," J. Eng. Power., (1972) 207-213.

139. Bammert, K., and H. Sandstede, "Influences of Manufacturing Tolerances and Surface Roughness of Blades on Performance of Turbines," J. Eng. Power, (1976) 29-36.

140. Smith, A.M.O., and D.W. Clutter, "The Smallest Height of Roughness Capable of Affecting Boundary-Layer Transition," J. Aerospace Sci., (1959) 229-245.

141. Klebanoff, P.S. and K.D. Tidstrom, "Mechanism by Which a Two-Dimensional Roughness Element Induces Boundary-Layer Transition," The Physics of Fluids, (1972) 1173-1188.

142. Schubauer, G.B., P.S. Klebanoff, and K.D. Tidstrom, "Measurements on the Effect of Two and Three-Dimensional Roughness Elements on Boundary Layer Transition," J. Aeron. Sci., (1955) 803-804.

143. Doenhoff, A.E., and E.A. Horton, "A low Speed Experimental Investigation of the Effect of a Sandpaper Type of Roughness on Boundary Layer Transition," NACA Technical Note, (1956), 3853.

144. Braslow, A.L., E.C. Knox, and E.A. Horton, "Effect of Distributed Three-Dimensional Roughness and Surface Cooling on Boundary Layer Transition and Lateral Spread of Turbulance at Supersonic Speeds, " NASA Technical Note D-53.

145. Tani- I., H. Komoda, Y. Komatsu, M. Iuchi: Aeron. Res. Inst. Tokyo University, Rep. 375 (1962)

146. Braslow, A.L.: NATO AGARD Rep. 254 (1960)

147. Paterson, J.B., Horton, E.A.: NASA Memo 2-8-59L (1959)

148. Gibbings, J.C., "On the Effect of a Narrow Band of Distributed Roughness Upon Boundary Layer Transition," J. Aerospace Sci., (1959) 843-844

149. Loftin, L.K., "Effects of Specific Types of Surface Roughness on Boundary Layer Transition," NACA ACR LSJ29a

150. Braslow, A.L., "Review of Factors Affecting Boundary Layer Transition," NASA Tech Note D-3384 (1966)

151. Guven, O., V.A. Patel, and C. Farell, "Surface Roughness Effects on the Mean Flow Past Circular Cylinders," Iowa Institute of Hydraulic Research Report No. 175, May 1975.

152. Guven, O., V.C. Patel, and C. Farell, "A Model for High-Reynolds-Numver Flow Past Rough-Walled Circular Cylinders," J. Fluids Eng., (1977) 486-493

153. Oka, S. and Z. Kostic, "Influence of Wall Proximity on Hot-Wire Velocity Measurements," DISA Information, No. 13 (May, 1972), 29-33.

154. Rhen, D.L., "An Investigation of the Effects of Surface Proximity and the Resulting Wire-to-Surface Heat Transfer on Hot-Wire Anemometer Data," AIAA Student Journal, Vol. 4, No. 1 (February, 1966), 24-29.

155. Kanevce, G. and S. Oka, "Correcting Hot-Wire Readings for Influence of Fluid Temperature Variations, "DISA Information, No. 15 (October, 1973), 21-24.

156. Wills, J.A.B., "The Correction of Hot-Wire Readings for Proximity to a Solid Boundary," J Fluid Mech, Vol. 11, Part 3 (1961), 388-396.

157. Horak, D., and H.R. Velkoff, "Direct Frequency Response of Hot-Wire and Hot-Wire and Hot-Film Anemometers," to be presented in the 1979 ASME Winter Annual Meeting.

158. Kovasznay, L.S.G., H. Komoda, and B.R. Vasudeva, Proc. 1962 Heat Transfer and Fluid Mech. Inst. 1-26 (Stanford University Press, Stanford, 1962).

*U.S.Government Printing Office: 1979 — 657-002/111


ILME